



Actinobacteria Isolation from Forest Soils and Determination of Biological Activities

Pervin Soyer¹ , Yağmur Tunalı^{1*} 

¹Anadolu University, Faculty of Pharmacy, Department of Pharmaceutical Microbiology, 26470, Eskişehir, Turkey.

Abstract: Actinobacteria bacterial group has one of the most populous population in microorganisms that extends very different and extensive habitats on earth especially the main character of the natural soil habitats. Since old times, bioactive metabolites of soil microorganisms have been studied and the results have provided that metabolites of these microorganisms have significant benefits to science, medicine, agriculture, and the pharmaceutical industry. In this study, isolation of Actinobacteria strains from forest soils, identification of morphological and molecular features, extraction of the bioactive metabolite of isolates and determination the antimicrobial, antibiofilm, and cytotoxic activities of bioactive extract were tested. The microbiological isolation methods for collected forest soil samples were used and after the determination of their morphological and molecular features, isolates were defined as *Brevibacterium spp.* that is a member of Actinobacteria. The antibiotic resistance of the isolates was determined by different methods and different concentrations of standard antibiotics. The chromium tolerance of isolates was also determined. The bioactive metabolites of isolates were produced in a modified medium and extracted. The antimicrobial, antibiofilm, cytotoxic activities of bioactive metabolites were determined against standard microorganisms and *Artemia salina* larvae were used as a test organism for cytotoxic tests. In the present study, results provided information about Actinobacteria that were isolated from forest soils. Isolates have antibiotic resistance and chromium tolerance abilities. Moreover, it has been shown that the Actinobacteria group is the largest bioactive metabolite producing group in terms of both antibacterial and antifungal activity and also contains a wide range of other compounds such as antibiofilm and cytotoxic compounds. The antimicrobial (MIC) concentrations of bioactive metabolites were detected 2500 µg/mL for standard bacteria cultures and 1250 µg/mL for yeasts. The antibiofilm (MBEC) value was determined at 1250 µg/mL. The 2500 µg/mL concentration of the extract was found to be the effective cytotoxic value. The results provide *Brevibacterium spp.* isolates have industrial and pharmaceutical potential and more detailed pharmaceutical researches are planned.

Keywords: Actinobacteria, *Brevibacterium*, antibacterial, antifungal

Submitted: December 09, 2019. **Accepted:** February 21, 2020.

Cite this: Soyer P, Tunalı Y. Actinobacteria Isolation from Forest Soils and Determination of Biological Activities. JOTCSA. 2020;7(2):327-34.

DOI: <https://doi.org/10.18596/jotcsa.657180>.

***Corresponding author.** E-mail: yagmurt@anadolu.edu.tr. Tel: 0532 554 6003.

INTRODUCTION

Soil is a highly complex, heterogeneous, and nutrient-limited environment consisting of an organic matrix with liquid and gaseous pores possessing the highest microbial diversity on the Earth (1). Molecular phylogenetic analyses reveal that the soil and rhizosphere can contain thousands of unique bacterial species per gram (2). The

phylum of Actinobacteria is well-known for its ability to produce a wealth of natural products with structural complexity and with diverse biological activities (3). Actinobacteria bacterial group has one of the most populous populations of microorganisms that extend very different and extensive habitats on earth. Actinobacteria and its members are the main characteristics of natural soil habitats. Especially, forest soils are eligible habitats for soil

microorganisms, it contains organic-inorganic materials, various organisms, and their wastes. Actinobacteria are *Gram*-positive, free-living, saprophytic bacteria, widely distributed in soil, water, and colonizing plants with a filamentous structure.

Bacteria produce a vast array of secondary metabolites, which have diverse and important ecological functions. It has become increasingly clear that secondary metabolite production often is triggered by intra- and inter-specific interactions between soil bacteria. Soil bacteria produce a large number of secondary metabolites that have many different physicochemical and biological properties (1). Bioactive metabolites of microorganisms especially soil microorganisms have studied for many years and the results have provided that metabolites of soil microorganisms have significant benefits to science, medicine, agriculture, and the pharmaceutical industry. Actinobacteria have also ability to synthesize antiviral (4), antibacterial, antifungal (5), antibiofilm, antitumoral (6), insecticidal (7), antioxidative (8), anti-inflammatory (9), anti-biofouling (10), immunosuppressive (11), anti-parasitic (7), plant-growth-promoting and herbicidal compounds (12), enzyme inhibitors (6) and industrially important enzymes. From the 22,500 biologically active compounds that have been obtained from microbes, 45% are produced by Actinobacteria, 38% by fungi, and 17% by unicellular bacteria (13).

The main focus of this study was to isolate, characterize and identification of Actinobacteria strains that were collected from forest soils in the Çanakkale-Gelibolu region in Turkey. The isolated Actinobacteria strain was grown in special media and extracted to obtain the bioactive metabolite in crude extract form. The collected crude extract was evaluated with its antibacterial, antifungal, antibiofilm, and cytotoxic features.

EXPERIMENTAL SECTION

Isolation and characterization

The soil samples were collected from 6 to 10 cm depth from forest regions in Çanakkale-Gelibolu, Turkey. For sampling, moist and fertile soils that are rich in organic matter were selected.

After collection, soil samples were serially diluted up to 10^{-5} and inoculated to special isolation modified media. The content of this medium was as follows: Dextrose (4 g/L), yeast extract (4 g/L), malt extract (10 g/L), CaCO₃ (calcium carbonate) (2 g/L) and agar (4 g/L). The cultures were incubated at 37 °C for 3-5 days (14). This culture-dependent isolation method was continued until the pure colonies shown on the agar surface typically resemble Actinobacteria. The morphological characterization of these colonies determined by using the *Gram* staining method.

Molecular identification

The selected pure cultures were identified by using their 16S rRNA (ribosomal RNA) sequence. After, DNA isolation PCR (Polymerase Chain Reaction) amplification methods were used. The 27F/1492R universal primers were used and 1450 base pairs of 16S rRNA were amplified by using PCR. Two primers 27F (5'-AGAGTTTGATCMTGGCTCAG-3') and 1492R (5'-TACGGYTACCTTGTTACGACTT-3') were used. Sequencing was performed by using the EURX Gene Matrix Bacterial Genomic DNA Purification Kit. The PCR protocol used was as follows: 95 °C for 5 minutes, 56 °C for 40 seconds, 72 °C for 60 seconds, 35 cycles of denaturation at 95 °C for 40 seconds, annealing at 56 °C for 40 seconds, and elongation at 72 °C for 45 seconds. Amplification was followed by a final extension at 72 °C for 5 minutes. After the PCR reaction was completed, 10 µL of the obtained PCR product was electrophoresed on a 1% 1× Tris-acetate-EDTA agarose gel containing ethidium bromide. PCR products were produced for bidirectional sequence analysis by mixing with their respective forward and reverse primers. The analyses were carried out in duplicate with the Sanger sequencing device and the Big Dye Terminator v 3.1 Cycle Sequencing Kit (Applied Biosystems). The 16S rRNA gene sequence was compared to a sequence in the public database using basic local alignment search tool (BLAST - Basic Local Alignment Search Tool) on the national center for biotechnology information (NCBI (National Center for Biotechnology Information)) website (www.ncbi.nlm.nih.gov). The homology of the 16S rRNA sequence of the isolate was analyzed by using BLAST software (15,16).

Determination of the antimicrobial resistance of isolates

Antibiotic resistance was determined by the disc diffusion method. The antibiotic resistance of Actinobacteria culture were determined both by disc diffusion and microbroth dilution methods against standard antibiotic discs; AmC-30 (amoxicillin+clavulanic Acid 30/10 µg), SAM-20 (ampicillin+sulbactam 10/10 µg), IPM-10 (imipenem 10 µg) B (bacitracin 0.004 µg), OFX-10 (ofloxacin 10 µg) and TEC-30 (teicoplanin 30 µg). 100 µL of Actinobacteria culture inoculated to MHA (Mueller Hinton Agar) and the standard antibiotic discs were put on the agar and incubated at 37°C, for 24 hours. After the incubation period, the inhibition zones around the discs were measured (17). The microbroth dilution method (minimum inhibitory concentration - MIC) was defined as the lowest concentrations necessary for the inhibition of growth. 6 different concentrations (156.25, 78.125, 39.062, 19.53, 9.75, and 4.87 µg/mL) of standard antibiotics chloramphenicol, amoxicillin and ampicillin were used. Overnight microorganism culture was adjusted to McFarland's 0.5 standard. 100 µL of each antibiotic concentrations and 100 µL of microorganism cultures were inoculated to the

well plates and incubated at 37°C, for 24 hours. After the incubation period, the wells were stained by 20 µL resazurin dye to observe the color difference between dead and living cells.

Screening of the chromium tolerance

Potassium chromate (K₂CrO₄) and chromium(III) chloride (CrCl₃) salts were used at 100, 75, 50, 25, and 12.5 mg/100 mL concentrations. The chromium powders were added to PYE (peptone, yeast extract) and MHA (Mueller Hinton Agar) at proper concentrations by using the agar dilution method (18). The 50 µL of Actinobacteria culture was inoculated to the medium and incubated at 37°C, 96 hours. Microbroth dilution method was also used at 25, 12.5, 6.25, 3.125, and 1.562 mg/100 mL concentrations. 100 µL of K₂CrO₄ and CrCl₃ was added to *Brevibacterium* sp. that adjusted to McFarland 0.5 and incubated at 37°C, for 24 hours. Following the incubation period, a 150 µL aliquot was taken from each concentration wells and inoculated to MHA and incubated at 37°C, 96 hours. After the incubation, colonies on the plate were counted.

Fermentation and extraction of bioactive metabolites from *Brevibacterium*

For the fermentation step, a submerged culture method was used. The pure *Brevibacterium spp.* isolate was grown in the modified medium containing; 4 g/L of glucose, 10 g/L of malt extract, 4 g/L of yeast extract, 1 g/L of K₂HPO₄ (potassium hydrogen phosphate), MgSO₄ (magnesium sulfate), NaCl (sodium chloride), 0.001 g/L of FeSO₄ (iron(II) sulfate) and 2 g/L of CaCO₃ (calcium carbonate). The prepared cultures were incubated 37°C, for 7 days. After the incubation period, organic solvent extraction was performed. The broth was filtered through a Whatman No.1 filter and cultures were extracted three times with equal volume of ethyl acetate (EtOAc) at a 1:1 ratio. Then the EtOAc solution was evaporated for dryness by using a rotary evaporator at 30°C, 80 rpm, under 187 mbar vacuum and the crude extract was collected (19).

Determination of minimum inhibitory concentration (MIC) of bioactive metabolite

5 different concentrations crude extract were applied to *Escherichia coli* ATCC 35218, *Staphylococcus aureus* ATCC 29213, *Klebsiella pneumoniae* ATCC 700603, *Bacillus subtilis* NRRL B478, *Staphylococcus epidermidis* ATCC 14990, *Streptococcus pyogenes* ATCC 13615, *Listeria monocytogenes* ATCC 19111 and *Candida albicans* ATCC 90028 species by using 96 well plate assay. *Brevibacterium* crude extract was weighed and dissolved in %5 DMSO. Proper concentrations were

2500, 1250, 625, 312, and 156 µg/mL. Overnight microorganism cultures were adjusted to McFarland 0.5 standard. 100 µL of each extract concentrations and 100 µL of each microorganism cultures were inoculated to the well plates and incubated at 37 °C, for 24 hours. %5 DMSO, ketoconazole for fungi and chloramphenicol for bacteria species were also used as a control with 100, 50, 25, 12.5, 6.25, 3.125, 1.562, 0.781, 0.390, and 0.195 µg/mL values. After incubation period wells were stained by 20 µL resazurin dye to observe the color difference between dead and living cells (20, 21).

Biofilm eradication assay of bioactive metabolite

Microbial biofilms are communities of microorganisms embedded in a self-producing matrix, forming on living and nonliving surfaces. The inhibition effect of crude extract on biofilm formation was evaluated in 96-well plates. Briefly, overnight *Staphylococcus aureus* ATCC 29213, *Staphylococcus epidermidis* ATCC 14990, *Candida albicans* ATCC 90028 cultures were adjusted to McFarland 0.5 standard. 200 µL of each bacteria were inoculated to the well plates and incubated at 37 °C, for 48 hours to form the biofilm at the bottom of the wells. After the incubation period, wells were gently washed twice with 100 µL of 0.9% NaCl (physiological saline). 100 µL of concentrations (1250, 625, 312, 156, and 78 µg/mL) of crude extract were added to each well and incubated at 37°C, 24 hours. After the incubation period, wells were stained by 20 µL resazurin dye. (22, 23, 24)

Brine shrimp lethality test of bioactive metabolite

A 24-h LC₅₀ (lethal concentration) bioassay was performed in a 96 well plate using nauplii of the Brine shrimp *Artemia salina* (25). Commercially sold *Artemia* mix was used. 18 g of the *Artemia* mix was poured to the 500 mL of distilled water and incubated 48-52 hours at 30 °C. After larvae had been seen, they were taken and counted. Brine shrimp lethality bioassay was determined with crude extract concentrations; 2500, 1250, 625, 312, and 156 µg/mL with 10 *Artemia salina* larvae in each concentration wells. After 24 hours incubation period, the alive larvae were counted.

RESULTS AND DISCUSSION

Isolation, characterization and molecular identification of Actinobacteria

In the present study, 25 Actinobacteria strains were isolated from collected soil samples. *The Gram* staining method was applied to all of these isolates. Some of them are shown in Figures below 1. a, b, c.

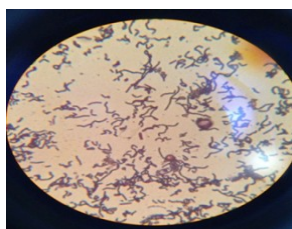


Figure 1.a



Figure 1.b

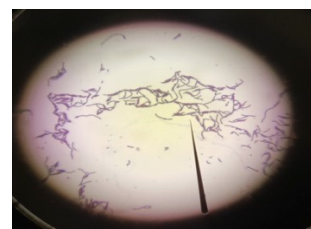


Figure 1.c.

Actinobacteria isolates after the Gram staining method.

The selected pure cultures were identified by using their 16S rRNA sequence. The results showed that most of them identified as *Brevibacterium spp.* BLAST analysis of the isolate showed that it is 100% similar to *Brevibacterium spp.* called *Brevibacterium frigoritolerans* (Accession Numbers: MN062932.1 and MN845150.1) which are the many *Brevibacterium* species available in the Gen Bank. *Brevibacterium* is one of the soil microbial communities that uncommon members of the Actinobacteria class. *Brevibacterium* is a member of the Actinobacteria phylum and genus of the Brevibacteriaceae family that is aerobic, non-sporulating, Gram-positive rod to coccoid shape and grows in a saline environment.

Determination of the antibiotic resistance of isolates

The antibiotic resistance of these isolates was determined by using standard antibiotic discs; AmC-30 (amoxicillin+clavulanic acid 30/10 µg), SAM-20 (ampicillin+sulbactam 10/10 µg), IPM-10 (imipenem 10 µg), B (bacitracin 0.004 µg), OFX-10 (ofloxacin 10 µg) and TEC-30 (teicoplanin 30 µg). It showed the most sensible reaction to IPM-10 (imipenem 10 µg). Also, the other values are shown in Table 1. Additionally, the MIC values are 78.125 µg/mL for chloramphenicol and 4.87 µg/mL for amoxicillin and ampicillin.

Table 1. Antibiotic resistance results from the disc diffusion method in terms of millimeters (mm).

Standard Antibiotic Discs	<i>Brevibacterium spp.</i> inhibition zone diameters (mm)
AmC-30	19
SAM-20	16
IPM-10	20
TEC-30	8
OFX-10	12
B-0.04	0

Screening of the chromium tolerance

While 150-160 colonies were counted in chromium(III) chloride (CrCl_3) plate at 50 mg/100 mL concentration, 25 mg/100mL concentration plate formed 200-300 colonies. In 50 mg/100 mL potassium chromate (K_2CrO_4) plate 50-100 colonies and in 25 mg/100 mL plate 100-150 colonies were counted. Additionally, at the results of microbroth dilution for chromium(III) chloride (CrCl_3) and potassium chromate (K_2CrO_4), there was no formation of colonies. The test will be repeated using different concentrations. Chromium is one of the poisonous polluting metal ions that is found in soils. Several studies have demonstrated

Brevibacterium spp. has chromium tolerance and chromium degradation abilities. Hence, chromium tolerance of isolates was tested by the agar dilution method. It showed significant tolerance to potassium chromate (K_2CrO_4) and chromium(III) chloride (CrCl_3) salts.

Determination of minimum inhibitory concentration (MIC) of bioactive metabolite

The MIC value of bioactive metabolite extract was tested at 2500, 1250, 625, 312, 156 µg/mL concentrations. The results are shown in Tables 2 and 3. The yeast species are more sensitive than bacteria species.

Table 2. MIC values of metabolite and chloramphenicol against bacteria species.

Microorganisms	MIC Values ($\mu\text{g/mL}$)	
	Bioactive Metabolites	Chloramphenicol
<i>Escherichia coli</i> ATCC 35218	2500	78.125
<i>Staphylococcus aureus</i> ATCC29213	2500	4.882
<i>Listeria monocytogenes</i> ATCC 19111	2500	9.765
<i>Klebsiella pneumonia</i> ATCC 700603	2500	19.531
<i>Bacillus subtilis</i> NRRL B478	2500	2.441
<i>Staphylococcus epidermidis</i> ATCC 14990	2500	9.765
<i>Streptococcus pyogenes</i> ATCC 13615	2500	39.0625

Table 3. MIC values of metabolites and ketoconazole against yeast species.

Microorganisms	MIC Values ($\mu\text{g/mL}$)	
	Bioactive Metabolites	Ketoconazole
<i>Candida albicans</i> ATCC 90028	1250	19.531
<i>Candida krusei</i> ATCC 6258	1250	39.0925

Several studies have demonstrated that secondary metabolites produced by soil bacteria can serve as weapons in microbial warfare, providing an advantage to producer strains when competing against other microbial competitors in the same ecological niche (26).

Biofilm eradication assay of bioactive metabolite

Antibiofilm studies demonstrated a dose-dependent activity. The antibiofilm activity of bioactive metabolite extract was examined by minimum biofilm eradication concentration (MBEC) assay. The antibiofilm value of bioactive metabolite extract was determined 1250 $\mu\text{g/mL}$ for *Staphylococcus aureus*, 1250 $\mu\text{g/mL}$ for *Staphylococcus epidermidis* and

1250 $\mu\text{g/mL}$ for *Candida albicans*. It means, the extract showed the same efficiency to selected microorganisms and eradicate their biofilm structure at the same dose. 1250 $\mu\text{g/mL}$ of bioactive metabolite extract is a proper concentration for eradicating the biofilm formation of tested microorganisms.

Brine shrimp lethality test of bioactive metabolite

The brine shrimp lethality test was determined at 2500, 1250, 625, 312, and 156 $\mu\text{g/mL}$ concentrations. The lethality values of *Artemia salina* larvae are shown in Table 4. 2500 and 1250 $\mu\text{g/mL}$ concentrations are the most effective doses on larvae. The larvae are counted out of 10 larvae.

Table 4. Results of the Brine shrimp lethality test.

Bioactive Concentrations ($\mu\text{g/mL}$)	Metabolite Amount of <i>Artemia salina</i> Larvae (out of 10)	Percentage (%) Effect of Bioactive Metabolite
2500	0	100%
1250	2	80%
625	3 \pm 1	60-70%
312	3 \pm 1	60-70%
156	4 \pm 1	50-60%

The cytotoxic efficacy of the bioactive metabolite extract is significantly observed at different concentrations. It can be used as an anticancer drug in cell culture studies. The studies will be continued to understand all of the efficacy mechanisms with different tests.

CONCLUSION

The search for novel microorganism species from soils has gained momentum in recent years. Nature acts as a prominent reservoir for isolating the microorganisms that have various biological activities. The results from in vitro experiments, a *Brevibacterium spp.* called *Brevibacterium frigoritolerans* was isolated. In this study, many biological activities of this isolate have been tested and proved. The isolated novel bacterial strain was

characterized by morphological, molecular, antimicrobial resistance, and chromium tolerance features and activities. For the determination of *Brevibacterium spp.* isolates antibiotic resistance, AmC-30 (amoxicillin+clavulanic acid 30/10 μg), SAM-20 (ampicillin+sulbactam 10/10 μg), IPM-10 (imipenem 10 μg), B (bacitracin 0.004 μg), OFX-10 (ofloxacin 10 μg) and TEC-30 (teicoplanin 30 μg) standard antibiotic discs were used. IPM-10 (imipenem 10 μg) was the most effective and B (bacitracin 0.004 μg) is not effective at all. Chromium is a heavy metal and causes environmental pollution. It accumulates in soil and is a very carcinogenic substance. For this reason, the chromium tolerance of *Brevibacterium spp.* isolates were determined. Das and Mishra showed that *Brevibacterium spp.* tolerates to potassium chromate (K_2CrO_4) (27). This research proved that

Brevibacterium spp. isolates tolerate both potassium chromate (K_2CrO_4) and chromium(III) chloride ($CrCl_3$) salts. The crude extract was checked for antibacterial, antibiofilm, and cytotoxic activities to identify the mechanisms of bioactive metabolite. *Brevibacterium spp.* showed different bioactive features, which highlighted its importance as potential pharmacological agents. Hence, there could be a probability of a new bioactive compound in the crude extract, which might provide a basis for further development of novel compounds from *Brevibacterium spp.* In Oskay's research, bioactive metabolites of Actinobacteria showed antimicrobial activities against *Staphylococcus aureus*, *Escherichia coli* and *Candida albicans* microorganisms (28). In the present study, bioactive metabolites of *Brevibacterium spp.* isolates that member of Actinobacteria showed antimicrobial activity against *Staphylococcus aureus* ATCC29213, *Escherichia coli* ATCC 35218, *Klebsiella pneumonia* ATCC 700603, *Bacillus subtilis* NRRL B478, *Staphylococcus epidermidis* ATCC 14990, *Streptococcus pyogenes* ATCC 13615 *Listeria monocytogenes* ATCC 19111, *Candida albicans* ATCC 90028, *Candida krusei* ATCC 6258 and antibiofilm activity against *Staphylococcus aureus* ATCC29213, *Staphylococcus epidermidis* ATCC 14990, *Candida albicans* ATCC 90028 at different concentrations of the crude extract. It has been previously shown that bioactive metabolites of Actinobacteria at 0.1-10 $\mu\text{g/mL}$ concentrations showed a 100% cytotoxic activity on *Artemia salina* larvae (29). In the current study, 80-100% cytotoxic activities at 2500 and 1250 $\mu\text{g/mL}$ concentrations were determined. There are limited data in the literature about the activities of *Brevibacterium* bioactive metabolites. This research also provided new insight into the development of good candidates for pharmaceutical and bioactive natural products. The development of new drugs can be a candidate for curing several types of diseases (30). The current attempt of using *Brevibacterium* isolates and its bioactive metabolites will be favorable for antimicrobial, antitumoral, antibiofilm and cytotoxic activity tests.

REFERENCES

1. Tyc O, Song C, Dickschat JS, Vos M, Garbeva P. The Ecological Role of Volatile and Soluble Secondary Metabolites Produced by Soil Bacteria. *Trend Microb.* 2017;25(4):280-92.
2. Uroz S, Buée M, Murat C, Frey-Klett P, Martin F. Pyrosequencing reveals a contrasted bacterial diversity between oak rhizosphere and surrounding soil. *Environ Microbiol.* 2010; 2:281-8.
3. Adegboye MF, Babalola O. Taxonomy and ecology of antibiotic producing *Actinomycetes*. *Afr J Agric Res.* 2012; 15:2255-61.
4. Sacramento DR, Coelho RRR, Wigg MD, Linhares LFTL, Santos MGM, Semedo LTAS. Antimicrobial and antiviral activities of an actinomycete (*Streptomyces sp.*) isolated from a Brazilian tropical forest soil. *World J Microbiol Biotechnol.* 2004; 20:225-9.
5. Zarandi ME, Bonjar GHS, Dehkaei FP, Moosavi SAA, Farokhi PR, Aghighi S. Biological control of rice blast (*Magnaporthe oryzae*) by use of *Streptomyces sindeneusis* isolate 263 in greenhouse. *Am J Appl Sci.* 2009;6:194-9.
6. Hong K, Gao AH, Xie QY, Gao H, Zhuang L, Lin HP. *Actinomycetes* for marine drug discovery isolated from mangrove soils and plants in China. *Mar Drugs.* 2009;7: 24-44.
7. Pimentel-Elardo SM, Kozytskam S, Bugni TS, Ireland CM, Moll H, Hentschel U. Antiparasitic compounds from *Streptomyces sp.* strains isolated from Mediterranean sponges. *Mar Drug.* 2010;8: 373-80.
8. Janardhan A, Kumar AP, Viswanath B, Saigopal DVR, Narasimha G. Production of bioactive compounds by *Actinomycetes* and their antioxidant properties. *Biotechnol Res Int.* 2014; 217030:1-9.
9. Renner MK, Shen YC, Cheng XC, Jensen PR, Frankmoelle W, Kauffman CA. Cyclomarins A-C, new anti-inflammatory cyclic peptides produced by a marine bacterium (*Streptomyces sp.*). *J Am Chem Soc.* 1999; 121:11273-6.
10. Xu Y, He H, Schulz S, Liu X, Fusetani N, Xiong H. Potent antifouling compounds produced by marine *Streptomyces*. *Biores Technol.* 2010; 101:1331-6.
11. Mann J. Natural products as immune suppressive agents. *Nat Prod Rep.* 2001; 18:417-30.
12. Sousa CS, Soares ACF, Garrido MS. Characterization of *Streptomyces* with potential to promote plant growth and biocontrol. *Sci Agric.* 2008;65:50-5.
13. Berdy J. Bioactive microbial metabolites: a personal view. *J Antibiot.* 2005; 58:1-26.
14. Yen H, Hsiao H, Chen L. The enhancement of rapamycin production using *Streptomyces hygrosopicus* through a simple pH-shifted control. *J Tai Ins Chem Engineers.*2013;44:743-7.
15. Rintala HA, Nevalainen A, Rönkä MS. PCR primers targeting the 16S rRNA gene for the specific detection of *Streptomyces*. *Mol Cell Probes.* 2001;15: 337-47.

16. Singh V, Praveen F, Khan CKM, Tripathi, Phylogenetics of an antibiotic producing *Streptomyces* strain isolated from soil. *Bioinformation*. 2009;4: 53-8.
17. Clark CL, Jacobs MR, Appelbaum PC. Antipeumococcal Activities of Levofloxacin and Clarithromycin as Determined by Agar Dilution, Microdilution, ETest and Disk Diffusion Methodologies. *J Clinical Microb*.1998;36(12):3579-84.
18. Poornima K, Karthik L, Swadhini SP, Mythili S, Sathiavelu A. Degradation of Chromium by Using a Novel Strains of *Pseudomonas* Species. *J Microb Biochem Technol*. 2010;2: 95-9.
19. Zhao S, Huang D, Qi H, Wen J, Jia X. Comperative metabolic profiling-based improvement of rapamycin production by *Streptomyces hygroscopicus*. *Appl Microb Biotech*. 2013: 97;5329-41.
20. CLSI. Performance standards for antimicrobial susceptibility testing informational supplement M100-S19. 29th ed. 2009.
21. Anderws JM. Determination of minimum inhibitory concentrations. *J of Antimic Chemot*. 2001; 48:5-16.
22. Teanpaisan R, Kawsud P, Pahumunto N, Puripattanavong J. Screening for antibacterial and antibiofilm activity in Thai medicinal plant extracts against oral microorganisms. *J Trad Compl Med*. 2017;7(2):172-7.
23. Cruz CD, Shah S, Tammela P. Defining conditions for biofilm inhibition and eradication assays for *Gram*-positive clinical reference strains. *BMC Microbiol*. 2018;173:1-9.
24. Chaieb K, Kouidhi B, Jrah H, Mahdouani K, Bakhrouf A. Antibacterial activity of Thymoquinone, an active principle of *Nigella sativa* and its potency to prevent bacterial biofilm formation. *BMC Complemen Alter Med*. 2011;11: 29.
25. Meyer BN, Ferrigni NR, Putnam JE, Jacobsen LB, Nichols DE, Mclaughlin JL. Brine shrimp: a convenient general bioassay for active plant constituents. *J Med Pl Res*. 1982;45;31-4.
26. Foster KR, Bell T. Competition, not cooperation, dominates interactions among culturable microbial species. *Curr Biol*. 2012; 22:1845-50.
27. Das A, Mishra S. Hexavalent chromium reduction and 16S rDNA identification of bacteria isolated from a Cr (VI) contaminated site. *Int J Microb*. 2008;7;1.
28. Oskay M. A Research on Isolation, Taxonomy and Fermentation Studies of *Streptomyces* Strains with High Antimicrobial Activity from Northern Cyprus Soils [Master of Science Thesis]. [Manisa]; Celal Bayar University, Institute of Science; 2006.
29. Yavuz M. Isolation of Secondary Metabolites of Local *Streptomyces* Species, Illumination of Their Structures and Investigation of Their Biological Activities [Doctoral Thesis]. [Diyarbakır], Dicle University Institute of Science and Technology; 2010.
30. Padma BJ, Saraswathi K, Arumugam P, Shiny RA. Isolation, characterization and evaluation of antioxidant activities of secondary metabolites producing *Actinomycetes* of terrestrial origin. *Int J of Res in Med Sci*. 2018;6(3):1017-28.



Bioremediation Potential of Immobilized *Corynebacterium kutscheri* in the Treatment of Tannery Industry Effluent from Challawa Industrial Estate, Kano State, Nigeria

Abdullateef Baba^{1,*} , Shuaibu Tela Garba¹  Hauwa Suleman Bello² 

¹Department of Chemistry, Faculty of Science, University of Maiduguri, Borno State, Nigeria

²Department of Microbiology, Faculty of Science, University of Maiduguri, Borno State, Nigeria

Abstract: In the present study, bioremediation potentials of indigenous bacteria (*Corynebacterium kutscheri*) in the treatment of tannery effluent was investigated. Industrial tannery effluent samples from Mamuda Tannery Industries in Challawa Industrial estate, Kano State, Nigeria were collected for a period of six months (August 2017 to January 2018) for the experiment. Bacteria were isolated from the effluents using serial dilution, immobilized on agar-agar and biochemical tests were carried out to identify the bacteria. Different masses (5 g, 10 g, 15 g, 20 g, and 25 g) of the identified bacteria were used in the treatment of 250 mL of the effluents. Temperature, pH, Biochemical Oxygen Demand (BOD), Chemical Oxygen Demand (COD), Suspended Solid (SS), Total Dissolved Solids (TDS), sulfate, phosphate, nitrate, chloride, and some heavy metals (Cr, Fe, Mn, Ni, Pb, Zn, Cd, and Cu) were determined before and after treatment of the effluents with the bacteria. The pre-treatment analysis showed that the values, 29.50±4.68, and 5.35±1.57, were observed for temperature (°C) and the pH respectively. The levels (mg/L), 26.17±9.49; 3106±2753; 562±482; 444±507; 97.20±146.80; 268.34±411.01; 8.82±34.71 and 22.59±19.64 were observed for BOD, COD, SS, TDS, nitrate, sulfates, phosphate, and chlorides, respectively. The concentration (mg/L) of the heavy metals, before treatment (with the bacteria) were as; Cr (7.528±4.530); Fe (1.263±0.502); Ni (0.023 ± 0.021); Mn (0.277 ± 0.03); Pb (0.304 ± 0.20); Zn (0.058± 0.05); Cd (0.068±0.02) and Cu (0.012 ±0.02). The bacteria were identified to be *Corynebacterium kutscheri*. The post-treatment analysis showed that the COD (1376±248–2681±867 mg/L) has the highest value while Cu (ND –0.007±0.00 mg/L) has the lowest value. The post-treatment analysis using the different masses of the *Corynebacterium kutscheri* indicates that there is a great decrease in the levels of the physicochemical parameters and the heavy metals as well when compared with the levels observed at the pre-treatment analysis. The decrease could be attributed to, not only due to the increase in the exact mass of the bacteria but also to the multiplicity in the mass of the *Corynebacterium kutscheri* which subsequently increases the surface area for the remediation. The average high percentage reduction (70% to 100%) of these parameters and heavy metals implies that the *Corynebacterium kutscheri* has a higher potential for the treatment of effluents from the textile industries.

Keywords: Bioremediation, *Corynebacterium kutscheri*, effluent, immobilization, tannery.

Submitted: November 07, 2019. **Accepted:** February 27, 2020.

Cite this: Baba A, Garba S, Bello H. Bioremediation Potential of Immobilized *Corynebacterium kutscheri* in the Treatment of Tannery Industry Effluent from Challawa Industrial Estate, Kano State, Nigeria. JOTCSA. 2020;7(2):335–50.

DOI: <https://doi.org/10.18596/jotcsa.643771>.

***Corresponding author.** E-mail: babslega@gmail.com; abelega2007@yahoo.com

INTRODUCTION

With rapid industrialization, water pollution has become a major problem. The characteristics of

industrial effluent depend upon the type of industrial raw material and the output of the product (1). Industrial effluents account for several point sources of water pollution, while developed nations adopt

stringent water quality requirement to control river pollution from point and non-point sources, the situation is different in the most developing countries like Nigeria. Wastewater treatment in Nigeria is not given the necessary priority it deserves and therefore, industrial wastes are discharged into receiving water bodies without treatment. The consequences of this include among others, river pollution, loss of aquatic life, uptake of polluted water by plants, disease burden, and shorter life expectancy in developing countries (2).

Tannery industrial wastewater is a serious consequence of the pollution point of view for streams, freshwater, and land used for agriculture. The lack of awareness in the modern industrial practice has resulted in the discharge of tannery effluents which exhibit the very high value of Cr, Sulfide, and chloride, Total Dissolved Solid (TDS), Total Suspended Solid (TSS), Biochemical Oxygen Demand (BOD) and Chemical Oxygen Demand (COD) in the water stream or land (3). Tannery effluent refers to as wastewater from the process of converting skin and hides into leather. The process of tanning requires a large volume of water, which is used to either cleanse the hides and skins or as an interaction medium between the hides and skin. During the tanning process, a large volume of effluents is discharged into the surrounding soil as well as a water source. These effluents may contain a variety of chemicals such as sodium sulfate, chromium sulfate, and non-ionic wetting agents that are used in the tanning process and may accumulate in the immediate environment of the tannery(4). There are two types of tanning. The first is the vegetable tanning in which plant extracts are employed to produce heavy leather such as belts and soles of footwear. The second is the chrome tanning which involves the treatment of skins/hides with chromium salts obtained by reduction of sodium dichromate reducing agent produces lighter leathers such as gloves and upper part of shoes. During the tanning process, at least about 300 kg chemicals are added per tonne of hides (5). A tannery is one of the important industries causing water pollution (6). There are more than 6000 tanneries in Nigeria with an annual processing capacity of 700,000 tons of hides and skins (7)(8). It was reported that the total amount of waste produced per slaughtered animal is approximately 35% of its weight (9). Also, for every 1000 kg of carcass weight, a slaughtered beef produces 5.5 kg of manure (excluding rumen contents or stockyard manure) and 100 kg of paunch manure (undigested food)(10). wastewater in the range of 30-35 L kg⁻¹ skin/hide processed with variable pH, BOD, COD, high concentrations of suspended solids, and tannins including chromium (11). A single tannery can cause the pollution of groundwater around the radius of 7-8 kilometers (7).

Tannery effluent, when discharged into water bodies, alters the physical, chemical, and biological characteristics of water and depletes the dissolved oxygen, increases alkalinity, suspended solids, and sulfides which are deleterious to fish and other aquatic lives (12). Many conventional processes such as oxidation, chemical, and biological processes were carried out to treat wastewater from tanneries (6). Biological processes have received more attention because of their cost-effectiveness, lower sludge production and environmental friendliness in contrast to chemical/physical methods which are invariably cost-intensive and cannot be conveniently employed in all industries, especially in developing and underdeveloped countries (12). Microbes in the environment play an important role in cycling and destroying pollutants through bio-degradation (11). In the course of the last two decades, a wide variety of technologies had been developed for clean-up operations of contaminated sites. Bioremediation has evolved as the most promising one because of its economical safety and environmental features since organic contaminants become transferred and some of them are fully mineralized. Bioremediation of tannery effluents is an attractive environment-friendly, safe and cost-effective alternative technology to conventional methods. Microbes in the environment play an important role in cycling and destroying them through bio-degradation (3).

Bioremediation is an option that offers the possibility to destroy or render harmless various contaminants using natural biological activity. It is based on the idea that all organisms remove substances from the environment to carry out growth and metabolism. The principles of bioremediation are that the microbe feeds on contaminants, digest it, and this waste is transformed into water and harmless gases which are later expelled out of the microbes. The resultant metabolic wastes that they produce are generally safe and somehow recycled into other products. Although the microorganisms are present in contaminated water, they cannot necessarily be there in the numbers required for bioremediation of the site. Their growth and activity must be stimulated. Naturally occurring degrade the hazardous organic wastes including xenobiotic compounds, such as pesticides, polycyclic aromatic hydrocarbons (PAHs) and polychlorinated biphenyls (PCBs) in due course of time. However, metallic residues cannot be degraded in composting but may be converted into organic combinations that have less bioavailability than mineral combinations of the heavy metals. Microbial transformation of metals serves various function generally, it occurs either by redox conversions of inorganic forms or conversions from inorganic to organic forms and vice versa. Bioremediation is amenable to a variety of organic and inorganic compounds and may be applied either *in situ* or *ex-situ*. In addition to this, it is easy to

implement and maintain, does not require the use of expensive equipment or highly specialized personnel and is environmentally friendly and aesthetically pleasing to the public (13).

Immobilized bacteria can withstand various temperatures, pH and substrate concentrations; consequently increasing the efficiency and the lifespan of the bacteria. Immobilized bacteria are widely applied in the treatment of wastewater and can be separated and recovered after the treatment with the same efficiency.

This study was carried out in Kano. Kano lies on Latitude 11°30'N and 8°30'N and Longitude 11°5'N and 8°5'E and 8°5'E in Northern Nigeria. It is one of the developed industrial cities in Nigeria. Tannery and textile-related activities are the dominating industries and this could be one of the reasons for her high population density(14). The climate is characterized by well-defined wet and dry seasons. The wet season spreads from May to October, August usually being the wettest whereas the dry season lasts from November to April. River Challawa originates from the Challawa Gorge dam in Challawa village and stretches to River Kano that empties into Lake Chad. The river receives waste from tanneries and textile industries, urban water storm, and agricultural runoffs from farming communities along its course. River Challawa serves as fishing, farming, and water supplies for the communities in the area. The domestic water supply for Challawa, Sharada, and Bompai industrial areas and their surroundings originates from the Challawa River (14). Several workers have studied bioremediation of tannery effluent using microorganisms. However, limited literature is available on the bioremediation of tannery effluent using immobilized bacterial cells in the Challawa industrial estate. This research work focused on the potential of the immobilized bacteria in the treatment of industry tannery effluent in the Challawa industrial estate.

MATERIAL AND METHODS

Sample Collection

Effluents were collected from the Mamuda Tannery Industry in Challawa Industrial Estates, Kano, Nigeria. The effluents were collected for a period of six months (August 2017 to January 2018). It was collected from the effluent reservoir in the industries in sterile 4-liter plastic containers with a unique identification number and was preserved using an ice-box that was transported to Microbiology Laboratory, Department of Microbiology, the Bayero University of Kano for analysis.

Sample Preparation and Analysis

Immediately after the collection of the effluent, pH, SS, TDS, COD, BOD, nitrate, sulfates, phosphates, chlorides, and heavy metals (Cr, Fe, Mn, Ni, Pb, Zn, Cd, and Cu) concentrations were determined.

pH was determined using Ecotests pH meter and TDS was determined using AQUALYTIC TDS-Salinometer. BOD was determined as described by the standard method (7). COD, SS, nitrate, sulfates, phosphates, and chlorides were determined using DR/2010 HACH portable data logging spectrophotometer (8). The heavy metals were determined using Atomic Absorption Spectrophotometer (BUCK Scientific ACCUSYS 211) according to the manufacturer's instructions.

Isolation and Identification of the Bacteria from the Tannery Effluents

The bacteria were isolated from the effluents using Serial Dilution according to the method described by APHA (15). The biochemical tests such as oxidase, catalase, coagulase, indole (from 1% tryptone broth), citrate (Simmons citrate agar), methyl red (5 drops of MR), nitrate reduction, Voges-Proskauer (VP), Starch Hydrolysis, Glucose, Maltose, and Lactose tests were carried out on the bacterial isolates to identify the bacteria through the bacteria biochemical characteristics according to Ajao *et. al.* (16).

Determination of Growth Rate of the Bacteria in Effluent Sample

The bacteria growth rates were determined by transferring 2 mL of the bacterial isolates from the tannery effluent in broth medium into 100 mL sterile effluents in conical flasks and kept in an incubator (Giffirin cool) for 10 days. Control was also set up by incubating another 100 mL each of the sterile effluents without the bacteria. The optical density of the content was determined at the wavelength of 600 nm on a daily interval and recorded.

Immobilization of Bacteria

Agar solution and inoculi were prepared separately. Fifty milliliters (50 mL) of nutrient broth each of the inoculi was prepared in a McCartney bottle and incubated for 24 hours. A solution of agar-agar was prepared by dissolving 10 g of the powder in distilled water and made up to 500 mL mark in an Erlenmeyer flask and was sterilized in an autoclave (280A) for 15 minutes and allowed to cool to 40-45 °C (16). Four milliliters (4 mL) of the bacterial isolates in the nutrient broth was mixed with 36 ml of the prepared agar-agar media in petri-dish plates and then allowed to solidify. This was kept in the refrigerator for bioremediation.

Bioremediation (Treatment) of the Effluents

The solidified agar block (immobilized bacteria) was cut into cubes using a sterile knife; 0.1 mL phosphate buffer (pH 7.0) was added and kept in the refrigerator for 1 hour for curing. The phosphate buffer was decanted after 1 hour and the cubes were washed with sterile distilled water 3-4 times before it was used. Five grams (5 g), 10 g, 15 g, 20 g and 25 g of the immobilized bacteria were then weighed (17).

Two liters (2 L) of the effluent was supplemented with the minimum basal medium in g/L: NaCl (0.8), $MgSO_4 \cdot 7H_2O$ (0.001), KH_2PO_4 (2), $NaNO_3$ (2), $CaCl_2 \cdot 2H_2O$ (0.5) and $NaHPO_4 \cdot 12H_2O$ (2) and sterilized in an autoclave at 121 °C for 15 minutes. Two hundred and fifty milliliters (250 mL) of the effluents were transferred into different 250 ml conical flasks. The content was covered with a cotton-wool ramped with foil paper to avoid contamination. Five grams (5 g) of the immobilized bacteria were quickly transferred into each of the effluents in the conical flasks in an inoculating chamber (18). The same procedures were carried out for the 10 g, 15 g, 20 g and 25 g of the immobilized bacteria in separate 250 mL effluents in conical flasks and agitated for ten days in a shaker incubator (Gallenkamp-OC-4364-L) at the temperature 30 °C and velocity of 60 rpm. The treated effluent samples were taken on the tenth day and analyzed for the parameters pH, SS, TDS, COD, BOD, nitrate, sulfates, phosphates, chlorides, and heavy metal concentrations (Post-treatment determination) at the different grams of bacteria to evaluate and compare the bioremediation efficiency.

Statistical Analysis

The data were represented as Mean \pm Standard deviation and analyzed statistically using one-way Analysis of Variance (ANOVA) and Tukey's HSD as Post Hoc Tests with the aid of SPSS 16.0. The correlation coefficient was also used to measure the strength of the relationship between the different masses of the bacteria and the parameters. All $p \leq 0.05$ were considered as statistically significant.

RESULTS AND DISCUSSION

Results of the Physico-Chemical Parameters and Heavy Metals in Industrial Effluents before the Bioremediation

Results of the physicochemical parameters in the industrial effluents before the bioremediation were shown in Table 1. The mean level of temperature (29.50 ± 4.68 °C) was found below the World Health Organization (WHO) (35 °C) and NESREA (National Environmental Standards and Regulatory Enforcement Agency) (40 °C) recommended standard limits; the average value of temperature observed in this present study is less than that observed (56.23 to 74.54 °C) by another researcher. High temperature brings down the solubility of gases in water that ultimately expresses as high BOD and COD (19). pH (5.35 ± 1.57) was below the WHO (7.0-8.5) and NESREA (6-9). Maheshwari et al. (2017) reported that the level of pH in the effluents from the tannery industry in Vaniyambadi, India was 6.5 which was higher than that observed in the present study (20).

BOD (26.17 ± 9.49 mg/L) was below the NESREA (200 mg/L) but above the WHO (10 mg/L). Maheshwari et al. (2017) reported that the level of BOD in the effluents from the tannery industry in Vaniyambadi, India was 348 mg/L which was higher than that observed in the present study. BOD is a measure of the content of organic substances in the wastewater which are biologically degradable with consumption of oxygen usually indicated as 5-day BOD. This is the amount of oxygen in milligrams per liter (mg/L) that consumed by microorganisms in 5 days at 20 °C for the oxidation of the biologically degradable substances contained in the water. The high values of BOD recorded are indicative of the presence of total solids in the effluents which are known to be organic with high oxygen demands for their oxidation under required conditions of temperature and oxidants and time, as a result, will naturally lead to the depletion of dissolved oxygen in the aqueous body. The biochemical oxygen demand of the untreated textile wastewater can cause rapid depletion of dissolved oxygen if it is directly discharged into the surface water sources another researcher (21).

The Chemical Oxygen demand (COD) is the amount of oxygen, in mg/L, required for the degradation of the compound of wastewater to occur. COD (3106 ± 2753 mg/L) above the WHO (40 mg/L) and NESREA (40 mg/L). The level of COD in the effluents from the tannery industry in Vaniyambadi, India was 860 mg/L (20) which was lower than that observed in the present study. The higher the COD value of wastewater, the more oxygen demand to discharge water bodies another researcher(22). Akan et al. (2009) reported that a high COD value shows that the effluents have high oxygen demanding wastes which cause the depletion of Dissolved Oxygen (DO) which is a fundamental requirement for aquatic life.

SS (562 ± 482 mg/L) is above the WHO (30 mg/L) and NESREA (10 mg/L). These high TSS values observed in all the industries understudied might be possible due to the presence of fine leather particles, residues from various chemical discharges and reagents from different waste liquors from tanneries and textile industries (23). The composition of solids present in tannery effluent mainly depends upon the nature and quality of hides and skins processed in the tannery (24). The average value of SS observed in this present study is less than that observed (3422 ± 122 to 3700 ± 122 mg/L) by Maheshwari et al. (2017). It is observed that a suspended solid absorb heat from sunlight, causing an increase in water temperature and subsequently decreases the level of dissolved oxygen (25).

TDS (444 ± 507 mg/L) was above the WHO (250 mg/L) but below the NESREA (500 mg/L). The composition of solids present in tannery effluent

mainly depends upon the nature and quality of hides and skins processed in the tannery (24).

Nitrate (97.20 ± 146.80 mg/L) was found above the WHO (50 mg/L) and NESREA (40 mg/L). Maheshwari et al. (2017) reported that the level of nitrate in the effluents from the tannery industry in Vaniyambadi, India was 95 mg/L which was lower than that observed in the present study. The high level of nitrate in the tannery effluents in the present study might be due to the release of ammonia from the delimiting process and the presence of nitrogen in proteinaceous materials from unhairing operations. Momodu et al. (2017) have reported the presence of nitrate in receiving water which can lead to extensive undesirable algal growth associated with eutrophication.

Sulfates (268.34 ± 411.01 mg/L) were below the NESREA (500 mg/L) but above the WHO (100 mg/L). The high level of sulfate in the tannery effluents in the present study might be due to the use of sulfuric acid. The sulfate and high phosphate concentration detected in the effluents are also known to cause eutrophication and algal boom (26).

Phosphate (18.82 ± 34.717 mg/L) was found far above WHO (0.1 mg/L) and NESREA (3.5 mg/L). The sulfate and high phosphate concentration detected in the effluents are also known to cause eutrophication and algal boom (26).

Chlorides (22.59 ± 19.64 mg/L) were below the recommended limits of WHO (250 mg/L) and NESREA (350 mg/L). The presence of chloride in the tannery effluents in the present study might be due to the use of sodium chloride in hide and skin preservation. Chlorides inhibit the growth of plants, bacteria, and fish in surface waters growing. The presence of these physicochemical parameters in the tannery effluent of the present study might be due to the nature of the raw materials and processes used in the tannery industries at the time of sampling.

The results of the heavy metals in the industrial effluents before the bioremediation were shown in Table 2. The mean level of chromium (7.528 ± 4.530 mg/L) was found above the WHO (0.05 mg/L) and the NESREA (0.5 mg/L) recommended standard limits. Maheshwari (20) reported that the level of chromium in the effluents from the tannery industry in Vaniyambadi, India was 435 mg/L which was higher than that observed in the present study. The high concentration of chromium might be due to the use of chromium salts for tanning processes. Chromium can cause allergic reactions in the skin, damage the lungs, and asthma attacks maximum concentration of 0.1 mg/L was set up (27).

Iron (1.263 ± 0.502 mg/L) was found above WHO (0.5 mg/L) and the NESREA (1.0 mg/L). Higher iron

content may produce undesirable effects such as astringent taste, coloration, turbidity, deposits, and growth of iron bacteria in pipes affecting the acceptability of water for domestic use. Iron is an essential element in Maheshwari nutrition, and the health effect of iron in drinking water may include warding off fatigue and anemia (28).

Manganese (0.277 ± 0.03 mg/L) was above the NESREA (0.01 mg/L) and the WHO (0.02 mg/L). In another study, 1.02 mg/L of manganese was reported Yusuff and Sonobare, 2004 (29). Depending upon the exposure route, manganese may be among the least toxic of the trace elements if ingested low IQ of children is attributed to high manganese intake and hence at high concentration lead to neurotoxins and harms the brain (30).

Nickel (0.023 ± 0.021 mg/L) was above the NESREA (0.01 mg/L) and the WHO (0.02 mg/L). The concentration of nickel in the effluents from textile industries in Kano ranged (3.11 to 3.4 mg/L) (31) which is the same order of magnitude reported in the study by Ali et al (32). The most obvious anthropogenic source of nickel is scrap metal waste, notably alloyed metals including stainless steel. Nickel is considered as an essential trace element at very low concentrations. It does bioaccumulate in aquatic systems, and as such elevations above normal concentrations can result in deleterious aquatic effects (25).

Lead (0.304 ± 0.20 mg/L) was above the WHO (0.05 mg/L) and NESREA (0.1 mg/L). Galadima et al. (2012) (30) reported that the concentration of lead in the effluents from textile industries in Kano ranged (2.45 to 2.46 mg/L) which is the same order of magnitude reported in the study by Ali et al (32). Excess quantities of lead may impact Maheshwari health, especially affecting small children (33). The value 0.646 mg/L and 0.289 mg/L were reported for lead in wastewater samples from the textile industry in Kaduna (33).

Zinc (0.058 ± 0.05 mg/L) was below the WHO (5 mg/L) and the NESREA (0.2 mg/L). The concentration of zinc in the effluents from textile industries in kano ranged from 2.52 to 2.45 mg/L (31), which is the same order of magnitude reported by Ali et al. (2009). Zinc is a trace element that is essential for Maheshwari health; the danger of which can be to an unborn child when mothers absorbed large concentration of zinc and other health problem such as stomach cramps, skin irritation, vomiting and anemia (34).

Cadmium (0.068 ± 0.02 mg/L) was above the NESREA (0.01 mg/L) but below the WHO (0.5 mg/L). Galadima et al. (2012) reported that the concentration of cadmium in the effluents from textile industries in Kano ranged from 1.23 to 2.06 mg/L, which is the same order of magnitude

reported by Ali et al. (2009). Cadmium is a nonessential trace element that enters the environment via anthropogenic activities such as industrial effluent, sewage-sludge, fertilizers, and pesticides. Cadmium adsorbs strongly to sediments and organic matter (35). It has a range of negative physiological effects on the organism, such as decreased growth rates and negative effects on embryonic development and children are likely to be exposed to cadmium when is highly toxic and absorbed in the skin and can cause lung damage and irritation with shortness of breath dry throat, headache, vomiting, extreme restlessness or irritability, etc (36). Other potential long-term effects are pulmonary damage and fragile bones (37).

Copper (0.012 ± 0.02 mg/L) was found below WHO (1.00 mg/L) but above NESREA (0.01 mg/L) the recommended limits. Galadima et al. (2012) reported that the concentration of copper in the effluents from textile industries in Kano ranged from 1.06 to 1.01 mg/L. Copper is a reddish metal in a color that occurs naturally in rocks, soil, water, industrial activities, and sediment and has some practical uses in our society and are found in pipes, electrical wiring, and coins. The level of copper reported from the textile industry in Lagos ranged from 4.0 mg/L to 5.14 mg/L (29). Copper is generally remobilized with acid-base ion exchange or oxidation mechanism (33).

The presence of these heavy metals may be due to the addition of some raw materials containing these ions during the production process. It has been reported that the major problem associated with industrial effluents is the presence of heavy metal ions, which arise from the material used in the production process or a considerably high amount, from metal-containing raw materials (37). Heavy metals present as impurities in dye effluents or chelated as part of dye molecules. In metal complex dyes, the metal is coordinated or forms a chemical bond with the organic dye molecules. Thus, it is an indispensable constituent of dye and governs the fastness in absorbing colors. The highest value of heavy metal ions in the effluents severely affects soil fertility and depletes the soil quality and its nutrients. Besides, the variations of heavy metals concentration in the wastewater sample were due to the different types of dyestuff used in a different production of the threads when the samples were taken. The concentration of heavy metals could be a serious environmental nuisance if a large volume of such effluents is released into the environment regularly without proper treatment (31). In line with the findings by Yusuff and Sonibare (2004), Dan Azumi and Bichi (14) analyzed heavy metal in Kano from Challawa industrial estate and found high concentrations of metal ions. The presence of these heavy metals in the tannery effluent of the present study might be due to the nature of the raw materials and processes used in the textile industries at the time of sampling.

Table 1: Mean values (mg/L) \pm S.D of physicochemical parameters in effluents from the industries before and after treatment of the effluents with the different masses of the bacteria.

Parameter	Before	After				
		5 g	10 g	15 g	20 g	25 g
Temperature($^{\circ}$ C)	29.50 \pm 4.68					
pH	5.35 \pm 1.57					
COD	3106 \pm 2753	1376ab \pm 248	1588a \pm 489	2279b \pm 924	2681b \pm 867	1881ab \pm 626
BOD	26.17 \pm 9.49	0.81c \pm 0.67	0.80b \pm 0.61	0.80b \pm 0.61	0.58bc \pm 0.45	0.73b \pm 0.38
SS	562 \pm 482	118ab \pm 136	230ab \pm 252	78ad \pm 89	196bd \pm 302	273ab \pm 375
TDS	444 \pm 507	27be \pm 16	25bc \pm 15	25bc \pm 16	27bc \pm 18	25bd \pm 20
Nitrate	97.20 \pm 146.80	18.97a \pm 15.93	14.43a \pm 8.88	18.67a \pm 16.94	26.52a \pm 13.06	20.28a \pm 7.85
Chloride	22.59 \pm 19.64	12.90a \pm 18.39	3.95bc \pm 4.78	8.87a \pm 10.95	5.54ab \pm 4.66	8.25a \pm 10.68
Sulfate	268.34 \pm 411.01	18.12a \pm 19.26	15.99a \pm 17.37	5.95b \pm 8.91	13.31b \pm 18.55	8.59b \pm 12.82
Phosphate	18.82 \pm 34.71	2.03a \pm 3.11	1.90a \pm 3.15	2.10a \pm 3.00	1.76b \pm 2.74	1.76b \pm 2.64

Replicate= 6 (months), Within the columns, means with different letters are statistically different ($p < 0.05$).

Table 2: Mean values (mg/L) ± S.D of heavy metals in effluents from the industries before and after the treatment of the effluents with the different masses of the bacteria.

Parameter	Before	After				
		5 g	10 g	15 g	20 g	25 g
Cr	0.171a±0.12	0.049a±0.05	0.046a±0.07	0.013a±0.02	ND	0.170a±0.00
Fe	0.822±0.63	0.532c±0.11	0.488b±0.18	0.485b±0.36	0.202a±0.21	0.287ab±0.29
Mn	0.217a±0.48	0.002a±0.00	ND	ND	ND	ND
Ni	0.285±0.06	0.180a±0.07	0.180a±0.09	0.100a±0.10	0.070a±0.11	0.055a±0.11
Pb	0.273±0.20	0.118a±0.05	0.076a±0.04	0.073a±0.04	0.051a±0.05	0.043a±0.05
Zn	0.035±0.03	0.028a±0.02	0.028ac±0.03	0.027a±0.02	0.020ab±0.02	0.013a±0.02
Cd	0.068±0.02	0.058a±0.02	0.058a±0.03	0.050a±0.02	0.058a±0.03	0.063a±0.02
Cu	0.172±0.16	0.125b±0.12	0.068b±0.08	0.122b±0.13	0.100b±0.11	0.078b±0.08

Replicate= 6 (months), Within the columns, means with different alphabets are statistically different (p<0.05).

Table 3. Preliminary identification of the bacterial isolates.

Gram staining	Shape	Spore formation
+	Rod	-

+ = Positive - = Negative

Table 4. Biochemical characteristics of the bacterial isolates.

Citrate	Catalase	Coagulase	Starch	Glucose	Oxidase	Lactose	Mannitol	Maltose	MR	Nitrate Reduction
-	+	+	+	+	-	-	-	+	-	-

MR=Methyl Red

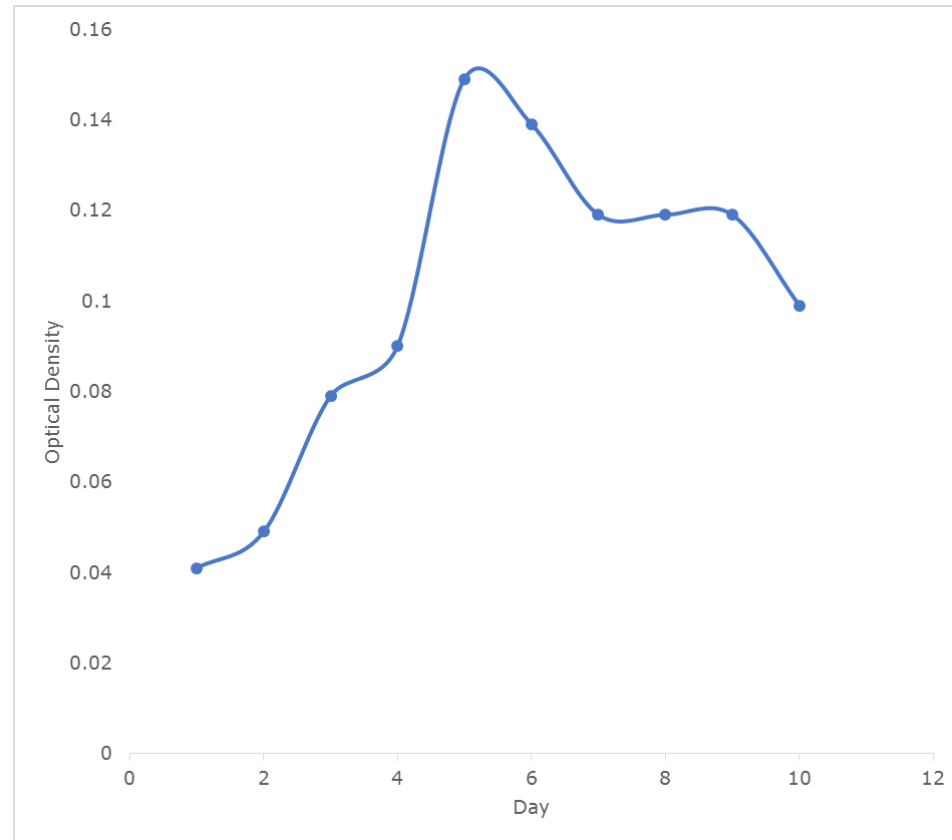


Figure 1: Growth rates (Cells/mL/day) of the *Corynebacterium kutscheri* in the effluent sample from the tannery industry.

Table 5: The correlation coefficient (r) between different masses of bacteria and physicochemical parameters.

Parameter	Correlation coefficient (r)	Percent dependence (rxrx100) (%)
SS	0.54*	30
TDS	-0.35	12
BOD	-0.62	39
COD	0.63*	40
NITRATE	0.53*	28
SULFATE	-0.68	46
PHOSPHATE	-0.69	48
CHLORIDE	-0.37	14

The correlation coefficient (r) with * is statistically significant ($p < 0.05$).

SS=Suspended Solid, TDS=Total Dissolved Solid, BOD=Biochemical Oxygen Demand and COD=Chemical Oxygen Demand

Table 6: The correlation coefficient (r) between different masses of bacteria and heavy metals.

Heavy metals	Correlation coefficient (r)	Percent dependence (rxrx100) (%)
Cr	-0.29	9
Fe	-0.85	72
Mn	-0.76	58
Ni	-0.99	97
Pb	-0.89	79
Zn	-1.00	99
Cd	0.33	11
Cu	-0.39	15

The correlation coefficient (r) with * is statistically significant ($p < 0.05$).

Table 7: Percentage reduction of the physicochemical parameters after-treatment of the effluents (250 mL) with the different masses (5 g, 10 g, 15 g, 20 g, and 25 g) of the *Corynebacterium kutscheri*.

Parameter (mg/L)	Percentage reduction (%)				
	5 g	10 g	15 g	20 g	25 g
COD	56	49	27	14	39
BOD	97	97	97	98	97
SS	79	59	86	65	51
TDS	94	94	94	94	94
Nitrate	80	85	81	73	79
Chloride	43	83	61	75	63
Sulfate	93	94	98	95	97
Phosphate	89	90	89	91	91

Table 8: Percentage reduction of the heavy after-treatment of the effluents (250 mL) with the different masses (5 g, 10 g, 15 g, 20 g, and 25 g) of the *Corynebacterium kutscheri*.

Parameter (mg/L)	Percentage reduction (%)				
	5 g	10 g	15 g	20 g	25 g
Cr	33	60	28	46	52
Fe	42	55	62	54	75
Mn	36	57	71	50	86
Ni	38	43	50	64	72
Pb	48	58	51	67	73
Zn	17	26	34	40	51
Cd	15	15	27	15	7
Cu	86	43	100	71	86

Results of the Preliminary Identification and Biochemical Characteristics of the Bacterial Isolates

Results of preliminary identification and biochemical characteristics of bacterial isolates were shown in Tables 3 and 4 respectively. After 48 hours of incubation, the nutrient agar media plates were checked for bacteria growth. The results showed that the bacterial isolate was found to be gram-positive, rod-shaped and recorded negative results for spore formation. The results of the biochemical test indicated that the bacteria were positive for catalase, maltose, glucose, starch hydrolysis, and coagulase tests. The bacteria showed negative results for citrate, oxidase, nitrate reduction, MR, lactose and mannitol tests. Base on the Preliminary Identification and biochemical test results, the bacteria isolated were identified to be *Corynebacterium kutscheri* (*C. kutscheri*).

Mohammed *et al.*, (2012) (3) investigated the enriched inoculums of *Corynebacterium sp* and *Pseudomonas putida*, separately inoculated into anthracene-contaminated water at the temperature of 28 °C under an optimum pH of 7.2 for 96 hours. Maheshwari *et al.*, (2017) (20) isolated and immobilized *Pseudomonas putida* and *Bacillus cereus* isolated from the tannery effluents of Vaniyambadi, India.

Figure 1 shows the growth rates of *C. kutscheri* in the effluent sample from the tannery industry. The initial growth phase of the *C. kutscheri* occurred on the 3rd day of incubation as the growth rate increases up to the 5th-day incubation when the maximum growth was observed. Beyond the 5th day, the growth of the bacteria declined (which might be due to a shortage of nutrients in the effluents) until it reached its phase of death (which might be due to the unavailability of nutrients in the effluents). This implies that the isolate can bioremediate most in the effluent on 5th day.

Results of the Physicochemical Parameters and Heavy Metals in the Industrial Effluents after the Bioremediation

Table 1 shows the mean results of the physicochemical parameters in the industrial effluents before and after the bioremediation using the different masses (5 g, 10 g, 15 g, 20 g, and 25 g) of the *C. kutscheri*. Also, Table 5 shows the results of the correlation coefficient (r) between the different mean masses of bacteria and the physicochemical parameters.

The mean value (mg/L) of the SS after the bioremediation varies between 78±89 and 273±375. The relative potential or efficiency of the different masses of the *C. kutscheri* in remediating the SS was in the order 15 g>5 g>20 g>10 g>25 g. A positive and significant correlation (0.54*) exists between the masses of the *C. kutscheri* and the SS.

There was a low correlation (30 %) between the masses of the *C. kutscheri* and the SS.

The mean value (mg/L) of the TDS after the bioremediation was between 25 ± 15 and 27 ± 16 . A negative and no significant correlation (-0.35) exist between the masses of the *C. kutscheri* and the TDS. There was a low correlation (12%) between the masses of the *C. kutscheri* and the TDS.

The mean value (mg/l) of the BOD after the bioremediation varies between 0.58 ± 0.45 and 0.81 ± 0.67 . In the present study, the values of the BOD agree with the report Maheshwari *et al.* (2017) (20) in which the concentration of nitrate decreased in biologically (immobilized *Pseudomonas putida* and *Bacillus cereus*) treated tannery wastewater. The relative potential or efficiency of the different masses of the *C. kutscheri* in remediating the BOD was in the order 20 g > 25 g > 15 g = 10 g > 5 g. A negative and no significant correlation (-0.62) exists between the masses of the *C. kutscheri* and the BOD. There was a low correlation (39%) between the masses of the *C. kutscheri* and the BOD.

The mean value (mg/L) of the COD after the bioremediation varies between 1376 ± 248 and 2681 ± 867 . In the present study, the values of the COD agree with the report Maheshwari *et al.* (2017) (20) in which the concentration of nitrate decreased in biological (immobilized *Pseudomonas putida* and *Bacillus cereus*) treated tannery wastewater. The relative potential or efficiency of the different masses of the *C. kutscheri* in remediating the COD was in the order 5 g > 10 g > 25 g > 15 g > 20 g. A positive and significant correlation (0.63*) exists between the masses of the *C. kutscheri* and the COD. There was a low correlation (40 %) between the masses of the *C. kutscheri* and the COD.

The mean value (mg/L) of the nitrate after the bioremediation varies between 14.43 ± 8.88 and 26.52 ± 13.06 . In the present study, the values of the nitrate agree with the report Maheshwari *et al.* (2017) (20) in which the concentration of nitrate decreased in biological (immobilized *Pseudomonas putida* and *Bacillus cereus*) treated tannery wastewater. The relative potential or efficiency of the different masses of the *C. kutscheri* in remediating the nitrate was in the order 10 g > 5 g > 15 g > 25 g > 20 g. A positive and significant correlation (0.53*) exists between the masses of the *C. kutscheri* and nitrate. There was a low correlation (28%) between the masses of the *C. kutscheri* and the nitrate.

The mean value (mg/L) of the sulfate after the bioremediation varies between 5.95 ± 8.91 and 18.12 ± 19.26 . The relative potential or efficiency of the different masses of the *C. kutscheri* in remediating the sulfate was in the order 15 g > 25 g > 20 g > 10 g > 5 g. A negative and no significant

correlation (-0.68) exist between the masses of the *C. kutscheri* and the sulfate. There was an average correlation (46 %) between the masses of *C. kutscheri* and the sulfate.

The mean value (mg/L) of the phosphate after the bioremediation varies between 1.76 ± 2.64 and 2.10 ± 3.00 . The relative potential or efficiency of the different masses of the *C. kutscheri* in remediating the phosphate was in the order 25 g > 20 g > 10 g > 5 g > 15 g. A negative and no significant correlation (-0.69) exist between the masses of *C. kutscheri* and the phosphate. There was an average correlation (48%) between the masses of *C. kutscheri* and the phosphate.

The mean value (mg/L) of the chloride after the bioremediation varies between 5.54 ± 4.66 and 12.90 ± 18.39 . The relative potential or efficiency of the different masses of the *C. kutscheri* in remediating the chloride was in the order 10 g > 20 g > 25 g > 15 g > 5 g. A negative and no significant correlation (-0.37) exist between the masses of *C. kutscheri* and the chloride. There was a very low correlation (14%) between the masses of *C. kutscheri* and the chloride. The decrease in the concentration of the physicochemical parameters after the bioremediation was not only due to the increase in the mass of *C. kutscheri* but might be also due to the increase in surface area of the different mass of *Corynebacterium Kutscheri*.

Table 2 shows the mean results of the heavy metals in the industrial effluents before and after the bioremediation using the different masses (5 g, 10 g, 15 g, 20 g, and 25 g) of the *C. kutscheri*. Also, Table 6 shows the results of the correlation coefficient (r) between the different mean masses of bacteria and heavy metals.

The mean value (mg/L) of the chromium after the bioremediation varies between 3.048 ± 2.70 and 5.416 ± 4.07 . This is in agreement with the work of Maheshwari *et al.* (2017) (22) in which the concentration of chromium decreased in biologically (immobilized *Pseudomonas putida* and *Bacillus cereus*) treated tannery wastewater. The relative potential or efficiency of the different masses of the *C. kutscheri* in remediating the chromium was in the order 10 g > 25 g > 20 g > 5 g > 15 g. A negative and no significant correlation (-0.29) exists between the masses of the *C. kutscheri* and the chromium. There was a very low correlation (9%) between the masses of the *C. kutscheri* and the chromium.

The mean value (mg/L) of the iron after the bioremediation varies between 0.310 ± 0.20 and 0.732 ± 0.11 . The relative potential or efficiency of the different masses of the *C. kutscheri* in remediating the iron was in the order 25 g > 15 g > 10 g > 20 g > 5 g. A negative and no significant correlation (-0.85) exist between the masses of the

C. kutscheri and the iron. There was a high correlation (72%) between the masses of the *C. kutscheri* and the iron.

The mean value (mg/L) of the manganese after the bioremediation varies between 0.003 ± 0.01 and 0.015 ± 0.01 . The relative potential or efficiency of the different masses of the *C. kutscheri* in remediating the manganese was in the order 25 g > 15 g > 10 g > 20 g > 5 g. A negative and no significant correlation (-0.76) exists between the masses of the *C. kutscheri* and the manganese. There was an average correlation (58 %) between the masses of the *C. kutscheri* and the manganese.

The mean value (mg/L) of the nickel after the bioremediation varies between 0.077 ± 0.06 and 0.172 ± 0.05 . The relative potential or efficiency of the different masses of the *C. kutscheri* in remediating the nickel was in the order 20 g > 25 g > 15 g > 10 g > 5 g. A negative and no significant correlation (-0.99) exists between the masses of *C. kutscheri* and the nickel. There was a very high correlation (97%) between the masses of the *C. kutscheri* and the nickel.

The mean value (mg/L) of the lead after the bioremediation varies between 0.082 ± 0.11 and 0.158 ± 0.20 . The relative potential or efficiency of the different masses of the *C. kutscheri* in remediating the lead was in the order 25 g > 20 g > 10 g > 15 g > 5 g. A negative and no significant correlation (-0.89) exists between the masses of the *C. kutscheri* and the lead. There was a high correlation (79%) between the masses of the *C. kutscheri* and the lead.

The mean value (mg/L) of the zinc after the bioremediation varies between 0.028 ± 0.03 and 0.048 ± 0.04 . The relative potential or efficiency of the different masses of the *C. kutscheri* in remediating the zinc was in the order 20 g > 25 g > 15 g > 10 g > 5 g. A negative and no significant correlation (-1.00) exist between the masses of the *C. kutscheri* and the zinc. There was a very high correlation (99%) between the masses of the *C. kutscheri* and the zinc.

The mean value (mg/L) of the cadmium after the bioremediation varies between 0.050 ± 0.02 and 0.063 ± 0.02 . The relative potential or efficiency of the different masses of the *C. kutscheri* in remediating the cadmium was in the order 15 g > 5 g > 20 g = 1 g > 25 g. A positive and no significant correlation (0.33) exists between the masses of the *C. kutscheri* and the cadmium. There was a very low correlation (11%) between the masses of the *C. kutscheri* and the cadmium.

The mean value (mg/L) of the copper after the bioremediation varies between not detected and 0.007 ± 0.00 . The relative potential or efficiency of

the different masses of the *C. kutscheri* in remediating the copper was in the order 15 g > 25 g > 20 g > 5 g > 10 g. A negative and not significant correlation (-0.39) exists between the masses of the *C. kutscheri* and the copper. There was a low correlation (15%) between the masses of the *C. kutscheri* and the copper. There was a reduction in the concentration of all the heavy metals after the bioremediation process when compared with the concentration of the raw samples before the bioremediation. This is in agreement with the work of Maheshwari *et al.* (2017) in which the concentration of chromium decreased in biologically (immobilized *Pseudomonas putida* and *Bacillus cereus*) treated tannery wastewater. This is also in line with the report made by Ajao *et al.* (2011) and Galadima *et al.* (2012). Also, Table 6 shows the results of the correlation coefficient (r) between the different mean masses of bacteria and heavy metals. In the present study, the decrease in the concentration of the heavy metals after the bioremediation was not only due to the increase in the mass of the bacteria but might be also due to the increase in surface area of the different mass of the bacteria.

Percentage reduction of the physicochemical parameters and the heavy metals by the *Corynebacterium Kutscheri*

Table 7 shows the percentage reduction of the physicochemical parameters after the treatment of the effluents (250 mL) by the different masses (5 g, 10 g, 15 g 20 g, and 25 g) of the *C. kutscheri*. The percentage reduction (%) of SS ranged (51-86); TDS (94); BOD (97-99); COD (14-56); nitrate (73-85); chloride (43-83); sulfate (93-98); phosphate (89-92).

Table 8 shows the percentage reduction of the heavy metals after-treatment of the effluents (250 mL) with the different masses (5 g, 10 g, 15 g 20 g, and 25 g) of the *C. kutscheri*. The percentage reduction (%) of Cr ranged (28-60); Fe (42-75); Mn (36-86); Ni (38-72); Pb (48-73); Zn (17-51); Cd (7-27) and Cu (43-100). Maheshwari *et al.* (2017) studied the bioremediation by free and immobilized bacteria isolated from tannery effluent. The percentage reduction of nitrate and nitrite was ranged from 45 to 75% when treated with *P. putida*, whereas they were ranged from 60 to 79% on the 15th day of the treatment. The level of BOD was reduced drastically after the 15th day of exposure by the free cells of both bacteria. The maximum percentage of reduction (83%) was shown by immobilized *B. cereus*. The percent reduction of COD ranged from 16% to 65% in both bacterial strains. The percentage of removal of Cr(VI) was 86% and 91% for free and immobilized cells, respectively. In *B. cereus* treated sample, it reached 84% and 89% on the 15th day respectively. It was concluded that both *P. putida* and *B. cereus* investigated in this study are highly recommended

for beneficial bioremediation applications for *in-situ* and off-site removal of pollutants.

Bioremediation of textile industrial effluent using the mixed culture of *Pseudomonas aeruginosa* and *Bacillus subtilis* immobilized on agar-agar in a bioreactor was carried out by Ajao et al. (2011). The result indicates overall % reduction in COD, BOD, nitrate, sulfate, phosphates as 83%, 97%, 61.3%, 62.8%, 61.2% respectively. Heavy metals were also bio-sorbed. It was concluded that immobilized cells represent a promising application in the bioremediation of textile industrial effluent and possible reusability of the cells for its commercial application can be achieved.

In general, immobilization makes the enzyme more resistant to temperature, pH, and substrate concentration swings giving it a longer lifetime and higher productivity per active unit (35). Although several workers described microbial degradation of tannery effluent, limited literature is available on the bioremediation of tannery effluent using immobilized bacterial cells in the present study area.

CONCLUSION

The tannery industrial effluent samples contained variable levels of the physicochemical parameter and heavy metals, in which some of them were higher than the recommended standard limits. The presence of these physicochemical parameters and heavy metals might be due to the nature of the raw materials and processes used in the tannery industries at the time of sampling. Based on the preliminary identification and biochemical test results, the bacterial isolate was identified to be *C. kutscheri*. There was an overall decrease in the concentration of the physicochemical parameters and the heavy metals after the bioremediation using the different masses of the immobilized *C. kutscheri*. However, the decrease was not only due to the increase in the mass of the *C. kutscheri* but might be also due to the increase in surface area of the different mass of the immobilized *C. kutscheri*. The average high percentage reduction (70% to 100%) of these parameters and heavy metals implies that the immobilized *C. kutscheri* is having a higher potential for the treatment of the tannery industrial effluents.

ACKNOWLEDGMENTS

The authors are grateful to the Kano State Ministry of Environment for their support in obtaining the effluent samples.

REFERENCES

1. Kamat DV, Kamat SD. Bioremediation of industrial effluent containing reactive dyes. International Journal of Environmental Sciences.

2015; 5(6): 1078-84. Doi: <http://10.0.23.200/ijes.2014050100101>.

2. Ado A, Gumel SM, Garba J. Industrial effluents as major source of water pollution in Nigeria: An overview. Am J Chem Appl. 2014;1(5):45-50.

3. Mohammed A, Sekar P, George J. Efficacy of microbes in bioremediation of tannery effluent. Intl J Curr Res. 2001;3(4):324-6.

4. Tudunwada IY, Essiet EU, Mohammed SG. THE EFFECTS OF TANNERY SLUDGE ON HEAVY METALS CONCENTRATION IN CEREALS ON SMALL-HOLDER FARMS IN KANO, NIGERIA. Notulae Botanicae Horti Agrobotanici Cluj-Napoca. 2007 Aug 5;35(2):55-60.

5. Adekunle AS, Eniola ITK. Impact of industrial effluents on quality of segment of Asa river within an industrial estate in Ilorin, Nigeria. New York Science Journal. 2008;1(1):17-21.

6. El-Bestawy E. Biological treatment of leather-tanning industrial wastewater using free living bacteria. 2013;

7. Omoleke II. Management of environmental pollution in Ibadan, an African city: the challenges of health hazard facing government and the people. Journal of HMaheshwarin Ecology. 2004;15(4):265-75.

8. Singh N, Sharma BK, Bohra PC. Impact assessment of industrial effluent of arid soils by using satellite imageries. Journal of the Indian Society of Remote Sensing. 2000;28(2-3):79.

9. The World Bank. Nigeria - Strategic options for redressing industrial pollution (English) | The World Bank [Internet]. 1995 [cited 2020 Mar 6]. Available from: <http://documents.worldbank.org/curated/en/287401468333530717/Nigeria-Strategic-options-for-redressing-industrial-pollution>

10. Verheijen L, Wiersema D, Pol LH, De Wit J. Management of wastes from animal product processing. Livestock and environment, Finding a balance. International Agriculture Center, Wageningen, The Netherlands. 1996;

11. Zahoor A, Rehman A. Isolation of Cr(VI) reducing bacteria from industrial effluents and their potential use in bioremediation of chromium containing wastewater. Journal of Environmental Sciences. 2009 Jan 1;21(6):814-20.

12. Noorjahan CM. Physicochemical characteristics, identification of bacteria and biodegradation of industrial effluent. Journal of bioremediation and Biodegradation. 2014;5(3).

13. Sen R, Chakrabarti S. Biotechnology – applications to environmental remediation in resource exploitation. *Current Science*. 2009;97(6):768–75.
14. Dan’Azumi S, Bichi MH. INDUSTRIAL POLLUTION AND HEAVY METALS PROFILE OF CHALLAWA RIVER IN KANO, NIGERIA. *Journal of Applied Sciences in Environmental Sanitation*. 2010;5(1).
15. Greenberg AE, Clesceri LS, Eaton AD. *Standard Methods for Examination of Water and Wastewater-APHA*. Washington, DC. 1992;
16. Ajao AT, Adebayo GB, Yakubu SE. Bioremediation of textile industrial effluent using mixed culture of *Pseudomonas aeruginosa* and *Bacillus subtilis* immobilized on agar-agar in a bioreactor. *J Microbiol Biotech Res*. 2011;1(3):50–6.
17. Adinarayana K, Jyothi B, Ellaiah P. Production of alkaline protease with immobilized cells of *Bacillus subtilis* PE-11 in various matrices by entrapment technique. *AAPS PharmSciTech*. 2005;6(3):E391–7.
18. Margesin R, Schinner F. Bioremediation (natural attenuation and biostimulation) of diesel-oil-contaminated soil in an alpine glacier skiing area. *Appl Environ Microbiol*. 2001;67(7):3127–33.
19. Akan JC, Ogugbuaja VO, Abdulrahman FI, Ayodele JT. Pollutant levels in effluent samples from tanneries and textiles of Kano industrial areas, Nigeria. *Global journal of pure and applied sciences*. 2009;15(3–4).
20. BIOREMEDIATION BY FREE AND IMMOBILIZED BACTERIA ISOLATED FROM TANNERY EFFLUENT - Google Search [Internet]. [cited 2020 Mar 6]. Available from: <https://www.google.com/search?client=firefox-b-d&q=BIOREMEDIATION+BY+FREE+AND+IMMOBILIZED+BACTERIA+ISOLATED+FROM+TANNERY+EFFLUENT>
21. Babu BV, Rana HT, Ramakrishna V, Sharma M. COD reduction of reactive dyeing effluent from cotton textile industry. *Journal of the Institution of Public Health Engineers India*. 2000;4:5–11.
22. Akan JC, Moses EA, Ogugbuaja VO, Abah J. Assessment of tannery industrial effluents from Kano metropolis, Kano State, Nigeria. *Journal of Applied Sciences*. 2007;7(19):2788–93.
23. Haile A. Physico-chemical characterization of tannery effluent and its impact on the nearby river. *Journal of Environmental Chemistry and Ecotoxicology*. 2016 Jun 30;8:44–50.
24. Islam BI, Musa AE, Ibrahim EH, Sharafa SAA, Elfaki BM. Evaluation and Characterization of Tannery Wastewater. 2014;10.
25. KMaheshwarir K, Saravana Devi S, Krishnamurthi K, Gampawar S, Mishra N, Pandya GH, et al. Decolorisation, biodegradation and detoxification of benzidine based azo dye. *Bioresour Technol*. 2006 Feb;97(3):407–13.
26. Momodu O, Ekundayo AO, Momodu IS, Iyayi AF, Ohaga S, Momoh D. Pollution Monitoring and Control in Rubber Industry in Nigeria. :6.
27. Rajendran P, Gunasekaran P. Nanotechnology for bioremediation of heavy metals. In: *Environmental bioremediation technologies*. Springer; 2007. p. 211–21.
28. Kaushik S. Bio-sorption of hexavalent chromium using bacterial isolates [PhD Thesis]. M. Phil. Dissertation. School of Energy and Environment Studies. Devi ...; 2003.
29. Yusuff RO, Sonibare JA. Characterization of textile industries’ effluents in Kaduna, Nigeria and pollution implications. *Global Nest: the int J*. 2004;6(3):212–21.
30. Agency) F (Federal EP. Guidelines and standards for environmental pollution control in Nigeria. FEPA Lagos; 1991.
31. BIOREMEDIATION OF TEXTILE INDUSTRIES EFFLUENTS USING SELECTED BACTERIAL SPECIES IN KANO, NIGERIA BY GALADIMA ADAMU DAGONA BSc. (UNIMAID, 2007) (M.SC./SCIE/10738/2008-2009) - Google Search [Internet]. [cited 2020 Mar 5]. Available from: <https://www.google.com/search?client=firefox-b-d&q=BIOREMEDIATION+OF+TEXTILE+INDUSTRIES+EFFLUENTS+USING+SELECTED+BACTERIAL+SPECIES+IN+KANO+%2C+NIGERIA+BY+GALADIMA+ADAMU+DAGONA+BSc.+%28UNIMAID%2C+2007%29+%28M.SC.+%2FSCIE%2F10738%2F2008-2009%29>
32. Ali N, Hameed A, Ahmed S. Physicochemical characterization and bioremediation perspective of textile effluent, dyes and metals by indigenous bacteria. *Journal of hazardous materials*. 2009;164(1):322–8.
33. Orisakwe OE. Environmental pollution and blood lead levels in Nigeria: who is unexposed? *International journal of occupational and environmental health*. 2009;15(3):315–7.
34. Organization WHO. Air quality guidelines: global update 2005: particulate matter, ozone, nitrogen dioxide, and sulfur dioxide. World Health Organization; 2006.

35. Dos Santos AB, Bisschops IAE, Cervantes FJ. Closing process water cycles and product recovery in textile industry: perspective for biological treatment. *Advanced biological treatment processes for industrial wastewaters*. 2006;1:298–320.
36. Chong K, Wang W-X. Bioavailability of sediment-bound Cd, Cr and Zn to the green mussel *Perna viridis* and the Manila clam *Ruditapes philippinarum*. *Journal of Experimental Marine Biology and Ecology*. 2000;255(1):75–92.
37. Prasad AA, Rao KB. Physico chemical characterization of textile effluent and screening for dye decolorizing bacteria. *Global journal of biotechnology and biochemistry*. 2010;5(2):80–6.



Comparative DFT Study of a Ruthenium Complex

Nil Ertekin Binbay^{1*}  

¹Dicle University, 21280, Diyarbakir, Turkey

Abstract: A comparative density functional theory (DFT) study of the Ruthenium complex (pentamethylcyclopentadienyl)(diisopropylmethylphosphine)(chloro)(trichlorosilyl)ruthenium hydride is reported. The molecule contains a ruthenium (Ru) atom, which, like other transition metals, is computationally difficult to handle due to the near degeneracy of their electronic states. Calculations were carried out in the gas phase using GAMESS software (the General Atomic and Molecular Electronic Structure System), which is an ab-initio quantum chemistry package. Five different basis sets were used, namely: Sapporo non-relativistic SPK DZP, SBKJ, 3-21G, STO3G, and STO6G. The molecule was optimized in quintuplicate with each of the basis sets. The computational results were compared with real X-ray data to assess how well the basis sets worked for a molecule containing a transition metal such as ruthenium. As the most computationally expensive basis set, the Sapporo non-relativistic SPK DZP was expected to give the most accurate results. However, unexpectedly, 3-21G, a computationally cheaper basis set, exhibited the best performance.

Keywords: SBKJ, 3-21G, STO-6G, Ruthenium, DFT.

Submitted: May 21, 2019. **Accepted:** March 14, 2020.

Cite this: Ertekin Binbay N. Comparative DFT Study of a Ruthenium Complex. JOTCSA. 2020;7(2):351–60.

DOI: <https://doi.org/10.18596/jotcsa.568062>.

***Corresponding author.** E-mail: nbinbay@gmail.com, Tel: +90 541 609 8307

INTRODUCTION

Density functional theory (DFT), as the most common computational method for molecular calculations, has been used for decades to investigate the properties of molecules and molecular systems by ab-initio calculations. (1–6) It has been applied to a wide range of real atomic systems, including transition metal (TM) complexes. (3,7–11) However, it is well known that TM complexes are computationally difficult as they have unique properties, such as near degenerate electronic states, which lead to less accurate computational results than for other atomic types. (8–11) Nonetheless, DFT is still the most used computational approach as there is no better alternative (with a lower computational cost and better accuracy) available. (6)

Owing to the errors that arise in quantum chemical calculations of TM complexes, it is necessary to investigate suitable computational methods to

minimize calculation errors. One of the most effective ways of determining the effectiveness of computational methods is to compare their results with real experimental data. By doing so, we aim to contribute to search for better parameter sets that give better results for ab-initio quantum chemical calculations of TM complexes, and also to contribute to the improvement of computational approaches by adding some new data to the existing literature.

Scientists need to know how much improvement they can expect from using a more computationally expensive model (for instance, when computation time is doubled). Therefore, expected improvements in accuracy with increased computational resources need to be investigated in order to decide if a particular model is worthwhile. The most effective way of doing this is to carry out comparative studies with new models and real data and contribute to the available literature, as with the current study. Moreover, these types of studies should include models that are both computationally cheap and expensive for comparison and accuracy. Hence, the

main aim of the current work is to determine the effectiveness of the computationally expensive Sapporo non-relativistic SPK DZP and SBKJ basis sets by comparison to the computationally cheaper STO3G, STO6G, and 3-21G.

The CAM-B3LYP functional, which was recently introduced, solves the long-range self-interaction error problem with its range-separated structure. (12,13) Furthermore, it has been used for transition metal complexes in previous studies.(14–17) Hence, it was also selected for investigation in our current study. As our results showed, it is an efficient functional for optimization of the ruthenium complex since it gave tolerable bond length errors according to the comparison of the calculated results with the real X-ray data, even for the computationally cheaper basis sets.

Here, five different basis sets were investigated for the optimization of the structure of (pentamethylcyclopentadienyl) (diisopropylmethylphosphine)(chloro) (trichlorosilyl)ruthenium hydride, and the calculated results were compared against real X-ray data for the molecule.(18)

RESULTS AND DISCUSSION

The optimized geometry of the molecule is given in Figure 1. As can be seen in Figure 1, Ru is bonded

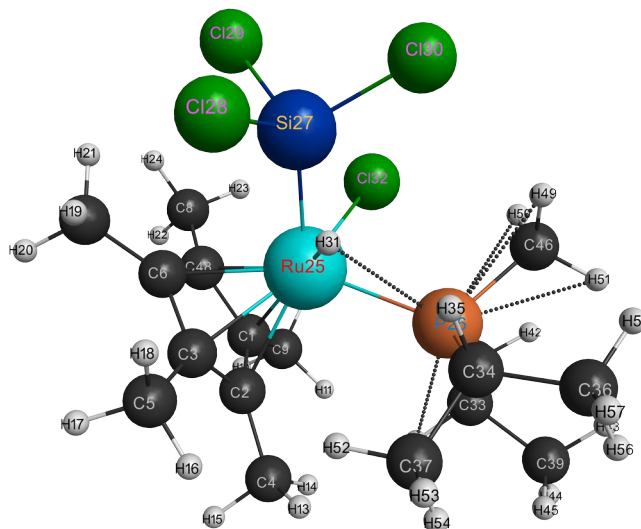


Figure 1: Optimized geometry of the molecule, as determined by the Sapporo non-relativistic SPK DZP basis set.

The calculated bond lengths of the molecule are given in Table 1, and the percentage of calculation errors for each bond and each method are presented in Table 2. As can be seen from Tables 1 and 2, the overall performance of the basis sets varies greatly, while the performance of individual

MATERIALS AND METHODS

All calculations were carried out using GAMESS software (the General Atomic and Molecular Electronic Structure System), which is an ab-initio quantum chemistry package.(6,19) The hybrid Becke three-parameter Lee–Yang–Parr, modified by the Coulomb-attenuating method (CAM-B3LYP) was selected for this work as exchange correlation functional.(12) Five different basis sets were used to optimize the structure of the molecule: SBKJ (Stevens, Bash, Krauss, and Jasien) valence, Sapporo non-relativistic SPK DZP, 3-21G, STO3G, and STO6G.(20–24) All calculations were performed in the gas phase and all of the optimizations started from the same molecular configuration. All of the computational parameters were kept the same for all calculations, except for the basis sets. After the optimizations, frequency calculations were also carried out with the same levels of theory to confirm that there were no imaginary frequencies, hence the optimized conformations are confirmed as real minima on the potential energy surface.

to five ring carbons (C1, C2, C3, C6, C48) and four other atoms (Si27, P26, Cl32, and H31) in half-sandwich form.

basis sets also varies with the type of bonded atom. For instance, according to Table 1, the STO-6G basis set gives better performance than the STO-3G basis set for all of the bonds. Besides, STO-6G gives more errors for Ru bonds (with near 25%) than the C-C bonds (with near 4%).

Table 1: Bonded atoms and bond lengths calculated using basis sets and determined experimentally with X-ray data.

Atom 1	Atom 2	X-ray (Å)	SBKJ (Å)	Sapporo SPK (Å)	DZP	3-21G (Å)	STO-3G (Å)	STO-6G (Å)
C1	C2	1.414	1.425	1.419		1.407	1.508	1.356
C1	C9	1.496	1.512	1.495		1.495	1.527	1.514
C2	C4	1.484	1.513	1.496		1.499	1.517	1.517
C3	C2	1.441	1.449	1.427		1.447	1.351	1.519
C3	C5	1.497	1.516	1.499		1.500	1.519	1.524
C3	C6	1.442	1.453	1.439		1.454	2.102	1.474
C33	C38	1.530	1.548	1.534		1.544	1.557	1.554
C33	C39	1.532	1.546	1.529		1.539	1.552	1.553
C34	C36	1.525	1.546	1.531		1.540	1.554	1.554
C34	C37	1.526	1.545	1.527		1.540	1.555	1.551
C48	C1	1.447	1.464	1.443		1.465	1.467	1.565
C48	C8	1.496	1.510	1.493		1.495	1.487	1.522
C6	C48	1.415	1.428	1.414		1.417	1.768	1.454
C6	C7	1.500	1.514	1.496		1.499	1.466	1.502
P26	C33	1.861	1.875	1.861		1.852	1.884	1.913
P26	C34	1.848	1.880	1.868		1.857	1.889	1.905
P26	C46	1.822	1.841	1.820		1.821	1.857	1.859
Ru25	C1	2.316	2.335	2.252		2.365	1.638	2.507
Ru25	C2	2.345	2.365	2.309		2.400	2.310	2.548
Ru25	C3	2.229	2.256	2.233		2.234	1.591	1.679
Ru25	C48	2.241	2.280	2.240		2.281	1.578	1.638
Ru25	C6	2.240	2.284	2.262		2.270	1.458	1.654
Ru25	Cl32	2.413	2.449	2.430		2.427	1.679	1.752
Ru25	P26	2.369	2.440	2.410		2.377	4.890	1.785
Ru25	Si27	2.315	2.374	2.341		2.307	1.767	1.833
Si27	Cl28	2.099	2.134	2.127		2.102	2.040	2.054
Si27	Cl29	2.089	2.105	2.093		2.066	2.044	2.043
Si27	Cl30	2.092	2.110	2.089		2.075	2.055	2.049

Table 2: Percentage calculation errors for each bond by basis set.

Atom 1	Atom 2	Error SBKJ	% %	Error Sapporo SPK DZP	% %	Error 3-21G	% %	Error STO-3G	% %	Error STO-6G	% %
C1	C2	0.78		0.35		-0.50		6.65		-4.10	
C1	C9	1.07		-0.07		-0.07		2.07		1.20	
C2	C4	1.95		0.81		1.01		2.22		2.22	
C3	C2	0.56		-0.97		0.42		-6.25		5.41	
C3	C5	1.27		0.13		0.20		1.47		1.80	
C3	C6	0.76		-0.21		0.83		45.77		2.22	
C33	C38	1.18		0.26		0.92		1.76		1.57	
C33	C39	0.91		-0.20		0.46		1.31		1.37	
C34	C36	1.38		0.39		0.98		1.90		1.90	
C34	C37	1.25		0.07		0.92		1.90		1.64	
C48	C1	1.17		-0.28		1.24		1.38		8.15	
C48	C8	0.94		-0.20		-0.07		-0.60		1.74	
C6	C48	0.92		-0.07		0.14		24.95		2.76	
C6	C7	0.93		-0.27		-0.07		-2.27		0.13	
P26	C33	0.75		0.00		-0.48		1.24		2.79	
P26	C34	1.73		1.08		0.49		2.22		3.08	
P26	C46	1.04		-0.11		-0.05		1.92		2.03	
Ru25	C1	0.82		-2.76		2.12		-29.27		8.25	

Ru25	C2	0.85	-1.54	2.35	-1.49	8.66
Ru25	C3	1.21	0.18	0.22	-28.62	-24.67
Ru25	C48	1.74	-0.06	1.78	-29.59	-26.91
Ru25	C6	1.96	0.98	1.34	-34.91	-26.16
Ru25	Cl32	1.51	0.73	0.60	-30.40	-27.38
Ru25	P26	2.98	1.72	0.32	106.39	-24.66
Ru25	Si27	2.54	1.12	-0.35	-23.68	-20.82
Si27	Cl28	1.67	1.33	0.14	-2.81	-2.14
Si27	Cl29	0.77	0.19	-1.10	-2.15	-2.20
Si27	Cl30	0.86	-0.14	-0.81	-1.77	-2.06

Figure 2 shows a comparison of the calculated C-C bond lengths with those obtained from the X-ray data, and Figure 3 shows the errors in the calculated C-C bond lengths. As shown in Figures 2 and 3, the Sapporo non-relativistic SPK DZP basis set gives the best approximation of the C-C bond lengths, while STO-3G gives the worst approximation. The most significant error for the C-

C bond lengths was in relation to the C6 position calculated using the STO-3G basis set; 45% error was seen for the C3-C6 bond and 24% for the C6-C48 bond. On the other hand, when we look at the overall picture in Figure 2, it is clear that all of the approximations are in tolerable agreement with the C-C bond lengths determined via X-ray data, except for those obtained using the STO-3G basis set.

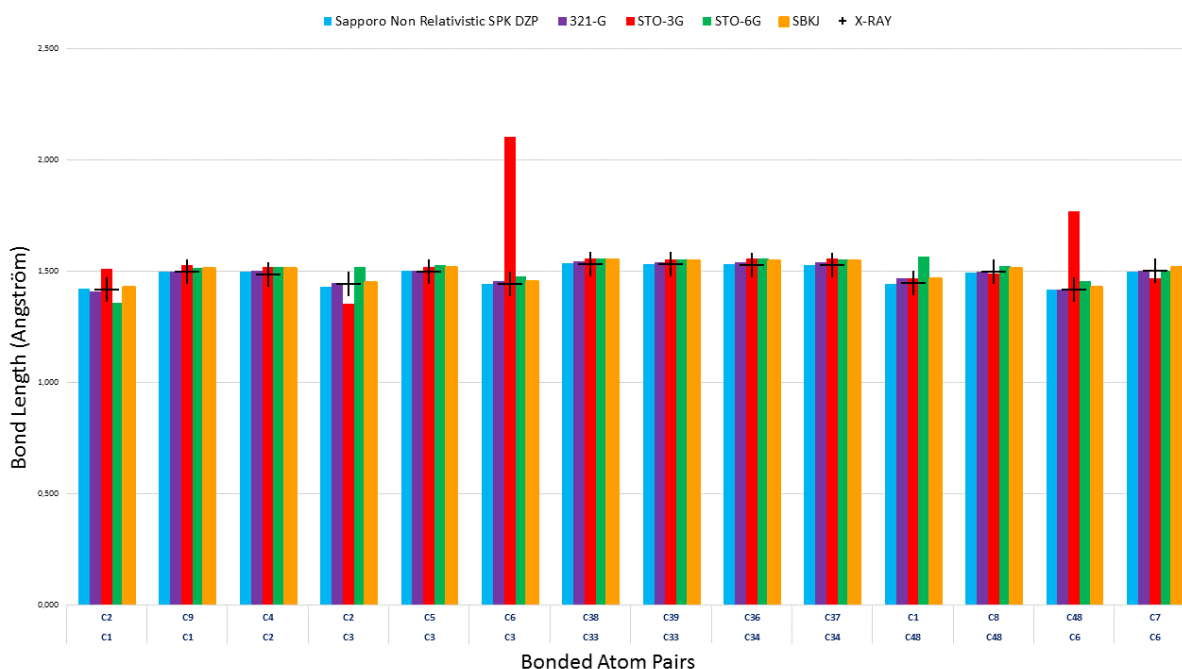


Figure 2: Comparison of calculated C-C bond lengths with those obtained from X-ray data.

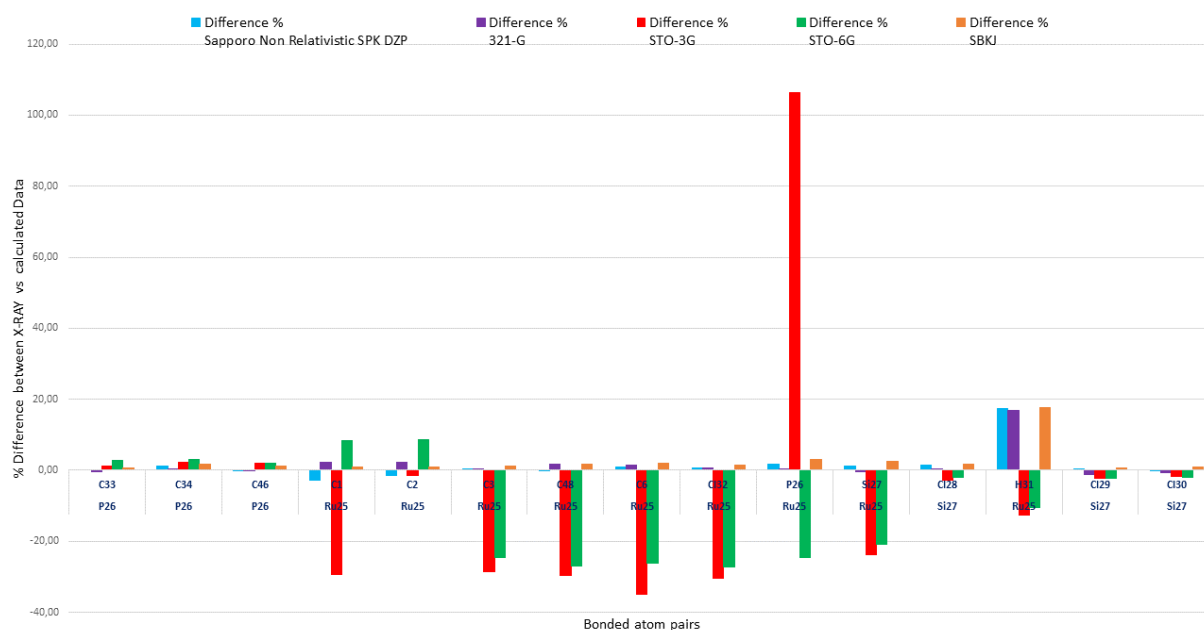


Figure 5: Percentage differences between calculate and experimentally determined bond lengths for Ru, Si, Cl, and P atoms.

Figure 4 shows a comparison of the calculated and experimentally obtained bond lengths for Ru, Si, Cl, and P atoms, while Figure 5 shows the percentage errors for these calculated bond lengths. It can be clearly seen that the performance of the basis sets differs significantly for Ru bonds, while closer agreement was observed for P–C and Si–Cl bonds. Clearly, neither of the Slater-type orbital basis sets (STO-3G nor STO-6G) give a good fit for Ru bonds. Although the STO-6G basis set shows better performance than the STO-3G, as expected, both approximations give intolerable errors for Ru bonds. Thus, this type of basis set is not recommended for quantum chemical calculations for complexes with

transition metals such as Ru. The best performance for Ru bonds surprisingly came from 3-21G, a computationally cheaper method, rather than from the more computationally expensive Sapporo non-relativistic SPK DZP or SBKJ basis sets.

Figure 6 shows a comparison of the calculated and experimentally determined C–H bond lengths, and Figure 7 shows the percentage errors for the calculated C–H bond lengths. The results show that each of the five basis sets gave larger errors for H atoms than for any other atoms. All of the basis sets gave longer bond lengths than those obtained from the X-ray data for all H bonds.



Figure 6: Comparison of calculated C–H bond lengths with those obtained from X-ray data.

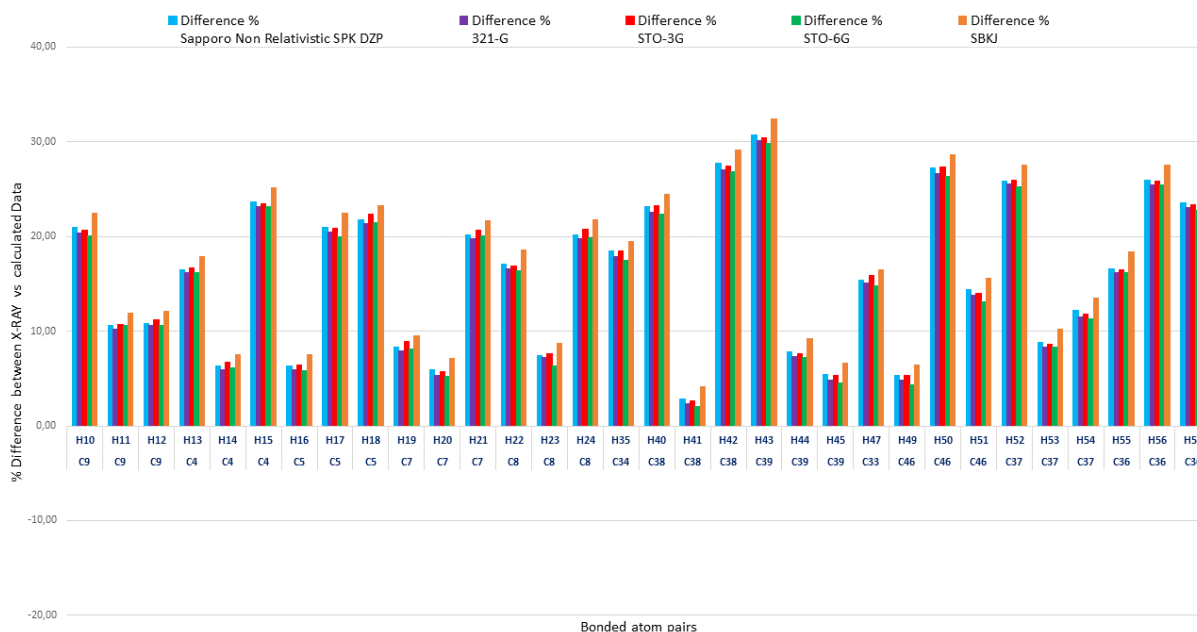


Figure 7: Percentage errors for calculated C–H bond lengths.

The calculation times and RMS (Root Mean Square) errors for specific bond types are presented in Table 3. The table shows that the fastest method is STO-3G with 604 minutes; hence, it is the cheapest method in a computational sense. However, STO-3G is the worst method when considering the percentage errors for all bond types.

On the other hand, the Sapporo non-relativistic SPK DZP basis set is the slowest one at 5290.2 minutes,

requiring an eight-fold longer calculation time than STO-3G. The Sapporo non-relativistic SPK DZP basis is the most computationally expensive method used in this work. Although it gave the most accurate results for C–C bond lengths, as expected, this was unexpectedly not the case for Ru bonds or C–H bonds.

Surprisingly, 3-21G, the second-cheapest method in computational terms with 640.7 minutes, gave the

most accurate results for Ru bonds with a 4.501% RMS error, and the second-most accurate results for C–C and C–H bonds with results very close to those obtained using the best-performing basis set.

Hence, when all of the bonds are considered with total RMS errors, 3-21G exhibits the best performance, being superior to the other more computationally expensive basis sets.

Table 3: The RMS error percentages for bonded atom groups and the calculation times.

Basis Set	Total calculation time (min)	Total RMS error	C–C bonds RMS error	Ru bonds RMS error	C–H bonds RMS error
Sapporo SPK DZP	5290.2	13.057	0.401	4.636	17.735
3-21G	640.7	12.722	0.687	4.501	17.275
STO-3G	604.0	22.059	14.221	33.428	17.623
STO-6G	1517.7	14.974	3.256	16.530	17.005
SBKJ	1300.9	13.983	1.124	4.795	18.968

The performance of each of the basis sets is shown graphically in Figure 8, which shows all the calculation times and the RMS error percentages for all bond types and all basis sets. Thus, we can compare both the calculation times and the errors simultaneously to compare the performances of all

basis sets. Clearly, the Sapporo non-relativistic SPK DZP and the 3-21G basis sets have similar error rates for all types of bonds, while there is a large gap between their calculation times (88.17 hour vs. 10.68 hour).

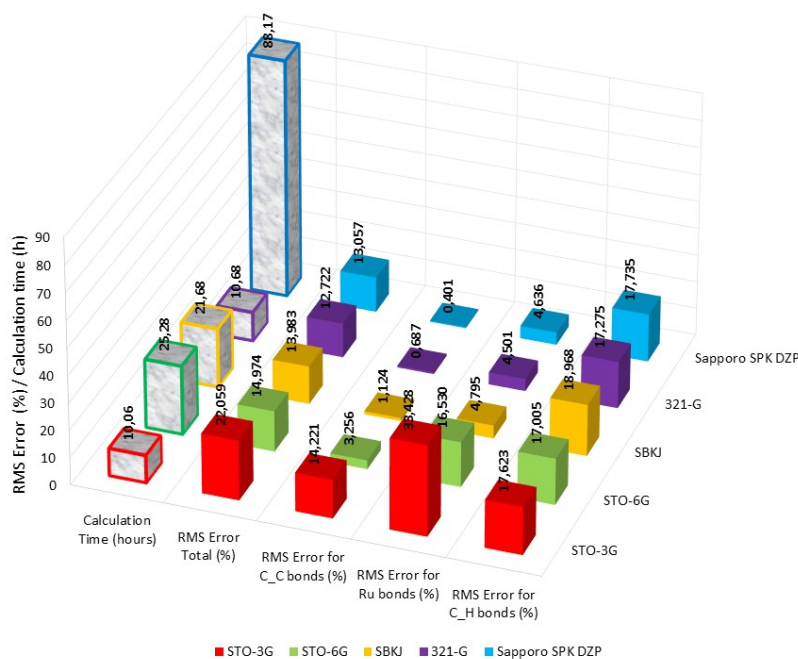


Figure 8: 3D graph comparing the performance of the basis sets, showing the RMS error percentages and calculation times for each basis set and each bond type.

CONCLUSIONS

Considering the overall picture in Figure 8, the following conclusions can be drawn:

- a) Slater-type orbital (STO -*G) basis sets are not recommended for complexes involving Ru and similar transition metals.
- b) All of the tested methods exhibited some difficulties in calculating H bonds, but the Slater-type orbital basis sets (STO-6G and even STO-3G) performed better than the other tested basis sets.

STO-6G gives the smallest RMS error for H bonds, as seen in Figure 8.

- c) The Sapporo non-relativistic SPK DZP, 3-21G, and SBKJ valence basis sets give similar error rates for C–C and Ru bonds, but with radically different calculation times of 5290.2 min, 640.7 min, and 1300.9 min, respectively.

- d) Hence, among those tested in this work, the 3-21G basis set shows the best performance with a short computation time and high accuracy, and it is recommended for use for complexes with Ru and similar transition metals.

REFERENCES

- Hohenberg P, Kohn W. Inhomogeneous Electron Gas. *Phys Rev.* 1964 Nov 9;136(3B):B864-71.
- Kohn W, Sham LJ. Self-Consistent Equations Including Exchange and Correlation Effects. *Phys Rev.* 1965 Nov 15;140(4A):A1133-8.
- Harvey JN. On the accuracy of density functional theory in transition metal chemistry. *Annu Rep Sect C Phys Chem.* 2006;102:203.
- Fey N, Ridgway BM, Jover J, McMullin CL, Harvey JN. Organometallic reactivity: the role of metal-ligand bond energies from a computational perspective. *Dalton Trans.* 2011;40(42):11184.
- Chermette H. Density functional theory. *Coord Chem Rev.* 1998 Dec;178-180:699-721.
- Dykstra CE, editor. *Theory and applications of computational chemistry: the first forty years.* 1st ed. Amsterdam ; Boston: Elsevier; 2005. 1308 p.
- Davidson ER. *Computational Transition Metal Chemistry.* *Chem Rev.* 2000 Feb;100(2):351-2.
- Zhao Y, Truhlar DG. Comparative assessment of density functional methods for 3d transition-metal chemistry. *J Chem Phys.* 2006 Jun 14;124(22):224105.
- Schultz NE, Zhao Y, Truhlar DG. Density Functionals for Inorganometallic and Organometallic Chemistry. *J Phys Chem A.* 2005 Dec;109(49):11127-43.
- Furche F, Perdew JP. The performance of semilocal and hybrid density functionals in 3d transition-metal chemistry. *J Chem Phys.* 2006 Jan 28;124(4):044103.
- Kameno Y, Ikeda A, Nakao Y, Sato H, Sakaki S. Theoretical Study of $M(\text{PH}_3)_2$ Complexes of C_{60} , Corannulene ($\text{C}_{20}\text{H}_{10}$), and Sumanene ($\text{C}_{21}\text{H}_{12}$) ($M = \text{Pd}$ or Pt). Unexpectedly Large Binding Energy of $M(\text{PH}_3)_2$ (C_{60}). *J Phys Chem A.* 2005 Sep;109(35):8055-63.
- Yanai T, Tew DP, Handy NC. A new hybrid exchange-correlation functional using the Coulomb-attenuating method (CAM-B3LYP). *Chem Phys Lett.* 2004 Jul;393(1-3):51-7.
- Cramer CJ, Truhlar DG. Density functional theory for transition metals and transition metal chemistry. *Phys Chem Chem Phys.* 2009;11(46):10757.
- Son J-H, Ohlin CA, Casey WH. A new class of soluble and stable transition-metal-substituted polyoxoniobate: $[\text{Cr}_2(\text{OH})_4\text{Nb}_{10}\text{O}_{30}]^{8-}$. *Dalton Trans.* 2012;41(41):12674.
- Elius Hossain Md, Mahmudul Hasan Md, Halim ME, Ehsan MQ, Halim MA. Interaction between transition metals and phenylalanine: A combined experimental and computational study. *Spectrochim Acta A Mol Biomol Spectrosc.* 2015 Mar;138:499-508.
- Cong S, Yan LK, Wen SZ, Guan W, Su ZM. Quantum chemical studies of Lindqvist-type polyoxometalates containing late 3d transition metals ($[(\text{py})\text{MIIW}_5\text{O}_{18}]_4^-$ ($M = \text{Fe}, \text{Co}, \text{Ni}$)): MII-N bonding and second-order nonlinear optical properties. *Theor Chem Acc.* 2011 Dec;130(4-6):1043-53.
- Shakerzadeh E, karbasiyuon M. Electro-optical properties of bowl-like B36 cluster doped with the first row transition metals: A DFT insight. *Phys E Low-Dimens Syst Nanostructures.* 2019 Oct;114:113599.
- Osipov AL, Gerdov SM, Kuzmina LG, Howard JAK, Nikonov GI. Syntheses and X-ray Diffraction Studies of Half-Sandwich Hydridosilyl Complexes of Ruthenium. *Organometallics.* 2005 Feb;24(4):587-602.
- Schmidt MW, Baldrige KK, Boatz JA, Elbert ST, Gordon MS, Jensen JH, et al. General atomic and molecular electronic structure system. *J Comput Chem.* 1993 Nov;14(11):1347-63.
- Stevens WJ, Krauss M, Basch H, Jasien PG. Relativistic compact effective potentials and efficient, shared-exponent basis sets for the third-, fourth-, and fifth-row atoms. *Can J Chem.* 1992 Feb;70(2):612-30.
- Binkley JS, Pople JA, Hehre WJ. Self-consistent molecular orbital methods. 21. Small split-valence basis sets for first-row elements. *J Am Chem Soc.* 1980 Jan;102(3):939-47.
- Hehre WJ, Stewart RF, Pople JA. Self-Consistent Molecular-Orbital Methods. I. Use of Gaussian Expansions of Slater-Type Atomic Orbitals. *J Chem Phys.* 1969 Sep 15;51(6):2657-64.
- Collins JB, von R. Schleyer P, Binkley JS, Pople JA. Self-consistent molecular orbital methods. XVII. Geometries and binding energies of second-row molecules. A comparison of three basis sets. *J Chem Phys.* 1976 Jun 15;64(12):5142-51.

24. Gordon MS, Binkley JS, Pople JA, Pietro WJ, Hehre WJ. Self-consistent molecular-orbital methods. 22. Small split-valence basis sets for second-row elements. J Am Chem Soc. 1982 May;104(10):2797-803.



Catalytic performance of polyvinylidene fluoride (PVDF) supported TiO₂ additive at microwave conditions

Huseyin Gumus^{1*}  

¹University of Bilecik Seyh Edebali, Vocational School of Osmaneli, 11500, Osmaneli, Bilecik/Turkey

Abstract: TiO₂ is a widely used additive material to improve the properties of filtration membranes. As far as its contribution to filtration performance, TiO₂ acts as a catalytic agent. In this study, the catalytic activity of TiO₂ added PVDF flat sheets (membranes) prepared by the phase inversion method, and we tested them on the oxidation of benzyl alcohol at microwave irradiation. We investigated the structure, thermal behaviors, and morphology of samples by FTIR, TG-DTA, and SEM analysis, respectively. Contact angle measurements determined the hydrophilicity, and we observed the interaction between TiO₂ and PVDF chain. TiO₂-added PVDF membranes had improved filtration and rejection performance. 32.4% BSA rejection was obtained with composites while it was 7.5% for the pristine membrane. We obtained 93.86% conversion and 56% selectivity with composites in a microwave-assisted batch reactor. The decomposition of the polymer increased with a 6% additive due to the catalytic effect of TiO₂ then, and it decreased with further loading. We obtained detailed evidence by activation energies (E_a) of decomposition calculated by Kissinger's method. The microwave-assisted catalytic effect of TiO₂ inside the polymeric matrix promise to obtain fast, high yielded, and disposable membrane materials for catalytic reactors to in-situ production of fine chemicals.

Keywords: Alcohol oxidation, filtration membranes, PVDF, degradation, TiO₂.

Submitted: August 26, 2019. **Accepted:** March 24, 2020.

Cite this: Gumus H. Catalytic performance of polyvinylidene fluoride (PVDF) supported TiO₂ additive at microwave conditions. JOTCSA. 2020;7(2):361-74.

DOI: <https://doi.org/10.18596/jotcsa.610886>.

***Corresponding author.** E-mail: (huseyin.gumus@bilecik.edu.tr), Tel: (+90 228 214 1841), Fax: (+90 228 214 1342).

INTRODUCTION

Filtration and separation membranes caused great interest in obtaining more improved performance, such as high purity, fast, and easy yields. One of the most effective routes to obtain highly efficient filtration membranes was the preparation of composites, which are a combination of two or more components. Zeolite, metal oxides, carbon-based molecular sieves, and clays were commonly used organic/inorganic filler materials into the polymer matrix (1). Researchers preferred TiO₂ as additive materials for filtration membranes due to their multi-functional properties such as providing thermal and physical resistance, tunable pore, and channels in addition to its photocatalytic activity (2). Degradation of organic compounds were

conducted by using TiO₂ at the form of suspended in solution or immobilized to support by NIPS, TIPS and spinning processes or grafting to membrane surface (3-9). Among those, suspended TiO₂ provided high activity, but separation from the solution and regeneration became an environmental issue, so it restricts the usage of suspension. Researchers adopted the application of the TiO₂-immobilized polymer matrix, and they used composite membranes, mainly separation of particles, degradation of organic contaminants, production of fine chemicals, and bacterial removal. Researchers used Ag particles combined with TiO₂-Perlite for the degradation of methylene blue removal under UV light radiation (10). Hydroxyl groups that emerged on the surface of composites turned to hydroxyl radicals when UV

radiation exposed to them, and these induced to the decomposition of organic dye, waste, and bacteria.

Some authors also prepared TiO₂ dispersed filtration membranes and investigated in terms of additive size, additive ratio, as far as they met the composition, and coagulation conditions (11,12). An extended summary was reported by Mendret et al. about TiO₂-deposited polymers, particularly for the combination of TiO₂ and PVDF (13). TiO₂ provided excellent hydrophilicity and permeation to filtration membranes. Mainly, embedded membranes having nanosized particles performed better antifouling properties compared with their pristine forms (14,15). Self-cleaning ability is related to the photocatalytic activity of TiO₂ immobilized on the membranes.

Some authors prepared additive contained polymeric or ceramic matrixes to achieve instant reaction of substrates during filtration as catalytic membrane reactors. The common advantages of these systems are easy reaction and separation with low cost and reusability. Some researchers conducted phenol hydroxylation and p-aminophenol production by hydrogenation of p-nitrophenol on ceramic membrane reactors with high yield (16,17). For the oxidation of phenol with peroxide, the authors used a packed bed reactor consisting of FeZSM-5 zeolite immobilized on silicon carbide (SiC) foam catalyst. At 60 °C and 1 mL min⁻¹ flow, the researchers obtained 3.4 kJ mol⁻¹ activation energy of phenol degradation with 95 h⁻¹ turnover frequency. These kinds of systems require polymeric materials that have high physical and chemical resistance. PVDF is known for its high chemical, physical, and thermal resistance, and we see its use for chemical reactors and applications using UV light irradiation (18).

On the other hand, TiO₂ can be used to dispose of polluting polymers, organics, and polymeric materials economically, for instance, the application of polyethylene degradation by PAM grafted TiO₂ (19). A group of researchers investigated the photocatalytic degradation of the polystyrene matrix by the immobilized TiO₂, and they recorded a decrease at the molecular weight of the polymer (20). Thermal behaviors are also essential indicators about the resistance capacity of polymer, and those provide information about the interaction of additive with a polymer matrix (21).

In general, under appropriate rates, TiO₂ contributed better thermal stability to the polymer matrix. Polymer coated by nucleated additives induces crystalline formation on polymer during the phase separation (22–24). According to literature overviewed, TiO₂ immobilized/embedded/

coated polymeric composite membranes have better thermal resistance in addition to improved flux, rejection, and other filtration properties compared with pristine forms.

In this study, we aimed to determine the catalytic and thermal oxidative degradation properties and their filtration performance of TiO₂-blended PVDF membranes prepared at different mass ratios. In distinct energy supply, we conducted the oxidation experiments of benzyl alcohol in a microwave radiated batch reactor cooled with a condenser. We also investigated the polymer decomposition behaviors of TiO₂ (inside the structure) by detailed thermal analysis and decomposition enthalpies calculated by the Kissinger's method. We evaluated whether these are usable or not as a catalytic membrane at microwave conditions to get a fast and environmentally friendly design.

We tested only 0.5-4% TiO₂ contained filtration membranes in terms of filtration performances due to the inconvenience of the filtration ability of high loading composites. We also investigated the effect of additive ratio and dispersion of particles on the membrane properties on the heat resistance of composite membrane and disposal method for polymeric waste by the obscured thermal-oxidative activity of TiO₂ in addition to its well-known photocatalytic activity.

EXPERIMENTAL SECTION

Materials

Polyvinylidene fluoride, PVDF (Solef 6010), was used as the polymer material without any purification with N, N-dimethylformamide (DMF; Sigma Aldrich) as a solvent and distilled water. For the synthesis of TiO₂, titanium(IV) isopropoxide, Ti[OCH(CH₃)₂]₄ (284.22 g/mol, 97% w/w, 0.960 g/mL), sodium chloride, NaCl (58.44 g/mol), ethanol, C₂H₅OH (46.06 g/mol, 0.789 g/mL) were purchased from Sigma-Aldrich. We used a model protein-solution with bovine serum albumin, BSA (MW: 66000 Da, ≥98% purity, Sigma Aldrich) with boric acid, H₃BO₃ (MW: 61.83 g/mol, Sigma-Aldrich), ortho-phosphoric acid, H₃PO₄ (MW: 98 g/mol, Sigma-Aldrich) and acetic acid, CH₃COOH (MW:60.05 g/mol, 99.7%, Sigma-Aldrich) as acidity adjustment. We procured benzyl alcohol and hydrogen peroxide (30% w/v) from Panreac.

Preparation of TiO₂ and TiO₂-PVDF composite membranes

We prepared the TiO₂-blended PVDF membranes by wet-phase inversion technique determined in a report (25). To synthesize TiO₂ particles, titanium(IV) isopropoxide (0.11 mol/L) and NaCl solution (%1 w/w) were mixed in a round-bottomed flask and stirred with a magnetic stirrer for ten minutes. We then left the obtained slurry to

rest for approximately 12 hours. It was then filtered and washed with hot ethanol and water. The precipitate was dried at 60 °C and ground to powder at the size of 5-100 µm. An appropriate amount of dry solid was weighed and dissolved in DMF by ultrasonication. We added it to the polymer solution obtained by dissolving PVDF (1.6 g) in DMF (10 mL) as a 14% mass ratio in terms of polymer to solvent. The mixture of PVDF/DMF/TiO₂ was stirred at 250 rpm at 65 °C for 12 hours, and we kept it in the ultrasonication bath for 10 minutes to obtain a homogeneous dispersion. The mixture was waited for a time to prevent air

bubbles and cast on to a flat surface (15 cm x 15 cm) uniformly by a 300 µm casting knife at 25 °C. After exposure to air for 10 seconds, we quickly immersed the glass plate into the coagulation bath. Figure 1 represents the steps of preparation. Membranes were dried and used for characterization and alcohol oxidation. We stored the filtration membranes in distilled water for filtration experiments. Membranes contain TiO₂ at the rate of 0, 0.5, 1, 2, 4, 6, and 8% according to the total mass of combination were determined as PVDF, T05-P, T1-P, T2-P, T4-P, T6-P, and T8-P respectively.

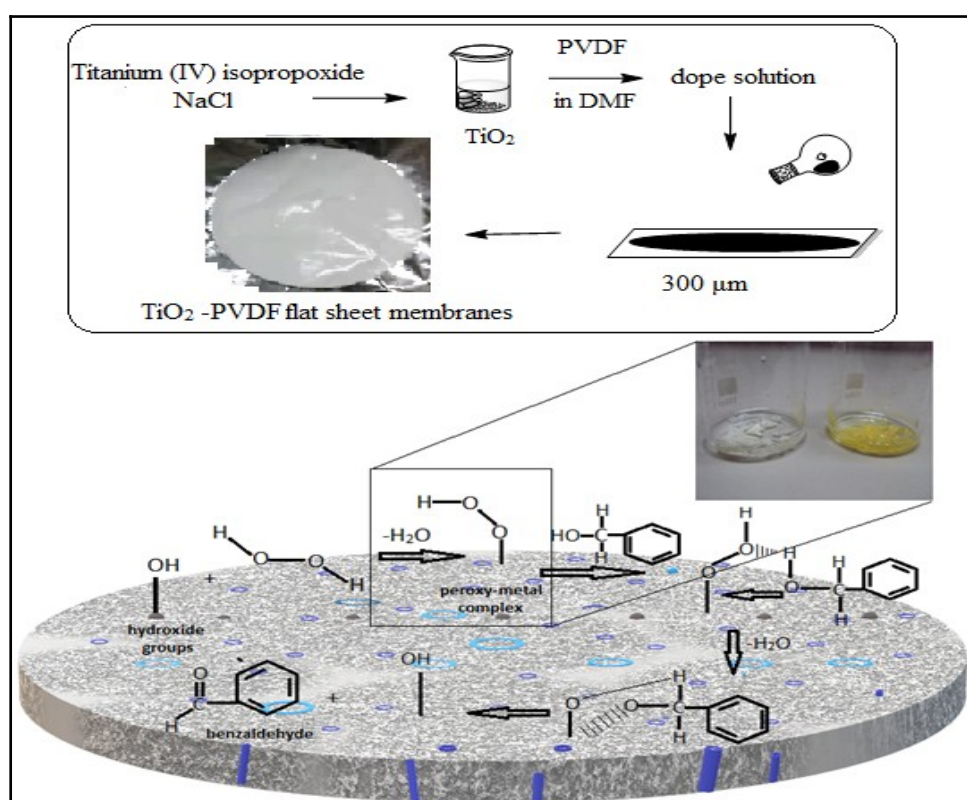


Figure 1: Illustration for the preparation of TiO₂-PVDF and peroxy metal complex.

Characterization of TiO₂ and TiO₂-PVDF composite membranes

We recorded the FTIR spectra of TiO₂ and membranes in the region between 4000 and 650 cm⁻¹ by a Perkin-Elmer FTIR spectrometer. Thermal stability and content of inorganic matter of samples were investigated by the thermogravimetric analyzer (TG-DTA, Exstar 7020) under the aerial atmosphere. We have adjusted typical conditions as about 5-7 mg of sample weight and 20 °C/min heating rate. We evaluated the thermal decomposition effect of TiO₂ to polymer, and we heated the samples in 50-1000 °C temperature range by 5, 10, 15, 20 and 30 °C/minute heating rates. The hydrophilicity of membranes was analyzed by a KSV Attention contact angle analyzer (Finland) at 25 °C temperature. The morphology of membranes was

examined by Carl Zeiss ULTRA Plus SEM device (Germany) at 10 kV. We photographed the cross-section images of samples broken in liquid nitrogen. As a model contaminant, we used BSA to determine membrane performance. We have analyzed the absorbance of the contaminant with a UV-visible spectrophotometer (PG Instruments, T80) at 280 nm wavelength (24).

We determined the water uptake capacity (WU) of membranes stored in water by measuring the weight of wet (W_w) and dried (W_d) membranes dried at 40 °C in a vacuum oven for 2 hours. We used Equation 1 to calculate.

$$WU(\%) = \frac{W_w - W_d}{W_w} \times 100$$

(1)

Pore percentage called as membrane porosity (PO) was calculated by following eq. (2):

$$PO(\%) = \frac{W_w - W_d}{dA\delta} \times 100 \quad (2)$$

Where d is the density of deionized water at 25 °C (the temperature of studies conducted), A is the area of the membrane (cm²) and δ is the thickness of wet membrane (cm).

Water flux, rejection and antifouling performances of composite membranes

We measured the pure water flux (PWF) performances of membranes by collecting the permeated water (L/m²h) at ultrafiltration cross-flow membrane cell. We adjusted the transmembrane pressures (TMP) as 100, 200, and 300 kPa after pre-conditioning of membranes for 1-3 h (26-27). We calculated WF by Equation (3) (28).

$$WF = \frac{V}{At} \quad (3)$$

where V is the volume of water-permeated (L), A is the surface of the membrane (1.7x10⁻³ m²), and t represents the sampling time (h). Compaction factor (CF) means the physical resistance of membranes, and we calculated that by dividing the initial WF_i value by constant WF_c value. We prepared the 0.5 g/L BSA solution with phosphate buffer (0.01 mol/L, pH:7.4) and filtered it at 200 kPa. We determined the concentration of BSA in collected permeate with a UV-Vis spectrophotometer and calculated the rejection performance with Equation (4).

$$R(\%) = \left(1 - \frac{C_p}{C_f}\right) \times 100 \quad (4)$$

Where C_p and C_f stand for the concentration of initial and final solutions of BSA, respectively.

Catalytic activity experiments

A previous study investigated the catalytic activities on benzyl alcohol conversion of TiO₂-PVDF samples in a batch reactor (29) We put 0.02 g of TiO₂-PVDF membrane pieces (1.5x1.5 cm) kept in benzyl alcohol for the diffusion of the substrate into a 50 mL reaction cup along with 1 mmol benzyl alcohol and 1 mmol H₂O₂. We then applied 500 W microwave radiation in a cooled microwave oven for 8 minutes. We analyzed a sample with GC, taken from the reaction mixture with a syringe (without any filtration). We washed the pieces of the membrane with acetone and used these samples three times. We performed the calculation of conversion and benzaldehyde selectivity of samples according to Equations 6 and 7. We used powder TiO₂ as a catalyst with the same reaction conditions. We filtered the sample taken from the powder catalyst with a syringe filter before injection to the column.

$$Conversion\% (C\%) = \frac{C_{alcohol(initial)} - C_{alcohol(final)}}{C_{alcohol(initial)}} \times 100 \quad (6)$$

$$Selectivity\% (S\%) = \frac{\text{Amount of benzaldehyde}}{\text{Amount of all products}} \times 100 \quad (7)$$

RESULTS AND DISCUSSION

FTIR analysis of TiO₂ and TiO₂-PVDF membranes

We carried out FTIR analyses to understand the interaction of TiO₂ and the polymer chain. We have observed satisfactory evidence proving the blend of TiO₂ with a chain structure of PVDF in Figure 2.

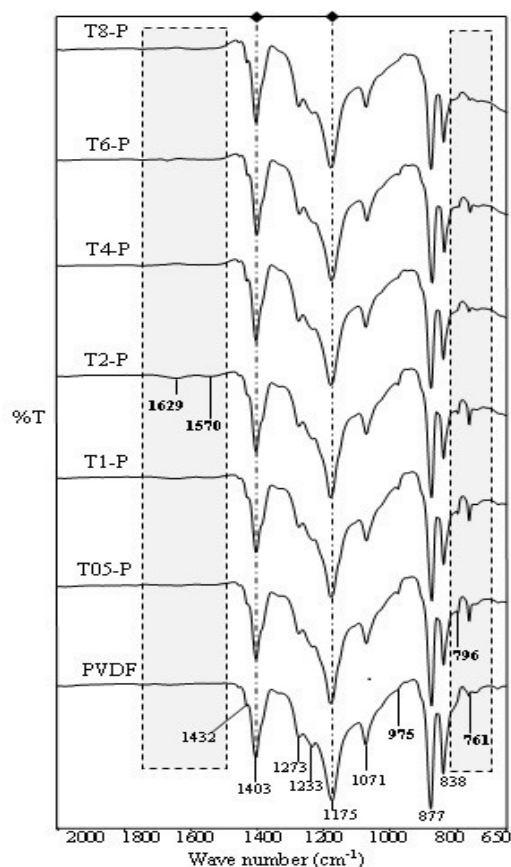


Figure 2: FT-IR spectra of TiO₂-PVDF samples.

α -phases of PVDF ascribed with 761, 796, and 975 cm^{-1} bands disappeared with increasing TiO₂ amount. This outcome indicated the formation of an amorphous structure with increased TiO₂ loading. We could see the superimposed FTIR bands of pristine and composites at the high wavenumber, but deviations emerged at the bands of 761, 976, and 1233 cm^{-1} due to increasing TiO₂. We observed characteristic CH₂ and CF₂ stretching vibrations at 1403, and 877-1175 cm^{-1} ,

respectively, and CF stretching bands of the PVDF chain at 1071 cm^{-1} . We obtained an essential indication for TiO₂ and PVDF interaction with the band at ca. 1570 cm^{-1} indicating the presence of OH groups on TiO₂ bonding with the PVDF chain (30-32). The band at 1629 cm^{-1} emerged due to the presence of the Ti-O-Ti structure and indicated possible hydrogen bonding between the oxygen of TiO₂ and fluorides of PVDF (23-25, 33). Figure 3 represents the possible bonding.

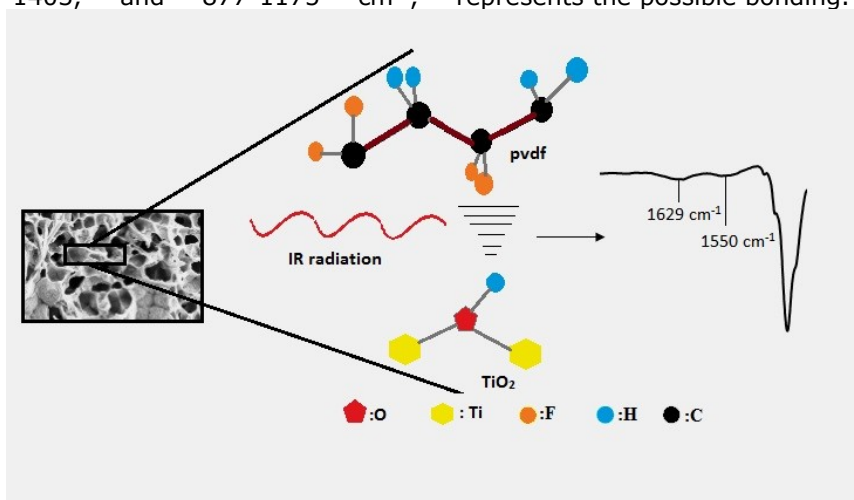


Figure 3: Estimated bonding of Ti-O-Ti with PVDF chain.

Morphology of composites

Figure 4 presents the cross-section SEM images of the composites to understand better the effect of TiO_2 addition on the structure of the membrane.

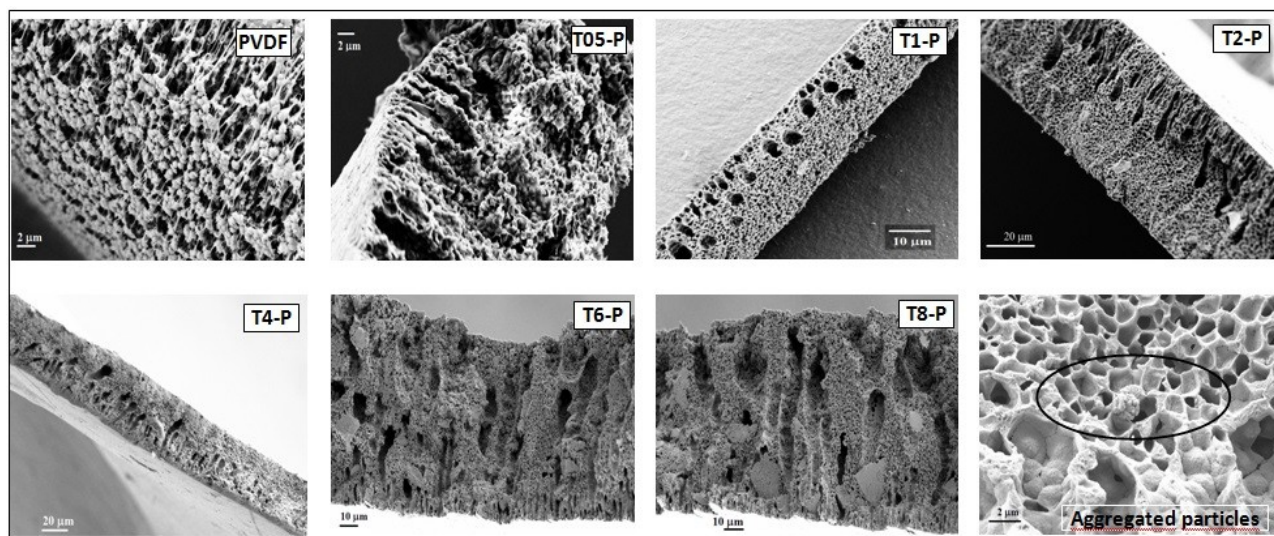


Figure 4: SEM images of TiO_2 -PVDF samples.

Bare PVDF and additive contained samples showed different morphology as mainly symmetric and asymmetric forms. PVDF membrane structure, having large holes among the polymer clusters, became sponge-like as could be seen at the image of T1-P with macroscopic voids. We observed that, for T2-P and T4-P, the uniform membrane structure consisting of finger-like pores connected to the sponge side. In general, we obtained appropriately dispersed particles for the samples which have finger-like pores, despite the aggregated TiO_2 remnants available among the pores. We also observed a severe deviation from uniformity for samples containing additive amounts at 6% and further.

Furthermore, a high amount of additive pressed the micro-pores and channels, which determine the permeation and rejection performances of membranes. Additive, along with the solvent type, has a prominent effect on the formation of membrane structure such as a sponge, macro, and finger-like properties according to the affinity of water (11). Researchers reported the crystalline form of TiO_2 and DMF as a solvent to result in a

thicker structure of hollow fiber membranes (34-35).

High water affinity of TiO_2 accelerated to mixing of coagulation water with polymer solvent (DMF) during phase inversion. Thus, the solvent separation occurred faster than additive-free samples. Due to the hydrophobic nature of PVDF, polymeric lumps formed containing large holes at the bare PVDF membrane. Structural changes observed by SEM images were compatible with the permeation results presented in Figure 6. With the further amount of TiO_2 deposition, convenient finger-like structures of membrane began to turn on dense sponge-like with large agglomeration. 4% TiO_2 amount was concluded as a maximum ratio to obtain sufficient filtration behavior.

Thermal analysis and thermal catalytic activity of composites

The thermal stability of samples was analyzed by TG and DTA to understand the effect of additive on to polymeric structure at the temperature ranges of 30-1000 °C (Figure 5). Ash contents obtained for the PVDF and TiO_2 contained PVDF samples were different from the additive ratios.

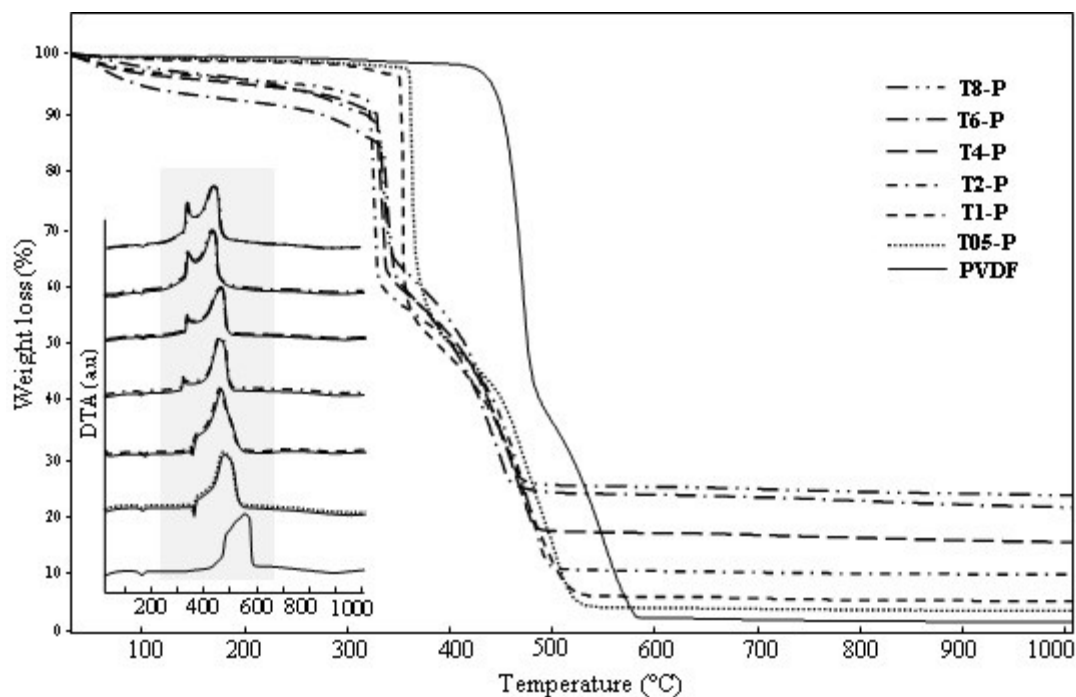


Figure 5: TG and DTA curves of TiO₂-PVDF samples.

During the calculation of the dope solution, only polymer and additives burned along with a small amount of solvent in the thermal analyzer. After the exposure of samples to heat, the remaining weight indicated to TiO₂ inside the membranes. The process burned all of the organic contents of the polymer. In Figure 5, we recorded that the degradation of neat PVDF started at 470 °C, whereas the degradation temperatures of composites were between 348-339 °C, which was a lower temperature than neat PVDF. We know that TiO₂ deposition onto polymeric support has

two opposite effects for the thermal behaviors of the samples. (1) TiO₂ may cover the surface of the polymer and improve the thermal resistance of the composite by protecting the polymer from direct exposing of oxygen or (2) thermal catalytic oxidation of TiO₂ may be dominant, and it may increase the thermal degradation of the organic structure due to thermal catalytic effect of TiO₂ at high temperatures (36). Patra and coworkers explained the increasing thermal resistance for the additive containing samples due to the escape of the radicals (20).

Table 1: Thermal behaviors of TiO₂-PVDF samples.

Sample	t _{onset} (°C)	t _{max} (°C)	t _{endset} (°C)	t% ₁₀ (°C)
PVDF	374	470	593	450
T05-P	351	362	546	361
T1-P	328	348	565	347
T2-P	328	348	541	347
T4-P	300	326	523	321
T6-P	312	332	503	320
T8-P	305	339	494	288

Rather than shielding, the catalytic thermal decomposition effect of additives dominated, and it decreased the on-set and max temperatures of TiO₂ contained samples (Table 1). Thermal degradation of samples accelerated, and end-set temperatures were recorded between 494-565 °C, whereas it was 593 °C for neat PVDF. Reduced degradation temperature values of additive containing samples are clear indicators for the thermal decomposition effect of TiO₂. Differential

thermal analysis (DTA) curves confirmed the results of the thermal degradation of the polymeric structure (Figure 5). Exothermic peaks of PVDF at 440-560 °C emerged after the burning of organic components was observed at lower temperatures with increasing TiO₂ amounts. Besides, we observed for T4-P, T6-P, and T8-P one more exothermic peak, which represents degradation, and these were different from PVDF. An endothermic peak at around 170 °C may

correspond to the melting point of polymer (37). Increasing of additive resulted in a decrease at the crystallinity of polymer, and TiO₂ clusters started to agglomerate differently. A disordered structure meant weakened binding of OH groups on TiO₂ with a PVDF chain pointed by FTIR results (see the section about FTIR). That induced the degradation effect of TiO₂ at high temperatures. We conducted the thermal analysis of samples to demonstrate the degradation effect of the additive at high heating rates: 5, 10, 15, 20, 30 °C/minute, and activation energy of samples were calculated by Kissinger’s method (38) according to TG results obtained under air. We calculated the activation

energies of degradation by linearization of β/T_{max}^2 versus $1/T_{max}$ according to Equation 1.

$$\left(\frac{\beta}{T_{max}^2}\right) = \left(\frac{AR}{E_a}\right) - \frac{E_a}{RT_{max}} \tag{1}$$

Where β is the heating rate, A is a pre-exponential factor, E_a is the calculated activation energy for degradation of samples, and R is the universal gas constant. By using the maximum degradation occurred, we calculated the activation energy values. We presented T_{max} and E_a values calculated by the mentioned method in Table 2.

Table 2: T_{max} and degradation energy values of TiO₂-PVDF samples.

TiO ₂ content (Wt. %)	5	10	15	20	30	E _a (kJ/mol)
-	447	470	444	460	482	193.5
0.5	342	362	334	345	353	135.8
1	340	348	355	365	378	138.5
2	335	347	348	355	374	136.9
4	314	326	337	347	366	95.1
6	329	332	336	343	351	217.4
8	334	339	339	344	351	305.5

The E_a of PVDF was 193.5 kJ/mol, and it was observed as 136.9 and 95.1 kJ/mol for T2-P and T4-P respectively under the air atmosphere. Thermal properties of composites given in Table 1 and Figure 5 are compatible with the activation energy values. In general, activation energy decreased with an increased amount of additive, relatively with changes of T_{onset} and T_{max} values. E_a values provided clear information about how the additive rate affected the degradation process. To bare TG results, very little increase was observed for max decomposition as can be assumed negligible. But 217.4 and 305.5 kJ/mol E_a values recorded for T6-P and T8-P respectively indicated that further loading of additive prevented the

degradation of the polymer due to the shielding effect of agglomerated spherical TiO₂ clusters. The thermal stability of PVDF decreased because of the thermal oxidative effect of TiO₂ until the 4% TiO₂, which is the final sufficient composition as a filtration membrane. After that activation energy increased, the shielding effect became dominant when the 6% and further additive loadings. We have observed competition between shielding and thermal decomposition effects until the 6% additive.

Filtration Performances of composites

We tested the water flux (WF) of membranes cross-flow filtration system (see Figure 6).

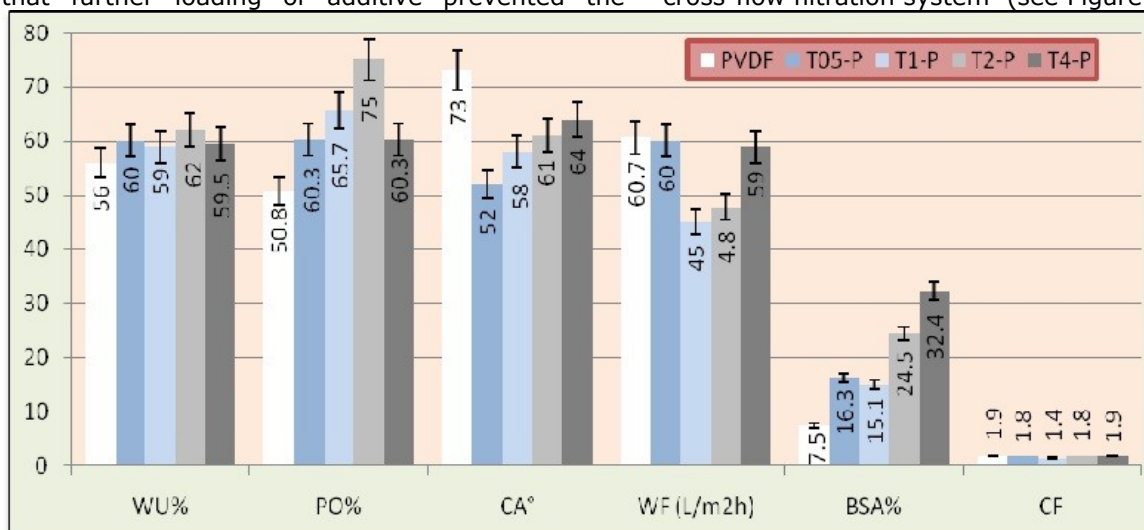


Figure 6: Filtration performances of PVDF and TiO₂-PVDF samples.

WF values decreased with increasing hydrophilic TiO₂ additive, which is controversial with the phenomena of the more hydrophilic, the more improved in water flux (39). Water permeation is commonly not only depending on hydrophilicity but also porosity, thickness, and water uptake (11). T2-P showed the highest porosity and water uptake for T2-P, which were 75% and 62%, respectively. Porosity and water uptake values of composite membranes were higher than that of the pristine PVDF membrane. As a controversy, water permeation of composites was lower than the PVDF membrane. In that case, we understood that the thickness and pore size determined the permeation performances of membranes. We saw the formation of a large number of small pores during phase separation. That was result of accelerated process induced by hydrophilic additives with increasing porosity. A relative change was observed among the porosity and water uptake values. Porosity and water uptake of PVDF were 50.8% and 56% respectively. High porosity with low water uptake of composites was also another proof for the existence of small pores. Effect of hydrophilic additive was confirmed by contact angle measurements. It is known that the smaller contact angle means the better hydrophilicity (40). Lower contact angle values were obtained for all samples compared with contact angles of PVDF (73°). Roughness of membrane surface suppressed the hydrophilic character of additive with further TiO₂ loading ratios. Due to agglomerated particles contact angles values were began to rise. Thick skin layer had a respectable effect on filtration performance and physical properties of membranes. Formation

of a thicker and stuck layer was induced by increasing viscosity of dope solution. That was confirmed by lower compaction values of membranes. Denser composition of composite membranes performed lower compaction values. We have concluded that the type and amount of additive have a considerable effect on the pores, voids, and channels of all structures with physical effects. BSA rejection performances were investigated to interpret structural characteristics of membranes. Dense structure of membrane provided an advantage as high rejection performance. 32.4% BSA rejection values was obtained for T4-P sample while it was only 7.5% for PVDF. Permeable polymeric lumps determined in SEM images of PVDF (Figure 4), provided low rejection although moderate flux. New structures formed by TiO₂ addition presented tightened skin which was beneficial for filtration and higher rejection. Generally it was known that particle accumulation on the surface occurs by electrostatic interaction between surface and particles (38). Flux recovery values a little reduced due to the interaction of BSA and surface groups. The roughness of the membrane promoted to an accumulation of rejected particles on the surface of the membrane.

The catalytic activity of composites

We have used a round-bottomed flask to test the catalytic activity of TiO₂-PVDF flat sheets on benzyl alcohol oxidation. We adjusted the alcohol and peroxide ratio to 1:1 with 0.06 g catalyst without solvent. We put the reaction flask cooled with a condenser into the microwave furnace. Table 3 shows the results of optimization experiments.

Table 3: Conversion and benzaldehyde selectivity of TiO₂-PVDF composite samples.

Entry	Catalyst (amount, g)	Temperature (°C)	Reaction Time (min.)	Conversion-selectivity (%)
1	-	R.T.	240	-
2	-	80	240	-
3	-	80*	8	-
4	TiO ₂ (0.06)	R.T.	240	-
5	TiO ₂ (0.06)	80	240	26.2-33.5
6	TiO ₂ (0.06)	80*	8	86.0-4.4
7	T2-P (0.06)	R.T.	240	-
8	T2-P (0.06)	80	240	25.5 - 45
9	T05-P (0.06)	80*	8	-
10	T1-P (0.06)	80*	8	53.15 -21.4
11	T2-P (0.06)	80*	8	67 - 29
12	T4-P (0.06)	80*	8	62.9-45.4
13	T6-P (0.06)	80*	8	66.6-16.2
14	T8-P (0.06)	80*	8	27-26
15	T4-P (0.02)	80*	8	70.7 - 36
16	T4-P (0.04)	80*	8	76.9 - 5.9
17	T4-P (0.08)	80*	8	54 - 20
18**0	T4-P (0.06)	80*	8	48.46 - 4.35
19**0.2	T4-P (0.06)	80*	8	59.4 - 34.3
20**0.4	T4-P (0.06)	80*	8	62.5 - 48

21**0.6	T4-P (0.06)	80*	8	56.37- 56
22**0.8	T4-P (0.06)	80*	8	56.5 - 56
23**1	T4-P (0.06)	80*	8	73 - 38.7
24**1.5	T4-P (0.06)	80*	8	93.86 - 5.84
25-300W	T4-P (0.06)	80*	8	76 - 17
26-700W	T4-P (0.06)	80*	8	70 - 36
2. reuse	T4-P (0.06)	80*	8	63.4 - 74
3. reuse	T4-P (0.06)	80*	8	80 - 37
4. reuse	T4-P (0.06)	80*	8	59 - 35

We carried out the reaction in a 50 mL flask with a condenser in a 500 W microwave, with 1 mmol H₂O₂ and 1 mmol benzyl alcohol ratio unless otherwise stated. We introduced the mixture to an HP-5 column for GC analysis.

*: in microwave radiation.

** :H₂O₂: Benzyl alcohol ratio (mol)

We investigated the effects of various parameters on the reaction yield. A high conversion with high selectivity was a considerable result. A satisfactory result was obtained with 0.06 g T4-P sample. That was directly related to easy transferring of substrate to active sites of catalyst. Structural properties such as pore distribution, pore radius, cross-section thickness, and the additive were essential determiners of substrate flow and, consequently, the reaction yield. Moderate pores provided easy transferring of substrate conversely, pressed structure complicated transportation. As could be seen, T4-P has a more hydrophobic character inferred from its high contact angle and low water uptake capacities. That makes it more attractive to organic substrate. The more organic substrate diffused inside the active sites give the more selectivity. On the other hand, selectivity performance of T4-P may due to its prevention effect of over peroxide transferring due to its hydrophobicity. Experiments conducted to

understand peroxide ratio at the reaction yield supported this estimation. High conversion but low selectivity was obtained with increased peroxide ratio. That meant that benzyl alcohol was converted into other oxidation products. Changes of peroxide alcohol ratio may resulted in different products (39). 0.4 (H₂O₂: benzyl alcohol molar ratio) was considered as optimum peroxide amount. The results of 0 and 0.2 ratios specified stoichiometric peroxide shortage. Reason for low selectivity, although increased peroxide ratio may be decomposition or transferring problem of peroxide (29). The catalyst amount had a direct effect on the product type. Highest conversion was obtained when the TiO₂-PVDF was 0.04 g but low selectivity. It decreased when it was further than 0.06 g. Increase at the conversion was related with high amount of catalysis. However, the exact reason may be over-oxidation of benzaldehyde or direct conversion of benzoic acid to its by-products (see Figure 7) (41).

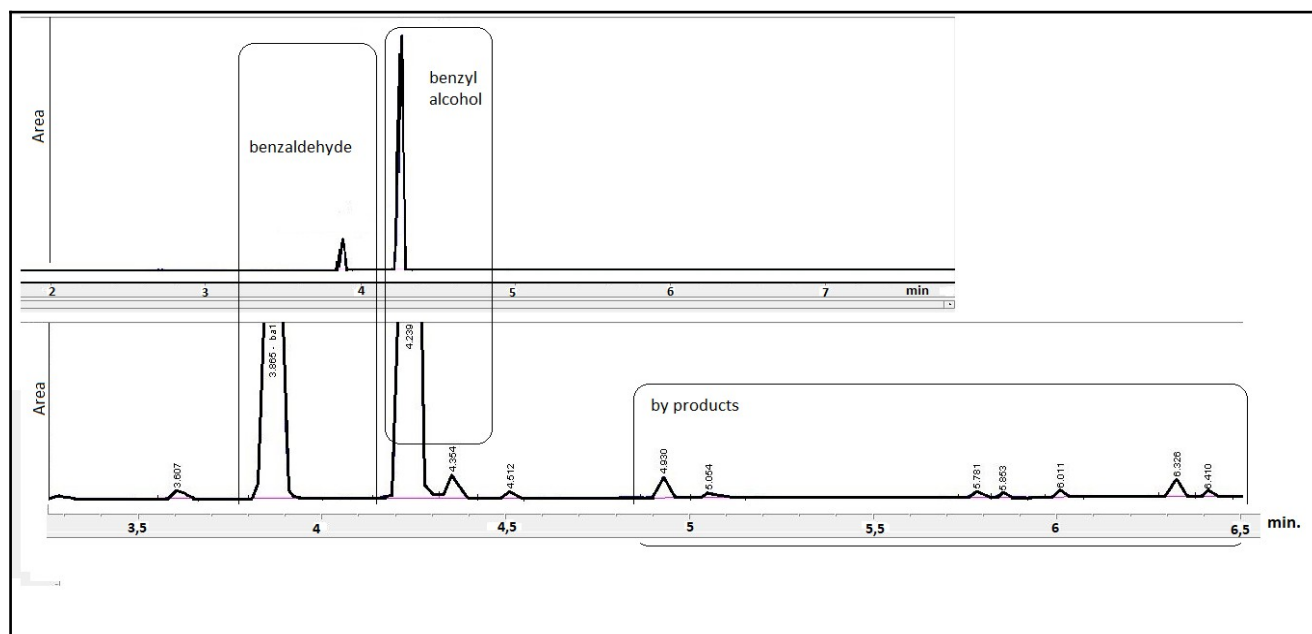


Figure 7: GC peaks of benzaldehyde and other products.

In this study, we saw that complex peroxy-metal structures formed as a result of the interaction of hydrogen peroxide and metals on the catalyst (Figure 1). During the oxidation, peroxide decomposed quickly in the presence of a high amount of catalyst to give active hydroxyl radicals. Even though a high number of hydroxyl radicals desired to the conversion of a substrate, the formation of active reactants quickly may cause over oxidation of reactant, consequently low selectivity. We did not observe notable results with different microwave radiation. (see Table 3). We separated TiO₂-PVDF pieces from the mixture and washed with acetone, then reused three times. Washing with organic solvent wiped off all organic residues and opened the channels. However, the structure gets shrunk with further reuse due to microwave radiation. Benzyl alcohol conversion and benzaldehyde selectivity decreased gradually, with ongoing usage. TiO₂ embedded PVDF flat sheets performed moderate yield in addition to easy usage, low cost, and fast results at solvent-free area. The advantages of easy separation from the reaction mixture without solvent and reusability were considered remarkable output for oxidation reactions.

CONCLUSION

We combined the well-known advantages of TiO₂ additive on PVDF membranes to obtain sufficient, fast, and environmentally friendly chemical production systems with microwave radiation. TiO₂ provided improvement filtration and better BSA rejection by increasing hydrophilicity of the polymeric matrix for almost all membranes. 4% TiO₂ contained samples presented 32.4% BSA rejection while it was only 7.5% for PVDF. TiO₂ interaction with PVDF ascribed by the FTIR bands of Ti-OH and Ti-O-Ti vibrations.

We found a clear insight by the thermal behaviors of TiO₂ on the membrane structure, which are not available in the primary thermal analysis results. Activation energies belong to polymeric decomposition were recorded at different heating rates. Unlike preventing effect, TiO₂ induced thermal decomposition of the polymer due to its catalytic activity, especially at high temperatures.

TiO₂-PVDF membrane pieces were used as a microwave-induced catalyst to obtain benzaldehyde from benzyl alcohol in a batch reactor. 62.9% conversion and 45.4% selectivity with the T4-P sample. We investigated the possibility of faster and cleaner in-situ production of fine chemicals on the TiO₂-catalyzed filtration system combined with microwave radiation. TiO₂-added PVDF self-recyclable membranes have a high potential to the production of chemicals on

filtration systems with microwave energy, besides their well known hydrophilic, antifouling, and high rejection properties.

ACKNOWLEDGEMENTS

This research did not receive any specific grant from funding agencies in the public, commercial, or not for profit sectors.

Availability of the data

The processed data required to reproduce these findings are available to download from [<https://data.mendeley.com/datasets/w2678cnzsg/1>].

REFERENCES

1. Xu Z, Wu T, Shi J, Teng K, Wang W, Ma M, et al. Photo catalytic antifouling PVDF ultra filtration membranes based on synergy of graphene oxide and TiO₂ for water treatment. *Journal of Membrane Science*. 2016;520:281–93.
2. Nor NAM, Jaafar J, Ismail AF, Mohamed MA, Rahman MA, Othman MHD, et al. Preparation and performance of PVDF-based nanocomposite membrane consisting of TiO₂ nanofibers for organic pollutant decomposition in wastewater under UV irradiation. *Desalination*. 2016;391:89–97.
3. Laohaprapanon S, Vanderlipe AD, Doma BT, You SJ. Self-cleaning and antifouling properties of plasma-grafted poly(vinylidene fluoride) membrane coated with ZnO for water treatment. *Journal of the Taiwan Institute of Chemical Engineers*. 2017;70:15–22.
4. Munoz-Bonilla A, Kubacka A, Fernandez-Garcia M, Ferrer M, Fernandez-Garcia M, Cerrada ML. Visible and ultraviolet antibacterial behavior in PVDF-TiO₂ nanocomposite films. *European Polymer Journal*. 2015;71:412–22.
5. You SJ, Semblante GU, Lu SC, Damodar RA, Wei TC. Evaluation of the antifouling and photo catalytic properties of poly(vinylidene fluoride) plasma-grafted poly(acrylic acid) membrane with self-assembled TiO₂. *Journal of Hazardous Materials*. 2012;237–238:10–9.
6. Kim BS, Lee J. Macroporous PVDF/TiO₂ membranes with three-dimensionally interconnected pore structures produced by directional melt crystallization. *Chemical Engineering Journal*. 2016;301:158–65.
7. Wang Q, Wang X, Wang Z, Huang J, Wang

- Y. PVDF membranes with simultaneously enhanced permeability and selectivity by breaking the tradeoff effect via atomic layer deposition of TiO₂. *Journal of Membrane Science*. 2013;442:57–64.
8. Zhang X, Wang Y, You Y, Meng H, Zhang J, Xu X. Preparation, performance and adsorption activity of TiO₂ nanoparticles entrapped PVDF hybrid membranes. *Applied Surface Science*. 2012;263:660–5.
9. Shi F, Ma Y, Ma J, Wang P, Sun W. Preparation and characterization of PVDF / TiO₂ hybrid membranes with different dosage of nano-TiO₂. *Journal of Membrane Science*. 2012;389:522–31.
10. Duranoğlu D. Preparation of TiO₂/perlite composites by using 23-1 Fractional Factorial Design. *Journal Of The Turkish Chemical Society, Section A: Chemistry*. 2016; 3(3):299-312.
11. Cao X, Ma J, Shi X, Ren Z. Effect of TiO₂ nanoparticle size on the performance of PVDF membrane. *Applied Surface Science*. 2006;253(4):2003–10.
12. Oh SJ, Kim N, Lee YT. Preparation and characterization of PVDF/TiO₂ organic-inorganic composite membranes for fouling resistance improvement. *Journal of Membrane Science*. 2009;345(1–2):13–20.
13. Méricq J-P, Mendret J, Brosillon S, Faur C. High performance PVDF-TiO₂ membranes for water treatment. *Chemical Engineering Science*. 2015;123:283–91.
14. Wei Y, Chu HQ, Dong BZ, Li X, Xia SJ, Qiang ZM. Effect of TiO₂ nanowire addition on PVDF ultra filtration membrane performance. *Desalination*. 2011;272(1–3):90–7.
15. Wang Q, Wang Z, Zhang J, Wang J, Wu Z. Antifouling behaviors of PVDF/nano-TiO₂ composite membranes revealed by surface energetics and quartz crystal microbalance monitoring. *RSC Adv*. 2014;4(82):43590–8.
16. Torlak Y. Polyoxotungstate/oxy-graphene nanocomposite multilayer films for electro catalytic hydrogen evolution. *Journal of the Turkish Chemical Society, Section A: Chemistry*. 2018;
17. Ou X, Pilitsis F, Jiao Y, Zhang Y, Xu S, Jennings M, et al. Hierarchical Fe-ZSM-5/SiC foam catalyst as the foam bed catalytic reactor (FBCR) for catalytic wet peroxide oxidation (CWPO). *Chemical Engineering Journal*. 2019;362(July 2018):53–62.
18. Fadaei A, Salimi A, Mirzataheri M. Structural elucidation of morphology and performance of the PVDF/PEG membrane. *Journal of Polymer Research*. 2014;21(9).
19. Liang W, Luo Y, Song S, Dong X, Yu X. High photo catalytic degradation activity of polyethylene containing polyacrylamide grafted TiO₂. *Polymer Degradation and Stability*. 2013;98(9):1754–61.
20. Patra N, Salerno M, Malerba M, Cozzoli PD, Athanassiou A. Improvement of thermal stability of poly(methyl methacrylate) by incorporation of colloidal TiO₂ nanorods. *Polymer Degradation and Stability*. 2011;96(7):1377–81.
21. Yang W, Wang H, Zhu X, Lin L. Development and Application of Oxygen Permeable Membrane in Selective Oxidation of Light Alkanes. *Topics in Catalysis*. 2005;35(1–2):155–67.
22. Songur Z, Acar M. Chloromethylation of Polysulfone. *Journal of the Turkish Chemical Society, Section A: Chemistry*. ; 1(1):5.
23. Shi F, Ma J, Wang P, Ma Y. Effect of quenching temperatures on the morphological and crystalline properties of PVDF and PVDF-TiO₂ hybrid membranes. *Journal of the Taiwan Institute of Chemical Engineers*. 2012;43(6):980–8.
24. Li W, Li H, Zhang YM. Preparation and investigation of PVDF/PMMA/TiO₂ composite film. *Journal of Materials Science*. 2009;44(11):2977–84.
25. Dehestaniathar S, Khajelakzay M, Ramezani-Farani M, Ijadpanah-Saravi H. Modified diatomite-supported CuO-TiO₂ composite: Preparation, characterization and catalytic CO oxidation. *Journal of the Taiwan Institute of Chemical Engineers*. Elsevier Ltd.; 2016;58:252–8.
26. Hashino M, Hiram K, Ishigami T, Ohmukai Y, Maruyama T, Kubota N, et al. Effect of kinds of membrane materials on membrane fouling with BSA. *Journal of Membrane Science*. 2011;384(1–2):157–65.
27. Abdelrasoul A, Doan H, Lohi A. Fouling in Membrane Filtration and Remediation Methods. In: *Mass Transfer - Advances in Sustainable Energy and Environment Oriented Numerical Modeling*. 2013.
28. Anvari A, Yancheshme AA, Rekaabdar F, Hemmati M, Tavakolmoghadam M, Safekordi A. Erratum to: PVDF/PAN Blend Membrane: Preparation, Characterization and Fouling Analysis (*J Polym Environ*, (2017), 25, 1348,

10.1007/s10924-016-0889-x). Journal of Polymers and the Environment. 2017;25(4):1359–60.

29. Gumus H. Performance investigation of Fe₃O₄ blended poly (vinylidene fluoride) membrane on filtration and benzyl alcohol oxidation: Evaluation of sufficiency for catalytic reactors. Chinese Journal of Chemical Engineering. Elsevier B.V.; 2019;27(2):314–21.

30. Mokhtari-Shourijeh Z, Montazerghaem L, Olya ME. Preparation of Porous Nanofibers from Electrospun Polyacrylonitrile/Polyvinylidene Fluoride Composite Nanofibers by Inexpensive Salt Using for Dye Adsorption. Journal of Polymers and the Environment. 2018;26(9):3550–63.

31. Shi F, Ma Y, Ma J, Wang P, Sun W. Preparation and characterization of PVDF/TiO₂ hybrid membranes with different dosage of nano-TiO₂. Journal of Membrane Science. 2012;389:522–31.

32. Kubacka A, Ferrer M, Cerrada ML, Serrano C, Sanchez-Chaves M, Fernandez-Garcia M, et al. Boosting TiO₂-anatase antimicrobial activity: Polymer-oxide thin films. Applied Catalysis B: Environmental. 2009;89(3–4):441–7.

33. Attarchi N, Montazer M, Toliyat T. Ag/TiO₂/γ-CD nano composite: Preparation and photo catalytic properties for methylene blue degradation. Applied Catalysis A: General. 2013;467:107–16.

34. He X, Sanders S, Aker WG, Lin Y, Douglas J, Hwang H. Assessing the effects of surface-bound humic acid on the phototoxicity of anatase and rutile TiO₂ nanoparticles in vitro. Journal of Environmental Sciences. 2015;2:50–60.

35. García-Fernández L, García-Payo MC, Khayet M. Effects of mixed solvents on the structural morphology and membrane distillation performance of PVDF-HFP hollow fiber membranes. Journal of Membrane Science. 2014;

36. J. L. Falconer, K. A. Magrini-Bair. Photo catalytic and Thermal Catalytic Oxidation of Acetaldehyde on Pt/TiO₂. Journal of Catalysis. 1998;179:171–8.

37. Figoli A, Simone S, Criscuoli A, Al-Jilil SA, Al Shabouna FS, Al-Romaih HS, et al. Hollow fibers for seawater desalination from blends of PVDF with different molecular weights: Morphology, properties and VMD performance. Polymer. Elsevier Ltd; 2014;55(6):1296–306.

38. Sánchez-Jiménez PE, Criado JM, Pérez-Maqueda LA. Kissinger kinetic analysis of data obtained under different heating schedules. Journal of Thermal Analysis and Calorimetry. 2008;

39. Saleh TA, Gupta VK. Synthesis and characterization of alumina nano-particles polyamide membrane with enhanced flux rejection performance. Separation and Purification Technology. 2012;

40. Molinari R, Poerio T. Preparation, characterisation and testing of catalytic polymeric membranes in the oxidation of benzene to phenol. Applied Catalysis A: General. 2009;358(2):119–128.

41. Zhu Y, Wang B, Wang H, Liu X, Licht S. Towards efficient solar STEP synthesis of benzoic acid: Role of graphite electrode. Solar Energy. Elsevier Ltd; 2015;113:303–12.



Poly(*o*-aminobenzyl alcohol) Films with and without Organic Compound on AISI 316 Surface; Synthesis and the Corrosion Performances

Ali Tuncay OZYILMAZ¹  , Begüm OZGEN¹,  , Cumali CELIK²  

¹ Hatay Mustafa Kemal University, Faculty of Arts and Sciences, Department of Chemistry, Antakya / Hatay, Turkey

² University of Yalova, Yalova Vocational School, Property Protection and Security Department, Yalova, Turkey

Abstract: In this work, we obtained the anticorrosive properties of polymer films (SS/PABA and SS/PABA-ORG) synthesized on stainless steel surface by adding an organic substance to aniline derived *o*-aminobenzyl alcohol monomer synthesis medium. Firstly, we prepared the polymer coating bath by dissolving 0.15 M *o*-aminobenzyl alcohol monomer in the electrolyte solvent containing acetonitrile and 0.15 M LiClO₄. From this bath, poly (*o*-aminobenzyl alcohol) (PABA) film was synthesized in 30 segments by cyclic voltammetry (CV) technique at a scanning rate of 50 mV/s at a potential range of -0.20/1.80 V on the AISI 316 (SS) working electrode in contrast to the platinum electrode. For the synthesis of organic structure doped polymer film (PABA-ORG), we repeated the same synthesis process by dissolving C₂₁H₂₇NO_{2(k)} (ORG) at low concentration in the same bath. We investigated the corrosion performances of bare SS, SS/PABA, and SS/PABA-ORG substrates, using open circuit potential – time, anodic polarization, and AC impedance techniques in the solution of corrosion study. As a result, we observed that the organic additive added to the synthesis medium caused changes in the synthesis behavior of PABA. Corrosion performance tests showed that PABA and PABA-ORG films increased the corrosion protection performance of the SS electrode, and we observed a reduction of the corrosion rate of the SS electrode.

Keywords: corrosion; electropolymerization; *o*-aminobenzyl alcohol; AISI316.

Submitted: November 02, 2019. **Accepted:** March 24, 2020.

Cite this:

DOI: <https://doi.org/10.18596/jotcsa.641851>.

Corresponding author. E-mail: atuncay@mku.edu.tr.

INTRODUCTION

Corrosion is the physical and chemical erosion of metals and a momentous event that can cause serious harm to humanity despite today's developing technology. This phenomenon is because metals generally undergo electrochemical and chemical reactions within the atmosphere due to environmental factors. So the materials might receive severe damage. To prevent these damages and losses, researchers have been developing various methods and materials for years. Stainless steel, which is one of these materials, is resistant to many corrosive environments with its quality and

stable oxide layers formed by chromium and nickel metals in its compositions. However, it can corrode faster than expected in environments containing chloride and sulfate (1-3). AISI 316 series stainless sheets of steel, which are frequently preferred by the industry due to their cheapness, easy availability, and machinability, also have the disadvantage mentioned in such environments. Although there are many methods used to prevent this and increase the protective effect of stainless steel, conductive polymer coatings have received much attention in the literature recently (4-10). In particular, polyaniline and its derivatives are conductive polymers that are frequently studied and

give fruitful results. The main characteristics of conductive polymers are their high conductivity, corrosion-resistant, and non-corrosive enough to be brought to the metal level.

Furthermore, their electrochemical coating on technical metals results in meager costs, under constant potential, constant current, and cyclic voltammetry. Besides, one of the commonly applied techniques in recent years is cyclic voltammetry. In this technique, after the monomer oxidation, the polymer film is converted into induction and oxidation forms during synthesis. After the monomer oxidation, there is a conversion of the polymer film into induction and oxidation forms during synthesis. As known, once most inorganic inhibitors are harmful to the environment, organic inhibitors containing amine groups are useful to prevent corrosion. Amine-based inhibitors compose a thin adsorbed layer on the substrate, and this layer has a polymeric structure and is extremely protective against corrosion (11-13). The research made in the literature shows that the organic structure can add to the matrix of conductive polymer films (14). This study aim is to investigate the anti-corrosive properties of poly (o-aminobenzyl alcohol) synthesized from an aniline derived monomer o-aminobenzyl alcohol on AISI 316 stainless steel. Also, we synthesized the polymer coating (PABA-ORG) obtained in a mixture solution including o-aminobenzyl alcohol (ABA) and 2,6-di-*tert*-butyl-4- $\{(E)-[4-(4-hydroxyphenyl)imino]methyl\}$ phenol (M_w : 325.45) (ORG) compound having varying degree of hydrophobic chain length and the steric environment on AISI 316 stainless steel (SS) in $LiClO_4$ + acetonitrile medium. We explored the

corrosion performances of PABA coatings synthesized without and with 0.50 mM ORG compound in a 3.5 % NaCl solution. We evaluated the electrochemical measurement techniques of PABA polymer films with and without ORG compound obtained on SS (SS/PABA and SS/PABA-ORG) and bare SS.

MATERIALS AND METHODS

All electrochemical experiments were carried out with three-electrode in single-cell technique on CH Instruments electrochemical workstation. In the experiment cells, Ag/AgCl (3M KCl) and square platinum plate with a surface area of 0.25 cm² electrodes were reference and counter electrodes, respectively. AISI 316 electrode with a 0.50 cm² surface was the working electrode. Shortly before use, the SS electrode surface was carefully polished with 400 and 1200 grid abrasive paper, respectively, and washed with acetone+ethanol (1:1) mixture and bi-distilled water in this order. For the poly (o-aminobenzyl alcohol) (PABA) coating, we dissolved 0.15 M o-aminobenzyl alcohol monomer in acetonitrile (ACN) containing 0.15 M lithium perchlorate. Electropolymerization was carried out by cyclic voltammetry (CV) technique in 30 segments between -0.20 and 1.80 V at a scan rate of 50 mV s⁻¹. The fitting curves in the Nyquist and Bode diagrams in Figure 5c were analyzed using the ZView2 software. The structure of the organic compound named 0.50 mM 2,6-di-*tert*-butyl-4- $\{(E)-[4-(4-hydroxyphenyl)imino]methyl\}$ phenol (M_w : 325.45) joined to the PABA polymer film is given in Figure 1. The electropolymerization of PABA polymer film containing an organic compound (PABA-ORG) we applied the same process as that of PABA polymer film.

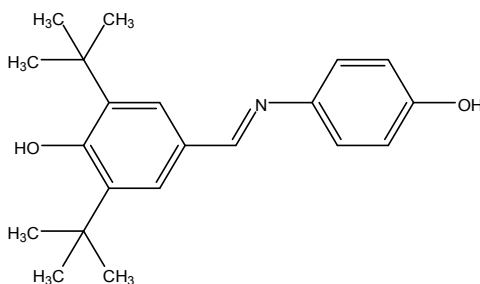


Figure 1: Chemical structure of the organic compound.

RESULTS AND DISCUSSION

Synthesis of the Polymeric Film

In this study, we synthesized PABA film in 0.15 M o-aminobenzyl alcohol (ABA) monomer dissolved in the solution of $LiClO_4$ in ACN by CV technique in one step. We coated Poly (o-aminobenzyl alcohol) (PABA) homopolymer films with and without organic compound (ORG) of 0.50 mM concentration on the

surface of the SS electrode using cyclic voltammetry at a scan rate of 50 mV/s. Figure 2 shows the film growth curves observed for SS in 0.15 M ABA (a) and 0.15 M ABA + 0.50 mM organic compound (ABA-ORG) (b) containing 0.15 M $LiClO_4$ + ACN solution. Film growth curves of electrodes obtained in both ORG compound-containing and ORG compound-free PABA medium, which are referred to here as SS/PABA-ORG and SS/PABA respectively,

showed in Figure 2. We obtained the works at a scan rate of $50 \text{ mV}\cdot\text{s}^{-1}$.

We carried out 30 segments for the synthesis of PABA or PABA-ORG coating on the SS electrode. Both coated electrodes exhibited entirely different electrochemical behavior in CV curves. The anodic current values increased after the potential value of 0.89 V during the first cycle in ABA monomer containing $\text{LiClO}_4 + \text{ACN}$ solution, while we observed them after the potential value of 0.88 V for $\text{LiClO}_4 + \text{ACN} + \text{ABA}$ monomer mixture with the organic compound. The 8.84×10^{-4} , a peak current value obtained for the ABA monomer medium, was related to the monomer oxidation of *o*-aminobenzyl alcohol on the SS electrode. The monomer oxidation process in ABA and ORG compound mixture moved to previous potential value, while its current intensities were incredibly high as $1.12 \times 10^{-3} \text{ A}$ than that the presence of only ABA. This case clarifies itself for being a better conductive medium in the presence of ORG compound concerning only the presence of ABA. It showed that the addition of ORG

compound to ABA solution provided an increase in the electropolymerization rate.

Furthermore, because it was not observed an additional oxidation peak in cyclic voltammogram (Figure 2b), we concluded that the organic compound is of high purity. Also, we did not observe the dissolution of the SS electrode for both coated electrodes. On the other hand, the peak current increases obtained for monomer oxidation of coated SS electrodes were significantly high in the first anodic cycles, while their values decreased with increasing cycle numbers. These behaviors of SS electrode in LiClO_4 and ACN medium containing ABA with and without ORG compound could be explained by the lower conductive surface of synthesized PABA film, for the SS electrode surface. Moreover, monomer oxidation peak intensities recorded for ABA + ORG compound mixture were comparatively higher when compared with that of only the ABA medium. After the growth of the polymer film, the process covered the SS electrode surface, a green uniform film for both *o*-aminobenzyl alcohol conditions with and without ORG compound.

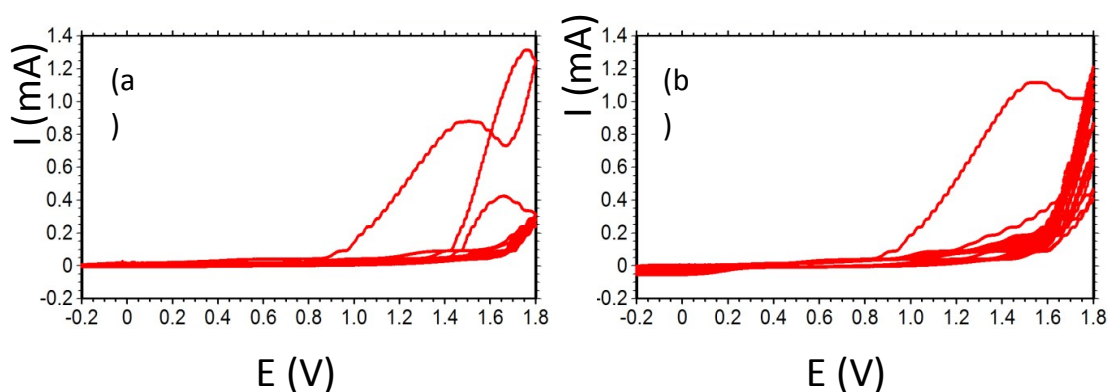


Figure 2: CVs of SS/PABA (a) and SS/PABA-ORG (b) homopolymer film synthesis.

Corrosion protection abilities of coated electrodes

The anticorrosive properties of the PABA and PABA-ORG coated SS electrodes in 3.5 % NaCl were evaluated with EIS, E_{ocp} -time plots, and anodic polarization plot.

We plotted the E_{ocp} values of SS, SS/PABA, and SS/PABA-ORG electrodes against the exposure time at the first half-hour and different exposure times (see Figure 3). Initially, the E_{ocp} measurement of bare SS metal was -0.234 V , while these values recorded for SS/PABA and SS/PABA-ORG electrodes in 3.5 % NaCl electrolyte solution were 0.140 V and 0.070 V , respectively. The E_{ocp} values obtained for uncoated and deposited electrodes shifted to an anodic direction in time. Yet, the E_{ocp} measurements of the SS/PABA-ORG electrode raced to the cathodic direction for a short time after 1654 s of exposure

time. We reported these values of SS/PABA to shift to the positive domain to 0.165 V . Afterwards, according to our observations, the E_{ocp} values of SS/PABA-ORG electrode shifted to the anodic domain from 0.053 to 0.206 V , between 2 and 168 h of exposure time (see Figure 3b). These values recorded for SS/PABA electrode remained constant close to the same potential value for 168 min.

Consequently, we noticed that the SS/PABA-ORG substrate had significantly positive potential region comparison with the only PABA deposited SS metal. We attributed these positive measurements obtained for the SS/PABA-ORG electrode to the formation of, especially nickel and chromium oxide layers, which built up with an extended immersion period, at metal/polymer interface. On the other hand, the E_{ocp} measurements of bare SS metal were carried to the cathodic region from -0.076 to -0.124

V, between 2 and 168 h of immersion period. This case indicated that chloride ions increased the active dissolution of SS the underlying chromium

and nickel oxide layer utilizing its aggressive property and small ion diameter.

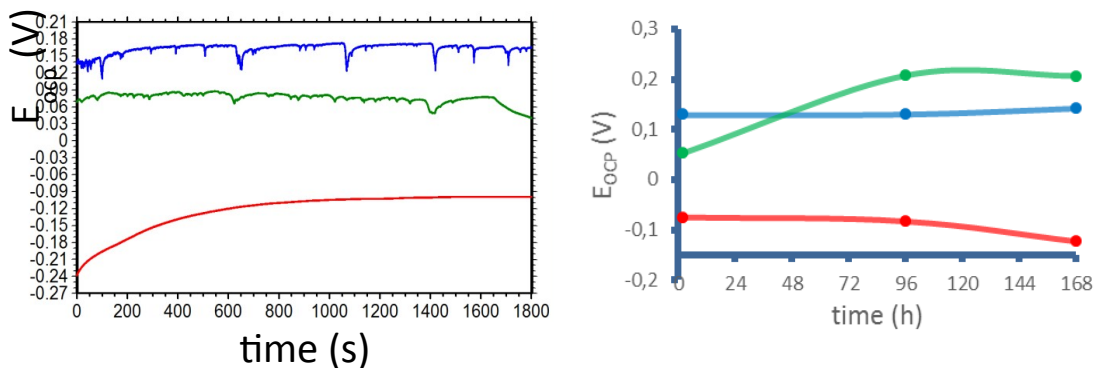


Figure 3: Open circuit potential-time plots of **SS**, **SS/PABA**, and **SS/PABA-ORG** electrodes at first half-hour (a) and different immersion times (b).

Figure 4 compares the anodic polarization plots of SS, SS/PABA, and SS/PABA-ORG substrates after 168 h of exposure period in the solution of corrosion. In the presence of bare SS, we determined the corrosion potential value (E_{corr}) as -0.130 V. Besides, the current values obtained for bare SS were highest when compared with those of coated SS electrodes. This case showed active dissolved of stainless steel in the wider potential region, while current values of the SS electrode remained almost constant in the high potential domain, owing to the formation of chromium and nickel oxide layers. On the other hand, the corrosion potential values of SS/PABA and SS/PABA-ORG electrodes were anodic direction when compared with that of the bare SS electrode. Therefore, this result implied conversion of SS electrode from

anodic dissolution to chromium and nickel oxide layers under the catalyzing effect of polymer film after the corrosive types reached to the SS. The E_{corr} values of polymer film coated electrodes were high due to oxide layers formation and reduction of PABA film. As a result, stabilities of PABA and PABA-ORG coatings were high while permeability was low in aggressive medium and ensured important anodic protection on SS in extended time. Also, the current values of SS/PABA and SS/PABA-ORG electrodes were significantly lower than that of the bare SS electrode. This case showed the effective barrier properties of polymer coatings on the SS electrode. The lowest current values recorded for PABA-ORG coating indicated that ORG compound addition to poly(o-aminobenzyl alcohol) structure exhibited an excellent barrier property on the SS surface.

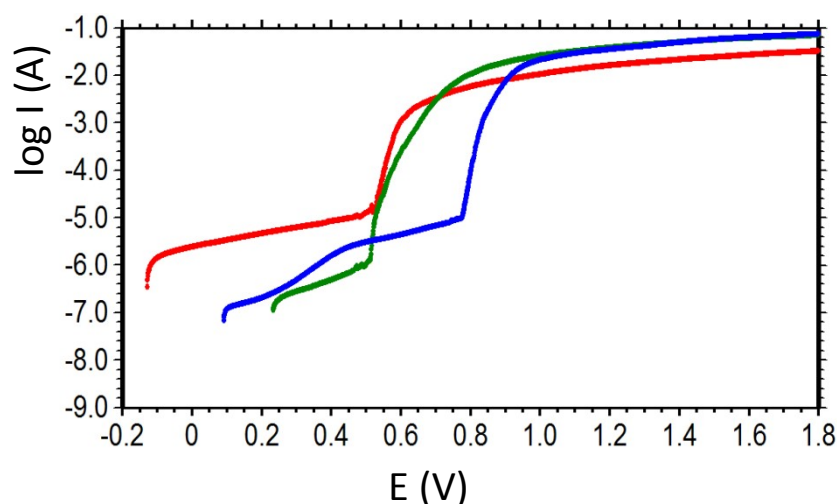


Figure 4: Anodic polarization plots of **SS**, **SS/PABA**, **SS/PABA-ORG** electrodes, after 168h of exposure time.

The Nyquist diagrams obtained for uncoated SS and PABA coated SS (SS/PABA), and PABA-ORG coated

SS are present in Figure 5 for 2, 96, and 168 h of immersion times in the solution of corrosion. There

was a depressed semicircle for metal corrosion at the high-frequency region for bare and deposited electrodes. In Nyquist curves, a one-time constant defined as depressed semicircle at the high-frequency region gave the polarization resistance (R_p). The R_p value obtained for the bare SS electrode was the sum of the resistance of oxide layers (R_o) and the charge transfer resistance (R_{ct}) corresponding to the metal/solution interface formed at the bottom of the pores. In contrast, the fact that almost all curves obtained for coated electrodes were composed of a depressed semicircle gives the R_p value, including the R_o , the R_{ct} , and the polymer film resistance (R_{pf}). Besides, the linear region at the low-frequency side of the Nyquist plots recorded for all of them denoted the presence of Warburg impedance (Z_w) showing a noticeable formation of layers, after 2 h of immersion time in Figure 5a. Warburg impedance assumes the diffusion resistance consisting of corrosion types of the substrate because of being at approx. 45° of angle, in phase angle, $(-)$ -log f plots (14-18). The observation of the linear portion at the low-frequency district showed that the coating had active barrier property.

Consequently, we observed a typical charge transfer process occurring under diffusion control as a linear part. As a result, ion diffusion processes taking place through the pores of the coating and oxide layers towards the underlying metal surface at a metal/solution interface denoted the presence of Warburg impedance. We observed that the bare SS electrode had important anti-corrosion properties due to the formation of stable chromium and nickel oxide layers, after 2 h of the exposure period. In the case of uncoated SS and coated electrodes, there was still a linear portion defined as the Warburg impedance at the lowest frequency domain, which indicated the active protective properties of the oxide and polymer films on surfaces, after 96 h. Nevertheless, we noticed on phase angle-logf plot that the $(-)$ values of coated electrodes obtained a maximal value at approx. 60° (Figure 5b). Higher $(-)$ values of PABA and PABA-ORG polymer film coated SS electrodes attributed to limited corrosive products diffusion process taking place through the

pores of the coating and the formation of new oxide films towards the underlying SS surface at metal/solution interface (14-18). In Figure 5c, the incremental R_p value of depressed semicircle obtained polymer-coated both electrodes at the high frequency indicated the growth of the passive films consisted of nickel and chromium oxides, metal/polymer interface. In the presence of SS/PABA and SS/PABA-ORG electrodes, the one-time constant at high frequency composed of the total resistance of R_{ct} value corresponding to the dissolution of metal at the bottom of the pores, R_{pf} value and R_o value. The linear portion at the low-frequency region of the Nyquist curves denoted the presence of Warburg impedance, pointing out an unusual formation of films (14-18). It is also well known that Warburg coefficient (σ) values give an idea about the diffusability of ion through the polymer film and oxide layers or only the former. We investigated the diffusive properties of polymer films deposited on the SS surface and calculated the Warburg coefficients with details given in the literature (17-18) and (see Table 1). The σ value of SS/PABA and SS/PABA-ORG electrodes was comparatively higher when compared with that of uncoated SS substrate, after 168 h of immersion period (Table 1). We obtained this highest σ value obtained for SS/PABA-ORG electrode by investigation of the $(-)$ -logf plot. In $(-)$ -log f plot, the peak representing polarization resistance expanding between mid and low frequencies in the curve of SS/PABA-ORG electrode indicated the highest phase angle than those of SS/PABA and bare SS electrodes (Figure 5B(c)). So, it was evident that on SS electrode coated with PABA polymer in the organic compound medium had lower porosity structure and number (or only the former), when compared with that of only PABA polymer. As a result, these low porosity properties allowed the limited ion diffusion from the pores of the coating on the metal surface. So, organic compound situated in polymer film structure reduced more the porosity structure of SS electrode by more catalyzing the formation of oxide layers on the SS surface with time. Consequently, the more formation of nickel and chromium oxide layers on the SS surface inhibited mainly the dissolution of stainless steel metal.

Table 1: Corrosion performance values of coated and uncoated SS electrodes, after 168 h period of immersion.

Electrode	E_{OCP} (mV)	R_p (k Ω)	σ ($\Omega \cdot s^{-1/2}$)
SS	-124	5.08	2200.79
SS/PABA	148	30.80	10484.84
SS/PABA-ORG	206	31.16	12576.56

CONCLUSIONS

In this study, we have synthesized PABA film with and without organic compound on the SS surface by cycling the potential in $LiClO_4$ + acetonitrile solution.

The cyclic voltammetric curves demonstrated that PABA coatings synthesized with and without organic compound medium had different morphologic structure and different potential values of monomer oxidation. We investigated the corrosion

performances of SS/PABA and SS/PABA-ORG electrodes in a 3.5 % NaCl solution. It was evaluated with E_{ocp} -time curves, anodic polarization curves, and the AC impedance diagrams and of PABA polymer films synthesized with and without ORG compound obtained on SS surface. This study clearly showed that all the PABA-ORG coating provided valuable protective property against corrosive types such as aggressive chloride ions.

The Nyquist diagrams revealed that PABA-ORG film exhibited significant catalytic efficiency on the formation of protective oxide layers on the SS surface when compared with only PABA film. Consequently, PABA-ORG coating was low permeable and high stability under aggressive chloride medium and ensured exceptional anodic protection on SS over a longer time.

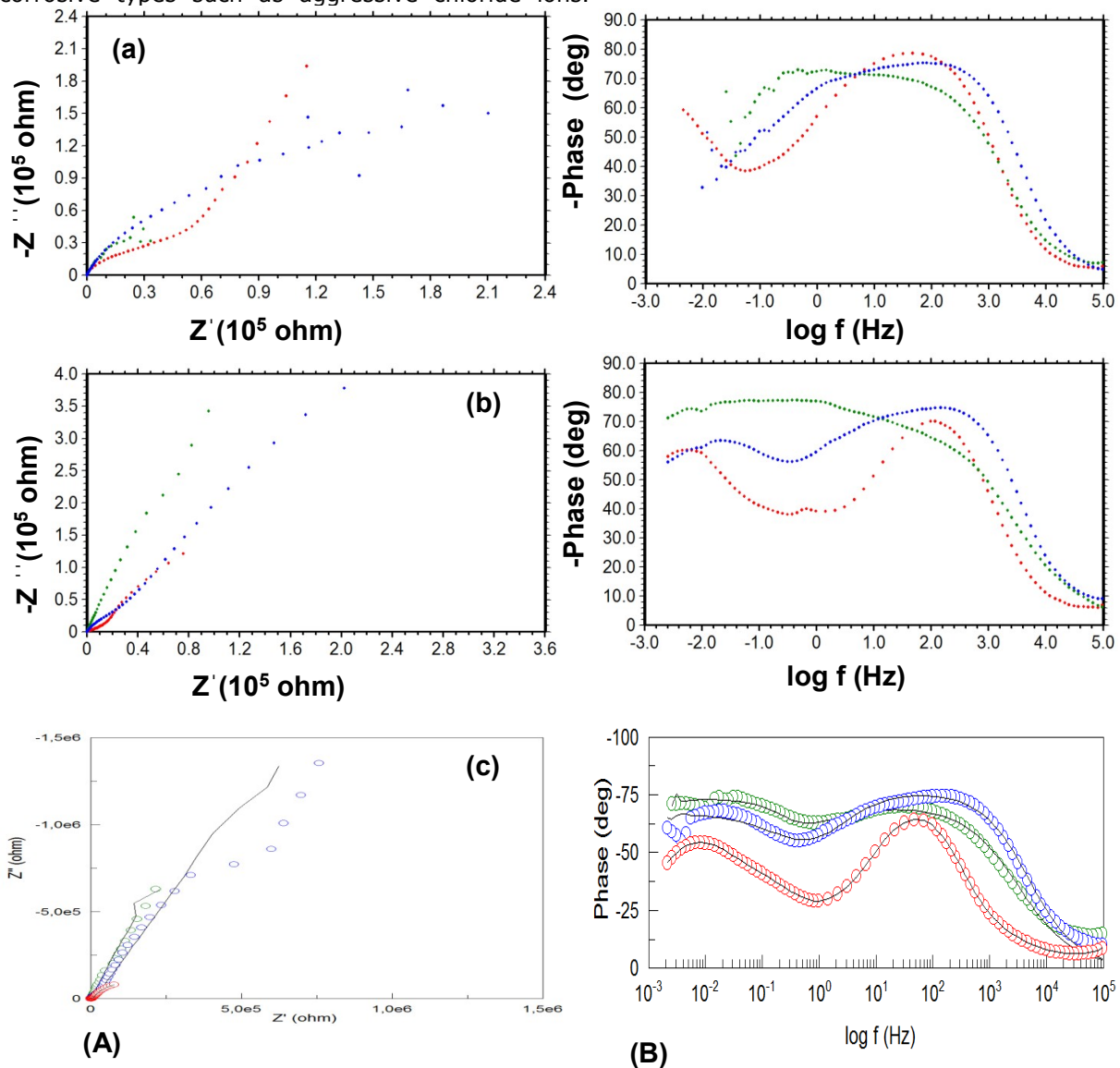


Figure 5: Nyquist (A) and Bode (B) curves recorded for **SS**, **SS/PABA** and **SS/PABA-ORG** electrodes after 2 (a), 96 (b) and 168 (c) h of exposure time in 3.5 % NaCl solution.

ACKNOWLEDGMENTS

This study has been supporting from Hatay Mustafa Kemal University Coordinatorship of Scientific Research Projects by Project No: 19.YL.005. This paper was presented orally at the 2nd International Eurasian Conference on Biological and Chemical Sciences (EurasianBioChem 2019) held in Ankara between 28 – 29 June 2019.

REFERENCES

1. Perez N., *Electrochemistry and Corrosion Science*, Kluwer Academic Publishers, 2004, ISBN: 1-4020-7744-0.
2. Creus J, Mazille H, Idrissi H, Porosity evaluation of protective coatings onto steel, through electrochemical techniques. *Surf. Coat. Technol.*,

- 2000; 130; 224–232. [https://doi.org/10.1016/S0257-8972\(99\)00659-3](https://doi.org/10.1016/S0257-8972(99)00659-3).
3. Sohi MH, Jalali M, Study of the corrosion properties of zinc-nickel alloy electrodeposits before and after chromating. *J. Mater. Process. Tech.* 2003; 138: 63-66, [https://doi:10.1016/S0924-0136\(03\)00050-5](https://doi:10.1016/S0924-0136(03)00050-5).
4. Toprak Doşlu S, Doğru Mert B, Yazıcı B, Polyindole top coat on TiO₂ sol-gel films for corrosion protection of steel. *Corros. Sci.* 2013; 66(8): 51-58, <https://doi.org/10.1016/j.corsci.2012.08.067>.
5. Deshpande PP, Jadhav NG, Gelling VJ, Sazou D, Conducting polymers for corrosion protection: a review. *J. Coat. Technol. Res.* 2014; 11(4): 473–494, <https://doi:10.1007/s11998-014-9586-7>.
6. Ates M, A review on conducting polymer coatings for corrosion protection. *J Adhes. Sci. Technol.*, 2016; 30(14): 1510–1536, <https://doi.org/10.1080/01694243.2016.1150662>.
7. González MB, Saidman SB, Electrodeposition of polypyrrole on 316L stainless steel for corrosion prevention. *Corros. Sci.*, 2011; 53(1): 276–282, <https://doi.org/10.1016/j.corsci.2010.09.021>.
8. Jadhav N, Gelling VJ, Synthesis and Characterization of Micaceous Iron Oxide/Polypyrrole Composite Pigments and Their Application for Corrosion Protection of Cold Rolled Steel. *Corrosion.* 2014;70 (5):464–474, <https://doi.org/10.5006/0980>.
9. Bereket G, Hur E. The Corrosion Protection of Mild Steel by Single Layered Polypyrrole and Multilayered Polypyrrole/Poly(5-amino-1-naphthol) Coatings. *Prog. Org. Coat.* 2009; 65 (1):116–124, <https://doi.org/10.1016/j.porgcoat.2008.10.005>.
10. Bajat JB, Maksimovic MD, Miskovic-Stankovic VB, Zec S, Electrodeposition and characterization of Zn-Ni alloys as sublayers for epoxy coating deposition. *J. Appl. Electrochem.* 2001; 31: 355-361, <https://doi.org/10.1023/A:101758001>.
11. Ozyilmaz AT, Avsar B, Ozyilmaz G, Karahan IH, Camurcu T, Colak F, Different copolymer films on ZnFeCo particles: Synthesis and anticorrosion properties. *Appl. Surf. Sci.* 2014; 318: 262-268, <https://doi.org/10.1016/j.apsusc.2014.04.177>.
12. Ozyilmaz AT, Akdag A, Karahan IH, Ozyilmaz G, The influence of polyaniline (PANI) coating on corrosion behaviour of zinc-cobalt coated carbon steel electrode. *Prog. Org. Coat.* 2013; 76(6): 993-997, <http://doi.org/10.1016/j.porgcoat.2012.10.020>.
13. Bagherzadeh M, Haddadi H, Iranpour M, Electrochemical evaluation and surface study of magnetite/PANI nanocomposite for carbon steel protection in 3.5 % NaCl. *Prog. Org. Coat.* 2016; 101: 149-160, <https://doi.org/10.1016/j.porgcoat.2016.08.011>.
14. Ozyilmaz AT, Aydin AE, Akdag A, Anticorrosive properties with catalytic behaviour of primer PANI film and top PPy coating synthesised in presence of novel norephedrine based amino alcohol compound. *T. I. Met. Finis.* 2014; 92(1): 34-40, <https://doi.org/10.1179/0020296713z.000000000134>.
15. Lorenz WJ, Mansfeld F, Determination of corrosion rates by electrochemical DC and AC methods. *Corros. Sci.* 1981; 21: 647–672, [https://doi.org/10.1016/0010-938x\(81\)90015-9](https://doi.org/10.1016/0010-938x(81)90015-9).
16. Mansfeld F, Use of electrochemical impedance spectroscopy for the study of corrosion protection by polymer-coatings. *Appl. Electrochem.* 1995; 25: 187-202, <http://doi:10.1007/bf00262955>.
17. Walter GW, A review of impedance plot methods used for corrosion performance analysis of painted metals. *Corros. Sci.*, 1986; 26(9): 681-703, [http://doi:10.1016/0010-938x\(86\)90033-8](http://doi:10.1016/0010-938x(86)90033-8).
18. Ozyilmaz AT, Ozyilmaz G, Yigitoglu O, Synthesis and characterization of poly(aniline) and poly(o-anisidine) films in sulphamic acid solution and their anticorrosion properties. *Prog. Org. Coat.* 2010; 67: 28-37. <http://doi:10.1016/j.porgcoat.2009.09.010>.



Identifying the Novel Pyrimidine-Based CDK2 Inhibitors as Anticancer Agents Using Text-Mining and Combined Molecular Modeling Approaches

Kader ŞAHİN^{1*}  , Serdar DURDAĞI¹  

¹Computational Biology and Molecular Simulations Laboratory, Department of Biophysics, School of Medicine, Bahcesehir University, Istanbul, Turkey

Abstract: The cycline-dependent kinase (CDK) protein is a vital target used in anti-cancer drug designing studies. Many FDA-approved drugs, including anti-cancer drugs, use pyrimidine as a crucial fragment. In the current study, a small molecule database (Specs SC) that text mining studies include more than 210.000 compounds, and we filtered 6668 molecules that carry "pyrimidine" fragments. We then screened these compounds at the binding pocket of CDK-2 target using molecular docking and molecular dynamics (MD) simulations approaches. Besides, we compared the binding free energies of screened compounds with pyrimidine-based FDA-approved anti-cancer drug Abemaciclib which targets CDK. Based on the comparison of docking scores of screened compounds, we used top-7 hits in 100 ns MD simulations. We also applied the same MD simulations protocol (100 ns) to the Abemaciclib-bound CDK-2 complex structure. We then calculated the average Molecular Mechanics/Generalized Born Surface Area (MM/GBSA) energies. Our MM/GBSA results showed that 6 out of 7 compounds have better MM/GBSA scores than FDA-approved compound Abemaciclib. Thus, together with a combination of text mining and integrated molecular modeling approaches, we identified novel pyrimidine-based hits against CDK.

Keywords: CDK inhibitors, virtual screening, text mining, molecular docking, molecular dynamics simulations, pyrimidines.

Submitted: March 09, 2020. **Accepted:** March 28, 2020.

Cite this: Şahin K, Durdağı S. Identifying the Novel Pyrimidine-Based CDK2 Inhibitors as Anticancer Agents Using Text-Mining and Combined Molecular Modeling Approaches. JOTCSA. 2020;7(2):383-402.

DOI: <https://doi.org/10.18596/jotcsa.701243>.

***Corresponding author.** E-mail: sahkader@hotmail.com.

INTRODUCTION

Cycline-dependent kinases (CDKs) are the catalytic subunits of a large family of serine/threonine protein kinases, having crucial roles in the regulation of cell cycle progression.

There are two main groups in the family: Cell cycle CDKs and transcriptional CDKs (1). We often observe the over-expression of CDKs in many cancer types; thus, their inhibition may lead to cell cycle arrest or apoptosis (2). Although the human genome encodes 21 CDKs, researchers have shown that only seven (CDK1-

4, 6, 10, 11) of them indeed play a direct role in the progression of the cell cycle. Thus, targeting the CDK enzyme function is a rational approach to prevent unregulated cancer cell proliferation, and the authors considered these targets in many anti-cancer drug design studies (3, 4). Pyrimidine derivatives have attracted considerable interest in recent years in diverse biological problems (5, 6). Experts use pyrimidine derivatives in many different biological applications, including anti-tumor (7), antiviral (7, 8), antioxidant (9), antifungal (10), and hepatoprotective (11) roles. FDA-approved drug Brigatinib (marketed as Alunbrig) is a pyrimidine-based small-molecule used in targeted cancer therapy (12). Another FDA-approved drug Abemaciclib (commercial terms Verzenio and Verzenios) specifically targets CDK. Physicians mainly use them in advanced or metastatic breast cancer treatment. However, it has some adverse side effects such as diarrhea, nausea, vomiting, leukopenia (i.e., low white blood cell count) including neutropenia, anemia, thrombocytopenia (i.e., low platelet count), stomach pain, fatigue, decreased appetite, and headache (13, 14). Therefore, in the current study, pyrimidine-based new lead compounds targeting CDK were investigated using integrated text-mining and molecular modeling approaches. For this aim, we used MarvinSketch software (15) in 210,596 molecules obtained from Specs-SC drug-like small molecule database in an IUPAC text file format. We then screened this text file by a Python-based text mining in-house script and identified 6668 molecules as compounds that include the "pyrimidine" phrase in their text files. Moreover, we used these filtered compounds at the active site of the CDK-2 enzyme, and screened compounds were ranked based on their interaction energy scores. We used top-7 compounds that show better docking scores than FDA-approved drug Abemaciclib in molecular dynamics (MD) simulations. Trajectory frames collected throughout the MD simulations were used in Molecular Mechanics/Generalized Born Surface Area (MM/GBSA) calculations and based on average MM/GBSA scores, we identified novel 6 pyrimidine-based small molecules that have better MM/GBSA scores than Abemaciclib (Table 1).

MATERIALS AND METHODS

Data Collection

Text mining helps find significant molecules by quickly screening them from large databases using keywords (16). In this study, 210,596 molecules obtained from Specs-SC were prepared in the IUPAC text file format using

MarvinSketch software. We then screened this text file to find pyrimidine-based molecules using a Python-based text mining and obtained 6,668 molecules.

Ligand Preparation

Ligand preparation consists of the analysis of a 3D structure of a ligand, generation, and optimization steps. We have prepared 6,668 compounds using the OPLS-2005 forcefield (17) LigPrep module (18) of the Maestro Molecular Modeling Suit. A problem to be addressed is the ionization of the ligand in physiological conditions. We have used the Epik module (18) at the physiological pH of 7.4 for potential ionization states. We also produced all possible stereoisomers and tautomers and considered 32 structures per ligand.

Protein Preparation

We obtained the CDK-2 target from the protein data bank (PDB), and a 2XMY PDB-coded protein structure was used (19). We fixed the missing side chains, backbone atoms, and loops with Prime (20). For protonation states, structural optimization and minimization, the PROPKA and OPLS-2005 force field were used, respectively (21). We considered water molecules around 5.0 Å of the co-crystallized ligand in the docking simulations.

Molecular Docking Simulations

Molecular docking studies investigate interactions occurring in protein-protein or ligand-protein complexes and rank candidate poses according to predicted affinity scoring functions (22). Docking processes predict ligands to bind with the most appropriate conformation in the binding pocket of the target protein using different algorithms. We used Glide to carry out the molecular docking between the investigated ligands and CDK-2 protein to obtain the binding poses as well as docking scores of the studied ligands (23). The conformations obtained during the docking were ranked using the Glide score function (24). Residues set the binding pocket within 10 Å vicinity of a co-crystallized ligand. All ligands were initially docked into the binding pocket of CDK using a grid-based docking program Glide standard precision (SP) of Maestro Molecular Modeling pocket (20, 23) and requested 10 docking poses for each ligand (25, 26).

Molecular Dynamics (MD) Simulations

There is evidence that some systems require MD simulations to discover proper binding fit (27). Long MD simulations can find more and energetically favorable configurations. MD simulations were implemented up to 100 ns using Desmond V.4.9 to investigate the conformational stability of the complexes of selected hit molecules with CDK-2 (28). We solvated the complex structures in the orthorhombic simple point charge (SPC) water model (29).

Moreover, we neutralized the systems with counter ions (0.15 M NaCl solution). We set the system as Lennard-Jones interactions cutoff of 10 Å on periodic boundary conditions (23). We used a 2.0 fs time step in the integration steps.

We have used Nose-Hoover thermostat (30) and Martyna-Tobias Klein protocols (31) to control the temperature and pressure of the systems at 310 K and 1 bar, respectively.

Molecular Mechanics/Generalized Born Surface Area (MM/GBSA)

Protein-ligand complexes were also analyzed by MM/GBSA to estimate the free binding energies of studied ligands. The MM/GBSA calculations were applied to complex structures using Schrödinger's Prime module (20). The software extracted the frames of ligand-protein complexes from the MD trajectory of each complex at every 10 ps. For protein flexibility, we used the VSGB solvation model (32), which is a realistic parameterization of the solvation and OPLS-2005 force field.

Therapeutic Activity Prediction

Binary QSAR models in MetaCore/MetaDrug underwent therapeutic activity prediction, pharmacokinetic predictions, and ADME/toxicity profile for the compounds under investigation. It is an advanced data analysis program based on protein-protein interactions, protein-DNA interactions, disease, and toxicity. In Metacore/Metadrag, the software normalized the predicted therapeutic activity values to 0 and 1 (i.e., 0 meaning inactive, 1 meaning active molecules). Therapeutic activity results of selected 7 hit compounds, and the FDA-approved two drugs (Abemaciclib and Ribociclib) are in Table 1. Also, we carried out the therapeutic activity calculations for specific CDK2 inhibitors (A-674563 and MK-8776). Activity values of A-674563 and MK-8776 are 0.44 and 0.79, respectively.

RESULTS AND DISCUSSION

The current study aims to identify novel pyrimidine-based small compounds against CDK-2 from a small molecule library using combined text mining and molecular modeling approaches. For this aim, we used the Specs SC database, which includes 210,596 drug-like compounds. Figure 1 summarizes the flowchart of all applied procedures in the current study. All 210,596 compounds imported from the Specs-SC database in .sdf file format were converted to .name IUPAC text file format with MarvinSketch program (MarvinSketch, 2018) and identified 6,668 compounds that contain the phrase "pyrimidine." We then converted these compounds to .sdf file format and prepared 2D molecular structures of selected pyrimidine-derivatives to energetically optimized 3D structures using the LigPrep module of Maestro molecular modeling Suite. Afterward, we used these prepared compounds in molecular docking simulations. These 6,668 pyrimidine derivative compounds were screened at the active site of the CDK-2 (PDB ID: 2XMY) using a grid-based docking program Glide/SP (standard precision). Docking scores of these compounds were measured, and selected top-7 compounds for MD simulations to better understand their structural and dynamical profiles at the active site of the enzyme. Trajectory frames of each complex system were collected and analyzed throughout the MD simulations. Figure 2 shows MM/GBSA free energy plots of each selected hits, as well as FDA-approved drugs Abemaciclib and Ribociclib. Table 1 summarizes the top-docking scores and average MM/GBSA binding free energies of selected hit compounds as well as FDA-approved compounds. Docking scores of Glide/SP for the selected hit compounds are similar. However, a few selected compounds (i.e., compounds 2523, 2657, and 6447) have in a different range of MM/GBSA scores. There are a few reasons. (i) Some of the hit compounds (i.e., compound 2523) do not maintain their initial docking poses (Figure S13); (ii) Used docking scoring functions and MM/GBSA scoring functions are different; thus they may not necessarily produce the same ranking. For this reason, we also performed docking simulations using another docking program GOLD. As well as, instead of a prolonged (100-ns) MD simulations, we also repeated simulations with three times with short (10-ns) MD simulations for selected hit compounds and FDA-approved drugs (Abemaciclib, Ribociclib) and specific CDK-2 inhibitors (A-674563 and MK-8776), (Table S1). GOLD docking scores showed that selected hit compounds 6447 and 2657 also have high docking scores. Besides, Figures S1, S2, and S3 give the protein RMSD plot of compounds 2657, 5925, and 6447 during 10 ns simulations,

respectively. The results show that the average ΔG values obtained as a result of 10 ns simulations are very close to each other.

We provided, in Figure 3, the protein (Ca) RMSD plots of selected 7 hit compounds and FDA-approved drug Abemaciclib. RMSD plots of all studied systems show that all the systems reach the equilibrium after the 20-ns time scale. The deviations from the initial conformations are not significant ($<4.0 \text{ \AA}$). Within the studied systems, the Mol-236 lead compound had higher structural fluctuations compared to other systems.

Together with protein-RMSDs for the studied systems, we further measured the ligand-RMSDs. We plotted two different ligand RMSD graphs: LigFitLig and LigFitProt. While we considered the rotational motion in LigFitLig RMSDs, throughout the MD simulations, we adopted the translational motion of the ligand in LigFitProt RMSDs. Thus, in LigFitLig, heavy atoms of the ligand align themselves, and we recorded the deviations from the initial conformation throughout the simulation. However, in LigFitProt RMSDs, heavy atoms of ligand aligned to the backbone atoms of protein, and we measured the deviations from the initial positions as RMSDs. Ligand RMSD shows how stable the ligand is regarding the protein and its binding pocket. We showed the LigFitProt's RMSD of a ligand when we first matched the protein-ligand complex with the reference protein backbone, and then the RMSD of the ligand heavy atoms is determined. If the measured values are significantly larger than the protein's RMSD, then the ligand is likely to have diffused away from its original binding position. LigFitLig displays a ligand's RMSD that is aligned and measured just according to its reference conformation. This value for RMSD measures the internal fluctuations in the ligand atoms.

Figure 4 shows the LigFitProt RMSD plots of studied ligands. As it can be seen clearly from the Figure, most of the studied ligands do not have significant translational changes throughout the MD simulations. We observed the maximum deviations for FDA-approved drug Abemaciclib, Mol-2655 and Mol-2657, which have around 5.0 \AA throughout the simulations. Results show that studied systems tightly bound to the binding pocket of the target structure; thus, they do not diffuse from their initial positions.

Figure 5 shows the LigFitLig RMSD plots of studied ligands. As we can see from the RMSD plots, all the ligands have less than 3.0 \AA average RMSD values that represent the structural stability of studied compounds at the active site of the target protein. We also investigated the root-mean-square fluctuation (RMSF) values of studied compounds to check the effect of each ligand to the target protein structure. (Figure 6) Residue numbers around

40, 70, and 150 have higher fluctuations compared to other regions when the studied compounds bind.

We showed the 2D ligand interaction diagrams of hit compound Mol-2657 in Figure 7. The compound constructs stable non-bonded chemical interactions with mainly following residues throughout the MD simulations: Lys20, Lys129, Asn132, and Asp145.

Figure 8 displays a time-line representation of the interactions and contacts (H-bonds, Hydrophobic, Ionic, Water Bridges). The top panel shows the total number of specific contacts produced throughout the MD simulation period by the protein with the ligand. The bottom panel displays which residues interact with the ligand in each trajectory frame. Many residues allow more than one direct interaction with the ligand, defined by darker orange color, depending on the scale to the right of the map. Figure 8 displays that Mol-2657 constructs critical chemical interactions with residues Lys129, Asn132, and Asp 145, which are stable throughout the simulation time.

We screened the therapeutic activity values of selected 7 hit compounds against cancer using binary quantitative structure-activity relationship (QSAR) models in Metacore/Metadug. Therapeutic activity values of all selected compounds greater than 0.5 (Table 1).

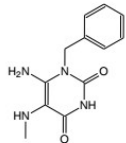
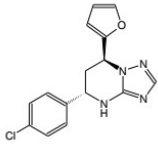
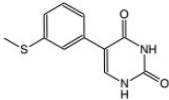
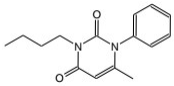
CONCLUSION

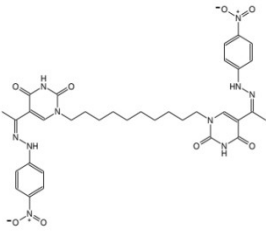
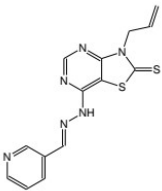
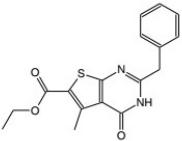
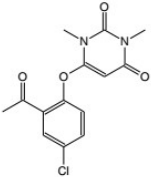
In this study, we carried out advanced integrated text mining, virtual screening, and hybrid molecular modeling strategies to identify the pyrimidine-based inhibitors targeted to the binding site of CDK-2. Thus, we have selected 6,668 pyrimidine derivatives from the small molecule database of Specs-SC for this aim. We screened these identified compounds against the CDK-2 target using molecular docking and used the top-docking poses of selected 7 hits in long MD simulations (100 ns). MM/GBSA binding free energy calculations have been conducted for all ligands. We also performed the same protocol (100 ns molecular dynamics simulation) for the FDA-approved drug Abemaciclib. The therapeutic activities of the selected 8 compounds were screened in Metacore/Metadug using binary QSAR models. We evaluated the docking scores and MM/GBSA scores in Table 1. We observed that the compound 2523 has a high docking score, however its corresponding MM/GBSA score was low compared to MM/GBSA scores of other compounds. When we visualize the trajectory

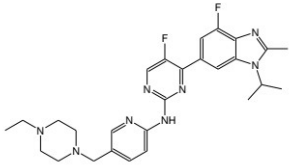
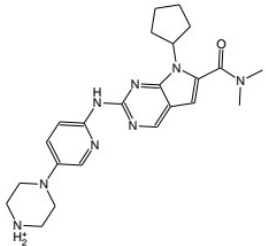
frames throughout the simulations, we observed that this compound does not stay at the binding pocket throughout the simulations and loses its initial docking pose. (see Figure S11) Thus, we have not evaluated the binding energy of compound 2523. Here, we showed

that integrated text-mining and molecular modeling approaches leading to 7 novel pyrimidine-based CDK-2 inhibitors. Thus, such new compounds may open new paths for developing small inhibitors against CDK-2.

Table 1. 2D structures, top-docking scores in Glide/SP and Gold, and average MM/GBSA scores of selected 7 hits and FDA-approved 2 CDK inhibitors.

Compounds	2D Structure	Glide Docking Score (kcal/mol)	Gold Docking Score (kcal/mol)	MM/GBSA (kcal/mol)	Predicted Therapeutic activity
Mol-30		-9.359	-4.956	-48.91±3.29	0.53
Mol-236		-9.385	-6.453	-46.52±3.95	0.75
Mol-2623		-9.382	-6.882	-52.85±4.64	0.52
Mol-2655		-9.298	-6.963	-47.32±3.58	0.53

Compounds	2D Structure	Glide Docking Score (kcal/mol)	Gold Docking Score (kcal/mol)	MM/GBSA (kcal/mol)	Predicted Therapeutic activity
Mol-2657		-9.573	-7.533	-74.38±7.91	0.69
Mol-5925		-9.746	-7.00	-51.90±3.02	0.74
Mol-6447		-9.317	-7.675	-62.14±3.20	0.56
Mol-2523		-9.373	-5.969	NA	0.30

Compounds	2D Structure	Glide Docking Score (kcal/mol)	Gold Docking Score (kcal/mol)	MM/GBSA (kcal/mol)	Predicted Therapeutic activity
Abemaciclib		-6.818	-9.170	-45.49±5.90	0.78
Ribociclib		-5.187	-7.568	-47.40±3.16	0.68

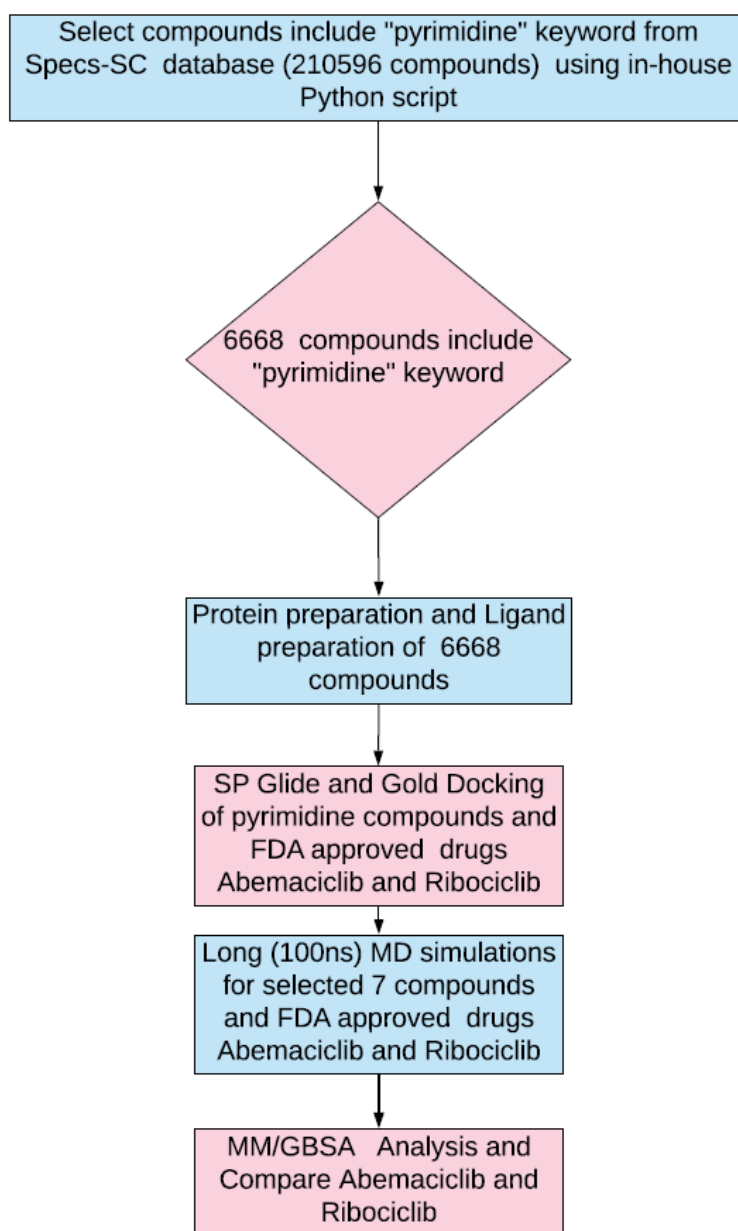


Figure 1: Applied virtual screening workflow at the current study.

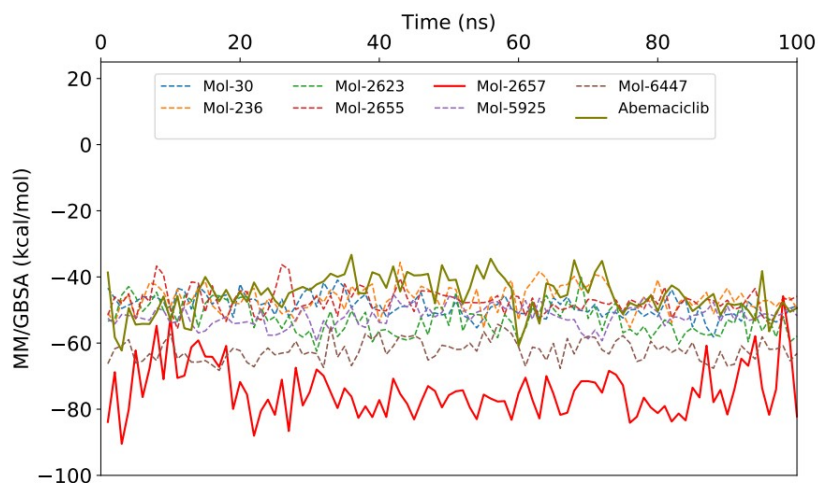


Figure 2: MM/GBSA plots of selected 7 compounds and FDA-approved drug Abemaciclib during the MD simulations.

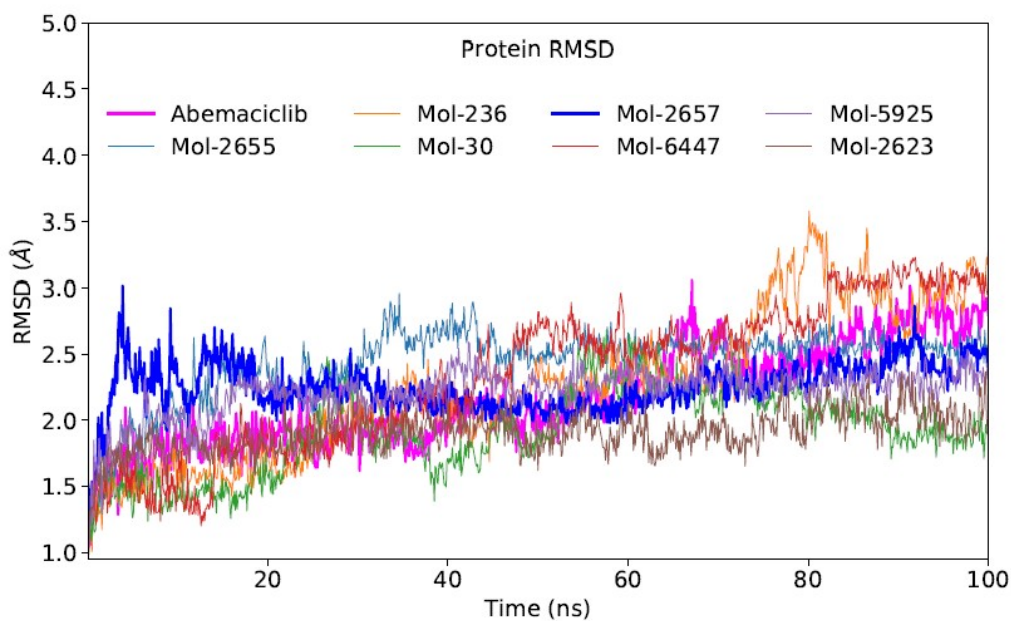


Figure 3: Protein-RMSD plots of selected 7 compounds and FDA-approved drug Abemaciclib throughout the MD simulations.

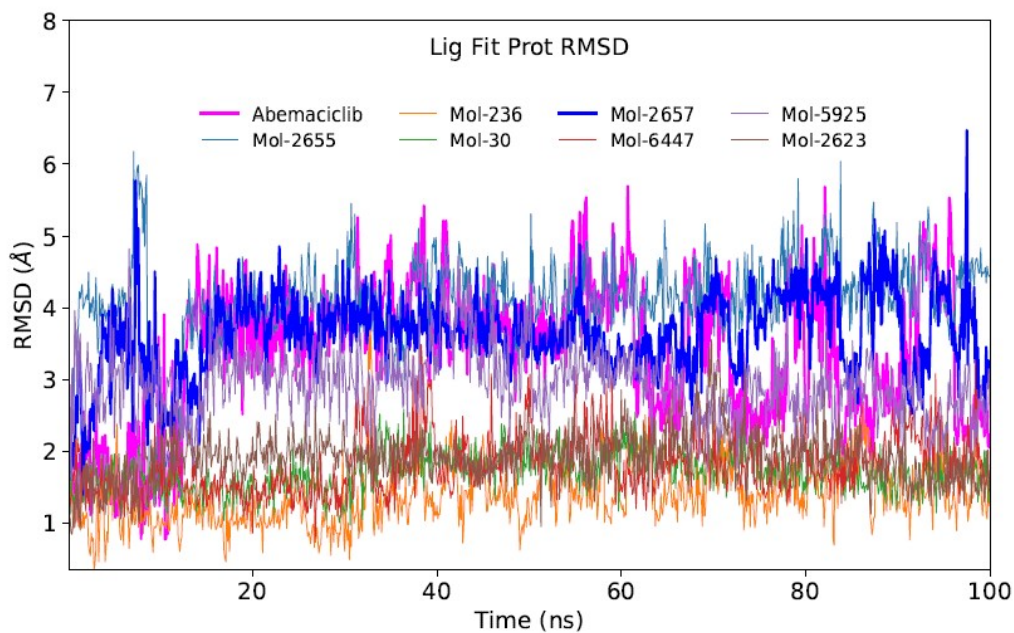


Figure 4: LigFitProt RMSD graph for selected 7 compounds and FDA-approved drug Abemaciclib.

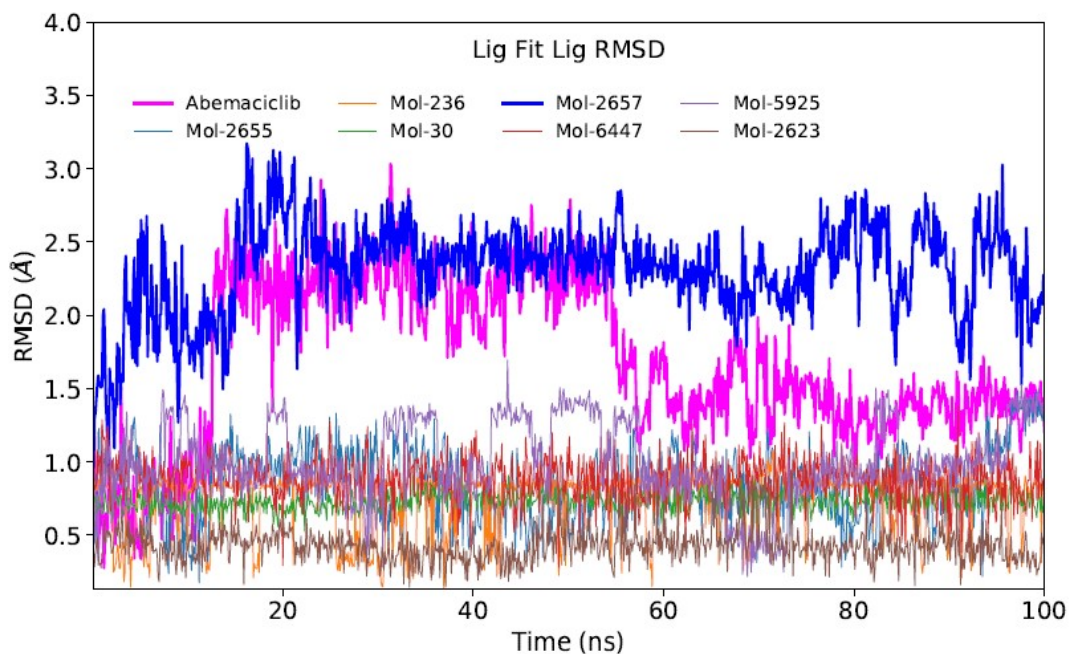


Figure 5: LigFitLig RMSD graph for selected 7 compounds and FDA-approved drug Abemaciclib.

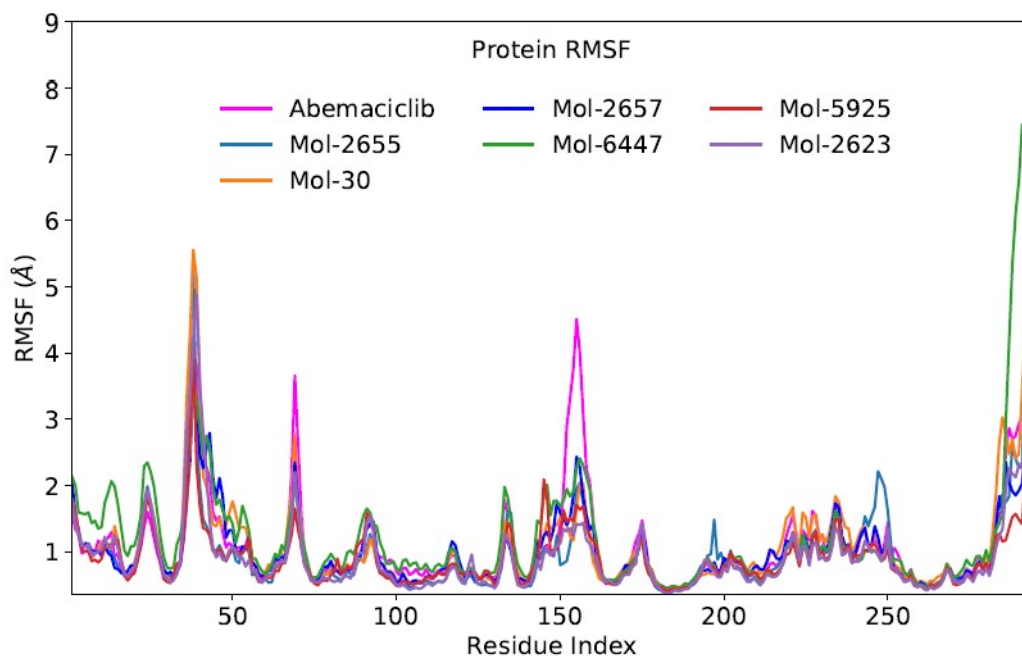


Figure 6: RMSF plots for selected 7 hit compounds and FDA-approved drug Abemaciclib.

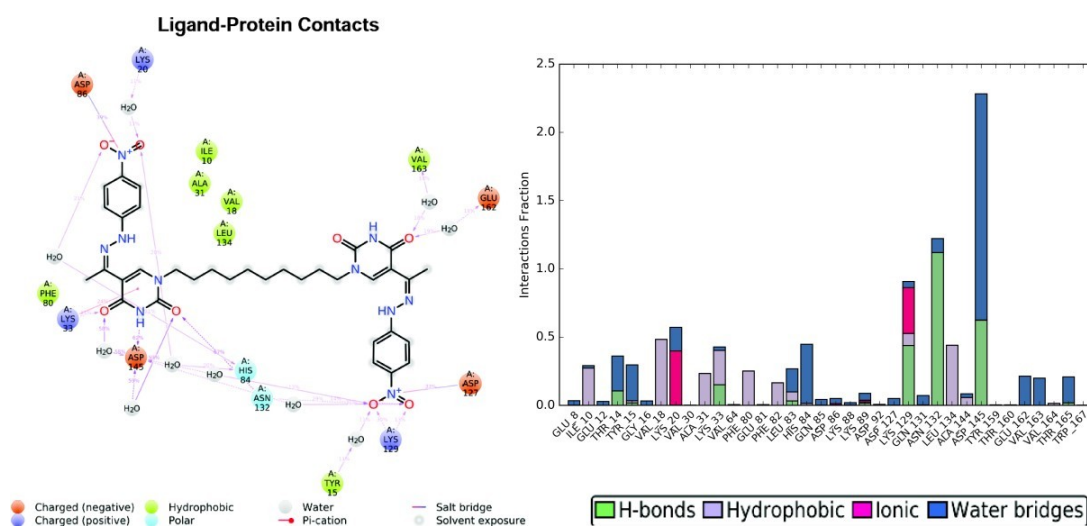


Figure 7: Mol-2657's 2D ligand interaction graph. The figure also shows interaction fractions throughout the simulations.

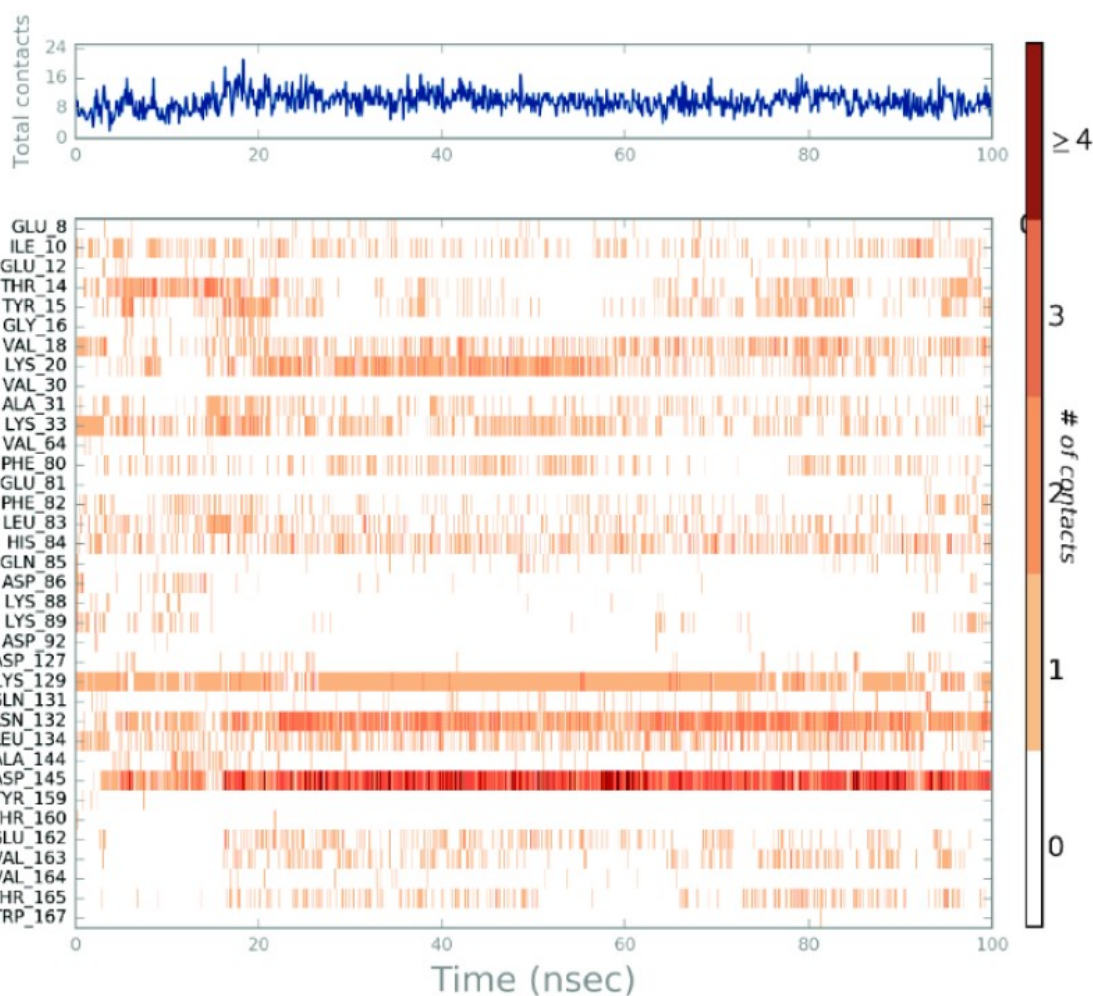


Figure 8: Protein-ligand interactions throughout the simulations. While top-panel shows total contacts with the ligand, the bottom-panel represents the formed and broken interactions between the protein and ligand during the simulation.

REFERENCES

- Hirose Y, Ohkuma Y. Phosphorylation of the C-terminal domain of RNA polymerase II plays central roles in the integrated events of eucaryotic gene expression. *Journal of Biochemistry*. 2007;141(5):601–8.
- Shapiro GI, Harper JW. Anticancer drug targets: cell cycle and checkpoint control. *Journal of Clinical Investigation*. 1999 ;104(12):1645–53.
- Barriere C, Santamaria D, Cerqueira A, Galan J, Martin A et al. Mice thrive without Cdk4 and Cdk2. *Molecular Oncology*. 2007;1(1):72–83.
- Malumbres M, Barbacid M. Cell cycle, CDKs and cancer: a changing paradigm. *Nature Reviews Cancer*. 2009;9(3):153–66.
- Clark A. Natural products as a resource for new drugs. *Pharmaceutical Research*. 1996;13:1133–44.
- Melik-Ogandzhanyan RG, Khachatryan VE, Gapoyan AS. Furo-, Thieno-, and Pyrrolo-[2,3-d]pyrimidines. *Russian Chemical Reviews*. 1985;54(3):262–76.
- Sanghvi YS, Larson SB, Matsumoto SS, Nord LD, Smee DF et al. Antitumor and antiviral activity of synthetic alpha and beta-ribonucleosides of certain substituted pyrimido[5,4-d]pyrimidines: a new synthetic strategy for exocyclic aminonucleosides. *Journal of Medicinal Chemistry*. 1989;32(3):629–37.
- Tenser RB, Gaydos A, Hay KA. Inhibition of herpes simplex virus reactivation by dipyradamole. *Antimicrobial Agents and Chemotherapy*. 2001;45(12):3657–9.
- de-la-Cruz JP, Carrasco T, Ortega G, Sanchez de-la-Cuesta F. Inhibition of ferrous induced lipid peroxidation by pyrimido-pyrimidine derivatives in human liver membranes. *Lipids*. 1992; 27(3):192–4.

10. Sharma P, Rane N, Gurram VK. Synthesis and QSAR studies of pyrimido[4,5-d]pyrimidine-2,5-dione derivatives as potential antimicrobial agents. *Bioorganic & Medicinal Chemistry Letter*. 2004;14(16):4185–90.
11. Ram VJ, Goel A, Sarkhel S, Maulik PR. A convenient synthesis and hepato protective activity of imidazo[1,2-]pyrimido[5,4-]pyrimidine, tetraazaacenaphthene and tetraazaphenalene from cyclic ketene aminals through tandem addition-cyclization reactions. *Bioorganic & Medicinal Chemistry*. 2002;10(5):1275–80.
12. Huang WS, Liu S, Zou D, Thomas M, Wang Y. et al. Discovery of Brigatinib (AP26113), a Phosphine Oxide-Containing, Potent, Orally Active Inhibitor of Anaplastic Lymphoma Kinase. *Journal of Medicinal Chemistry*. 2016;59(10):4948–64.
13. Corona SP, Generali D. Abemaciclib: a CDK4/6 inhibitor for the treatment of HR+/HER2- advanced breast cancer. *Drug Design, Development and Therapy*. 2018;12:321–30.
14. Krallinger M, Valencia A. Text-mining and information-retrieval services for molecular biology. *Genome Biology*. 2005;6(7):224.
15. MarvinSketch 18.30.0, Chemaxon, 2018.
16. Banks JL, Beard HS, Cao Y, Cho AE, Damm W et al. Integrated Modeling Program, Applied Chemical Theory (IMPACT). *Journal of Computational Chemistry*. 2005;26(16):1752–80.
17. Kakarala KK, Jamil K, Devaraji V. Structure and putative signaling mechanism of Protease activated receptor 2 (PAR2) - a promising target for breast cancer. *Journal of Molecular Graphics and Modelling*. 2014;53:179–99.
18. Shelley JC, Cholleti A, Frye LL, Greenwood JR, Timlin MR et al. Epik: a software program for pK(a) prediction and protonation state generation for drug-like molecules. *Journal of Computer-Aided Molecular Design*. 2007;21(12):681–91.
19. Wang S, Griffiths G, Midgley CA, Barnett AL, Cooper M et al. Discovery and characterization of 2-anilino-4- (thiazol-5-yl)pyrimidine transcriptional CDK inhibitors as anticancer agents. *Cell Chemical Biology*. 2010;17(10):1111–21.
20. Jacobson MP, Pincus DL, Rapp CS, Day TJ, Honig B et al. A hierarchical approach to all-atom protein loop prediction. *Proteins*. 2004;55(2):351–67.
21. Protein preparation, version 2.5, Schrödinger, LLC, New York, 2011.
22. Sledz P, Caflisch A. Protein structure-based drug design: from docking to molecular dynamics. *Current Opinion in Structural Biology*. 2018;48:93–102.
23. Friesner RA, Banks JL, Murphy RB, Halgren TA, Klicic JJ et al. Glide: a new approach for rapid, accurate docking and scoring. 1. Method and assessment of docking accuracy. *Journal of Medicinal Chemistry*. 2004;47(7):1739–49.
24. Raha K, Merz KM. A quantum mechanics-based scoring function: Study of zinc ion-mediated ligand binding. *Journal of the American Chemical Society*. 2004;126(4):1020–1.
25. Subhani S, Jayaraman A, Jamil K. Homology modelling and molecular docking of MDR1 with chemotherapeutic agents in non-small cell lung cancer. *Biomedicine & Pharmacotherapy*. 2015;71:37–45.
26. Roy S, Kumar A, Baig MH, Masajik M, Provaznik I. Virtual screening, ADMET profiling, molecular docking and dynamics approaches to search for potent selective natural molecules based inhibitors against metallothionein-III to study Alzheimer's disease. *Methods*. 2015; 83:105–10.
27. Hou T, Wang J, Li Y, Wang W. Assessing the performance of the MM/PBSA and MM/GBSA methods. 1. The accuracy of binding free energy calculations based on molecular dynamics simulations. *Journal of Chemical Information and Modeling*. 2011;51(1):69–82.
28. Desmond, version 4.9, Schrödinger, LLC, New York, 2011.
29. Berendsen HJC, Postma JPM, van Gunsteren WF, Hermans J. *Interaction Models for Water in Relation to Protein Hydration* pages 331–342. Springer Netherlands, Dordrecht. 1981.
30. Hoover WG. Canonical dynamics: Equilibrium phase-space distributions. *Physical Review A*. 1985;31(3):1695–7.
31. Ma Z, Tuckerman M. Constant pressure ab initio molecular dynamics with discrete variable representation basis sets. *The Journal of Chemical Physics*. 2010;133(18):184110.
32. Li J, Abel R, Zhu K, Cao Y, Zhao S, Friesner RA. The VSGB 2.0 model: a next generation energy model for high resolution protein structure modeling. *Proteins*. 2011;79 (10):2794–812.

SUPPLEMENTARY INFORMATION

Table S1. Molecular dynamics simulations results of selected 7 hit compound, FDA-approved two drugs (Abemaciclib and Ribociclib) and two selective CDK2 inhibitors (A-674563 and MK-8776)

Compounds	Gold Docking Scores (kcal/mol)	MD_1 (10 ns) (ΔG /kcal/mol)	MD_2 (10 ns) (ΔG /kcal/mol)	MD_3 (10 ns) (ΔG /kcal/mol)	Average (ΔG /kcal/mol)
30	-4.956	-46.13	-46.15	-47.59	-46.62
236	-6.453	-47.37	-46.99	-42.95	-45.77
2657	-7.533	-75.19	-82.62	-75.62	-77.81
5925	-7.000	-51.46	-53.85	-55.04	-53.45
6447	-7.675	-60.63	-56.98	-60.32	-59.31
2523	-5.969	-43.47	-40.95	-39.53	-41.31
2655	-6.963	-45.13	-45.08	-45.99	-45.40
Abemaciclib	-9.170	-41.75	-39.04	-40.05	-40.28
Ribociclib	-7.568	-49.40	-52.64	-50.99	-51.01
A-674563	-9.685	-46.98	-47.75	-47.24	-47.32
MK-8776	-7.529	-42.12	-44.35	-44.90	-43.79

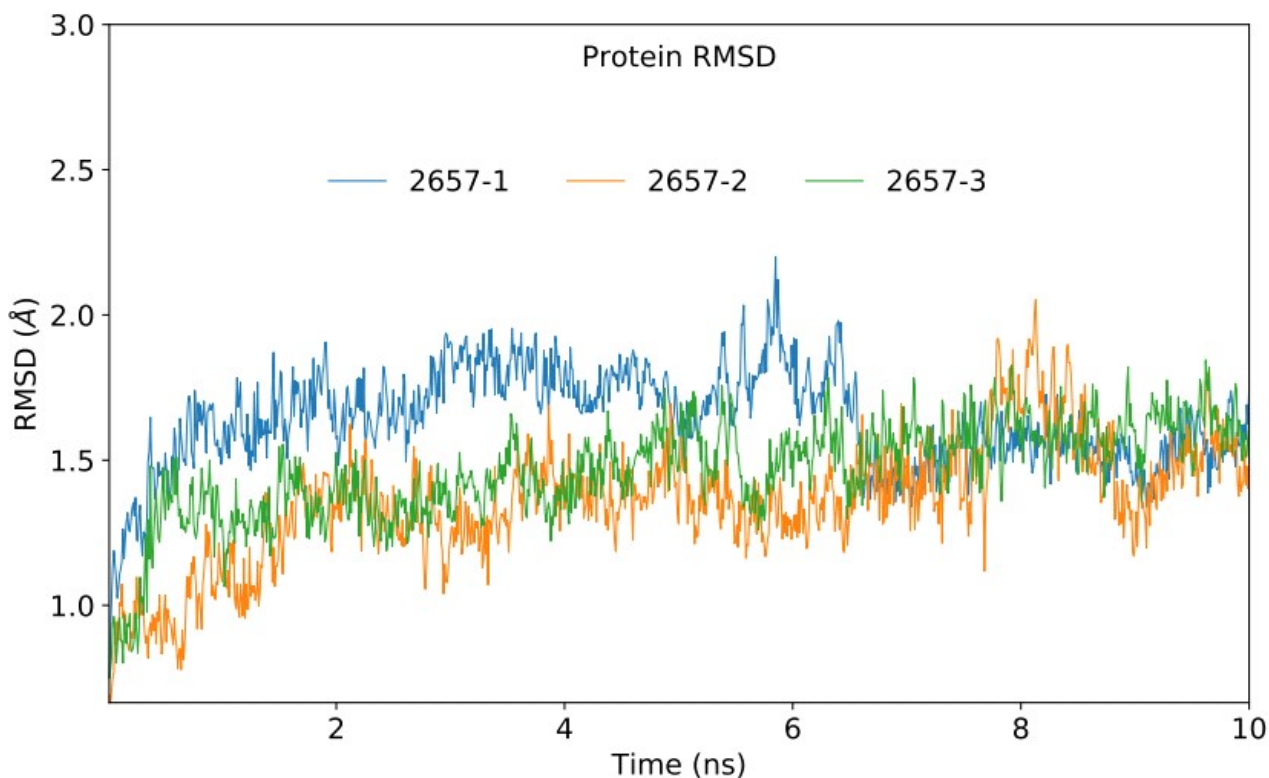


Figure S1: Protein RMSD plot of compound 2657 as a result of 3 separate 10 ns simulations.

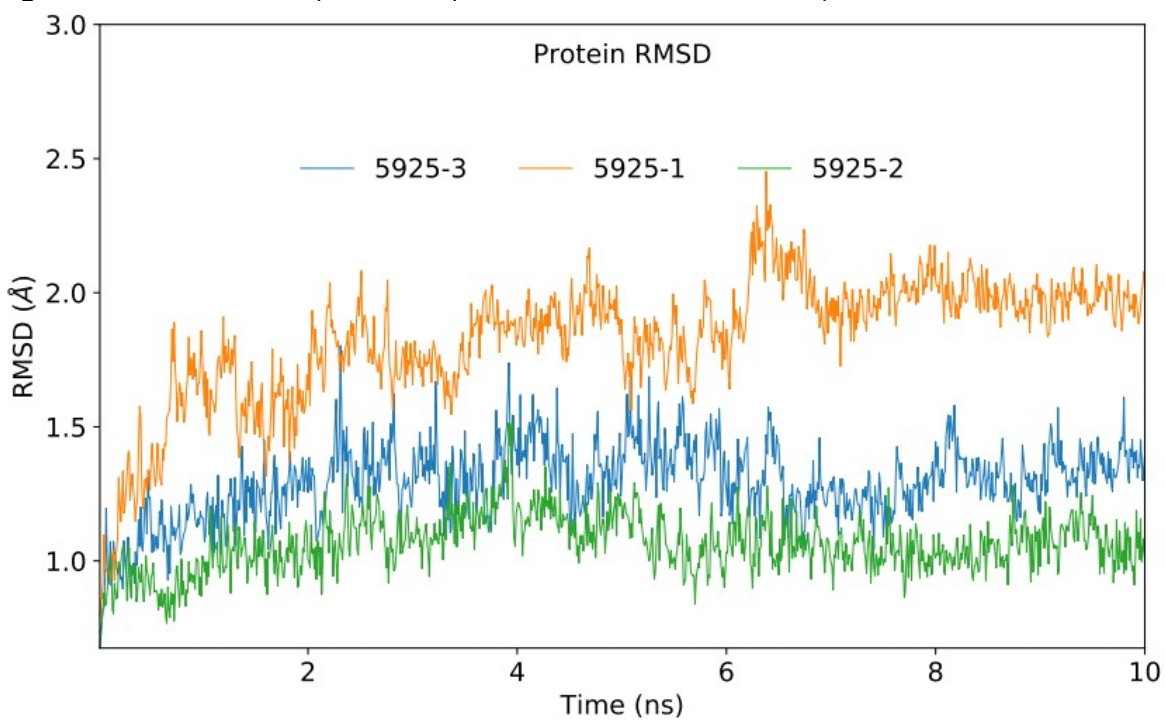


Figure S2: Protein RMSD plot of compound 5925 as a result of 3 separate 10 ns simulations.

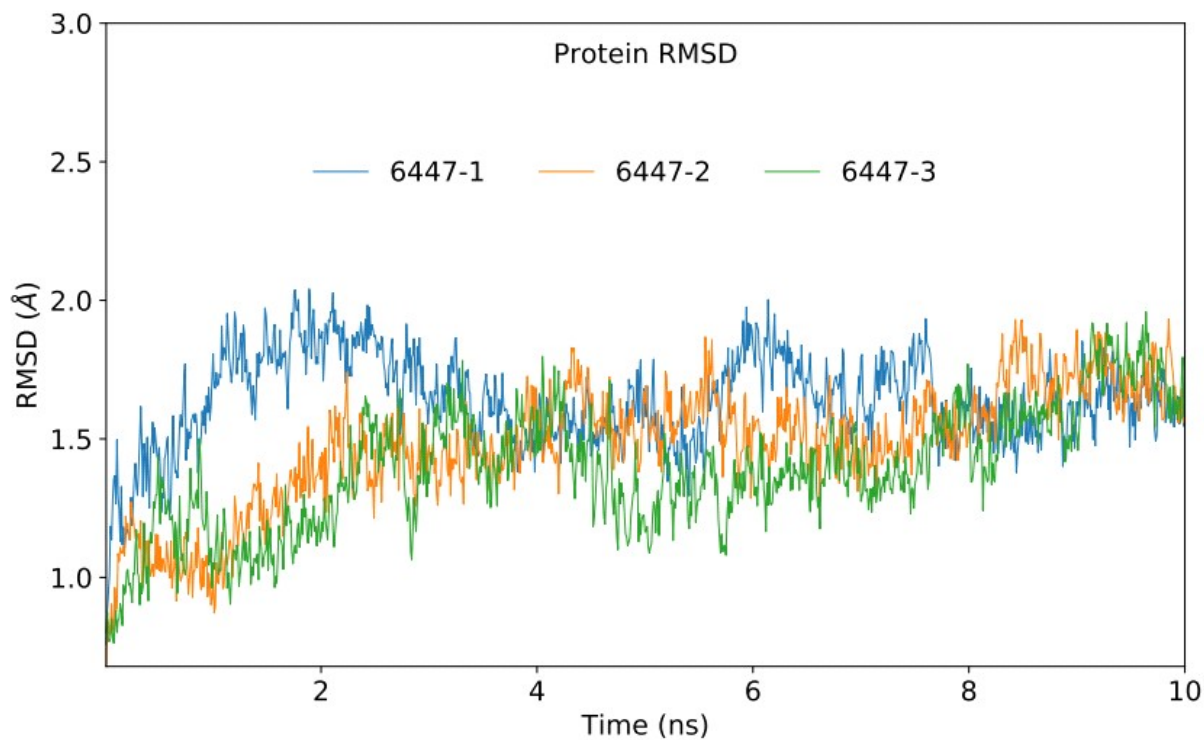


Figure S3: Protein RMSD plot of compound 6447 as a result of 3 separate 10 ns simulations.

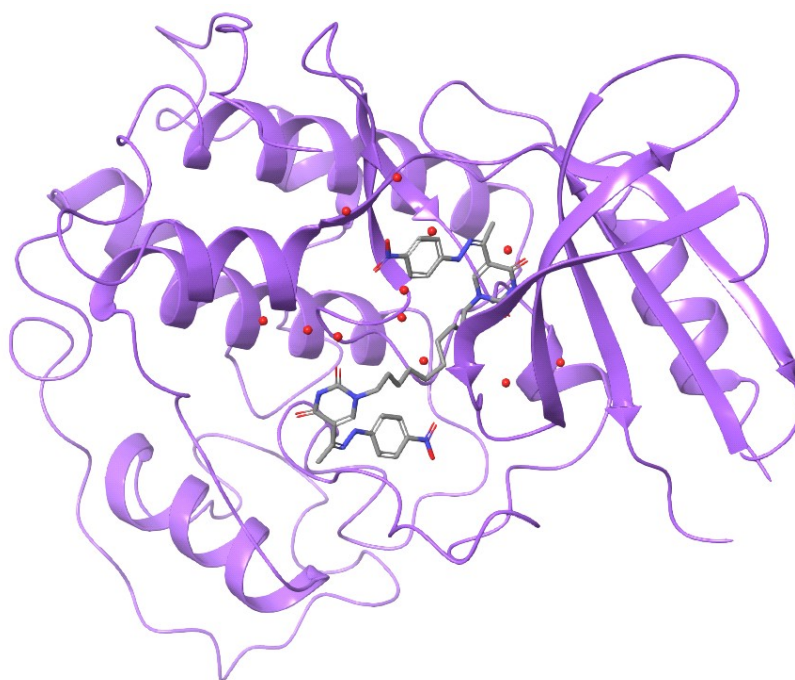


Figure S4: 2XMY-Compound 2657 complex structure.

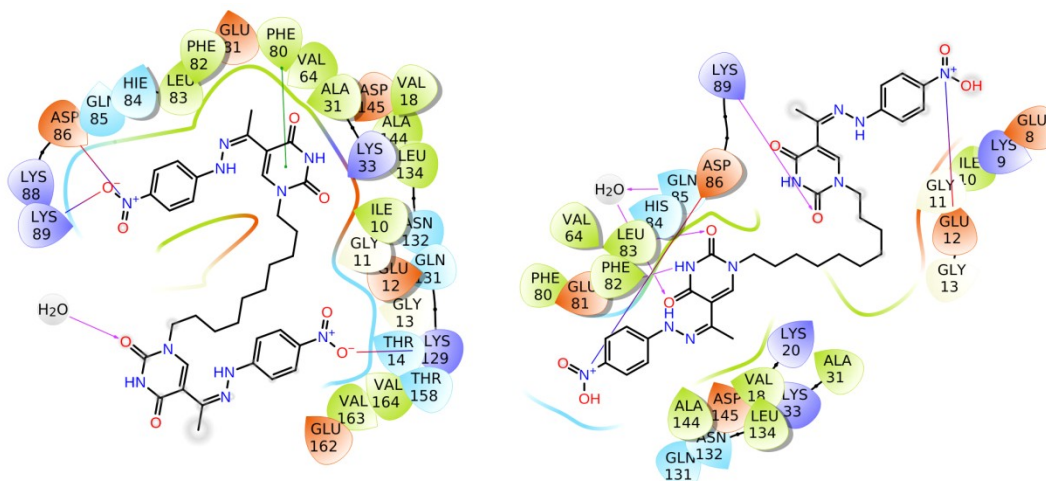


Figure S5: Ligand interactions diagram of compound 2657 (left Glide docking and right Gold docking)

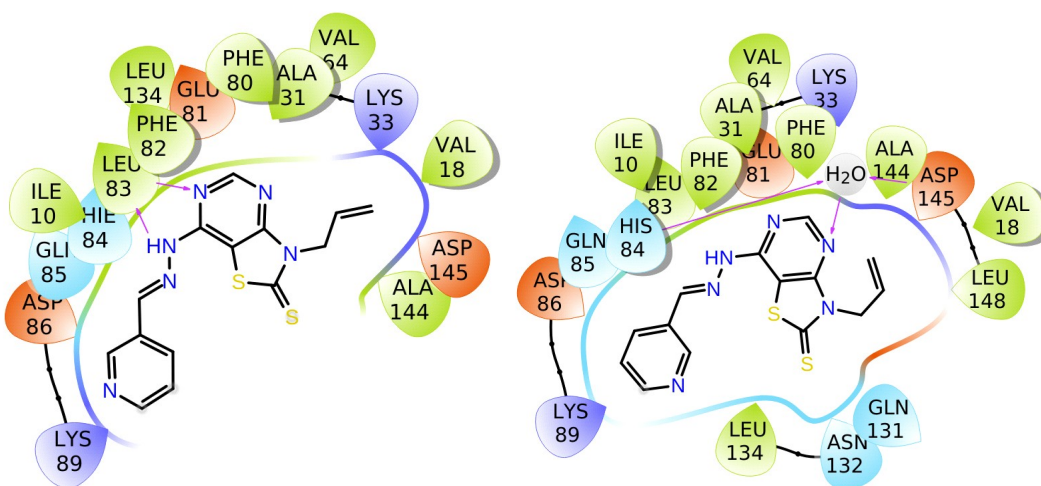


Figure S6: Ligand interactions diagram of compound 5925 (left Glide docking and right Gold docking)

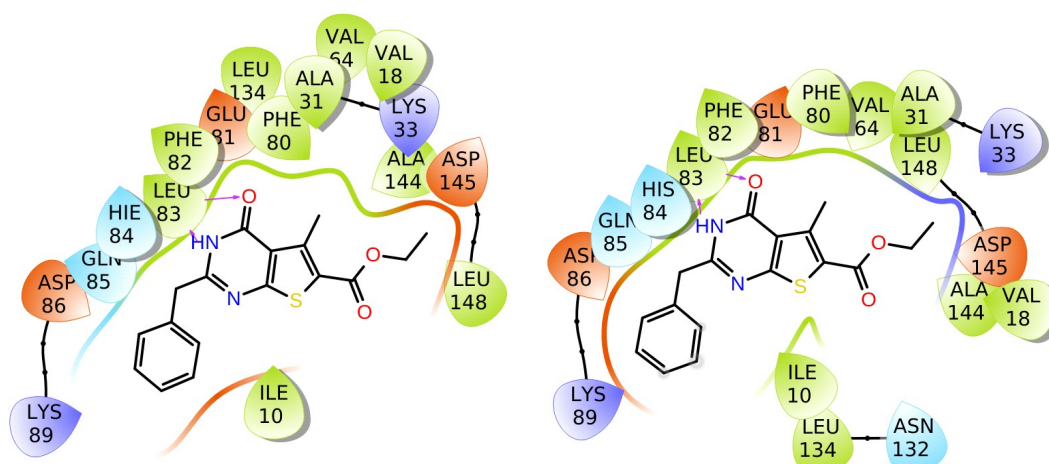


Figure S7: Ligand interactions diagram of compound 6447 (left Glide docking and right Gold docking)

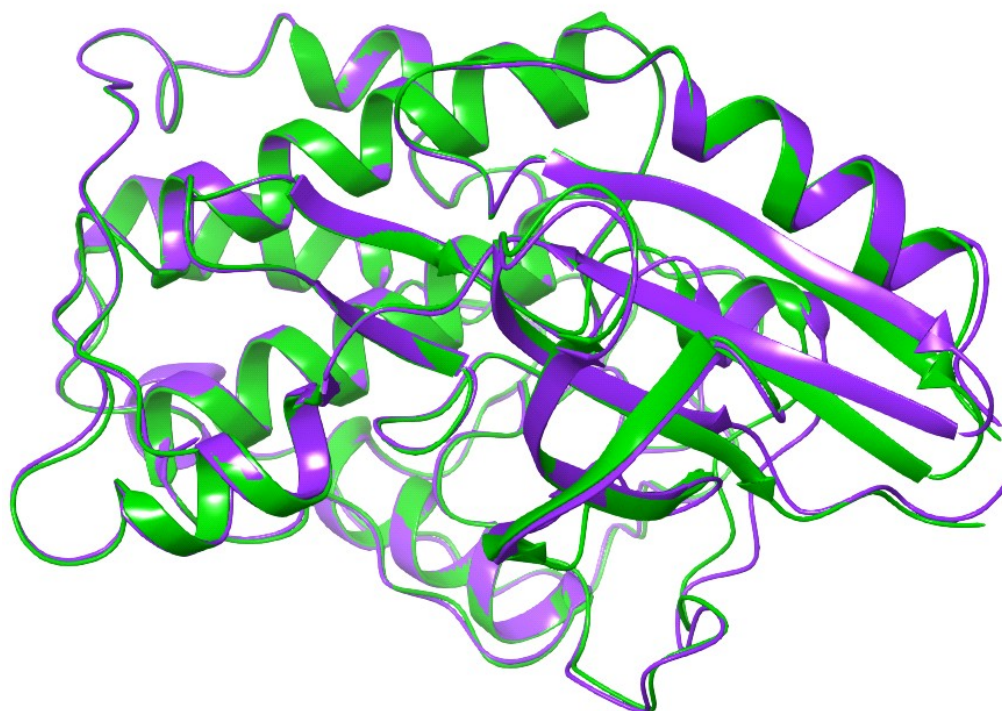


Figure S8: Alignment of 2XMY and 2XNB (Alignment Score: 0.014 ; RMSD: 0.583 A)

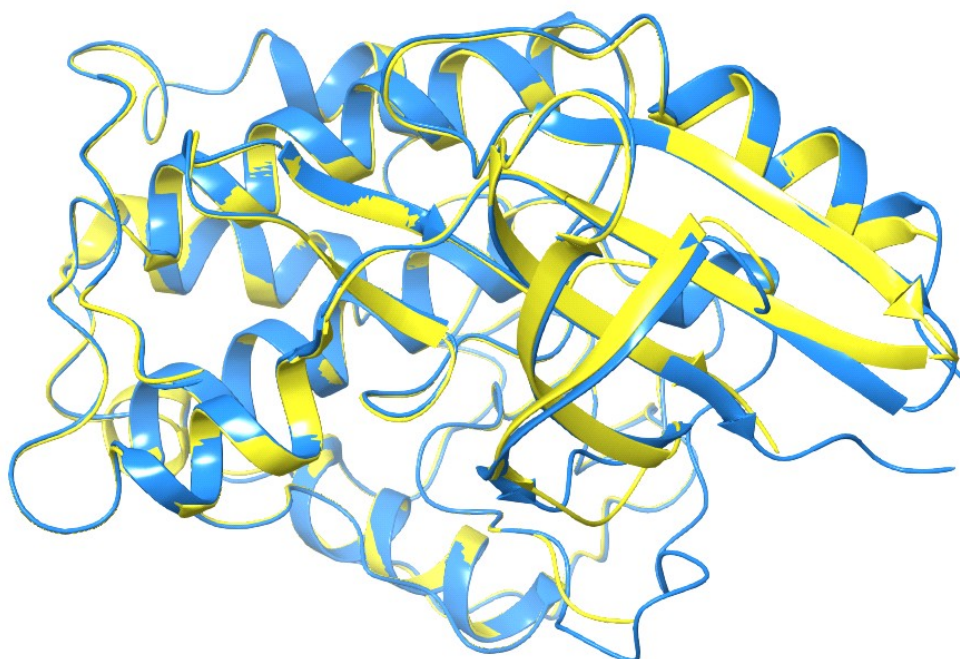


Figure S9: Alignment of 2XMY and 2W05 (Alignment Score: 0.016; RMSD: 0.629 A)

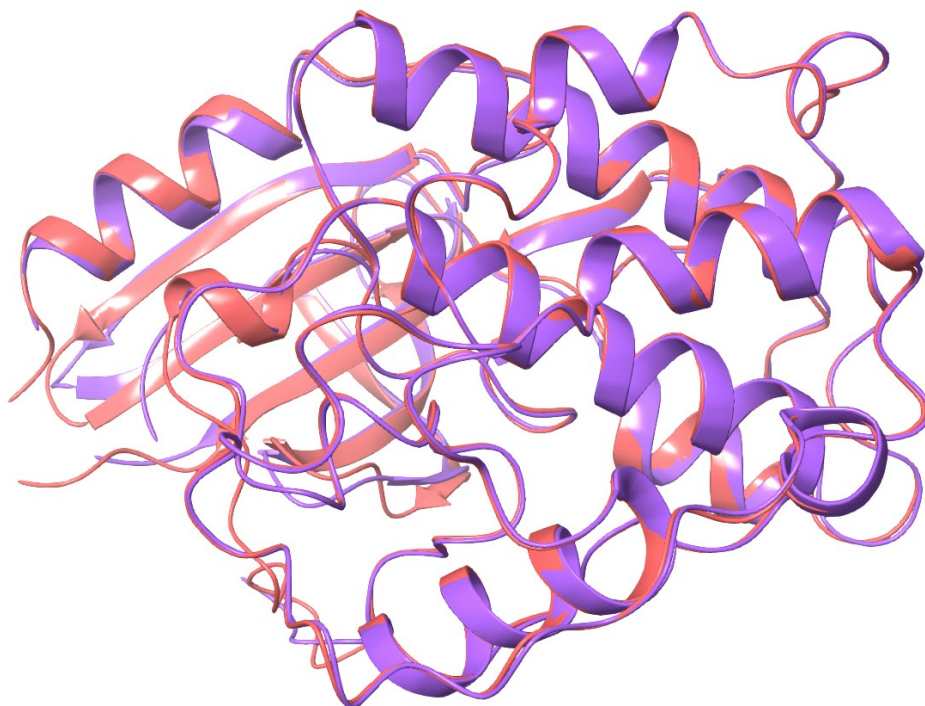


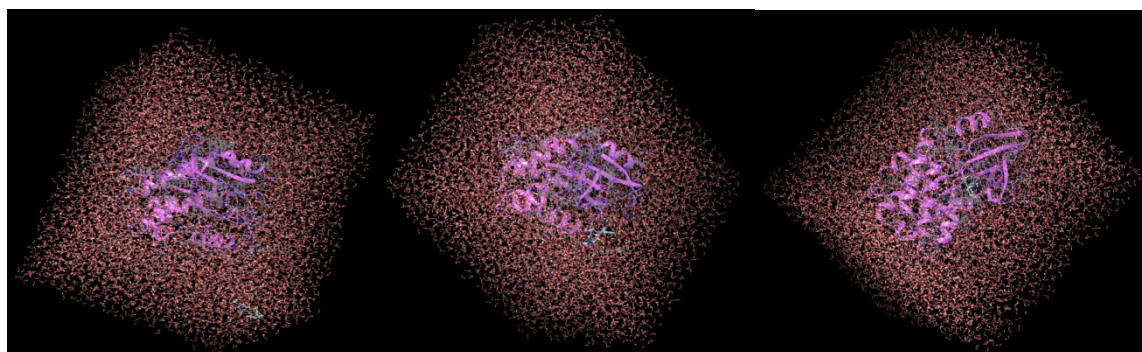
Figure S10: Alignment of 2XMY and 1Y91 (Alignment Score: 0.018; RMSD: 0.670 A)

Table S2: A method development-validation1.

Title	Stars	t Q	Job Name	docking score
glide-dock_SP_validation_se...				
2XMY - minimized	☆☆☆		glide-dock_SP_validat...	
2m	☆☆☆	0	glide-dock_SP_validat...	-8.629
2c	☆☆☆	0	glide-dock_SP_validat...	-7.510
2c	☆☆☆	0	glide-dock_SP_validat...	-7.510
2d	☆☆☆	0	glide-dock_SP_validat...	-7.428
2n	☆☆☆	0	glide-dock_SP_validat...	-7.077
2h	☆☆☆	0	glide-dock_SP_validat...	-6.729
glide-dock_SP_validation_se...				
2XMY - minimized	☆☆☆		glide-dock_SP_validat...	
2i	☆☆☆	0	glide-dock_SP_validat...	-7.499
2l	☆☆☆	-1	glide-dock_SP_validat...	-7.490
2j	☆☆☆	0	glide-dock_SP_validat...	-6.880
2k	☆☆☆	-1	glide-dock_SP_validat...	-4.472

Table S3. A method development-validation2.

Title	omer probability	docking score
glide-dock_SP_validation_set3_inactive_...		
2XMY - minimized		
12	1.000	-8.839
17	1.000	-8.174
16	1.000	-6.361
glide-dock_SP_validation_set3_active_pv...		
2XMY - minimized		
11e	1.000	-9.554
11a	1.000	-9.273
11h	1.000	-7.286



FigureS11: Initial (right), after 60 ns (center) and last (left) poses of compound 2523 throughout 100 ns molecular dynamics simulations.



Assessment of Elemental Content, Antioxidant Activity, and Total Phenolic Content of *Vitis sylvestris* Gmelin

Nagihan Karaaslan Ayhan^{1,2}  

¹Munzur University, Tunceli Vocational School, Department of Chemistry and Chemical Processing Technologies, Tunceli, Turkey.

²Munzur University, Rare Earth Elements Application and Research Center, Tunceli, Turkey.

Abstract: In this study, we determined the Cu, Fe, Mn, and Zn contents of *Vitis sylvestris* Gmelin using flame atomic absorption spectrometry (FAAS), and examined the antioxidant properties of *Vitis sylvestris* Gmelin using radical scavenging capacities and total phenolic content tests. We found the average elemental contents; Cu, Fe, Mn, and Zn as 1.506 ± 0.042 mg/kg, 0.796 ± 0.020 mg/kg, 2.333 ± 0.033 mg/kg, and 3.191 ± 0.262 mg/kg, respectively. When we examined the antioxidant activity tests applied to different extracts, we determined the highest extraction yield with the methanol extract. DPPH radical scavenging activity, ABTS radical scavenging activity, and total phenolic content values in methanol extract were determined to be respectively 3.957 ± 0.146 mg TEAC/g fw, 9.062 ± 0.273 mg TEAC/g fw, and 2.365 ± 0.028 mg GAE/g fw. When we evaluated the antioxidant activity and total phenolic content results for all extracts statistically, we determined that there was generally a statistically significant difference between each extract ($p < 0.01$). *Vitis sylvestris* Gmelin has high antioxidant content when considering the data obtained. Also, we determined that it is an effective candidate in the protection against reactive oxygen species.

Keywords: *Vitis sylvestris* Gmelin, elemental content, antioxidant activity, extraction.

Submitted: February 15, 2020. **Accepted:** April 07, 2020.

Cite this: Karaaslan Ayhan N. Assessment of Elemental Content, Antioxidant Activity, and Total Phenolic Content of *Vitis sylvestris* Gmelin. JOTCSA. 2020;7(2):405-10.

DOI: <https://doi.org/10.18596/jotcsa.689329>.

***Corresponding author. E-mail:** nkaraaslan@munzur.edu.tr. Tel: +90 428 213 17 94.

INTRODUCTION

Copper (Cu), iron (Fe), manganese (Mn), and zinc (Zn) are essential elements for human health and should be taken into the body to maintain many important metabolic activities in the human body (1, 2). These elements play an essential role in the growth, development, and health of the human body (2-5). We can find Cu in the structure of many enzymes; similarly, Zn is defined as a co-factor in some enzymes and is involved in various metabolic activities. For example, if we do not take copper and zinc into the human body in sufficient quantities, then the bodily functions may be adversely affected. Consuming various vegetables,

fruits, and food products supply the essential elements needed by the human body.

Antioxidants protect our body against diseases by reacting with almost all classes of compounds in the structure of living organisms, by taking a role in the reduction of reactive oxygen species (ROS), which cause significant damage. Antioxidant compounds have an essential role against diseases such as cancer, diabetes, gastrointestinal diseases, neurodegenerative diseases, and aging caused by excessive reactive oxygen species. Many synthetic antioxidant compounds are available, but it is clear that these compounds have toxic and mutagenic effects. In recent years, we started to prefer

natural antioxidant compounds rather than synthetic ones, and we can take these compounds from various sources, including vegetables and fruits. Fruits and vegetables are rich antioxidant sources concerning phenolic compounds, anthocyanins, vitamins, and mineral elements in the literature (6, 7). Authors state that the adverse effects of free radicals reduce by consuming foods, including antioxidants, because of their positive effects on health (6, 8-10).

Turkey, a country rich in fruit and vegetable varieties, is a potential source of phenolic compounds, and one of them is wild grapes and grape varieties (11, 12). In the literature, there are studies about antioxidant activity, phenolic, vitamin, and elemental content of wild grapes grown in different regions (13-16). As a result of biodiversity, which is emerging due to physical geography characteristics, climate differences, and abundant water resources, it is determined that there is no data about wild edible *Vitis sylvestris* Gmelin reported (17) to naturally grown in Pertek-Tunceli district (Turkey). In this context, we investigated the element content, antioxidant activity, and total phenolic content of *Vitis sylvestris* Gmelin.

MATERIAL AND METHOD

Reagents and standards

All chemicals and solvents used in sample and standard solution preparation were of analytically pure grade and obtained from Sigma-Aldrich and Merck. We used ultrapure water (Milli-Q, Millipore 18.2 $\mu\Omega$ cm⁻¹) in the experimental studies. We drew calibration graphs by standard solutions prepared in different concentration levels and used these graphs to evaluate the obtained data.

Element contents were determined using Perkin Elmer AAnalyst 800 flame atomic absorption spectrometer (FAAS) (Perkin Elmer, Inc., Shelton, CT, USA). The operation conditions are as follows: We set the wavelength and slit width for Cu, Fe, Mn, Zn respectively 324.8-07 nm, 248.3-0.2 nm, 279.5-0.2 nm, 213.9-0.7 nm, and acetylene and air flow rate was 2.0 L/min and 17.0 L/min. We used a Shimadzu 1800 UV-Vis spectrophotometer for antioxidant activity measurements.

Sample preparation

Vitis sylvestris Gmelin (wild grape) naturally grown in Pertek-Tunceli, Turkey was gathered manually on the season, and then samples were mixed, washed with tap water, lastly passed through deionized water. We then stored them in the freezer until the analysis time.

Wet Digestion procedure for elemental analyses: We separated *Vitis sylvestris* Gmelin samples into

small pieces, transferred approximately a 1-g sample into the beakers, and dissolved with 2 mL of concentrated 1:1 HNO₃: H₂O₂ mixture. We evaporated the samples near dryness with occasional stirring and repeated the same procedure once again. We completed the final volumes to 5 mL with 1.0 M HNO₃ and centrifuged to obtain homogeneous solutions. We carried out elemental analyses in the solutions using FAAS. Blank samples and standard reference materials (0.25 g) (NIST-1547 peach leaves) were also prepared using the same procedure and analyzed. We expressed the results as mean values \pm standard deviation of three independent analyses based on fresh weight.

Extraction procedure for antioxidant activity: We separated *Vitis sylvestris* Gmelin samples into small pieces, approximately 5 g samples transferred into the beakers, and acidified 10 mL of extraction solvents such as water, acetonitrile, and methanol with 0.1% HCl to the samples. We then mixed the samples with extraction solvents for 60 min at room temperature and then centrifuged (10 min at 5000 rpm). We passed the clear solutions through a 0.45 μ m injection filter. For DPPH and ABTS radical scavenging activities, we applied total phenolic content tests to different sample extracts. We expressed the results as mean values \pm standard deviation of three independent analyses based on fresh weight.

Antioxidant Activity Tests

DPPH radical scavenging activities in the extracts were determined using the method applied by Brand-Williams et al. (18). We made the volumes of extracts taken in a certain amount to 2.5 mL with DPPH solution and then incubated for 30 min at room temperature. We used a UV-Vis spectrophotometer for the absorbance measurements of the solutions at 517 nm. Trolox was the standard and stated the results as Trolox equivalent on fresh weight (mg TEAC/g fw).

We used the method proposed by Re et al. (19) to measure ABTS radical scavenging activity of the sample extracts. The extracts were made up to 2.5 mL with ABTS solution and incubated at room temperature for 30 minutes in the dark. At the end of the incubation time, we measured the absorbance values with a UV-Vis spectrophotometer at 734 nm. Trolox was the standard, and we stated the results as Trolox equivalent on fresh weight (mg TEAC/g fw).

Determination of Total Phenolic Content

We determined the total phenolic contents by measuring the absorbance value of the color formed by adding the Folin-Ciocalteu reactant and 2% sodium carbonate solution to the extracts (20). We determined the absorbance values by

measuring with a UV-Vis spectrophotometer at 755 nm after 30 minutes of incubation at room temperature. The standard was gallic acid and we expressed the experimental data in terms of gallic acid equivalent on fresh weight (mg GAE/g fw).

We used GraphPad Software (version 5.01 for Windows, GraphPad Software, USA) for the statistical analyses for antioxidant activity and total phenolic content. We established the significance between the groups using the one-way analysis of variance (ANOVA) and Tukey's multiple comparison tests. We considered the differences statistically significant when $p < 0.01$.

RESULTS AND DISCUSSION

We used FAAS to determine Cu, Fe, Mn, and Zn contents in *Vitis sylvestris* Gmelin. We found the Cu, Fe, Mn, and Zn contents were 1.506 ± 0.042 mg/kg, 0.796 ± 0.020 mg/kg, 2.333 ± 0.033 mg/kg, and 3.191 ± 0.262 mg/kg, respectively. We tested the accuracy of the method with standard reference material (NIST-1547 peach leaves). We determined the certified values for this standard reference material to be 3.75 ± 0.37 mg/kg for Cu, 219.8 ± 6.8 mg/kg for Fe, 97.8 ± 1.8 mg/kg for Mn, and 17.94 ± 0.53 mg/kg for Zn. In the present study, we found the Cu, Fe, Mn, and Zn contents obtained with the used method to be 3.48 ± 0.25 mg/kg, 198.7 ± 7.0 mg/kg, 90.1 ± 2.1 mg/kg, and 17.08 ± 0.48 mg/kg, respectively. We found the recovery values for these elements to be 93% for Cu, 90 % for Fe, 92% for Mn, and 95% for Zn.

A literature study has reported that Cu, Fe, Mn, and Zn concentrations in grapes found from 0.4 ± 0.1 to 2.4 ± 0.1 $\mu\text{g/g}$, 6.6 ± 0.1 to 14.8 ± 0.3 $\mu\text{g/g}$, 3.1 ± 0.2 to 41.8 ± 0.2 $\mu\text{g/g}$, and 2.1 ± 0.1 to 20.4 ± 1.0 $\mu\text{g/g}$ in a study, respectively (21). In another study, researchers determined the element contents in the grape as 2.6 ± 0.1 $\mu\text{g/g}$ for Cu, 3.8 ± 0.2 $\mu\text{g/g}$ for Fe, 3.4 ± 0.2 $\mu\text{g/g}$ for Mn, and 2.2 ± 0.1 $\mu\text{g/g}$ for Zn (22). Researchers examined the elemental contents of some fruits and vegetables in a study. They found Cu and Zn concentrations in the grape to be 3.5 mg/kg and 6.1 mg/kg, respectively (23). In the present study, the data concerning elemental contents were compatible, found with the literature data.

We determined the antioxidant activity of *Vitis sylvestris* Gmelin using DPPH and ABTS radical scavenging activities and total phenolic content tests, applying these tests to the extracts of the samples processed with water, acetonitrile and methanol, and evaluated the results statistically. There is a mention in a literature report that antioxidant activity results changed significantly depending on the solvent type (24-27). In the current study, we applied the antioxidant activity and total phenolic content test applied to different extracts; we obtained the highest results for all tests with methanolic extracts. As seen in Figure 1, average DPPH radical scavenging activity results were determined to be 0.537 ± 0.060 mg TEAC/g fw for aqueous extracts, 3.785 ± 0.077 mg TEAC/g fw for acetonitrile extracts, 3.570 ± 0.08 mg TEAC/g fw for ethanolic extracts, and 3.957 ± 0.146 mg TEAC/g fw for methanolic extracts. We evaluated the results statistically. We found out that there were statistically significant differences between acetonitrile, ethanolic and methanolic extracts of aqueous extracts, and also between ethanolic and methanolic extracts. On the other hand, we determined that there were no statistically significant differences between ethanol and methanol extracts of acetonitrile extracts ($p < 0.01$).

We found the average ABTS radical scavenging activity results for water, acetonitrile, ethanol, and methanol extracts as 2.285 ± 0.120 mg TEAC/g fw, 7.984 ± 0.355 mg TEAC/g fw, 8.471 ± 0.642 mg TEAC/g fw, and 9.062 ± 0.273 mg TEAC/g fw, respectively (Figure 2). When we examined the data statistically, we determined that there were statistically significant differences between acetonitrile, ethanolic, and methanolic extracts against aqueous extracts, and also between acetonitrile and methanolic extracts. On the other hand, we found that there were no statistically significant differences between acetonitrile and methanol extracts of ethanol extracts ($p < 0.01$). While we found the highest total phenolic content in methanolic extracts (2.365 ± 0.028 mg GAE/g fw), the lowest total phenolic content was in aqueous extracts (0.592 ± 0.045 mg GAE/g fw) (Figure 3). When we statistically compared the data for total phenolic contents, we found that there was a statistically significant difference between every two extracts except for acetonitrile and ethanolic extracts ($p < 0.01$).

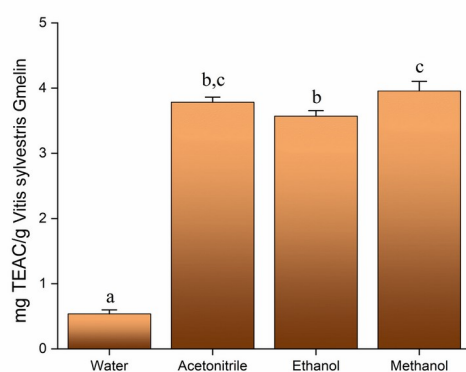


Figure 1: DPPH radical scavenging activity of *Vitis sylvestris* Gmelin.

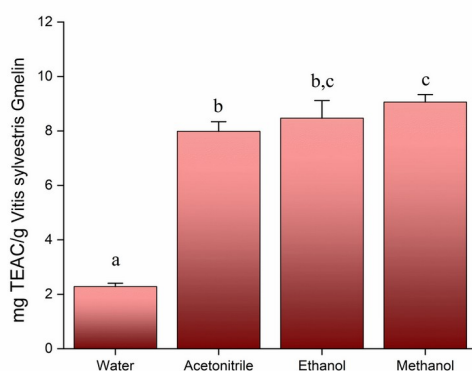


Figure 2: ABTS radical scavenging activity of *Vitis sylvestris* Gmelin.

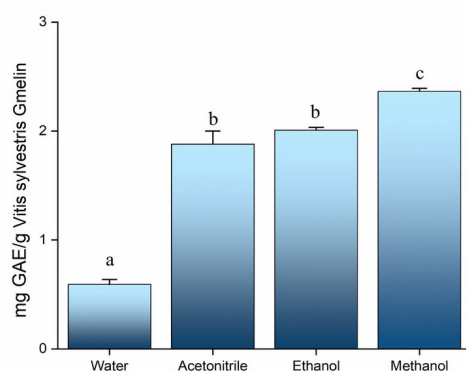


Figure 3: Total phenolic content of *Vitis sylvestris* Gmelin.

In a study, researchers examined phenolic profile and antioxidant activity of different grape varieties and reported total phenolic content results in a range from 0.44 ± 0.02 to 7.94 ± 0.19 mg gallic acid equivalents/g grape sample (28). Antioxidant activity of black grape obtained applying different drying methods determined with DPPH and ABTS assay, total phenolic content tests. Literature reports that antioxidant activity results changed

depending on different drying methods. The highest value for total phenolic content found to be 20.21 mg/g DW in fresh grapes, but this value in the freeze-, oven- and sun-dried samples continued to decrease. The values of DPPH and ABTS antioxidant activities in fresh grapes determined as 66.07 mmol TE/kg DW and 137.65 mmol TE/kg DW (29). Total phenolic compounds of red grape varieties examined by Correia and

Jordão found to be average 1341.0 mg/L, and antioxidant capacities determined varying from 3.96 to 32.96 mm/L Fe(II) (30). The results in the presented study were compatible with those found in the literature. Researchers determined that the data changed importantly depending on different conditions such as drying method, extraction method, and solvent type, as stated in the literature (24-27, 30).

CONCLUSIONS

In this study, we investigated the elemental content and antioxidant activity of *Vitis sylvestris* Gmelin. Elemental analysis results carried out as applied to the wet digestion method were determined to be 1.506 ± 0.042 mg/kg for Cu, 0.796 ± 0.020 mg/kg for Fe, 2.333 ± 0.033 mg/kg for Mn, and 3.191 ± 0.262 mg/kg for Zn, respectively. We have found that DPPH and ABTS radical scavenging activity, total phenolic content results tested with different polar solvents are 3.957 ± 0.146 mg TEAC/g fw, 9.062 ± 0.273 mg TEAC/g fw, 2.365 ± 0.028 mg GAE/g fw for methanol extracts determined as the best solvents. *Vitis sylvestris* Gmelin naturally grown in Pertek, Tunceli; according to the obtained results can be evaluated as an antioxidant food, especially, we will add new data with this study about the fruit to the literature.

CONFLICT OF INTEREST

The author declares no conflict of interest.

REFERENCES

- Martínez-Ballesta MC, Dominguez-Perles R, Moreno DA, Muries B, Alcaraz-López C, Bastías E, et al. Minerals in plant food: effect of agricultural practices and role in human health. A review. *Agron Sustain Dev*. 2010 Apr;30(2):295–309.
- Yin Y, Li Y, Li Q, Jia N, Liu A, Tan Z, et al. Evaluation of the Relationship Between Height and Zinc, Copper, Iron, Calcium, and Magnesium Levels in Healthy Young Children in Beijing, China. *Biol Trace Elem Res*. 2017 Apr;176(2):244–50.
- Salgueiro MJ, Zubillaga MB, Lysionek AE, Caro RA, Weill R, Boccio JR. The role of zinc in the growth and development of children. *Nutrition*. 2002 Jun;18(6):510–9.
- Đermanović M, Miletić I, Pavlović Z. A Comparative Analysis of the Contents Of Iron, Zinc, Copper, Manganese, and Calcium in the Collective Diet Of Preschool Children in the Northwestern Region of Bosnia. *Biol Trace Elem Res*. 2017 Jan;175(1):27–32.
- Cao J, Gao Z, Yan J, Li M, Su J, Xu J, et al. Evaluation of Trace Elements and Their Relationship with Growth and Development of Young Children. *Biol Trace Elem Res*. 2016 Jun;171(2):270–4.
- Manach C, Scalbert A, Morand C, Rémésy C, Jiménez L. Polyphenols: food sources and bioavailability. *The American Journal of Clinical Nutrition*. 2004 May 1;79(5):727–47.
- Hanasaki Y, Ogawa S, Fukui S. The correlation between active oxygens scavenging and antioxidative effects of flavonoids. *Free Radical Biology and Medicine*. 1994 Jun;16(6):845–50.
- Robards K, Antolovich M. Analytical Chemistry of Fruit Bioflavonoids A Review. *Analyst*. 1997;122(2):11R-34R.
- Zhu F. Anthocyanins in cereals: Composition and health effects. *Food Research International*. 2018 Jul;109:232–49.
- M. Calderon-Montano J, Burgos-Moron E, Perez-Guerrero C, Lopez-Lazaro M. A Review on the Dietary Flavonoid Kaempferol. *MRMC*. 2011 Apr 1;11(4):298–344.
- Karataş DD, Karataş H, Laucou V, Sarikamiş G, Riahi L, Bacilieri R, et al. Genetic diversity of wild and cultivated grapevine accessions from southeast Turkey. *Hereditas*. 2014 Oct;151(4–5):73–80.
- Ergül A, Perez-Rivera G, Söylemezoğlu G, Kazan K, Arroyo-Garcia R. Genetic diversity in Anatolian wild grapes (*Vitis vinifera* subsp. *sylvestris*) estimated by SSR markers. *Plant Genet Res*. 2011 Aug;9(3):375–83.
- Dastoor R, Bakhshi D, Aliakbar A. Resveratrol and other phenolic compounds from wild grape *Vitis vinifera*. ssp *sylvestris*. *JBES*. 2017;11(4):121–30.
- Jiménez M, Juárez N, Jiménez-Fernández VM, Monribot-Villanueva JL, Guerrero-Analco JA. Phenolic compounds and antioxidant activity of wild grape (*vitis tiliifolia*). *Italian Journal of Food Science [Internet]*. 2017 Nov 21 [cited 2020 Apr 7];30(1). Available from: <http://doi.org/10.14674/IJFS-975>
- Margaryan K, Melyan G, Vardanyan D, Devejyan H, Aroutiounian R. Phenolic content and antioxidant activity of Armenian cultivated and wild grapes. Aurand J-M, editor. *BIO Web Conf*. 2017;9:02029.

16. Revilla E, Bellido A, Yus J, Ortiz P, Carrasco D, Arroyo RA. Flavonols in skins of wild grapes (*Vitis vinifera* L., subsp. *sylvestris* (Gmelin) Hegi). Aurand J-M, editor. BIO Web Conf. 2016;7:01018.
17. Doğan A. Pertek (Tunceli) yöresinde etnobotanik araştırmalar [PhD Thesis]. [İstanbul]: Marmara University; 2014.
18. Brand-Williams W, Cuvelier M, Berset C. Use of a Free Radical Method to Evaluate Antioxidant Activity. *Lebensm-Wiss u-Technol.* 1995;28:25–30.
19. Re R, Pellegrini N, Proteggente A, Pannala A, Yang M, Rice-Evans C. Antioxidant activity applying an improved ABTS radical cation decolorization assay. *Free Radical Biology and Medicine.* 1999 May;26(9–10):1231–7.
20. Singleton V, Rossi J. Colorimetry of Total Phenolics with Phosphomolybdic-Phosphotungstic Acid Reagents. *American Journal of Enology and Viticulture.* 1965;16:144–58.
21. Unsal Y, Yilmaz E, Soylak M, Tuzen M. Trace element contents of raisins, grape and soil samples from Incesu-Kayseri, Turkey. *Fresenius Environmental Bulletin.* 2013;22(5):1441–5.
22. Yami SG, Chandravanshi BS, Wondimu T, Abuye C. Assessment of selected nutrients and toxic metals in fruits, soils and irrigation waters of Awara Melka and Nura Era farms, Ethiopia. *SpringerPlus.* 2016 Dec;5(1):747.
23. Aydinalp C, Marinova S. Concentration of Cu and Zn in Some fruits and Vegetables grown in north western Turkey. *Bulgarian Journal of Agricultural Science.* 2012;18(5):749–51.
24. Mitic M, Kostic D, Pavlovic A, Dimitrijevic D, Veljkovic J. Effects of solvent extraction system on concentration and antioxidant activity of strawberry phenolics. *Agro Food Industry Hi-Tech.* 2014;25(5):24–8.
25. Boulekbache-Makhlouf L, Medouni L, Medouni-Adrar S, Arkoub L, Madani K. Effect of solvents extraction on phenolic content and antioxidant activity of the byproduct of eggplant. *Industrial Crops and Products.* 2013 Aug;49:668–74.
26. Karaaslan MG, Karaaslan NM, Ates B. Investigation of Mineral Components and Antioxidant Properties of a Healthy Red Fruit: Cornelian Cherry (*Cornus mas* L.). *Journal of the Turkish Chemical Society, Section A: Chemistry.* 2018 Nov 17;1319–26.
27. Karaaslan NM, Karaaslan MG, Ates B. Effects of Some Extraction Solvents on the Antioxidant Properties of Strawberry Fruit. *International Journal of Pure and Applied Sciences [Internet].* 2018 Dec 27 [cited 2020 Apr 7]; Available from: <http://dergipark.gov.tr/doi/10.29132/ijpas.354885>
28. Di Lorenzo C, Colombo F, Biella S, Orgiu F, Frigerio G, Regazzoni L, et al. Phenolic profile and antioxidant activity of different grape (*Vitis vinifera* L.) varieties. Aurand J-M, editor. *BIO Web Conf.* 2019;12:04005.
29. Çoklar H, Akbulut M. Effect of sun, oven and freeze-drying on anthocyanins, phenolic compounds and antioxidant activity of black grape (Eksikara)(*Vitis vinifera* L.). *South African Journal of Enology and Viticulture.* 2017;38(2):264–272.
30. Correia AC, Jordão AM. Antioxidant capacity, radical scavenger activity, lipid oxidation protection analysis and antimicrobial activity of red grape extracts from different varieties cultivated in Portugal. *Natural Product Research.* 2015 Mar 4;29(5):438–40.



Graphene Oxide-Ionic Liquid Used as Solid-Phase Microextraction Coating for Polyphenolic Compounds' Extraction and Determination with GC-MS After On-Fiber Derivatization in Wine

Paniz Tashakkori¹  , Aylin Altinisik Tagac²  , Melek Merdivan²  *

¹Graduate School of Natural and Applied Science, Dokuz Eylul University, Tinaztepe Campus, Izmir 35160, Turkey.

² Faculty of Science, Chemistry Department, Dokuz Eylul University, Tinaztepe Campus, Izmir 35390, Turkey.

Abstract: We describe the use of a home-made fiber coated by graphene oxide modified by an ionic liquid having methylimidazolium cation with an amino-functional group for the extraction of polyphenolic compounds (P.C.s). We then performed the determination by gas chromatography coupled with mass spectrometry after on-fiber derivatization. The authors optimized the main parameters influencing the extraction and derivatization processes. The on-fiber derivatization was employed within 15 min at 60 °C using 20 µL of trimethylsilyl reagents. Under the optimized conditions, the calibration curves for 12 P.C.s were linear from 0.1 to 1000 µg/L, and the detection limits were between 0.02 and 0.1 µg/L. We determined the single fiber repeatability obtained for all calibration points and the fiber to fiber reproducibility for 100 µg/L to be < 14.82% and < 5.87%, respectively. The extraction efficacy of the home-made fiber due to high intermolecular and electrostatic attractions was much better than the commercial fibers. We successfully applied the method to the analysis of P.C.s in wine samples with the recoveries from 72.8 to 99.9%.

Keywords: GO-[APMIM][NTf2] coated fiber, SPME-GC-MS, polyphenolic compounds, derivatization on-fiber, wine samples.

Submitted: November 29, 2019. **Accepted:** April 12, 2020.

Cite this: Tashakkori P, Altinisik Tagac A, Merdivan M. Graphene Oxide-Ionic Liquid Used as Solid-Phase Microextraction Coating for Polyphenolic Compounds' Extraction and Determination with GC-MS After On-Fiber Derivatization in Wine. JOTCSA. 2020 Apr;7(2):411-26.

DOI: <https://doi.org/10.18596/jotcsa.652794>.

***Corresponding author: E-mail:** melek.merdivan@deu.edu.tr. Phone: +902323018693.

INTRODUCTION

Polyphenolic compounds (P.C.s) are involved in color formation in plants, and plants can also synthesize some new polyphenolic compounds to protect against pathogens in stress situations (1). Polyphenolic compounds are essential in terms of their positive effects on human health. Their antimutagenic, anticarcinogenic, antioxidant, anti-inflammatory, antiallergic, and antipathogenic properties are reported (2, 3). Wine is a significant natural antioxidant source when compared to other alcoholic beverages (4).

Because of the complexity of the sample matrix, literature mentions of sample pretreatment techniques, including liquid-liquid extraction (LLE), solid-phase extraction (SPE), stir bar sorptive extraction (SBSE), and solid-phase microextraction (SPME) before their chromatographic detection for extraction and preconcentration of polyphenolic compounds in wine samples (5-8). SPME, an equilibrium-based sample pretreatment technique, provides a single-step analysis by integrating sampling, extraction, preconcentration, and sample introduction for the target analytes. The main advantages of SPME are fast mass transfer, its solvent-free, and simple nature, and lower sample volume (9). Enrichment of organic compounds from

Tashakkori P, Altinisik Tagac A, Merdivan M. JOTCSA. different kinds of sample matrices is essential, and so new coatings must be developed on fibers for SPME. Literature suggests the orientation of the preparation of new coating materials to the selectivity performance to target analytes as well as the development of more durable, firmer, and highly consistent supports (10).

Graphene oxide (G.O.) obtained by oxidation of epoxy (C-O-C), hydroxyl (C-OH), carbonyl (C=O) and carboxylic acid (COOH) groups from basal and surface corners of a single graphite layer has excellent properties such as large surface area, excellent structure, and good chemical stability (11). Recently, graphene oxide-based materials have been progressed and used as coating materials in the sample preparation technique such as SPME, SPE because of its facile functionalization (12, 13). Ionic liquids (I.L.s), being potential environmentally friendly solvents, have a great attraction in separation science due to low volatility, high viscosity, excellent thermal stability, and high polarities (14). Besides, its use as stationary phase in liquid chromatography, gas chromatography, and capillary chromatography, and extraction material in micro liquid extraction techniques, I.L.s have been preferred in SPE and SPME as sorbent and coating material both alone and grafted on different supports such as graphene oxide and carbon nanotubes to improve extraction efficiency and stability (15-18).

So far, liquid chromatography-diode array detector (LC-DAD) and liquid chromatography-mass spectrometry (LC-MS) techniques have been reliable solutions for the determination of P.C.s. However, rarely has gas chromatography-mass spectrometry (GC-MS) been preferred due to the need for derivatization for polar P.C.s. In the literature, direct methods (19,20), solid supported-LLE (SS-LLE) (5), SPE method using molecularly imprinted polymers (6), and SPME method using commercial polyalcoholic fiber (P.A.) (8) are available. Along with them, application of carbowax-templated resin (CW/TPR) (21), polystyrene-divinylbenzene-polyacrylonitrile (PS-DVB-PAN) coated fiber (22), and poly(ionic liquid)-based molecularly imprinted polymer (PIL-MIP)-coated fiber (23) before L.C. to wine, fruit juices, and beer samples. Many extraction techniques including LLE (24), liquid-liquid microextraction (LLME) (25), SPE using Oasis MAX cartridges (26), SPSE using polydimethylsiloxane (PDMS) coated stir bar (27), SPME with P.A. fiber (28- 30) are present for the determination of P.C.s in wine, fruit juice, and medicinal plant samples before GC-MS/FID or multidimensional GC-MS techniques. Despite the most probable preference of L.C. methods, G.C. can also be a choice for the determination of P.C.s in a complex sample matrix. GC-MS technique has some advantages such as better chromatographic separation using a capillary column, improved detectability, lower matrix effects, more accurate

2020; 7(2): 411- 426.

RESEARCH ARTICLE

result, cost-effectiveness, and a more straightforward interface concerning LC-MS.

References concerning the SPME-GC-MS method using only commercial fibers are available for some polyphenolic compounds such as resveratrol, gallic acid, caffeic acid, p-coumaric acid, ferulic acid, syringic acid, and protocatechuic acid (28-30). SPME fibers coated with graphene oxide modified with ionic liquids having vinyl- and benzylimidazolium by sol-gel technique have been performed and used for extraction and determination of phthalate esters and polyaromatic hydrocarbons in water and coffee samples in our previous studies (18, 32). In this work, the extraction performance of coating possessing graphene oxide modified with amino-terminated methylimidazolium cation was evaluated for the analysis of twelve P.C.s (syringic acid, protocatechuic acid, cinnamic acid, p-coumaric acid, sinapinic acid, ferulic acid, caffeic acid, quercetin, kaempferol, chlorogenic acid, resveratrol, and gallic acid) in wine using direct immersion-SPME coupled with GC-MS. The graphene oxide-(1-(3-aminopropyl)-3-methylimidazolium bis(trifluoromethylsulfonyl)imide) (GO-[APMIM][NTf₂]) coated fiber was prepared with layer by layer coating technique onto the surface of stainless steel wire using a crosslinker agent. We performed the derivatization of P.C.s using trimethylsilyl (TMS) reagents on the fiber. The authors compared the efficiency of GO-[APMIM][NTf₂] coated fiber with commercial fibers and G.O. coated fiber. Finally, we applied the optimized SPME method for the determination of P.C.s in real white, red, and fruit wine samples.

MATERIALS AND METHODS

Chemicals and Materials

We procured the P.C. standards (caffeic acid, gallic acid, quercetin, kaempferol, chlorogenic acid, resveratrol, syringic acid, protocatechuic acid, cinnamic acid, p-coumaric acid, sinapinic acid, and ferulic acid) from Alfa Aesar (Karlsruhe, Germany). We also purchased ethyltrimethylsilane (ETMS), N,O-bis(trimethylsilyl) trifluoroacetamide (BSTFA), and trimethylchlorosilane (TMCS) as derivatization compounds from the same vendor. 1-Methylimidazole, 3-bromopropylamine hydrobromide, bis(trifluoromethane) sulfonimide lithium (LiNTf₂), and graphene oxide (2 mg/ mL, dispersion in water) were obtained from Sigma-Aldrich (St. Louis, USA). We purchased the modified dihydroxyethylene urea as a cross-linking from Hunstman (Utah, USA). All other used reagents were of analytical reagent grade. Deionized water was obtained from a Milli-Q water purification system (Millipore, Bedford, USA). We procured a manual SPME holder, amber glass vials (20 mL) with screw caps and polytetrafluoroethylene/silicone septa, and polyacrylate (PA, 85 μm), divinylbenzene/carboxen/polydimethylsiloxane (DVB/CAR/PDMS, 50/30 μm),

Tashakkori P, Altinisik Tagac A, Merdivan M. JOTCSA. carboxen/polydimethylsiloxane (CAR/PDMS, 85 μm) and carbowax/ polyethylene glycol (CW/PEG, 60 μm) fibers from Supelco (Bellefonte, USA). Using a 5 μL microsyringe from Hamilton (Reno, USA), we produced the SMPE fibers and obtained a stainless steel wire having O.D. 150 μm from a local market (Istanbul, Turkey).

Stock standard solution of 1000 mg/L of each P.C.s was prepared using methanol and stored at $-18\text{ }^{\circ}\text{C}$. The intermediate solution of the mixture standard of P.C.s was prepared at 200 mg/L in methanol and stored at $4\text{ }^{\circ}\text{C}$. We prepared the pH 8 buffer solution using 1 M tris(hydroxymethyl)aminomethane hydrochloride (Tris-HCl).

The analyzed samples, including red wine, white wine, and fruit wines, were purchased from local supermarkets in Izmir. The alcohol content was in the range of 12%-13.8% for the studied wines. The bottles of wine were stored at $4\text{ }^{\circ}\text{C}$ and protected from light before analysis. The authors prepared synthetic wine solutions including 12% (v/v) of ethanol with pH adjusted to 3.5 by tartaric acid for optimization and performance evaluation of the DI-SPME method.

Instrumentation

We performed the G.C. analysis on a Trace 1300 gas chromatograph QP2010 equipped with an ISQ QD single quadrupole mass spectrometer and split/splitless injector (Thermo Scientific, USA). A TG-5MS fused silica capillary column (30.0 m \times 0.25 mm I.D., 0.25 μm film thickness) supplied from Thermo Scientific (West Palm Beach, FL, USA) was used. High purity helium was employed as the carrier gas, at a flow rate of 1.2 mL min $^{-1}$. We employed the following separation temperature program in G.C. for TMS derivatives: initially oven temperature held at $80\text{ }^{\circ}\text{C}$ for 3 min, then programmed at $10\text{ }^{\circ}\text{C min}^{-1}$ to $220\text{ }^{\circ}\text{C}$ (held for 4 min), finally increased to $280\text{ }^{\circ}\text{C}$ at $20\text{ }^{\circ}\text{C min}^{-1}$ (held for 2 min). The injection port temperature was at $250\text{ }^{\circ}\text{C}$ for GO-[APMIM][NTf2] coated SPME fiber. We carried out all injections on the splitless mode for 5 min. After each analysis, we heated all fibers at a desorption temperature for 5 min in the extra G.C. injection port to prevent carry-over effects. The authors operated the MS in the electron impact

2020; 7(2): 411- 426.

RESEARCH ARTICLE

(E.I.) at 70 eV under selected ion monitoring mode (SIM) by monitoring two relevant m/z fragments for TMS derivatives given in Table S1. The GC-MS ion source and interface were set at $250\text{ }^{\circ}\text{C}$ and $280\text{ }^{\circ}\text{C}$, respectively. Figure 1 gives the chromatogram of P.C.s and their M.S. spectra.

The Fourier transform infrared (FTIR) spectra of G.O. and GO-[APMIM][NTf2] were obtained by using a Thermo Fisher Scientific Nicolet iS10 model FTIR Spectrometer. We employed thermogravimetric analysis (TGA) for investigation of their thermal properties. The TGA was performed between 30 and $450\text{ }^{\circ}\text{C}$ at a rate of $10\text{ }^{\circ}\text{C/min}$ under a nitrogen atmosphere with a Perkin-Elmer Diamond TG/DTA instrument. X-ray Diffractometer measurements were made by a Philips X'Pert PROBE model with a monochromatic Cu-K α X-ray source at $2\theta = 10\text{-}60^{\circ}$. The authors evaluated the surface morphology GO-[APMIM][NTf2] coated fiber with scanning electron microscopy (SEM, Carl Zeiss 300VP, Jena, Germany).

Derivatization Procedure

By on-fiber derivatization process, the fibers after SPME firstly were inserted into a flask, dried under nitrogen atmosphere for 5 min and then transferred into the headspace of a 1.5 mL glass vial containing 20 μL of BSTFA: TMCS (9:1, v:v) solution and held at $60\text{ }^{\circ}\text{C}$ for 15 min.

Preparation of the Fiber

After etching of stainless steel wire as previously described (18), the tip of wire was dipped into dihydroxyethylene urea cross-linking reagent for 1 h, then inserted into G.O. dispersion in water for 30 min. These steps were repeated for three times for efficient coating. We dipped the G.O. coated fiber vertically into the 0.02 g [APMIM][NTf2], which was synthesized according to the previous methods given in the literature (18, 33), in 5 mL of methanol for 2 h at room temperature. This step was repeated in sextuplicate to increase the thickness of the fiber coating. Then, the home-made fiber prepared was dried at room temperature overnight and conditioned in sextuplicate in the injection port of G.C. at $250\text{ }^{\circ}\text{C}$ for 5 min under nitrogen atmosphere.

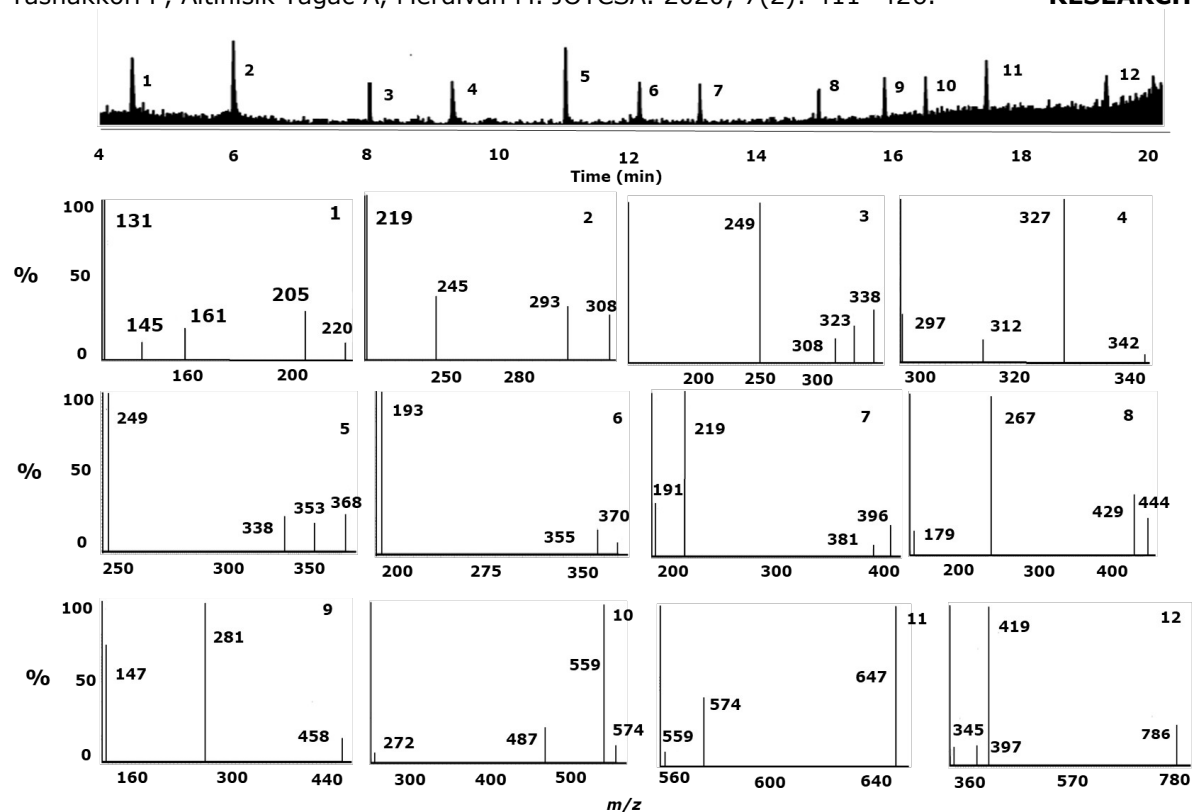


Figure 1. Chromatogram of P.C.s standards and M.S. spectra of P.C.s by the proposed method. Peak identification: (1) cinnamic acid, (2) p-coumaric acid, (3) ferulic acid, (4) syringic acid, (5) sinapinic acid, (6) protocatechuic acid, (7) caffeic acid, (8) resveratrol, (9) gallic acid, (10) kaempferol, (11) quercetin, (12) chlorogenic acid.

The characterization results of GO-[APMIM][NTf2] coating material by FTIR, XRD and T.G. were shown in Figure S1. FTIR (cm⁻¹): 2914, 1847, 1578, and 1456. XRD (2 θ) = 23.67°, 38.17° and 40.51°. TG (25-450°C): from 100% to 70% weight loss.

DI-SPME Procedure for Analysis of P.C.s

Firstly, synthetic wine or wine sample solution was prepared by adjusting pH to 8 and placed into a 20-mL amber glass vial. The vial was placed in a metallic block on a magnetic heater. After equilibration for 5 min, the 1 cm tip of the GO-[APMIM][NTf2] coated SPME fiber was exposed to the test solution at adjusted temperature for a particular time while stirring at 400 rpm using a stirring bar. Extractions were performed using a metallic block and a heater with a magnetic stirrer. After extraction, the fiber was dried under a nitrogen stream for 5 min, derivatized by BSTFA:TMCS mixture, and inserted into GC-MS for analyzing P.C.s. Because of the complex composition of wine, we have used two home-made fibers prepared in the extraction experiments. Using one prepared GO-[APMIM][NTf2] coated fiber, we were successful to perform 150 injections with no remarkable decrease in recovery and repeatability.

RESULTS AND DISCUSSION

Optimization of the Derivatization Process

G.C. analysis needs a derivatization procedure for hydroxyl functional groups. The most commonly used derivatization reagents are TMS reagents containing N-methyl-N-(trimethylsilyl)trifluoroacetamide), N-methyl-N-tert-butylidimethylsilyl-trifluoroacetamide, BSTFA and TMCS for derivatization of polyphenolic compounds and their metabolites (25, 28, 34, 35). TMS reagents are hydrolyzed in aqueous solutions. Because of this, the SPME fiber after extraction was dried under nitrogen atmosphere. Therefore, drying time for fiber after extraction, suitable derivatizing reagent and volume, and time and temperature of derivatization were investigated. The optimal conditions to get the highest signal came to an agreement at 60 °C for 15 min using 20 μ L of BSTFA: TMCS (9:1) after drying the fiber for 5 min under nitrogen gas for all P.C.s studied following the extraction.

Optimization of the SPME Conditions

SPME experimental conditions such as sample pH, ionic strength, extraction temperature, and extraction time were investigated to obtain reproducible results with high extraction performance of the GO-[APMIM][NTf2] coated SPME

Tashakkori P, Altinisik Tagac A, Merdivan M. JOTCSA. 2020; 7(2): 411- 426.

fiber for P.C.s by using DI-SPME method. We carried out all the experiments in triplicate using synthetic wine sample solutions containing 100 µg/L P.C.s standard and reported the mean values.

Sample pH and Ionic Strength

The pH of a sample solution affects the retention of analytes on the surface of the coating material of SPME fiber. It is possible to observe an interaction between the analyte and the sorbent when the polarities of them are close to each other. The pH of the sample is adjusted to obtain reproducible extraction efficiency, taking into account the pKa of analytes. Depending on the pKa values of P.C.s, we performed the extraction experiments to control the effect of pH at pH 4 and 8. The authors saw that the extraction efficiencies of P.C.s studied were higher at pH 8 except syringic acid and gallic acid (Figure 2A). The reason is that the P.C.s studied were ionized mainly at pH 8 and the sorption between the ionized P.C.s and imidazolium cation took place by electrostatic interaction. Besides, the aromatic ring and -O.H., -OCH₃ and -COOH groups in P.C.s caused dipole-dipole and π-π interactions during the sorption to the surface of GO-[APMIM][NTf₂] coated fiber. The time of analysis is optimal at pH 8 and selected for further studies because the peak areas of most P.C.s studied were high at pH 8.

In HS-SPME and rarely in DI-SPME methods, increasing the ionic strength of the aqueous solution improved the peak areas, favoring the extraction of analytes into the fiber and solubility of the extracted compounds. Thus, we investigated the impact of ionic strength on the uptake of P.C.s after exposure to the fiber at three different NaCl concentrations (0%, 10%, and 25%, w/v). As seen in Figure 2B, the addition of NaCl caused a slight increase in the

RESEARCH ARTICLE

peak areas of P.C.s (10%, w/v) initially and then led to a more decrease in the extraction efficiency. The presence of a high amount of salt may cause an increase in the viscosity of the solution, which decreases the mass transfer rate and affects the peak areas of P.C.s negatively. So, we used 10% NaCl solution as a test for further experiments.

Extraction Temperature and Extraction Time

Extraction temperature is an essential factor for the extraction efficiency. It influences the mass transfer and affects the extraction time in the SPME method. Therefore, we investigated the effect of extraction temperature on the extraction efficiency of P.C.s by exposing the fiber to the sample solution at 30 and 70 °C for 30 min. Figure 2C shows the temperature profiles obtained. The authors achieved the highest extraction efficiency at 30 °C for all P.C.s. Increasing temperature caused a decline in the peak areas of P.C.s. This event may be explained by that the high temperature causes a rapid motion of neutral or ionized P.C.s but decrease the diffusion of P.C.s on fiber coating due to the exothermic extraction process (36). The researchers performed subsequent experiments at 30 °C for the home-made fiber because of the maximum extraction efficiency at this temperature.

The extraction time deals with the interaction of analytes in solution and fiber coating in SPME. The extraction time was investigated from 15 to 90 min at 30 °C by stirring at 400 rpm to acquire the adsorption equilibrium for P.C.s on the fiber surface. As shown in Figure 2D, the peak areas of all P.C.s reached the maxima in 30 min. Thus, considering the extraction efficacy and the analytical time, 30 min was chosen as the optimized fiber exposure time.

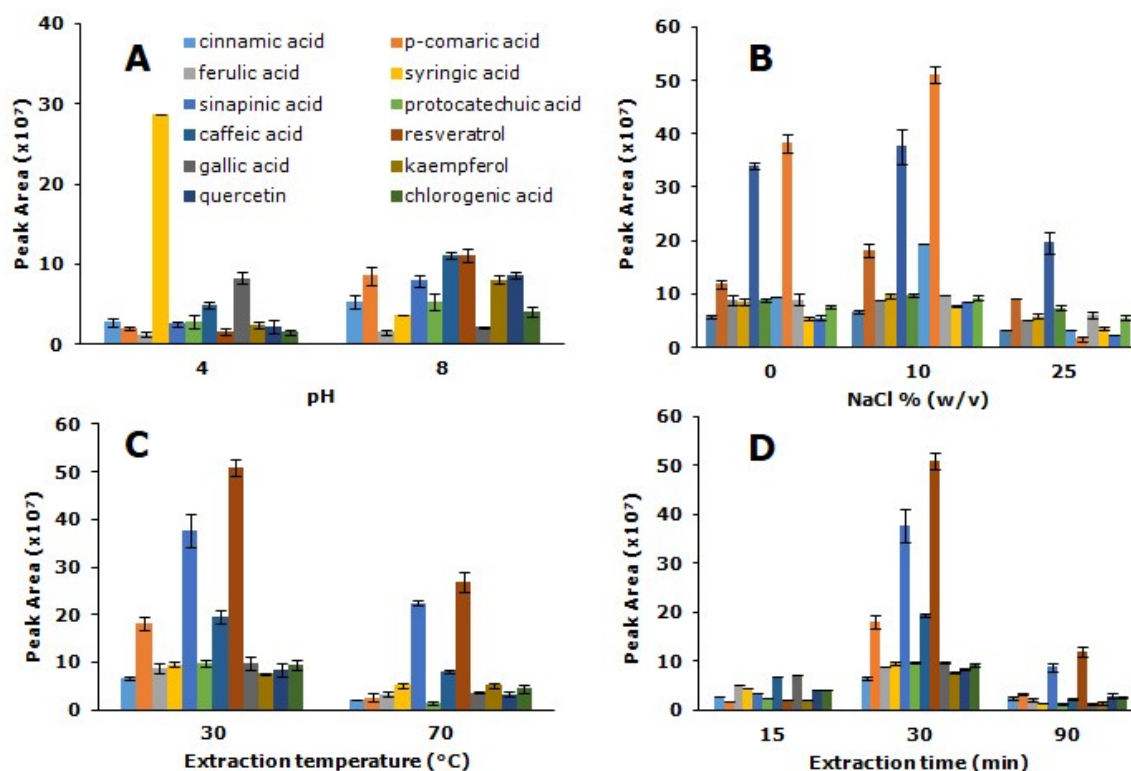


Figure 2. Effects of pH of sample solution (A), ionic strength (B), extraction temperature (C), and extraction time (D) of GO-[APMIM][NTf₂] fiber on the DI-SPME method.

Comparison of Extraction Efficiency of GO-[APMIM][NTf₂] Coated Fiber with Commercial Fibers and G.O. Coated Fiber

DI-SPME method was also optimized for P.A., DVB/CAR/PDMS, CAR/PDMS, and CW/ PEG commercial SPME fibers to compare their extraction efficiency with the GO-[APMIM][NTf₂] coated fiber. These fibers were conditioned on the injection port of G.C. before the extraction experiments at 280 °C, 270, 300, and 240 °C for P.A., DVB/CAR/PDMS, CAR/PDMS, and CW/ PEG for 30 min according to the manufacturer recommendation, respectively. We carried out the SPME extraction experiments in the range of 15- 60 min with 100 µg/L P.C.s solution at pH 8 and 400 rpm to obtain the optimum extraction time. The authors obtained the highest extraction efficiency as 30 min for all commercial SPME fibers.

We studied the extraction temperature at 30 and 70 °C at the optimized extraction time. The experimental results indicated that the optimum extraction temperature was 30 °C for all commercial fibers. Although the optimal extraction parameters of commercial fibers are the same as the GO-[APMIM][NTf₂] coated fiber, the extraction efficiency of the home-made coated fiber was much higher than those commercial fibers (Figure 3). Within the commercial SPME fibers, the peak area of cinnamic acid and kaempferol with P.A. fiber and the peak area of cinnamic acid with CW/PEG fiber were only higher than that of the home-made fiber. As seen in Figure 2, the presence of [APMIM][NTf₂] caused much increase in the extraction efficacy of P.C.s with respect to only G.O. coated fiber.

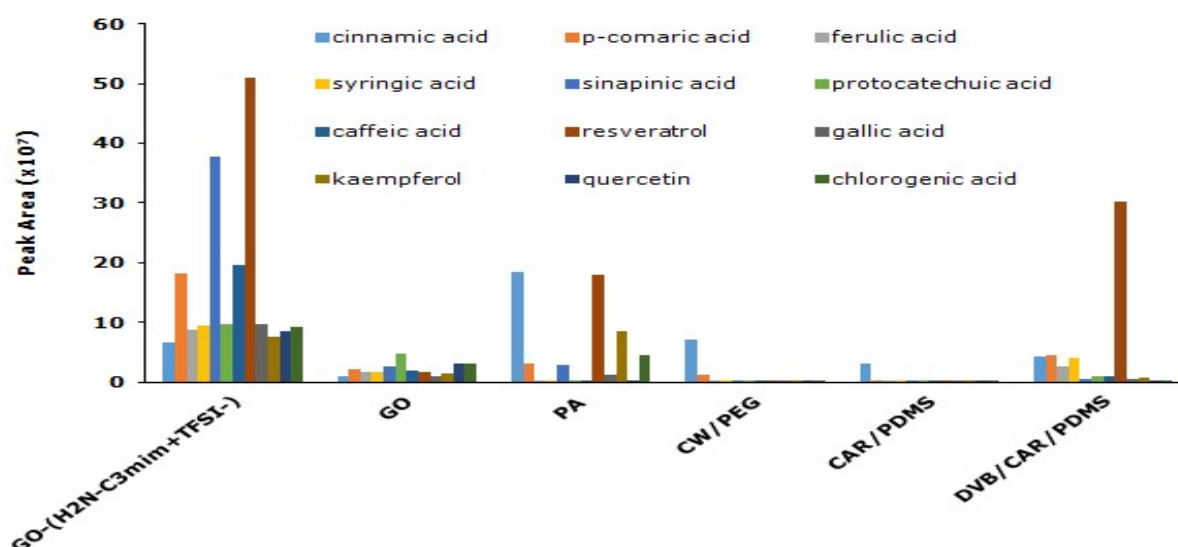


Figure 3. Comparison of the extraction efficiencies of GO-[APMIM][NTf₂] coated fiber with G.O. coated and P.A., CAR/PDMS, DVB/CAR/PDMS, and CW/ PEG commercial fibers. Conditions: C_{PCs} = 100 µg/L; sample pH = 8; stirring rate = 400 rpm; extraction temperature = 30 °C; extraction time = 30 min.

Table 1. Analytical figures of merit for GO-[APMIM][NTf₂] coated fiber in DI-SPME-GC-MS method.

PCs	Linear range (µg/L)	R ²	LOD (µg/L)	Precision (RSD, %)	Fiber-to-Fiber (RSD, %)
Cinnamic acid	0.1-1000	0.998	0.05	2.48-11.37	2.39
p-Coumaric acid	0.25-1000	0.998	0.1	2.22-9.23	2.79
Ferulic acid	0.25-1000	0.998	0.1	2.57-9.68	2.18
Syringic acid	0.1-1000	0.999	0.02	1.32-14.82	4.68
Sinapinic acid	0.1-1000	0.997	0.02	0.71-13.29	3.04
Protocatechuic acid	0.1-1000	0.997	0.02	0.92-8.42	5.71
Caffeic acid	0.25-1000	0.997	0.05	3.48-14.74	1.64
Resveratrol	0.1-1000	0.997	0.02	0.93-10.53	4.79
Gallic acid	0.25-1000	0.997	0.02	0.90-9.85	2.33
Kaempferol	0.1-1000	0.997	0.02	0.78-9.85	5.87
Quercetin	0.1-1000	0.998	0.02	3.14-9.24	4.06
Chlorogenic acid	0.1-1000	0.997	0.02	2.73-11.92	2.25

Table 2. Comparison of the proposed method with previous SPME and other extraction methods for determination of P.C.s studied.

	Coating Material/ Sorbent	Extraction type	Sample	PCs	LR ($\mu\text{g/L}$)	LOD ($\mu\text{g/L}$)	RSD (%)	Recovery (%)	Refs
LC-DAD	MIP	SPE	wine	GA	10-70*	0.4*	6.4-8.0	89.1-98.3	(6)
GC-MS		LLME	plasma	Phenolic acids	0.1-4.5 10-5000	0.1* 0.5-16.9	7.0-8.1 3.8-18.4	95-100 80-110	(25)
LC-FLD	PDMS CW/TPR	SBSE SPME	Wine, must, fruit juice	trans-res trans-res/ cis-res	0.5-50 5-150/ 2-150	0.1 2/0.5	6.9 5.3/4.8	82-105	(21)
LC-DAD	PA	SPME	Wine, spirit, grape juice	res	0.1-500	0.4	6.5-12.6	92.2-99.4	(8)
GC-MS	PDMS stir bar	SBSE	Wine	res, picetannol	0.2-1	0.004-0.015	5-9	79-109	(27)
GC-MS	PA	SPME	Wine and grape	res	1-150	0.09	2.4	85-116	(28)
LC-DAD	PIL/MIP	SPME	Fruit juice and beer	CA FA	0.1-200 0.05-200	0.019-0.024 0.011-0.042	2.3-8.2 4.6-8.0	80.1-111 72.1-109	(23)
LC-MS/MS	PS-DVB-PAN	SPME	Wine, berry, grape	CA res	1.5-500 5-500	0.5 1.5	5 4	82 77	(22)
Multidimensional GC-MS	PA	SPME	Wine	res	10-5000	7.08	3.0-9.2	72.7-94.7	(29)
GC-MS	Oasis MAX	SPE	Wine	trans-res	up to 2500	0.24	8	92.5-108.2	(26)
GC-FID	PA	SPME	Synthetic solution	pCuA, SyA, PrA, FA, CA, GA	2.2-354.4	0.01-1.77	9.78-17.89	-	(30)
GC-MS	GO-[APMIM][NTf2]	SPME	Wine	CnA, SyA, SnA, PrA, Res, Kfl, Qcn, ChA pCuA, FA, CA, GA	0.1-1000 0.25-1000	0.02-0.05 0.02-0.1	0.78-11.92 0.90-14.74	72.8-99.9 80.7-99.8	This study

LC-FLD: Liquid chromatography-fluorescence detector MEPS: Microextraction packed sorbent,

CnA: Cinnamic acid, SyA: Syringic acid, SnA: Sinapinic acid, PrA: Protocatechuic acid, Res: resveratrol, Kfl: Kaempferol, Qcn: Quercetin, ChA: Choloregenic acid, pCuA: p-Coumaric acid, F.A.: Ferulic acid, CA: Caffeic acid, GA: Gallic acid. * $\mu\text{g/mL}$

Surface Morphology of GO-[APMIM][NTf2] Coated Fiber

We characterized the surface morphology of the G.O. and GO-[APMIM][NTf2] material by SEM (Figure 4). In Figure 4a, it is evident G.O. sheets seem the sheet-like structure with a smooth surface and wrinkled edge. After a combination with I.L. (Figure 4b), the coating material had a rougher surface, which pointed out that I.L. stacks assembled on the surface of the G.O. layers. The

GO-[APMIM][NTf2] is porous with a much rougher surface, which indicates that the coating material has a large surface area. Figure 4c-d shows that the coating possessed a homogeneous and porous structure. The porous structure of the coating could have increased the available surface area of the fiber, as well as its extraction ability. From the SEM images in Figure 4c-d, the coating thickness was determined as 27.5 μm for the GO-[APMIM][NTf2] coating material.

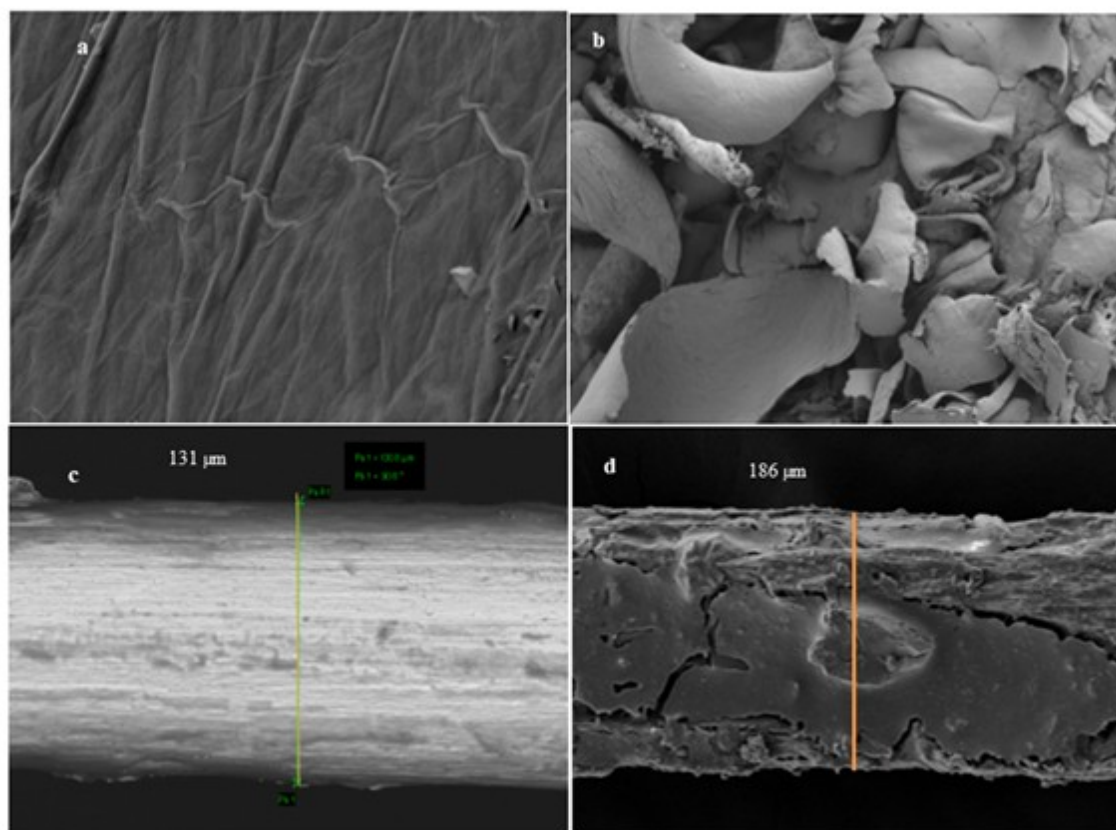


Figure 4. SEM images of GO, 2 μm , 10000 X (a); GO-[APMIM][NTf2] 20 μm , 500 X (b); etched stainless steel fiber, 20 μm , 1000 X (c); GO-[APMIM][NTf2] fiber, 20 μm , 1000 X (d).

Application to Real Sample Analysis

The proposed GO-[APMIM][NTf2] coated fiber was used for the analysis of twelve P.C.s in red wine, white wine, and fruit wine samples by DI-SPME-GC-MS method (Table 3). By SPME, known as a non-exhaustive method, the amount of analytes found in the sample represents the free concentration of analytes (20). We examined the recoveries of 12 P.C.s by spiking 5 and 200 $\mu\text{g L}^{-1}$ concentration of P.C.s to the wine samples to evaluate the accuracy

of the proposed DI-SPME-GC-MS method with the home-made coated fiber. As shown in Table 3, we acquired the recoveries of P.C.s in the range of 75.4- 99.8 % for red wine, 75.2- 99.9 % for white wine, and 71.2- 99.7 % for fruit wines with the RSDs less than 13.71% depending on the P.C.s and samples. Figure 5 shows the typical chromatograms of fruit wines, white wine, and red wine samples as blank and red wine spiked of P.C.s standard.

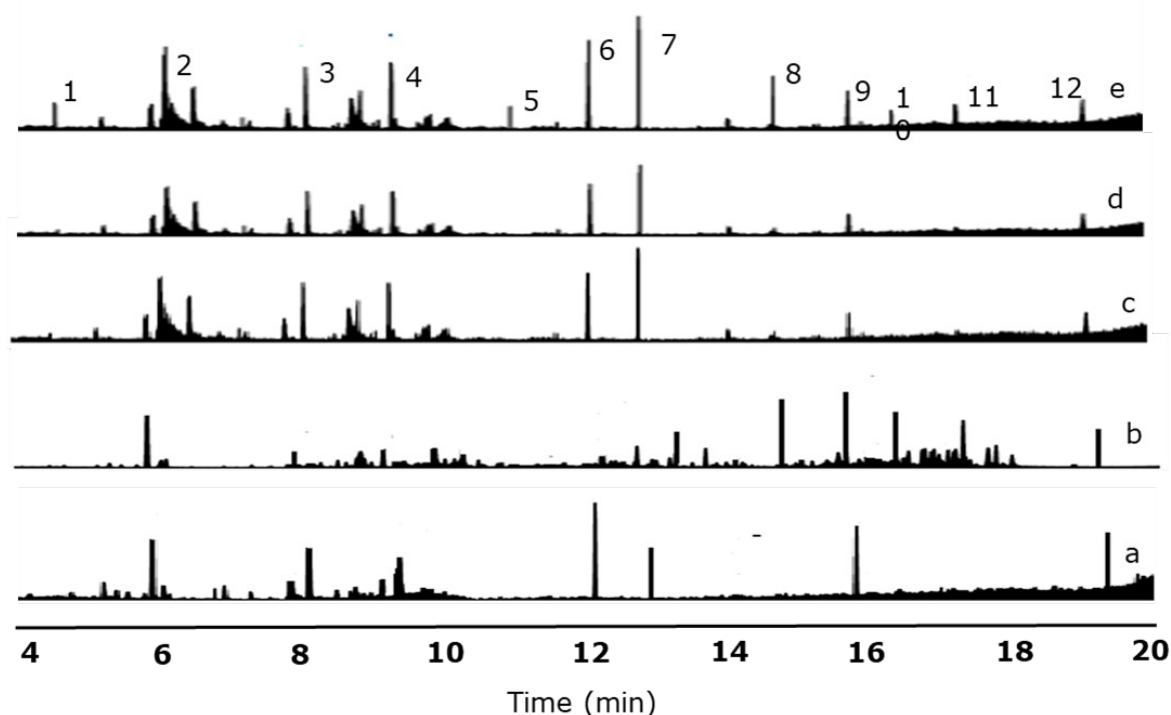


Figure 5. Chromatograms of P.C.s for wine samples by the proposed method. (a) blank melon wine, (b) blank blueberry wine, (c) blank white wine, (d) blank red wine, and (e) blank red wine spiked with P.C.s at 20 µg L⁻¹. Peak identification: (1) cinnamic acid, (2) p-coumaric acid, (3) ferulic acid, (4) syringic acid, (5) sinapinic acid, (6) protocatechuic acid, (7) caffeic acid, (8) resveratrol, (9) gallic acid, (10) kaempferol, (11) quercetin, (12) chlorogenic acid.

CONCLUSION

The GO-[APMIM][NTf₂] coated fiber was prepared and successfully applied for the determination of P.C.s in wine samples by the proposed DI-SPME under optimized conditions (30 °C, 30 min, 5 min desorption) and on-fiber derivatization (20 min) combined to GC-MS method. The developed home-made fiber exhibits high durability, excellent thermal behavior, high fiber-to-fiber reproducibility, and long term stability without a reduction in the extraction performance after more than 150 extraction cycles. Also, the extraction efficiency of the GO-[APMIM][NTf₂] coated fiber was much better than the studied commercial fibers (P.A.,

CAR/PDMS, DVB/CAR/PDMS, and CW/PEG). The prepared fiber presents a wide linear range, low LODs, and excellent repeatability and reproducibility in the determination of the P.C.s in different kinds of wine samples. Besides, by using the home-made SPME fiber, good recoveries for the analysis of P.C.s were succeeded in the wine samples.

The performance of the present coating material could be due to electrostatic interactions between imidazolium cation and the P.C.s, as well as the π-π and dipole-dipole interactions with G.O. and I.L., and the P.C.s. Thus, GO-[APMIM][NTf₂] coated fiber can be taken into account as SPME fiber for the extraction of P.C.s in various kinds of food samples.

Table 3. Analytical results of P.C.s* in wine samples (n= 3).

Wine samples	Added (µg/L)		CnA	pCuA	FA	SnA	CA	ChA	SyA	PrA	GA	Kfl	Qcn	Res
Red	0	Found	58.3±7.1	255.7±0.3	382.0±0.3	ND	2.8±0.2	108.0±0.6	270.0±0.6	1.4±0.8	194.0±3.2	233.0±12.3	103.7±0.9	81.5±0.6
	5	RR,RS D(%)	96.7±6.13	97.6±9.7	97.5±8.4	75.4±7.2	84.0±8.9	98.9±2.4	99.7±3.9	91.6±7.1	99.8±6.3	99.5±10.6	99.2±6.8	98.9±0.2
	200	RR,RS D(%)	95.2±5.2	96.8±7.2	96.4±3.3	79.2±4.9	87.5±1.5	89.9±2.5	96.8±1.0	92.5±6.6	90.1±5.6	98.1±6.2	94.3±5.4	97.6±1.0
White	0	Found	2.9±0.7	69.6±0.9	85.1±0.4	ND	308.0±1.4	7.8±2.7	54.8±0.2	496.0±0.1	491.0±4.9	ND	ND	ND
	5	RR,RS D(%)	89.4±5.3	95.18±.3	99.0±12.4	75.22±.8	99.6±1.8	86.0±9.4	98.1±6.6	99.9±4.0	99.9±7.8	83.5±10.1	80.5±8.3	80.0±4.9
	200	RR,RS D(%)	91.8±2.5	93.1±5.8	91.9±1.5	78.4±2.4	97.4±3.8	92.9±6.5	93.4±1.3	97.3±0.9	97.3±4.0	88.9±8.1	88.7±5.8	84.7±0.6
Black mulberry	0	Found	ND	238.0±0.1	301.0±0.2	ND	415.5±2.7	447.5±0.1	280±0.5	1.6±0.4	407.0±0.8	ND	338.0±1.8	ND
	5	RR,RS D(%)	86.4±.5	99.4±6.8	99.6±3.1	76.6±9.2	96.5±5.6	99.6±5.7	99.5±6.6	81.6±5.4	99.6±2.4	78.2±4.4	99.5±1.1	86.2±10.2
	200	RR,RS D(%)	92.60±0.8	93.6±0.2	93.8±3.5	80.9±0.9	93.3±3.6	95.1±1.2	93.4±0.3	83.7±3.2	92.9±2.9	89.9±2.1	94.7±0.3	88.8±5.4
Blueberry	0	Found	ND	107.0±0.8	ND	ND	415.5±4.5	3.7±0.5	ND	1.7±0.2	416.0±2.1	448.5±7.9	469.0±6.7	482.0±0.2
	5	RR,RS D(%)	82.2±8.3	88.7±8.3	80.7±8.1	77.6±3.1	99.5±5.2	82.2±6.3	80.0±10.5	79.6±8.4	99.6±8.2	99.6±6.9	99.7±7.8	99.7±4.5
	200	RR,RS D(%)	88.5±4.6	86.1±5.1	82.4±4.1	85.1±2.3	96.8±6.5	91.0±4.7	83.8±4.3	83.2±5.2	86.1±0.9	86.2±5.0	87.1±1.9	83.0±3.5
Melon	0	Found	ND	371.0±1.8	311.0±2.0	ND	453.0±0.1	294.0±0.2	272.0±4.5	441.0±7.9	312.0±0.8	ND	ND	ND
	5	RR,RS D(%)	81.8±4.63	99.7±1.3	99.8±1.5	73.4±7.7	99.8±0.9	99.6±1.8	99.6±3.9	99.9±0.6	99.8±1.8	84.2±4.8	84.4±5.1	81.6±1.4
	200	RR,RS D(%)	93.7±1.3	95.7±0.5	95.9±0.8	89.9±0.1	96.4±0.7	95.1±0.8	92.4±0.7	96.0±0.6	91.4±0.9	93.5±1.1	88.5±1.2	96.5±2.8
Red plum	0	Found	ND	448.0±8.5	364.0±4.2	ND	957.0±6.6	314.0±4.2	ND	ND	ND	398.0±8.5	975.0±10.6	ND
	5	RR %,RSD	84.6±4.8	99.7±1.3	99.5±6.0	75.2±1.4	99.8±6.8	99.4±3.9	78.8±8.4	72.8±7.2	77±.64.1	99.±51.9	99±.89.2	76.2±6.6
	200	RR %,RSD	91.0±4.4	98.3±1.4	93.1±3.5	85.1±4.4	95.1±0.8	97.4±3.0	89.5±7.9	83.0 ±3.2	81.7±2.7	96.6±2.2	97.0±0.5	93.3±4.3

^aValues are mean ± standard deviation^bRR : Relative recovery; ND: not detected

* P.C.s; CnA: Cinnamic acid, SyA: Syringic acid, SnA: Sinapinic acid, PrA: Protocatechuic acid, Res: t-resveratrol, Kfl: Kaempferol, Qcn: Quercetin, ChA: Chlorogenic acid, pCuA: p-Coumaric acid, F.A.: Ferulic acid, CA: Caffeic acid, GA: Gallic acid

ACKNOWLEDGMENTS

This work was supported by the Dokuz Eylul University research foundation (grant number DEU 2018.KB.FEN.033).

SUPPORTING INFORMATION SUMMARY

Details of parameters of SIM mode for P.C.s after derivatization and characterization studies of GO-[APMIM][NTf₂] coating material are given in the supporting information.

REFERENCES

1. Pourcel L, Routaboul J, Cheynier V, Lepiniec L, Debeaujon I. Flavonoid oxidation in plants: from biochemical properties to physiological functions. *Trends in Plant Science*. 2007 Jan;12(1):29–36.
2. Lesschaeve I, Noble AC. Polyphenols: factors influencing their sensory properties and their effects on food and beverage preferences. *The American Journal of Clinical Nutrition*. 2005 Jan 1;81(1):330S-335S.
3. Cardona F, Andrés-Lacueva C, Tulipani S, Tinahones FJ, Queipo-Ortuño MI. Benefits of polyphenols on gut microbiota and implications in human health. *The Journal of Nutritional Biochemistry*. 2013 Aug;24(8):1415–22.
4. Klatsky AL. Wine, Liquor, Beer, and Mortality. *American Journal of Epidemiology*. 2003 Sep 15;158(6):585–95.
5. Nave F, Cabrita MJ, da Costa CT. Use of solid-supported liquid-liquid extraction in the analysis of polyphenols in wine. *Journal of Chromatography A*. 2007 Oct;1169(1–2):23–30.
6. Denderz N, Lehotay J. Using of molecularly imprinted polymers for determination of gallic and protocatechuic acids in red wines by high performance liquid chromatography. *Journal of Chromatography A*. 2014 Dec;1372:72–80.
7. Cacho JI, Campillo N, Viñas P, Hernández-Córdoba M. Stir bar sorptive extraction with gas chromatography-mass spectrometry for the determination of resveratrol, piceatannol and oxyresveratrol isomers in wines. *Journal of Chromatography A*. 2013 Nov;1315:21–7.
8. Aresta A, Cotugno P, Massari F, Zamboni C. Determination of Trans-resveratrol in Wines, Spirits, and Grape Juices Using Solid-Phase Micro Extraction Coupled to Liquid Chromatography with UV Diode-Array Detection. *Food Anal Methods*. 2018 Feb;11(2):426–31.
9. Arthur CL, Pawliszyn Janusz. Solid phase microextraction with thermal desorption using fused

- silica optical fibers. *Anal Chem*. 1990 Oct;62(19):2145–8.
10. Souza-Silva ÉA, Jiang R, Rodríguez-Lafuente A, Gionfriddo E, Pawliszyn J. A critical review of the state of the art of solid-phase microextraction of complex matrices I. Environmental analysis. *TrAC Trends in Analytical Chemistry*. 2015 Sep;71:224–35.
11. Dreyer DR, Park S, Bielawski CW, Ruoff RS. The chemistry of graphene oxide. *Chem Soc Rev*. 2010;39(1):228–40.
12. Ye N, Shi P. Applications of Graphene-Based Materials in Solid-Phase Extraction and Solid-Phase Microextraction. *Separation & Purification Reviews*. 2015 Jul 3;44(3):183–98.
13. Dahaghin Z, Mousavi HZ, Sajjadi SM. Synthesis and Application of Magnetic Graphene Oxide Modified with 8-Hydroxyquinoline for Extraction and Preconcentration of Trace Heavy Metal Ions. *ChemistrySelect*. 2017 Jan 23;2(3):1282–9.
14. Anderson JL, Armstrong DW, Wei G-T. Ionic Liquids in Analytical Chemistry. *Anal Chem*. 2006 May;78(9):2892–902.
15. Berthod A, Ruiz-Ángel MJ, Carda-Broch S. Recent advances on ionic liquid uses in separation techniques. *Journal of Chromatography A*. 2018 Jul;1559:2–16.
16. Hou X, Guo Y, Liang X, Wang X, Wang L, Wang L, et al. Bis(trifluoromethanesulfonyl)imide-based ionic liquids grafted on graphene oxide-coated solid-phase microextraction fiber for extraction and enrichment of polycyclic aromatic hydrocarbons in potatoes and phthalate esters in food-wrap. *Talanta*. 2016 Jun;153:392–400.
17. Li G, Ho Row K. Ionic liquid based on imidazolium cation to modify functional materials on separation of active compounds. *Journal of Liquid Chromatography & Related Technologies*. 2018 Oct 2;41(15–16):937–48.
18. Tashakkori P, Erdem P, Merdivan M, Bozkurt SS. Determination of Phthalate Esters in Water and Coffee by Solid-Phase Microextraction Using Vinyl Terminated Imidazolium Based Ionic Liquid Grafted on Graphene Oxide Coatings. *ChemistrySelect*. 2019 Feb 28;4(8):2307–13.
19. Tian Y, Gou X, Niu P, Sun L, Guo Y. Multivariate Data Analysis of the Physicochemical and Phenolic Properties of Not from Concentrate Apple Juices to Explore the Alternative Cultivars in Juice Production. *Food Anal Methods*. 2018 Jun;11(6):1735–47.

- Tashakkori P, Altinisik Tagac A, Merdivan M. JOTCSA. 2020; 7(2): 411- 426.
20. Anli E, Vural N, Demiray S, Özkan M. Trans-resveratrol and Other Phenolic Compounds in Turkish Red Wines with HPLC. *Journal of Wine Research*. 2006 Aug;17(2):117–25.
21. Viñas P, Campillo N, Hernández-Pérez M, Hernández-Córdoba M. A comparison of solid-phase microextraction and stir bar sorptive extraction coupled to liquid chromatography for the rapid analysis of resveratrol isomers in wines, musts and fruit juices. *Analytica Chimica Acta*. 2008 Mar;611(1):119–25.
22. Mirnaghi FS, Mousavi F, Rocha SM, Pawliszyn J. Automated determination of phenolic compounds in wine, berry, and grape samples using 96-blade solid phase microextraction system coupled with liquid chromatography–tandem mass spectrometry. *Journal of Chromatography A*. 2013 Feb;1276:12–9.
23. Chen L, Huang X. Preparation and application of a poly (ionic liquid)-based molecularly imprinted polymer for multiple monolithic fiber solid-phase microextraction of phenolic acids in fruit juice and beer samples. *Analyst*. 2017;142(21):4039–47.
24. Canini A, Alesiani D, D’Arcangelo G, Tagliatesta P. Gas chromatography–mass spectrometry analysis of phenolic compounds from Carica papaya L. leaf. *Journal of Food Composition and Analysis*. 2007 Nov;20(7):584–90.
25. Bustamante L, Cárdenas D, von Baer D, Pastene E, Duran-Sandoval D, Vergara C, et al. Evaluation of microextraction by packed sorbent, liquid-liquid microextraction and derivatization pretreatment of diet-derived phenolic acids in plasma by gas chromatography with triple quadrupole mass spectrometry. *J Sep Sci*. 2017 Sep;40(17):3487–96.
26. Montes R, García-López M, Rodríguez I, Cela R. Mixed-mode solid-phase extraction followed by acetylation and gas chromatography mass spectrometry for the reliable determination of trans-resveratrol in wine samples. *Analytica Chimica Acta*. 2010 Jul;673(1):47–53.
27. Cacho JJ, Campillo N, Viñas P, Hernández-Córdoba M. Stir bar sorptive extraction with gas chromatography–mass spectrometry for the determination of resveratrol, piceatannol and oxyresveratrol isomers in wines. *Journal of Chromatography A*. 2013 Nov;1315:21–7.
28. Viñas P, Campillo N, Martínez-Castillo N, Hernández-Córdoba M. Solid-phase microextraction on-fiber derivatization for the analysis of some polyphenols in wine and grapes using gas chromatography–mass spectrometry. *Journal of Chromatography A*. 2009 Feb;1216(9):1279–84.
29. Cai L, Koziel JA, Dharmadhikari M, (Hans) van Leeuwen J. Rapid determination of trans-resveratrol in red wine by solid-phase microextraction with on-fiber derivatization and multidimensional gas chromatography–mass spectrometry. *Journal of Chromatography A*. 2009 Jan;1216(2):281–7.
30. Citová I, Sladkovský R, Solich P. Analysis of phenolic acids as chloroformate derivatives using solid phase microextraction–gas chromatography. *Analytica Chimica Acta*. 2006 Jul;573–574:231–41.
31. Angioni A, Pintore GAM, Caboni P. Determination of Wine Aroma Compounds by Dehydration Followed by GC/MS. *Journal of AOAC INTERNATIONAL*. 2012 May 1;95(3):813–9.
32. Erdem P, Tashakkori P, Merdivan M, Bozkurt SS. Ionic liquid-based graphene oxide-coated fiber for headspace-solid phase microextraction of polycyclic aromatic hydrocarbons in water samples. *Turkish Journal of Chemistry*. 2019;43:1383–97.
33. Yang H, Shan C, Li F, Han D, Zhang Q, Niu L. Covalent functionalization of polydisperse chemically-converted graphene sheets with amine-terminated ionic liquid. *Chem Commun*. 2009; (26):3880.
34. Yuan S, Liu Z, Lian H, Yang C, Lin Q, Yin H, et al. Simultaneous determination of eleven estrogenic and odorous chloro- and bromo-phenolic compounds in surface water through an automated online headspace SPME followed by on-fiber derivatization coupled with GC-MS. *Anal Methods*. 2017;9(33):4819–27.
35. Proestos C, Sereli D, Komaitis M. Determination of phenolic compounds in aromatic plants by RP-HPLC and GC-MS. *Food Chemistry*. 2006 Mar;95(1):44–52.
36. Xie L, Liu S, Han Z, Jiang R, Liu H, Zhu F, et al. Preparation and characterization of metal-organic framework MIL-101(Cr)-coated solid-phase microextraction fiber. *Analytica Chimica Acta*. 2015 Jan;853:303–10.

Graphene Oxide-Ionic Liquid Used as Solid-Phase Microextraction Coating for Polyphenolic Compounds' Extraction and Determination with GC-MS After On-Fiber Derivatization in Wine

Paniz Tashakkori, Aylin Altinisik Tagac, Melek Merdivan*
Supporting Information

Table S1. Parameters of SIM mode for PCs after derivatization.

Compound	Molecular weight	TMS groups	TMS derivatized molecular weight	t _R (min)	Characteristic fragments ^[a]
Cinnamic acid	148	1	220	4.48	<u>131</u> , 161, 205, 145, 220
p-Coumaric acid	164	2	308	6.01	<u>219</u> , 293, 245, 308
Ferulic acid	194	2	338	8.07	<u>249</u> , 323, 338, 219
Syringic acid	198	2	342	9.30	<u>327</u> , 342, 312, 297
Sinapinic acid	224	2	368	11.01	<u>353</u> , 368, 338, 249
Protocatechuic acid	154	3	370	12.13	<u>193</u> , 370, 355, 73
Caffeic acid	180	3	396	13.04	<u>291</u> , 396, 381, 73
Resveratrol	228	3	444	14.71	<u>267</u> , 179, 429, 444
Gallic acid	170	4	458	15.82	<u>281</u> , 147, 179, 458
Kaempferol	286	4	574	16.44	<u>487</u> , 574, 559, 272
Quercetin	302	5	662	17.35	<u>647</u> , 574, 559, 662
Chlorogenic acid	354	6	786	19.16	<u>419</u> , 786, 397, 345

[a] Quantitations are underlined.

Characterization of GO-[APMIM][NTf₂] coating material

In the FTIR study (Figure S1(A)), as well as the main peaks of GO, the presence of IL was verified by the peaks at 2914, 2847, 1578 and 1456 cm⁻¹ corresponding to the stretching vibrations of C-H in imidazole ring, aliphatic groups, C-N and C=N groups in imidazole ring, respectively. In thermal gravimetric analysis curves (Figure S1(B)), GO-[APMIM][NTf₂] coating with fewer thermally labile oxygen functional groups has a mass loss in the range of 200-450°C at the low slope (from 95% to 70% weight loss) beside the moisture loss at 150 °C. In XRD powder patterns (Figure S1(C)), the appearance of new peaks at 2θ = 23.67°, 38.17° and 40.51° explain the exfoliation of GO due to the removing of water molecules and the oxide groups and interaction with IL.

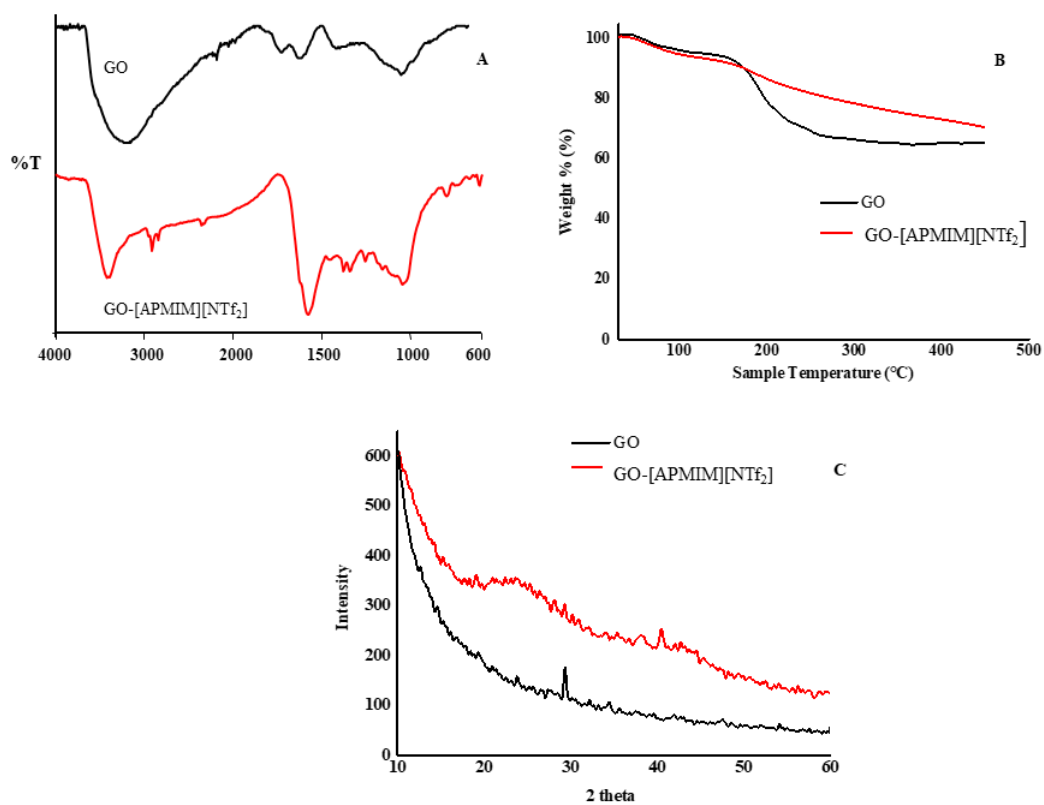


Figure S1: FTIR spectra (A), thermogravimetric analysis (B), and XRD patterns of GO and GO-[APMIM][NTf₂] (C).



Eco-friendly Synthesis of Quinoxaline Derivatives Using Mineral Fertilizers as Heterogeneous Catalysts

Badr Malek , Imane Bahammou , Omar Zimou , Achraf El Hallaoui , Rachida Ghailane , Said Boukhris , Abdelaziz Souizi* 

Laboratory of Organic, Organometallic and Theoretical Chemistry, University Ibn Tofail, B.P. 133, Kenitra, Morocco

Abstract: The synthesis of quinoxaline derivatives were heterogeneously catalyzed by phosphate-based catalyst fertilizers, MAP, DAP, or TSP. The reaction affords the desired products in excellent yields at ambient temperature. A series of studies were conducted to investigate the effect of solvent reaction, its volume, and catalyst amount. A study of the recyclability of catalysts removed from the reaction mixture by simple filtration was also carried out to find that the three phosphate-based catalysts retain their catalytic activities up to six cycles.

Keywords: Phosphate, Fertilizers, MAP, DAP, TSP, Quinoxaline, Heterogeneous catalysts.

Submitted: June 12, 2019. **Accepted:** April 24, 2020.

Cite this: Malek B, Bahammou I, Zimou O, El Hallaoui A, Ghailane R, Boukhris S, et al. Eco-friendly Synthesis of Quinoxaline Derivatives Using Mineral Fertilizers as Heterogeneous Catalysts. JOTCSA. 2020;7(2):427-40.

DOI: <https://doi.org/10.18596/jotcsa.577101>.

***Corresponding author. E-mail:** Souizi@yahoo.com (A. Souizi), Tel: +212661183260.

INTRODUCTION

Since the US Environmental Protection Agency (EPA) had developed the concept of "green chemistry" to protect human health and environment (1), enormous research efforts have been devoted to designing clean and eco-friendly chemical processes (2-4). In this area, considerable interests have focused on heterogeneous catalysis (5-7) due to its advantages to reduce energy consumption but to recover and recycle the used catalyst. Thereby, a large variety of heterogeneous catalysts have been developed and widely used to carry out numerous organic syntheses (8). Among the greener catalysts developed, phosphate-based minerals appear as the obvious choice for Moroccan researchers as they represent the first mining wealth of their country. For this reason, they contribute to the valorization of these minerals as promising catalysts. S. Sebti and co-workers were the first team to introduce natural (9), doped (10) or modified (11) phosphate not only as

heterogeneous catalysts for organic reactions but also as the support of metal catalysts (12-13).

Motivated by the desire to introduce a new generation of phosphate-based heterogeneous catalysts, our laboratory was particularly interested in the catalytic performance evaluation of some phosphate fertilizers for Knoevenagel condensation and 1-(benzothiazolylamino)-methyl-1-2-naphthol derivatives (14-15).

In continuation of our ongoing effort to extend the application of these novel fertilizer phosphates as green and reusable heterogeneous catalysts, we develop in the present paper a straightforward and efficient process to synthesize quinoxaline derivatives utilizing phosphate-based catalysts, mono-ammonium phosphate (MAP), di-ammonium phosphate (DAP), or triple superphosphate (TSP).

The quinoxaline derivatives are a class of nitrogen-containing fused heterocyclic compounds, which

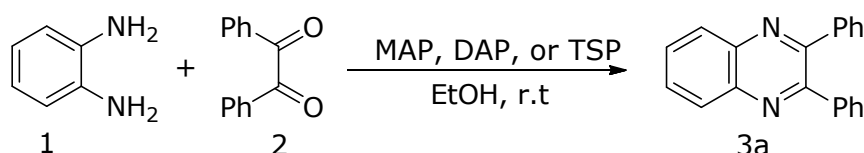
attracted considerable interest since their basic skeleton involved as a core structure of several drug molecules such as quinacillin (15), brimonidine (16), varenicline (17), clofazimine (18), echinomycin (19-20) and actinomycin (21). Some other quinoxaline-containing compounds have shown many biological properties (22), such as antimicrobial (23), antidiabetic (24), anti-inflammatory (25), antioxidant (25), anticancer (26), antileishmanial and antitrypanosomal (27) activities. Additionally, quinoxaline derivatives act as inhibitors of the aldose reductase enzyme (28) and the kinase protein (29). Furthermore, the quinoxaline structural nucleus has recently identified to possess inhibitory effects on the corrosion of some metals (30-32).

In light of their importance, numerous methods have been designed to synthesize quinoxaline derivatives. Most broadly, they involve 1,4-addition of 1,2-diamines to diazenylbutenes (33), oxidative cyclization of α -haloketones and 1,2-diamines (34), oxidative coupling of epoxides with ene-1,2-diamines (35), and condensation of 1,2-diamines with 1,2-dicarbonyl compounds (36-37). The latter method was chosen as the reaction model.

EXPERIMENTAL

Chemicals and instruments

Chemicals were purchased from Fluka or Aldrich companies. The spectral data were compared with those of the known compounds reported in the literature. Melting points were recorded on a Wagner & Munz HEIZBANK Kofler bench. Thin layer chromatography (TLC) on silica gel SIL G/UV 254 plates were used to monitor the progress of the reactions.



Scheme 1. Condensation of 1,2-diamines with 1,2-dicarbonyl compounds.

Table 1. Results and physical characteristics of 2,3-diphenylquinoxaline **3a**.

Entry	Catalyst	Time ^a	Yield ^b (%)
1	-	60	23
2	MAP	4	94
3	DAP	2	99
4	TSP	2	96

^a Time reported in min monitored by TLC. ^b Isolated yields.

These encouraging results prompted us to investigate the solvent effect on the reaction. The results displayed in Table 2 show that the reagents react efficiently in the different solvents. However, the yields decreased smoothly when the reaction is

Synthesis of quinoxaline derivatives: General procedure

In a typical reaction, to a solution of 1,2-diamine (1 mmol) and 1,2-dicarbonyl (1 mmol) in EtOH (2 mL) was added phosphate-based catalyst MAP, DAP or TSP (0.006 g). The resulting mixture stirred at 800 rpm at ambient temperature for appropriate reaction time as indicated by TLC. The solid product formed was dissolved in hot EtOH and filtered to separate the catalyst, and the resulting filtrate was placed in ice-bath to give a pure product as crystals. All prepared products were identified as based on comparison of their melting points and their ¹H NMR and ¹³C NMR data with authentic samples reported in the literature. Supplementary material includes the NMR data is joined to this paper.

Recyclability of MAP, DAP and TSP

The recyclability of the catalyst was examined using the model reaction under optimized reaction conditions. The catalyst is recovered by simple filtration at the end of the reaction, washed with hot EtOH, dried at oven at 80 °C for 6 hours, and then reused.

RESULTS AND DISCUSSION

In a preliminary study, the condensation of 1,2-diamines **1** with 1,2-dicarbonyl **2** (Scheme 1) chosen as a test reaction for the catalytic activity of catalysts MAP, DAP, and TSP. Table 1 gathers the results and noticeably displays that in the presence of catalysts, the reaction led to the expected product in higher yields (94-99%) within shorter reaction times (Table 1, entries 2-4).

carrying out in cyclohexane and THF. The best yields are obtained in EtOH. Consequently, we chose it as an optimal solvent for this reaction to avoid the use of the toxic solvent and thus to contribute to the protection of the environment.

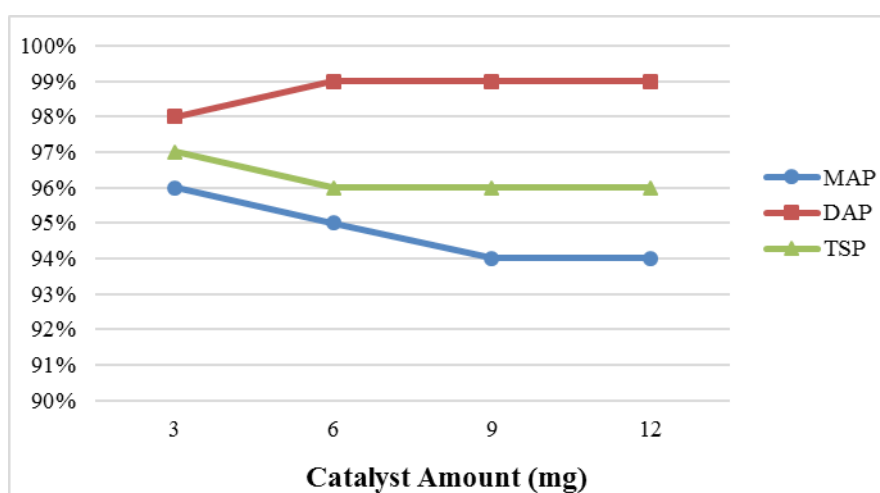
Table 2. Solvent effect on the quinoxaline **3a** synthesis ^a.

Entry	Solvent	Catalyst	Time (min)	Yield ^b (%)
1		MAP	4	94
2	EtOH	DAP	2	99
3		TSP	2	96
4		MAP	4	95
5	MeOH	DAP	2	96
6		TSP	2	90
7		MAP	4	98
8	Isopropanol	DAP	2	96
9		TSP	2	89
10		MAP	4	92
11	CH ₃ CN	DAP	2	95
12		TSP	2	94
13		MAP	4	92
14	AcOEt	DAP	2	94
15		TSP	2	94
16		MAP	4	94
17	Dioxane	DAP	2	93
18		TSP	2	92
19		MAP	4	92
20	CHCl ₃	DAP	2	93
21		TSP	2	90
22		MAP	4	87
23		DAP	2	86
24	Cyclohexane	TSP	2	82
25		MAP	4	73
26	THF	DAP	2	78
27		TSP	2	74

^a Reaction conditions: 1,2-diamine (1 mmol) and 1,2-dicarbonyl (1 mmol), Solvent (2 mL), 0.006 g of catalyst, r.t.; ^b Isolated yields.

Further experiments were conducted to determine the optimum catalyst loading. As revealed in Figure 1, yields increase smoothly with about 1% when DAP amount increases, and decrease smoothly with 2% or 1% when MAP and TSP amounts increase, this result allows us to deduce that the amount of

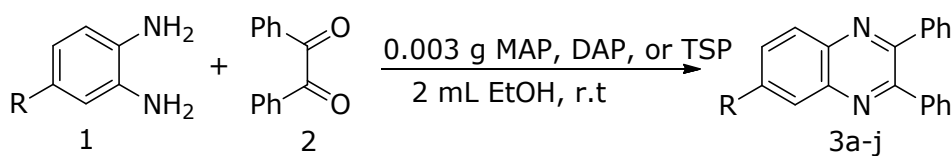
the optimal catalyst is 0.003 g, thus this quantity is widely sufficient to give good yields at 96% for MAP, at 98% for DAP and at 97% for TSP. One can also notice that the reaction times are concise 4, 2 and 2 min in the presence of MAP, DAP, and TSP catalysts, respectively.

**Figure 1.** Effect of the catalyst amount on the quinoxaline **3a** synthesis.

In order to explore the reliability of the protocol developed to synthesize the quinoxaline derivatives, various aryl 1,2-diamines were condensed with

various 1,2-dicarbonyl compounds (Scheme 2) under the optimal reaction conditions. Table 3 shows that the heterogeneous catalysts MAP, DAP,

and TSP afford the products in high to excellent yields 89-99% in short reaction times 2-4 min.



Scheme 2. Condensation of aryl 1,2-diamines with 1,2-dicarbonyl compound.

Table 4 collects the yields and reaction times of the condensation of 1,2-diamines with 1,2-dicarbonyl catalyzed by MAP, DAP, and TSP and those brought out in the literature. As can be seen, phosphate

fertilizers MAP, DAP, and TSP underwent the reaction more rapidly than $\text{Fe}_3\text{O}_4@\text{SiO}_2\text{-imid-PMA}^n$, VO_2 , and MIL-101-Cr-NH- RSO_3H , though the yields were comparable.

Table 4. Comparison between the present results and those given in the literature.

Entry	Catalyst	Condition	Time (min)	Yield (%)	Ref
1	$\text{Fe}_3\text{O}_4@\text{SiO}_2\text{-imid-PMA}^n$ (0,5 mol%)	EtOH, r.t.	10	97	(38)
2	VO_2 (3 mol%)	EtOH, r.t.	20	96	(39)
3	MIL-101-Cr-NH- RSO_3H (3.9 mol%- SO_3H)	MeOH, 45 °C	12	93	(40)
4	MAP (0.003 g)	EtOH, r.t.	4	96	This work
5	DAP (0.003 g)	EtOH, r.t.	2	98	This work
6	TSP (0.003 g)	EtOH, r.t.	2	97	This work

The catalytic efficiency of the catalyst is determined not only by its capacity to lead to the formation of the desired product with a good yield and short reaction time but also by its recyclability and its

natural regeneration. Finally, it seemed necessary to check the reusability of the three catalysts (MAP, DAP, and TSP) in the optimum reaction conditions.

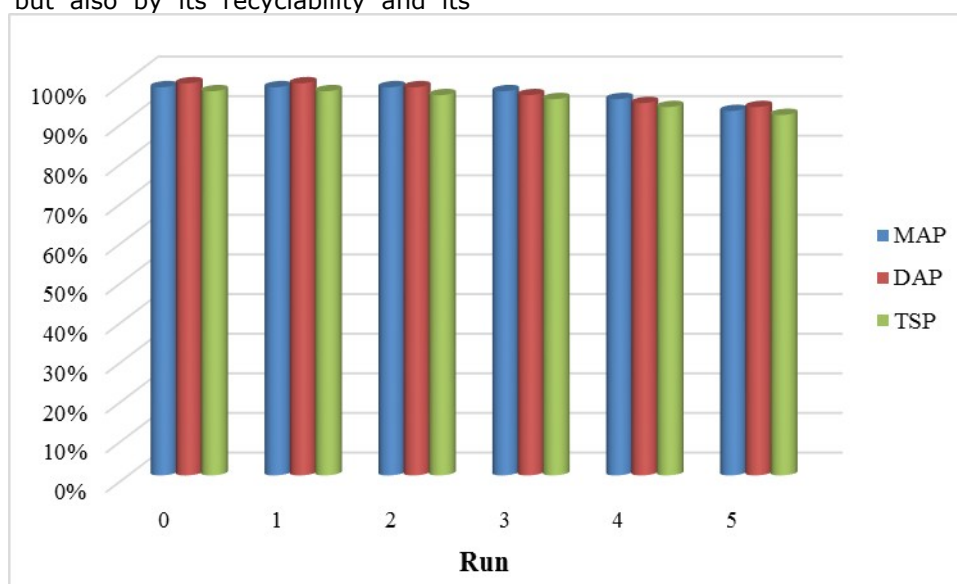
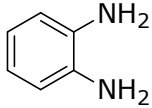
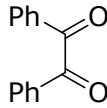
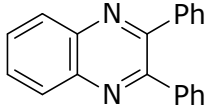
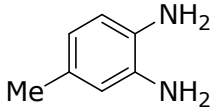
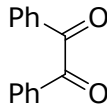
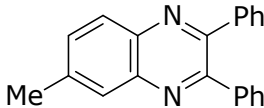
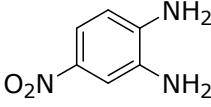
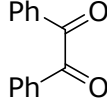
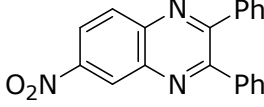
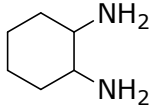
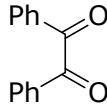
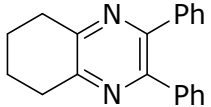
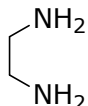
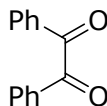
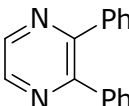
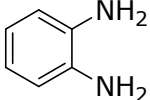
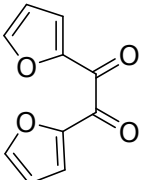
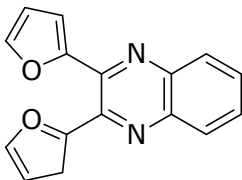
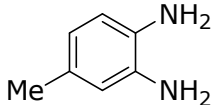
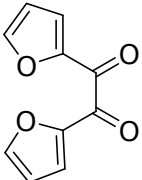
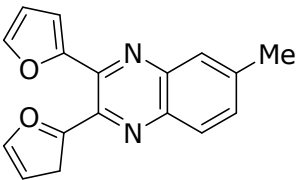
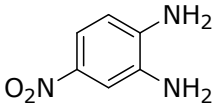
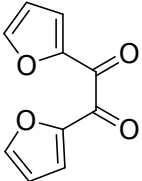
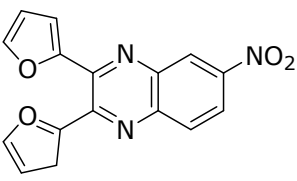
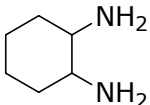
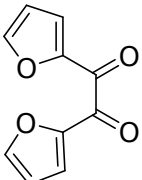
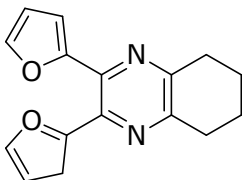
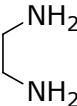
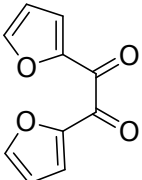
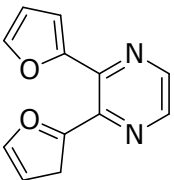


Figure 2. Recyclability of MAP, DAP, and TSP (0.003 g) in the condensation of 1,2-diamines with 1,2-dicarbonyl compounds at optimal conditions.

The catalysts remain functional throughout the six runs with a slight loss of their catalytic capacity that can be estimated by about 5% in yield.

Table 3. Quinoxaline derivatives synthesis catalyzed by MAP, DAP, and TSP at room temperature ^a.^a Reaction conditions: 1,2-diamine (1 mmol) and 1,2-dicarbonyl (1 mmol), EtOH (2 mL), 0.003 g of catalyst, r.t. ^b Isolated yields.

Entry	aryl 1,2-diamines	1,2-dicarbonyl	Product	Molecular weight (g/mol)	Catalyst	Time (min)	Yield ^b (%)	TON	TOF (h ⁻¹)
1(3a)				282.3	MAP	4	96	36.67	547.31
					DAP	2	98	43.17	1308.18
					TSP	2	97	75.78	2296.36
2(3b)				296.4	MAP	4	97	37.16	554.63
					DAP	2	98	43.17	1308.18
					TSP	2	99	77.34	2343.64
3(3c)				327.3	MAP	4	95	36.39	543.13
					DAP	2	94	41.41	1254.85
					TSP	2	97	75.78	2296.36
4(3d)				314.4	MAP	4	88	33.71	503.13
					DAP	2	90	39.65	1201.51
					TSP	2	90	70.31	2130.60
5(3e)				232.28	MAP	4	90	34.48	514.63
					DAP	2	88	38.77	1174.85
					TSP	2	91	71.09	2154.24

6(3f)				262.26	MAP	4	90	34.48	514.63
					DAP	2	93	40.97	1241.51
					TSP	2	91	71.09	2154.24
7(3g)				276.29	MAP	4	94	36.02	537.61
					DAP	2	92	40.53	1228.18
					TSP	2	97	75.78	2296.36
8(3h)				307.26	MAP	4	91	34.86	520.29
					DAP	2	89	39.21	1188.18
					TSP	2	92	71.87	2177.88
9(3i)				266.29	MAP	4	86	32.95	491.79
					DAP	2	89	39.21	1188.18
					TSP	2	88	68.75	2083.33
10(3j)				212.2	MAP	4	88	33.72	503.28
					DAP	2	86	37.88	1147.88
					TSP	2	90	70.31	2130.61

CONCLUSION

To sum up the present study, phosphate-based fertilizers MAP, DAP, and TSP act as active heterogeneous catalysts for the synthesis of quinoxalines from various 1,2-diamines and 1,2-dicarbonyl compounds at ambient temperature. The optimum reaction conditions were not determined only by choice of the "greener" solvent and its volume, but also by the determination of the most appropriate weight of the catalyst, in order to present an environmentally benign protocol for this synthesis. Moreover, the study of the recyclability results shows that the catalysts can be quickly recovered and reused for at least six runs.

REFERENCES

- Anastas PT, Warner JC. *Green Chemistry: Theory and Practice*. Oxford 1998; 29.
- Xu F, Wang C, Wang H, Li X, Wan B. Eco-friendly synthesis of pyridines via rhodium-catalyzed cyclization of diynes with oximes. *Green Chemistry* 2015; 17(2): 799-803.
- Shingalapur RV, Hosamani KM. An Efficient and Eco-Friendly Tungstate Promoted Zirconia (WO_x/ZrO₂) Solid Acid Catalyst for the Synthesis of 2-Aryl Benzimidazoles. *Catalysis Letters* 2010; 137(1-2): 63-8.
- Chakrabarty M, Sarkar S. Novel clay-mediated, tandem addition-elimination-(Michael) addition reactions of indoles with 3-formylindole: an eco-friendly route to symmetrical and unsymmetrical triindolylmethanes. *Tetrahedron Letters* 2002; 43(7): 1351-3.
- Shu XZ, Nguyen S C, He Y, Oba F, Zhang Q, Canlas C, Somorjai GA, Alivisatos AP, Toste FD. Silica-Supported Cationic Gold(I) Complexes as Heterogeneous Catalysts for Regio- and Enantioselective Lactonization Reactions. *J. Am. Chem. Soc.* 2015; 137(22): 7083-6.
- Sun J, Zhan WW, Akita T, Xu Q. Toward Homogenization of Heterogeneous Metal Nanoparticle Catalysts with Enhanced Catalytic Performance: Soluble Porous Organic Cage as a Stabilizer and Homogenizer. *J. Am. Chem. Soc.* 2015; 137(22): 7063-6.
- Chughtai AH, Ahmad N, Younus HA, Laypkov A, Verpoort F. Metal-organic frameworks: versatile heterogeneous catalysts for efficient catalytic organic transformations. *Chemical Society Reviews* 2015; 44(19): 6804-49.
- Pirkanniemi K, Sillanpää M. Heterogeneous water phase catalysis as an environmental application: a review. *Chemosphere* 2002(10); 48: 1047-60.
- Abba MO, Gonzalez-DelaCruz VM, Colón G, Sebti S, Caballero A. In situ XAS study of an improved natural phosphate catalyst for hydrogen production by reforming of methane. *Applied Catalysis B: Environmental* 2014; 150-151: 459-65.
- Sebti S, Smahi A, Solhy A. Natural phosphate doped with potassium fluoride and modified with sodium nitrate: efficient catalysts for the Knoevenagel condensation. *Tetrahedron Letters* 2002; 43(10): 1813-5.
- Ramanarivo HR, Solhy A, Sebti J, Smahi A, Zahouily M, Clark J, Sebti S. An Eco-Friendly Paradigm for the Synthesis of α -Hydroxyphosphonates Using Sodium-Modified Fluorapatite under Solventless Conditions. *ACS Sustainable Chemistry & Engineering* 2013; 1(4): 403-9.
- Hassine A, Sebti S, Solhy A, Zahouily M, Len C, Hedhili MN, Fihri A. Palladium supported on natural phosphate: Catalyst for Suzuki coupling reactions in water. *Applied Catalysis A: General* 2013; 450: 13-8.
- Hassine A, Bouhrara M, Sebti S, Solhy A, Mahfouz R, Luart D, Len C, Fihri A. Natural Phosphate-supported Palladium: A Highly Efficient and Recyclable Catalyst for the Suzuki-Miyaura Coupling Under Microwave Irradiation. *Current Organic Chemistry* 2014; 18(24): 3141-8.
- Bahammou I, Esaady A, Boukhris S, Ghailane R, Habbadi N, Hassikou A, Souizi A. Direct use of mineral phosphate fertilizers MAP, DAP, and TSP as heterogeneous catalysts in organic reactions. *Mediterr.J.Chem.*, 2016; 5(6): 615-23.
- Zimou O, Malek B, Elhallaoui A, Ghailane T, Ghailane R, Boukhris S, Habbadi N, Hassikou A, Souizi A. Valorization of the Phosphate Fertilizers Catalytic Activity in 1- (Benzothiazolylamino) Methyl-2-Naphthol Derivatives Synthesis. *Bulletin of Chemical Reaction Engineering & Catalysis* 2019; 14 (2): 238-46.
- Hugo WB, Stretton RG. Action of Quinacillin on *Staphylococcus aureus*. *Nature* 1964; 202: 1217.
- Toris CB, Gleason ML, Camras CB, Yablonski ME. Effects of Brimonidine on Aqueous Humor Dynamics in Human Eyes. *Archives of Ophthalmology* 1995; 113(12): 1514-7.
- Chávez JJE, Merino V, Cervantes ML, Cruz IMR, Guerrero DQ, Quintanar AG. The Use of Iontophoresis in the Administration of Nicotine and New Non-Nicotine Drugs through the Skin for Smoking Cessation. *Current Drug Discovery Technologies* 2009; 6(3): 171-85.
- Arbiser JL, Moschella SL. Clofazimine: A review of its medical uses and mechanisms of action. *Journal of the American Academy of Dermatology* 1995; 32(2): 241-7.
- Dell A, Williams DH, Morris HR, Smith GA, Feeney J, Roberts GCK. Structure revision of the antibiotic echinomycin. *J. Am. Chem. Soc.* 1975; 97(9): 2497-502.
- Bailly C, Echepare S, Gago F, Waring M. (1999) Recognition elements that determine affinity and sequence-specific binding to DNA of 2QN, a biosynthetic bis-quinoline analogue of echinomycin, *Anti-Cancer Drug Design* 1999; 14(3): 291-303.
- Taylor J. Inhibition of interferon action by actinomycin. *Biochemical and biophysical research communications* 1964; 14: 447-51.
- Pereira J A, Pessoa A M, Cordeiro MNDS, Fernandes R, Prudêncio C, Noronha JP, Vieira M. Quinoxaline, its derivatives and applications: A State of the Art review. *European Journal of Medicinal Chemistry* 2015; 97: 664-72.

24. Vieira M, Pinheiro C, Fernandes R, Noronha JP, Prudêncio C. Antimicrobial activity of quinoxaline 1,4-dioxide with 2- and 3-substituted derivatives. *Microbiological Research* 2014; 169(4): 287-93.
25. Bahekar RH, Jain MR, Gupta AA, Goel A, Jadav PA, Patel DN, Prajapati VM, Patel PR. (2007) Synthesis and Antidiabetic Activity of 3,6,7-Trisubstituted-2-(1H-imidazol-2-ylsulfanyl)quinoxalines and Quinoxalin-2-yl isothioureas. *Arch. Pharm. Chem. Life Sci*, 340(7): 359-66.
26. Burguete A, Pontiki E, Hadjipavlou-Litina D, Ancizu S, Villar R, Solano B, Moreno E, Torres EE, Pérez S, Aldana I, Monge A. (2011) Synthesis and Biological Evaluation of New Quinoxaline Derivatives as Antioxidant and Anti-Inflammatory Agents. *Chemical Biology & Drug Design* 2011; 77(4): 255-67.
27. Cogo J, Kaplum V, Sangi DP, Ueda-Nakamura T, Corrêa AG, Nakamura CV. Synthesis and biological evaluation of novel 2,3-disubstituted quinoxaline derivatives as antileishmanial and antitrypanosomal agents. *European Journal of Medicinal Chemistry* 2014; 90: 107-23.
28. Tseng CH, Chen YR, Tzeng CC, Liu W, Chou CK, Chiu CC, Chen YL. Discovery of indeno[1,2-b]quinoxaline derivatives as potential anticancer agents. *European Journal of Medicinal Chemistry* 2015; 108: 258-73.
29. Sarges R, Lyga J W. Synthesis and aldose reductase inhibitory activity of N-1, N-4-disubstituted 3,4-dihydro-2(1H)-quinoxalinone derivatives. *Journal of Heterocyclic Chemistry* 1988; 25(5): 1475-9.
30. Schepetkin IA, Kirpotina LN, Khlebnikov AI, Hanks TS, Kochetkova I, Pascual DW, Jutila MA, Quinn MT. Identification and Characterization of a Novel Class of c-Jun N-terminal Kinase Inhibitors. *Molecular Pharmacology* 2012; 81(6): 832-45.
31. Saranya J, Sounthari P, Parameswari K, Chitra S. Acenaphtho[1,2-b]quinoxaline and acenaphtho[1,2-b]pyrazine as corrosion inhibitors for mild steel in acid medium, *Measurement* 2016; 77: 175.
32. Olasunkanmi LO, Kabanda MM, Ebenso EE. Quinoxaline derivatives as corrosion inhibitors for mild steel in hydrochloric acid medium: Electrochemical and quantum chemical studies. *Physica E* 2016; 76: 109-26.
33. Zarrouk A, Zarrok H, Salghi R, Hammouti B, Al-Deyab SS, Touzani R, Bouachrine M, Warad I, Hadda T B. A Theoretical Investigation on the Corrosion Inhibition of Copper by Quinoxaline Derivatives in Nitric Acid Solution, *International Journal of Electrochemical Science* 2012; 7: 6353-64.
34. Aparicio D, Attanasi OA, Filippone P, Ignacio R, Lillini S, Mantellini F, Palacios F, Santos JMDL. Straightforward Access to Pyrazines, Piperazinones, and Quinoxalines by Reactions of 1,2-Diaza-1,3-butadienes with 1,2-Diamines under Solution, Solvent-Free, or Solid-Phase Conditions. *Journal of Organic Chemistry* 2006; 71(16): 5897-905.
35. Singh SK, Gupta P, Duggineni S, Kundu B. Solid Phase Synthesis of Quinoxalines. *Synlett* 2003; 14: 2147-50.
36. Taylor EC, Maryanoff CA, Skotnickilc JS. Heterocyclization with cyano and sulfonyl epoxides. Preparation of quinoxalines and tetrahydro quinoxalines. *Journal of Organic Chemistry* 1980; 45(12): 2512-5.
37. Kamal A, Babu KS, Hussaini SA, Mahesh R, Alarifi A. Amberlite IR-120H, an efficient and recyclable solid phase catalyst for the synthesis of quinoxalines: a greener approach. *Tetrahedron Letters* 2015; 56(21): 2803-8.
38. Huang T, Jiang D, Chen J, Gao W, Ding J, Wu H. Silica Sulfuric Acid (SSA)/Polyethylene Glycol (PEG) as a Recyclable System for the Synthesis of Quinoxalines and Pyrazines, *Synthetic Communications* 2011; 41(22): 3334-43.
39. Javidi J, Esmailpour M. Fe₃O₄@SiO₂-imid-PMAN magnetic porous nanosphere as recyclable catalyst for the green synthesis of quinoxaline derivatives at room temperature and study of their antifungal activities. *Materials Research Bulletin* 2016; 73: 409-22.
40. Digwal CS, Yadav U, Sakla AP, Ramya PVS, Aaghaz S, Kamal A. VOSO₄ catalyzed the highly efficient synthesis of benzimidazoles, benzothiazoles, and quinoxalines. *Tetrahedron Letters* 2016; 57(36): 4012-6.
41. Andriamitantsoa RS, Wang J, Dong W, Gao H, Wang G. SO₃H-functionalized metal-organic frameworks: an efficient heterogeneous catalyst for the synthesis of quinoxaline and derivatives. *RSC Advances* 2016; 6: 35135-43.

Eco-friendly Synthesis of Quinoxaline Derivatives Using Mineral Fertilizers as Heterogeneous Catalysts

Badr Malek, Imane Bahammou, Omar Zimou, Achraf El Hallaoui, Rachida Ghailane, Said Boukhris, Abdelaziz Souizi*

Laboratory of Organic, Organometallic and Theoretical Chemistry, University Ibn Tofail, B.P. 133, Kenitra, Morocco

* Correspondence: Souizi@yahoo.com (A. Souizi),
Tel: +212661183260

Supplementary Information

2,3-diphenylquinoxaline (3a, Table 3, Entry 1). M.p.: 127-128°C (126-127°C³⁶⁻³⁷); ¹H NMR (300 MHz, DMSO-d₆): δ (ppm): 7.32-7.36 (m, 6H); 7.42-7.46 (m, 4H); 7.86-7.88 (m, 2H); 8.14-8.16 (m, 2H). ¹³C NMR (300 MHz, DMSO-d₆): δ (ppm): 128.50; 129.22; 129.26; 130.16; 130.84; 139.23; 140.93; 153.49.

6-methyl-2,3-diphenylquinoxaline (3b, Table 3, Entry 2). M.p.: 121-122°C (120-122°C³⁶⁻³⁷); ¹H NMR (300 MHz, DMSO-d₆): δ (ppm): 2.47 (s, 3H); 7.30-7.47 (m, 6H); 7.68-7.71 (m, 4H); 7.92 (m, 1H); 8.01 (m, 1H); 8.04 (m, 1H). ¹³C NMR (300 MHz, DMSO-d₆): δ (ppm): 21.83; 127.96; 128.82; 129.15; 130.13; 133.02; 139.42; 141.00; 152.56; 153.30.

6-nitro-2,3-diphenylquinoxaline (3c, Table 3, Entry 3). M.p.: 141-142°C (140-142°C³⁷); ¹H NMR (300 MHz, DMSO-d₆): δ (ppm): 7.36-7.46 (m, 6H); 7.47-7.54 (m, 4H); 8.38 (m, 1H); 8.58 (m, 1H); 8.93 (m, 1H). ¹³C NMR (300 MHz, DMSO-d₆): δ (ppm): 124.05; 129.87; 130.29; 138.45; 139.69; 143.46; 148.11; 155.86; 156.51.

2,3-Diphenyl-5,6,7,8-tetrahydroquinoxaline (3d, Table 3, Entry 4). M.p.: 153-154°C (152-155°C³⁷); ¹H NMR (300 MHz, DMSO-d₆): δ (ppm): 1.99-2.03 (m, 4H), 3.11 (m, 4H), 7.30-7.33 (m, 6H), 7.44-7.49 (m, 4H). ¹³C NMR (300 MHz, DMSO-d₆): δ (ppm): 22.9, 32.0, 128.2, 128.4, 129.9, 139.2, 149.8, 151.1.

2,3-Diphenylpyrazine (3e, Table 3, Entry 5). M.p.: 119-120°C (121-122°C³⁷); ¹H NMR (300 MHz, DMSO-d₆): δ (ppm): 7.30-7.37 (m, 6H), 7.43-7.48 (m, 4H), 8.62 (s, 2H). ¹³C NMR (300 MHz, DMSO-d₆): δ (ppm): 128.6, 128.9, 129.8, 139.0, 142.4, 153.1.

2,3-di(furan-2-yl)quinoxaline (3f, Table 3, Entry 6). M.p.: 133-135°C (134-136°C³⁶⁻³⁷); ¹H NMR (300 MHz, DMSO-d₆): δ (ppm): 6.59 (m, 2H), 6.68 (m, 2H), 7.65 (m, 2H), 7.79 (m, 2H), 8.17 (m, 2H). ¹³C NMR (300 MHz, DMSO-d₆): δ (ppm): 112.00, 112.93, 129.06, 130.67, 140.71, 142.85, 144.22.

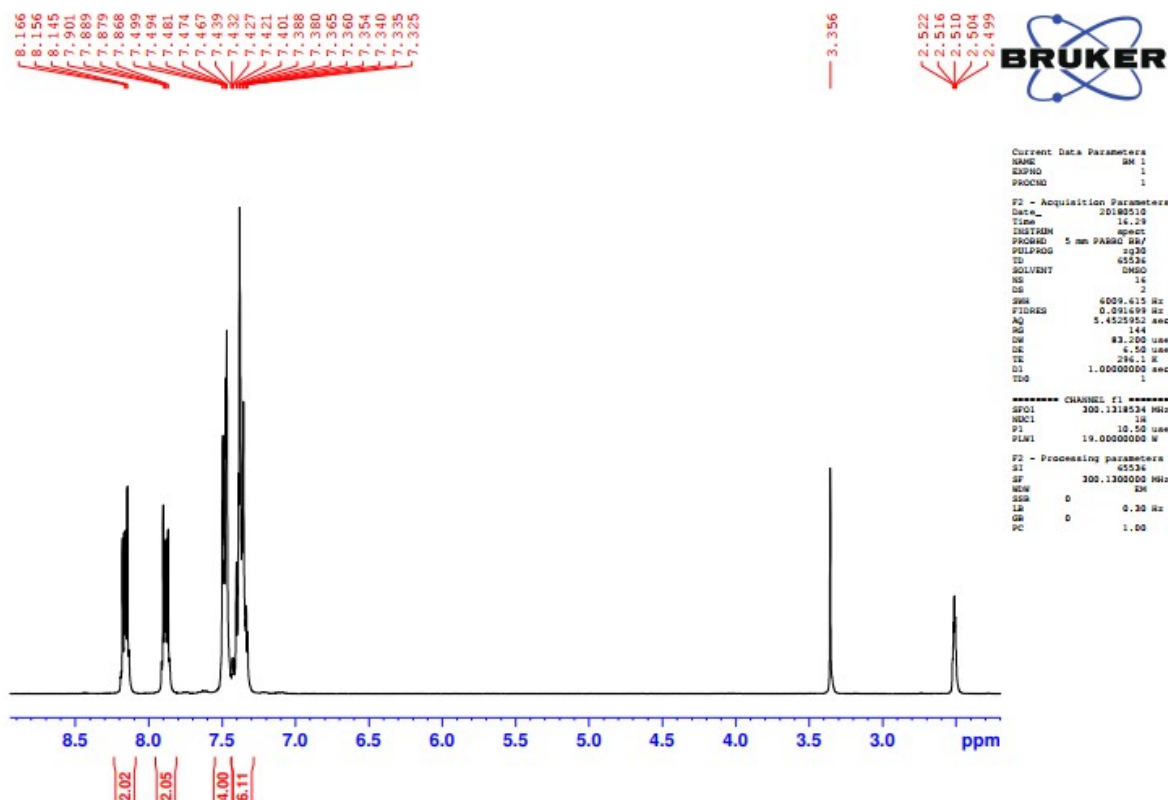
2,3-di(furan-2-yl)-6-methylquinoxaline (3g, Table 3, Entry 7). M.p.: 124-125°C (122-124°C³⁶⁻³⁷); ¹H NMR (300 MHz, DMSO-d₆): δ (ppm): 6.71 (m, 4H), 7.68 (m, 3H), 7.99 (s, 1H), 7.99 (m, 1H). ¹³C NMR (300 MHz, DMSO-d₆): δ (ppm): 21.46, 111.42, 111.97, 112.40, 127.30, 127.88, 132.21, 138.53, 139.98, 140.65, 141.12, 141.92, 143.35, 143.52, 150.40.

2,3-di(furan-2-yl)-6-nitroquinoxaline (3h, Table 3, Entry 8). M.p.: 154-156°C (152-154°C³⁶⁻³⁷); ¹H NMR (300 MHz, DMSO-d₆): δ (ppm): 6.62-6.65 (m, 2H), 6.97 (m, 2H), 7.68 (m, 2H), 8.32 (m, 1H), 8.59 (m, 1H), 9.04 (m, 1H). ¹³C NMR (300 MHz, DMSO-d₆): δ (ppm): 111.38, 111.52, 113.55, 114.38, 122.49, 123.98, 129.47, 137.98, 141.88, 142.98, 143.45, 143.95, 144.41, 146.64, 148.89, 148.98.

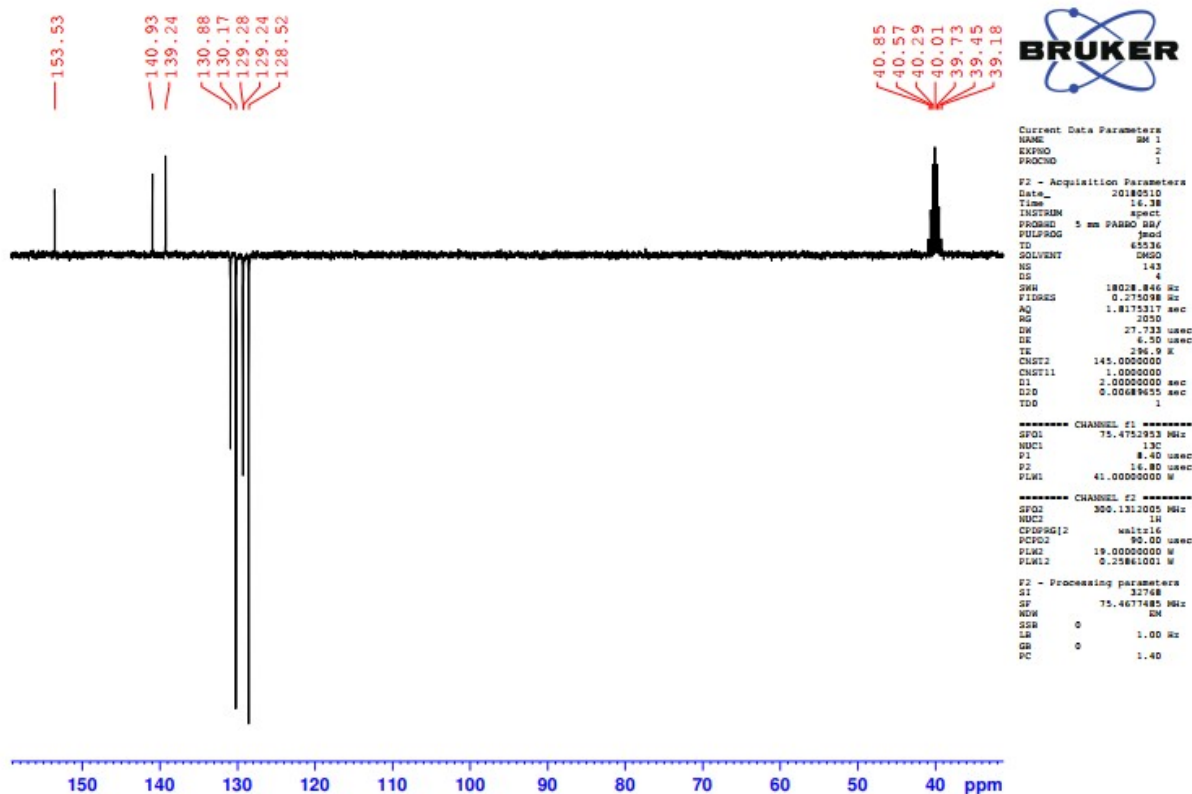
2,3-Di(2-furyl)-5,6,7,8-tetrahydroquinoxaline (3i, Table 3, Entry 9). M.p.: 150°C (150-151°C³⁷); ¹H NMR (300 MHz, DMSO-d₆): δ (ppm): 1.91-1.97 (m, 4H), 2.99-3.04 (m, 4H), 6.45-6.51 (m, 4H), 7.50-7.51 (m, 2H). ¹³C NMR (300 MHz, DMSO-d₆): δ (ppm): 22.65, 31.87, 111.34, 111.63, 139.22, 143.35, 150.77, 150.81.

2,3-Di(2-furyl)pyrazine (3j, Table 3, Entry 10). M.p.: 77-78°C (78-80°C³⁷); ¹H NMR (300 MHz, DMSO-d₆): δ (ppm): 6.53-6.72 (m, 4H), 7.56-7.57 (m, 2H), 8.53 (m, 2H). ¹³C NMR (300 MHz, DMSO-d₆): δ (ppm): 111.82, 112.15, 112.33, 141.76, 143.84, 150.40.

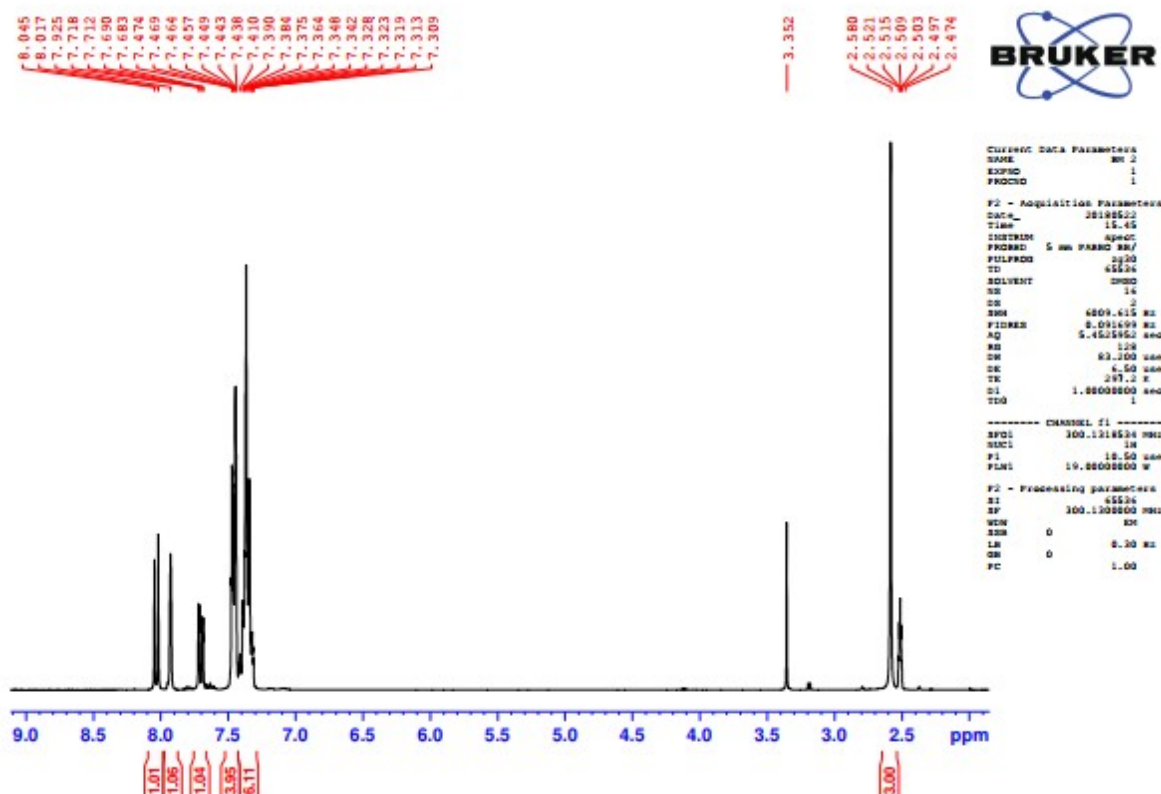
¹H and ¹³C NMR spectra of Quinoxalines:



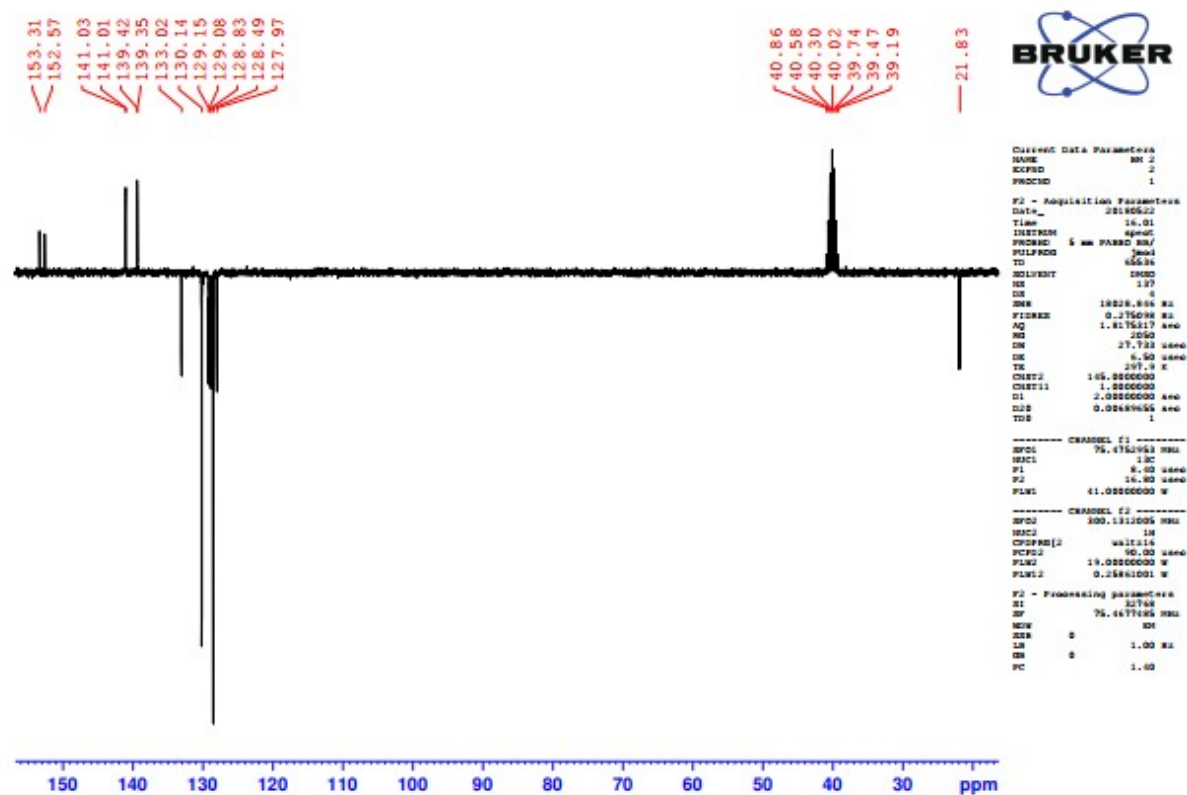
¹H NMR spectrum of 2,3-diphenylquinoxaline (DMSO-d₆).



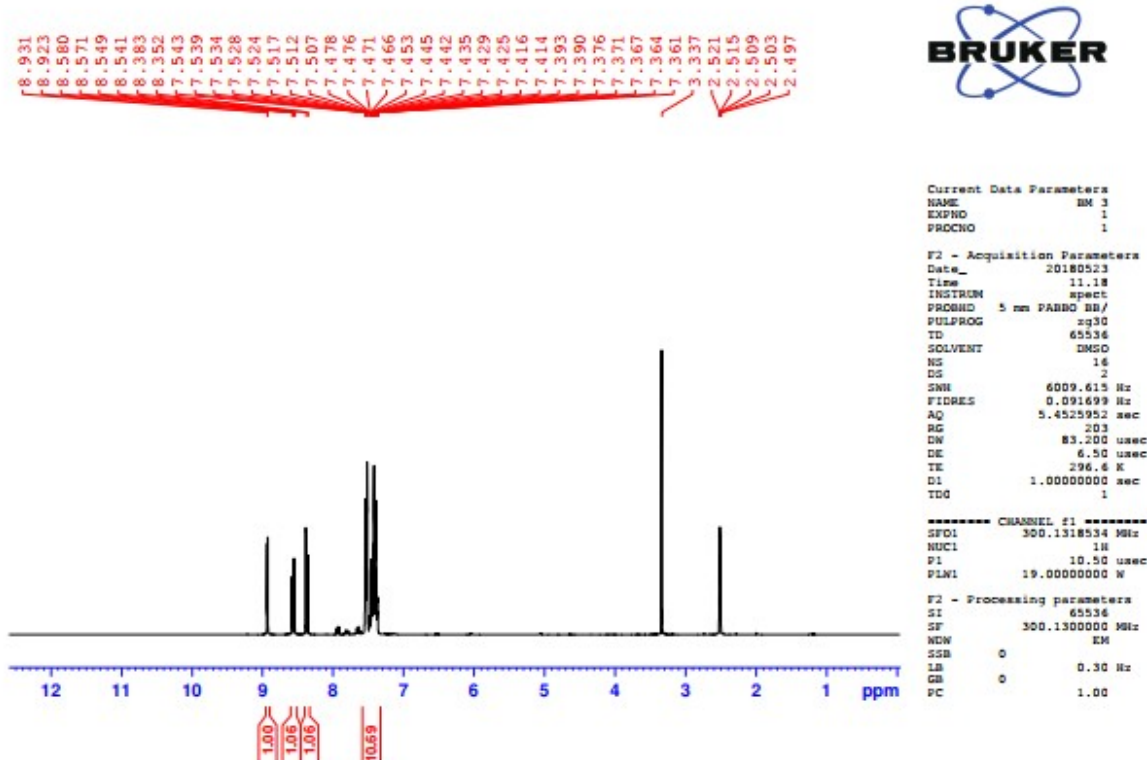
¹³C NMR spectrum of 2,3-diphenylquinoxaline (DMSO-d₆).



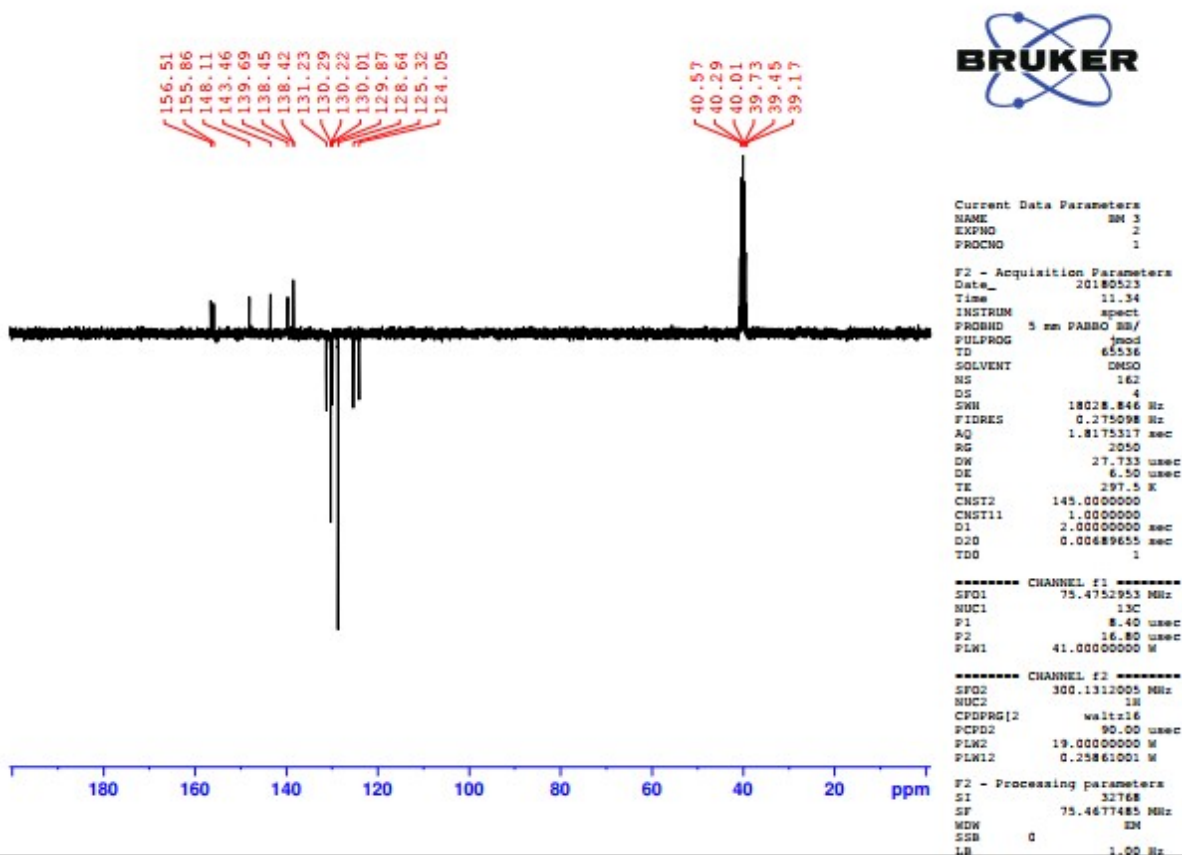
¹H NMR spectrum of 6-methyl-2,3-diphenylquinoxaline (DMSO-d₆).



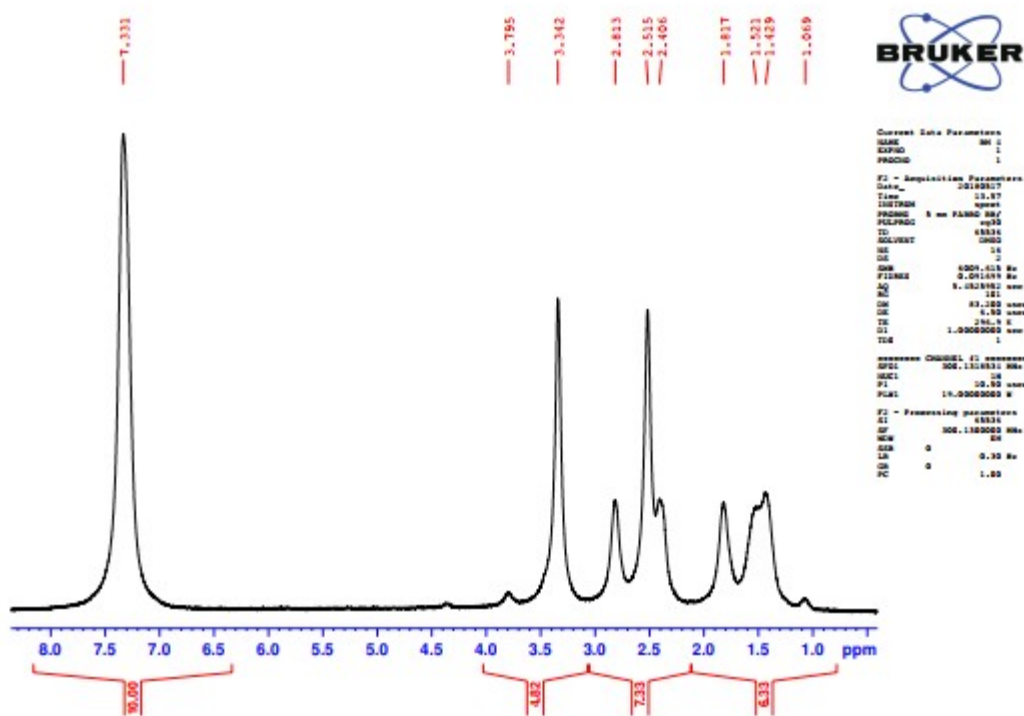
¹³C NMR spectrum of 6-methyl-2,3-diphenylquinoxaline (DMSO-d₆).



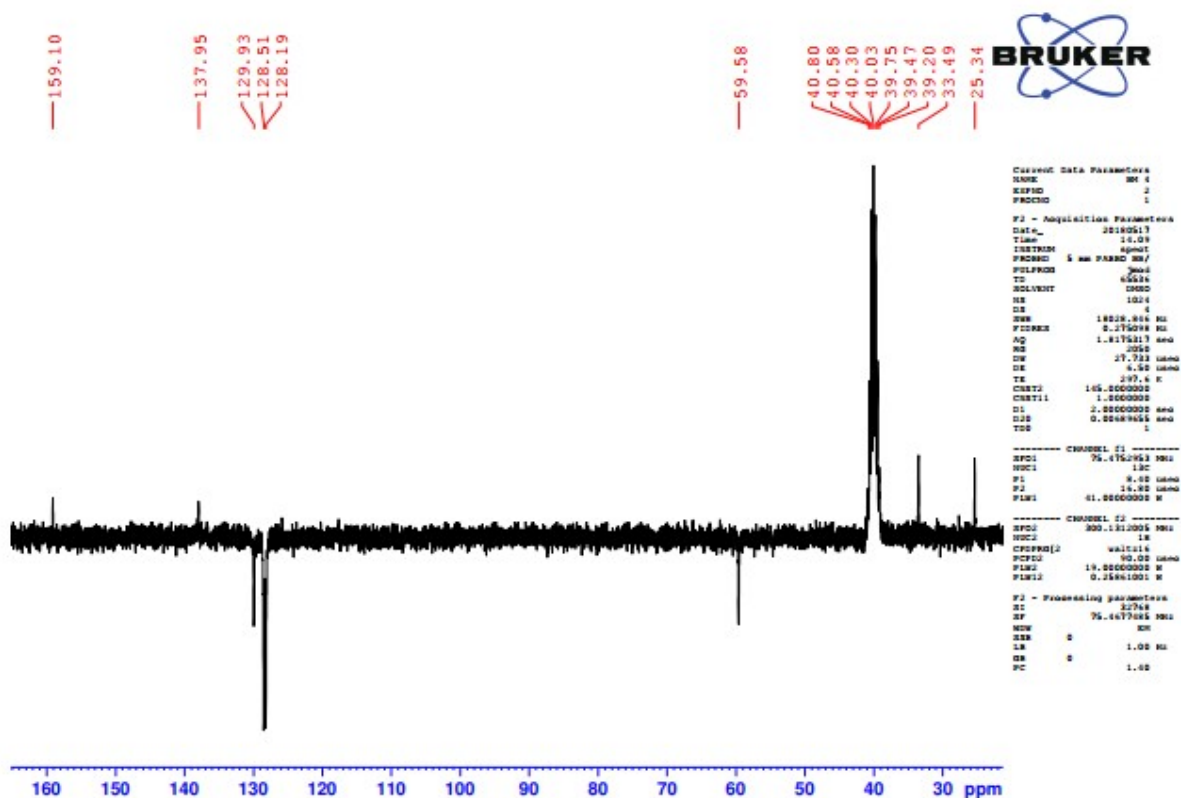
¹H NMR spectrum of 6-nitro-2,3-diphenylquinoxaline (DMSO-d₆).



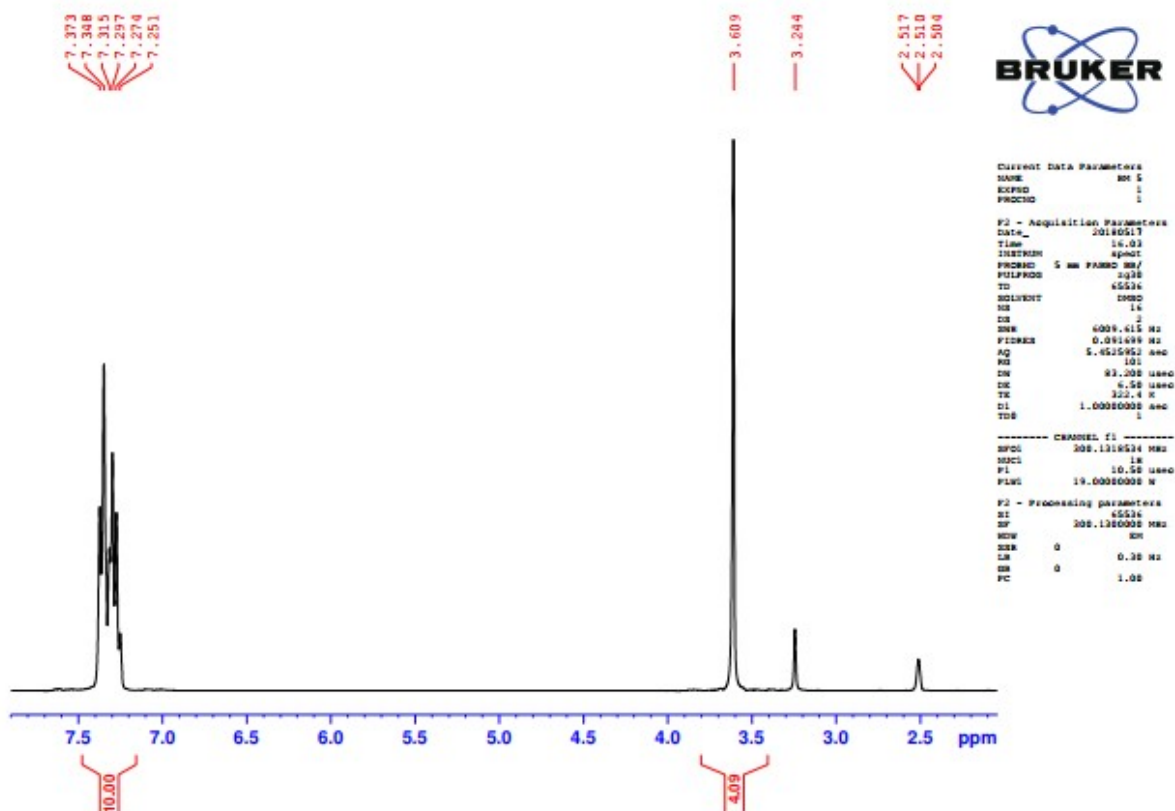
¹³C NMR spectrum of 6-nitro-2,3-diphenylquinoxaline (DMSO-d₆).



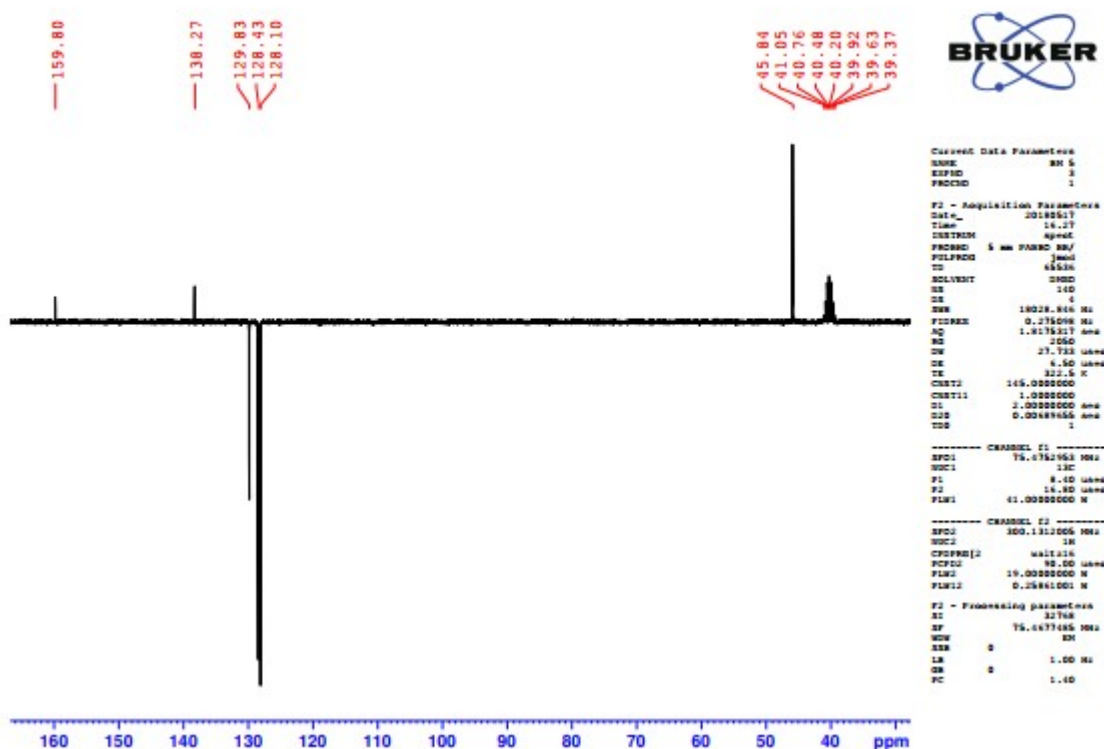
¹H NMR spectrum of 2,3-Diphenyl-5,6,7,8-tetrahydroquinoxaline (DMSO-d₆).



¹³C NMR spectrum of 2,3-Diphenyl-5,6,7,8-tetrahydroquinoxaline (DMSO-d₆).



¹H NMR spectrum of 2,3-Diphenylpyrazine (DMSO-d₆).



¹³C NMR spectrum of 2,3-Diphenylpyrazine (DMSO-d₆).



The Evaluation of Syngas Loss from Disposable Syringe Sampling System: A Case Study

Gábor Nagy^{1*}  , Mária Ambrus²  

¹University of Miskolc, Faculty of Materials Science and Engineering, Institute of Energy and Quality, 3515, Miskolc, Hungary.

²University of Miskolc, Faculty of Earth Science and Engineering, Institute of Raw Material Preparation and Environmental Processing, 3515, Miskolc, Hungary.

Abstract: The main advantage of standard gas sampling methods is their capability to keep a consistent gas composition from sampling to the analysis. On the other hand, the disadvantages include the price and possible fragility of the sampling equipment and the speed of sampling. Thus, a new tool was required with low cost and fast sampling during fieldwork. Disposable plastic syringes fulfill all these requirements with the additional advantage of applicability for multiple samplings. With the utilization of 3-way stopcocks, a filter media, and a butterfly needle, a simple but efficient sampling system was prepared. Even though the holding time of specific components is not as high as it is for a standard sample holder, the precise analysis of the gas samples is possible. After 3 hours of holding time, the concentration decrease was 0.4% CO, 1.6% CO₂, 8.0% H₂, 0.2% CH₄, 0.5% C₂H₄, 0.8% C₂H₆, 3.5% H₂S (3-part syringe) and 2.5% H₂S (2-part syringe) In the article, equations are proposed for the examined components so that the measured concentrations could be adjusted based on the elapsed time from sampling. Syringes have been successfully utilized in the field of applied pyrolysis, for small and pilot-scale experiments, and can even be used in an industrial environment.

Keywords: gas sampling method, syngas, GC, disposable syringe

Submitted: November 10, 2019. **Accepted:** May 03, 2020.

Cite this: Nagy G, Ambrus M. The Evaluation of Syngas Loss from Disposable Syringe Sampling System: A Case Study. JOTCSA. 7(2):441-8.

DOI: <https://doi.org/10.18596/jotcsa.644994>.

***Corresponding author.** E-mail: nagy.gabi@uni-miskolc.hu.

INTRODUCTION

As the energy demand of humanity is getting higher, the available energy resources must be used with the best possible efficiency. The most common utilization of solid fuels is energy production via thermochemical processes, which include, for example, combustion, gasification, and pyrolysis. Combustion is the most frequently used thermochemical process; however, the role of pyrolysis and gasification is predicted to increase in the future in both energy production and further branches of industry. During combustion, carbon monoxide, water, and heat are produced from the solid matter at high temperature, in the presence of oxygen to achieve complete combustion (1-3). In the case of gasification, the solid base material is

turned into gaseous fuel – syngas – at high temperature and during partial oxidation. The main constituents of syngas are carbon monoxide and hydrogen (4). As a result, syngas can be widely used as a base material in the chemical industry, for energy or synthetic natural gas production as well (5). Pyrolysis can be carried out at a lower temperature than gasification, and usually in the absence of air. The final products, beside syngas, include significant amounts of liquid hydrocarbons such as pyrolysis oil and tar, as well as char that can be further utilized via combustion or gasification.

To adequately control both pyrolysis and gasification processes, the composition of the produced gas should be known. The compositions of the gases can

vary greatly depending on the base material, the type of technology used, and the parameters of the experiment. The quantity of the following components should be monitored:

- carbon monoxide (CO): the main component; the highest possible quantity should be in the syngas;
- hydrogen (H₂): the main component; the highest possible quantity should be in the syngas;
- oxygen (O₂): produced if there is a leakage in the system, so its determination is essential;
- hydrocarbons (C_xH_y): fundamentally, the generation of methane is expected, but a high amount of ethane and ethene can be produced if the holding time in the reactor is short; their production is mostly a characteristic of pyrolysis, but their presence during gasification is disadvantageous, implying that the technology should be changed;
- carbon dioxide (CO₂): due to the addition of an oxidizing medium, partial oxidation occurs during gasification and CO₂ is produced; the regulation of the quantity of the oxidizing medium can lead to the maximization of CO and the minimization of CO₂ production;
- hydrogen sulfide (H₂S): produced from base materials with high sulfur content in the sub-stoichiometric environment; essential to know its quantity for environmental considerations and the utilization of the gas.

Gasification and pyrolysis experiments of various base materials – coals, biomasses, wastes – had been conducted with small-scale and pilot-sized (Figure 1.) systems for many years to optimize syngas production. In the case of the lab-scale system, the tests were fast, so frequent sampling was necessary to determine if any parameters of the experiments had to be changed. On the other hand, the use of the pilot-sized system required a more significant number of samplings from several gas outlets to monitor the various technological steps.

Thus, the preparation of a sampling technique appropriate for both systems was required with the following criteria:

- sampling should be fast, to monitor sudden changes in the gas composition;
- the sampling system could be used not only in laboratory conditions but for in situ samplings;
- it should be cheap, as a high number of samples are needed in case of further analyses;
- the internal volume should be suitable to take samples of varying quantities (e.g., the produced gas quantity is small in the lab-scale system);
- the gas composition should stay nearly constant in the sample holder until the analysis.

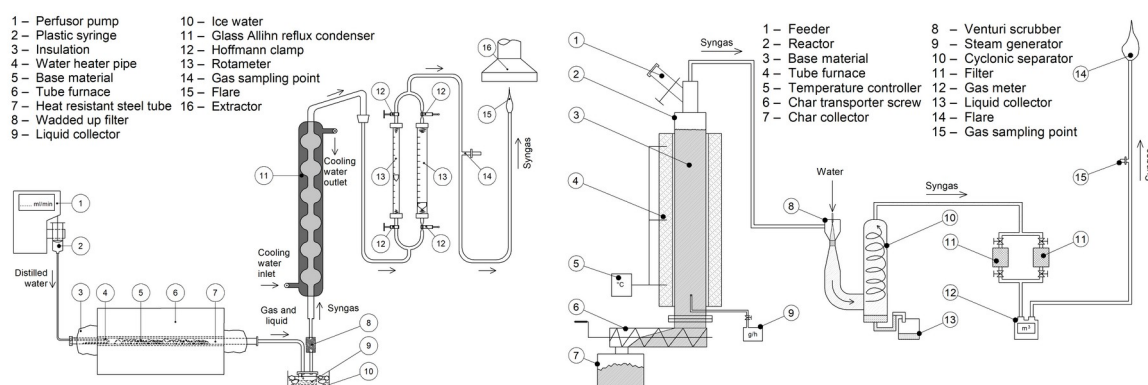


Figure 1: Lab-scale pyrolysis system (left) and pilot size gasification system (right).

The most frequent gas sampling methods (canister, sample cylinder, sampling bag, different types of sampling bulbs and gas-tight syringes) focus on holding the samples for a long time, e.g., bags for 2 days, canisters for 30 days (6). Thereby, the same gas composition is assured for the analysis as the composition during sampling. The volume of the samplers is at least 100-500 cm³, which makes the flushing and filling take several minutes, especially if the sampler is rigid. These properties of standard tools can be disadvantageous in case of experiments of smaller-scale. Glass gas-tight syringes provide fast sampling with low volume. However, they are fundamentally used for normal laboratory conditions and are not suitable for fieldwork in a dusty or contaminated environment. Furthermore, such

syringes are fragile and easily blocked, rendering them single-use samplers if the immediate analysis is not possible – as it is the case for our systems.

Thus, disposable plastic 3-part syringes were tested as samplers. Some of the main advantages of syringes, in contrast with the current sampling methods, are the speed of sampling, which is less than 0.5 minute, including the assembly of the sampler system and the cost, which can be a fraction of the price of the other samplers. Some examples of the approximate average retail prices of certain samplers in 2019 were as follows:

- 1 L multi-layer foil gas sampling bag with valve and septum: 17 EUR / 19 USD;
- 125 mL glass gas sampling bulb with stopcock and septum: 233 EUR / 269 USD;

- 250 mL polypropylene gas sampling bulb with stopcock: 100 EUR / 111 USD;
- 250 μ L gas-tight syringe: 78 EUR / 86 USD;

In contrast, the proposed sampling system from disposable syringes would cost 1.1 EUR / 1.2 USD, with 0.6 EUR / 0.7 USD per sample using one butterfly needle and one flushing syringe.

Syringes are mainly used in the medical field. Their significance is rather low in the case of chemical analysis, where they are almost solely used as liquid feeders (7, 8). Furthermore, the application of disposable syringes as gas samplers has been examined in a few publications. During their experiments to analyze greenhouse gas fluxes between the soil and the atmosphere, Collier et al. (9) prepared a static chamber and collected gas samples from the chamber headspace using disposable syringes. The samples were immediately injected into vials, so there was no change in the gas composition during sampling. De Quirós et al. (10) used disposable insulin syringes to sample bubbles in the cardiovascular system of stranded cetaceans. After sampling, the contents were injected into a vacutainer. The reason to use disposable syringes was the inapplicability of gas-tight syringes (fragile and easily clogged) during fieldwork.

The gas holding capability of plastic syringes is scarcely tested. Cho et al. studied the air contamination of CO₂-filled empty syringes with time both mathematically and experimentally. However, as the syringes were not closed off in any way, the results were not useful for the current experiment (11). On the other hand, plastic syringes filled with sulfur hexafluoride and perfluoropropane, sealed off with a plastic cap, and a 3-way stopcock were used by Ohji et al. (12), and the concentration decrease of these was examined concerning time for 24 hours. The concentration in their experiments decreased by 1-1.5 % for a 3-way stopcock and by 60-63 % for the plastic cap of the syringe. According to these results, the two

examined components can be stored with minimal concentration decrease in a syringe with a stopcock for one day. The investigation of the effects of syringe material (plastic and glass), storage time (0 and 30 min) and storage temperature (0-4 and 22 °C) on normal arterialized blood gas values (12 vol % O₂ and 5 vol% CO₂) was carried out by Knowles et al. (13). It was concluded that samples from plastic syringes should be instantly analyzed, while glass syringes should be used to store the samples.

Syringes are adequate for few-second-long medical processes. However, they are subjected to higher and longer stress during gas sampling, holding, and injection. Furthermore, these otherwise disposable tools could be reusable in case of gas sampling. After sampling, the storability of the gas is dependent on the material of the syringe and the stopcock. The barrel of the 3-part syringe is made from polypropylene, the base material of the plunger is isopropylene, the body of the stopcock is polycarbonate, and the handle is polyethylene. Among these polymers, polypropylene and polyethylene are not considered gas-tight materials, so the gas sample loss had to be examined. Moreover, if H₂S is present in the gas, it can be bound by the rubber plunger. There are some commercially available 2-part syringes, but these are difficult to obtain in large size (50 mL). On the other hand, 3-part syringes with rubber plunger are better sealed and provide easier plunger sliding, compared to the 2-part ones. Thus, 3-part syringes sealed with 3-way stopcocks were used for the experiments to test their performance as syngas samplers and sample holders. With high gas quantities kept in the samplers, the changes in gas composition were tested at various time intervals.

MATERIALS AND METHOD

Materials

Calibration gas from Linde was used to model raw syngas. The exact gas composition is summarized in Table 1.

Table 1: The gas mixture used to test the method.

Gases, gas mixtures	Composition, vol%
Hydrogen	50
Carbon monoxide	25
Carbon dioxide	12
Methane	6
Ethane	3
Ethylene	2
Hydrogen sulfide	2

Romed type 2-part and 3-part disposable plastic syringes (50 mL), B.Braun type 3-way stopcocks, household cotton wool, and B.Braun type 23G scalp vein butterfly needle were used to prepare the

sampling system (23G = 0.023" outside diameter of the needle). The assembled gas sampling system is illustrated in Figure 2.

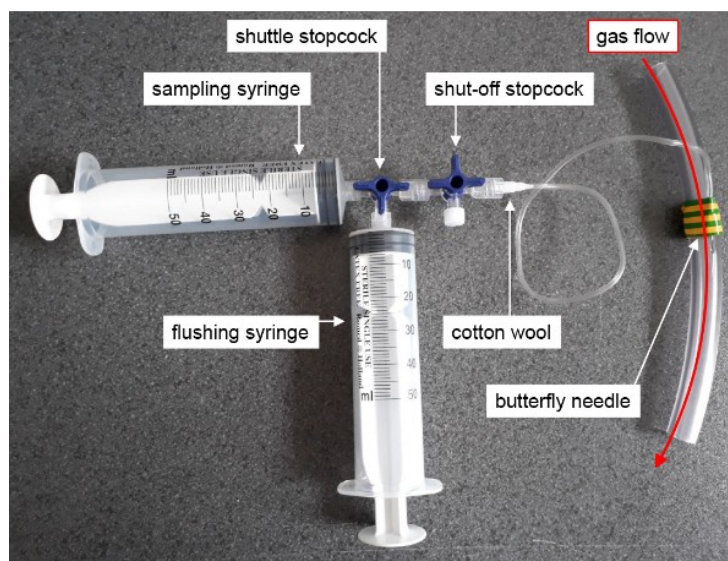


Figure 2: The gas sampling system.

Methods

The sampling method was prepared with the usage of simple medical infusion tools. Disposable syringes were used for both gas sampling and injecting the sample to a gas chromatograph for analysis. Plastic single-use syringes are available with standard conical Luer connectors (14). The two most widespread types are Luer-Slip and Luer-Lock connectors. In the case of Luer-Slip connectors, the connecting item – for example, needle, stopcock, injector, etc. – can be simply slipped in or on the cone-shaped connector. The connectors are kept together by frictional force. As the connectors can be easily disconnected, the proper connection should always be monitored. Considering that the Luer-Lock type connectors require the two connecting items to be screwed together, making disconnection significantly harder, Luer-Lock connectors were chosen.

A piece of cotton wool is used as a gas filter because of its high specific surface. It is supposed to separate materials that are either solid or able to condense and were not separated by the gas cleaning equipment. Thus, the gas chromatograph can further be protected.

Additionally, a tap or inlet is necessary where a plastic, rubber, or silicone tube can be connected to the sampler. Various sized needles were tested to connect the tube with the sampler. The trial of various types of needles revealed that using a relatively thin needle can cause many problems: the needle can bend, slip out of its plastic socket and cause injuries, get clogged and make the sampling longer because of the small inside diameter. The use of a thick needle can result in a giant hole on the tube, and, in the case of rigid tubes, gases can escape, and most of the produced components during syngas production are toxic and flammable. Thus, a 23G-25G size butterfly needle was chosen

for the experiments. The tube can be pierced slantwise with the butterfly needle, just like it is done in case of blood tests or infusions, with the wings taped to the tube to keep it in position.

After assembling the sampling system, the steps of the sampling are the following (Figure 3.):

- Put the shuttle stopcock in a position that allows gas to flow through all three passages (Figure 3/a.). The shut-off stopcock should be mirroring the shuttle stopcock, the passages parallel to the gas flow opened, and the perpendicular passage closed. This way, both syringes can be filled with the gas.
- The tube of the butterfly needle should be flushed with the sample gas, by using one of them as a flushing syringe (Figure 3/b.). As the sample gas enters the tube, the residing air is sucked to the flushing syringe. The total inner volume of the stopcock, the butterfly needle, and its tube is around 1.3 mL, so approximately 10-15 mL gas is necessary for complete flushing.
- Turning the shuttle stopcock closes the passage to the flushing syringe (Figure 3/c.), so the clean sample can only flow to the sampling syringe (Figure 3/d.).
- When sampling is finished, the sampling syringe can be closed off by further turning the shuttle stopcock, opening the passage to the flushing syringe (Figure 3/e.). The gas from the flushing syringe can be injected back to the original gas flow (Figure 3/f.). Therefore it enables the user to protect themselves from the toxic components that could be released after the sampling process.
- The final step is to disconnect the empty flushing syringe and the shuttle and sampling stopcocks after the shut-off stopcock is closed (Figure 3/g.). The sample can be held in the sealed syringe that can be connected to the sampling loop of the gas chromatograph (Figure 3/h.).

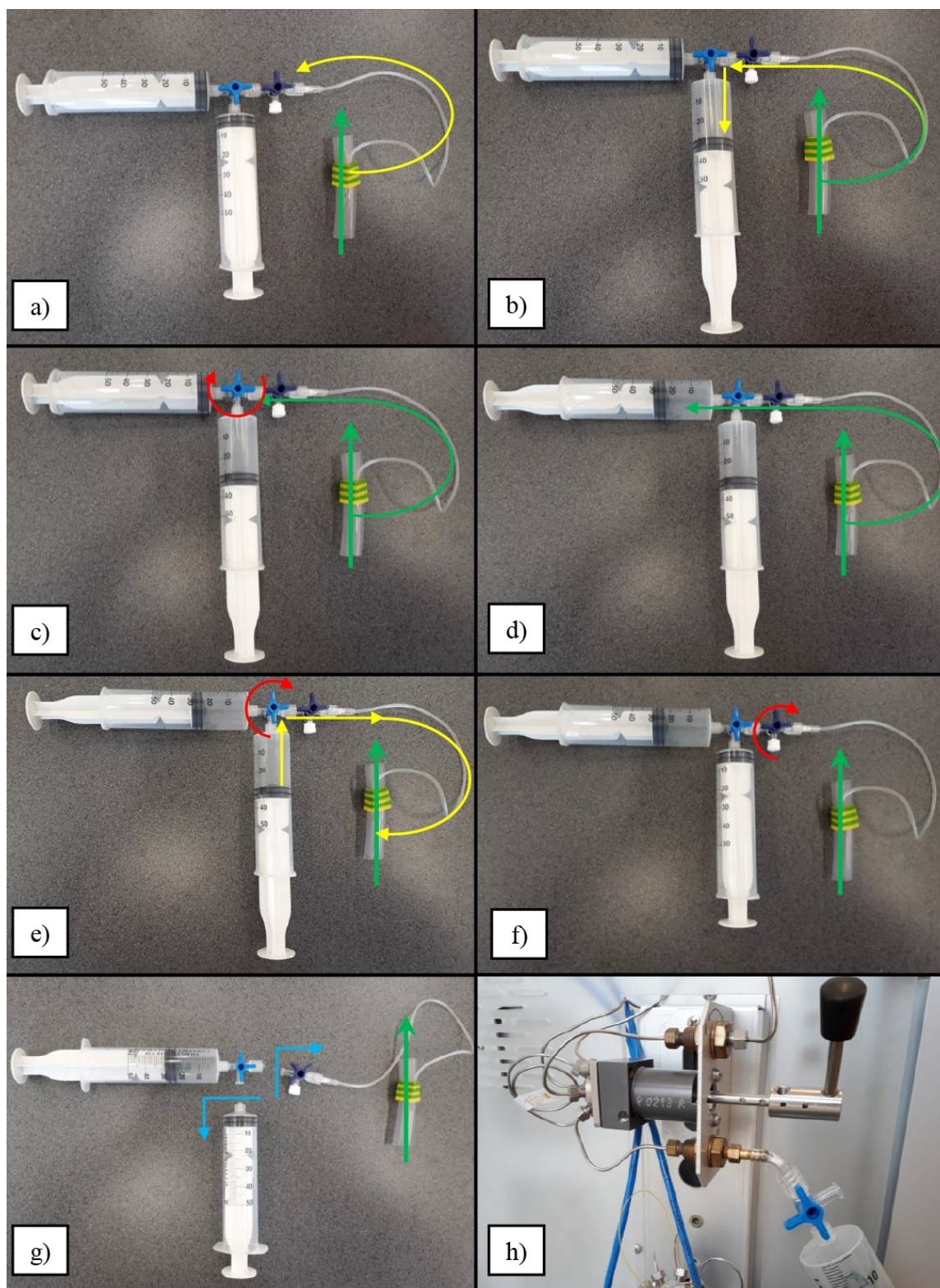


Figure 3: The operation of the sampling system.

(a – connecting the sampler to the sampling point; b – filling the flushing syringe with air/previous sample; c – closing the flushing syringe; d – sampling; e – stopping the gas sample flow; f – closing off the sampling point; g – removing the sampling syringe; h – attaching the sampling syringe to the gas chromatograph)

A Dani Master gas chromatograph with a TCD detector was used to test the gas holding capability

of the syringes. The gas chromatograph operating conditions can be seen in Table 2.

Table 2: GC operation conditions.

Detector	Thermal Conductivity Detector (TCD)
Temperature	110 °C
Voltage	4 V
Signal range	1
Sample injection	Loop, 200 µL
Injector	S/SL
Mode	Splitless
Split purge	10 mL/min
Temperature	40 °C
Pressure control	400 kPa
Carrier gas	Helium 6.0
The first column (Q-Bond 1)	Restek RT-Q-Bond (Fused Silica PLOT)
Length x Inner diameter x Film thickness	30 m x 0.32 mm x 10 µm
The second column (Q-Bond 2)	Restek RT-Q-bond (Fused Silica PLOT)
Length x Inner diameter x Film thickness	15 m x 0.53 mm x 20 µm
The third column	Restek RT-Msieve 5A (Fused Silica PLOT)
Length x Inner diameter x Film thickness	30 m x 0.53 mm x 50 µm
Configuration of the column with software*	
Length x Inner diameter x Film thickness	45 m x 0.32 mm x 20 µm
Oven temperature	36 °C
Method events	Times of switching the valve
flow in all three columns	0 – 1.80 min
flow in only the Q-Bond column	1.80 – 5.70 min
flow in all three columns	5.70 – 12.5 min
Aux gas	Nitrogen 5.0
Aux gas pressure	270 kPa
Cycle time	12 min
Evaluation software	Clarity 3.0.6.589

*The software can recognize only one column, so column parameters that could substitute for all three columns and result in realistic carrier gas flow values had to be entered.

Samples were analyzed immediately, and 3, 6, 9, 12, 18, 24, 36, 48, 59, 70, 95, and 120 hours after sampling. The calibration of the instrument was checked after 9, 18, and 24 hours and corrected if necessary. Furthermore, the start-up of the instrument was always followed by calibration (before the 36-, 48-, 95- and 120-hour examination).

RESULTS AND DISCUSSION

As some experiments require much more samplings as the laboratory system can analyze at once, the period during which the samples can be used with relatively low concentration change had to be tested, because these syringes were designed to hold liquids, the composition of the gas inside changes over time as air enters the syringe. For these tests, various gas mixtures were prepared from the gases available and sealed inside the syringe with the stopcock. The gas mixtures were kept on room temperature and were not exposed to direct sunlight. The composition was analyzed at given time intervals. The signals given by the original mixture were considered 100%, and the changes related to this are shown in Figure 4. The decrease in the quantity of the components can be described with polynomials in two or three variables. Moreover, exponentials are also indicated

in the figure with the coefficient of determination for each equation.

The yellow zones in Figure 4. demonstrate the range of the standard deviations of the measurements. It can be observed for all examined components, that the standard deviation of the measurements increased as the elapsed time became longer between the sampling and the measurement. Thus, the shorter the elapsed time is before measurement, the better the proposed equations are to describe the changes in composition.

In the case of CO, CO₂, CH₄, C₂H₄, and C₂H₆, a similar trend was experienced in the concentration changes. The decrease in H₂ and H₂S amount (in a 2-part syringe) showed a correlation, however, due to the better sealing ability of the syringes with rubber plunger, no further investigations were carried out about the composition changes in 2-part syringes. The evolution of the H₂S content (in a 3-part syringe) shows significantly distinct characteristics. The comparison of the diagrams reveals that the decrease of hydrogen content is the most significant for approximately the first 13 hours, then the decrease in the concentration of hydrogen sulfide becomes drastically higher (in a 3-part syringe).

The reason for this phenomenon can be explained by the examination of the used syringe. Both polypropylene (barrel) and polyethylene (handle) are non-polar molecules. Hydrogen is also non-polar and has the smallest size among the examined components, so it is expected to escape at the fastest rate from the syringe (15). However, the plunger is made from isoprene, and sulfur is used for crosslinking. The crosslinking of sulfur between the double-bonds of the isoprene chains is called vulcanization (16). The quantity of sulfur affects the characteristics of the product; for example, increasing sulfur content results in higher rigidity. As the plunger is soft and able to deform, many unsaturated bonds can be found between the

isoprene chains. Thus, instead of escaping to the atmosphere, hydrogen sulfide diffuses into the plunger material at a faster rate than hydrogen could escape through the wall of the syringe. The characteristic odor of hydrogen sulfide can be smelled on the plunger for several weeks after the analysis of hydrogen sulfide-containing samples, and this can, therefore, be further proven. The plunger also becomes gradually more rigid after 30-50 samplings, and sliding it in the barrel also becomes difficult, as the plunger is further vulcanized due to the diffusion of sulfur. This issue can be avoided with the use of a 2-part syringe in case of hydrogen sulphide containing samples.

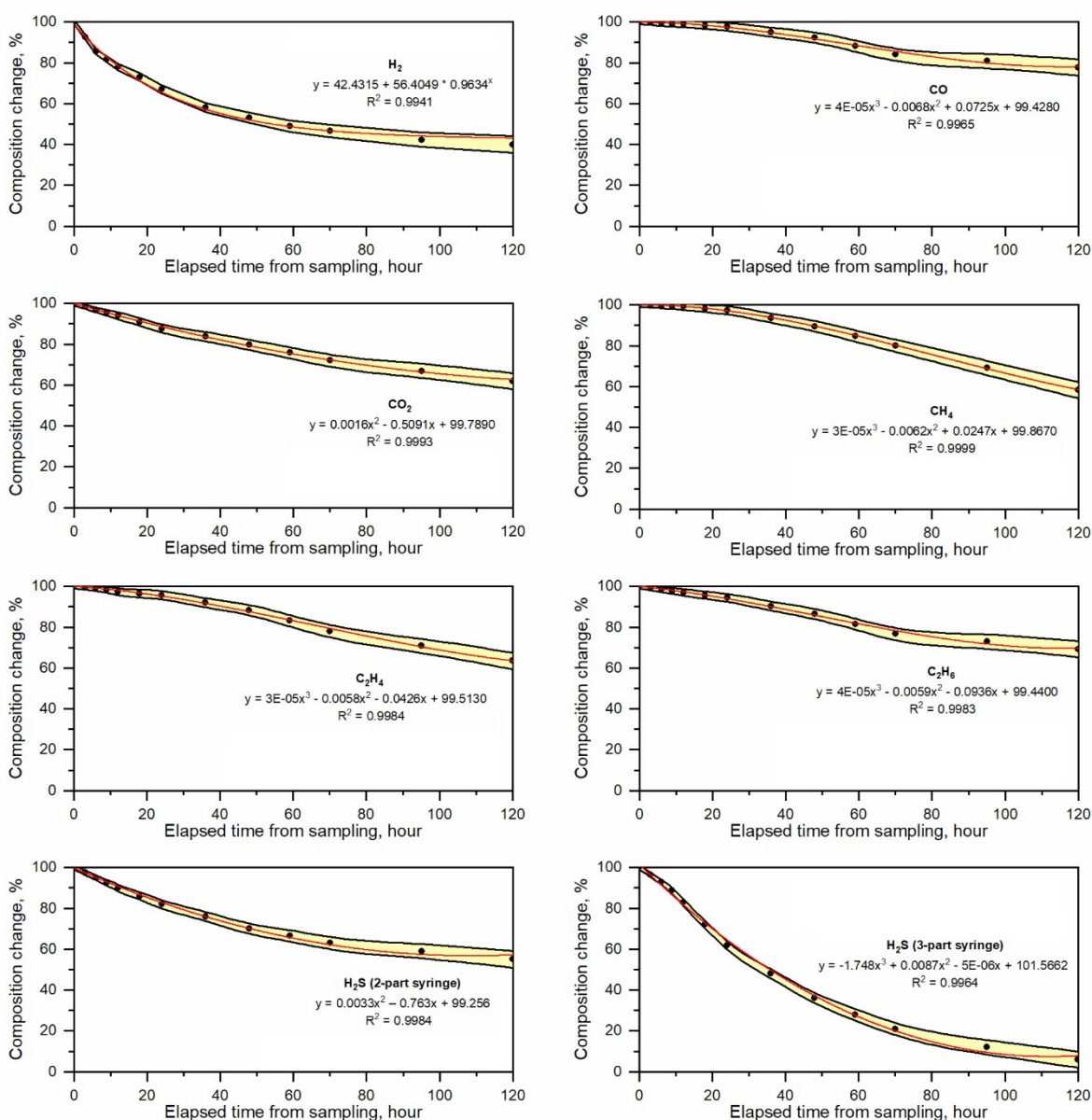


Figure 4: The changes in the composition of the calibration gas in the syringe in relation to time.

Ideally, the measurement of the stored gases should be carried out immediately after sampling as the component concentration decreases over time.

In case of the first measured time (3 hours), the concentration decrease was 0.4% CO, 1.6% CO₂, 8.0% H₂, 0.2% CH₄, 0.5% C₂H₄, 0.8% C₂H₆, 3.5%

H₂S (3-part syringe) and 2.5% H₂S (2-part syringe). However, the initial concentration can be calculated using the equations given in Figure 4. Since the standard deviation for each component increases over time, the measurements should be carried out as soon as possible.

CONCLUSIONS

A new gas sampling technique for systems of various sizes was developed, using disposable plastic syringes with stopcocks and a butterfly needle, and the syngas holding capability of the syringes after sampling was examined. The hydrogen content decreases exponentially, making it one of the earliest components to leave the sample holder, along with H₂S in the 3-part syringe. Equations describing the expected gas composition related to the holding time were also proposed, making it possible to calculate the original composition and concentration of the examined gas samples. As the standard deviations of the equations also increase over time, the accuracy of the calculations decreases. Thus, the initial measurement of the samples is suggested.

ACKNOWLEDGEMENT

The described article was carried out as part of the EFOP-3.6.1-16-2016-00011 "Younger and Renewing University – Innovative Knowledge City – institutional development of the University of Miskolc aiming at intelligent specialisation" project implemented in the framework of the Szechenyi 2020 program. The realization of this project is supported by the European Union, co-financed by the European Social Fund.

REFERENCES

1. Kumar V, Nanda M. Biomass Pyrolysis-Current status and future directions. *Energy Sources Part a-Recovery Utilization and Environmental Effects*. 2016;38(19):2914-21.
2. Stiegel GJ, Ramezan M. Hydrogen from coal gasification: An economical pathway to a sustainable energy future. *International Journal of Coal Geology*. 2006;65(3-4):173-90.
3. Sansaniwal SK, Pal K, Rosen MA, Tyagi SK. Recent advances in the development of biomass gasification technology: A comprehensive review. *Renewable & Sustainable Energy Reviews*. 2017;72:363-84.
4. Basu P. *Biomass Gasification and Pyrolysis - Practical Design and Theory*. Kidlington: Elsevier Inc.; 2010.
5. Nagy G, Wopera A, Koos T, Szabo R. The pyrolysis of canteen waste and oak mixtures in various ratios. *Energy Sources Part A-Recovery Utilization and Environmental Effects*. 2018;40(18):2124-36.
6. Swift J, Liss LA, Durand B. *Indoor air sampling and evaluating guide*. Boston: Commonwealth of Massachusetts Department of Environmental Protection; 2002.
7. Chiu G. Use of plastic syringes as measuring pipettes. *Journal of Chemical Education*. 1992;69(8):666.
8. Caletka R. Application of disposable plastic syringes in analytical-chemistry. *Fresenius Zeitschrift Fur Analytische Chemie*. 1982;311(2):124-5.
9. Collier SM, Ruark MD, Oates LG, Jokela WE, Dell CJ. Measurement of Greenhouse Gas Flux from Agricultural Soils Using Static Chambers. *Jove-Journal of Visualized Experiments*. 2014(90):8.
10. de Quiros YB, Gonzalez-Diaz O, Saavedra P, Arbelo M, Sierra E, Sacchini S, et al. Methodology for in situ gas sampling, transport and laboratory analysis of gases from stranded cetaceans. *Scientific Reports*. 2011;1:10.
11. Cho DR, Cho KJ, Hawkins IF. Potential air contamination during CO₂ angiography using a hand-held syringe: Theoretical considerations and gas chromatography. *Cardiovascular and Interventional Radiology*. 2006;29(4):637-41.
12. Ohji M, Adachi F, Tano Y. Sulfur hexafluoride and perfluoropropane do not escape from a plastic syringe closed with a stopcock. *American Journal of Ophthalmology*. 1997;123(5):709-11.
13. Knowles TP, Mullin RA, Hunter JA, Douce FH. Effects of syringe material, sample storage time, and temperature on blood gases and oxygen saturation in arterialized human blood samples. *Respiratory Care*. 2006;51(7):732-6.
14. Conical fittings with 6 % (Luer) taper for syringes, needles and certain other medical equipment - Part 2: Lock fittings. Switzerland: International Organization for Standardization; 1998.
15. Karger-Kocsis J. *Polypropylene - An A-Z reference*: Kluwer; 1999.
16. Mark JE, Erman B, Roland M. *The Science and Technology of Rubber - 4th Edition*. Oxford: Academic Press; 2013.



Spectral, DFT, molecular docking and antibacterial activity studies of Schiff base derived from furan-2-carbaldehyde and their metal(II) complexes

Manjuraj T.^{1*}  , Yuvaraj TCM¹  , Jayanna N.D.²  , Shreedhara S H³ ,
Sarvajith M S⁴  

¹Department of Chemistry, Sahyadri Science College (Auto), Shimoga, Karnataka INDIA.

²Department of Chemistry, S. S. M. S. College, Athani, 59104, Belagaum, Karnataka, INDIA.

³Sahyadri Science College (A) Shivamogga, INDIA.

⁴Manipal Institute of technology, Manipal, INDIA.

Abstract: Metal(II) complexes of cobalt(II) (1), copper(II) (2), nickel(II) (3), and zinc(II) (4) with Schiff base ligand derived from furan-2-carbaldehyde were synthesized and elucidated by IR, electronic, mass, ¹H NMR, and magnetic susceptibility measurements. Using DFT-based optimization of structures, bond length, bond angle, HOMO-LUMO energy gaps, and molecular electrostatic potential maps (MEP) of ligand and complexes 1-3 were theoretically calculated at the B3LYP/LANL2DZ level of theory. HOMO-LUMO energy gap was calculated which allowed the calculation of comparable properties like chemical hardness, chemical inertness, and chemical potential. The Ni(II) and Cu(II) complexes showed potent inhibition against all the bacterial strains. In comparison with antibacterial activity, molecular docking studies were carried out with protein receptor SEC2 (PDB: 1STE) in *Staphylococcus aureus*.

Keywords: Furan-2-carbaldehyde, Metal complexes, DFT, Antibacterial, Molecular docking.

Submitted: October 06, 2018. **Accepted:** May 04, 2020.

Cite this: Manjuraj T, Juvaraj T, Jayanna N. Spectral, DFT, molecular docking and antibacterial activity studies of Schiff base derived from furan-2-carbaldehyde and their metal(II) complexes. JOTCSA. 2020;7(2):449-62.

DOI: <https://doi.org/10.18596/jotcsa.467859>.

***Corresponding author. E-mail:** manjuraj877@gmail.com.

INTRODUCTION

The Schiff base ligands with nitrogen and oxygen donor atoms act as good chelating agents for the transition and non-transition metal ions. The azomethine (-CH=N-) linkage present in Schiff base ligands and its metal (II) complexes show a wide range of biocidal activities such as antibacterial (1) antifungal (2) anti-inflammatory

(3) anticancer, anti-diabetic (4), and antitumor activities. Furthermore, the interactions of these complexes with DNA have gained much attention due to their possible applications as new therapeutic agents (5-7). The high affinity for the chelation of the Schiff bases towards the transition metal ions is utilized in preparing their complexes in the solid form (8-10). The tractability of Schiff base ligands can be

enhanced by hydrogenation of (C=N) bands, and they should thus coordinate metal ions more easily. For these explanations, condensed Schiff bases have newly expanded significant consideration (11). Herein we report the synthesis and characterization of furan-2-ylmethylidene-hydrazinylidene-ethyl-phenol [AF], which is derived from 2-[(1E)-1-hydrazinylidene-ethyl] phenol and 2-furancarboxaldehyde and its metal(II) complexes.

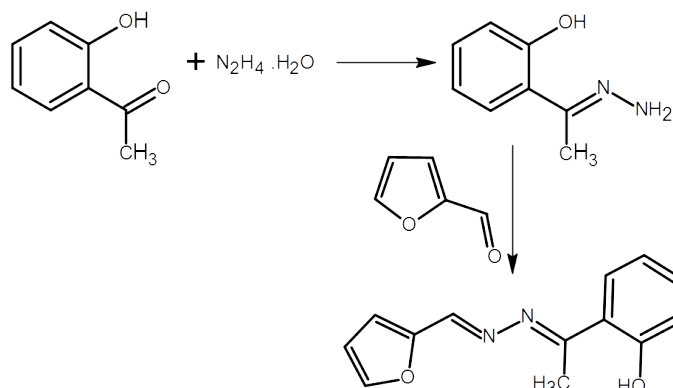
EXPERIMENTAL

All the chemicals used were of analytical grade and were as procured. The reagent grade chemicals 2-hydroxyacetophenone, hydrazine hydrate, 2-furancarboxaldehyde, and metal(II) salts were purchased from Sigma-Aldrich and used without further purification. The melting point had been recorded on an electro-thermal melting factor apparatus and are uncorrected. ¹H-NMR spectra were recorded on a Bruker 400 MHz spectrometer at IISc, Bangalore, and Karnataka, INDIA. The chemical shifts have been proven in δ values (ppm) with tetramethylsilane

(TMS) as an internal standard. LC-MS changed into acquired the usage of a C-18 column on Shimadzu, LCMS 2010A, Japan. The FT-IR spectra of the compounds were taken as KBr pellets (100 mg), the usage of Shimadzu FT-IR spectrometer. Magnetic susceptibility has been measured at 35 °C through the Gouy technique.

Synthesis of 2-[(1E)-1-[(2E)-(furan-2-ylmethylidene) hydrazinylidene] ethyl] phenol [AF]

The Schiff base ligand was prepared by refluxing 2-hydroxyacetophenone (4.02 g, 0.02 mol) and hydrazine hydrate, each dissolved in 30 mL ethanol with continuous stirring. The stirring was continued for 3 h and to obtain the white product. A solution of the isolated 2-[(1E)-1-hydrazinylidene ethyl]phenol (2.7g 0.02 mol) in 10 mL ethanol was then refluxed with an ethanolic solution of furan-2-carbaldehyde (1.8 g, 0.02 mol) for 5 h after adding 1 mL of glacial acetic acid (Scheme 1). The obtained solid product was filtered off, washed several times with methanol and recrystallized from hot methanol, and dried over anhydrous CaCl₂.



Scheme 1: Synthesis of Schiff base ligand AF .

Yield: 78%; M.p.: 178–180 °C, Anal. Calc. for C₁₃H₁₂N₂O₂ = C(68.41%) H(5.30%) and N(12.27%), Found: C(67.11%) H(5.68%) and N(11.94%), LC-MS: m/z 228 [M+1].

Synthesis of metal complexes

Ethanolic solution of metal(II) chlorides [Co(II), Ni(II), Cu(II) and Zn(II)] (2 mmol) added in drops to an ethanolic solution of the ligand (AF) (4 mmol) and the mixture was refluxed on a water bath for 3–4 h. The solid complexes obtained was filtered, washed with hot ethanol and dried in vacuum over anhydrous calcium chloride.

Co(II) Complex [1]:- Pale yellow solid, yield: 61%. Mp: > 300 °C. Anal. C(53.44%), H(3.79%), Co(10.09%), N(9.59%), Cl(12.13%), Found: C(53.62%), H(4.03%), Co(10.44%), N(10.21%), Cl(11.82%), 23 $\lambda\text{m cm}^{-2} \Omega^{-1} \text{mol}^{-1}$.

Ni(II) Complex [2]:- Light green solid, yield: 53%. Mp: > 300 °C Anal. C(52.37%), H(3.61%), Ni(10.21%), N(8.89%), Cl(12.05%), Found: C(52.62%), H(3.91%), Ni(10.44%), N(9.22%), Cl(12.63%), 21 $\lambda\text{m cm}^{-2} \Omega^{-1} \text{mol}^{-1}$.

Cu(II) Complex [3]:- Dark brown solid, yield: 55%. Mp: > 300 °C Anal. C(55.12%), H(4.19%), Cu(12.11%), N(8.66%), Cl(13.22%), Found: C(55.41%), H(4.51%), Cu(11.81%), N(8.05%), Cl(13.87%), $28 \text{ } \mu\text{m cm}^{-2} \Omega^{-1} \text{ mol}^{-1}$

Zn(II) Complex [4]:- Light cream solid, yield: 62%. Mp: > 300 °C Anal. C(51.43%), H(4.16%), N(8.12%), Zn(9.12%), Cl(10.18%), Found: C(51.92%), H(3.83%), Zn(8.78%), N(8.73%), Cl(10.51%), $21 \text{ } \mu\text{m cm}^{-2} \Omega^{-1} \text{ mol}^{-1}$.

Biological studies

Antibacterial assay

The obtained compounds were screened *In-vitro* against *S. aureus*, *B. Subtilis*, and *S. Pneumonia* (gram-positive) *P. aeruginosa* and *K. pneumonia* (gram-negative) bacterial strains by using disc diffusion method (12, 13). Ciprofloxacin was used as a standard for the current study with a concentration of about 10 $\mu\text{g}/\text{disc}$. Sterile molten Muller and Hynton agar cooled to 45 °C was injected with different strains. Fresh inocula containing $\sim 100 \text{ cells mL}^{-1}$ were used. Homogeneously, the inoculums were transferred on to a molten agar media with sterile cotton swabs by disease-free technique. A Whatman, no 2 filter paper disc of 6 mm diameter containing 200 $\mu\text{L}/\text{disc}$ of sample, was placed over the inoculated medium. The plates were left uninterrupted at room temperature for two hours and incubated at 37 °C for 24 h. Zone inhibition was measured with the zone reader scale.

In-silico docking studies

HEX 8.0 docking software in support with the discovery visualizer studios were used to perform interaction studies with protein receptor SEC2 (PDB: 1STE) in *Staphylococcus aureus* obtained from RCSB protein data bank (14).

RESULTS AND DISCUSSION

The metal (II) complexes are soluble in DMSO, DMF, and are sparingly soluble in chloroform. The complexes are stable at room temperature. The elemental analysis data of the ligand [AF] and its metal complexes [Co(II), Ni(II), Cu(II) and Zn(II)] indicate that the metal to ligand ratio is 1:2.

¹H NMR and Mass spectra

To identify the structure of free ligand AF, the resonance signals at δ 12.12, δ 7.11–7.75, δ 3.52–3.81, and δ 2.75–2.95 ppm are due to OH, Ar-protons, $-\text{CH}_2$, and $-\text{CH}_3$, respectively. The

sharp peak at 8.08 ppm corresponding to ($-\text{CH}=\text{N}-$) proton is shifted towards the upper field, which proves the formation of coordination bond between the metal and imine nitrogen. The deprotonation of OH proton has been observed in the spectrum of Zn(II) complex, which supports the phenolic oxygen atom was coordinated with metal ions and ¹H NMR spectra of ligand AF and Zn(II) complex provided in the supplementary file.

The mass spectrum of ligand (AF) shows (Fig. 3) a well-defined molecular ion peak at m/z 288, which is equivalent with (M+ 1), was proposed molecular formula weight of ligand. The molecular ion peaks of the Cu(II), Co(II) Ni(II) and Zn(II) complexes were appeared at m/z of 588.93, 584.31, 584.07 and 590.79 respectively, which are equivalent to the stoichiometric ratio of 1:2 (M:L) type. Further, the observed molecular mass in all the spectra of the prepared complexes are in consistency with their proposed molecular structures.

IR spectra

The ligand AF showed the characteristic band at 3334 cm^{-1} due to stretching vibrations of OH group and the absorption bands of 2920, 1590, 1298, 916 and 1357 cm^{-1} are due to Ar-CH, C=N, C-O, N=N and $-\text{CH}_3$ respectively (15). The OH stretching vibrations have disappeared with complexation in the metal (II) complexes, indicating coordination through the OH group. Additional support by the $\nu(\text{C-O})$ stretching shifted to the lower frequency at $1245\text{--}1253 \text{ cm}^{-1}$. The C=N band also shifted lower frequency by $1512\text{--}1589 \text{ cm}^{-1}$ indicating coordination of azomethine nitrogen (16, 17). The new IR bands witnessed in the range at $570\text{--}522 \text{ cm}^{-1}$ in the spectra of the metal complexes suggest the presence of M-O bonding in their structure, and M-N bands are tentatively assigned to absorptions in the regions $443\text{--}499 \text{ cm}^{-1}$ (18).

Electronic spectra

The electronic spectra of the ligand AF and their metal complexes are set in Table 1. The uncoordinated ligand showed two absorptions bands at 250, 290 nm due the $\pi \rightarrow \pi^*$, $n \rightarrow \pi^*$, for (C=N) groups respectively (19, 20), and for the metal complexes, the bands appeared clearly in the range of 460 to 785 nm due to the $\pi \rightarrow d_x^2 - y^2$ and /or $(\pi \sigma) \rightarrow d_x^2 - y^2$ LMCT transition in all complexes (21-23).

Table 1: UV-Visible Bands of the AF and their metal complexes.

Compound	Solvent	λ_{\max} in (cm^{-1})	Transition	Magnetic moment (BM)	Geometry
Co(II)-AF	DMF	16,150 20,270	${}^4\text{T}_{1g}(\text{F}) \rightarrow \text{A}_{2g}(\text{F})$ ${}^4\text{T}_{1g}(\text{F}) \rightarrow {}^4\text{T}_{1g}(\text{P})$	4.81	Octahedral
Ni(II)-AF	DMF	10,354 17,556 23,712	${}^3\text{A}_{2g}(\text{F}) \rightarrow {}^3\text{T}_{2g}(\text{F})$ ${}^3\text{A}_{2g}(\text{F}) \rightarrow 3\text{T}_{1g}(\text{F})$ ${}^3\text{A}_{2g}(\text{F}) \rightarrow {}^3\text{T}_{1g}(\text{P})$	3.11	Octahedral
Cu(II)-AF	DMF	13,478- 14,331	${}^2\text{E}_g \rightarrow {}^2\text{T}_{2g}$	1.92	Distorted Octahedral
Zn(II)-AF	-	-	-	-	Diamagnetic complex

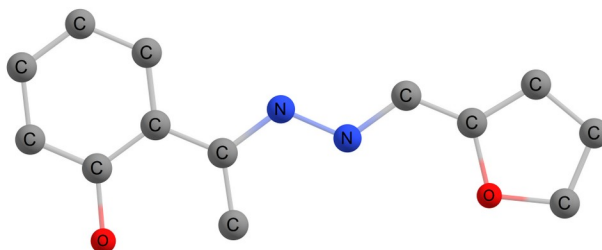
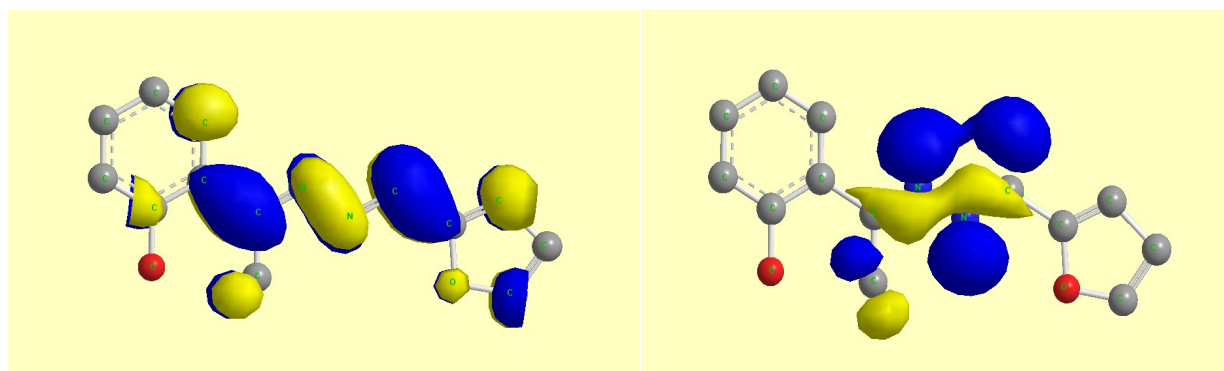
Computational studies

The calculations, optimized geometry of ligand, Co(II), and Ni(II) complexes are carried out with Gaussian 09 software using B3LYP/6-311, +G(d,p)(5D, 7F) basic set in the gas phase (24).

Frontier molecular orbital analysis (FMOs) and Molecular electrostatic potential (MEP)

In FMOs, the HOMO act as donor and LUMO as electron acceptor between the occupied and unoccupied molecular orbitals are shown in Figures 1 and 4. The energy gap ΔE of HOMO-LUMO for the ligand is 0.917 eV, in which HOMO

orbital is delocalized on the nitrogen atom and CH_3 group while the LUMO orbital is occupied on phenyl and thiophene rings (25). The energy gaps ΔE of Co(II) and Ni(II) complexes are 2.311 and 2.778 eV. In HOMO orbitals for Co(II) and Ni(II) complexes are mainly delocalized on corresponding metal ions and thiophene and phenyl rings. Whereas in LUMO, electrons are concentrated on nitrogen, methyl group, and some part of metal ions. These tell us the chemical reactivity and stability of the ligand and their corresponding metal (II) complexes (26).

**Figure 1:** Optimized geometry of schiff base AF.**Figure 2:** $E_{\text{LUMO}}-E_{\text{HOMO}}$ [-4.820 eV and -3.903 eV] molecular Schiff base AF.**Molecular electrostatic potential (MEP)**

MEP relates to the chemical reactivity and electronegativity by the electron and proton of

the molecules (Figure 5). Red color shows the negative electrostatic potential and mostly contains on the nitrogen and methyl moiety,

whereas the blue color represents the positive electrostatic potential contains on the phenyl and OH group of the molecule. The potential shows

the oxygen is nucleophilic center nitrogen acts as an electrophilic center and gives molecular interactions in the compounds (27).

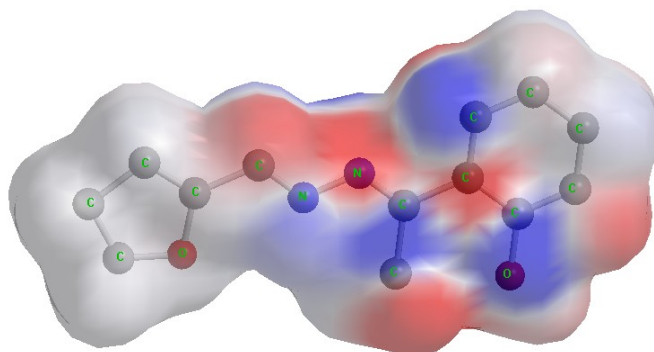


Figure 3: Molecular electrostatic potential (MEP) of ligand

Table 2: Selected parameters of Schiff base AF.

Bond	Bond length (Å)	Angle (°)	Dihedral angle (°)
C(8)-C(10)	1.540	N(9)-C(8)-C(10)	119.999
N(9)-N(11)	1.352	C(8)-N(9)-N(11)	120.000
N(11)-C(17)	1.244	N(9)-N(11)-C(17)	120.000
C(12)-O(13)	1.410	O(13)-C(12)-C(14)	110.999
C(12)-C(14)	1.324	O(13)-C(12)-C(17)	124.499
C(12)-C(17)	1.540	C(14)-C(12)-C(17)	124.500
O(13)-C(15)	1.410	C(12)-O(13)-C(15)	104.000

The energy gaps ΔE of Co(II) and Ni(II) complexes are 2.311 and 2.778 eV. In HOMO orbitals for Co(II) and Ni(II) complexes are mainly delocalized on the corresponding metal ions and thiophene and phenyl rings. Whereas in LUMO, electrons are concentrated on nitrogen, the methyl group, and some part of metal ions.

These tell us the chemical reactivity and stability of the ligand and their corresponding metal Co(II) and Ni(II) complexes and represented in Figures 5 and 6, and for Cu(II) and Zn(II) complexes were represented in supplementary file (28).

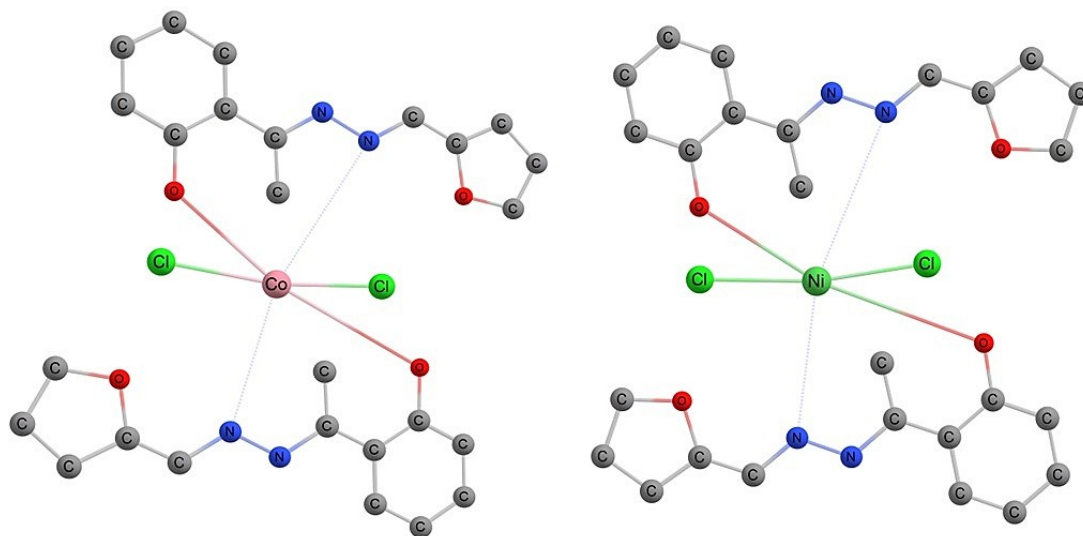


Figure 4: Optimized geometry of Co(II) and Ni(II) complexes.

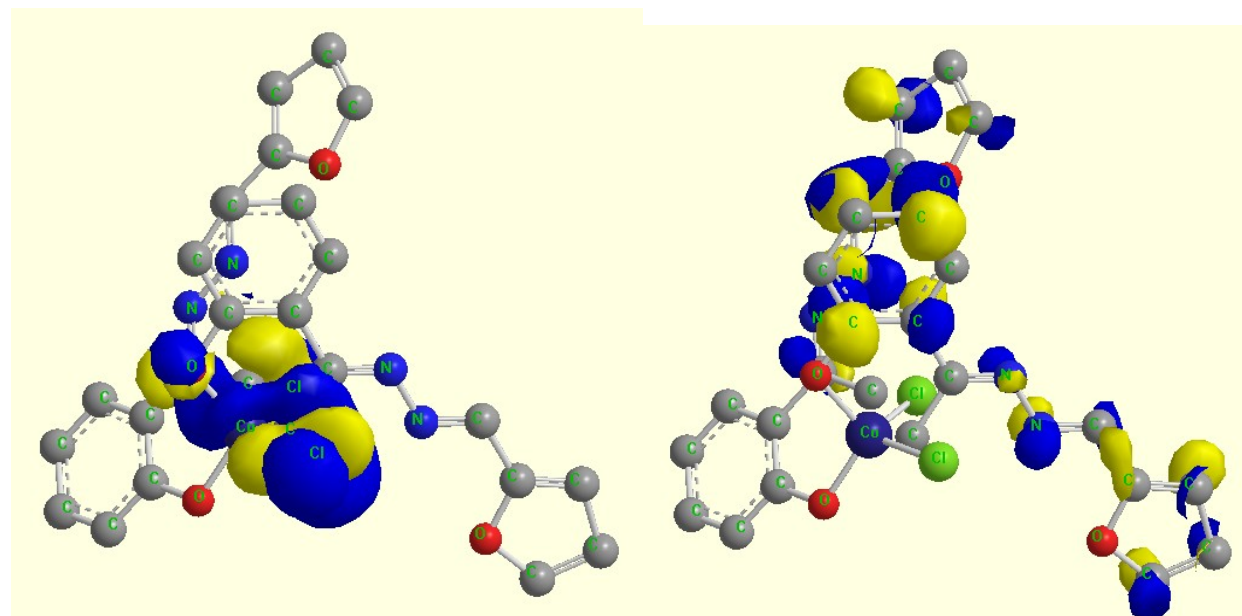


Figure 5: $E_{LUMO}-E_{HOMO}$ [-4.951 eV and -2.631eV] molecular orbitals of Co(II) complexes.

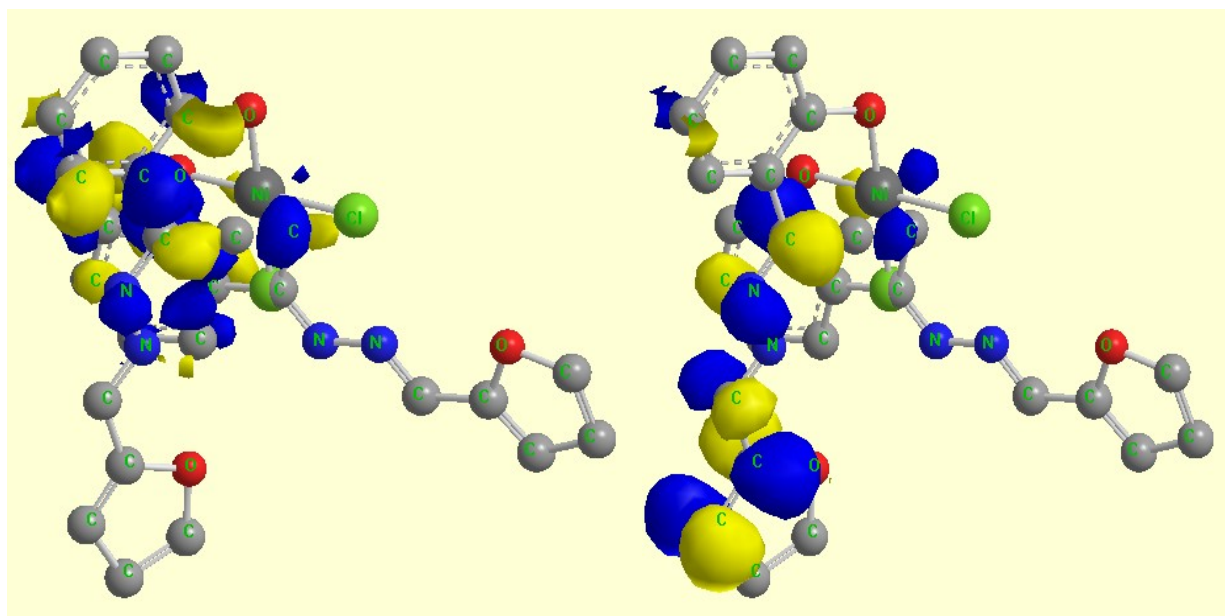


Figure 6: $E_{\text{LUMO}}-E_{\text{HOMO}}$ [-8.811eV and -6.033 eV] molecular orbitals of Ni(II) complexes.

Biological studies

Antibacterial activity

The obtained results of the antibacterial assay of synthesized compounds have given in Table 3. The Ni(II) and Cu(II) complexes showed potent inhibition against all the bacterial strains, in which *B. subtilis* and *K. pneumonia* showed the

highest activity towards these cell lines. On the other hand, Co(II) complex showed promising activity towards gram-negative bacterial strains of *P. aeruginosa* and *B. subtilis*. While the ligand AF and Zn(II) showed the least activity towards all the bacterial strains (29, 30).

Table 3: Antibacterial data of AF and their metal complexes.

Compounds	<i>P.aeruginosa</i>	<i>K. pneumonia</i>	<i>B. subtilis</i>	<i>S. pneumonia</i>	<i>S. aureus</i>
AF	6	8	9	8	7
Co(II)	12	13	15	13	13
Ni(II)	15	18	19	15	12
Cu(II)	15	18	20	17	16
Zn(II)	12	13	15	11	13
Ciprofloxacin	16	19	22	18	17

Molecular docking

In accordance with antibacterial activity, it is significant to carry out *in silico* docking studies. The protein receptor SEC2 (PDB: 1STE) in *Staphylococcus aureus* revealed that the excellent docking interactions with different amino acids and E-total score (31). The Ni(II) complex showed excellent binding affinity towards enzyme receptor 1STE of -287.16

kcal/mol, while Co(II) and Cu(II) complexes also exhibit good binding interactions docking score of -257.11 and -222.99 kcal/mol. But the ligand, AF, showed the least binding interactions of -155.73 kcal/mol. The ligand and the receptor interactions involve binding with different amino acids like His6, Phe20, Thr136, Ser165, Phe167, Glu198, Phe200, Val236, Thr237, Leu250, and Leu253.

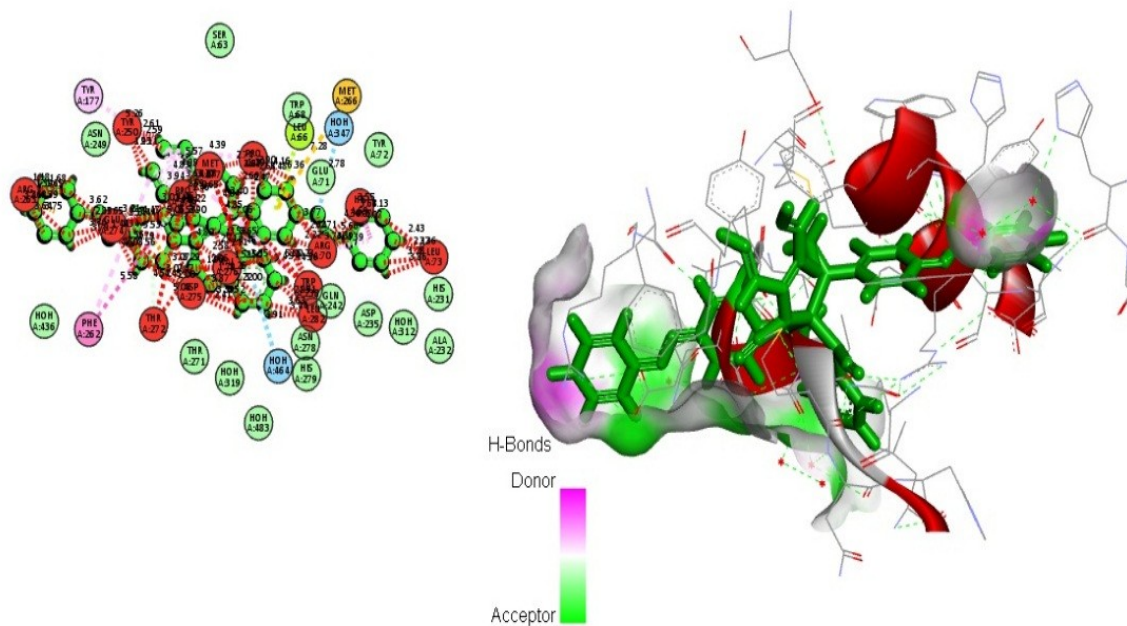


Figure 7: 3D and 2D binding interactions of Co(II) complex with PDB: 1STE.

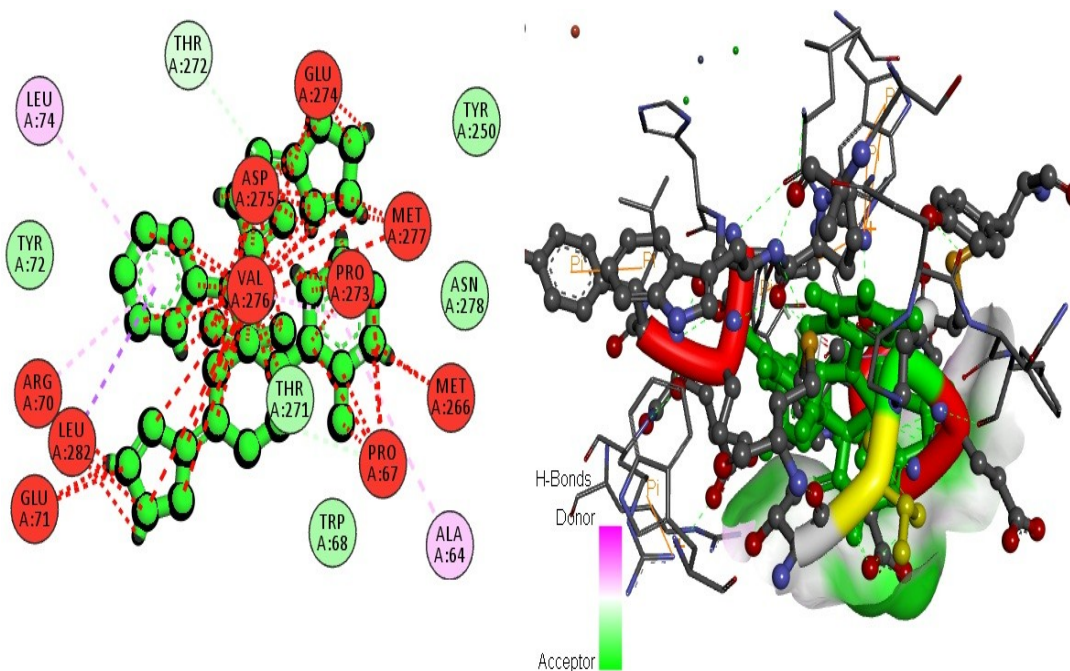


Figure 8: 3D and 2D binding interactions of Ni(II) complex with PDB: 1STE.

CONCLUSION

The synthesized compounds were characterized by spectral and analytical data. The bidentate nature of ligand indicates the bonding through (-OH) and (C=N) groups. The Co(II), Ni(II)

complexes suggest the octahedral geometry and the Cu(II) complex exhibits The theoretical study using DFT/B3LYP supports experimental pieces of evidence of the binding sites of the ligand, geometry and the stability of the complexes. *B. subtilis* and *K. pneumonia* showed the highest

activity towards Ni(II) and Cu(II) complexes, The docking study revealed that Co(II) and Cu(II) complexes showed binding interaction with several amino acid residue of the protein receptor SEC2 (PDB: 1STE) in *Staphylococcus aureus*.

REFERENCES

- Asghar SF, Yasin KA, Habib-ur-Rehman, Aziz S. Synthesis and cyclisation of 1,4-disubstituted semicarbazides. *Natural Product Research*. 2010 Mar 10;24(4):315-25.
- Rajesh-Rane A, Shital-Naphade S, Pavan Kumar, Mahesh Palkar B, Mahamadhanif Shaikh S, Rajshekhar Karpoomath. Synthesis of novel 4-nitropyrrole-based semicarbazide and thiosemicarbazide hybrids with antimicrobial and anti-tubercular activity. *Bioorganic & Medicinal Chemistry Letters*. 2014 Jul 24;10: 3079-3083.
- Pituchaa M, Karczmarzykb Z, Kosikowska U, and Malm A. Synthesis, Experimental and Theoretical Study on the Structure of Some Semicarbazides with Potential Antibacterial Activity. *Zeitschrift für Naturforschung B*. 2011 Apr 66;(5) 971-87.
- Rafat-Mohareb M. and Abeer Mohamed A. Uses of 1-Cyanoacetyl-4-Phenyl-3-Thiosemicarbazide in the Synthesis of Antimicrobial and Antifungal Heterocyclic Compounds. *International Research Journal of Pure & Applied Chemistry*. 2012 Jul 2(2): 2012 144-155.
- Gursoy A, Terzioglu N, Otuk G. Synthesis of some new hydrazide-hydrazones, thiosemicarbazides and thiazolidinones as possible antimicrobials. *European Journal of Medicinal Chemistry*. 1997 Jun 32(9):753-757.
- Narang KK, Singh VP. Synthesis and characterization of cobalt (II), nickel (II), copper (II) and zinc (II) complexes with acetylaceton bis-benzoyl hydrazone and acetylaceton bis isonicotinoyl hydrazone. *Transition Metal Chemistry*. 1993 Dec 10(18): 287-90.
- El-Azab AS, El-Tahir KEH. Synthesis and anticonvulsant evaluation of some new 2,3,8-trisubstituted-4(3H)-quinazoline derivatives. *Bioorganic & Medicinal Chemistry Letters*, 2012 Oct 22(1): 327-33.
- Aly MM, Mohamed YA, El-Bayouki KAM, Basyouni WM, Abbas SY. Synthesis of some new 4(3H)-quinazolinone-2-carboxaldehyde thiosemicarbazones and their metal complexes and a study on their anticonvulsant, analgesic, cytotoxic and antimicrobial activities. *European Journal of Medicinal Chemistry*, 2010 Apr 45(8): 3365- 73.
- Azam F, Alskas IA, Khokra SL, Prakash O. Synthesis of some novel N 4 - (naphtha[1,2-d]thiazol-2-yl) semicarbazides as potential anticonvulsants. *European Journal of Medicinal Chemistry*. 2009 Nov 44(1): 203-11.
- Shashikumar ND, Krishnamurthy G, Bhojya-Naik HS, Lokesh MR, Jithendra-kumara KS. Synthesis of new biphenyl-substituted quinoline derivatives, preliminary screening and docking studies. *Journal of chemical sciences*. 2014 Jan 126(1): 205-12.
- Manjuraj T, Krishnamurthy G, Yadav D. Bodke, BhojyaNaik H.S, Metal complexes of quinolin-8-yl [(5-methoxy-1H-benzimidazol-2-yl)sulfanyl]acetate: Spectral, XRD, thermal, cytotoxic, molecular docking and biological evaluation. *Journal of Molecular Structure, Volume 1148, (15): 2017; 231-7.*
- Harinath Y, Subbarao D, Suresh C, Sessaiah K. Synthesis, characterization and studies on antioxidant and molecular docking of metal complexes of 1-(benzo[d]thiazol-2-yl)thiourea. *Journal of Chemical Sciences*. 2016 Jan 128(1): 43-51.
- Hall Parsonage D, Poole LB, Karplus PA. Structural evidence that peroxiredoxin catalytic power is based on transition-state stabilization. *Journal of Molecular Biology*. 2010 10; 402(1):194-209.
- Abdel Nasser MA, Alaghaz-Badr A, El-Sayed A, Ahmed, El-Henawy, Reda, Ammar AA. Synthesis, spectroscopic characterization, potentiometric studies, cytotoxic studies and molecular docking studies of DNA binding of transition metal complexes with 1,1-diaminopropane-Schiff base. *Journal of Molecular Structure*, 2013 Dec 1035(12): 83-93.
- Mohammed Shafeeulla R, Ganganaik Krishnamurthy, Halehatti S. Bhojynaik, Manjuraj T. Synthesis, Cytotoxicity, and Molecular Docking Study of Complexes Containing Thiazole Moiety. *Journal of the turkish chemical society. section A: chemistry*. 2017 Aug 4(3): 787-810.
- Nakamoto K, *Infrared and Raman Spectra of Inorganic and Coordination Compounds*. In:Chalmers JM, Griffiths PR, editors. *Handbook of vibrational spectroscopy*, Chichester, UK: John Wiley & Sons, Ltd; 2006.
- Sangeetha Gowda KR, Bhojya-Naik HS, Vinay-Kumar B, Sudhamani CN, Sudeep HV, Ravikumar-Naik TR, Krishnamurthy G. Synthesis, antimicrobial, DNA-binding and photonuclease studies of Cobalt(III) and Nickel(II) Schiff base complexes. *Spectrochimica Acta Part A: Molecular and Biomolecular Spectroscopy*. 2013 Jun 105(10): 229-237.
- Emelda AR, Jayachandramani N, Ravichandran S. Synthesis, Characterization and Antimicrobial Study of a New Mannich Base, N-(1-Piperidinobenzyl)benzamide and its Transition Metal(II) Complexes. *Asian Journal of Chemistry*. 2008 Feb 2(20): 2485-2490.

19. Ashraf A, Siddiqui WA, Akbar J, Mustafa G, Krautscheid H, Ullah N. Metal complexes of benzimidazole derived sulfonamide: Synthesis, molecular structures and antimicrobial activity. *Inorganica Chimica Acta*. 2016 Mar (443): 179–85.
20. Lever A.B.P. *Inorganic electronic spectroscopy*. 2nd ed. Amsterdam ; New York: Elsevier; 1984 863.
21. El-Gammal OA, Mostafa MM. Synthesis, characterization, molecular modeling and antioxidant activity of Girard's T thiosemicarbazide and its complexes with some transition metal ions *Spectrochimica Acta Part A: Molecular and Biomolecular Spectroscopy*, 2014 Mar(127): 530–42.
22. Rahaman F, Mruthyunjayaswamy BHM. Synthesis, spectral characterization and biological activity studies of transition metal complexes of Schiff base ligand containing indole moiety. *Complex Metals*. (31): (2014); 88–95.
23. Bal M, Ceyhan G, Avar B, Köse M, Kayraldiz A, Kurtoğlu M. Synthesis and X-ray powder diffraction, electrochemical, and genotoxic properties of a new azo-Schiff base and its metal complexes. *Turkish journal of chemistry*. 2014 Dec 12(38): 22-241.
24. Joseph J, Mehta HB. Synthesis, characterization, and thermal analysis of transition metal complexes of polydentate ONO donor Schiff base ligand. *Russian Journal of Coordination Chemistry*. 2007 Mar 12(33): 124-129.
25. Donia A. M, Al-Ansi T. Y and Othman M. Q., *Journal of Thermal Analysis*. (50) 1997 857.
26. Venugopala Reddy KR, Keshavayya J, Seetharamappa J. Synthesis, spectral, magnetic and thermal studies on symmetrically substituted metal (II) 1,3,8,10,15,17,22,24-octachloro phthalocyanines, *Dyes Pigments*, 2003 Nov (59):237-244.
27. Yapati H, Devineni S.R, Chirumamilla S, Kalluru S. Synthesis, characterization and studies on antioxidant and molecular docking of metal complexes of 1-(benzo[d]thiazol-2-yl)thiourea. *Journal of Chemical Sciences*. 2016 Jan (128): 43–51.
28. Bhimagouda-Patil S, Krishnamurthy G, Bhojya-Naik HS, Prashant R. Latthe, Manjunath-Ghate. Synthesis, characterization and antimicrobial studies of 2-(4-methoxy-phenyl)-5-methyl-4-(2-arylsulfanyl-ethyl)-2,4-dihydro-[1,2,4] triazolo-3-ones and their corresponding sulfones. *European Journal of Medicinal Chemistry* 2014 12(45): 3329-3334.
29. Jayamani A, Sengottuvelan N, Chakkaravarthi G, Synthesis, structural, electrochemical, DNA interaction, antimicrobial and molecular docking studies on dimeric copper(II) complexes involving some potential bidentate ligands. *Polyhedron* 2014 Feb 81(12): 764–76.
30. Manjuraj T, Krishnamurthy G, Yadav D. Bodke, BhojyaNaik H.S, Synthesis, XRD, thermal, spectroscopic studies and biological evaluation of Co(II), Ni(II) Cu(II) metal complexes derived from 2-benzimidazole. *Journal of Molecular Structure*, Volume 1171; 2018: 481-487.
31. Yuvaraj T. C. M, Parameshwara Naik P, Venkatesh T.V, Krishnamurthy G, Manjuraj T, Synthesis, spectral studies, XRD, thermal analysis and biological screening of metal complexes derived from (N-(3-methoxyphenyl)-2-[(2E)-3-phenylprop-2-enoyl]hydrazinecarboxamide. *Journal of the Turkish chemical society. Section A: chemistry*. 2018; 5(3): 845-856.

Spectral, DFT studies, molecular docking and antibacterial activity of Schiff base derived from furan-2-carbaldehyde and their metal (II) complexes

Manjuraj T.^{1*}  , Yuvaraj TCM¹  , Jayanna N.D²  , Shreedhara S H³  ,
Sarvajith M S⁴  

Supplementary Figures

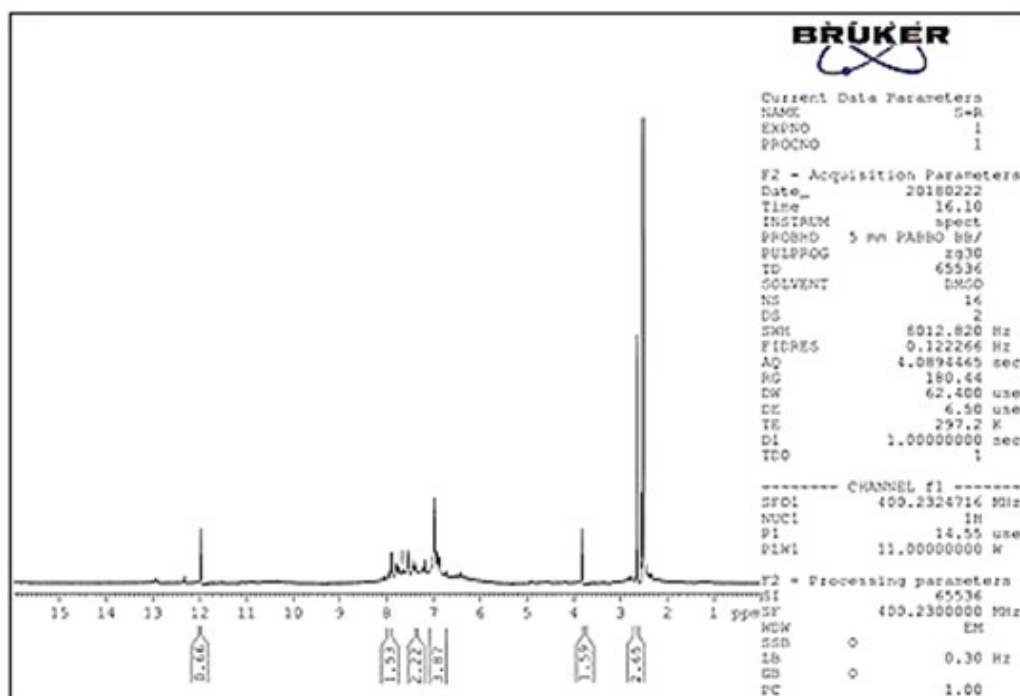


Figure S1: ¹H NMR spectrum of AF.

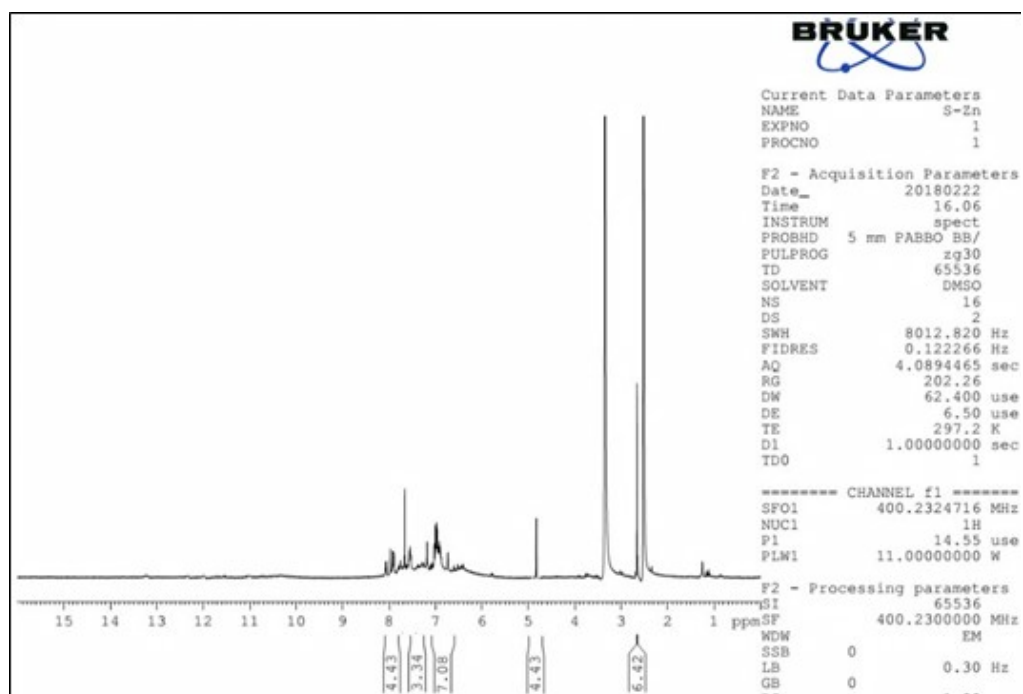


Figure S2: ¹H NMR of Zn(II) complex.

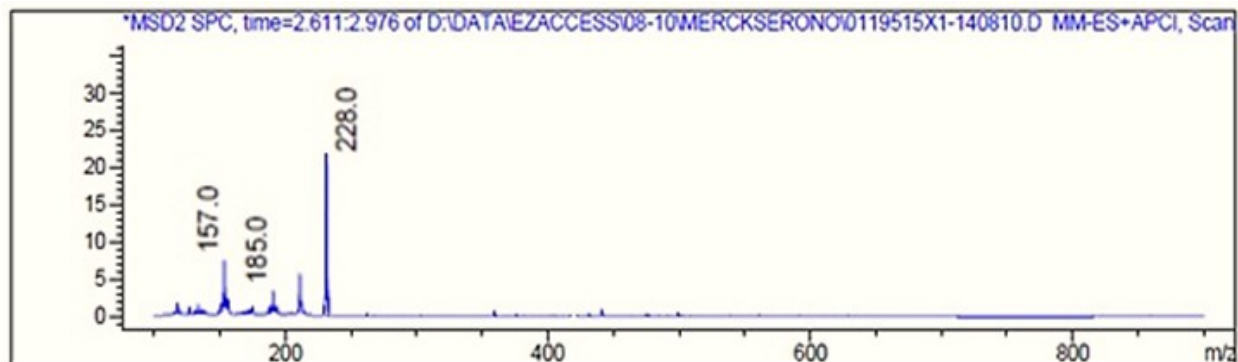


Figure S3: LCMS spectrum of Ligand AF.

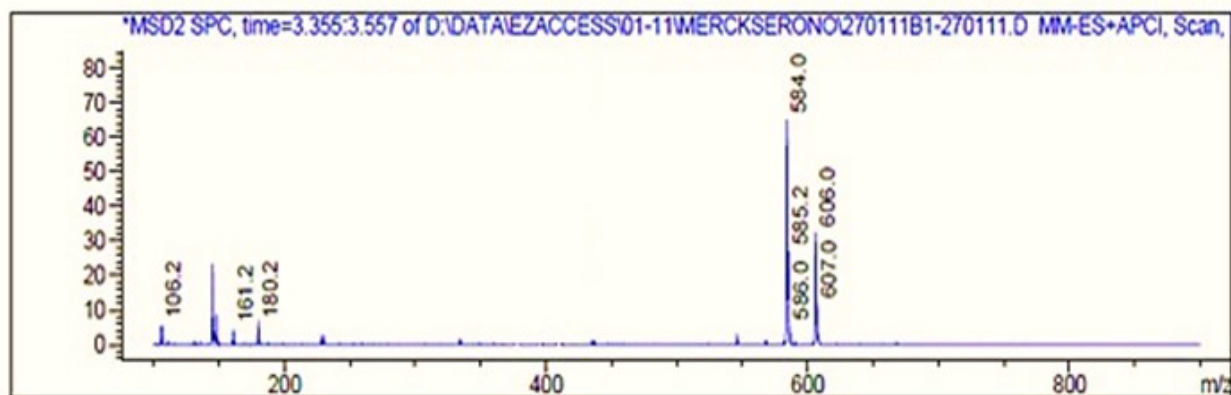


Figure S4: LCMS spectrum of Ni(II) complex .

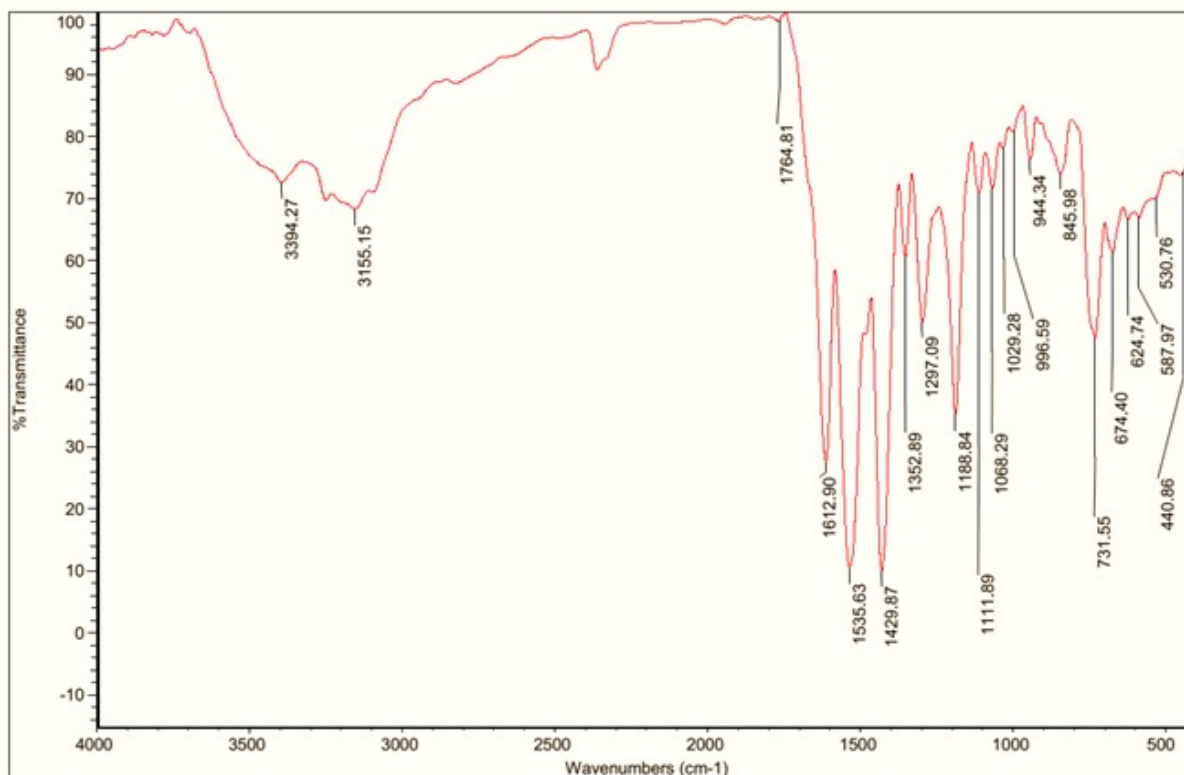


Figure S5: FT-IR Spectrum of Ligand AF .

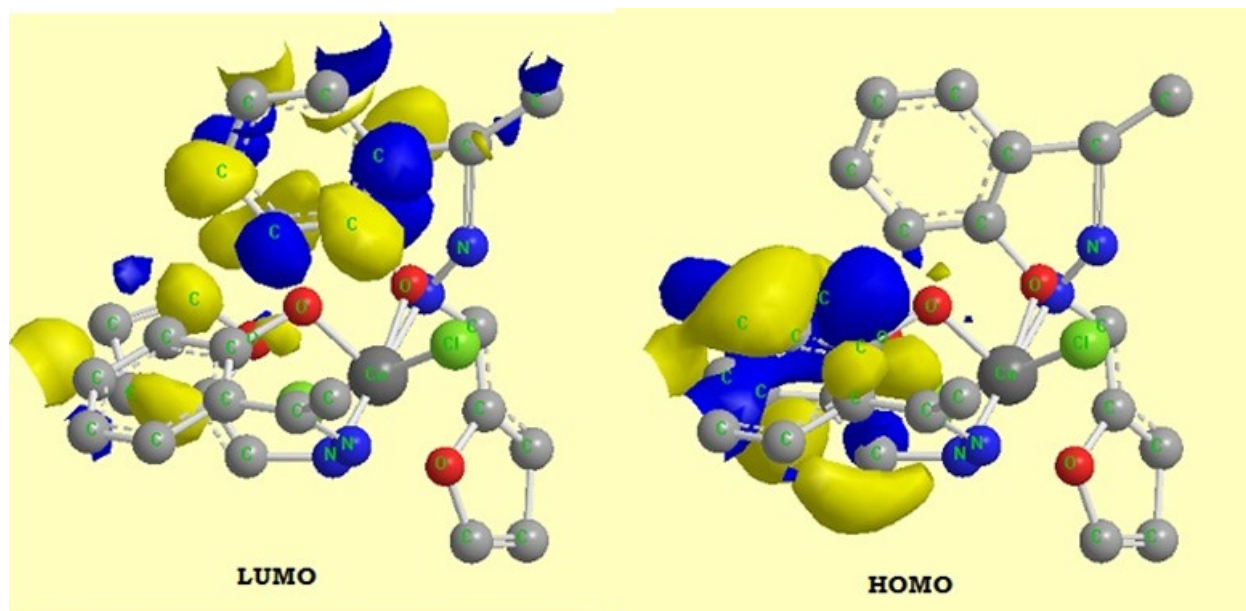


Figure S6: $E_{LUMO}-E_{HOMO}$ [-5.114 eV and -2.231eV] molecular orbitals of Cu(II) complexes.

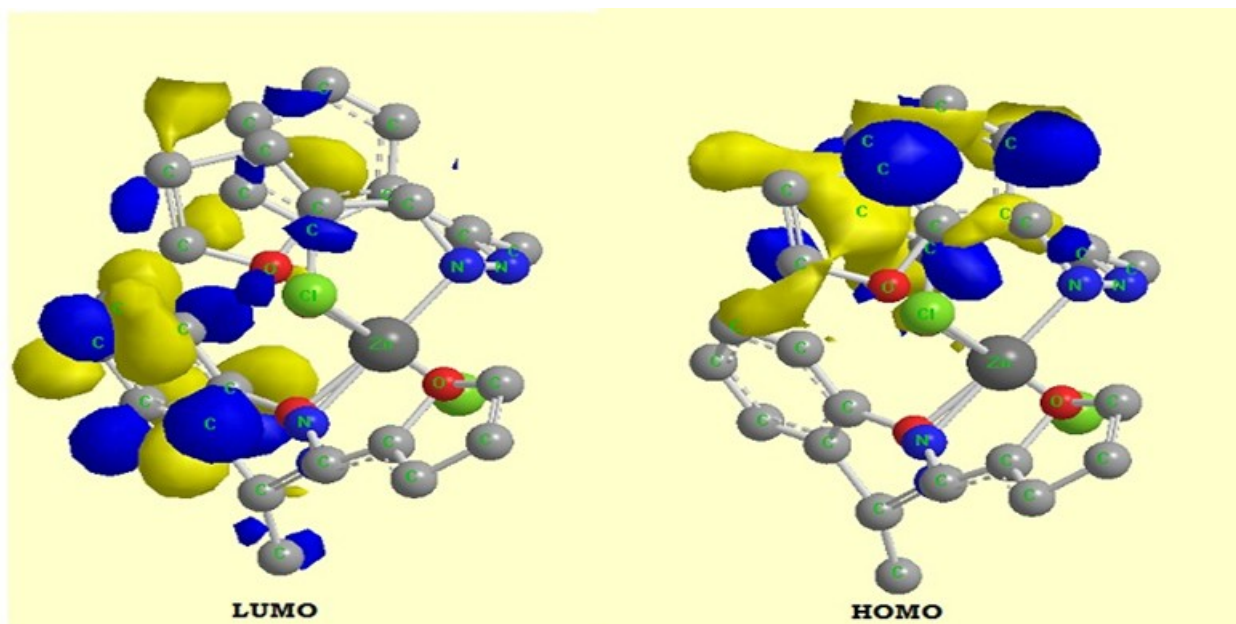


Figure S7: $E_{\text{LUMO}}-E_{\text{HOMO}}$ [-6.221 eV and -4.241eV] molecular orbitals of Zn(II) complexes.



Dyeing Polyester, Cotton and Wool with Some Schiff Bases Derived from 4-chloroaminophenol and Various Benzaldehydes

Demet GÜRBÜZ^{1*}  

¹University of Istanbul-Cerrahpasa, Faculty of Engineering, Department of Chemistry, 34320, Istanbul, Turkey.

Abstract: Dyeability of ten Schiff bases obtained from 4-chloroaminophenol and various benzaldehydes including methyl, chloro, bromo, nitro, methoxy, and hydroxy groups were investigated on polyester, cotton and wool fibers. The dry/wet rubbing and washing fastness of the compounds were measured. It is observed that the rubbing and washing fastness values are varying at the 4 – 5 range (1: weak, 5: excellent). The lightness (**L**), red-greenness (**a**), and yellow-blueness (**b**) properties of the compounds were also investigated. It was observed that the dyeing properties of the compounds change depending on the substituent positions, and the substituent effect is observed on wool mostly. Especially, 3- and 5-methyl derivatives (**VIII** and **IX**) exhibit similar behavior toward polyester and cotton while they behave differently on wool in point of the **L**, **a**, and **b** values. On the other hand, it can be claimed that chlorine substituent increases the **L** value on wool.

Keywords: Schiff bases, dyeability, polyester, cotton, wool.

Submitted: April 04, 2020. **Accepted:** May 04, 2020. (This will be filled in by the journal staff).

Cite this: Gürbüz D. Dyeing Polyester, Cotton and Wool with Some Schiff Bases Derived from 4-chloroaminophenol and Various Benzaldehydes. JOTCSA. 2020; 7(2): 463-70.

DOI: <https://doi.org/10.18596/jotcsa.714635>.

***Corresponding author.** E-mail: demet@istanbul.edu.tr.

INTRODUCTION

Schiff bases have considerable interest due to a large number of biological activities, including anticancer (1-3), antibacterial (4-6), antiviral (7-9), antifungal (10-12), antimalarial (13), urease inhibition (14-15), antioxidant agents (16-17) and DNA binding ability (18-19). The presence of C=N functional group in Schiff bases is responsible for the biological activities (20). Intramolecular hydrogen bonding between the phenolic group and the azomethine nitrogen atoms of Schiff bases derived from aromatic o-hydroxy aldehydes impacts the properties of various molecular systems and plays an essential role in many biochemical reactions (21).

Besides, the synthesis of Schiff bases has been increasing attention in synthetic organic chemistry, because of their potential applications in biological

modeling, catalysis, design of molecular magnets and materials chemistry (22-24) and also widely used as chelating agents (25-27), as corrosion inhibitors (28-29), as an herbicide (30), as textile dyes (31), as stabilizers in polymer chemistry (32).

Polyester is a synthetic fiber which is the most widely used in the textile industry due to their advantageous properties, including high tenacity, good resistance to chemicals, and deformation. Polyester fiber is preferred because of its hydrophobic nature and has a highly compact structure that permits efficient dyeing at high temperatures with disperse dyes.

The present study reports the investigation of the dyeability of some Schiff bases synthesized from 4-chloroaminophenol and various benzaldehydes. Polyester, cotton, and wool fabrics dyeing with conventional aqueous dyeing (batch dyeing) methods are studied in this context.

EXPERIMENTAL SECTION

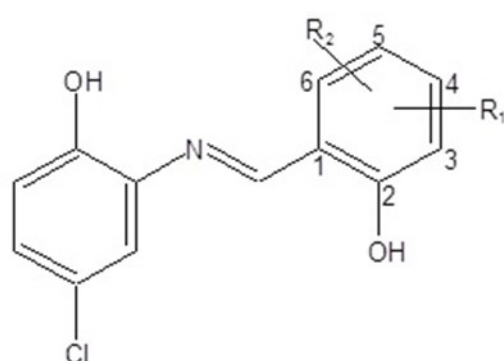
General

All reagents were commercially available and used as received without further purification. Elemental analysis data were recorded on a Thermo Finnigan Flash EA 1112 analyzer. The FTIR spectra were obtained with a Bruker Optics Vertex 70 spectrometer (ATR). UV-Visible spectra were measured using a Perkin Elmer Lambda 25 UV/Visible Spectrophotometer. The Electron Spray Ionization-Mass Spectroscopy (ESI-MS) analyses were recorded on a Thermo Finnigan LCQ Advantage MAX LC/MS/MS. Dyeing was performed

at a TERMAL Dyeing Lab. Machine. The used polyester (110 g/m²), wool (120 g/m²), and cotton (110 g/m²) fabrics for dyeing procedure are 100% woven. Decacid Sab was used as a dispersing agent.

General Procedure for the Preparation of Schiff Bases

The Schiff bases were synthesized by condensation of 4-chloro-2-aminophenol (1.44 g; 10 mmol) with an appropriate aldehyde (e.g., 2,4-dihydroxybenzaldehyde for **V**, 1.38 g; 10 mmol) in 20 mL of EtOH. This mixture was stirring under reflux for 3h. After the heading, the mixture was allowed to cool to room temperature. The solid product was separated by filtration and then crystallized from CH₃OH (33-34).



Compound	R ₁	R ₂
I	H	5-Br
II	H	5-Cl
III	3-Br	5-Cl
IV	3-Cl	5-Cl
V	4-OH	H
VI	3-OCH ₃	H
VII	4-OCH ₃	H
VIII	3-CH ₃	H
IX	H	5-CH ₃
X	H	5-NO ₂

Scheme 1. The chemical structures of Schiff bases **I** – **X** used in this study.

I: Yellow-orange solid. Yield: 90%, m.p.: 201 °C. Elemental analysis: Calculated for C₁₃H₉BrClNO₂: C, 47.82; H, 3.28; N, 4.56; Found: C, 47.81; H, 2.78; N, 4.29. FT-IR (ATR, v/cm⁻¹): 3071 m,br, 2925 m,br, 2854 m,br, 2587 m, 1628 m, 1607 w, 1504 s, 1288 m, 1231 m, 1177 m, 1123 m, 816 m, 656 m, 525 w. UV (10⁻⁴ M, in methanol): 456 sh, 364 m,br, 262 m, 214 s. MS (ESI), m/z (%) (MA: 326.57 g/mol): 324.6 (38.0, [M-2]⁺), 325.4, 326.7, 327.5, 328.6, 329.7.

II: Orange solid. Yield: 96%, m.p.: 203 °C. Elemental analysis: Calculated for C₁₃H₉Cl₂NO₂: C, 54.17; H, 3.41; N, 5.08; Found: C, 55.34; H, 3.22; N, 4.96. FT-IR (ATR, v/cm⁻¹): 3072 m,br, 2926 m,br, 2542 m,br, 1628 s, 1452 m, 1208 m, 1154 m, 1093 m, 1018 m, 910 m, 831 s, 698 w. UV (10⁻⁴ M, in methanol): 452 w,br, 364 m,br, 269 m, 234 sh, 215 s. MS (ESI), m/z (%) (MA: 282.12 g/mol): 280.6 (100, [M-2]⁺), 281.7 (11.7, [M-1]⁺), 282.5 (65.6, [M]⁺), 283.6 (8.1, [M+1]⁺), 284.5 (9.6, [M+2]⁺).

III: Orange solid. Yield: 93%, m.p.: 271 °C. Elemental analysis: Calculated for C₁₃H₈BrCl₂NO₂: C, 43.40; H, 2.19; N, 3.70; Found: C, 43.25; H, 2.32; N, 3.88. FT-IR (ATR, v/cm⁻¹): 3214 m,br, 3059 m,br, 2925 m,br, 1628 s, 1499 s, 1438 m, 1305 m,

1226 s, 1145 m, 1021 m, 915 m, 845 m, 739 m, 664 m. UV (10⁻⁴ M, in methanol): 462 w,br, 440 sh, 367 m,br, 269 m, 211 s. MS (ESI), m/z (%) (MA: 361.02 g/mol): 358.8 (41.4, [M-2]⁺), 359.9 (6.0, [M-1]⁺), 360.8 (100, [M]⁺), 361.7 (15.9, [M+1]⁺), 362.5 (49.7, [M+1]⁺), 363.2 (43.0, [M+2]⁺), 364.1 (9.8; [M+3]⁺), 364.8 (11.7, [M+4]⁺), 365.7 (5.0, [M+5]⁺).

IV: Orange solid. Yield: 95%, m.p.: 279 °C. Elemental analysis: Calculated for C₁₃H₈Cl₃NO₂: C, 49.18; H, 2.74; N, 4.56; Found: C, 49.32; H, 2.55; N, 4.42. FT-IR (ATR, v/cm⁻¹): 3164 m,br, 3063 m,br, 2921 m, 1628 s, 1508 s, 1438 m, 1217 s, 1149 m, 1034 m, 854 m, 761 m, 660 w. UV (10⁻⁴ M, in methanol): 463 m,br, 437 sh, 365 m,br, 269 m, 213 s. MS (ESI), m/z (%) (MA: 316.57 g/mol): 314.7 (87.2, M-2), 316.6 (100, [M]⁺), 317.7 (14.6, [M+1]⁺), 318.6 (31.5, [M+2]⁺), 319.5 (5.4, M+3), 320.5 (4.4, M+4).

V: Dark yellow solid. Yield: 73%, m.p.: 221 °C. Elemental analysis: Calculated for C₁₃H₁₀ClNO₂: C, 58.89; H, 3.84; N, 5.50; Found: C, 59.22; H, 3.82; N, 5.31. FT-IR (ATR, v/cm⁻¹): 3178 m,br ●(OH), 3072 m,br, 2926 m, 2553 m,br, 1637 s, 1592 m, 1269 s, 1228 s, 1131 m, 989 m, 915 m, 849 m, 790 m, 662 w. UV (10⁻⁴ M, in methanol): 422 m,br, 352

m,br, 269 m, 228 sh, 212 s. MS (ESI), m/z (%) (MA: 263.67 g/mol): 264.5 (38.0, [M+1]⁺), 265.8 (17.2, [M+2]⁺), 509.3 (100, [2M-OH]), 511.3 (71.9), 525.5 (56.7), 526.5 (20.8), 527.5 (22.0).

VI: Bright yellow solid. Yield: 85%, m.p.: 219 °C. Elemental analysis: Calculated for C₁₄H₁₂ClNO₃ : C, 60.82; H, 4.46; N, 5.01; Found : C, 60.55; H, 4.36; N, 5.04. FT-IR (ATR, v/cm⁻¹): 3071 m,br, 2970 m,br, 2909 m,br, 1649 s, 1621 s, 1592 m, 1525 m, 1504 s, 1479 s, 1429 s, 1278 m, 1226 s, 903 m, 831 m, 800 m, 772 m, 656 m. UV (10⁻⁴ M, in methanol): 446 sh, 426 m,br, 351 s,br, 304 m,br, 285 sh, 242 s,br, 215 sh. MS (ESI), m/z (%) (MA: 277.50 g/mol): 276.67 (77.6, [M-1]⁺), 278.69 (100, [M+1]⁺), 280.16 (30.4, [M+3]⁺).

VII: Red solid. Yield: 50%, m.p.: 145 °C. Elemental analysis: Calculated for C₁₄H₁₂ClNO₃ : C, 60.75; H, 4.48; N, 5.00; Found : C, 60.55; H, 4.36; N, 5.04. FT-IR (ATR, v/cm⁻¹): 3054 m,br, 3002 m,br, 2930 m,br, 1623 s, 1594 m, 1504 s, 1443 m, 1251 m, 1140 m, 906 m, 827 m, 799 m, 646 m. UV (10⁻⁴ M, in methanol): 482 w,br, 373 m,br, 354 sh, 273 s, 252 sh, 236 s,br, 219 sh. MS (ESI), m/z (%) (MA: 277.50 g/mol): 276.72 (100, [M-1]⁺), 278.71 (71.3, [M+1]⁺), 280.37 (24.4, [M+3]⁺).

VIII: Light orange solid. Yield: 97%, m.p.: 220 °C. Elemental analysis: Calculated for C₁₄H₁₂ClNO₂ : C, 64.20; H, 4.83; N, 5.42; Found : C, 64.25; H, 4.62; N, 5.35. FT-IR (ATR, v/cm⁻¹): 3071 m,br, 2920 m, 2673 m,br, 2562 m,br, 1624 s, 1595 sh, 1441 m, 1232 s, 1162 m, 1036 m, 817 m, 762 m, 662 w. UV (nm, 10⁻⁴ M, in methanol): 452 w,br, 352 m,br, 269 m,br, 215 s. MS (ESI), m/z (%) (MA: 261.70 g/mol): 262.6 (100, [M+1]⁺), 263.5 (30.7, [M+2]⁺).

IX: Orange solid. Yield: 85%, m.p.: 173 °C. Elemental analysis: Calculated for C₁₄H₁₂ClNO₂ : C, 64.34; H, 4.51; N, 5.11; Found : C, 64.25; H, 4.62; N, 5.35. FT-IR (ATR, v/cm⁻¹): 3428 m, 2925 m, 1631 s, 1585 m, 1508 s, 1438 m, 1294 m, 1240 m, 1162 m, 922 m, 822 m, 656 w. UV (nm, 10⁻⁴ M, in methanol): 451 w,br, 359 m,br, 269 m, 237 sh, 214 s. MS (ESI), m/z (%) (MA: 261.70 g/mol): 262.5 (31.6, [M+1]⁺), 261.6 (10.5, [M]⁺), 260.6 (100, [M-1]⁺).

X: Yellowish orange solid. Yield: 74%, m.p.: 268 °C. Elemental analysis: Calculated for C₁₃H₉ClN₂O₄ : C, 53.44; H, 3.26; N, 9.74; Found : C, 53.35; H, 3.10; N, 9.57. FT-IR (ATR, v/cm⁻¹): 3066 m, 2925 m,br, 2774 m,br, 2557 m,br, 1649 s, 1623 s, 1446 m, 1391 m, 1296 s, 1238 m, 1192 m, 1151 m, 1100 m, 1038 m, 901 m, 837 m, 755 m, 639 m. UV (nm, 10⁻⁴ M, in methanol): 461 sh, 426 m,br, 350 m,br, 269 m, 262 m, 211 s. MS (ESI), m/z (%) (MA: 292.67 g/mol): 290.3 (100, [M-2]⁺), 292.4 (65.7, [M]⁺), 293.5 (29.3, [M+1]⁺) 294.5 (28.6, [M+2]⁺).

Dyeing Polyester Fabrics

The polyester samples were dyed with an HT sample dyeing machine. Dyebath was prepared with dye, which was synthesized, nonionic dispersant (0.5 g/L), and CH₃COOH (pH~5) with a liquor ratio of 1:20. The temperature was raised to 130 °C at a rate of 3 °C/min. Within 30 min. and the dyeing continued for 60 min. After completion of dyeing, reduction cleaning of the samples were rinsed with warm water and were subjected to neutralization with a solution containing Na₂S₂O₄ and NaOH (2 g/L each) at 70 °C for 10 min. To remove the superficial dye, the polyester was rinsed with cold water at 50 °C for 10 min. and washed with water and air-dried.

Dyeing Cotton Fabrics

The cotton samples were dyed with an HT sample dyeing machine. Dyebath was prepared with dye, which was synthesized, nonionic dispersant (0.5 g/L), and Na₂CO₃ (pH~10) with a liquor ratio of 1:20. The temperature was raised to 90 °C at a rate of 6 °C/min within 30 min, and the dyeing continued for 90 min. After completion of dyeing, the samples were rinsed two times for 10 min. with water at 60 °C and air-dried.

Dyeing Wool Fabrics

The wool samples were dyed with an HT sample dyeing machine. Dyebath was prepared with dye, which was synthesized, nonionic dispersant (0.5 g/L), and CH₃COOH (pH~5) with a liquor ratio of 1:20. The temperature was raised to 80 °C at a rate of 8 °C/min and then held at this temperature for 90 min. and the dyeing continued for 60 min. After completion of dyeing, the samples were removed, thoroughly rinsed with water for 10 min. at 40 °C and air-dried.

Color Fastness Tests

The reduction cleaning of the dyed samples was measured using the ISO 105 C06 standard method, and ECE was used as washing detergent for this test. The Greyscale was used for evaluating the change in shade and staining of adjacent multifiber test fabrics. Color fastness to rubbing test was evaluated according to the ISO105-X122002 standard method. The color of the dyed fabrics was measured using ISO7724/1 standard method

RESULTS AND DISCUSSIONS

The Schiff bases used in this study were reported previously (33- 34). The physicochemical and spectroscopic data of the Schiff bases are given at Experimental Section.

Tables 1, 3, and 5 show the washing and rubbing fastness test results of dyes on polyester, cotton, and wool fabrics. Washing and rubbing fastness values of the compounds for polyester, cotton, and wool are detected as 4 or 5, which considered that these values are specified at the 1 - 5 range (1:

weak, 4: good, 5: excellent). It can be said that the compounds give good fastness properties for washing and rubbing levels as well.

The lightness (**L**), red-greenness (**a**), and yellow-blueness (**b**) properties of the compounds, containing different substituents on polyester, wool, and cotton fibers are shown in Tables 2, 4, and 6.

The following points are found by examining the lightness (**L**), red-greenness (**a**) and yellow-blueness (**b**) values of the compounds for polyester fabric (Table 2): The **L** value of the compound **VI** (3-methoxy derivative) is highest, that of **III** (3-Br,5-Cl derivative) is lowest although all **L** values are close to each other (between 68.11 and 53.61). Similarly, all the **a** and **b** values are close to each other, also. The highest **a** and **b** values are belonging to 3-Me (**VIII**) and 5-Br (**I**) derivatives, 14.52 and 43.34; the lowest ones are 10.27 (**VII**: 4-methoxy) and 30.01 (**III**: 3-Br,5-Cl), respectively.

It is seen that the **L** and **b** values of 5-Br derivative (**I**) are higher than those of 5-Cl derivative (**II**),

whereas the **a** value is lower (Table 2). The bromo substituent at the ortho position (**III**: 3-Br,5-Cl) decreases the **L**, **a**, and **b** values comparing to the chloro derivative (**IV**: 3-Cl,5-Cl) on polyester fabric. It is observed that the **L** value of the 5-Br derivative (**I**) is highest among the compounds having chloro and bromo substituents, namely **I**, **II**, **III**, and **IV**. The **L** and **a** values of the 4-methoxy derivative (meta position, **VII**) are lower (66.73 and 10.27, respectively) than those of 3-methoxy derivative (**VI**; L: 68.11, a: 13.41) whereas the **b** value is higher (42.43) than that of **VI** (36.39) towards to polyester fabric (Table 2). The **L** value of the 3-Me derivative (**VIII**: methyl group at ortho position) is lower than that of 5-Me derivative (**IX**: methyl group at the para position) whereas the values of **a** and **b** are higher than that of 3-Me derivative.

It is seen that the highest **L** value is belonging to 5-Br derivative (**I**) for cotton fabrics (Table 4), whereas the nitro derivative (**X**) shows the lowest **L** value. The highest **a** and **b** values are shown by the compound **VIII** (3-Me derivative); the lowest **a** and **b** values are exhibited by **I** and **II** (5-Br and 5-Cl derivatives), respectively.

Table 1. Color fastness of the compounds on polyester fabric.⁽¹⁾

Compound	Washing fastness							Rubbing fastness	
	Color Change	Staining ⁽²⁾						Dry	Wet
		AC	CO	PA	PES	PAN	WO		
I	4-5	4-5	4	4-5	4-5	4-5	4-5	4-5	4
II	4	4-5	4	4	5	5	4	4-5	5
III	4	5	4	4	5	5	4	4-5	5
IV	4	4-5	4	4	5	5	4	4-5	5
V	4	4-5	4	4-5	5	4-5	4	5	4
VI	5	5	4	5	5	5	5	5	4-5
VII	5	5	4	4-5	5	5	4-5	5	5
VIII	4	4	4	4	4	4	4	4	4
IX	4	4	4	4	4	4	4	4	4
X	4-5	5	4	4	5	5	4	4-5	5

¹ The changes are graded with marks 1 - 5 (1: weak, 5: excellent)

² AC: Acetate cellulose, CO: Cotton, PA: Polyamide, PES: Polyester, PAN: Polyacrylonitrile, WO:wool

Table 2. Lightness (L), red-greenness (a) and yellow-blueness (b) values for polyester (D65).⁽¹⁾

Compound	L ⁽²⁾	a ⁽²⁾	b ⁽²⁾	Compound	L ⁽²⁾	a ⁽²⁾	b ⁽²⁾
I	64.01	10.59	43.34	VI	68.11	13.41	36.39
II	55.52	14.00	37.55	VII	66.73	10.27	42.43
III	53.61	11.74	30.01	VIII	64.64	14.52	39.08
IV	60.84	12.18	36.51	IX	63.78	12.63	33.42
V	56.32	14.37	43.04	X	59.75	12.68	37.54

¹: D65: daylight lamp.

² **L**: Lightness (low or negative value: darkness, high or positive value: lightness); **a**: Red-greenness (low or negative value: green, high or positive value: red); **b**: Yellow-blueness (low or negative value: blue, high or positive value: yellow).

Table 3. Color fastness of the compounds on cotton fabric.⁽¹⁾

Compound	Washing fastness							Rubbing fastness	
	Color Change	Staining ⁽²⁾						Dry	Wet
		AC	CO	PA	PES	PAN	WO		
I	5	4-5	4	4	4-5	5	4	4-5	4
II	5	4-5	4	4-5	4-5	4-5	4	4-5	4
III	4-5	4	4	4	5	5	4	4-5	4
IV	4-5	4	4	4	4	3-4	4	4-5	4
V	4	4-5	4	4	4-5	5	4	5	4
VI	4	4-5	4	4	4-5	5	4	5	4
VII	4	4-5	4	4	4-5	5	4	5	4
VIII	4	4	4	4	4	5	4	5	4
IX	4	4	4	4	4	4	4	4	4
X	4	4	4	4	5	5	4	4	4

Table 4. Lightness, red-greenness and yellow-blueness values for cotton (D65).⁽¹⁾

Compound	L ⁽²⁾	a ⁽²⁾	b ⁽²⁾	Compound	L ⁽²⁾	a ⁽²⁾	b ⁽²⁾
I	85.20	2.68	11.45	VI	82.66	4.39	16.96
II	82.24	5.03	10.04	VII	82.04	4.08	18.66
III	77.16	6.47	25.64	VIII	74.28	7.86	26.53
IV	81.53	4.96	15.73	IX	84.30	2.78	16.26
V	77.96	6.16	14.65	X	71.22	4.95	13.47

Table 5. Color fastness of the compounds on wool fabric.⁽¹⁾

Compound	Washing fastness							Rubbing fastness	
	Color Change	Staining ⁽²⁾						Dry	Wet
		AC	CO	PA	PES	PAN	WO		
I	4	4	4	4	4	4	4	5	4
II	4	4	4	4	4	4	4	5	4
III	4	4	4	4	5	5	4	5	4
IV	4	4	4	4	4	4	4	5	4
V	4-5	4-5	4	4-5	4-5	5	4-5	4-5	4
VI	4-5	4-5	4	4	4-5	5	4	4-5	4
VII	4	4-5	4	4	4-5	5	4	4-5	4
VIII	4	4	4	4	4	5	4	4	4
IX	4	4	4	4	4	4	4	4	4
X	4	4	4	4	5	5	4	4	4

Table 6. Lightness, red-greenness and yellow-blueness values for wool (D65).⁽¹⁾

Compound	L ⁽²⁾	a ⁽²⁾	b ⁽²⁾	Compound	L ⁽²⁾	a ⁽²⁾	b ⁽²⁾
I	54.83	12.20	41.08	VI	52.70	14.71	39.60
II	90.46	2.02	-6.25	VII	49.83	15.05	40.31
III	64.86	8.37	10.52	VIII	46.34	14.41	35.83
IV	90.94	1.73	-5.10	IX	90.58	0.38	-2.07
V	37.48	18.01	38.86	X	38.16	14.93	33.15

It is observed that the **L** and **b** values of 5-Br derivative (**I**) are higher than those of 5-Cl derivative (**II**), whereas the **a** value is lower for cotton fabric (Table 4). On the other hand, the chloro substituent at ortho position (**IV**: 3-Cl,5-Cl) increases **L** value whereas decreases the **a** and **b** values compared to those of the bromo derivative (**III**: 3-Br,5-Cl). The **L** value of the 5-Br derivative (**I**) is highest among the compounds having chloro and bromo substituents, namely **I**, **II**, **III**, and **IV** (similarity to the polyester fabric). In the compounds **VI** (3-methoxy, ortho position) and **VII** (4-methoxy, meta position), the **L** and **a** values are close to each other, whereas the methoxy group at the meta position (**VII**) increases the **b** value according to the ortho position. It is seen that the methyl group at the para position (**IX**) increases the **L** value according to the ortho position methyl group (**VIII**) (84.30 and 74.28 respectively) whereas decreases **a** and **b** values (Table 4).

The **L**, **a**, and **b** values for wool fabrics (Table 6) are in a wide range according to the polyester and cotton. These ranges are 90.94 – 37.48, 18.01 – 0.38, and 41.08 – (-6.25) for **L**, **a**, and **b**, respectively. The highest **L**, **a**, and **b** values belong to **IV**, **V**, and **I**, respectively, whereas the lowest **L**,

a, and **b** values are exhibited by the compounds **V**, **IX**, and **II**, respectively. Interestingly, compound **V** (4-OH derivative) has the highest **a** and lowest **L** values.

By comparing **I** and **II** for wool fabric (Table 6), it is seen that the **L** value of **II** (5-Cl derivative) is relatively high than that of **I** (5-Br derivative) (90.46 and 54.83, respectively). The **a** and **b** values of **II** (2.02, -6.25) are relatively low, according to those of **I** (12.20 and 41.08). There is a similar situation for **III** (3-Br,5-Cl) and **IV** (3-Cl,5-Cl): The **L** value of **IV** is considerably high (64.86 and 90.94 for **III** and **IV**, respectively) and the **a** and **b** values (1.73 and -5.10 for **IV**, respectively) are considerably low according to those of **III** (8.37 and 10.52). From these results, it can be claimed that chloro substituent increases **L** value whereas decreases the **a** and **b** values in case of wool. The **L**, **a**, and **b** values are close to each other for 3-methoxy and 4-methoxy derivatives (**VI** and **VII**) on wool. The **L** values are 90.58 and 46.34 for **IX** and **VIII**, respectively: The methyl group at para position (**IX**) increases the **L** value whereas decreases the **a** and **b** (0.38 and -2.07) values considerably according to the methyl group at ortho position (**VIII**: 14.41 and 35.83).

Tables 2, 4, and 6 reveal that the **a** and **b** values are higher for polyester and wool fabrics according to that of cotton fabric. In addition, it is interesting that the **b** values of the compounds **III**, **IV**, and **IX** are negative. It is considered that the **b** value of **IX** (5-Me derivative) is negative (-2.07) for wool, although that of the **VIII** (3-Me derivative) is a reasonably positive value such as 35.83. These two compounds (**VIII** and **IX**) show similar behavior toward polyester and cotton while behaving differently on wool in point of the **L**, **a**, and **b** values. Contrarily for wool, there is no significant difference in the polyester and cotton fabrics comparing their **L**, **a**, and **b** values.

As a conclusion, it is observed that the compounds have **L**, **a**, and **b** values at a wide range of wool fabric. It means that the substituent effect is seen more clearly in wool fabrics. Besides, it can be concluded that the position of the substituents is significant on dyeing properties even if slightly, comparing the **VI** with **VII** and **VIII** with **IX**, the derivatives including the methyl and methoxy groups.

It is possible to say that comparing Tables 2, 4, and 6, the **L** values are inversely proportional to **a** and **b** values, generally: If the **L** values are high, **a** and **b** values are low.

CONCLUSIONS

In this study, dry/wet rubbing and washing fastnesses of some Schiff bases derived from 4-chloroaminophenol and various benzaldehydes including methyl, chloro, bromo, nitro, methoxy, and hydroxy groups were investigated on polyester, wool and cotton fibers. The compounds exhibit good or excellent rubbing and washing fastness characteristics. Also, the lightness (**L**), red-greenness (**a**), and yellow-blueness (**b**) properties of the compounds were investigated. Dyeing properties of the compounds depend on the substituent positions, and the change in dyeing properties resulted from substituent effect is observed on wool mostly. Interestingly, the **L**, **a**, and **b** values of 3-Me and 5-Me derivatives (**VIII** and **IX**) are close to each other on polyester and cotton; however, they show significant differences in wool fabric (substituent position effect).

On the other hand, it can be claimed that chlorine substituent increases **L** value on wool. Schiff base substituents cause various effects on the fabrics. These result from interactions between the functional groups on the molecule and the fabrics depending on their structure.

ACKNOWLEDGMENTS

This study was funded by Scientific Research Projects Coordination Unit of Istanbul University – Cerrahpaşa.

REFERENCES

1. Poonia K, Siddiqui S, Arshad M, Kumar D. In vitro anticancer activities of Schiff base and its lanthanum complex. *Spectrochim. Acta. A. Mol. Biomol. Spectrosc.* 2016;155:146-54.
2. Wang M, Wang LF, Li YZ, Li QZ, Xu ZD, Qu DM. Antitumour activity of transition metal complexes with the thiosemicarbazone derived from 3-acetyllumbiferone. *Transit Met Chem.* 2001;26:307-10.
3. Mokhles MA, Ammar AL, Hanan AM, Samia AM, Mamdouh MA, Ahmed AE. Synthesis, anticancer activity and molecular docking study of Schiff base complexes containing thiazole moiety. *Beni-Suef Univ. J. Appl. Sci.* 2016;5:85-96.
4. Matar SA, Talib WH, Mustafa MS, Mubarak MS, AlDamen MA. Synthesis, characterization, and antimicrobial activity of Schiff bases derived from benzaldehydes and 3,3'-diaminodipropylamine. *Arab. J. Chem.* 2015;8:850-7.
5. Venugopal KN, Jayashree BS. Microwave-induced synthesis of Schiff bases of bromcoumarins as antibacterials. *Indian J. Pharm. Sci.* 2008;70:88-91.
6. Pandeya SN, Sriram D, Nath G, DeClercq E. Synthesis, antibacterial, antifungal and anti-HIV evaluation of Schiff and Mannich bases of isatin derivatives with 3-amino-2-methylmercapto quinazolin-4(3H)-one. *Pharm Acta Helv.* 1999;74:11-7.
7. Holla BS, Akberali PM, Shivananda MK. Studies on nitrophenylfuran derivatives: Part XII. Synthesis, characterization, antibacterial and antiviral activities of some nitrophenylfurfurylidene-1,2,4-triazolo[3,4-*b*]-1,3,4-thiadiazines. *Il Farmaco.* 2001;56:919-27.
8. Jarrahpour A, Khalili D, De Clercq E, Salmi C, Brunel JM. Synthesis, antibacterial, antifungal and antiviral activity evaluation of some new bis-Schiff bases of isatin and their derivatives. *Molecules.* 2007;12:1720-30.
9. da Silva CM, da Silva DL, Modolo LV, Alves RB, de Resende MA, Martins CVB, de Fatima A. Schiff bases: A short review of their antimicrobial activities. *J Adv Res.* 2011;2:1-8.
10. Singh H, Yadav LDS, Mishra SBS. Studies on some antifungal transition metal chelates of N-(5-phenyl-1, 3, 4-thiadiazol-2-yl) dithiocarbamic acid. *J Inorg Nucl Chem.* 1981;43:1701-4.
11. Joseyphus RS, Nair MS. Antibacterial and Antifungal Studies on Some Schiff Base Complexes of Zinc (II). *Mycobiology.* 2008;36:93-8.
12. Walsh OM, Meegan MJ, Prendergast RM, Nakib TA. Synthesis of 3-acetoxazetidin-2-ones and 3-hydroxyazetidin-2-ones with antifungal and antibacterial activity. *Eur J Med Chem.* 1996;31:989-1000.

13. Harpstrite SE, Collins SD, Oksman A, Goldberg DE, Sharma V. Synthesis, characterization, and antimalarial activity of novel schiff-base-phenol and naphthalene-amine ligands. *Med. Chem.* 2008;4(4):392-5.
14. Aslam MAS, Mahmood SU, Shahid M, Saeed A, Iqbal J. Synthesis, biological assay in vitro and molecular docking studies of new Schiff base derivatives as potential urease inhibitors. *Eur. J. Med. Chem.* 2011;46:5473-9.
15. Sangeeta S, Ahmad K, Noorussabah N, Bharti S, Mishra M.K, Sharma SR, Choudhary M. Synthesis, crystal structures, molecular docking and urease inhibition studies of Ni(II) and Cu(II) Schiff base complexes. *J. Mol. Struct.* 2018;1156:1-11.
16. Anouar EH, Raweh S, Bayach I, Taha M, Baharudin MS, Di Meo F, Hasan MH, Adam A, Ismail NH, Weber JF, Trouillas P. Antioxidant properties of phenolic Schiff bases: structure-activity relationship and mechanism of action. *Journal of Computer-Aided Mol. Des.* 2013;27:951-64.
17. Aziz AN, Taha M, Ismail NH, Anouar EH, Yousuf S, Jamil W, Awang K, Ahmat KAN, Khan KM, Kashif SM. Synthesis, crystal structure, DFT studies and evaluation of the antioxidant activity of 3,4-dimethoxybenzamine Schiff bases. *Molecules* 2014;19:8414-33.
18. Jamshidvand A, Sahihi M, Mirkhani V, Moghadam M, Mohammadpoor-Baltork I, Tangestaninejad S, Rudbari HA, Kargar H, Keshavarzi R, Gharaghani S. Studies on DNA binding properties of new Schiff base ligands using spectroscopic, electrochemical and computational methods: Influence of substitutions on DNA-binding. *J. Mol. Liq.* 2018;253:61-71.
19. Mahmood K, Hashmi W, Ismail H, Mirza B, Twamley B, Akhter Z, Rozas I, Baker RJ. Synthesis, DNA binding and antibacterial activity of metal (II) complexes of a benzimidazole Schiff base. *Polyhedron.* 2019;157:326-34.
20. Dhanaraj CJ, Nair MS. Synthesis, characterization, and antimicrobial studies of some Schiff-base metal(II) complexes. *J Coord Chem.* 2009;62:4018-28.
21. Szady-Chelmieniecka A, Grech E, Rozwadowski Z, Dziembowska T, Schilf W, Kamiński B. Multinuclear NMR study of the intramolecular hydrogen bond in Schiff-Mannich bases. *J Mol Struct.* 2001;565:125-8.
22. Jones RD, Summerville DA, Basolo F. Synthetic oxygen carriers related to biological systems. *Chem Rev.* 1979;17:139-79.
23. Hadjoudis E, Mavridis IM. Photochromism and thermochromism of Schiff bases in the solid state structural aspects. *Chem Soc Rev.* 2004;33:579-88.
24. Bhat K, Chang KJ, Aggarwal MD, Wang WS, Penn BG, Frazier DO. Synthesis and characterization of various Schiff bases for non-linear optical applications. *Mater Chem Phys.* 1996;44:261-6.
25. Mahmoud MR, El-Gyar SA, Moustafa AA, Shaker A. Ni(II) complexes of some polyfunctional n-Naphthylideneamino acids. *Polyhedron.* 1987;6:1017-20.
26. Qing-Yu H, Zheng-Hua M, Ya-Me Z. Preparation and oxygenation of manganese(II) complexes of imines derived from salicylaldehyde and amino acids. *J Coord Chem.* 1990;21:199-207.
27. Memon SQ, Memon N, Mallah A, Soomro R, Khuhawar MY. Schiff Bases as Chelating Reagents for Metal Ions Analysis. *Current Analytical Chem.* 2014;10:393-417.
28. Prajila M, Joseph A. Inhibition of mild steel corrosion in hydrochloric using three different 1,2,4-triazole Schiff's bases: A comparative study of electrochemical, theoretical and spectroscopic results. *J Mol Liq.* 2017; 241:1-8.
29. Gupta NK, Quraishi MA, Verma C, Mukherjee AK. Green Schiff's bases as corrosion inhibitors for mild steel in 1 M HCl solution: experimental and theoretical approach. *RSC Advances.* 2016; 104:102076-87.
30. Samadhiya S, Halve A. Synthetic utility of Schiff bases as potential herbicidal agents. *Orient J. Chem.* 2001;17 (electronic).
31. Papic S, Koprivanac N, Grabaric Z, Parac-Osterman D. Metal complex dyes of nickel with Schiff bases. *Dyes and Pigments.* 1994;25:229-40.
32. Ahmed DS, El-Hiti GA, Hameed AS, Yousif E, Ahmed A. New tetra-Schiff bases as efficient photostabilizers for poly(vinyl chloride). *Molecules.* 2017;22:1506-21.
33. Cinarli A, Gürbüz D, Tavman A, Birteksöz AS. Spectral characterization and antimicrobial activity of some Schiff bases derived from 4-chloro-2-aminophenol and various salicylaldehyde derivatives. *Chinese J Chem.* 2012;30:449-59.
34. Cinarli A, Gürbüz D, Tavman A, Birteksöz AS. Synthesis, spectral characterizations and antimicrobial activity of some Schiff bases of 4-chloro-2-aminophenol. *Bull Chem Soc Ethiop.* 2011;25:407-17.



Design of Novel Benzimidazole Derivatives as Potential α -amylase Inhibitors by 3D-QSAR Modeling and Molecular Docking Studies

Khalil El Khatabi , Ilham Aanouz , Reda El-Mernissi , Ayoub Khaldan ,
 Mohammed Aziz Ajana* , Mohammed Bouachrine , Tahar Lakhlifi 

University of Moulay Ismail, Faculty of Science, MCNSL, Meknes, Morocco.

Abstract: The enzyme α -amylase belongs to the highly conserved glycoside hydrolase family which is regarded as a good target for the discovery of antidiabetic agents. Following a 3D-QSAR study on forty-five 2-aryl benzimidazole derivatives which have been reported as potential insulin-independent antidiabetic agents. The results revealed that the CoMFA values were found to be 0.696 and 0.860 for Q^2 and R^2 respectively; while for the CoMSIA, the Q^2 and R^2 values were found to be 0.514 and 0.852 respectively. Both models were derived from a training set of thirty-seven compounds based on an appropriate method of alignment, while the predictive ability was approved by a test set containing eight compounds with r_{ext}^2 values of 0.990 and 0.987, respectively. Moreover, the contour maps generated from CoMFA and CoMSIA models provided much helpful information to figure out the structural requirements that influence the activity. To further reinforce the 3D-QSAR results, the molecular docking method was implemented which led to the design of new potential insulin-independent antidiabetic compounds with high predicted activity values.

Keywords: 3D-QSAR, Molecular modeling, Computational study, Benzimidazole, α -amylase inhibitors.

Submitted: March 12, 2020. **Accepted:** May 10, 2020.

Cite this: El Khatabi K, Aanouz I, El-Mernissi R, Khaldan A, Ajana MA, Bouachrine M, et al. Design of Novel Benzimidazole Derivatives as Potential α -amylase Inhibitors by 3D-QSAR Modeling and Molecular Docking Studies. JOTCSA. 2020;7(2):471-80.

DOI: <https://doi.org/10.18596/jotcsa.703026>.

***Corresponding author.** E-mail: a.ajanamohammed@fs.umi.ac.ma.

INTRODUCTION

Diabetes mellitus (DM) is a chronic metabolic syndrome of multiple etiology characterized by hyperglycemia as its initial symptoms and glucose intolerance. The disease can be simply classified into insulin secretion (type 1 diabetes) or insulin action (type 2 diabetes) (1,2). The digestive enzyme, α -Amylase, is the main form of amylase belonging to the family of glycoside hydrolases and found principally in pancreatic fluid and saliva. It is responsible for the biosynthesis of glycoproteins with an important role in the digestion of carbohydrate in the small intestine. Acute renal necrosis, cancer of urinary bladder, and active pyelonephritis are some urinary disorders and causes due to increasing the level of this

enzyme(3). The glycoside hydrolases family can be isolated from many organisms including humans (4), animals (5,6), plants (7), and bacteria (8).

Benzimidazoles are a class of heterocyclic compounds that attracts much attention as promising bioactive molecules. Furthermore, benzimidazole is one of the privileged pharmacophores in drug discovery acting as a good ligand towards the transition metal ions using the nitrogen atom (9). This is due to their various reported anti-tumor (10), anti-fungal (11), anti-inflammatory (12), antiviral (13), anti-ulcerative (14), and antimicrobial activities (15).

The structural parameters along with the application of the 3D-QSAR modeling and molecular docking

methods have proved to be a promising avenue for structure-based drug design that can provide quantitative forecasts of activity and predict the activity of new organic compounds with a lowered economic investment costs (16). The current study aimed to explore the 3D-QSAR and molecular docking approaches (17) on a series of benzimidazole derivatives against α -amylase in order to develop a correlation between their inhibitory activities and structural characteristics. This would eventually facilitate the design and optimization of new potential α -amylase inhibitors with potent activities.

MATERIALS AND METHODS

Dataset

A set of forty-five compounds with their reported α -amylase inhibition activities, IC_{50} was obtained from the literature (18). And the corresponding IC_{50} values (μM) were converted into the pIC_{50} values (Table 1). The dataset was split into the training set (37 molecules) and test set (8 molecules). Both sets were selected at random to create the quantitative model.

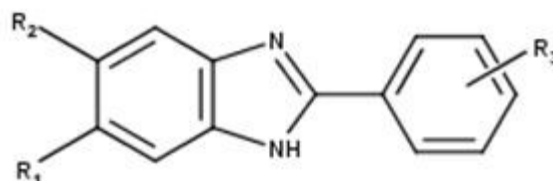


Figure 1. The structural template of the benzimidazole derivatives, **1-45**.

Table 1. IC_{50} values of the reported 2-Aryl benzimidazole derivatives against α -amylase.

Training/ Test	Comp.	R ₁	R ₂	R ₃	pIC_{50}
Test	1*	H	H	2-Cl-3-OCH ₃	5.562
Test	2*	H	H	2-OH-3-OCH ₃ -6-Br	5.605
Training	3	H	H	3,4-diOCH ₃ -6-Br	5.821
Training	4	H	H	2-OH-3-Br-5-Cl	5.555
Training	5	CH ₃	CH ₃	3,6-diOH	5.524
Training	6	CH ₃	CH ₃	4-OCH ₃ -6-F	5.555
Training	7	CH ₃	CH ₃	5-OCH ₃ -6-Cl	5.546
Training	8	CH ₃	CH ₃	4,5,6-triOCH ₃	5.638
Test	9*	CH ₃	CH ₃	2-OH-3-OCH ₃ -6-Br	5.585
Training	10	CH ₃	CH ₃	3,4-diOCH ₃ -6-Br	5.829
Training	11	CH ₃	CH ₃	3,5-diOCH ₃ -4-Br	5.790
Training	12	CH ₃	CH ₃	3-I-4-OH-5-OCH ₃	5.751
Training	13	CH ₃	CH ₃	3-Cl-5-Br-6-OH	5.530
Training	14	CH ₃	CH ₃	3,5-diCl-6-OH	5.520
Training	15	H	F	4,6-diOH	5.520
Training	16	H	F	4-OCH ₃ -6-F	5.790
Test	17*	H	F	2-OCH ₃ -5-Br	5.585
Test	18*	H	F	5-OCH ₃ -6-Cl	5.580
Training	19	H	F	4-OAc-5-OCH ₃	5.770
Training	20	H	F	4,5,6-triOH	5.595
Training	21	H	F	3,5-diOCH ₃ -4-OH	5.603
Training	22	H	F	2-OH-3-OCH ₃ -6-Br	5.663
Training	23	H	F	3,4-diOCH ₃ -6-Br	5.804
Training	24	H	F	4,5-diOCH ₃ -6-Cl	5.591
Training	25	H	F	3,5-diCl-6-OH	5.542
Training	26	H	F	3-Cl-5-Br-6-OH	5.543
Training	27	H	Cl	4-OAc-5-OCH ₃	5.774
Training	28	H	Cl	5-OCH ₃ -6-Cl	5.555
Training	29	H	Cl	2-OCH ₃ -5-Br	5.581
Test	30*	H	Cl	4-OCH ₃ -6-F	5.562
Training	31	H	Cl	3,4-diOCH ₃ -6-Br	5.761
Training	32	H	Cl	3-I-4-OH-5-OCH ₃	5.793
Test	33*	H	Cl	3-Cl-5-Br-6-OH	5.543
Training	34	H	Cl	4,5-diOCH ₃ -6-Cl	5.821
Training	35	H	Cl	3,5-diOCH ₃ -4-Br	5.790
Training	36	H	Cl	2-Br-5-OCH ₃ -6-OH	5.655
Training	37	H	Cl	3,5-diOCH ₃ -4-OH	5.598
Training	38	H	NO ₂	4-OAc-5-OCH ₃	5.761

Training/ Test	Comp.	R ₁	R ₂	R ₃	pIC ₅₀
Training	39	H	NO ₂	4-OCH ₃ -6-F	5.560
Training	40	H	NO ₂	5-OCH ₃ -6-Cl	5.556
Training	41	H	NO ₂	2-Br-5-OCH ₃ -6-OH	5.640
Training	42	H	NO ₂	3,4-diOCH ₃ -6-Br	5.749
Training	43	H	NO ₂	3-I-4-OH-5-OCH ₃	5.764
Training	44	H	NO ₂	3-Cl-5-Br-6-OH	5.542
Test	45*	H	NO ₂	2-F-5-Br	5.634

Molecular modeling

The studied molecules were constructed and minimized using the SKETCH option in SYBYL-X 2.0 program package (19) running on a windows 10, 64 bit workstation/ASUS, under the Tripos standard force field (20) with Gasteiger-Hückel atomic partial charges (21) by the Powell method with a convergence criterion of 0.01 kcal/mol Å. Sybyl program provides a molecular design environment to identify, predict and analyze molecular behavior.

Molecular alignment

Molecular alignment aims to build an efficiency of the 3D-QSAR models. The studied molecules were stratified on the common core; 2-aryl benzimidazole using the simple alignment protocol in Sybyl (22). Compound **10** was selected as a representative template for superimposing structures as shown in Figure 2.

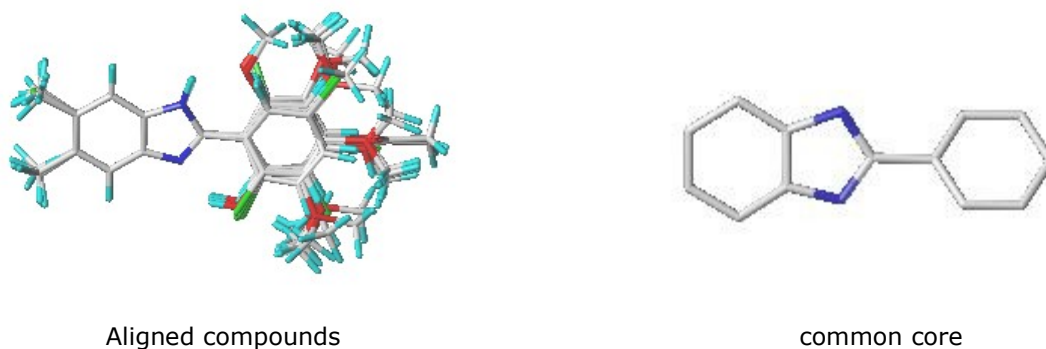


Figure 2. 3D-QSAR aligned molecules using compound 10 as a template.

3D QSAR analyses

On the basis of molecular alignment protocol which is considered as one of the most crucial factors that affects the accuracy of 3D-QSAR models, comparative molecular field analysis (CoMFA) (23) and comparative molecular similarity indices analysis (CoMSIA) (24) models were developed to derive a linear relationship between the obtained QSAR models and α -amylase enzyme inhibitory activities. 3D-QSAR study was performed with the default parameters; the minimum sigma (column filtering) is set to 2.0 kcal/mol and the energy cutoff values of 30 kcal/mol (25).

The partial least squares (PLS) regression method was adopted to derive 3D-QSAR models (26). Hence the PLS with leave-one-out cross-validation was implemented to produce the coefficient of cross-validation correlation (Q^2) with an optimum number of components (N). And the non-cross validation was carried out to get the correlation coefficient (R^2), F-test value (F) and the standard error of estimate (SEE). Consequently, the best QSAR model is selected based on the high Q^2 value ($Q^2 > 0.50$) and R^2 value ($R^2 > 0.60$), an optimal number of component values, and low standard error estimation (SEE). Furthermore, the external

validation was performed to evaluate the sturdiness of the generated 3D-QSAR models using eight molecules as a test set. Where the best value of $r_{\text{ext}}^2 > 0.6$ indicated that the predictive power of derived QSAR model was good (27).

Molecular Docking

The docking was carried out to further explore the binding interactions of the molecules in the active site of the α -amylase enzyme and confirm the contour maps results of CoMFA as well as the CoMSIA using the Surflex-Docking method (19). Further, the results were analyzed using PyMol (28) and Discovery studio 2016 softwares (29). The crystal structure of the α -amylase enzyme (PDB code: 1HNY) with the co-crystallized ligand removed was utilized for this study. Using the Discovery Studio 2016, the protein was prepared by the addition of polar hydrogens and Kohlman charges while removing water molecules from the 1HNY receptor. The 3D structure of the representative compound **10** was geometrically optimized and energetically minimized using default parameters and consequently docked into the active site of the α -amylase enzyme.

Y-Randomization test

The Y-Randomization test was performed to value the vigor of both models (30), and the inhibition activities ($-\log IC_{50}$) were shuffled many times. A new 3D-QSAR model was generated for each iteration. Besides, the low Q^2 and R^2 values pointed out that the results were not due to a chance correlation.

RESULTS AND DISCUSSION**3D-QSAR**

Based on the 3D-QSAR modeling, it appeared that the models might play substantial roles in predicting new potent insulin-independent antidiabetic agents as contained in the summary of PLS analyses (Table 2). Obviously, for the CoMFA model, the coefficient of cross-validated, Q^2 value was 0.696 with 2 as the optimized component, N. While the R^2 , SEE and F-

test values were 0.860, 0.041 and 104.72, respectively. It thus implied that the high Q^2 , R^2 and F values along with low SEE value, suggest a good statistical correlation and reasonable predictive capability of the obtained models. Furthermore, the high r_{ext}^2 (0.990) value of the external validation exhibits a high level of reliability in the current study. Similarly, the ratio of steric to electrostatic contributions were set at 51:49, which means that both fields are much explanatory.

The most accurate CoMSIA model which involved the steric, electrostatic, hydrophobic, H-bond acceptor and donor fields showed Q^2 , N, R^2 , SEE, and F values of 0.514, 3, 0.852, 0.042 119.904 respectively. The r_{ext}^2 value obtained was 0.987 which approved the prediction ability of the obtained model. The experimental and predicted pIC₅₀ are shown in Table 3.

Table 2. PLS statistical parameters.

Model	Q^2	R^2	SEE	F	N	r_{ext}^2	Fractions				
							Ster	Elect	Hyd	Acc	Don
CoMFA	0.696	0.860	0.041	104.72	2	0.990	0.514	0.486	-	-	
CoMSIA	0.514	0.852	0.042	63.55	3	0.987	0.084	0.471	0.229	0.138 0.077	

Table 3. Experimental and predicted pIC₅₀ of forty-five benzimidazole derivatives (*:test set)

Comp.	Experimental pIC ₅₀	predicted pIC ₅₀		Comp.	Experimental pIC ₅₀	predicted pIC ₅₀	
		CoMFA	CoMSIA			CoMFA	CoMSIA
1*	5.562	5.559	5.558	22	5.663	5.663	5.653
2*	5.605	5.647	5.645	23	5.804	5.846	5.847
3	5.821	5.861	5.858	24	5.591	5.655	5.658
4	5.555	5.563	5.562	25	5.542	5.574	5.574
5	5.524	5.493	5.493	26	5.543	5.578	5.578
6	5.555	5.634	5.630	27	5.774	5.751	5.752
7	5.546	5.541	5.542	28	5.555	5.588	5.587
8	5.638	5.664	5.659	29	5.581	5.553	5.549
9*	5.585	5.568	5.601	30*	5.562	5.557	5.557
10	5.829	5.817	5.816	31	5.761	5.755	5.758
11	5.790	5.755	5.756	32	5.793	5.760	5.760
12	5.751	5.714	5.713	33*	5.543	5.586	5.586
13	5.530	5.523	5.525	34	5.821	5.721	5.716
14	5.520	5.521	5.521	35	5.790	5.738	5.740
15	5.520	5.518	5.521	36	5.655	5.663	5.658
16	5.790	5.685	5.684	37	5.598	5.693	5.695
17*	5.585	5.544	5.541	38	5.761	5.736	5.739
18*	5.580	5.578	5.570	39	5.560	5.655	5.6657
19	5.770	5.749	5.750	40	5.556	5.556	5.557
20	5.595	5.513	5.517	41	5.640	5.56	5.655
21	5.603	5.688	5.686	42	5.749	5.715	5.720
				43	5.764	5.726	5.727
				44	5.542	5.493	5.557
				45*	5.634	5.616	5.617

Interpretation of graphical contours

The graphical contour maps were created to visualize areas where the activity can be increased or decreased. Figures 3 and 4 show the CoMFA and CoMSIA contour maps respectively for compound **10** as a representative molecule.

CoMFA contour maps

The electrostatic fields are presented with red (20% contribution) and blue (80% contribution) contours, while the steric fields are presented with green (80% contribution) and yellow (20% contribution) contours. The bulky substituents are preferred around green areas, whereas yellow areas' bulky substituents are not preferred (Figure 3).

As depicted in Figure 3, a relatively big yellow contour was observed around the phenyl group which could be favored to activity while the small-sized green contour around the C-3 position indicated that less bulky group at this position would

not be favorable for increasing the activity, which could be demonstrated by compounds **4**, **13**, **14**, **25**, **26**, **33** and **44**. For example, the compounds **13** ($pIC_{50} = 5.530$) and **14** ($pIC_{50} = 5.520$), with halogens at the 3 and 5 positions of the phenyl moiety, showed low activities than that of compound **10** ($pIC_{50} = 5.829$), with OCH_3 and H groups at the same positions, respectively.

Moreover, figure 3 revealed that that phenyl group with the electropositive substituents may increase the activity around the blue contours. As such three major space-favorable blue regions were distributed around the ortho, meta and para positions of the phenyl ring. This indicated that the existence of these electron donor groups at these positions could increase the activity. Therefore, electropositive and less bulky groups are required at these positions which could easily reach the binding pocket in the enzyme active sites and present high α -amylase inhibition affinity.

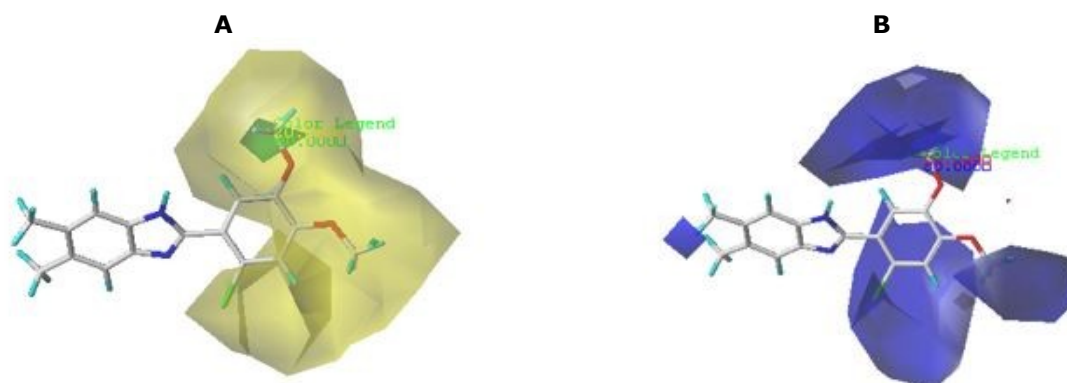


Figure 3. Analysis of CoMFA contour maps. **(A)** Steric field; **(B)** Electrostatic field.

CoMSIA contour map

The CoMSIA contour maps for the steric and electrostatic fields were found to be similar to the corresponding CoMFA fields. Therefore, the focus was directed towards the remaining parameters. Hence according to the CoMSIA fractions presented in Table 2, the electrostatic (0.471); H-bond acceptor (0.138); and hydrophobic fields (0.229) were found to be the major fields that could describe the activity.

The contour map for the hydrophobic field (Figure 4(a)) is depicted in yellow domains (80% contribution) and white domains (20% contribution) in which hydrophobic substituents are predicted to enhance the biological activity in yellow contours, whereas in white domain, hydrophobic groups were not favored. The yellow contour near the ortho position of the phenyl group brought to light that the hydrophobicity could play a crucial role in the activity. For example, compound **23** ($pIC_{50} = 5.804$) with a -Br group at the C-2, which is falls within the

yellow contours, exhibited higher activity than those with no hydrophilic groups such as; compounds **15** ($pIC_{50} = 5.520$) and **26** ($pIC_{50} = 5.542$), which lead into increase of activity. Moreover, two white contours near the C-3 and C-5 positions of the phenyl group pointed that the presence of a hydrophobic group especially halogens in this region may not be beneficial to the biological activity. For instance, compounds **4** ($pIC_{50} = 5.555$) and **33** ($pIC_{50} = 5.543$) with halogens groups at C-3 and C-5 position of the phenyl moiety exhibit lowest activities than that of the corresponding compound **10** ($pIC_{50} = 5.829$).

The CoMSIA hydrogen bond acceptor field (Figure 4(b)), is displayed in magenta (80% contribution) and red (20% contribution) contours, representing favorable and unfavorable positions for H-bond acceptors respectively. A relatively big red contour was observed around C-2, C-3 and C-4 positions of the phenyl group which has been proven to be a disadvantage to activity due to the existence of H-

bond acceptor substituent at one or two of these positions. Whereas, the magenta contour around the C-5 position of the phenyl moiety is crucial for significant inhibitory activity. These characteristics may explain significant α -amylase inhibitory activity for compounds with no hydrogen bond acceptor groups such as; compound **11** and compound **10**, respectively. For instance, compound **11** ($pIC_{50} = 5.790$) without any substituent and compound **10** ($pIC_{50} = 5.829$) with a -Br showed high activities.

Y-randomization test

Table 4 shows the results of seven random shuffles for the Y-randomization test. For every iteration, a set of Q^2 and R^2 of new QSAR models is generated.

In the contour map of H-bond donor field, as shown in Figure 4(c), the cyan (80% contribution) and the purple (20% contribution) contours represent areas with favorable and unfavorable H-bond donor groups respectively. A big-sized cyan contour is found around the phenyl ring, indicating that H-bond donor substituents in this area are predicted to enhance biological activity.

As a result, the Q^2 and R^2 values were low. Thus allowing to conclude that the probability of random correlations was excluded.

Table 4. Q^2 and R^2 values of the Y-randomization test.

Iteration	CoMFA		CoMSIA	
	Q^2	R^2	Q^2	R^2
1	0.082	0.128	0.048	0.134
2	0.125	0.317	0.121	0.242
3	0.199	0.421	0.178	0.391
4	0.167	0.360	0.142	0.308
5	-0.214	0.248	-0.199	0.195
6	0.099	0.126	0.092	0.102
7	0.137	0.301	0.129	0.284

Molecular docking

To reinforce the 3D-QSAR results, the molecular docking technique was applied to investigate the different interactions of benzimidazole derivatives in the active site of α -amylase (PDB code: 1HNY) using the Surflex program. The potent compounds were found to be those that contain ortho Cl or Br atom, para and meta methoxy groups on the phenyl ring which could be responsible for these compounds' inhibitory activity. As depicted in Figure 5, the representative compound **10** which is originally reported to be the most effective compound was docked in the α -amylase enzyme active site. This enabled the understanding of the hydrophobic and

H-bond interactions between the active molecule and 1HNY receptor.

The blue and pink colors around C-2, C-3 and C-4 positions of the phenyl ring indicated that substituents with hydrophilic character and H-bond donor substituents are favored in these positions. The R1 and R2 substituents were found in the brown area which implied that the groups with the hydrophobic characters at these positions would be favored. The observations obtained from the hydrophobicity and H-bond surfaces are in agreement with the contour maps of CoMSIA model.

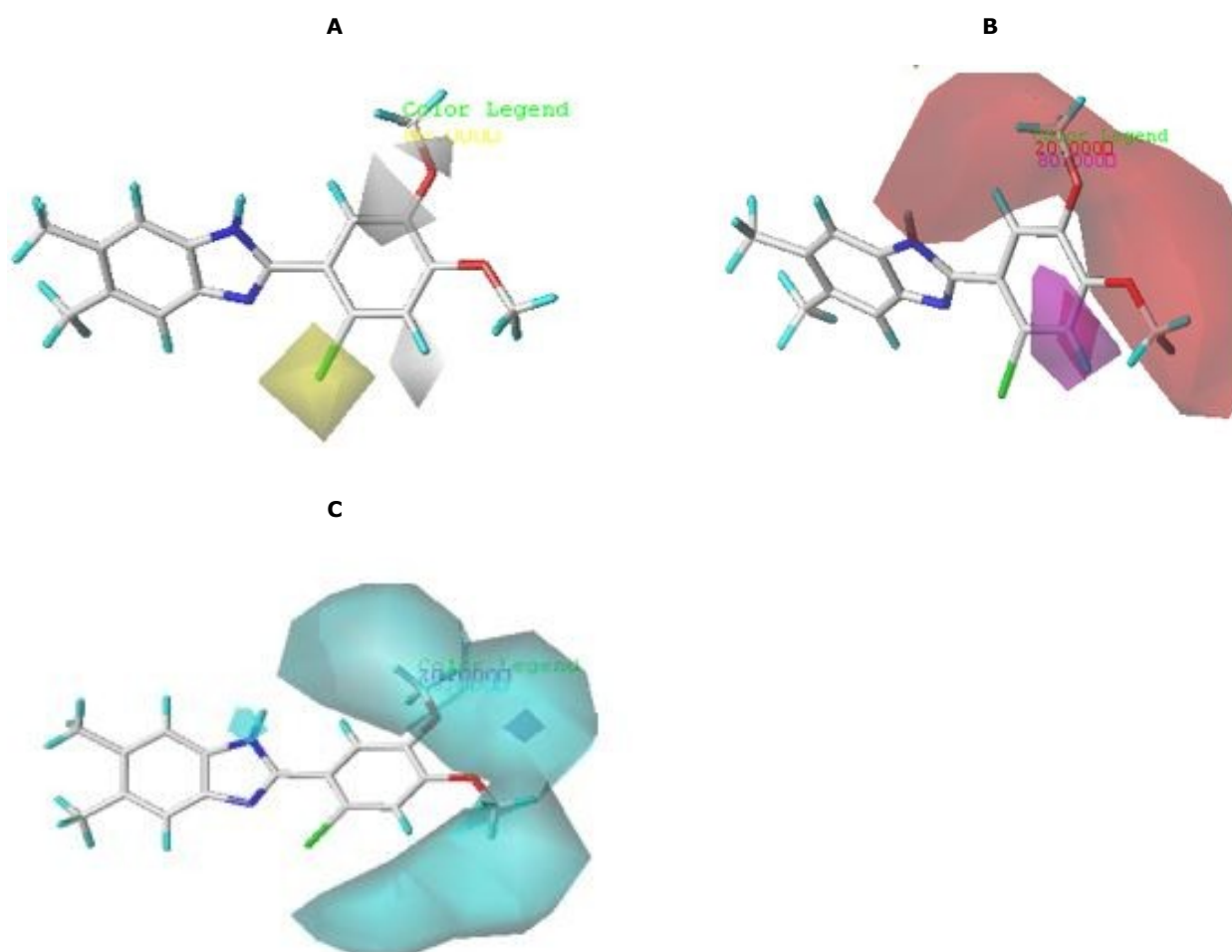


Figure 4. Analysis of CoMSIA contour maps. **(A)** Hydrophobic field; **(B)** H-bond acceptor field; **(C)** H-bond donor field

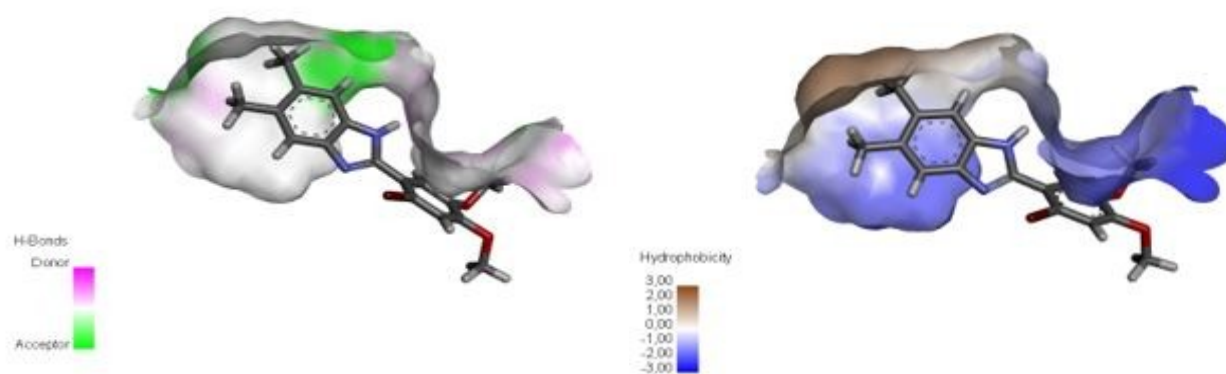


Figure 5. The docking pose of the active molecule and 1HNY receptor.

SAR summarized results

Figure 6 summarized the information derived from the 3D contour maps that satisfactorily matched the

results of molecular docking, which could be much helpful to propose new molecules with high predictive activities.

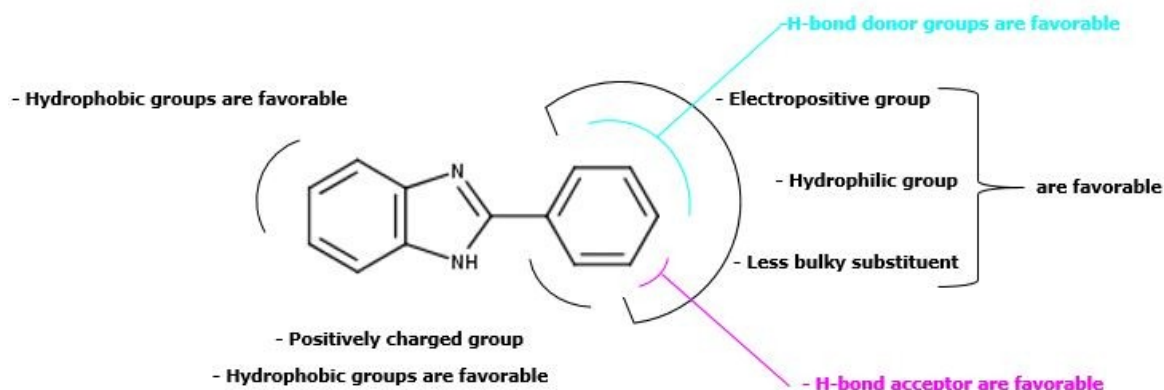


Figure 6. SAR-summarized results from the present work.

Newly designed compounds

Based on the information obtained from the 3D contour maps and molecular docking studies, five new 2-arylbenzimidazole derivatives which exhibited high pIC_{50} values were designed. The newly predicted compounds A1, A2, A3, A4 and A5

showed exceptionally improved inhibitory activity and higher total score (binding affinities) than that of compound 10 for both models, indicating their potential as new α -amylase inhibitors as shown in Table 5.

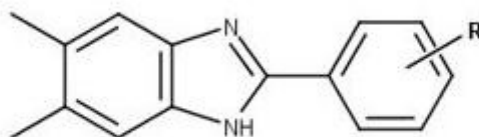


Figure 7. The structural template of the newly designed molecules.

Table 5. The pIC_{50} values of newly designed 2-arylbenzimidazole derivatives as α -amylase inhibitors.

N°	R	Predicted pIC_{50}		Total scoring
		CoMFA	CoMSIA	
Comp 10	3,4-diOCH ₃ -6-Br	5.817	5.816	1.7149
A1	2-OH-3-NHCH ₃	6.353	6.340	3.2841
A2	2-NH ₂ -3-OH	6.326	6.325	3.2719
A3	2,3,6-triOH	6.299	6.297	3.2722
A4	2-OH-3-NH ₂	6.092	6.101	2.9940
A5	2,4,6-triNH ₂	6.052	6.076	2.9866

CONCLUSION

The current study has provided some valuable information on the design of new potential insulin-independent antidiabetic agents. This has been achieved through investigating forty-five benzimidazole derivatives retrieved from the literature by molecular docking and 3D-QSAR studies. Graphical analyses of the optimal results obtained from the contour maps brought to light the

main structural requirements that may influence the activity. Moreover, the molecular docking analyses matched well with the results obtained from the contour maps which led to the design of five potent insulin-independent antidiabetic molecules and successfully predicted their α -amylase inhibitory activities.

ACKNOWLEDGEMENTS

We are grateful to the "Association Marocaine des Chimistes Théoriciens" (AMCT) for its pertinent help concerning the software programs.

REFERENCES

- Orbak R, Simsek S, Orbak Z, Kavrut F, Colak M. The Influence of Type-1 Diabetes Mellitus on Dentition and Oral Health in Children and Adolescents. *Yonsei Med J*. 2008;49(3):357-365.
- Latti BR, Kalburge JV, Birajdar SB, Latti RG. Evaluation of relationship between dental caries, diabetes mellitus and oral microbiota in diabetics. *J Oral Maxillofac Pathol JOMFP*. 2018;22(2):282.
- Gonick HC, Kramer HJ, Schapiro AE. Urinary β -Glucuronidase Activity in Renal Disease. *Arch Intern Med*. 1973;132(1):63-69.
- Kim D-H, Lee S-W, Han MJ. Biotransformation of Glycyrrhizin to 18 β -Glycyrrhetic Acid-3-O- β -D-glucuronide by *Streptococcus* LJ-22, a Human Intestinal Bacterium. *Biol Pharm Bull*. 1999;22(3):320-322.
- Abou-Haila A, Orgebin-Crist M-C, Skudlarek MD, Tulsiani DRP. Identification and androgen regulation of egasyn in the mouse epididymis. *Biochim Biophys Acta BBA - Mol Cell Res*. 1998;1401(2):177-186.
- Pereira W, Cruz A, Albuquerque E, Santos E, Oliveira A, Sales M, et al. Purification and Characterization of a β -Glucuronidase Present During Embryogenesis of the Mollusk *Pomacea* sp. *Protein Pept Lett*. 2005;12(7):695-700.
- Zhang C, Zhang Y, Chen J, Liang X. Purification and characterization of baicalin- β -d-glucuronidase hydrolyzing baicalin to baicalein from fresh roots of *Scutellaria viscidula* Bge. *Process Biochem*. 2005;40(5):1911-1915.
- Wang X, Liu Y, Wang C, Feng X, Li C. Properties and structures of β -glucuronidases with different transformation types of glycyrrhizin. *RSC Adv*. 2015;5(84):68345-68350.
- Küçükbay H. PART I: MICROWAVE-ASSISTED SYNTHESIS OF BENZIMIDAZOLES: AN OVERVIEW (UNTIL 2013). *J Turk Chem Soc Sect Chem* 2017; 4(1):1-22.
- Küçükbay H, Mumcu A, Tekin S, Sandal S. Synthesis and evaluation of novel N, N'-disubstituted benzimidazolium bromides salts as antitumor agents. *Turk J Chem*. 2016;40(3):393-401.
- Khabnadideh S, Rezaei Z, Pakshir K, Zomorodian K, Ghafari N. Synthesis and antifungal activity of benzimidazole, benzotriazole and aminothiazole derivatives. 2012;7(2):65-72.
- Sondhi SM, Singh N, Kumar A, Lozach O, Meijer L. Synthesis, anti-inflammatory, analgesic and kinase (CDK-1, CDK-5 and GSK-3) inhibition activity evaluation of benzimidazole/benzoxazole derivatives and some Schiff's bases. *Bioorg Med Chem*. 2006;14(11):3758-65.
- Salahuddin, Shaharyar M, Mazumder A. Benzimidazoles: A biologically active compounds. *Arab J Chem*. 2017;10:157-73.
- Carcanague D, Shue Y-K, Wuonola MA, Uria-Nickelsen M, Joubran C, Abedi JK, et al. Novel Structures Derived from 2-[[[2-Pyridyl)methyl]thio]-1 H -benzimidazole as Anti- *Helicobacter pylori* Agents, Part 2. *J Med Chem*. 2002;45(19):4300-9.
- Küçükbay H, Yılmaz Ü, Şireci N, Güvenç AN. Synthesis and antimicrobial activities of some bridged bis-benzimidazole derivatives. *Turk J Chem*. 2011;35(4):561-71.
- Ou-Yang S, Lu J, Kong X, Liang Z, Luo C, Jiang H. Computational drug discovery. *Acta Pharmacol Sin*. 2012;33(9):1131-40.
- Understanding the Basics of QSAR for Applications in Pharmaceutical Sciences and Risk Assessment 1, Kunal Roy, Supratik Kar, Rudra Narayan Das - Amazon.com [Internet]. available on: <https://www.amazon.com/Understanding-Applications-Pharmaceutical-Sciences-Assessment-ebook/dp/B00URFMD7Q>
- Adegboye AA, Khan KM, Salar U, Aboaba SA, Kanwal, Chigurupati S, et al. 2-Aryl benzimidazoles: Synthesis, In vitro α -amylase inhibitory activity, and molecular docking study. *Eur J Med Chem*. 2018;150:248-60.
- Sybyl-X [Internet]. omicX. available on: <https://omictools.com/sybyl-x-tool>
- Clark M, Cramer RD, Van Opdenbosch N. Validation of the general purpose tripos 5.2 force field. *J Comput Chem*. 1989;10(8):982-1012.
- Purcell WP, Singer JA. A brief review and table of semiempirical parameters used in the Hueckel molecular orbital method. *J Chem Eng Data*. 1967;12(2):235-46.
- SCIGRESS - a unique desktop molecular modeling software package [Internet]. available on: https://fqs.pl/en/chemistry/products/scigress?gclid=EAIaIQobChMIsrORqqe95wIVw7HtCh0bGAueEAAAYASAAEgJ0M_D_BwE
- Cramer RD, Patterson DE, Bunce JD. Comparative molecular field analysis (CoMFA). 1. Effect of shape on binding of steroids to carrier proteins. *J Am Chem Soc*. 1988;110(18):5959-67.
- Klebe G, Abraham U, Mietzner T. Molecular Similarity Indices in a Comparative Analysis (CoMSIA) of Drug Molecules to Correlate and Predict Their Biological Activity. *J Med Chem*. 1994;37(24):4130-46.
- Stähle L, Wold S. 6 Multivariate Data Analysis and Experimental Design in Biomedical Research. In: *Progress in Medicinal Chemistry* [Internet]. Elsevier; 1988:291-338. available on: <https://linkinghub.elsevier.com/retrieve/pii/S0079646808702819>
- Bush BL, Nachbar RB. Sample-distance partial least squares: PLS optimized for many variables, with application to CoMFA. *J Comput Aided Mol Des*. 1993;7(5):587-619.

27. Baroni M, Clementi S, Cruciani G, Costantino G, Riganelli D, Oberrauch E. Predictive ability of regression models. Part II: Selection of the best predictive PLS model. *J Chemom.* 1992;6(6):347-56.
28. DeLano WL. Pymol: An open-source molecular graphics tool. *CCP4 Newsl Protein Crystallogr.* 2002;40(1):82-92.
29. Discovery Studio Predictive Science Application | Dassault Systèmes BIOVIA [Internet]. available on: <https://www.3dsbiovia.com/products/collaborative-science/biovia-discovery-studio/>
30. Rücker C, Rücker G, Meringer M. γ -Randomization and Its Variants in QSPR/QSAR. *J Chem Inf Model.* 2007;47(6):2345-57.



SYNTHESIS, ANTIBACTERIAL ACTIVITY AND DOCKING STUDIES OF BENZYL ALCOHOL DERIVATIVES

Mamman Sulaiman¹  , Yusuf Hassan^{1*}  , Tugba Taskin-Tok²  ,
Xavier Siwe Noundou³  

¹Umaru Musa Yar'adua University, Faculty of Natural and Applied Sciences, Department of Chemistry, Katsina, Nigeria.

²Gaziantep University, Faculty of Arts and Sciences, Department of Chemistry, Gaziantep, Turkey.

³Rhodes University, Faculty of Science, Department of Chemistry, Grahamstown, South Africa.

Abstract: Benzyl alcohol derivatives were synthesized, and characterized using NMR and FTIR spectroscopic techniques. For the first time, the antibacterial activities of the synthesized compounds were examined using disc diffusion method by measuring the diameter of the zones of inhibition against *Staphylococcus aureus* and *Pseudomonas aeruginosa*. The results demonstrated that the activity was concentration dependant, and that the compounds were generally potent against *P. aeruginosa*. Only two of the compounds were active against *S. aureus*. In terms of broad spectrum activity, compound **2d** (35 mm) was found to exhibit a promising efficacy which surpassed that of the standard drug (amoxicillin). The binding of compounds **2a-e** to the glucosamine-6-phosphate synthase (GlcN-6-P) active-site revealed that all the synthesized compounds fitted into the GlcN-6-P active-site receptor cavity, exhibited potential hydrogen-bonding interactions with the proximal amino acid residues and aligned similar to amoxicillin. Interestingly, it has been found that the most active compound, **2d** also appeared to have a relatively low binding energy (-52.8901 kcal/mol).

Keywords: Benzyl alcohol derivatives, antibacterial activity, docking studies, glucosamine-6-phosphate synthase.

Submitted: February 21, 2020. **Accepted:** May 10, 2020.

Cite this: Sulaiman M, Hassan Y, Taşkın-Tok T, Noundou XS. SYNTHESIS, ANTIBACTERIAL ACTIVITY AND DOCKING STUDIES OF BENZYL ALCOHOL DERIVATIVES. JOTCSA. 2020;7(2):481-8.

DOI: <https://doi.org/10.18596/jotcsa.692113>.

***Corresponding author.** E-mail: (yusuf.hassan@umyu.edu.ng), Tel: (+234 803 062 1278).

INTRODUCTION

The continuous increase in the antibiotics resistance and the attendant scarcity of new antimicrobial agents is arguably one of the major challenges in public health today, especially in the developing countries where up to one-half of deaths are attributed to infectious diseases (1-4). This could particularly be seen in the level of antibiotics resistance associated with a number of staphylococcus species which causes respiratory and skin infections, as well as pseudomonas species which are also responsible for the gastrointestinal and urogenital diseases (5). For

instance, the clinical isolates of staphylococcus aureus — the leading cause of nosocomial infections — are becoming resistant to a range of popular antimicrobial agents such as vancomycin, trimethoprim-sulfamethoxazole, chloramphenicol, erythromycin, clindamycin, ciprofloxacin, penicillin, amikacin, tobramycin, and gentamicin (6).

In an attempt to address the aforementioned concerns, a number of workers have reported various bioactive molecules built around some promising scaffolds and assessed their antibacterial or antimicrobial potentials. These includes nitroimidazole derived oxazolidinones (7),

ciprofloxacin derivatives (8-11), icariin derivatives (12), 1-monolaurin (13), (*E*)-stilbene derivatives (14), benzimidazole-incorporated sulfonamide analogues (15), chalcone derivatives (16), 3-phenyl-1-methylquinolin-2-one derivatives (17), oxysterols (18), 2-thiazolylimino-5-arylidene-4-thiazolidinones (19), sulfonamide and carbamate derivatives of 5-Nitro-1H-indazole (20), polyfluorinated 4-thiazolidinone and α -aminophosphonic acid derivatives (21). Interestingly, we have noted a known bioactive scaffold that apparently escaped the attention of workers — benzyl alcohol.

Benzyl alcohol (Figure 1) is an aromatic alcohol commonly found in various essential oils such as jasmine, ylang-ylang, and hyacinth (22). Due to its antibacterial and antifungal activities, it is widely used as an ingredient in the manufacture of soaps, topical creams, skin lotions, shampoos, and facial cleansers. Unfortunately however, benzyl alcohol has been reported to be a contact allergen (23). It thus prompted us in this work to prepare benzyl alcohol derivatives in order to evaluate their structure activity relationships with the aim of developing lead compounds that could offer safe and efficacious oral or topical antibacterial agents.

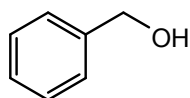


Figure 1. Structure of benzyl alcohol.

EXPERIMENTAL SECTION

Materials

All reagents and solvents were purchased from Aldrich and used as received. ^1H and ^{13}C NMR spectra were recorded on a Bruker AVANCE 400 spectrometer. IR spectra were recorded on a Perkin-Elmer FT-IR Spectrum BX spectrophotometer. Melting points were determined on an Electrothermal melting point apparatus and are uncorrected.

Methods

Chemistry

General Procedure for the preparation of benzyl alcohol derivatives (2a-e)

The aldehydes (13.2 mmol) were placed in a 250 mL round bottom flask containing ethanol (4 mL) and stirred at room temperature to obtain homogenous solutions. The resulting solutions were cooled on an ice bath prior to the addition of the reducing agent. Subsequently NaBH_4 (13.2 mmol) dissolved in 1M NaOH (3.8 mL) was slowly added over a period of 10 minutes. The resulting

mixture was stirred at room temperature for 10 minutes after which it was cooled and then treated with 6M HCl dropwise until the evolution of H_2 gas stopped. The pH was checked to make sure the solution was acidic, and further stirred for another 10 minutes to allow the appropriate product to precipitate. The products were collected by filtration, washed twice with ice-cold water and then transferred to a dry piece of filter paper and air dried. But in the case of compound **2d**, the crude mixture was extracted with chloroform which after evaporation afforded the product as a film-like solid.

4-hydroxy-3-methoxybenzyl alcohol, 2a

White powder, 93% yield, mp 112-114°C. ^1H NMR (400MHz, $\text{DMSO}_4\text{-d}_6$) δ ppm 3.71 (3H, s, OCH_3), 4.37 (2H, s, CH_2), 5.14 (1H, s, OH), 6.70 (2H, d, $J = 4$, Ar-H), 6.88 (1H, s, Ar-H), 8.88 (1H, s, Ar-OH); ^{13}C NMR (100MHz, $\text{DMSO}_4\text{-d}_6$) δ ppm 39.52, 55.80, 63.36, 111.32, 1115.35, 119.51, 133.72, 145.54, 147.67; IR 3503, 1509, 1259 cm^{-1} .

4-hydroxybenzyl alcohol, 2b

White powder, 87% yield, mp 260-265°C; ^1H NMR (400MHz, $\text{DMSO}_4\text{-d}_6$) δ ppm 4.37 (2H, s, CH_2), 5.07 (1H, s, OH), 6.71 (2H, d, $J = 8$, Ar), 7.11 (2H, d, $J = 8$, Ar), 9.36 (1H, s, Ar-OH); ^{13}C NMR (100MHz, $\text{DMSO}_4\text{-d}_6$) δ ppm 39.52, 63.09, 63.12, 115.10, 115.12, 128.43, 128.46, 132.94, 156.41, 156.42; IR 3377, 1513, 1233 cm^{-1}

4-nitrobenzyl alcohol, 2c

Yellow powder, 93% yield, mp 131-134°C. ^1H NMR (400MHz, $\text{DMSO}_4\text{-d}_6$) δ ppm 3.56 (2H, s, CH_2), 5.61 (1H, s, OH), 7.57 (2H, d, $J = 8$, Ar), 8.17 (2H, d, $J = 4$, Ar); ^{13}C NMR (100MHz, $\text{DMSO}_4\text{-d}_6$) δ ppm 39.52, 62.21, 123.49, 127.25, 148.50, 150.89 IR 3503, 1505, 1230 cm^{-1}

4-methoxybenzyl alcohol, 2d

Film-like white solid; 94% yield; mp 212-215°C; ^1H NMR (400MHz, $\text{DMSO}_4\text{-d}_6$) δ ppm 3.71 (3H, s, OCH_3), 4.40 (2H, s, CH_2), 5.15 (1H, s, OH), 6.87 (2H, d, $J = 8$, Ar), 7.22 (2H, d, $J = 8$, Ar); ^{13}C NMR (100MHz, $\text{DMSO}_4\text{-d}_6$) δ ppm 39.52, 55.22, 62.79, 113.67, 128.21, 128.82, 131.14, 134.60, 158.36, IR 3326, 1513, 1244 cm^{-1} .

4-bromobenzyl alcohol, 2e

Yellow powder; 95% yield; mp 212-215°C; ^1H NMR (400MHz, $\text{DMSO}_4\text{-d}_6$) δ ppm 4.46 (2H, s, CH_2), 5.38 (1H, s, OH), 7.27 (2H, d, $J = 8$, Ar), 7.48 (2H, d, $J = 8$, Ar); ^{13}C -NMR (100MHz, $\text{DMSO}_4\text{-d}_6$) δ ppm 39.52, 62.40, 62.43, 119.81, 119.83, 128.79, 131.12, 142.06; IR 3272, 1483, 1203 cm^{-1} .

Antibacterial Assay

Sourcing of Bacteria for Assay

The bacteria used for the assay were obtained from the Department of Microbiology, Umaru Musa Yar'adua University, Katsina, Nigeria. The Gram-positive bacterium, *Staphylococcus aureus* was cultured in the medium prepared from mannitol salt agar. While the Gram-negative *Pseudomonas aeruginosa* was cultured in the medium prepared from nutrient agar.

Preparation of culture media

50 g of nutrient agar was dissolved in 1800 mL distilled water, autoclaved at 121°C for 15 minutes, spread into eighty (80) petri dishes and allowed to solidify. The Gram positive and negative bacteria were each inoculated into forty (40) prepared petri dishes (24).

Preparation of the test concentrations

Twenty milligrams (20 mg) of the compounds were dissolved in 1 mL of DMSO to afford the stock solution. Using serial double dilution, six different concentrations (10^{-1} mg/mL, 10^{-2} mg/mL, 10^{-3} mg/mL, 10^{-4} mg/mL, 10^{-5} mg/mL, 10^{-6} mg/mL) of each compound were prepared (24).

In vitro assay of the activity of the synthesized compounds on *Staphylococcus aureus* and *Pseudomonas aeruginosa* culture

Discs were made from filter paper and dipped into the different concentrations prepared from the five synthesized compounds. The discs were then transferred into the six (6) prepared petri dishes for the Gram-positive and negative bacteria which gave a total of thirty (30) petri dishes for each

bacterium. The activity for each compound was determined by measuring the zones of inhibition (mm) of each bacterium after 24 hours of incubation (24).

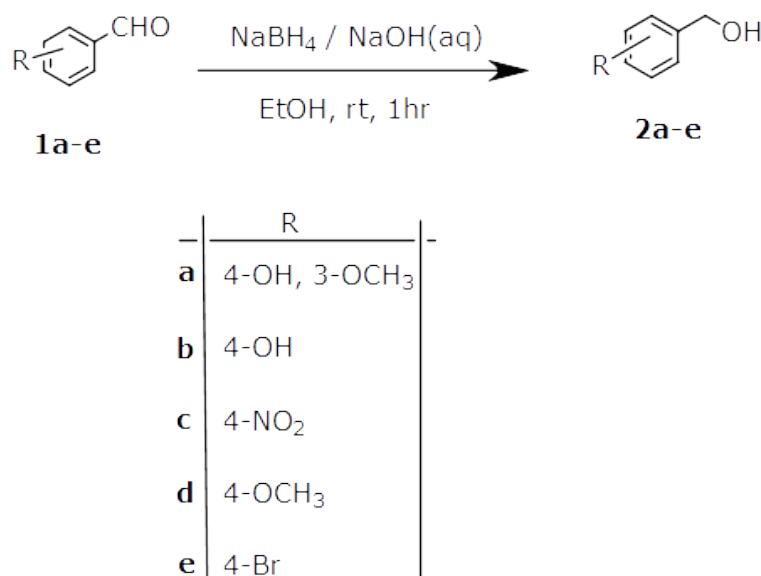
Molecular Docking studies

Discovery studio 2018 software was used to investigate the possible orientation and interactions of **2a-e** with glucosamine-6-phosphate GlcN-6-P synthase (25). The model structure of GlcN-6-P synthase, ID: 1XFF, was downloaded from the protein data bank. The target protein for molecular coupling was prepared based on the CHARMM force field with help of DS 2018. Structural and energy optimization of **2a-e** as ligands were prepared in DFT/B3LYP/6-31G base set using Gaussian 09 software. The docking studies estimate the binding site in the target model as GlcN-6-p synthase and the affinity of **2a-e** as ligands. CDOCKER was performed to place **2a-e** at the selected target binding sites. Docking results were evaluated with three-dimensional amino acid interactions and Binding energy values. Five possible structures of the ligands were generated and the best exposure was defined according to the lowest energy values for each complex.

RESULTS AND DISCUSSION

Chemistry

Benzyl alcohol derivatives, **2a-e** were synthesized (Scheme 1) by reacting the appropriate aldehyde with the basified solution of sodium borohydride, $\text{NaBH}_4/\text{NaOH}(\text{aq})$.



Scheme 1: Synthesis of benzyl alcohol derivatives.

Typically, the NaBH_4 solution in aqueous sodium hydroxide was slowly added to the appropriate

solution of aldehyde in ethanol. The resulting mixture was stirred at room temperature for a few minutes. This was followed with the addition of aqueous HCl which resulted in the evolution of hydrogen gas signifying the quenching of the excess NaBH₄. The corresponding alcohol product precipitated and collected by filtration. After additional washings, the product was air-dried and analyzed. The Nuclear magnetic resonance (NMR) spectroscopic data of compounds **2a-e** revealed the positions as well as the type of the proton and carbon in each compound. While the IR data gave the functional group present, particularly the hydroxyl (OH) functionality. Typically, the ¹H NMR spectrum of **2a** revealed a signal at 4.37 ppm assigned to the two protons of the methylene group, (-CH₂). Further upfield, the signal at 6.70 ppm appeared in the aromatic region of the spectrum and was integrated and assigned to the two aromatic protons closer to the methylene group. The ¹H NMR spectrum revealed that the signal at 3.71 ppm was for the three protons of the

methoxy group, (-OCH₃). Also the -OH proton attached to carbon-1 resonated at 5.14 ppm. The ¹³C NMR spectrum showed a distinct signal at 55.80 ppm which corresponded to the carbon atom of the methoxy group. The signal at 66.36 ppm was assigned to the methylene carbon, while the signals at 111.32 ppm, 115.35 ppm, 119.51 ppm, 133.72 ppm, 145.54 ppm and 147.67 ppm were assigned to the carbons of the benzene ring. From the IR spectrum of compound **2a**, it was deduced that the band at 3503 cm⁻¹ was due to the -OH stretching, while the C-O stretch (alcohol) was found at 1259 cm⁻¹.

Antibacterial Activity

The synthesized compounds were screened for *in vitro* antibacterial activity against Gram-positive and negative bacteria species, *Staphylococcus aureus* and *Pseudomonas aeruginosa* respectively using disc diffusion method. The result for the activity was expressed as the length of diameter of the zones of inhibition as given in Table 1.

Table 1: Antibacterial activity of benzyl alcohol derivatives^a

Compound	Organism	Zone of Inhibition (mm)					
		Conc (mg/mL)					
		10 ⁻¹	10 ⁻²	10 ⁻³	10 ⁻⁴	10 ⁻⁵	10 ⁻⁶
2a	<i>S. aureus</i>	08	00	00	00	00	00
	<i>P. aeruginosa</i>	27	11	11	09	08	08
2b	<i>S. aureus</i>	10	00	00	00	00	00
	<i>P. aeruginosa</i>	11	09	08	08	08	07
2c	<i>S. aureus</i>	08	08	07	00	00	00
	<i>P. aeruginosa</i>	07	00	00	00	00	00
2d	<i>S. aureus</i>	12	11	11	09	00	00
	<i>P. aeruginosa</i>	35	26	23	22	00	00
2e	<i>S. aureus</i>	00	00	00	00	00	00
	<i>P. aeruginosa</i>	12	11	07	00	00	00

^aAmoxicillin disc (30µg/mL): *S. aureus* = 24 mm; *P. aeruginosa* = 13 mm

Generally, the antibacterial activities of all the compounds appeared to be concentration dependant. In the case of Gram-positive bacterium (*S. aureus*), it was found that at the highest concentration (10⁻¹), compound **2d** showed a moderate activity (12 mm). While all other compounds relatively exhibited weak activities. Specifically, compounds **2b**, **2a** and **2c** have 10 mm, 08 mm and 08 mm zones of inhibition respectively. Compound **2e** did not show any activity at all concentrations. Regarding the Gram-negative bacterium (*P. aeruginosa*), all of the compounds except **2c** exhibited some degree of activities at more than one concentration. It was interestingly found that compound **2d**

demonstrated an excellent zone of inhibition (35 mm), and nearly matched the control antibiotic, amoxicillin even at a low concentration of 10⁻³ (23 mm). Compound **2a** has also showed a better activity at 10⁻¹ concentration (27 mm) than the control drug. Overall, it could be commented that compound **2d** appeared quite promising as it demonstrated the ability to inhibit the growth of both Gram-positive and negative bacteria.

Molecular Docking Studies

The enzyme glucosamine-6-phosphate (GlcN-6-P) synthase is responsible for the catalysis of first and rate-limiting step in hexosamine biosynthesis which give rise to uridine 5'-diphospho N-

acetylglucosamine (UDP-GlcNAc). Considering that UDP-GlcNAc is an essential building block in the fungal and bacterial cell walls, it thus becomes an interesting target for antifungal and antibacterial drug discovery (25).

Amoxicillin as the standard drug binds with GlcN-6-P synthase with binding affinity of -169.504 kcal/mol. The binding sites of amoxicillin on GlcN-6-P synthase target included twelve residues involved in the hydrogen bond, five residues involved in hydrophobic interaction and three residues involved in other interactions (Figure 2, left panel). There were two strongest hydrogen bonds that occurred with GLY99 with functional group O16 (bond length = 2.09381) and H27

(bond length = 2.72711). then with TRP24 through functional group H34 (bond length = 2.7042) and H41 (bond length = 2.9026). Similarly, another type of hydrogen bond designated as Carbon Hydrogen Bond has also occurred with GLY99 through functional group H43 (bond length = 2.10665).

The binding of compounds **2a-e** to the GlcN-6-P synthase active-site revealed that all the synthesized compounds fitted into the GlcN-6-N active-site receptor cavity, exhibited potential hydrogen-bonding as well as hydrophobic interactions with the proximal amino acid residues (Figure 2, right panel).

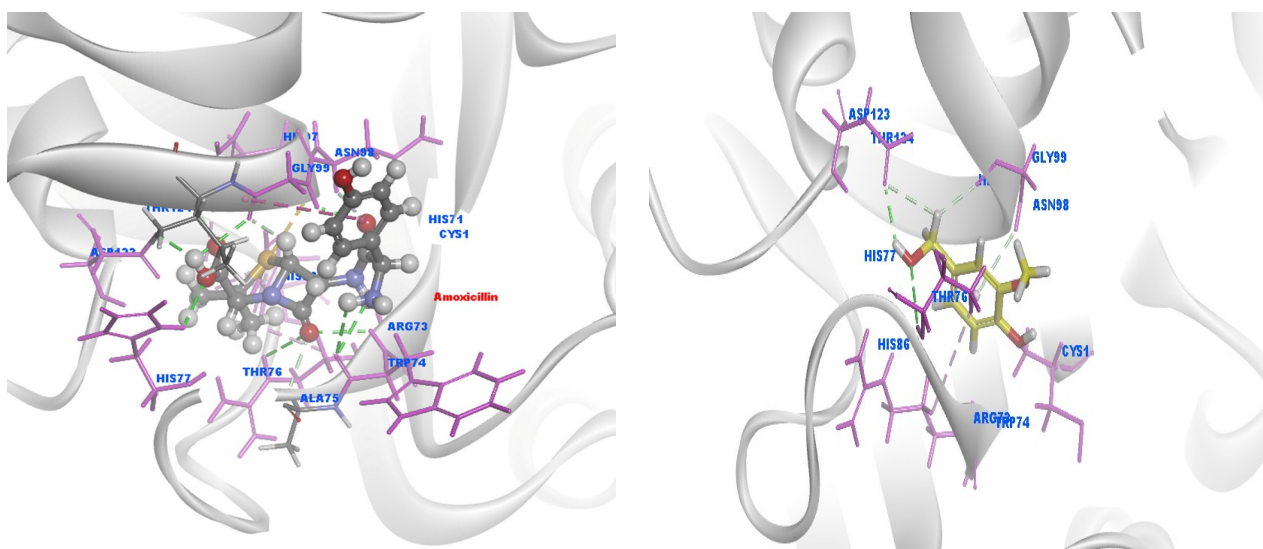


Figure 2. 3D interactions of amoxicillin as reference compound in the GlcN-6-P synthase binding region (left panel); Compound **2a** superimposed in the binding site of GlcN-6-P synthase (right panel).

Compound 2a was found to dock at seven sites (binding energy = -28.0758 kcal/mol). There were two hydrogen bond interactions with ASP123 through functional group H17 and H15 (bond length = 2.126 and 2.874 respectively). Another two hydrogen bonds were revealed with GLY99 through functional groups H15 and HN (bond length = 2.300 and 3.067 respectively). Other types of hydrogen bond as well as the hydrophobic interactions accounted for the remaining binding sites.

Compound 2b exhibited a total of nine docked interactions (binding energy = -34.4725 kcal/mol). One hydrogen bond with the residue ARG73 through functional group O9 (bond length = 2.456) and hydrophobic interaction with the same residue (bond length = 5.05659) were found. But for the residue TRP74, it was found that the conventional hydrogen bonds have occurred through functional groups O8 and H16 (bond length = 2.141 and

2.55708 respectively). The rest of the interactions have occurred with other residues through various functional groups.

Compound 2c docked with the enzyme (binding energy = -66.1382 kcal/mol) with lower energy than **2a** and **2b**. This might be due to the fact that there were some residues that each interacted multiple times with the compound. For instance, CYS1 interacted three times using different bonding types through functional groups O17, O18 and O19 (bond length = 4.4659, 1.86553 and 3.06222 respectively). Also the residue ARG73 doubly interacted using hydrogen bond through functional group O8 (bond length = 1.87337) and a hydrophobic interaction. Similarly, the residue ASP123 interacted using hydrogen bond through functional groups H15 and H13 (bond length = 3.08947 and 2.27452 respectively). In total, there were ten various interactions observed with compound **2c**.

Compound 2d (binding energy = -52.8901 kcal/mol) docked at a total of eight sites. It exhibited double interactions with ARG73, a hydrogen bonding through functional group O8 (bond length = 1.87521) and a hydrophobic interaction (bond length = 5.00408). The rest are single interactions with the remaining seven residues.

Compound 2e docked with the enzyme (binding energy = -74.6045 kcal/mol) at six sites which are fewer than all the compounds. It demonstrated double hydrophobic interactions with the residue HIS86 (bond length = 4.83674 and 4.91763). The remaining residues interacted singly through various bonding types.

Apparently, in terms of the binding energy, compound **2e** demonstrated the least value (-74.6045 kcal/mol) second to the standard drug, amoxicillin (-169.504 kcal/mol). This is in disagreement with the *in vitro* assay where compound **2d** exhibited the best zone of inhibition of the bacterial strains even better than the standard drug. Though it also possessed some significant low binding energy (-52.8901 kcal/mol). Mismatching of the results of biological assay with the docking studies had been observed in some works. For instance, a standard drug with the most potent *in vitro* bioactivity was found to exhibit a lesser docking score compared to the tested compounds and vice versa (26). Furthermore, some tested compounds exhibited similar *in vitro* bioactivities but appeared to differ in their docking results (27).

We opined that these discrepancies might be due to the fact that the tested compounds could be hitting targets other than the enzyme being studied. Other contributing factors might be due to the solubility issues, change in binding conformation of proteins, temperature and ionic strength of the buffer which influence entropy but often neglected in the docking software.

CONCLUSIONS

Benzyl alcohol derivatives were synthesized using simple NaBH₄ reduction. Although the compounds are known, but for the first time, their antibacterial activities have been investigated. And the results demonstrated that the activity was concentration dependant, and that the compounds were generally potent against *P. aeruginosa*. Only two of the compounds were active against *S. aureus*. In terms of broad spectrum activity, compound **2d** was found to exhibit a promising efficacy which surpassed that of the standard drug. In order to understand the mode of interaction of the compounds, an *in silico* studies were carried out by

docking the compounds against glucosamine-6-phosphate synthase (GlcN-6-P) as potential target. Interestingly, all the compounds fitted into the cavity and demonstrated a close alignment of the ligands with the enzyme active site. Of note was the binding energy of the most biologically active compound, **2d** which appeared to have a relatively favorable binding energy.

This work recommends further studies on the pharmacokinetic properties of compound **2d**. Based on the information obtained, it may also be subjected to *in vivo* studies to fully explore its potential as a possible lead that could be optimized to clinical trials in order to have a new antibacterial agent.

ACKNOWLEDGEMENT

Kabir Yahuza, Department of Microbiology, Umaru Musa Yar'adua University, Katsina, Nigeria is gratefully acknowledged for the antibacterial assay.

REFERENCES

1. Theuretzbacher U, Mouton JW. Update on antibacterial and antifungal drugs - Can we master the resistance crisis?. *Current Opinion in Pharmacology*. 2011;11: 429-32.
2. Walsh T, Toleman M. The emergence of pan-resistant gram-negative pathogens merits a rapid global political response. *Journal of Antimicrobial Chemotherapy*. 2012;67:1-3.
3. Awouafack MD, McGaw LJ, Gottfried S, Mbouangouere R, Tane P, Spiteller M, Eloff JN. Antimicrobial activity and cytotoxicity of the ethanol extract, fractions and eight compounds isolated from *Eriosema robustum* (Fabaceae). *BMC Complementary and Alternative Medicine*. 2013;13:1.
4. Srivastava J, Chandra H, Nautiyal AR, Kalra SJS: Antimicrobial resistance (AMR) and plant-derived antimicrobials (PDAMs) as an alternative drug line to control infections. *Biotechnology*. 2013;4:451-60.
5. Neu HC. The crisis in antibiotic resistance. *Science*. 1992;257:1064-73.
6. Lowy F. Antimicrobial resistance: the example of *Staphylococcus aureus*. *Journal of Clinical Investigation*. 2003;111:1265-73.
7. Varshney V, Mishra NN, Shukla PK, Sahu DP. Synthesis of nitroimidazole derived oxazolidinones as antibacterial agents. *European journal of medicinal chemistry*. 2010;45(2):661-6.

8. Gupta K, Pandeya SN, Pathak AK, Gupta A. Synthesis and Antibacterial Activity of Ciprofloxacin Derivatives. *Research Journal of Pharmacy and Technology*. 2011;4(2):308-14.
9. Ye FQ, Ding YM, Chen L, Ye S, Chen ZX. Synthesis and antibacterial activity of ciprofloxacin derivatives. *Acta pharmaceutica Sinica*. 2005;40(2):132-5.
10. Mokaber-Esfahani M, Eshghi H, Akbarzadeh M, Gholizadeh M, Mirzaie Y, Hakimi M, Lari J. Synthesis and Antibacterial Evaluation of New Pyrimidyl N-Ciprofloxacin Derivatives. *ChemistrySelect*. 2019;4(31):8930-3.
11. Rabbani MG, Islam MR, Ahmad M, Hossion AM. Synthesis of some NH-derivatives of ciprofloxacin as antibacterial and antifungal agents. *Bangladesh Journal of Pharmacology*. 2011;6(1):6-13.
12. Wang A, Xu Y. Synthesis and antibacterial activity of novel icariin derivatives. *Die Pharmazie-An International Journal of Pharmaceutical Sciences*. 2019;74(2):73-8.
13. Nitbani FO, Siswanta D, Sholikhah EN, Fitriastuti D. Synthesis and antibacterial activity 1-monolaurin. *Oriental Journal of Chemistry*. 2018;34(2):863.
14. Albert S, Horbach R, Deising HB, Siewert B, Csuk R. Synthesis and antimicrobial activity of (E) stilbene derivatives. *Bioorganic & medicinal chemistry*. 2011;19(17):5155-66.
15. Zhang HZ, He SC, Peng YJ, Zhang HJ, Gopala L, Tangadanchu VK, Gan LL, Zhou CH. Design, synthesis and antimicrobial evaluation of novel benzimidazole-incorporated sulfonamide analogues. *European journal of medicinal chemistry*. 2017;136:165-83.
16. Tiwari B, Pratapwar AS, Tapas AR, Butle SR, Vatkar BS. Synthesis and antimicrobial activity of some chalcone derivatives. *International Journal of ChemTech Research*. 2010;2(1):499-503.
17. Elenich OV, Lytvyn RZ, Blinder OV, Skripskaya OV, Lyavinets OS, Pitkovych Kh E, Obushak MD, Yagodinets PI. Synthesis and Antimicrobial Activity of 3-Phenyl-1-Methylquinolin-2-One Derivatives. *Pharmaceutical Chemistry Journal*. 2019; 52, 969-974.
18. Shingate BB, Hazra BG, Salunke DB, Pore VS, Shirazi F, Deshpande MV. Synthesis and antimicrobial activity of novel oxysterols from lanosterol. *Tetrahedron*. 2013;69(52):11155-63.
19. Paola V, Athina G, Kitka A, Matteo I, Franca Z. Synthesis and antimicrobial activity of novel 2-thiazolylimino-5-arylidene-4-thiazolidinones. *Bioorganic & Medicinal Chemistry*. 2006;14(11),3859-3864.
20. Kumar KP, Vedavathi P, Subbaiah KV, Reddy DV. Design, synthesis, spectral characterization and bioactivity evaluation of new sulfonamide and carbamate derivatives of 5-Nitro-1H-indazole. *Organic Communications*. 2017;10(3):239-249.
21. Abdel-Rahman RM, Ali TE. Synthesis and biological evaluation of some new polyfluorinated 4-thiazolidinone and α -aminophosphonic acid derivatives. *Monatshefte für Chemie-Chemical Monthly*. 2013;144(8):1243-52.
22. The Merck Index: An Encyclopedia of Chemicals, Drugs, and Biologicals (11th ed.), Merck, 1989, ISBN 091191028X, 1138.
23. NACDG Allergen: Benzyl alcohol. <https://www.the-dermatologist.com/article/7191> (accessed May 4, 2020).
24. Barakat A., Al-majid A.M., Shahidul M.I., Warad I., Masand V.H, Yousuf S., Choudhary M.I. (2016). Molecular structure investigation and biological evaluation of Michael adducts derived from dimedone. *Research on Chemical intermediates*. 2016; 42(5): 4041-4053.
25. Borowski E. Novel approaches in the rational design of antifungal agents of low toxicity. *Farmaco*. 2000; 55:206-208.
26. Patel MM, Patel LJ. Synthesis, molecular docking and antibacterial evaluation of some novel fluoroquinolone derivatives as potent antibacterial agents. *The Scientific World Journal*. 2014.
27. Alam MS, Jebins S, Rahman MM, Bari Md L. Biological and quantitative SAR evaluation and docking studies of (E)-N-benzylidenebenzo hydrazide analogues as potential antibacterial agents. *EXCLI Journal*. 2016; 15, 350-361.



Source Analysis of Heavy Metals and Polycyclic Aromatic Hydrocarbons from a Popular Dumpsite, Lagos State, Nigeria

Aminat Aderonke MOHAMMED^{1*}  , Pascal Okiroro INIAGHE²  ,
 Taofeeqat Omotayo ABU¹  , Mojeed Olalekan BELLO³  
 and Mariam Damilola ABDULKADIR¹  

¹Department of Industrial Chemistry, Faculty of Physical Science, University of Ilorin, Ilorin, Nigeria.

²Department of Chemistry, Faculty of Science, Federal University Otuoke, Nigeria.

³Department of Chemistry, Faculty of Science, University of Ilorin, Ilorin, Nigeria.

Abstract: In this study, landfill leachates and plants from Olusosun landfill in Ojota area of Lagos State, Nigeria were investigated. Physicochemical parameters, concentrations of heavy metals (HMs – Pb, Cd, Cr, Ni, Mn and Zn) and polycyclic aromatic hydrocarbons (PAHs) were determined in leachates while HMs and PAHs were determined in plants. Nitric and Perchloric acid mixtures were used for digesting both leachates and plant samples before quantification by atomic absorption spectrometry. Cold extraction was used for extracting PAHs and was quantified using gas chromatography-mass spectrometry. The range of results on HMs analysis were: leachates (mg/L) - Pb: 0.60 - 1.10, Cd: 0.04 - 0.05, Cr: 0.30 - 0.40, Ni: 0.13 - 0.19, Mn: 0.53 - 0.74 and Zn: 2.24 - 3.72; plants (mg/kg) – Pb: 1.0 - 6.0, Cd: 0.3 - 0.5, Cr: 0.0 - 4.0, Ni: 0.2 - 1.6, Mn: 10.1 - 41.2 and Zn: 0.0 - 13.2 respectively. For PAHs, the concentrations (mg/L) ranged from 0.10 - 0.24 and 0.09 - 0.31 mg/kg for leachates and plants respectively. Pearson correlation and principal component analysis identified the main sources of pollution in Olusosun landfill as anthropogenic. Proper management of the landfill is advised to prevent contamination of groundwater and surface waters.

Keywords: Landfill leachate, heavy metals, Olusosun, polycyclic aromatic hydrocarbons, plants.

Submitted: February 10, 2020. Accepted: May 15, 2020.

Cite this: MOHAMMED AA, INIAGHE PO, ABU TO, BELLO MO, ABDULKADIR MD. Source Analysis of Heavy Metals and Polycyclic Aromatic Hydrocarbons from a Popular Dumpsite, Lagos State, Nigeria. JOTCSA. 2020;7(2):489-504.

DOI: <https://doi.org/10.18596/jotcsa.687322>.

***Corresponding author. E-mail:** mohammed.aa@unilorin.edu.ng.

INTRODUCTION

Rapid urbanization and increasing population growth increase waste generation (1). Management of solid waste is an environmental challenge in many urbanized areas of the world (2). Landfilling is a standard method of waste disposal in several developing countries (3). However, the quality of many landfill sites is far from recommended standards mainly because the landfill systems are not correctly engineered and suited with the requisite leachate collection facilities and installation. These landfills thus serve as

repositories for many toxic substances (4,5). The extent of the threats posed by these landfills depends on the depth of the water table, the direction of the groundwater flow, permeability of the geologic strata, the concentration and level of pollutants in the leachates, and municipal solid waste type (6).

Leachates are mixtures of dissolved inorganic and organic compounds as well as microbes generated via the percolation of water through disposed of

solid wastes in a landfill (5). Several factors are responsible for leachates composition, including the kind of waste deposited on the landfill, degree of compaction, particle size, the composition of the wastes, the age of the landfill, the climate, hydrology of the site and other various peculiar conditions such as landfill design and type of liner used (7). Leachates can thus contain substantial amounts of organic (polycyclic aromatic hydrocarbons (PAHs), persistent organic pollutants (POPs), polychlorinated biphenyls (PCBs)) and inorganic (heavy metals) pollutants (8,9). They can also serve as indicators of environmental pollution through their ability to leak, percolate, and contaminate groundwater (10). There has been a growing interest regarding the possible harmful effects of PAHs released into the environment from anthropogenic sources as several PAHs have been reported to exhibit mutagenic and carcinogenic properties (3,11). Furthermore, uncontrolled inputs of heavy metals into the environment are unpleasant and undesirable due to non-biodegradability and bioaccumulation in soil, underground water, or plants; and the toxicity of several heavy metals is well documented in the literature. Leachate production via decayed solid waste materials mixed with precipitates of surface waters can bring about contamination of plants, surface and sub-surface water collection systems, and transportation of the contamination to the farther point of the ecosystem (12). While the volume of leachate generated in a landfill depends on the amount of solid waste deposited, water availability, condition of the landfill, and deposited refuse, as well as the soil condition (3). Leachate outflow and infiltration are reported to be the primary source of groundwater contamination from existing landfills (13). In Lagos metropolis, three dumpsites – Olusosun, Solus, and Abule-Egba – are in use, with Olusosun being the most active in terms of quantity of waste generated daily (14). There are

several reports on the state of different landfill sites in Lagos with particular interest on contamination of leachates and surrounding soils by heavy metals (10,15,16) and PAHs (17). However, the impact of heavy metals and PAHs from leachates on plants growing on the dumpsite is lacking. Therefore, in this study, the physicochemical properties, level of heavy metals and polycyclic aromatic hydrocarbons in leachates and plants from Olusosun dumpsite, were investigated

MATERIAL AND METHODS

Description of study area

Olusosun landfill is located in the Ojota area of Lagos State, Nigeria (Figure 1). It is known to be the most giant landfill in Lagos State and ranked among the biggest in the world. It has been in existence since 1978 (18), occupies 42 hectares of land, and receives approximately 40% of the total waste deposit Lagosians (19). It lies between latitude 6°. 20' N and longitude 3°. 20' E. Various human activities take place around this vicinity, including automobile repairs, petrol fueling stations (18), and motor parks. The landfill does not have any protective bottom layer constructed to protect leachate plumes from migrating into groundwater.

Sample collection

Five Leachate samples were collected from each of the three leachate streams flowing out of the base of the landfill to make a composite (L1). Another five leachate samples (L2) were collected from the main pond located within the vicinity of the landfill. Each of the composite samples was placed in 1L pre-cleaned plastic bottles with the cap securely tightened, preserved in ice-chest, taken to the laboratory, and stored in a refrigerator at 4 oC pending analysis. Sample bottles were rinsed with the leachates before sample collection.

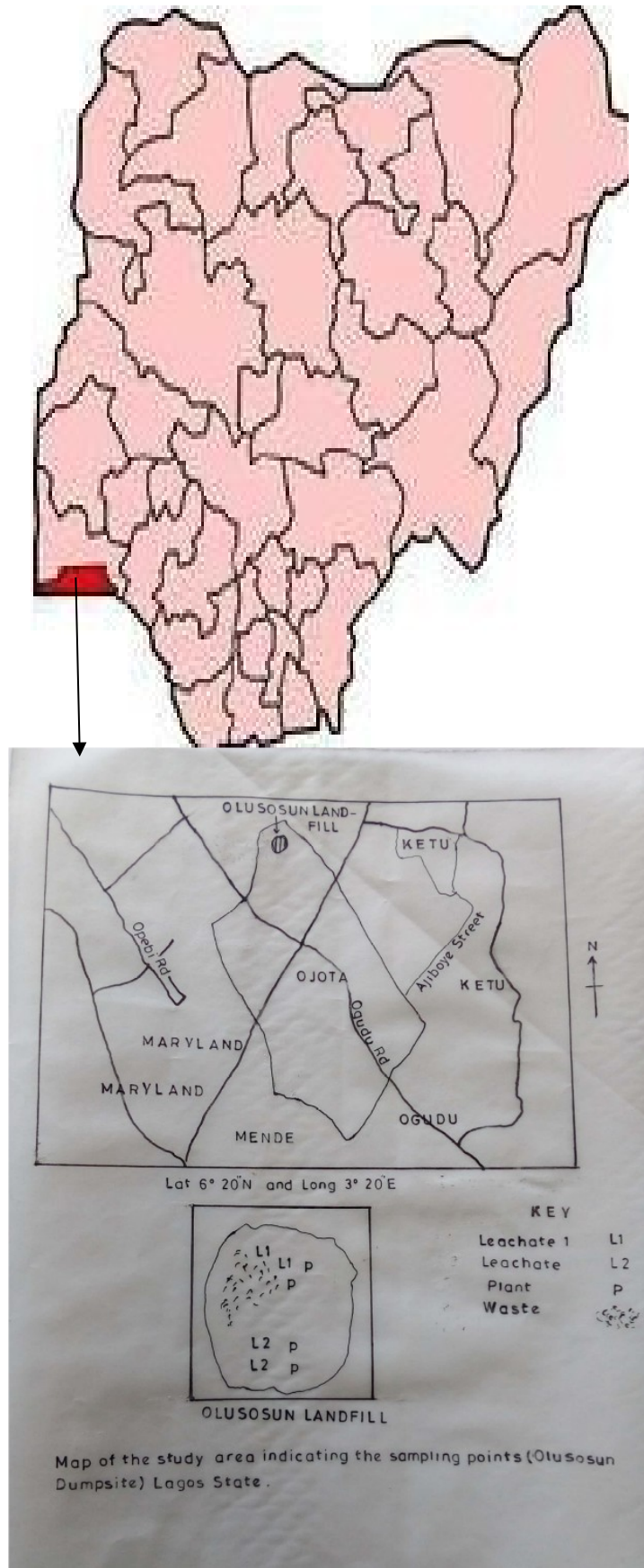


Figure 1: Map of the Study Area. (the red portion in the south-west quadrant).

The leaves of three different plants - pawpaw (*Carica papaya*, P₁), pepper (*Capsicum annum*, P₂) and banana (*Musa acuminata*, P₃) - were collected within the vicinity of L1 and L2. The collected plant leaves were placed in pre-cleaned polyethylene bags and transported to the laboratory. The plants were identified at the Department of Plant Biology, University of Ilorin, Nigeria. In the laboratory, the leaves were rinsed with tap water and distilled water and air-dried at room temperature. The dried samples were ground using an agate mortar and pestle and sieved using a 2 mm mesh size sieve.

Physico-chemical parameters

The pH of composite leachate samples was measured in-situ using a portable digital pH meter (pHep® Hanna, USA), which had been previously calibrated with buffer solutions of pH 4 and 7, respectively. The temperature was also determined in-situ using a thermometer. Electrical conductivity (EC) was measured with a conductivity meter calibrated with a potassium chloride solution. Colour was determined using colorimetry. Total dissolved solids (TDS) was determined gravimetrically by evaporating a known volume of leachate to dryness in a pre-weighed crucible on a steam bath. Total suspended solids (TSS) were also determined gravimetrically by evaporating a known volume of filtered leachate to dryness in a pre-weighed crucible on a steam bath. Biochemical oxygen demand (BOD), chemical oxygen demand (COD), chloride (Cl⁻), and hardness were determined titrimetrically. The concentration of sulfate (SO₄²⁻) was determined turbidimetrically, phosphate (PO₄³⁻) was determined via the colorimetric method, and nitrate (NO₃⁻) was determined using the brucine method (20).

Analysis of heavy metals in leachates and plant samples

50 mL of each leachate samples were treated with 10 mL of concentrated HNO₃ and 5 mL of HClO₄. The entire mixture was heated in a digestion block at 125 °C until white fumes are observed to confirm the complete utilization of the acid, and the volume was reduced to about 25 mL. The mixture was removed from the block, cooled, filtered using a Whatman No. 40 filter paper, transferred to a 50 mL volumetric flask and made up to mark with distilled water (21). Atomic absorption spectrophotometer (Buck Scientific Model 210 VGP, USA) was then used for quantification of the following metals: Pb, Cd, Cr, Ni, Mn, and Zn. All samples were prepared in duplicate.

For plant samples, approximately 5.00 g of each of the powdered leaf samples was placed in a 25 mL conical flask. 10 mL of concentrated HNO₃ was added, followed by 5 mL of HClO₄. The contents of the flask were heated at 150 °C for 1 hour in a fuming hood and then cooled to room temperature. After that, 20 mL of distilled water was added, and

the mixture was filtered using filter paper in a 50 mL volumetric flask (21). Atomic absorption spectrophotometer was also used for quantification of the following metals: Pb, Cd, Cr, Ni, Mn and Zn. All samples were prepared in duplicate.

Analysis of PAHs in leachate and plant leaves

For extraction and clean-up of PAHs in leachates, 100 mL of thoroughly mixed leachate sample was filtered using clean cotton wool to attain a clear solution without particles into a separating funnel. A 100 mL mixture of n-hexane and dichloromethane 1:1 (v/v) was added, and the separating funnel was left undisturbed on a retort stand for about 30 minutes. The separating funnel was then opened to drain the water phase while the organic phase was collected in a glass funnel containing 20 g of anhydrous sodium sulfate plugged with a ball of cotton wool. A second extraction was carried out on the organic phase and was re-extracted using a 50 mL mixture of dichloromethane and n-hexane 1:1 (v/v). The extract was concentrated to an absolute 20 mL prior to the determination of PAHs (22,23).

For plant leaves, a 2.00 g of each ground plant sample was weighed into a clean extraction container. 10 mL of dichloromethane was added and left for 20 minutes. Another 20 mL of dichloromethane was added again to the mixture and was then filtered into an extraction bottle. The extracted sample was concentrated to 3 mL for separation. The column was packed with 1 g of moderately packed cotton wool. 3 g of dried activated silica gel was then poured into the column, and 0.6 mL of sodium sulfate was added. The column was rinsed with 20 mL of dichloromethane to allow it to run through the silica gel. Pre-elution with dichloromethane (20 mL) was allowed to flow through the column for about 2 minutes, and 3 mL of the plant sample was poured immediately into the column. The stop-cork of the chromatographic column was opened, and the eluent was collected at intervals with a 10 mL graduated cylinder. Due to exposure of sodium sulfate to air, dichloromethane was added at intervals to the column in increments of 5 mL. The concentrated fractions were then transferred in a glass bottle with rubber crimps caps for GC-MS analysis (24). All samples were prepared in duplicate.

Extracts from leachates and plant leaves were analyzed for 16 PAHs by gas chromatography-mass spectrometry (GC-MS, Agilent 7890B GCMS, USA).

Data Analysis

All the experimental data were subjected to further statistical analyses such as Analysis of variance (ANOVA), Pearson correlation matrix, and principal component analysis to determine the source of pollution from the studied landfill (Olusosun) using Origin pro 2018.

RESULTS AND DISCUSSION

Physico-chemical properties of leachate

Physico-chemical properties of leachates obtained from Olusosun dumpsite are presented in Table 1. The pH values, ranging from 7.3 - 7.5, indicates slight alkalinity of the leachates. Leachate pH values are reported to increase with age and are usually greater than 7 (10,17,25). Values of pH greater than 7 may be attributed to high salinity, an increase in the utilization of unionized free volatile fatty acids by bacteria, and a decrease in short-chain fatty acids (26). The pH also serves as an indicator of the chemical state in which an environmental species will be present, and pH-dependent species such as heavy metals may become environmentally available at low pH (27). Hence, the metals' bioavailability might be low. Similarly, alkaline values have been reported for landfill leachates (10,16,17,26). The TDS values ranged from 5880 - 6500 mg/L. High TDS values imply the presence of a large concentration of soluble ions, leaching of the ions, and dissolved organic matter from the landfill caused by the hydrogeological, physical, and chemical conditions from the landfill, including chlorides, carbonates, phosphates, nitrates among others (27). The range of concentration values for TSS, BOD, COD, NO⁻, PO₄³⁻, Cl⁻, TH and SO₄²⁻ are: 1260-1805 mg/L, 640-

658.2 mg/L, 2788-2866 mg/L, 18.4-21.2 mg/L, 9.0-9.8 mg/L, 3439-3471 mg/L, 7305-7670 mg/L and 107-150 mg/L, respectively. All but SO₄²⁻ exceeded their respective limits set by WHO (29) and NESREA (30). A high BOD level implies that the leachate cannot undergo self-purification, and therefore require some form of pre-treatment. Similarly, a BOD/COD ratio greater than 0.2 indicates that the leachate is old and relatively stable (17). For Cl⁻, no harmful level is reported in humans, but high concentrations exceeding the 250 mg/L permissible limit may be harmful to and cause damage to plants. The concentration of sulfate at high amounts in landfill leachate is reported to depend on depends on the following factors: landfill age, composition of waste, the biological, physical, and chemical composition (31). Nitrate level concentration values are important factors in determining the extent of pollution in leachates. Phosphate at high concentrations can lead to oxygen depletion of water bodies via eutrophication with a response to an increasing level of nutrients due to the presence of phosphates and nitrates (32). The color of the leachates was found to be very black, which is a result of the changes in the oxidation state of Fe²⁺ (ferrous ions) to Fe³⁺ (ferric ions). The ferric ion forms ferric hydroxide colloids and fulvic complexes contributing to the blackish color of the leachates (26).

Table 1: Physico-chemical properties of leachates

Parameters	Leachates			
	L ₁	L ₂	*	**
Color	Black	Black	Colorless	-
pH	7.5±0.10	7.3±0.10	6.0 - 9.0	6.5 - 9.5
EC (µS/cm)	724.0±0.40	740.0±0.90	-	1000.0
TDS (mg/L)	6500.0±0.90	6880.0±1.30	500.0	500.0
Temperature (°C)	17.0±0.90	18.7±0.10	40.0	-
BOD (mg/L)	640.0±0.51	658.2±0.90	50.0	-
COD (mg/L)	2788.0±0.20	2868.0±1.10	90.0	-
Cl ⁻ (mg/L)	3439.0±0.80	3471.0±1.11	250.0	250.0
TH (mg/L)	7305.0±0.90	7670.0±0.71	-	180.0
TSS (mg/L)	1260.0±1.10	1505.0±0.92	25.0	-
SO ₄ ²⁻ (mg/L)	107.0±0.30	150.0±0.90	250.0	250.0
NO ₃ ⁻ (mg/L)	18.4±0.01	21.2±0.20	10.0	50.0
PO ₄ ³⁻ (mg/L)	8.0±0.50	9.8±0.03	2.0.0	-

*NESREA, 2011
 **WHO, 2007

Table 2: Pearson correlation matrix of the physicochemical parameters of leachate from Olusosun Landfill

	pH	EC	TDS	Temp.	BOD	COD	Cl⁻	TH	TSS	SO₄²⁻	NO₃⁻	PO₄³⁻
pH	1											
EC	-0.4096	1										
TDS	-0.8504	0.8283	1									
Temp.	-0.5903	0.9782	0.9267	1								
BOD	-0.8361	0.8429	0.9996	0.9363	1							
COD	-0.7219	0.9270	0.9780	0.9847	0.9832	1						
Cl ⁻	-0.8072	0.8692	0.9970	0.9530	0.9987	0.9912	1					
TH	-0.7665	0.8999	0.9897	0.9709	0.9932	0.9978	0.9978	1				
TSS	-0.8085	0.8681	0.9972	0.9523	0.9988	0.9909	0.9965	0.9977	1			
SO ₄ ²⁻	-0.7672	0.8994	0.9899	0.9706	0.9933	0.9977	0.9979	0.9968	0.9978	1		
NO ₃ ⁻	-0.9209	0.7329	0.9883	0.8583	0.9838	0.9346	0.9735	0.9563	0.9740	0.9565	1	
PO ₄ ³⁻	-0.9226	0.7298	0.9876	0.8560	0.9830	0.9330	0.9724	0.9549	0.9729	0.9552	0.9999	1

Two-tailed significance is used.

The physicochemical parameters for all the leachates were analyzed with Origin pro 2018 using one-way ANOVA (Analysis of variance), which shows that all the physicochemical parameters analyzed are significantly different ($p > 0.05$ level). Also, Pearson correlation was used to analyze the physicochemical parameters, as shown in Table 2 above. The pH shows a negative correlation with EC ($p = 0.7313$), TDS ($p = 0.3527$), Temp. ($p = 0.5980$), BOD ($p = 0.3697$), COD ($p = 0.4865$), TH ($p = 0.4440$), TSS ($p = 0.4006$), Cl^- ($p = 0.4020$), SO_4^{2-} ($p = 0.4434$), NO_3^- ($p = 0.2550$), PO_4^{3-} (0.2521). There was a positive correlation among other physicochemical parameters with which includes EC vs. TDS, SO_4^{2-} vs. NO_3^- , TH vs. PO_4^{3-} , BOD vs. Cl^- , Temp. vs. SO_4^{2-} , COD vs. TH, Cl^- vs. TH, TDS vs. Temp., TDS vs. BOD, Temp. vs. COD, EC vs. Temp., Cl^- vs. SO_4^{2-} , BOD vs. TSS, TDS vs. PO_4^{3-} , COD vs. SO_4^{2-} , TDS vs. TSS, BOD vs. COD, Temp. vs. TH, TSS vs. NO_3^- , BOD vs. TH, EC vs. NO_3^- , Cl^- vs. Temp., BOD vs. TSS, EC vs. TSS, TDS vs. NO_3^- , TH vs. SO_4^{2-} , Temp. vs. PO_4^{3-} , TH vs. NO_3^- , TSS vs. SO_4^{2-} , EC vs. BOD, and NO_3^- vs. PO_4^{3-} . With the results from Pearson correlation,

it can be deduced that the landfill is heavily polluted with diverse kinds of wastes dumped from the residents in this State.

Heavy metal concentrations in leachates and plant leaves

The concentrations of heavy metals (mg/L) in leachate samples were: 0.60 - 1.10 for Pb, 0.04 - 0.05 for Cd, 0.30 - 0.40 for Cr, 0.13 - 0.19 for Ni, 2.24 - 3.72 for Zn and 0.53 - 0.74 for Mn, respectively as shown from Figure 2 below. The increasing order of metals concentration metals in the leachate samples followed the order: Zn>Pb>Mn>Cr>Ni>Cd. These values are similar to the results obtained elsewhere (17) but slightly higher than those reported elsewhere (28). All analyzed metals in leachates samples exceeded their respective permissible limits set by WHO (29) and NESREA (30) except Cd, which was lower than the NESREA (30) permissible limit. The presence of heavy metals in both leachates can be attributed to the type of waste being deposited on the landfill site, which in turn is a function of the industrialized nature of the study areas.

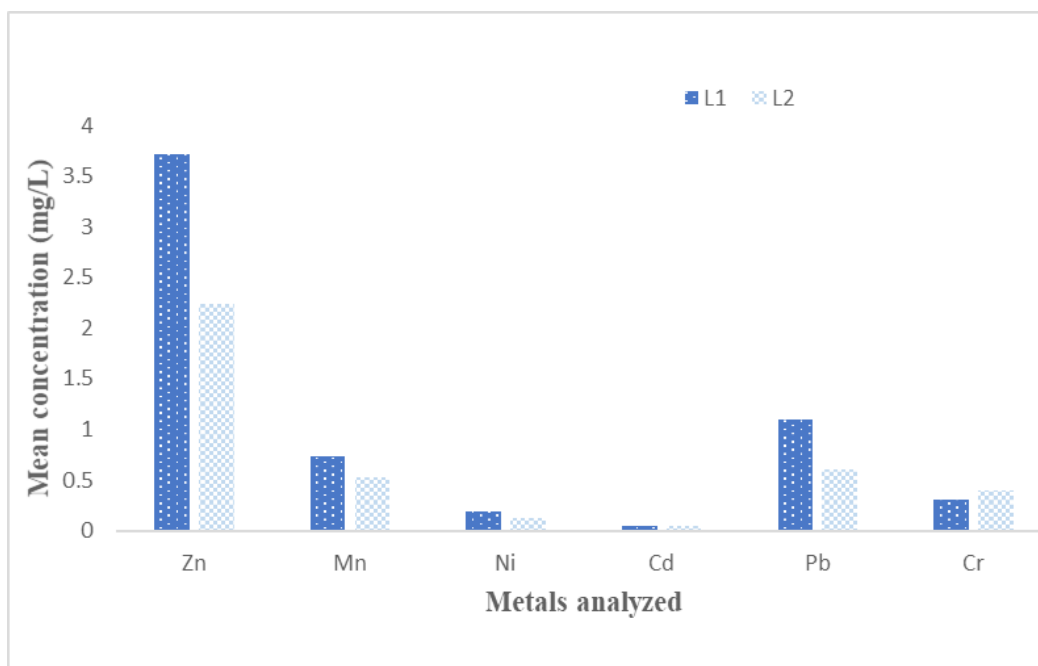


Figure 2: Metal concentrations in leachate samples.

The mean concentrations of heavy metals in plant samples analyzed are shown in Figure 3 below. The increasing order of metals concentration in plant samples followed the order: Mn>Zn>Pb>Cr>Ni>Cd.

The concentration of heavy metals in all plant samples were all below their respective permissible limits set by WHO (33) (50 mg/kg for Zn, 10 mg/kg for Ni, 0.02 mg/kg for Cd, 2 mg/kg for Pb and 1.3 mg/kg for Cr).

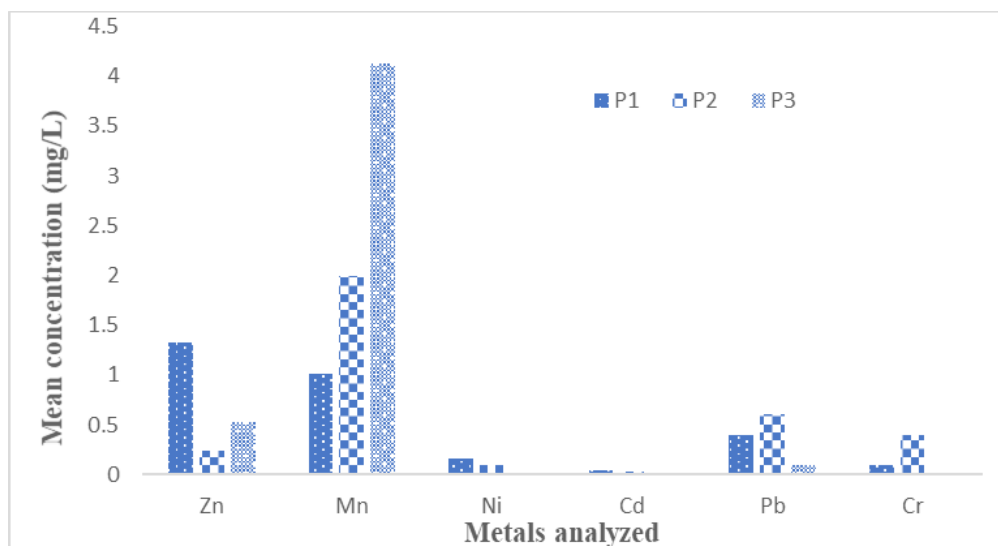


Figure 3: Metal concentrations in plant leaves.

Table 3: Pearson correlation matrix of heavy metals from leachates Samples in the Olusosun landfill.

	Zn	Mn	Ni	Cd	Pb	Cr
Zn	1					
Mn	0.9411	1				
Ni	0.7827	0.9471	1			
Cd	0.7278	0.4530	0.1429	1		
Pb	0.8967	0.9936	0.9774	0.3491	1	
Cr	0.1477	-0.1956	-0.5000	0.7857	-0.3054	1

Two tailed (p > 0.05 level)

Table 4: Pearson correlation matrix of heavy metals from the plant samples in the Olusosun landfill.

	Zn	Mn	Ni	Cd	Pb	Cr
Zn	1					
Mn	-0.5434	1				
Ni	0.7067	-0.9780	1			
Cd	0.7067	-0.9780	0.6215	1		
Pb	-0.1469	-0.7506	0.5960	0.5960	1	
Cr	-0.5171	-0.4376	0.2402	0.2402	0.9226	1

Two tailed (p > 0.05 level)

From Table 3 above, there is a strong positive correlation between Zn with other metals such as Mn (p = 0.2197), Ni (p = 0.4277), Cd (p = 0.4811), Pb (p = 0.2919) and Cr (p = 0.9057). Also, there is a positive correlation in Mn versus Ni (p = 0.2080), Mn versus Pb (p = 0.0723), Ni versus Pb (p = 0.1357), and Cd versus Cr (p = 0.4246) and slight correlation between Ni versus Cd (p = 0.9087), Mn versus Cd (p = 0.7007) and Cd versus Pb (p = 0.7730). A negative correlation was identified between Mn versus Cr (p = 0.8747), Ni versus Cr (p = 0.6667) and Pb versus Cr (p = 0.8024). The Pearson correlation of the plant samples is shown in Table 4 above. A negative correlation was identified between Zn vs. Mn (p = 0.6343), Zn vs. Cr (p = 0.6540), Mn vs. Ni (p = 0.1339), Mn vs. Pb (p = 0.4596), Mn vs. Cr (p = 0.7117) and slight correlation exist between Ni vs. Pb (p = 0.8456) and very strong correlation exist between Zn vs. Ni and Zn vs. Cd having the same

values (p = 0.5004), Ni vs. Cd, Cd vs. Pb are also having the same values (p = 0.5935). The correlation between the metals analyzed was from a similar source (34), and this confirmed that the landfill was contaminated with different composition of solid wastes dumped on this landfill, which percolated into soil and then contaminated the plants grown from this site. The relatively high concentrations recorded for Mn in plant leaves compared with leachate concentrations could be attributed to different degrees in bioaccumulation of Mn by the different plant laves studied.

The eigenvalues obtained from any data are used to determine components that are retained. A set of data has eigenvalues greater than unity indicates a component that is retained, but when it is less than unity, the component is not retained (35, 36). The scree plot of heavy metals in leachates and plants were shown from Figure 4 below. There were five

components from each scree plot of leachates and plants. Components 1 and 2 are retained with eigenvalues of 4.00 and 1.97 respectively for both leachates and plants, while other components (3-6) are not retained. However, components 1 and 2 are retained for leachates and plants because the eigenvalues are greater than unity, as shown in Figure 5. It is similar to the previous research from the assessment of heavy metals from roadside dust in Ilorin (36). The two principal components analysis (PC 1 and PC 2) from heavy metals in leachate samples has a variance of 66.99 % and 33.01%, respectively, as shown from Figure 6 below.

In the plant samples, the PC 1 and 2 have 66.05% and 33.95% variance, respectively, as shown from

Figure 6 below. PC 1 is strongly correlated with these metals (Zn, Mn, Ni, Cd, Pb) in leachates and negatively correlated with Cr while PC 2 is strongly correlated with Zn, Cd, and Cr, but negatively corrected with Mn, Ni, and Pb as shown from Table 5 below. Table 6 below indicates the PC 1 and PC2 of heavy metals in plant samples. PC 1 is strongly correlated with Zn, Ni, Cd, Pb, and Cr but negatively correlated with Mn. While PC 2 is strongly correlated with Mn, Pb, and Cr but negatively correlated with Zn, Ni, and Cd. With the statistical data from the principal component analysis, it can be deduced that the heavy metals from this landfill are heavily polluted by anthropogenic sources (17, 34, 37).

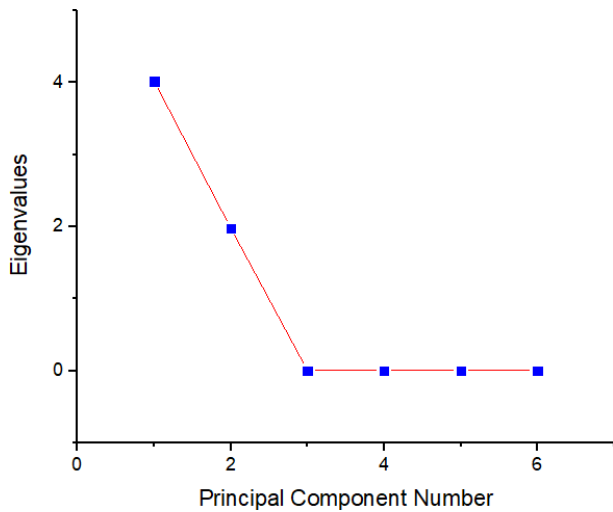


Figure 4: Screen plot of heavy metals in both plants and leachate samples.

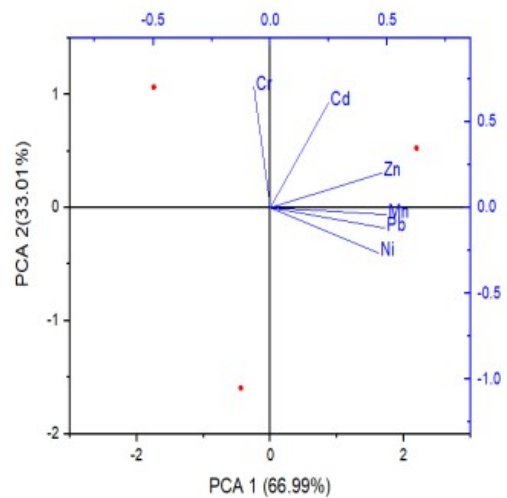


Figure 5: Bi-plot of heavy metals in plants leachates.

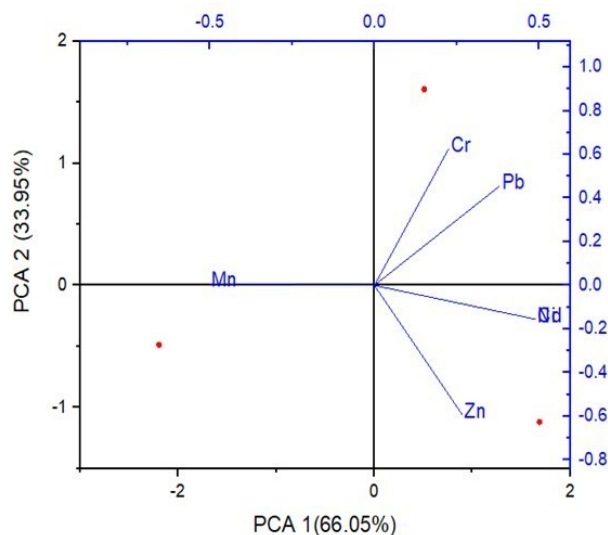


Figure 6: Bi-plot of heavy metals in leachates from Olusosun landfill.

Table 5: Extracted eigenvalues of the heavy metals in leachate samples.

	Coefficients of PC1	Coefficients of PC2
Zn	0.4781	0.2026
Mn	0.4980	-0.0397
Ni	0.4627	-0.2653
Cd	0.2504	0.6145
Pb	0.4916	-0.1198
Cr	-0.0701	0.7035

Table 6: Extracted eigenvalues of the heavy metals in leachate samples.

	Coefficients of PC1	Coefficients of PC2
Zn	0.2675	-0.5931
Mn	-0.5023	0.0091
Ni	0.4899	-0.1551
Cd	0.4899	-0.1551
Pb	0.3813	0.4562
Cr	0.2256	0.6260

Concentrations of PAHs in leachates and plant leaves

Table 7 shows the concentration of PAHs in leachate samples. Sixteen PAHs are recognized by the United States Environmental Protection Agency (EPA) and are classified as low molecular weight (LMW, petrogenic), medium molecular weight (MMW), and high molecular weight (HMW, pyrogenic). The following PAHs were detected in leachate and plant samples: HMW - chrysene, benzo(b)fluoranthene, and benzo(a)anthracene; MMW - pyrene and fluoranthene and LMW - phenanthrene. The concentration range (mg/L) for the detected PAHs in landfill leachates were: LMW: 0.17 - 0.22; MMW: 0.15 - 0.24 and HMW: 0.10 - 0.19 mg/L, respectively. The presence of LMW PAHs in the environment usually results from the emission of oil spills, noncombustible matter, and agricultural sources, while MMW and HMW PAHs are emitted mainly from sources like incomplete combustion/pyrolysis of organic matter and solid wastes, and incorporated into landfill leachate by rainwater (3). Municipal and waste discharge from industrial sites are part of the factors causing a high concentration of PAHs in leachates (38). The result of PAHs concentration in plant leaf samples is shown in Table 8. The concentration of PAHs in plant samples ranged between 0.09 - 0.31 mg/kg. Since P1 is far away and P2 and P3 are close, no PAHs were detected in P1, and some levels of PAH were found in P2 and P3.

Table 7: Concentration of polycyclic aromatic hydrocarbons found in leachates.

PAHs	Concentration (mg/L/)		Concentration (mg/L/)		
	L1	L2	PAHs	L1	L2
Anthracene	BDL	BDL	Pyrene	0.15	0.19
Acenaphthene	BDL	BDL	Perylene	BDL	BDL
Phenanthrene	0.22	0.17	Chrysene	0.10	0.13
Acenaphthylene	BDL	BDL	Benzo(b)fluoranthene	0.19	0.15
Naphthalene	BDL	BDL	Benzo(k)fluoranthene	BDL	BDL
Fluorene	BDL	BDL	Benzo(a)anthracene	0.14	0.16
Fluoranthene	0.21	0.24	Indeno(1,2,3-cd)pyrene	BDL	BDL
		$\Sigma=1.01$	$\Sigma= 1.04$		

Table 8: Concentration of PAHs in plant leaves.

PAHs	Concentration (mg/kg)		
	P1	P2	P3
Naphthalene	BDL	BDL	BDL
Acenaphthylene	BDL	BDL	BDL
Acenaphthene	BDL	BDL	BDL
Fluorene	BDL	BDL	BDL
Phenanthrene	BDL	0.31	0.19
Anthracene	BDL	BDL	BDL
Fluoranthene	BDL	0.16	0.14
Pyrene	BDL	0.24	0.11
Benz(a)anthracene	BDL	0.17	0.14
Chrysene	BDL	0.09	0.13
Benzo(b)fluoranthene	BDL	0.11	0.17
Benzo(k)fluoranthene	BDL	BDL	BDL
Benzo(a)pyrene	BDL	BDL	BDL
Indeno(1,2,3-cd)pyrene	BDL	BDL	BDL
Dibenzo(a,h)anthracene	BDL	BDL	BDL
Benzo (g,h,i) perylene	BDL	BDL	BDL

$\Sigma=0.0000 \Sigma= 1.08 \Sigma= 0.88$

Table 9: Pearson correlation matrices of PAHs from leachate samples in the Olusosun landfill.

	Phe	Flu	Pyr	Chy	Benzo(b)F	Benzo(a)A
	1					
Phe	0.0576	1				
Flu	0.8572	0.5636	1			
Pyr	0.8934	0.5000	0.9972	1		
Chy	0.4018	-0.8910	-0.1273	-0.0524	1	
Benzo(b)F	-0.7825	0.5766	-0.3500	-0.4193	-0.8846	1
Benzo(a)A	0.7924	0.6547	0.9934	0.9820	-0.2402	-0.2402

Phe- Phenanthrene; Flu- Fluoranthene; Pyr- Pyrene; Chy- Chrysene; Benzo (b)- Benzo(b)fluoranthene; Benzo(a)A- Benzo(a)anthracene

Table 10: Pearson correlation matrix of PAHs from plant samples in the Olusosun landfill.

	Phe	Flu	Pyr	Chy	Benzo(b)F	Benzo(a)A
Phe	1					
Flu	0.9477	1				
Pyr	0.7341	0.4790	1			
Chy	0.9995	0.9368	0.7559	1		
Benzo(b)F	-0.3192	3.61E-17	-0.8778	-0.3499	1	
Benzo(a)A	-0.4039	-0.0908	-0.9177	-0.4336	0.9959	1

The Pearson correlation of PAHs in leachates in shown from Table 9 above. A positive correlation exists between some PAHs found in leachates with significant difference >0.05 which includes: Pyr/Phe, Flu/Phe, Pyr/Flu, Chy/Phe, Benzo(a)A/flu, Benzo(b)F/ Flu, Benzo(a)A /Phe and a negative correlation exists between Benzo(b)F /Phe, Chy/Flu, Benzo(b)F/Phe, Benzo(b)/ Pyr, Benzo(a)A/ Benzo(b)F and Chy/Pyr. Also, a positive correlation

exists between Phe/Flu, Chy/Phe, Flu/Pyr, Benzo(b)F/ Benzo(a)A Pyr/Phe, Chy/Flu, Phe/Chy, Pyr/Chy, and negative correlation occurred between Phe/ Benzo(b)F, Phe/ Benzo(a)A, Chy/ Benzo(b)F, Benzo(a)A, Chy, Benzo(a)A/Pyr with a significant difference >0.05 in plants as shown in Table 10 above. It indicates that the source of contamination in this study is a result of different anthropogenic activities that take place in the landfill.

Table 11: Extracted eigenvalues of the PAH in leachate samples.

	Coefficients of PC1	Coefficients of PC2
Phenanthrene	0.4812	-0.1872
Fluoranthene	0.4716	0.2317
Pyrene	0.4825	0.1806
Chrysene	0.1013	-0.6957
Benzo(b)fluoranthene	-0.3174	0.5481
Benzo(a)anthracene	0.4498	0.3072

Table 12: Extracted eigenvalues of the PAH in plant samples removed from the plants.

	Coefficients of PC1	Coefficients of PC2
Phenanthrene	0.4415	0.3221
Fluoranthene	0.3495	0.5156
Pyrene	0.4706	-0.2109
Benz(a)anthracene	0.4483	0.3004
Chrysene	-0.3454	0.5217
Benzo(b)fluoranthene	-0.3757	0.4727

The variance of PAHs in leachate and plant samples analyzed are 66.98 %, 33.02 %; 69.02%, 30.98% for PC1 and PC2, respectively, as shown from Figures 7 and 8 below. The scree plot of PAHs in plants and leachates proved the components that are retained, as shown in Figure 8 below. Components 1 (4.34) and 2 (1.77) are retained because it is greater than unity (35, 36) while other components (3, 4 and 5) are not retained. There is a strong positive correlation between the PAHs in PC1 for leachate samples includes; Phenanthrene, Fluoranthene, Pyrene, Chrysene, and Benzo(a)anthracene but negative correlation occurred at Benzo(b)fluoranthene. While the positive correlation was seen between the PAHs in PC2 includes; Fluoranthene, pyrene,

Benzo(b)fluoranthene and Benzo(a)anthracene but negative correlation exists in Phenanthrene and Chrysene as shown from Table 11 above. For plant samples, a positive correlation exists between Phenanthrene, Fluoranthene, pyrene, Benzo(a)anthracene, and a negative correlation exists between Chrysene and Benzo(b)fluoranthene for PC1. A positive correlation exists between these PAHs (Phenanthrene, Chrysene, Fluoranthene, Benzo(b)fluoranthene and Benzo(a)anthracene) and pyrene only had a negative correlation in PC2 as shown from Table 12 above. However, the statistical data from this study confirmed that the source of PAHs was through resistance to environmental degradation, surface run-off (17), and type of waste deposited on the landfill.

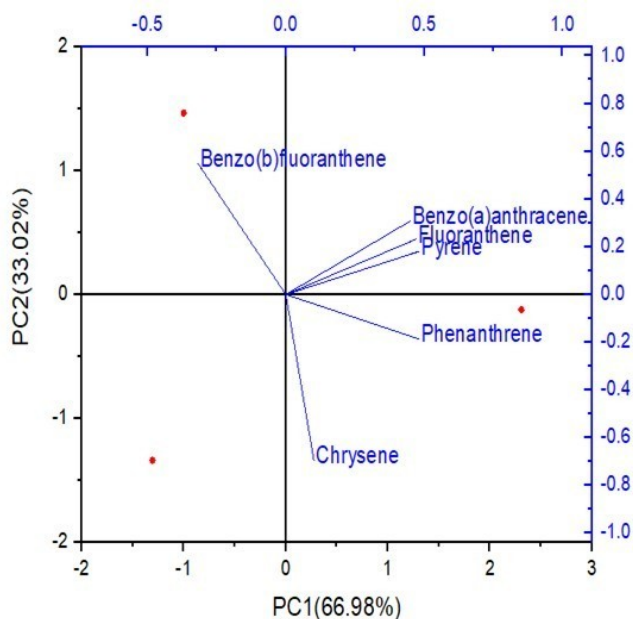


Figure 7: Biplot of the PAH in leachate samples.

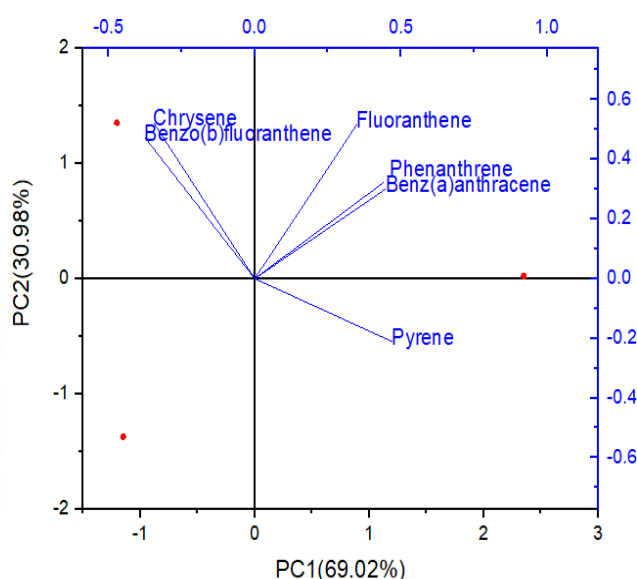


Figure 8: Bi-plot of PAH in plant samples.

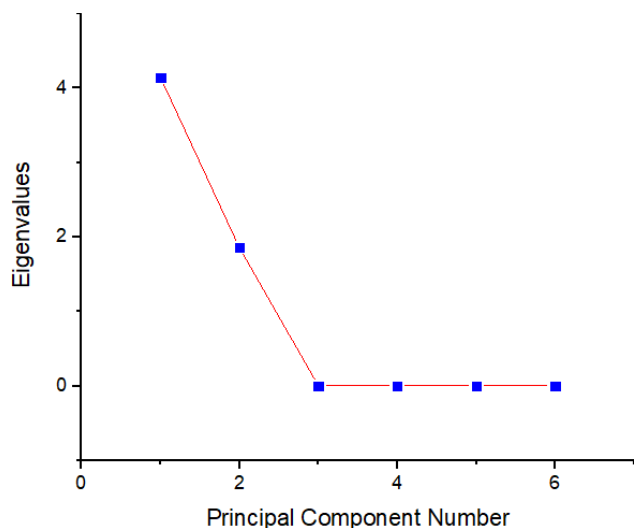


Figure 9: Screen plot of PAHs in plants.

CONCLUSION

Six (6) PAHs each were detected in both the plant and leachate samples analyzed, which includes the following: Chrysene, Benzo (b)fluoranthene, Benzo (a) anthracene, Phenanthrene, Pyrene, and Fluoranthene. Heavy metals such as Zinc (Zn), Lead Pb, Chromium (Cr), Manganese (Mn), Cadmium (Cd), and Nickel (Ni) were also detected. The majority of the physicochemical parameters analyzed were found to exceed their permissible limits set by WHO and NESREA. The source of pollution in this study is the same, and it is confirmed by the statistical analysis used. With the results obtained from this study, it could be deduced that the landfill is heavily polluted, and adequate management needs to be put in place by various agencies.

ACKNOWLEDGEMENT

The authors are grateful to the Department of Plant Biology, University of Ilorin, Ilorin, for the identification of the plant samples and Department of Industrial Chemistry, University of Ilorin, Ilorin, for providing the laboratory facilities used for this research.

CONFLICT OF INTEREST

All the authors declare no conflict of interest regarding this manuscript

REFERENCES

- Adeolu OA, Gbenga AA, Adebayo, AO. Municipal landfill leachate characterization and its induction of glycogen vacuolation in the liver of *Clarias gariepinus*: *International Journal of Environmental Protection* 2009; (2):20-4.
- Moqsud MA, Rahman MH. Biochemical quality of compost from kitchen garbage in Bangladesh. *Environmental Informalities Archive* 2004; (2): 635- 40.
- Zakaria MP, Geik KH, Lee WY, Hayet R. Landfill leachate as a source of polycyclic aromatic hydrocarbons (PAHs) to Malaysian waters. *Coastal Marine Science* 2005; 29(2): 116 -23.
- Mull EJ, Approaches toward sustainable urban solid waste management in Nigeria. *Iranian Journal of Environmental Health Sciences and Engineering* 2005; (6): 173 -80.
- Bakare AA, Alimba CG, Alabi, OA. Genotoxicity and mutagenicity of solid waste leachates: A review. *African Journal of Biotechnology* 2013; 12(27): 4206 - 20. doi: 10.5897/ajb2013.12014.
- Al-Khaldi S. Assessment of groundwater contamination vulnerability in the vicinity of Abqaiq landfill- A GIS Approach", King Fahd University of Petroleum and Minerals, Saudi Arabia, 2006.
- Rafizul IM, Alamgir M, Kraft E, Haedrich G. Bio-treatment of leachate generated from municipal solid waste in sanitary landfill lysimeter. 2nd International conference on solid waste management in developing Asian countries, KUEST, Bangladesh, 2011, pp. 191 - 3.
- Christensen TH, Kjeldsen P, Bjerg PL, Jensen DL, Christensen, JB, Baun A, Albrechtsen HJ, Heron G. Biogeochemistry of landfill leachate plumes. *Applied Geochemistry* 2000; (6): 659 - 718. doi: 10.1016/s0883-2927(00)00082-2
- Pivato A, Gaspari L. Acute toxicity test of leachates from traditional and sustainable landfills using luminescent bacteria. *Waste Management* 2005; (26): 1148 - 55. doi:10.1016/j.wasman.2005.10.008
- Ogundiran OO, Afolabi TA, Assessment of the physiochemical parameters and heavy metal toxicity of leachates from municipal solid waste open dumpsite. *International Journal of Environmental Science and Technology* 2008; 5(2): 243 - 50. doi:10.1007/bf03326018
- Hussein IA, Mona SMM. A review on polycyclic aromatic hydrocarbons:Source, environmental impact,

- effect on human health and remediation 2016(1):107 - 23. doi: 10.1016/j.ejpe.2015.03.011
12. Salami L, Fadayini O, Patinvoh RJ, Koleoba, O. Evaluation of leachate contamination potential of Lagos dumpsites using leachate pollution index. *British Journal of Applied Sciences and Technology* 2015; 5(1): 48 - 59. doi: 10.9734/bjast/2015/11707 .
13. Longe EO, Enekwechi LO. Investigation on potential groundwater impacts and influence of local hydrogeology on natural attenuation of leachate at a municipal landfill. *International Journal of Environmental Science Technology* 2007; 4(1):133 - 40.
14. Odunaiya CO. Repositioning solid waste management practices in cosmopolitan Lagos. Lagos State Polytechnic Inaugural Lecture Series No. 6, 2002, pp. 66
15. Oyetola OT, Babatunde AI. Effect of municipal solid waste in Olusosun dumpsite, Lagos state, Nigeria, *International Journal of Pure Applied Science* 2008; 2(1): 17 - 21.
16. Olujimi OO, Ajayi OL, Opotu OU. Toxicity Assessment of Olusosun and Igando leachates using the African catfish (*Clarias gariepinus*) as bioindicator species, part 1. *Ife Journal of science* 2015, 18(3): 693 - 701.
17. Oketola AA, Akpotu SO. Assessment of solid waste and dumpsite leachate and topsoil. *Chemistry and Ecology* 2015; 31(2): 134 - 46. doi.org/10.1080/02757540.2014.907280 .
18. Lagos Waste Disposal Board. Organization development and waste management system project, Lagos Waste Disposal Board. Assessment report, 2006, 1: 1-5.
19. Lagos Waste Management Authority, 2011. Olusosun Landfill site. Retrieved from: http://www.lawma.gov.ng/lawma_landfill.html
20. APHA (American Public Health Association) Standard methods for the examination of water and wastewater 23rd edition 2017, Washington, USA.
21. Kanmani S, Gandhimathi R. Assessment of heavy metal contamination in soil due to leachate migration from an open dumping site. *Applied Water Science* 2013; 3: 193 - 205. doi:10.1007/s13201-012-0072-z .
22. Farshid K, Amir HS, Rokhsare M. Determination of polycyclic aromatic hydrocarbons (PAHs) in water and sediments of the Kor River. *Iranian Middle - East Journal of Science Resources* 2011; 10(1):1 - 7.
23. Okoli CG, Ogbuagu DH, Gilbert CL, Madu S, Njoku RF. Proximal input of polynuclear aromatic hydrocarbons (PAHs) in groundwater sources of Okrika Mainland, Nigeria. *Journal of Environment Protection* 2011; (2): 848 - 54. doi:10.4236/jep.2011.26096 .
24. Ujowundu CO, Ihekweazu KL, Alisi CS, Ujowundu FN, Igwe CU. Procarcinogens: Polycyclic aromatic hydrocarbons and heavy metal content in some locally processed foods in South Eastern Nigeria. *British Journal of Applied Science Technology* 2014; 4(1): 249 - 60. doi: 10.9734/bjast/2014/4668 .
25. Chian E, DeWalle F. Sanitary landfill leachates and their treatment. *Journal of Environmental Engineering Division* 1976; ASCE (102): 411 - 31.
26. Chu L, Cheung K, Wong M. Variations in the chemical properties of landfill leachates. *Environmental Management* 1994; (18): 105 - 17. doi:10.1007/bf02393753 .
27. Tesi GO, Iniaghe PO, Iniaghe OP, Rotu AR. Assessment of the quality of water from boreholes and hand-dug wells of peri-urban towns in southern Nigeria. *Journal of Environmental Management Safety* 2013; 4(3): 39 - 46.
28. Adeyemi-Ale OA , Anifowoshe AT, Abdulkareem SI. Ecotoxicological Assessment of leachate from Amilegbe Dumpsite, Ilorin, Nigeria Using *Clarias gariepinus* (Burchell 1822) AND *Allium cepa*. *Agrosearch* (2018) 18 (2): 59 - 71. doi:10.4314/agrosh.v18i2.5
29. World Health Organization (WHO) Water for pharmaceutical use in quality assurance of pharmaceuticals. A compendium of guidelines and related materials, 2nd Updated Edition, World Health Organization, Geneva, 2007, pp. 170 -87.
30. National Environmental Standards and Regulations Enforcement Agency (NESREA) (Surface and Groundwater Quality Control) Regulations- Effluent discharges, irrigation and reuse standards, 2011.
31. Radojevic M, Bashkin V. Practical environmental analysis, Cambridge: The Royal Society Chemistry, London, 1999.
32. Schindler DW, Hecky RE, Findlay DL, Stainton MP, Parker BR, Paterson M, Beaty KG, Lyng M, Kasian SEM (2008) Eutrophication of lakes cannot be controlled by reducing nitrogen input: results of a 37-year whole ecosystem experiment. *Proceedings of National Academy of Science, USA*, 2008; (105): 11254 - 8. doi: 10.1073/pnas.0805108105 .
33. World Health Organization (WHO) Permissible limits of heavy metals in soil and plants (Geneva: World Health Organization), Switzerland, 1996.
34. Bhardwaj R, Gupta A, Garg JK (2017) Evaluation of heavy metal contamination using environmetrics and indexing approach for River Yamuna, Delhi stretch, India. *Water Science* 2017; (31): 52 - 66. doi: 10.1016/j.wsj.2017.02.002 .
35. Nair IV, Singh K, Arumugam M, Gangadhar K, Clarson, D. Trace metal quality of Meenachil River at Kottayam, Kerala (India) by principal component analysis. *World Applied Science* 2010; 9(10): 1100 - 7.
36. Okoro HK, Ogunsemoyin OT, Mohammed AA. Assessment of Heavy Metal Pollution Roadside Dusts from Selected Locations in Ilorin, Nigeria Using AAS Techniques. *Adamawa State University Journal of Science Research* 2016; 4(1): 1 - 12.
37. Jena VK, Sinha D. Ground water quality assessment by multivariate factor analysis. *Research Journal of Chemistry and Environment* 2017; 21(8): 21 - 5.

38. Baran S, Oleszczuk, P, Lesiuk A, Baranowska E. Trace metals and polycyclic aromatic hydrocarbons in surface sediment samples from the Narew River (Poland). Polish Journal of Environmental studies 2002; (11): 299 – 305.



A novel selective "turn-on" fluorescent sensor for Hg²⁺ and its utility for spectrofluorimetric analysis of real samples

Süreyya Oğuz TÜMAY*  

Department of Chemistry, Gebze Technical University, Gebze 41400, Kocaeli, Turkey.

Abstract: A novel anthracene-based dipodal Schiff base "turn-on" fluorescent sensor (**FS**) was designed and synthesized by accessible and straightforward Schiff base reaction of salicylaldehyde and 9,10-bis(aminomethyl)anthracene with high yield. The chemical characterization of fluorescent sensor **FS** was performed by standard spectroscopic techniques (MALDI-MS, FT-IR, ¹H, and ¹³C NMR), and photophysical properties were examined by UV-vis and fluorescent spectroscopies. The fluorescent sensor **FS** can coordinate with Hg²⁺ via Schiff base moiety when analytical signal as a "turn on" fluorescent response was obtained via anthracene moiety after coordination. Also, spectrofluorimetric analysis of Hg²⁺ was carried out using fluorescent sensor **FS** in environmental water samples after optimization required experimental conditions such as pH, the time before measurements, and photostability. According to obtained results, the presented fluorescent sensor can be used for selective and sensitive spectrofluorimetric determination of Hg²⁺.

Keywords: Schiff base, Fluorescent sensor, Spectrofluorimetry, Water samples, Mercury(II).

Submitted: May 06, 2020. **Accepted:** May 15, 2020.

Cite this: TÜMAY SO. A novel selective "turn-on" fluorescent sensor for Hg²⁺ and its utility for spectrofluorimetric analysis of real samples. JOTCSA. 2020;7(2):505-16.

DOI: <https://doi.org/10.18596/jotcsa.733160>.

***Corresponding author. E-mail:** sotumay@gtu.edu.tr. Tel: 00 90 262 6053106, Fax: 00 90 262 6053105.

INTRODUCTION

Although industrial and technological activities increase the quality of our life, it causes severe problems for environmental pollution and human health. Contamination of the environment with heavy metal ions led to potential damage to mankind due to the highly toxic effect of these ions even at low concentrations (1). Between these metal ions, Hg²⁺ is one of the most hazardous heavy metal ions because it can inhibit the activity of some biological species such as enzymes and proteins (2). Besides, it can be accumulating to the human body via the food chain and causes severe diseases of the central nervous system (3-5). Therefore, the United States Environmental Protection Agency (EPA) and World Health Organization (WHO) strongly limited the permissible concentration of Hg²⁺ ions in drinking

water in the range of several ppb (µg/kg) (6, 7). Although a significant number of analytical methods are used for detection and determination of Hg²⁺ ions up to now such as capillary electrophoresis (CE), liquid chromatography (LC), atomic absorption spectrometry (AAS), gas chromatography (GC), and atomic fluorescent spectrometry (AFS), these methods generally require preconcentration processes with extra chemicals (adsorbents or eluents), applied by expert users. In addition, they are not applied to in-field analysis (8-11). Fluorescent sensors, handling these disadvantages, attract attention for detection and determination of Hg²⁺ ions due to their several advantages such as simple operation, high sensitivity and selectivity, low cost, and real-time monitoring in-field analysis (12-14). Notably, the development of "turn-on" fluorescent sensors, which are selective for Hg²⁺, has become an

important research topic due to their increased sensitivity compared to "turn-off" fluorescent sensors. Because they can detect analytes via fluorescent signal increment, which led to more easy monitoring than fluorescent sensors that can detect analytes with fluorescent quenching (15-17), another important phenomenon is that heavy metal ions such as Hg^{2+} are known as quencher due to spin-orbit coupling (18). Therefore, developing a selective, sensitive, new, and simple "turn-on" fluorescent sensor for Hg^{2+} ions, which can be practicable to the spectrofluorimetric analysis of the environmental and biological sample is still an essential research area (19, 20).

Schiff bases, which are the essential class of organic compounds, can be obtained with the moderate reaction of primary amines with aldehydes/ketones. These kinds of compounds generally offer one-step synthesis processes in moderate conditions with high yield. Also, an imine bond, known as carbon-nitrogen double bond ($-\text{C}=\text{N}-$), is obtained as a result of Schiff base reaction can readily be used for coordination with metals (7, 21, 22). After coordination with metal ions, inhibition of the $\text{C}=\text{N}$ isomerization cause substantial fluorescent enhancement for such molecules, which is used as obtaining analytical signals (23). Also, according to previously published reports, it is well-known that via sulfur, oxygen, or nitrogen atoms, mercury ions can coordinate with fluorescent sensors (7, 13, 24). Therefore, Schiff base preparation methods can be used for obtaining Hg^{2+} ion-selective fluorescent sensors that containing anthracene with proper cavity and donor atoms due to its well-known optical and metal-binding properties (7, 25, 26). There are a few papers that existed in the literature regarding the develop fluorescent sensors, which are used for selective and sensitive detection of Hg^{2+} based on anthracene containing Schiff base systems (23, 27). However, some deficiencies regarding selectivity and applicability were observed in these reports (27). Thus, in this study, simple, accessible, and non-sulfur anthracene-based dipodal Schiff base fluorescent sensor for selective, sensitive, and simple quantification of Hg^{2+} ion in environmental water samples was prepared by the reaction of salicylaldehyde and 9,10-bis(aminomethyl)anthracene with high yield. The nitrogen and oxygen donor atoms provide the coordination capacity for Hg^{2+} ions (7, 13, 24) when anthracene core acts as a fluorophore for obtaining analytical signals. After full characterization of novel fluorescent sensor by MALDI-MS, FT-IR, NMR spectroscopies, required conditions were optimized and spectrofluorimetric determination of Hg^{2+} ions were carried out in environmental water samples.

EXPERIMENTAL

Materials and Instrumentation

The reagents and solvents which are used for preparation and fluorescent sensor application of **FS** purchased from commercially as follows: Anthracene, dichloromethane, 2-bromoethanol, paraformaldehyde, cetyltrimethylammonium bromide (CTAB), glacial acetic acid from Merck, 2,5-dihydroxybenzoic acid (MALDI-MS matrix) from Fluka, deuterated DMSO from Sigma-Aldrich and they were used as received. Inert argon atmosphere was used for the synthesis of **FS**.

Varian Eclipse spectrofluorometer and Shimadzu 2101 UV spectrophotometer were used for recording fluorescent and the electronic absorption spectra of **FS** in the UV-vis region. Also, spectrofluorimetric analysis in environmental water samples where 5 nm of slit width and 1 cm of path-length were used for all fluorescent measurements at 25°C were performed by Varian Eclipse spectrofluorometer. NMR (^1H and ^{13}C NMR), FT-IR, and mass analysis of **FS** were recorded with Varian INOVA 500 MHz spectrometer, Perkin Elmer Spectrum 100 spectrophotometer, and Bruker Daltonics Microflex MALDI-TOF mass spectrometer, respectively. Deuterated DMSO was used for all NMR measurements. The non-linear regression calculations were performed using Sigma-Plot 14.0.

All water samples were collected from Kocaeli/Sakarya in Turkey and filtered with filter paper (blue band). After that, they were acidified with nitric acid and kept at 4°C in a refrigerator before the spectrofluorimetric analysis. The presented spectrofluorimetric analysis performed without any enhancement processes via sensitive and selective complexation of **FS** with Hg^{2+} ion. The fluorescent signal of **FS** that raised via anthracene proportionally and gradually increased after treatment with 0.05-120.00 μM of Hg^{2+} . Spectrofluorimetric determination of Hg^{2+} ion in real samples was performed via analytical signals that were obtained by complexation of Hg^{2+} -**FS**, and the calibration curve was used for analysis with relative fluorescent response change. For determination of Hg^{2+} , 6.25×10^{-5} M of **FS** was prepared in DMSO. After taking 0.80 mL of **FS** from this solution, 1.70 mL of DMSO, 0.25 mL of Britton-Robinson buffer solution (pH 8.0), and 0.25 mL of sample was added onto volumetric flask (5 mL). After that, the volume of the flask was completed with deionized water to 5 mL and carefully shaken for 60 seconds. All spectrofluorimetric measurements were recorded at 426 nm.

Synthesis

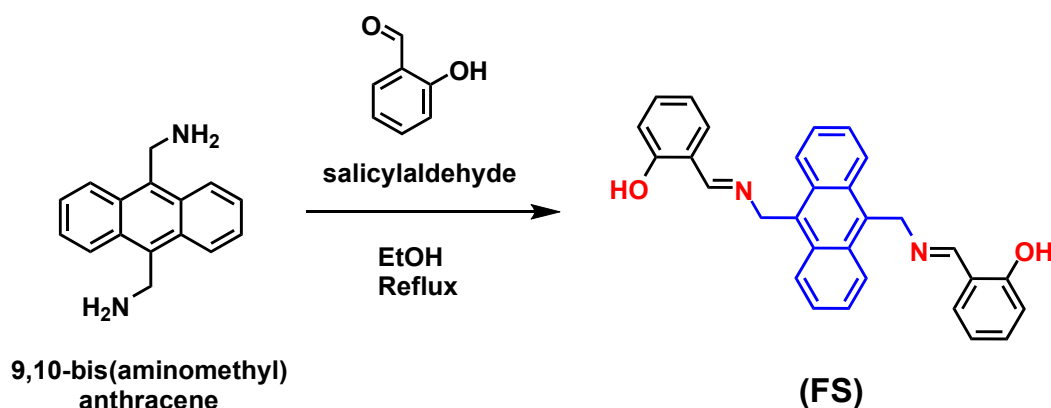
9,10-bis(aminomethyl)anthracene was synthesized and characterized according to literature (28) and **FS** was obtained as follows: 2.460 g of salicylaldehyde (0.0201 mol) dissolved in absolute ethanol in the stream of argon gas and refluxed for 30 minutes. Then, 4.750 g of 9,10-bis(aminomethyl)anthracene (0.0201 mol) and several drops of glacial acetic acid were added onto the solution of salicylaldehyde. The reaction mixture was refluxed during a day. Then the yellow precipitate was filtered with blue filter paper and washed three times with ethanol and n-hexane. **FS** was obtained as a yellow solid with 95% yield (8.488 g). FT-IR; 3271 cm^{-1} (-OH), 3061-3050 cm^{-1} (-ArH), 2917-2867 cm^{-1} (-C-H), 1634 cm^{-1} (-CH=N), 1600-1400 cm^{-1} (-C=C-), 1444.1-1335.1 cm^{-1} (-C-H-). $[\text{M}]^+$: 444.654 m/z (calc. $[\text{M}]^+$: 444.530). ^1H NMR in DMSO- d_6 at 25°C, δ_{ppm} ; 13.38 (s, 2H), 8.90 (s, 2H), 8.58 (dd, $J = 6.7, 3.2$ Hz, 4H), 7.67 (dd, $J = 6.7, 3.2$ Hz, 4H), 7.42 (d, $J = 7.8$ Hz, 2H), 7.27 (t, $J = 7.9$ Hz, 2H), 6.85 (t, $J = 7.5$ Hz, 2H), 6.77 (d, $J = 8.2$ Hz, 2H), 5.88 (s, 4H). ^{13}C NMR in in DMSO- d_6 at 25°C, δ_{ppm} ; 166.10,

160.27, 132.41, 131.72, 130.37, 129.82, 126.31, 125.05, 118.65, 116.41, 53.65.

RESULT AND DISCUSSION

Structural Characterization

The fluorescent sensor (**FS**) having a di-functional primer amine derivative of anthracene core was prepared by following the literature procedure (28). Briefly, 9,10-bis(bromomethyl)anthracene was obtained with high yield (96%) by the reaction of anthracene and HBr in the presence of paraformaldehyde and CTAB. After that, 9,10-bis(aminomethyl)anthracene, which is the di-functional primer amine derivative of anthracene core, was prepared in high yield (95%) by reaction of 9,10-bis(bromomethyl)anthracene and hexamethylenetetramine. Finally, the presented fluorescent sensor (**FS**) was prepared with high yield (95%) as a result of the Schiff base reaction of 9,10-bis(aminomethyl)anthracene and salicylaldehyde in ethanol (Scheme 1). During the preparation of **FS** with high yield, any purification process was not used except for washing and precipitation.



Scheme 1: The synthetic route of **FS**.

The chemical structure of the novel fluorescent sensor was investigated by FT-IR, MALDI-MS, and NMR (^1H and ^{13}C) spectroscopies. All results point out that the proposed structure of **FS** was consistent with characterization data. For instance, The FT-IR spectra of 9,10-bis(aminomethyl)anthracene, salicylaldehyde, and **FS** were depicted in Figure 1a. 9,10-bis(aminomethyl)anthracene demonstrated peaks at 1550 cm^{-1} , 2956-2867 cm^{-1} , 3078-3045 cm^{-1} and 3256-3167 cm^{-1} which assigned to stretching vibrations of -C=C-, -C-H, -ArH and -NH $_2$, respectively. Besides, -C=C-, -OH and -C=O stretching of the aldehyde functional groups of salicylaldehyde were observed at 1555 cm^{-1} , 3142 cm^{-1} and 1662 cm^{-1} , respectively. As can be seen from FT-IR spectra of **FS**, stretching vibrations of -C=C-, -CH=N, -C-H, -ArH and -OH were observed

at 1575 cm^{-1} , 1634 cm^{-1} , 2917-2867 cm^{-1} , 3061-3050 cm^{-1} and 3271 cm^{-1} , respectively (13, 29). Importantly, -C=O stretching of salicylaldehyde (1662 cm^{-1}) and -NH $_2$ stretching of 9,10-bis(aminomethyl)anthracene (3256-3167 cm^{-1}) were disappeared after the formation of **FS** which were important evidence for the proposed structure of **FS**. The ^1H NMR spectrum of **FS**, which recorded in DMSO- d_6 , was demonstrated in Figure 1b. The peak observed at 5.88 ppm was attributed to aliphatic methylene protons, which exist in the anthracene core, and aromatic protons of **FS** were observed between 8.59-6.76 ppm. Also, the imino proton was observed at 8.90 ppm while -OH proton existed at 13.38 ppm as a singlet peak. The integration value ratio of aromatic protons to methylene protons was 4: 1, which is an evidence

of compatibility with the proposed chemical structure.

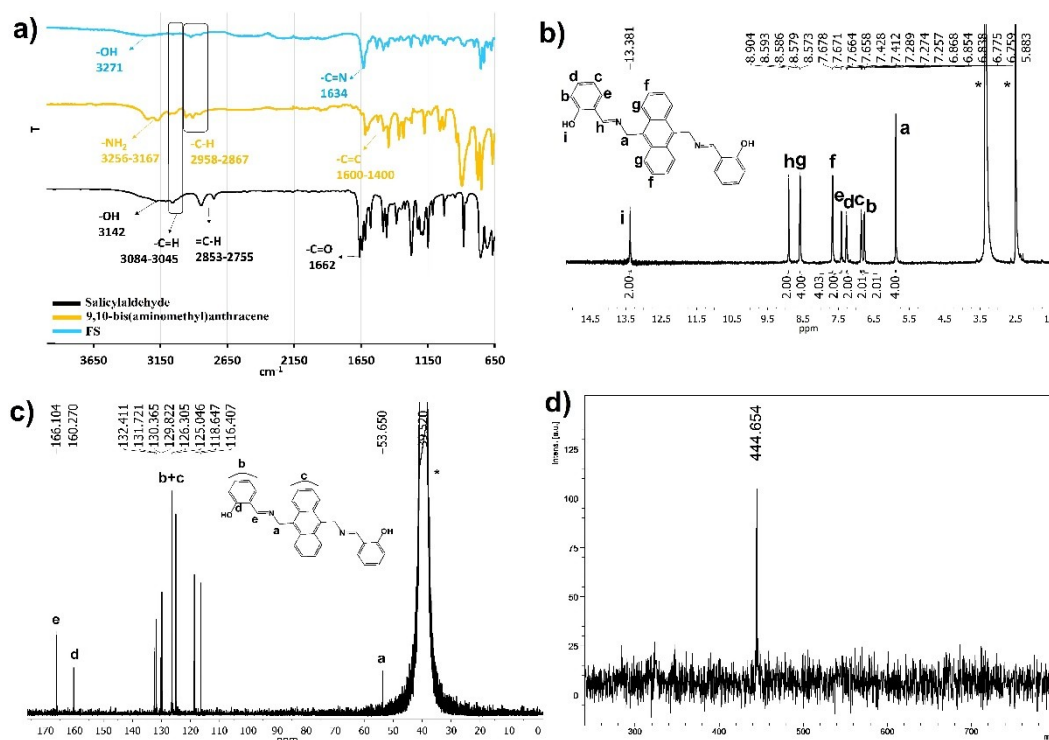


Figure 1: a) FT-IR spectra of 9,10-bis(aminomethyl)anthracene, salicylaldehyde, and **FS**, b) ¹H NMR (in DMSO-d₆), c) ¹³C NMR (in DMSO-d₆) and d) MALDI-MS spectrum of **FS**.

Photophysical Investigation

The photophysical properties of **FS** were investigated using electronic absorption in the UV-Vis region and fluorescent experiments. The effect of various solvents on UV-Vis absorption of 10 μM **FS** was investigated with various solvents such as n-hexane, THF, dichloromethane (DCM), acetonitrile (ACN), ethanol, DMSO, DMF, and water (Figure 2a). The UV-vis electronic absorption of **FS** reached maxima at 258 and 378 nm, which can be assigned to n-n* transition of anthracene moieties (30). Also, UV-Vis electronic absorption properties of **FS** were not changed by solvents except for absorbance values, which are presumably dissolution differences in various solvents. The

fluorescent sensor presented has high solubility in THF, dichloromethane, acetonitrile, DMSO, DMF, while it has low solubility in n-hexane, ethanol, and water only. UV-Vis electronic absorption properties of **FS** were examined at different concentrations in DMSO (Figure 2b). According to Figure 2b, absorbance values were proportionally decreased with decreasing concentrations of **FS** in UV-Vis electronic absorption spectra. The same situation was observed with other tested solvents, and molar absorptivities (ε) of compounds in various solvents were calculated. The fluorescent quantum yield (Φ) and other photophysical properties were summarized at Table 1.

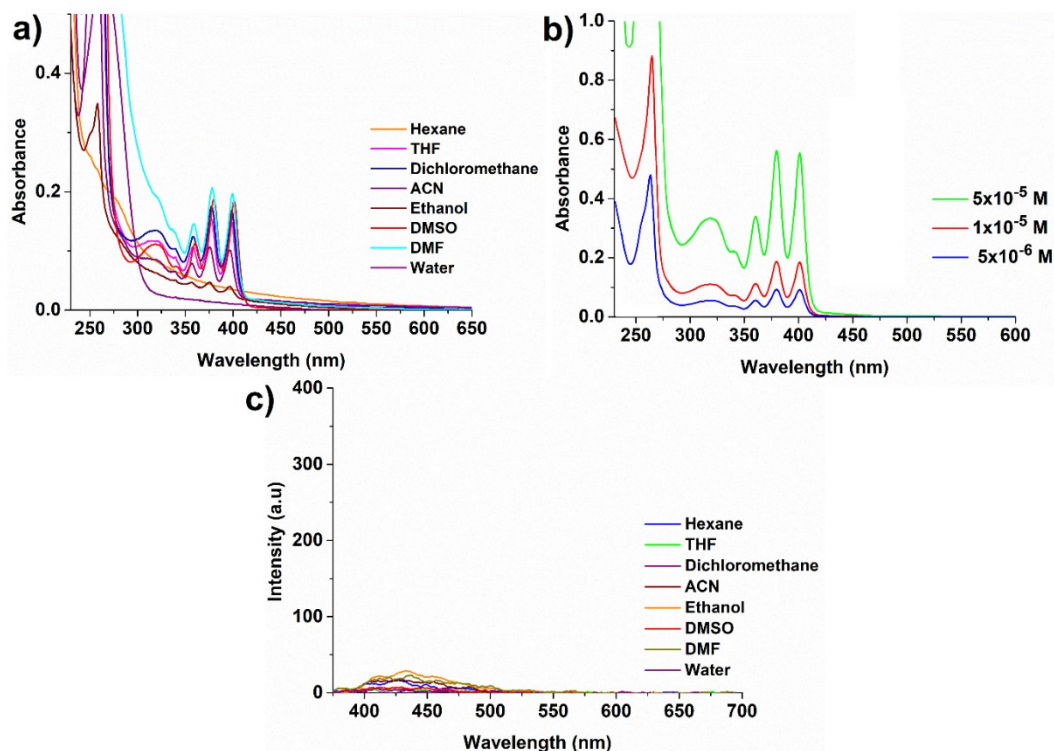


Figure 2: a) UV-Vis electronic absorption of 10 μM **FS** in different solvents, b) UV-vis electronic absorption of different concentrations of **FS** in DMSO, and c) fluorescent emission spectra of 10 μM **FS** in different solvents.

After the evaluation of the electronic absorption properties of **FS**, fluorescent emission properties of **FS** were examined with steady-state fluorescent measurements under the same conditions with UV-Vis absorption studies (Figure 2b). All fluorescent emission spectra of **FS** were recorded at 10 μM when excited at 360 nm. The effect of various solvents on fluorescent emission of **FS** was

investigated with the same solvent systems. In Figure 2b, the fluorescent sensor **FS** showed a very weak fluorescent signal at ~ 420 nm when excited at 360 nm. It is a well-known phenomenon for Schiff base due to photoinduced electron transfer (PET) process from Schiff base to fluorophore group of sensor (7, 23, 27, 29).

Table 1: Photophysical properties of **FS**.

λ_{abs} (nm)	λ_{ems} (nm)		ϵ ($\text{L}\cdot\text{mol}^{-1}\cdot\text{cm}^{-1}$) $\times 10^3$					Φ_f (%)	
			THF	DCM	ACN	Ethanol	DMSO		
FS 258, 378	426 (very weak)	(very	15.1	17.4	9.4	4.3	17.7	19.7	1.44

The fluorescent quantum yield (Φ_f) of **FS** was determined with the comparative method (Eq. (1)) (31). The quinine sulfate was used as a standard

for the calculation of Φ_f , because Φ_f of quinine sulfate was calculated as 0.54 in the literature (in 0.1 M H_2SO_4) (32).

$$\Phi_f = \Phi_{f_{\text{std}}} \frac{F \cdot A_{\text{std}} \cdot n^2}{F_{\text{std}} \cdot A \cdot n_{\text{std}}^2} \quad \text{Eq. (1)}$$

In Eq. (1), F_{std} , A_{std} , F and A represent the areas of fluorescent emission and electronic absorption curves of standard and **FS**, respectively at the excitation wavelengths. Besides, n_{std} and n demonstrate the refractive indices of solvents used for the standard and **FS**, respectively.

Fluorescent Sensor Property of **FS** and Optimization Studies

Fluorescent sensor property and selectivity of 10 μM **FS** was investigated in DMSO:water (pH 8.0, 1:1 v/v) against 120 μM of various metal ions (as nitrate salts) such as Mn^{2+} , Al^{3+} , Cs^+ , Ba^{2+} , Fe^{3+} , Ca^{2+} , K^+ , Cu^{2+} , Pb^{2+} , Hg^{2+} , Zn^{2+} , Mg^{2+} , Na^+ , Li^+ ,

Ni^{2+} , Ag^+ , Fe^{2+} , Cd^{2+} , Co^{2+} , Cr^{3+} by UV-Vis and fluorescent spectroscopies. The UV-Vis electronic absorption spectrum of **FS** significantly changes upon the addition of $120 \mu\text{M}$ Hg^{2+} ion when other metal ions did not cause any change under identical analytical conditions (Figure 3a). The absorption of **FS**, which at long wavelength centered at 378 nm , decreased ($\sim 50\%$) and other absorption, which centered at 258 nm red-shifted as 16 nm and observed at 274 nm . As a result of the electronic reorganization, an important color change was observed from yellow to colorless at daylight (Figure 3b). These changes in the UV-Vis absorption spectrum occurring by the addition of Hg^{2+} to **FS** can be assigned to the electronic reorganization after coordination of **FS** with Hg^{2+} (25, 33).

After the evaluation of UV-Vis response of **FS** towards various metal ions, fluorescent sensor properties of **FS** were investigated using fluorescent spectroscopy under identical analytical conditions with UV-Vis experiments (see Figure 3c); **FS** has a minimal fluorescent signal due to PET process from Schiff base to anthracene moiety when excited at 360 nm (34). After selective complexation of **FS** with the Hg^{2+} cation, the

fluorescent emission of **FS**, which originated from blue monomer emission of anthracene moiety, importantly increased at 426 nm . The change for fluorescent emission can be attributed to the chelation-enhanced fluorescence (CHEF) process, which occurred with selective complexation of **FS** with Hg^{2+} cation, and it inhibited the PET process (34). Importantly, except for Hg^{2+} , other tested metal ions did not demonstrate this effect and cause any "turn on" response on the fluorescent signal of **FS** (Figure 3c). As significant property of fluorescent sensors, selectivity of $10 \mu\text{M}$ **FS** in DMSO:water (pH 8.0, 1:1 v/v) over other competitive metal cations and anions was investigated with addition of Mn^{2+} , Al^{3+} , Cs^+ , Ba^{2+} , Fe^{3+} , Ca^{2+} , K^+ , Cu^{2+} , Pb^{2+} , Hg^{2+} , Zn^{2+} , Mg^{2+} , Na^+ , Li^+ , Ni^{2+} , Ag^+ , Fe^{2+} , Cd^{2+} , Co^{2+} , Cr^{3+} , Cl^- , F^- , NO_3^- , I^- , CO_3^{2-} , SO_4^{2-} . The selectivity studies were performed where concentration of other competitive species was $2400 \mu\text{M}$ (Figure 4). As seen in this figure, the effect of different competitive ions on relative fluorescent signal change of $10 \mu\text{M}$ **FS** in DMSO:water (pH 8.0, 1:1 v/v) were insignificant when compared with response of Hg^{2+} ion that clearly showed selectivity of **FS** against to Hg^{2+} .

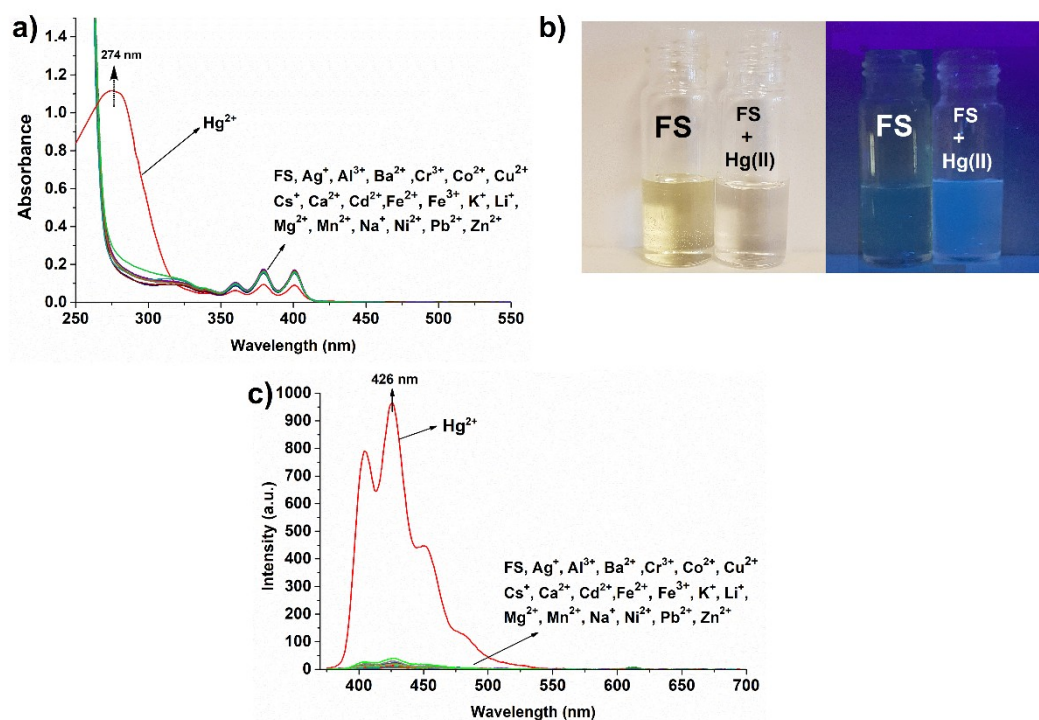


Figure 3: a) UV-vis electronic absorption, b) color change (daylight and 365 nm light source) and c) fluorescent emission spectra of $10 \mu\text{M}$ **FS** in DMSO:water (pH 8.0, 1:1 v/v) upon addition of $120 \mu\text{M}$ Hg^{2+} .

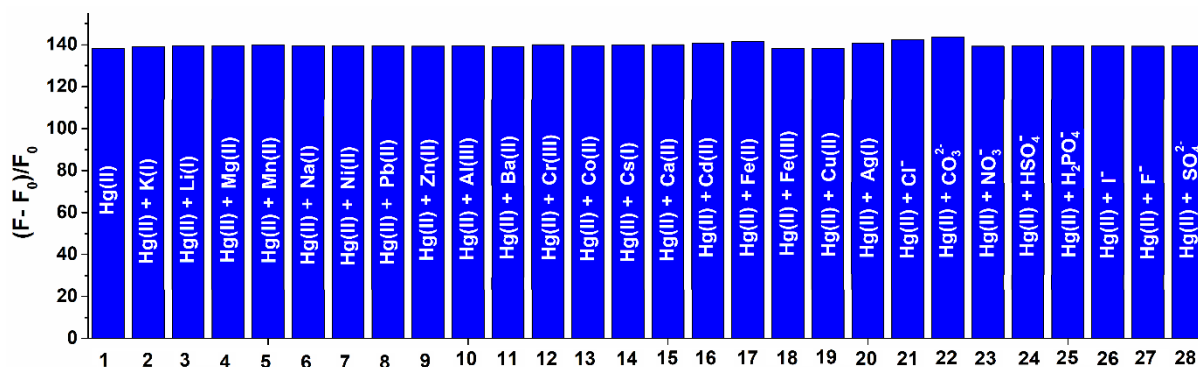


Figure 4: Relative fluorescent signal changes of 10 μM **FS** in DMSO:water (pH 8.0, 1:1 v/v, $\lambda_{\text{ex}}=360$ nm) upon addition of 120 μM Hg^{2+} + 2400 μM various metal ions.

The pH of analysis medium for fluorescent sensors which were designed for detection or determination of metal ions was important parameter, therefore, the effect of pH on relative fluorescent signal change of 10 μM **FS** in DMSO: water (1:1 v/v) with the addition of Hg^{2+} was investigated between pH 4 and 11 (29, 33) when other conditions kept steady. For that purpose, pH of 10 μM **FS** in DMSO: water (1:1 v/v) was adjusted by Britton-Robinson buffer (Figure 5a). As seen, the **FS**- Hg^{2+} complex is nearly pH-independent between pH 6.0–9.0 when considering the relative fluorescent signals. Therefore, the optimum pH was determined as 8.0 for the rest of the study, which demonstrated that **FS** could be used as a fluorescent sensor for spectrofluorimetric analysis of Hg^{2+} under neutral physical conditions (35). Then, the optimization of pH, effect of response time before the measurement was investigated for **FS** in DMSO: water (1:1 v/v) with the addition of Hg^{2+} ion when other parameters kept steady (Figure 5b). For that investigation, pH

of 10 μM **FS** DMSO:water (1:1 v/v) was adjusted 8.0 and 120 μM Hg^{2+} ion was added in this solution. Thereafter, obtained solution was carefully stirred up to 120 seconds and fluorescent spectra were recorded periodically. The results demonstrated that, after 60 seconds relative fluorescent signals remained nearly steady. Therefore, optimum time for measurement was determined as 60 second for determination of Hg^{2+} . To obtain accurate results in a spectrofluorimetric determination of a real sample using fluorescent sensors, the photostability of the sensor is highly essential. Accordingly, the photostability of **FS** and **FS**+ Hg^{2+} was investigated under optimized conditions. For that purpose, 120 μM of Hg^{2+} was added to 10 μM **FS** in DMSO:water (pH 8.0, 1:1 v/v) then stirred vigorously for 60 seconds and fluorescent responses observed between 1-60 minutes under daylight. As can be seen from Figure 5c, both **FS** and Hg^{2+} complex of **FS** was immensely photostable.

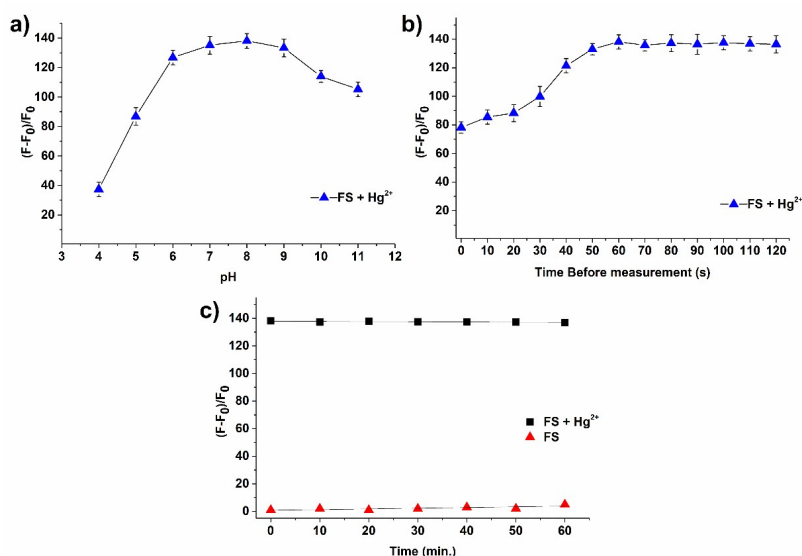


Figure 5: The effect of **a)** pH and **b)** measurement time on on relative fluorescent signal of **FS**+ Hg^{2+} and **c)** photostability of **FS** and **FS**+ Hg^{2+} (10 μM **FS** in DMSO:water (pH 8.0, 1:1 v/v, $\lambda_{\text{ex}}=360$ nm); 120 μM Hg^{2+}).

Complex formation of **FS** with Hg^{2+} ion was investigated by Job's plot (continuous variation) and non-linear curve fitting analysis in a buffered solution at pH 8.0 (36, 37). As can be seen from Figure 6a, maximum signal change was obtained at 0.5 in Job's plot, which revealed that stoichiometry of the **FS**- Hg^{2+} complex was 1:1. Besides, non-linear curve fitting analysis showed an inflection point at 1.0, which supports 1:1 binding mode (Figure 6b). With FT-IR analysis, we

obtained more information about the complexation of Hg^{2+} with **FS**, (Figure 6c). In the FT-IR spectrum of **FS**, -OH and C=N vibration peaks were observed at 3271 cm^{-1} and 1634 cm^{-1} , respectively. After treatment with Hg^{2+} , -OH vibration peak of **FS** disappeared, and the C=N vibration peak shifted to 1610 cm^{-1} proving that Hg^{2+} and **FS** had coordination via O- Hg^{2+} -N bond. According to the obtained results, the proposed binding mechanism for **FS**- Hg^{2+} was given in Figure 6d.

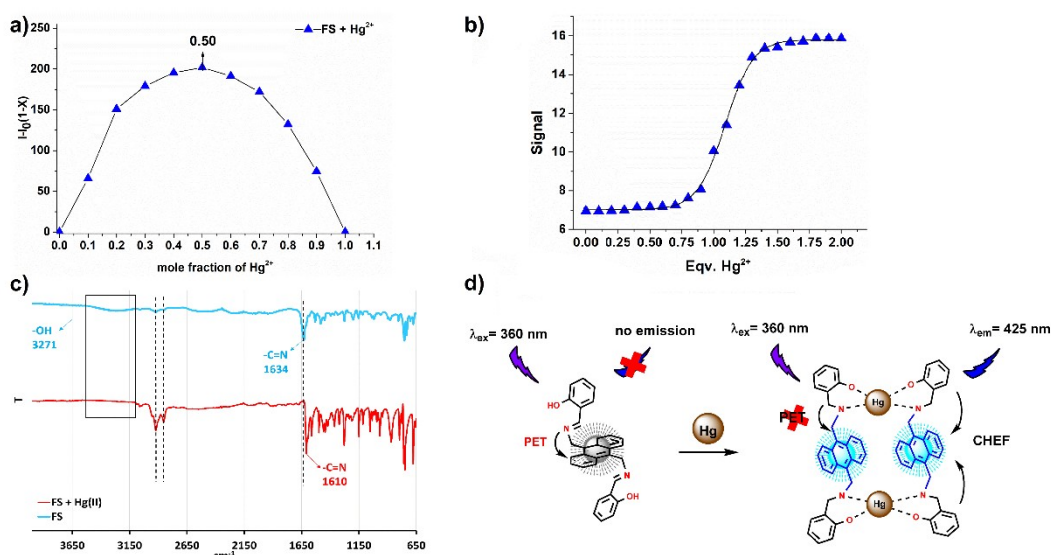


Figure 6: a) Job's Plot, b) non-linear curve fitting, c) FT-IR spectral analysis of **FS**+ Hg^{2+} and d) proposed binding mode for **FS**+ Hg^{2+} (10 μM **FS** in DMSO:water (pH 8.0, 1:1 v/v, λ_{ex} =360 nm).

Analytical Performance

The fluorescent response of **FS** towards to Hg^{2+} was also evaluated by fluorescent titration experiments under the optimized conditions (Figure 7a). As shown in Figure 7a, after gradual addition increased amount of Hg^{2+} to 10 μM **FS** in DMSO: water (pH 8.0, 1:1 v/v), fluorescent emission signal of **FS** at 426 nm was gradually and proportionally increased between 0.05-120.00 μM

Hg^{2+} which indicates the formation of **FS**+ Hg^{2+} complex. The calibration curve of **FS** for Hg^{2+} was given in Figure 7b, which demonstrated a good linear relationship ($R^2=0.9938$) between the relative fluorescent signal change and Hg^{2+} concentration between 0.05-120.00 μM . Also, linear regression equations for Hg^{2+} was determined as $(F-F_0)/F_0=1.1839[\text{Hg}^{2+}]-8.3709$.

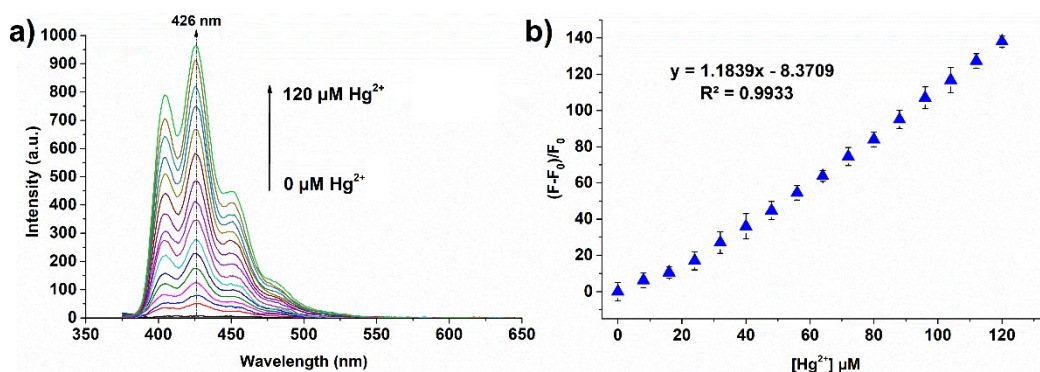


Figure 7: a) Fluorescent emission response of 10 μM **FS** in DMSO:water (pH 8.0, 1:1 v/v, λ_{ex} =360 nm) upon gradual addition of Hg^{2+} ion and b) calibration curve for Hg^{2+} ion.

The LOD, limit of detection, which calculated as dividing three times of the standard deviation of

the blank sample by the slope of the calibration graph ($3\sigma/K$) determined as 0.082 μM for Hg^{2+} ,

whereas the limit of quantification, LOQ, calculated as 0.246 μM for Hg^{2+} . Under optimized experimental conditions, the precision of the developed spectrofluorimetric determination method (N=10) was calculated as 2.58%, which assigned high precision and stability. All analytical parameters of **FS** for Hg^{2+} ion determination were given in Table 2. To evaluate the applicability of presented fluorescent sensor for

spectrofluorimetric analysis for Hg^{2+} in environmental water samples, **FS** was applied to seawater, lake, and tap water samples without any enhancement processes and obtained results given at Table 3. As seen in Table 3, obtained results for the spectrofluorimetric analysis of Hg^{2+} demonstrated high percentage recovery in environmental water samples and in a good agreement with to the spiked concentrations.

Table 2: Analytical parameters of **FS** for Hg^{2+} ion determination.

Excitation wavelength (nm)	360
Emission wavelength (nm)	426
Limit of detection (LOD) (μM)	0.082
Limit of quantification (LOQ) (μM)	0.245
Linear range (μM)	0.05-120
Optimum pH	8.0
Ligand concentration (μM)	2
Final volume (mL)	5
Solvent	DMSO:water (1:1 v/v)
Time before measurement (second)	60
Correlation coefficient (R2)	0.9938
Precision (RSD%)	2.58

Table 3: Spectrofluorimetric determination of Hg^{2+} in environmental water samples using **FS**.

Water sample	Spiked concentration of Hg^{2+} ions (μM)	Found (μM)	Recovery (%)
Seawater	20.00	20.59 \pm 0.52	102.95
	40.00	40.32 \pm 0.96	100.80
Lake water	20.00	20.29 \pm 0.35	101.45
	40.00	39.52 \pm 0.84	98.80
Tap water	20.00	19.20 \pm 0.28	96.00
	40.00	38.92 \pm 1.01	97.30

CONCLUSION

In summary, simple, efficient, and accessible anthracene-based dipodal Schiff base "turn-on" fluorescent sensor for Hg^{2+} ion was designed and synthesized via high yield Schiff base reaction of salicylaldehyde and 9,10-bis(aminomethyl)anthracene. The characterization of **FS** was performed by MALDI-MS, FT-IR, ^1H and ^{13}C NMR spectral methods. The photophysical and fluorescent sensor properties of **FS** were investigated by UV-Vis and fluorescent spectroscopies in different solvents. The presented fluorescent sensor demonstrated excellent selectivity and sensitivity towards Hg^{2+} over different competitive ions with "turn-on" response. The PET-triggered weak fluorescent response of **FS** was inhibited by coordination of Hg^{2+} via CHEF processes, and importantly "turn-on" fluorescent response was obtained at 426 nm. The binding mechanism of **FS** with Hg^{2+} was examined by electronic absorption and fluorescent spectroscopies. The LOD and LOQ were found to be 0.082 μM and 0.246 μM for Hg^{2+} , respectively. Finally, after the optimization of experimental conditions, spectrofluorimetric analysis of Hg^{2+} ions

was carried out in environmental water samples. According to obtained results, it can be said that **FS** is a selective and sensitive "turn-on" fluorescent sensor candidate for Hg^{2+} detection in aqueous media.

REFERENCES

- Duran C, Tumay SO, Ozdes D, Serencam H, Bektas H. Simultaneous separation and preconcentration of Ni(II) and Cu(II) ions by coprecipitation without any carrier element in some food and water samples. *International Journal of Food Science & Technology*. 2014;49(6):1586-92.
- Yan Z, Yuen M-F, Hu L, Sun P, Lee C-S. Advances for the colorimetric detection of Hg^{2+} in aqueous solution. *RSC Advances*. 2014;4(89):48373-88.
- Kim HN, Ren WX, Kim JS, Yoon J. Fluorescent and colorimetric sensors for detection of lead, cadmium, and mercury ions. *Chemical Society Reviews*. 2012;41(8):3210-44.

4. Taki M, Akaoka K, Iyoshi S, Yamamoto Y. Rosamine-Based Fluorescent Sensor with Femtomolar Affinity for the Reversible Detection of a Mercury Ion. *Inorganic Chemistry*. 2012;51(24):13075-7.
5. Liu D, Wang Y, Wang R, Wang B, Chang H, Chen J, et al. Fluorescein-based fluorescent sensor with high selectivity for mercury and its imaging in living cells. *Inorganic Chemistry Communications*. 2018;89:46-50.
6. Gao Y, De Galan S, De Brauwere A, Baeyens W, Leermakers M. Mercury speciation in hair by headspace injection-gas chromatography-atomic fluorescence spectrometry (methylmercury) and combustion-atomic absorption spectrometry (total Hg). *Talanta*. 2010;82(5):1919-23.
7. Tümay SO, Uslu A, Ardiç Alidağı H, Kazan HH, Bayraktar C, Yolaçan T, et al. A systematic series of fluorescence chemosensors with multiple binding sites for Hg(ii) based on pyrenyl-functionalized cyclotriphosphazenes and their application in live cell imaging. *New Journal of Chemistry*. 2018;42(17):14219-28.
8. Deng B, Xiao Y, Xu X, Zhu P, Liang S, Mo W. Cold vapor generation interface for mercury speciation coupling capillary electrophoresis with electrothermal quartz tube furnace atomic absorption spectrometry: Determination of mercury and methylmercury. *Talanta*. 2009;79(5):1265-9.
9. Mao Y, Liu G, Meichel G, Cai Y, Jiang G. Simultaneous Speciation of Monomethylmercury and Monoethylmercury by Aqueous Phenylation and Purge-and-Trap Preconcentration Followed by Atomic Spectrometry Detection. *Analytical Chemistry*. 2008;80(18):7163-8.
10. Nguyen TH, Boman J, Leermakers M, Baeyens W. Mercury analysis in environmental samples by EDXRF and CV-AAS. *Fresenius' Journal of Analytical Chemistry*. 1998;360(2):199-204.
11. Zheng C, Li Y, He Y, Ma Q, Hou X. Photo-induced chemical vapor generation with formic acid for ultrasensitive atomic fluorescence spectrometric determination of mercury: potential application to mercury speciation in water. *Journal of Analytical Atomic Spectrometry*. 2005;20(8):746-50.
12. Zhang C, Gao B, Zhang Q, Zhang G, Shuang S, Dong C. A simple Schiff base fluorescence probe for highly sensitive and selective detection of Hg²⁺ and Cu²⁺. *Talanta*. 2016;154:278-83.
13. Wei T-b, Gao G-y, Qu W-j, Shi B-b, Lin Q, Yao H, et al. Selective fluorescent sensor for mercury(II) ion based on an easy to prepare double naphthalene Schiff base. *Sensors and Actuators B: Chemical*. 2014;199:142-7.
14. Gujar V, Sangale V, Ottoor D. A Selective Turn off Fluorescence Sensor Based on Propranolol-SDS Assemblies for Fe³⁺ Detection. *Journal of Fluorescence*. 2019;29(1):91-100.
15. Kim K, Choi SH, Jeon J, Lee H, Huh JO, Yoo J, et al. Control of On-Off or Off-On Fluorescent and Optical [Cu²⁺] and [Hg²⁺] Responses via Formal Me/H Substitution in Fully Characterized Thienyl "Scorpionate"-like BODIPY Systems. *Inorganic Chemistry*. 2011;50(12):5351-60.
16. Long Y, Yang M-p, Yang B-q. Development and applications of two colorimetric and fluorescent indicators for Hg²⁺ detection. *Journal of Inorganic Biochemistry*. 2017;172:23-33.
17. Wang H, Li Y, Xu S, Li Y, Zhou C, Fei X, et al. Rhodamine-based highly sensitive colorimetric off-on fluorescent chemosensor for Hg²⁺ in aqueous solution and for live cell imaging. *Organic & Biomolecular Chemistry*. 2011;9(8):2850-5.
18. Burrell CN, Bodine MI, Elbjairami O, Reibenspies JH, Omary MA, Gabbai FP. Enhancement of External Spin-Orbit Coupling Effects Caused by Metal-Metal Cooperativity. *Inorganic Chemistry*. 2007;46(4):1388-95.
19. Coskun A, Akkaya EU. Signal Ratio Amplification via Modulation of Resonance Energy Transfer: Proof of Principle in an Emission Ratiometric Hg(II) Sensor. *Journal of the American Chemical Society*. 2006;128(45):14474-5.
20. Tian M, Ihmels H. Selective ratiometric detection of mercury(ii) ions in water with an acridinium-based fluorescent probe. *Chemical Communications*. 2009(22):3175-7.
21. Alizadeh K, Parooi R, Hashemi P, Rezaei B, Ganjali MR. A new Schiff's base ligand immobilized agarose membrane optical sensor for selective monitoring of mercury ion. *Journal of Hazardous Materials*. 2011;186(2):1794-800.
22. Quang DT, Wu J-S, Luyen ND, Duong T, Dan ND, Bao NC, et al. Rhodamine-derived Schiff base for the selective determination of mercuric ions in water media. *Spectrochimica Acta Part A: Molecular and Biomolecular Spectroscopy*. 2011;78(2):753-6.
23. Kaur B, Gupta A, Kaur N. A novel, anthracene-based naked eye probe for detecting Hg²⁺ ions in

aqueous as well as solid state media. *Microchemical Journal*. 2020;153:104508.

24. Zhou Y, Zhu C-Y, Gao X-S, You X-Y, Yao C. Hg²⁺-Selective Ratiometric and "Off-On" Chemosensor Based on the Azadiene-Pyrene Derivative. *Organic Letters*. 2010;12(11):2566-9.

25. Tümay SO, Yeşilot S. Tripodal synthetic receptors based on cyclotriphosphazene scaffold for highly selective and sensitive spectrofluorimetric determination of iron(III) in water samples. *Journal of Photochemistry and Photobiology A: Chemistry*. 2019;372:156-67.

26. Sie Y-W, Wan C-F, Wu A-T. A multifunctional Schiff base fluorescence sensor for Hg²⁺, Cu²⁺ and Co²⁺ ions. *RSC Advances*. 2017;7(5):2460-5.

27. Kaur B, Kaur N. Detection of Al³⁺ and Hg²⁺ ions with anthracene appended Schiff base and its reduced analogue. *Journal of Coordination Chemistry*. 2019;72(13):2189-99.

28. Ke C, Destecroix H, Crump MP, Davis AP. A simple and accessible synthetic lectin for glucose recognition and sensing. *Nature Chemistry*. 2012;4(9):718-23.

29. Mondal B, Banerjee S, Ray J, Jana S, Senapati S, Tripathy T. "Novel Dextrin-Cysteine Schiff Base: A Highly Efficient Sensor for Mercury Ions in Aqueous Environment". *ChemistrySelect*. 2020;5(6):2082-93.

30. Guven N, Camurlu P. Electrosyntheses of anthracene clicked poly(thienylpyrrole)s and investigation of their electrochromic

properties. *Polymer*. 2015;73:122-30.

31. Fery-Forgues S, Lavabre D. Are Fluorescence Quantum Yields So Tricky to Measure? A Demonstration Using Familiar Stationery Products. *Journal of Chemical Education*. 1999;76(9):1260.

32. Melhuish WH. QUANTUM EFFICIENCIES OF FLUORESCENCE OF ORGANIC SUBSTANCES: EFFECT OF SOLVENT AND CONCENTRATION OF THE FLUORESCENT SOLUTE¹. *The Journal of Physical Chemistry*. 1961;65(2):229-35.

33. Bayindir S. A simple rhodanine-based fluorescent sensor for mercury and copper: The recognition of Hg²⁺ in aqueous solution, and Hg²⁺/Cu²⁺ in organic solvent. *Journal of Photochemistry and Photobiology A: Chemistry*. 2019;372:235-44.

34. Xu Y, Mao S, Peng H, Wang F, Zhang H, Aderinto SO, et al. A fluorescent sensor for selective recognition of Al³⁺ based on naphthalimide Schiff-base in aqueous media. *Journal of Luminescence*. 2017;192:56-63.

35. Wee SS, Ng YH, Ng SM. Synthesis of fluorescent carbon dots via simple acid hydrolysis of bovine serum albumin and its potential as sensitive sensing probe for lead (II) ions. *Talanta*. 2013;116:71-6.

36. Chai SC, Lu J-P, Ye Q-Z. Determination of binding affinity of metal cofactor to the active site of methionine aminopeptidase based on quantitation of functional enzyme. *Anal Biochem*. 2009;395(2):263-4.

37. Chai SC, Ye Q-Z. Analysis of the stoichiometric metal activation of methionine aminopeptidase. *BMC Biochem*. 2009;10:32-.



Radionuclide Potential of Holocene Sediments in the West of Marmara Sea (Turkey)

Zeki Ünal YÜMÜN^{1*}   and Erol KAM²  

¹Namık Kemal University, Çorlu Engineering Faculty, Environmental Engineering Department, 59860 Çorlu, Tekirdağ, TURKEY, zyumun@nku.edu.tr

²Yıldız Technical University, Faculty of Arts and Sciences, Physics Department, Davutpaşa Campus, 34220 Esenler/ İstanbul, TURKEY, erolkam@yildiz.edu.tr

Abstract: Radionuclides that cause radioactive pollution descend to the bottom in marine and water environments such as heavy metals and accumulate in bottom sediments. It is useful to determine the radionuclides in these environments to control the radionuclide release and its damage. Radioactive pollution can harm people's life directly or through the food chain. In this study, natural and artificial radionuclide values were measured in Recent sediment samples taken from the seabed in the western part of the Marmara Sea. Gamma spectrometry method was used in radionuclide examinations. In gamma spectrometry studies of sediments, values of radionuclides (⁴⁰K, ¹³⁷Cs, ²²⁶Ra, ⁵⁴Mn, ⁹⁵Zr, and ²³²Th) were determined. Sea depths where 18 analyzed seafloor sediments are taken vary between 15-50 m. The determined radionuclide concentration activity values of the study area are ¹³⁷Cs (0.9 - 9.4 (Bq / kg)), ²³²Th (18.9 - 86 (Bq / kg)), ²²⁶Ra (10 - 50 (Bq / kg)), ⁴⁰K (24.4 - 670 (Bq / kg)), ⁵⁴Mn (0.71-0.9 (Bq / kg)) and ⁹⁵Zr (0.18 - 0.19 (Bq / kg)). These values were correlated with the United Nations Scientific Committee on the Effects of Atomic Radiation (UNSCEAR). The ²²⁶Ra series, ²³²Th series, and ⁴⁰K radionuclides accumulate naturally, and their concentrations increase gradually due to anthropogenic impurities. ²²⁶Ra values obtained across the study areas are within normal limits according to UNSCEAR values. ⁴⁰K and ²³²Th values were higher than UNSCEAR values in all locations. ¹³⁷Cs (0.9 - 9.4 (Bq / kg)) from almost all locations reveals a risky situation in terms of ambient conditions because this element cannot be found in the natural environment and can be found artificially as an end of radioactivity.

Keywords: ⁴⁰K, ¹³⁷Cs, ²²⁶Ra, ⁵⁴Mn, ⁹⁵Zr, ²³²Th, radionuclide, Marmara Sea.

Submitted: March 02, 2020. **Accepted:** May 15, 2020.

Cite this: YÜMÜN ZÜ, KAM E. Radionuclide Potential of Holocene Sediments in the West of Marmara Sea (Turkey). JOTCSA. 2020;7(2):517-24.

DOI: <https://doi.org/10.18596/jotcsa.696731>.

***Corresponding author. E-mail:** zyumun@nku.edu.tr.

INTRODUCTION

Humanity has lived with radiation continuously from the beginning of our existence. With the formation of the Earth, very long-lived (order of billion years) radioactive elements, inherently a part of nature, have created a natural and inevitably accepted natural radiation level in the environment (1).

Natural and anthropogenic radioactivity is related to the primary sources of radioactive composition encountered in marine, terrestrial, and atmospheric environments.

Natural airborne radiation is caused either by radioactive gases from various cracks in the earth (especially from radon gas) or by cosmic rays. The radioactivity in the soil is due to uranium, thorium, and other radioactive substances included in the

decomposition series of those radioisotopes. Radiation in water is due to the interaction of the radioactive sources in both the air and the soil with water (2).

Natural radionuclide concentrations are continually increasing in terrestrial and mainly marine environments. The reason for that is the rapid increase in the use of artificial fertilizers, fossil fuels, detergents, and pesticides and also the proliferation of phosphate processing plants (3). The most critical radioactive substances found in natural waters are uranium, thorium, radium, radon, strontium, potassium, carbon, and hydrogen (4). Radionuclides that cause artificial radioactivity are spread to the environment as a result of radiological activities, radioactive waste heaps, or nuclear accidents. Although those activities create a variety of different radionuclides, the ones that play an essential role in the radiation exposure of humans are the products of diffusion and activation (^{137}Cs and others). Those radionuclides may lead to internal and external radiation damage in the human body. Therefore, the radioactivity levels in environmental samples must be measured with an acceptable error so that the exposure dose can be accurately assessed (5).

Nuclear weapons trials that began in 1945 and continue to date, along with the Chernobyl (1986) and Fukushima (2011) nuclear reactor accidents, have resulted in high levels of artificial radionuclides spreading to the atmosphere.

Among radionuclides spreading to the environment since 1945 are the long-half-life radionuclides, including ^{14}C , ^{137}Cs , and ^{90}Sr , which are important for environmental and human health. Those radionuclides accumulate in the marine environment and the living body, damaging both living spaces and living things (6).

In Turkey, Aközcan (2012) (7) studied the distribution of natural radionuclide concentrations in sediment samples in Didim and Izmir Bay. In his study, the activity concentrations of ^{238}U , ^{226}Ra , ^{232}Th , and ^{40}K in sediments collected from two different locations in the Aegean Sea have been defined. The highest activity concentrations of ^{238}U and ^{232}Th were observed in sediments from the Gulf of Izmir. The highest activity concentrations of ^{40}K in sediments were measured from Didim (7). Aytaş et al. (2012)(8) evaluated thirty sediment samples from different distances along the Maritza and Tundja River. These samples were analyzed by gamma spectroscopy for ^{238}U , ^{232}Th , and ^{40}K .

The measured average activity concentrations of ^{238}U and ^{232}Th are above the world average, but the average activity concentration of ^{40}K is within the world average value (8).

Natural and artificial radioactivity assessment of dam lakes sediments in the Çoruh River (Turkey) was studied by Kobya et al. (2015) (9). In the study, ^{238}U , ^{232}Th , ^{40}K , and ^{137}Cs activity concentrations were determined. The mean concentrations of ^{238}U , ^{232}Th , ^{40}K , and ^{137}Cs were found to be 15.8, 13.9, 551.5 and 18.1 Bq/kg respectively in Deriner Dam Lake (zone 1); 3.7, 12.5, 473.8 and 6.8 Bq/kg in Borçka Dam Lake (zone 2); 14.4, 30.0, 491.7 and 18.2 Bq/kg in Muratlı Dam Lake (zone 3) was determined. The fact that the activity concentration values of radionuclide are maximum in the Deriner Dam Lake, where the sediment deposition is at its maximum level (9).

This study aims to determine natural and artificial radionuclide distribution in both intense industrialization and non-industrialized areas of the West of Marmara Sea by using gamma spectrometry and bring out the risky areas for human life.

MATERIALS AND METHOD

The study area covers the area between Silivri (Istanbul) and Tekirdağ-Gelibolu (Çanakkale) in the north and between Lapseki (Çanakkale) and Bandırma (Balıkesir) in the south in the Western Marmara Sea (Figure 1).

The bathymetry of the sea from which the samples were taken ranges from 20 m to 35 m. In the Marmara Sea, the Anatolian (Southern Marmara) and Thrace (Northern Marmara) shores show different characteristics. Thrace shores, which meet the sea with large plateaus, feature gulfs (Tekirdağ and Silivri Gulfs) with wide arcs and beaches with small coves that have turned into lagoons. On the other hand, the Anatolian coast features the gulfs (Izmit, Gemlik, Bandırma, and Erdek) extending in the east-west and south-north directions and the islands (Kızıladalar, İmralı, and Marmara Islands) located in front of the rugged coasts (10). Core samples taken from 29 locations (sediment from the seafloor) were used in the study (Figure 2). The samples were taken between 15.10.2016 and 20.10.2016, and the coordinates and depth information of the samples are given in Table 1.

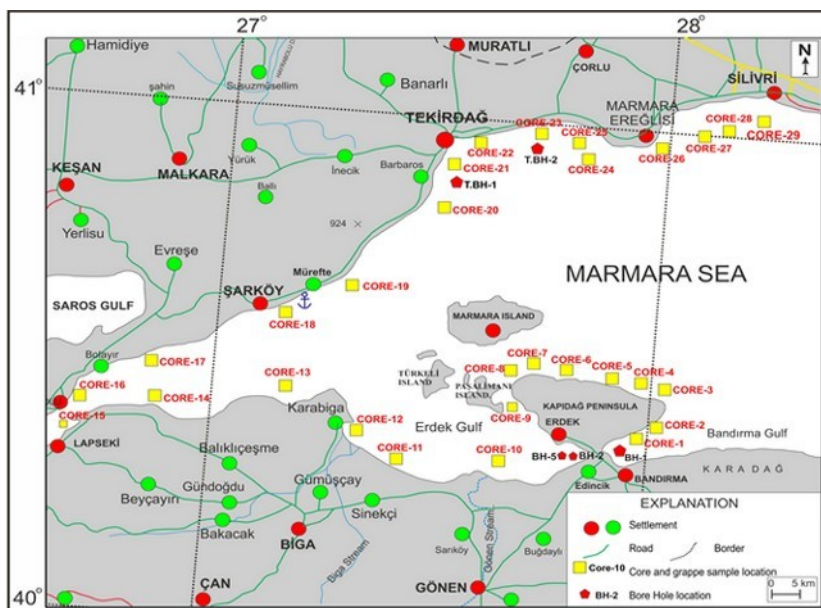


Figure 1. Location map of sample and study area.

Radionuclide analyses of the samples were made at the Çekmece Nuclear Research and Training Center. Samples were first dried at room temperature and prepared for analysis by sieving with 100-micron mechanical sieve. The samples were kept in the dry state for forty days were provided balance in radium, thorium, and other decomposition products. Concentration values of the radionuclides were analyzed using a Canberra GX5020 device.

The gamma activity peaks were: ^{238}U series, 609.3 keV; ^{232}Th series, 583 keV; ^{228}Ac , 911.2 keV; ^{226}Ra , 185.7 keV; ^{137}Cs , 661.7 keV; and ^{40}K , 1460.8 keV. In the gamma spectrometry analysis method, gamma ray-emitting radionuclides that irradiate at the energy range of 40 keV to 2000 keV are usually measured directly, without being separated from the sample matrix (such as air, water, soil, sediment, plant material, vegetable, and animal food.). Therefore, it is one of the most widely-used methods in the environmental analysis (5).

RESULTS

The range of radionuclide activity concentrations in the sediment samples, in Bq/kg, was 0.9–9.4 for ^{137}Cs ; 18.9–86 for ^{232}Th ; 10–50 for ^{226}Ra , and 24.4–670 for ^{40}K . Tables 2 and 3 present core sample radionuclide activities. The values were interpreted in comparison with the international average values as given in Table 4 (11).

In all locations, the analyses for ^{40}K were obtained in the core samples, the ^{40}K levels were above the world limits, whereas the ^{232}Th levels were below the limit in eleven locations and above world standard in eighteen locations. The values of ^{226}Ra were above the limit value at only one location (K-10, 50 Bq/kg). It is noteworthy that the ^{232}Th values (86–186 Bq/kg) reach the highest level in the Core-10 sample. One of the radioactive isotopes of cesium, ^{137}Cs , which is an alkali metal with similar chemical properties to potassium, reaches the highest value (9.4 Bq/kg) at the Core-20 location. That isotope has a considerably long physical half-life of 30.17 years; therefore, it is considered to be biologically hazardous for the ecosystem (12). The distributions of artificial and natural radionuclides at sea may differ from region to region, depending on various factors. The number of radionuclides deposited in marine environments vary with the physical and chemical properties of the radionuclide, dry or wet accumulation pattern, and topographic and meteorological environmental conditions (13).

Therefore, numerical results obtained from sediment samples show large variations. Figures 2, 3, 4, and 5 show the distribution of radionuclides for all sample locations in the west of the Marmara Sea. Figure 2 shows the map of ^{40}K , and radionuclides have been produced with the kriging method. Similarly, Figure 3 shows ^{226}Ra and Figure 4 shows ^{232}Th and Figure 5 shows ^{137}Cs radionuclides.

Table 1. Geographic coordinates of core samples.

CORE SAMPLE NUMBER	GPS-NO	DEPT H (M)	GEOGRAPHIC POSITION (WGS-84)		CORE SAMPLE NUMBER	GPS-NO	DEPTH (M)	GEOGRAPHIC POSITION (WGS-84)	
			East	North				East	North
CORE 1	116	30	058 14 59	447 46 77	Core 14a/b	142	29	049 02 82	447 33 47
CORE 2	117	29	058 49 85	447 66 92	Core 15	143	36	047 39 14	446 99 71
CORE 3	119	30	058 81 05	448 16 39	Core 16	144	43	047 29 08	447 24 87
CORE 3	120	35	058 62 29	448 27 80	Core 17	145	26	048 80 99	448 10 25
CORE 4A	121	30	058 23 93	448 35 51	Core 18	146	41	051 10 08	449 48 09
CORE 4B	123	32	058 22 60	448 39 37	Core 19	147	30	540197	4522435
CORE 4C	124	35	057 98 35	448 54 62	Core 20	148	33	542591	4530386
CORE 5	125	38	057 74 01	448 53 35	Core 21	149	32	546815	4533986
CORE 6A	126	40	056 68 40	448 63 34	Core 22	150	30	560139	4536953
CORE 7	127	48	056 21 01	448 68 10	Core 23	151	32	569767	4535792
CORE 8	128	39.5	055 81 97	448 48 62	Core 24	152	33	580368	4533824
CORE 9A	129	28	055 82 82	448 01 29	Core 25	153	33	588549	4541739
CORE 9B	137	32	055 83 61	447 97 91	Core 26	154	32	596782	4544493
CORE 10	138	19	055 62 81	446 36 87	Core 27	155	30	603222	4545684
CORE 11A/B	139	26	054 24 36	446 46 34	Core 28	156	31	540197	4522435
CORE 12	140	18	052 87 96	447 06 48	Core 29	157	35	542591	4530386
CORE 13	141	46	051 44 52	447 87 84					

Table 2. Results of gamma spectrometric analyses of core samples.

Sample	Radionuclide	Activity \pm Bq/kg	Sample	Radionuclide	Activity \pm Bq/kg
CORE-1	⁴⁰ K	490	CORE-10	¹³⁷ Cs	3.5
	¹³⁷ Cs	2.5		²²⁶ Ra	50
	²²⁶ Ra	30		²³² Th	86
CORE-2	²³² Th	42	CORE-11	¹⁵⁵ Eu	3.2
	¹³⁷ Cs	1.9		⁴⁰ K	670
	²²⁶ Ra	19.8		²³² Th	57
CORE-3	²³² Th	27.1	CORE-12	²²⁶ Ra	34
	²²⁶ Ra	25		¹³⁷ Cs	3.8
	²³² Th	28		⁵⁴ Mn	1.1
CORE-4	⁴⁰ K	24.4	CORE-13	²³² Th	49
	¹³⁷ Cs	1.4		²²⁶ Ra	28.2
	²³² Th	21.6		¹³⁷ Cs	4.9
CORE-5	⁵⁴ Mn	0.71	CORE-14	²³² Th	45
	⁴⁰ K	470		²²⁶ Ra	25.7
	¹³⁷ Cs	1.8		¹³⁷ Cs	2.2
CORE-6	²²⁶ Ra	21.5	CORE-15	^{95+Zr}	0.27
	²³² Th	30		⁴⁰ K	470
	⁴⁰ K	450		²³² Th	36
CORE-7	¹³⁷ Cs	1.3	CORE-16	²²⁶ Ra	25.2
	²²⁶ Ra	27		¹³⁷ Cs	0.90
	²³² Th	26		¹³⁷ Cs	3.2
CORE-8	¹³⁷ Cs	1.1	CORE-17	²²⁶ Ra	19.5
	²²⁶ Ra	24		²³² Th	36
	²³² Th	39		⁴⁰ K	600
CORE-9	^{95+Zr}	0.2	CORE-18	¹³⁷ Cs	4.7
	¹³⁷ Cs	1.1		²²⁶ Ra	24.9
	²²⁶ Ra	18.6		²³² Th	37
CORE-10	²³² Th	30	CORE-19	¹³⁷ Cs	1.6
	⁴⁰ K	470		²²⁶ Ra	18.9
	¹³⁷ Cs	0.9		²³² Th	26
CORE-11	²²⁶ Ra	19	CORE-20	²²⁶ Ra	10
	²³² Th	33		²³² Th	21
				⁴⁰ K	550
CORE-12			CORE-21	¹³⁷ Cs	1
				²²⁶ Ra	22
				²³² Th	38
CORE-13			CORE-22	^{95+Zr}	0.19
				⁴⁰ K	480
				²³² Th	24
CORE-14			CORE-23	²²⁶ Ra	19.2
				¹³⁷ Cs	0.8
				¹³⁷ Cs	1.3
CORE-15			CORE-24	²²⁶ Ra	16.1
				²³² Th	21.7
				⁴⁰ K	580
CORE-16			CORE-25	¹³⁷ Cs	1
				²²⁶ Ra	18.1
				²³² Th	24.8
CORE-17			CORE-26	²²⁶ Ra	20.9
				²³² Th	31

Table 3. Results of gamma spectrometric analyses of core samples (continuation of Table 2)

Sample	Radionuclide	Activity \pm Bq/kg	Sample	Radionuclide	Activity \pm Bq/kg
CORE-18	¹³⁷ Cs	4.8	CORE-24	²²⁶ Ra	10
	²²⁶ Ra	29		²³² Th	21
CORE-19	²³² Th	36	CORE-25	⁴⁰ K	550
	⁴⁰ K	650		¹³⁷ Cs	1
	¹³⁷ Cs	2.3		²²⁶ Ra	22
CORE-20	²²⁶ Ra	27.9	CORE-26	²³² Th	38
	²³² Th	39		^{95+Zr}	0.19
	⁴⁰ K	630		⁴⁰ K	480
CORE-21	¹³⁷ Cs	9.4	CORE-27	²³² Th	24
	²²⁶ Ra	20.5		²²⁶ Ra	19.2
	²³² Th	35		¹³⁷ Cs	0.8
CORE-22	¹³⁷ Cs	3.7	CORE-28	¹³⁷ Cs	1.3
	²²⁶ Ra	20.6		²²⁶ Ra	16.1
	²³² Th	30		²³² Th	21.7
CORE-23	¹³⁷ Cs	5.1	CORE-29	⁴⁰ K	580
	²²⁶ Ra	27		¹³⁷ Cs	1
	²³² Th	20.7		²²⁶ Ra	18.1
CORE-24	¹³⁷ Cs	1.7	CORE-30	²³² Th	24.8
	²²⁶ Ra	13.7		²²⁶ Ra	20.9
	²³² Th	18.9		²³² Th	31

Table 4. International average values of radionuclides (11) *Radionuclides* *International Average Limit Values*

<i>Radionuclides</i>	<i>International Average Limit Values</i>
^{232}Th	30 Bq/kg
^{226}Ra	35 Bq/kg
^{40}K	400 Bq/kg

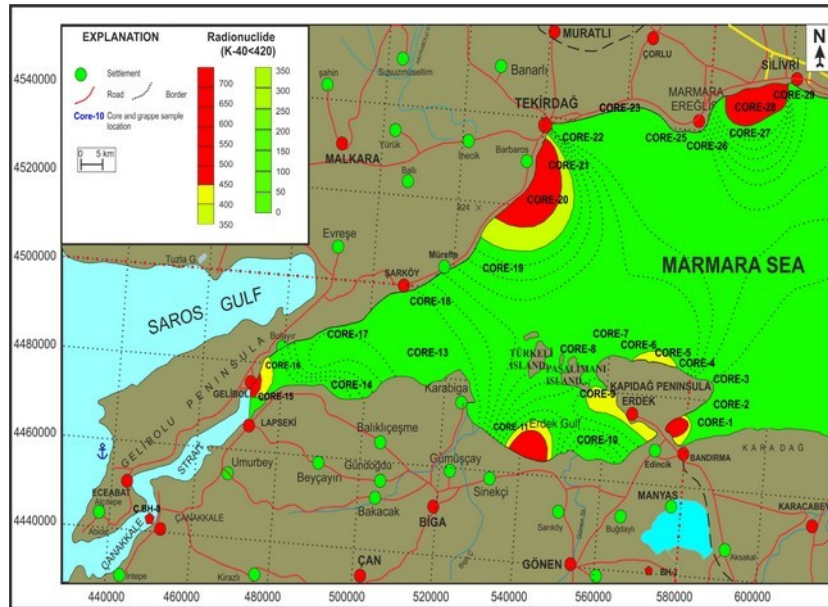


Figure 2. Distribution of the activity concentrations of ^{40}K (Bq/kg)

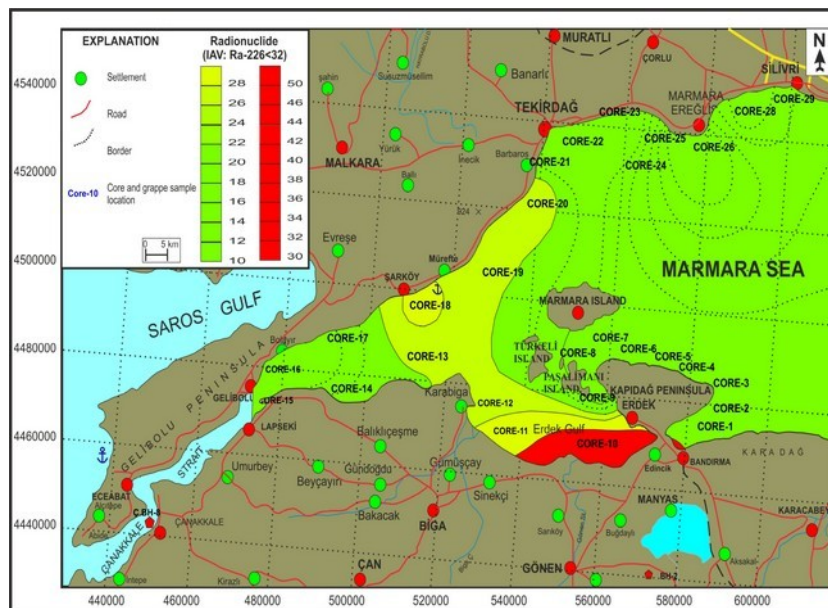


Figure 3. Distribution of the activity concentrations of ^{226}Ra (Bq/kg).

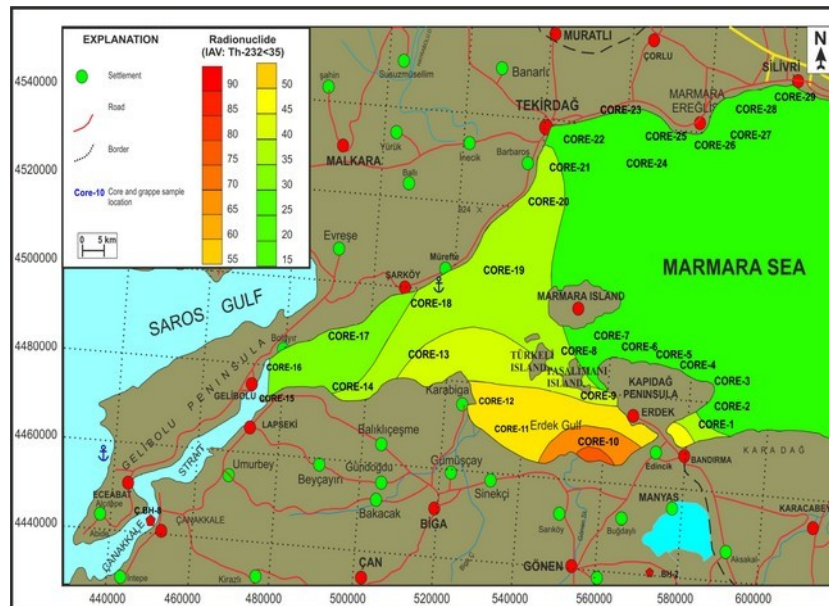


Figure 4. Distribution of the activity concentrations of ^{232}Th (Bq/kg).

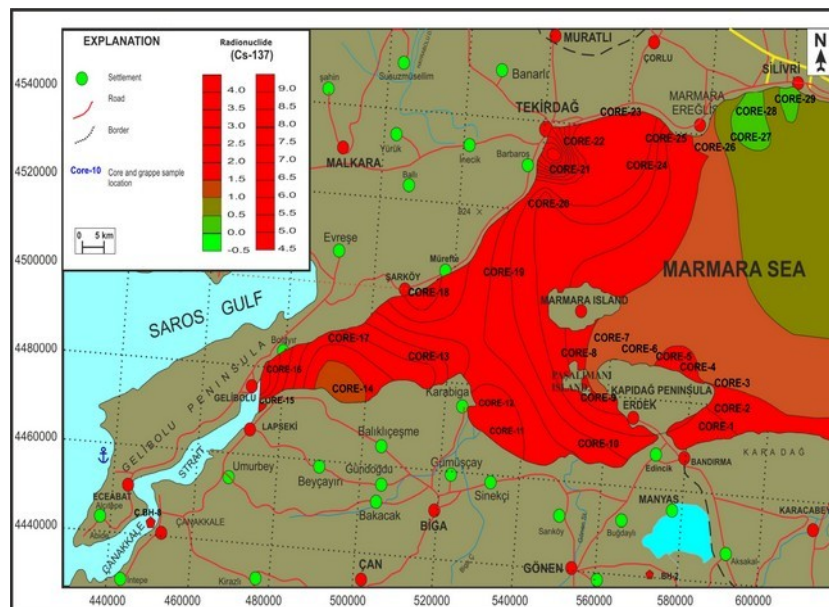


Figure 5. Distribution of the activity concentrations of ^{137}Cs (Bq/kg).

DISCUSSION AND CONCLUSION

In this study, core samples were collected from 29 different locations in the Marmara Sea for radioactivity analyses for ^{40}K , ^{232}Th , ^{137}Cs , ^{226}Ra , ^{54}Mn , and ^{95}Zr on the western coast of the Sea of Marmara. The Gamma Spectrometric Analysis method was used to determine the radioactivity properties of the sediments. The radionuclide concentration activity values in the sediment samples obtained from the locations, in Bq/kg, were ^{137}Cs , 0.9–9.4; ^{232}Th , 18.9–86; ^{226}Ra , 10–50; ^{40}K , 24.4–670; ^{54}Mn , 0.71–0.9; and ^{95}Zr , 0.18–0.19. These values were compared with data from the Turkish Atomic Energy Agency (TAEK) and the United Nations Scientific Committee on the Effects

of Atomic Radiation (UNSCEAR), and environmental analysis was also carried out. As a result of the analyses ^{40}K values were found to be zero in Core-2, Core-3, Core-4, Core-7, Core-8, Core-10, Core-12, Core-13, Core-15, Core-17, Core-18, Core-21, Core-23, Core-24, Core-27, and Core-29. The ^{137}Cs value was zero in Core-3 and Core-24, whereas it was determined to be 9.4 (Bq/kg) in Core-20. In the Core-11 sample taken from the Sea of Marmara (between Gönen Creek and Karabiga), the ^{40}K value was higher than those of other locations and higher than the average world value. On the contrary, ^{226}Ra values measured in all the core samples were below the limit values.

ACKNOWLEDGMENTS

The author thanks Yümün Mühendislik Ltd. Şti for their studies on drilling and core sampling and Melike ÖNCE, Sevinç YÜMÜN for the preparation of the samples in the laboratory and also for the separation studies of other fossils.

REFERENCES

1. TAEK. Radyasyon Kaynakları. Web. <http://www.taek.gov.tr/ogrenci/r05.htm> (In Turkish); 2012
2. Görür Ş. Investigation of the Relationship Between Environmental Radioactivity and Radioactivity in Dental Specimens. Cukurova University Institute Of Science Sciences, Graduate thesis. 2006; 1-74.
3. Topçuoğlu S. Radioactive Pollution of Seas. Web. <http://www.gelbalder.org/literatur/6238-deniz-kirliligi-analiz-yontemleri-iligili-uluslar-arasi-sozlesmeler-2.html>; 2012.
4. Tekirdağ Valiliği. Tekirdağ Province Environmental Status Report. T.C. Tekirdağ Governorship Provincial Environment and Forestry Directorate 285-286. 2009.
5. Ayçık GA, Onat NB, Ertürk MK, Topçuoğlu S, Köksal G, Yaşar S, Güngör N. Sampling, measurement and analysis methods for monitoring environmental radioactivity, Turkish Atomic Energy Authority. 2000.
6. Ergül HA. Investigation of some heavy metal, radionuclide, organic carbon and chlorophyll-a levels of sedimenting material in Oxide Zone in Trabzon region of Black Sea. PhD Thesis, Karadeniz Technical University Institute of Science and Technology, Department of Biology. 2004.
7. Aközcan S. Distribution of natural radionuclide concentrations in sediment samples in Didim and Izmir Bay (Aegean Sea-Turkey), Journal of Environmental Radioactivity. 2012; 112: 60-63.
8. Aytaş Ş, Yusan S, Aslani MA, Karali T, Turkozu D, A, Gök C, Erentürk S, Gökçe M, Oğuz KF. Natural Radioactivity of Riverbank Sediments of the Maritza and Tundja Rivers in Turkey. Journal of Environmental Science and Health, Part A. 2012; 47: 2163-2172.
9. Kobya Y, Taşkın H, Yeşilkanat CM., Varinlioğlu A, Korcak S. Natural and Artificial Radioactivity Assessment of Dam Lakes Sediments in Çoruh River, Turkey. Journal Radioanal Nucleid Chemical. 2015; 303: 287-295.
10. Bursa GC. Marmara Denizi. Web. <http://bgc.org.tr/ansiklopedi/marmara-denizi.html> [10].2015.
11. UNSCEAR. Sources and Effects of Ionizing Radiation. United Nations Scientific Committee On The Effects Of Atomic Radiation. Report to General Assembly with Scientific Annexes. United Nations, New York. 2000; 1, 1-659.
12. Aközcan S. Cs-137 Concentrations in Sediment and Waters of Büyük Menderes River and Dilek Peninsula Büyük Menderes Delta. Ekoloji. 2011; 20 (81): 55-60.
13. Aközcan S. Monitoring of Some Radionuclide and Heavy Metal Levels in Sediment, Sea Water and Different Marine Organisms in Didim and İzmir Bay (Turkish with English Abstract). PhD Thesis, Ege University Institute of Science, Department of Nuclear Science, İzmir. 2009.



Simple and sensitive detection of quercetin antioxidant by TEOS coated magnetic Fe₂O₃ core-shell

Ahmet ŞENOCAK*  

* Department of Chemistry, Gebze Technical University, 41400 Gebze, Kocaeli, Turkey

Abstract: In this study, α -Fe₂O₃ and tetraethyl orthosilicate (TEOS) coated Fe₂O₃ (TEOS@Fe₂O₃) was synthesized by the sol-gel method. The morphological properties and electrochemical detection of quercetin antioxidant with Fe₂O₃ and TEOS@Fe₂O₃ nanomaterials were evaluated. TEOS@Fe₂O₃ material was modified on a glassy carbon electrode (GCE) for the detection of quercetin with a linear range of 1.0-9.0 μ M by square wave voltammetry (SWV). TEOS@Fe₂O₃/GCE sensor ca 1.6 and 2.5 times more sensitive than Fe₂O₃/GCE and GCE. The quantification (LOQ) and detection (LOD) limits were found to be 306 and 92 nM for quercetin antioxidant on the TEOS@Fe₂O₃ modified electrode. Quercetin was also determined in an apple tea sample with a standard addition method, and the recovery of quercetin was obtained to be 104.16% and 106.04%. The results obtained from this study show that the TEOS@Fe₂O₃ modified electrode examined as a voltammetric sensor was found to be sensitive and straightforward to quercetin.

Keywords: Quercetin antioxidant; Magnetic nanoparticle; Electrochemical sensor, TEOS.

Submitted: May 06, 2020. **Accepted:** May 17, 2020.

Cite this: ŞENOCAK A. Simple and sensitive detection of quercetin antioxidant by TEOS coated magnetic Fe₂O₃ core-shell. JOTCSA. 2020;7(2):525-34.

DOI: <https://doi.org/10.18596/jotcsa.733141>.

*Corresponding author. E-mail: asenocak@gtu.edu.tr.

INTRODUCTION

Magnetite nanoparticles have attracted attention due to potential application in numerous biomedical applications and special physicochemical features, such as contrast agents in magnetic resonance imaging, carriers for targeted drug delivery, the magnetic separation in microbiology, biochemical sensing (1-3). Iron oxides nanoparticles have found extensive interest recently, and these materials often show unique magnetic, physical, catalytic, and optical features (4-6). These non-toxic and cheap nanomaterials are potential applications in high technology and used for enhanced the properties of storage media (7), in drug delivery, biosensors (8), and catalysts (9). The size and magnetic anisotropy of the particles are related to magnetization values of iron oxide nanostructures (10). Fe₂O₃ nanoparticles are exceptionally eco-friendly, rich in magnetite nanoparticles, economical, and highly resistant to corrosion, and they were also found to

be stable at room temperature (11). Therefore, Fe₂O₃ nanoparticles are applied to catalysts and a variety of soft and hard magnetic materials, and they have good biocompatibility (12, 13).

Recent studies have been shown that there is increasing interest in preventing diseases such as obesity, cardiovascular, inflammatory processes, cancer, and neurodegenerative disorders (14). These disorders can accelerate as people grow older, and their effects may be decreased by the intake of vegetables and fruits (15, 16). A diet containing Vitamin A and polyphenolic compounds, consideration of active nutrients in the prevention of disease because of oxidative stress, may decrease the effect (17). Moreover, the determination of antioxidants has increased to significant importance to protect from these disorders (18, 19). Flavonoids are naturally found in fresh vegetables and fruits, and they generally used as a component of health products and food additives (20). They show anti-

inflammatory and antioxidant properties concerning radical scavenging features of the compounds. Quercetin is a member of the flavonoid family, found in apples, onions, sweet pepper, grapes, celery, and honeysuckle. The antioxidant properties of quercetin have been extensively explored in the past studies (21, 22) due to other biological advantages such as anti-tumor, anti-viral, anti-allergic activities, reducing blood lipids and blood pressure (16, 23, 24). For this reason, developing sensitive, fast and straightforward determination methods of quercetin is vitally important.

Quercetin determination was carried out by traditional methods such as ultra-performance liquid chromatography (25), spectrofluorimetry (26, 27), and mass spectrometry (28), which are highly selective and sensitive. However, they are time-consuming, expensive, and complicated sample preparation. Voltammetric techniques are potentially applied for the determination of quercetin because of the electrochemical activity to overcome these difficulties (29). Therefore, Fe_2O_3 was coated TEOS to obtain $\text{TEOS@Fe}_2\text{O}_3$, which is a spherical material for the determination of quercetin via the electrochemical method for the first time. Due to higher surface area, well-designed material shape, and electroactive metal content, $\text{TEOS@Fe}_2\text{O}_3$ was tested in quercetin determination via signal amplification.

Herein, a magnetic nanoparticle of $\text{TEOS@Fe}_2\text{O}_3$ has been synthesized and successfully immobilized onto a GCE using an electrochemical sensor. The electrode showed impressive electrocatalytic action for the oxidation of quercetin, which is characterized by the enhancement of the highest current in both cyclic and square wave voltammetry techniques. After optimization, the electrode was used for quantification of quercetin in apple tea sample extracts. Experiments indicated that the $\text{TEOS@Fe}_2\text{O}_3$ based sensor was shown excellent electrocatalytic activity to quercetin.

EXPERIMENTAL

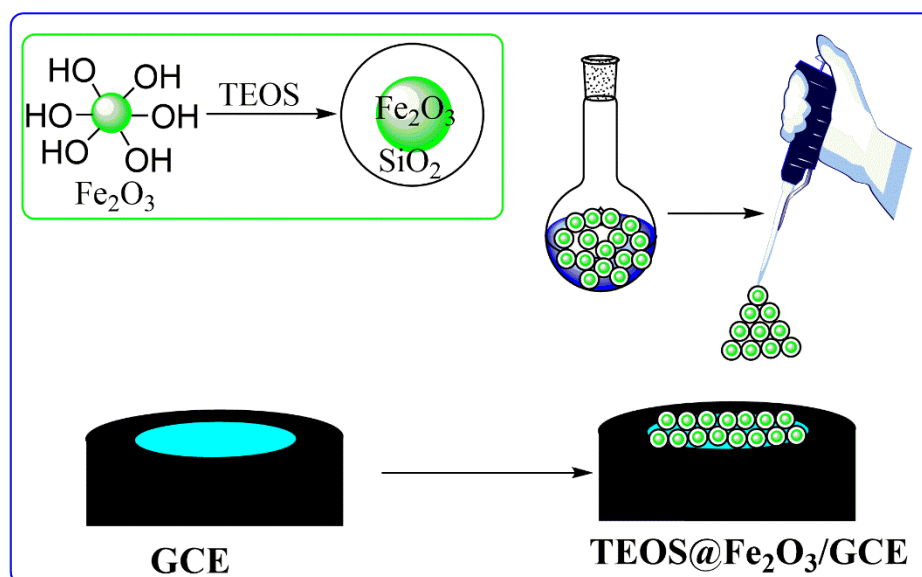
Materials and Characterization Techniques

$\text{Fe}(\text{NO}_3)_3 \cdot 9\text{H}_2\text{O}$ (98%), citric acid (98%) and quercetin (99%) were supplied from Sigma Aldrich, and stock solution of quercetin (concentration of 1 mM) was prepared daily. 0.1 M Britton-Robinson (BR) buffer solution, which was used as an electrolyte and prepared by boric, orthophosphoric, and acetic acids in pure water and kept at 4.0 °C. pH value of buffer solutions was adjusted by 5 M NaOH with a pH meter (Mettler Toledo, Switzerland). Voltammetric studies were carried by an electrochemical analyzer system of CH Instruments (CHI440B model, USA) at 25 °C. A three-electrode cell consisting of a counter, reference, and working electrodes are platinum wire, Ag/AgCl, and $\text{TEOS@Fe}_2\text{O}_3/\text{GCE}$, respectively.

Surface morphological properties of Fe_2O_3 and $\text{TEOS@Fe}_2\text{O}_3$ materials were performed by scanning (SEM) and transmission electron microscopic methods (TEM). The morphology of the synthesized hybrids was studied using an FEI (PHILIPS) XL30 SFEG scanning electron microscope. TEM images were obtained using an FEI TALOS F200S TEM instrument (accelerating voltage of 200 kV).

Preparation of Fe_2O_3 and $\text{TEOS@Fe}_2\text{O}_3$

Hematite ($\alpha\text{-Fe}_2\text{O}_3$) nanoparticles were prepared according to a simple method given in the literature with a slight modification (30, 31). Briefly, 10 mmol $\text{Fe}(\text{NO}_3)_3 \cdot 9\text{H}_2\text{O}$ and 12.5 mmol citric acid was dissolved in 60 mL of pure water and mixed ultrasonically for about 20 minutes. Then, 10 mL of ethanol was added, and the pH was adjusted to 5 with ammonia. The solution was taken into a beaker and boiled until obtaining a gel. It was transferred into an oven at 95 °C for drying. The dried gel was purged with pure N_2 gas for 30 minutes and placed to a tube furnace annealed to 400 °C for 3 hours. The final product was 1.5 g of $\alpha\text{-Fe}_2\text{O}_3$. The prepared $\alpha\text{-Fe}_2\text{O}_3$ particles were coated with silica using a sol-gel method (32). In a typical procedure, 100 mg of Fe_2O_3 was dispersed in absolute ethanol solution by ultrasonic bath, and 750 μL of NH_4OH and 400 μL of TEOS have added the suspension (Scheme 1, inset). The morphological analysis of samples was characterized by SEM and TEM.



Scheme 1. Schematic representation of the synthesis of TEOS@Fe₂O₃ material and fabrication of the sensor.

Preparation of the TEOS@Fe₂O₃ modified GCE

Scheme 1 depicts the fabrication procedure of the sensor based on the investigated TEOS@Fe₂O₃. The mirror-like clean surface of GCE was obtained with different size alumina powders ranging between 1.0 to 0.05 µm. Then GCE was cleaned after each polishing with ultra-pure water and ultrasonicated in acetone, HNO₃ solution (1:1, v/v), and double-distilled water, respectively. The cleaned GCE was then dried at room temperature until use. The TEOS@Fe₂O₃ modified GCE was obtained by drop-casting method. 2 mg of TEOS@Fe₂O₃ was placed into 1.0 mL ultra-pure water and stirred in an ultrasonic bath for 15 min to obtain well-dispersed 2 mg/mL suspension. An amount of 10 µL brownish-red suspension was transferred onto the cleaned surface of the electrode and dried at 40 °C. The obtained sensor electrode was taken as TEOS@Fe₂O₃/GCE.

Real samples assay procedure

Apple tea sample was purchased from a local market and weighed as 0.5 g and dissolved in ethanol (10.0 mL). The sample solution was well dispersed by an ultrasonic bath for 20 min. The supernatant of the dispersion was separated by centrifugation for 4 min at 3000 rpm. The sample solution was used to determination of quercetin without any further treatment. Electrochemical determination of quercetin was performed in the solution by the SWV technique from 0.0 to 1.0 V. All real sample detection measurements were applied three times at room temperature, and average values were taken to calculate the amount of quercetin antioxidants.

RESULTS AND DISCUSSION

Morphological Characterization of Fe₂O₃ and TEOS@Fe₂O₃

Morphological characterization of Fe₂O₃ and TEOS@Fe₂O₃ were investigated by scanning SEM TEM (Figure 2). Figure 2a demonstrates a typical SEM image of the α-Fe₂O₃ samples. As seen in this figure, pores structure can be monitored with an average size of 50-60 nm. SEM images also clearly showed the nanostructural homogeneities and remarkably unique neck-structured morphology, which could be the advantage of the penetration of antioxidant molecules. Figure 1b depicts the SEM image of TEOS@Fe₂O₃ particles. A large number of iron particles are monitored on the Si substrate with diameters in the range of 250-400 nm. Figure 2c and 2d show TEM images of the α-Fe₂O₃ and TEOS@Fe₂O₃ particles. Although Fe₂O₃ nanoparticles can be obtained as the shaping of many rough surfaces and different sizes, TEOS@Fe₂O₃ particles have almost uniform shapes. The spherical TEOS@Fe₂O₃ particle sizes were also confirmed by TEM. Besides, elemental analysis of the spherical structures, EDX analysis (installed in SEM) was carried out. The EDX analysis of the α-Fe₂O₃ particles represents the atomic percentage (%) of the O, Fe is 2:1, and the percentage of Fe, O, and Si in TEOS@Fe₂O₃ are 2:5:3.

Electrochemical Sensor Examination Tests of TEOS@Fe₂O₃ Material to Quercetin

The cleaned GCE was coated by 10 µL drop of the TEOS@Fe₂O₃ suspension (2 mg/mL) in ultra-pure water to provide the TEOS@Fe₂O₃/GCE sensor. The electrochemical sensor properties of TEOS@Fe₂O₃/GCE towards 6 µM quercetin were investigated by SWV methods with bare GCE, Fe₂O₃/GCE in a BR buffer solution (pH = 2) comparatively.

TEOS@Fe₂O₃/GCE sensor ca 2.5 and 1.6 times more sensitive than pristine GCE and Fe₂O₃/GCE, respectively (Figures 1a and 1b).

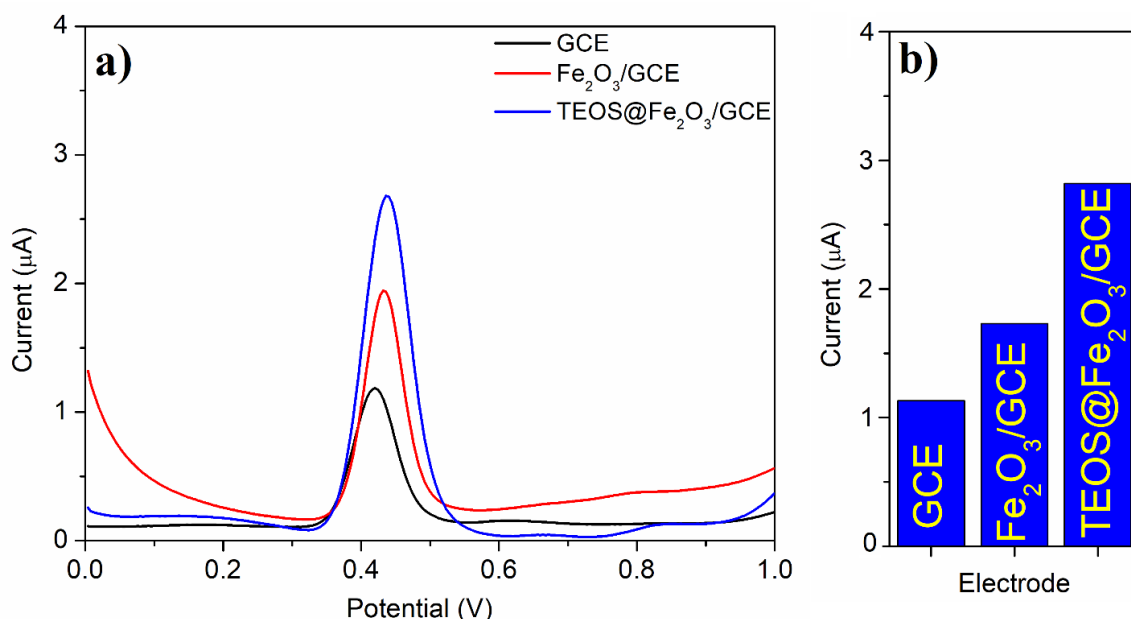


Figure 1. a) SWV response to 6 μM quercetin (pH=2) TEOS@Fe₂O₃/GCE in comparison with bare GCE and Fe₂O₃/GCE, b) their column graph.

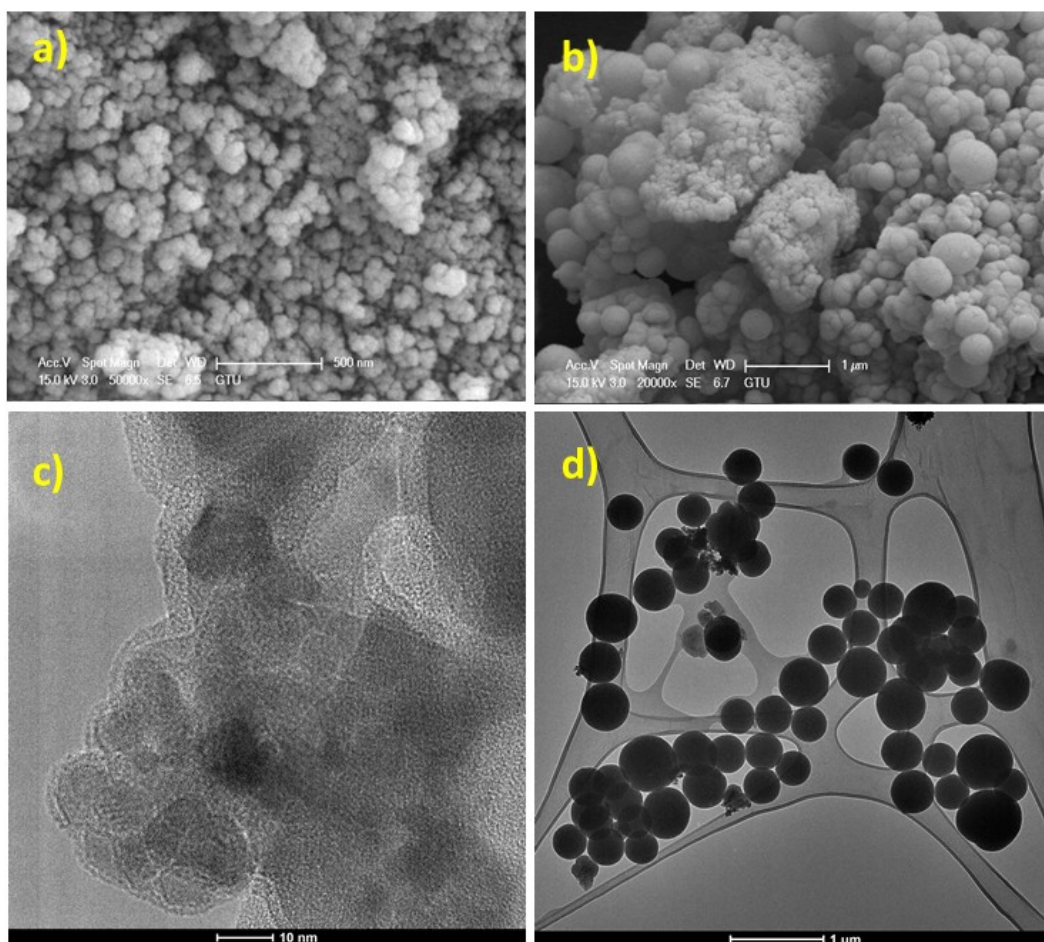


Figure 2. a) and b) SEM images, c) and d) TEM of images of Fe₂O₃ and TEOS@Fe₂O₃

The investigation of pH impact on voltammetric sensor features was also evaluated in BR buffer solution, and adjustments of pH were performed by NaOH solution (5.0 M). Figure 3a depicts the SWV responses of quercetin in the BR solutions with different pH values (2-7). The optimal pH value is found to be 2 because of better and higher peak current. When the acidic pH value comes out, the interaction between -OH functional groups in quercetin and electron-deficient boron atoms of in the BR are increased (33). Thus, it can be said that the reaction between the quercetin and the TEOS@Fe₂O₃ is a pH-dependent reaction.

Moreover, higher hydrophobic interaction and hydrogen bond formation occurs between spherical TEOS@Fe₂O₃ nanomaterial. Also, mass transfer of quercetin via diffusion happened very hard because

the at basic and neutral pH can limit the surface of the electrode and causes a decrease of the peak current. Due to the inhibition of quercetin antioxidant transfer by the absorption with OH functional groups, peak current values decreased suddenly. Quercetin's oxidation peak currents are almost invisible at high pH, along with a decrease of interaction between the buffer solution and OH of the quercetin (34). Therefore, the relationship between peak current and pH values (range of 2 to 7) was shown in **Figure 3b**, which demonstrates a linear decrease with a slope of 60.80 mV/pH. This value is very close to 59 mV/pH (Nernstian behavior) (29, 35). This voltammetric response has the same numbers of proton and electron ($y = -0.0608x + 0.5896$, $R^2 = 0.9961$) and in harmony with the electro-oxidation mechanism of quercetin (29).

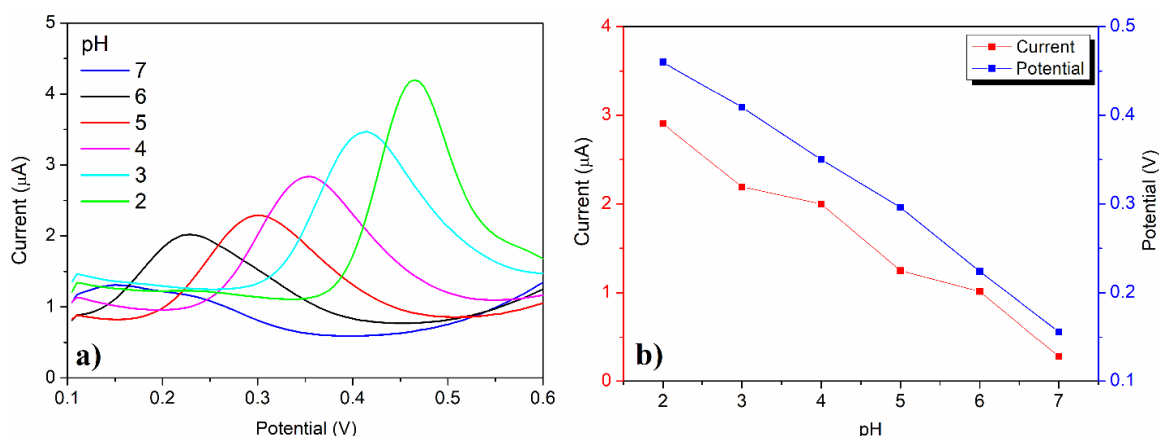


Figure 3. a) SWV responses at different pH values in the range of 2-7 and b) changes in pH with peak currents and peak potentials.

Not only electrokinetic behavior, both also analytical features performed by SWV and CV techniques. Figure 4a demonstrates the SWV responses obtained by different concentrations of quercetin on the TEOS@Fe₂O₃/GCE at the supporting electrolyte as a pH 2.0 BR buffer solution. As seen, this figure

with a concentration of quercetin ranging from 1.0 to 9.0 μ M was linearly increasing of peak current (Figure 4b). The LOQ and LOD of quercetin antioxidant were calculated as 306 and 92 nM ($y = 0.4632x - 0.0391$, $R^2 = 0.9956$) respectively.

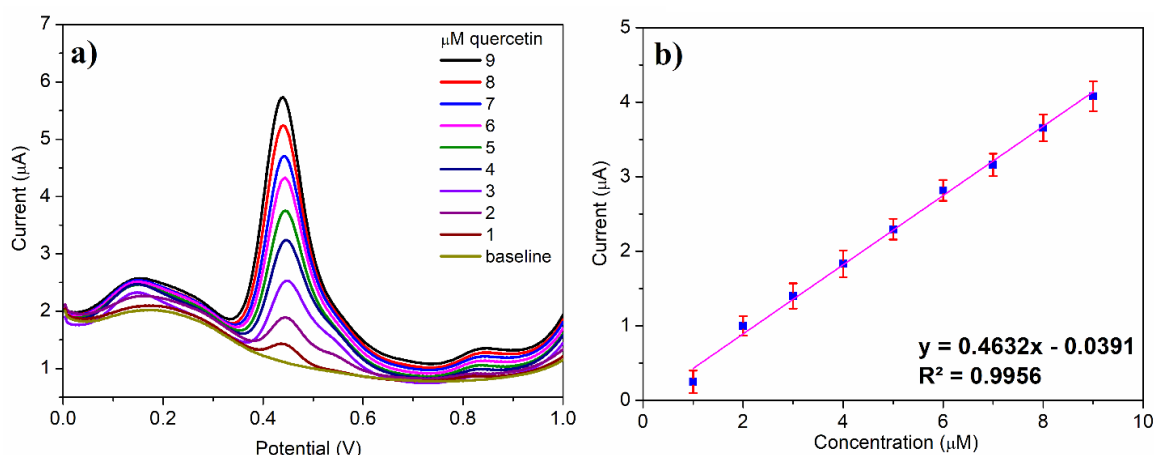


Figure 4. a) SWV responses at increasing concentrations of quercetin on the TEOS@Fe₂O₃ modified GCE and b) calibration graphs corresponding to (a).

CV measurements were carried out to determine the impact on the redox reaction mechanism of quercetin by the scan for gaining further information about the relationship between the scan rate and peak current. Figure 5a demonstrates the electrochemical measurements containing 6 μM quercetin, which was performed at the several scan rates (in the ranging from 25 to 500 mV/s) in the buffer (pH=2.0). As seen in Figure 5b, the peak current was increased linearly with an increase of

the scan rate (R^2 values were found to be 0.9979 and 0.9989 for oxidation and reduction). This linear correlation was pointed out that the electro-oxidation process of quercetin is controlled by adsorption in agreement with the previous works (36). Also, the quercetin has reversible electrode processes because it exhibited two peaks, which are an anodic peak at 490 mV and a cathodic peak at 430 mV.

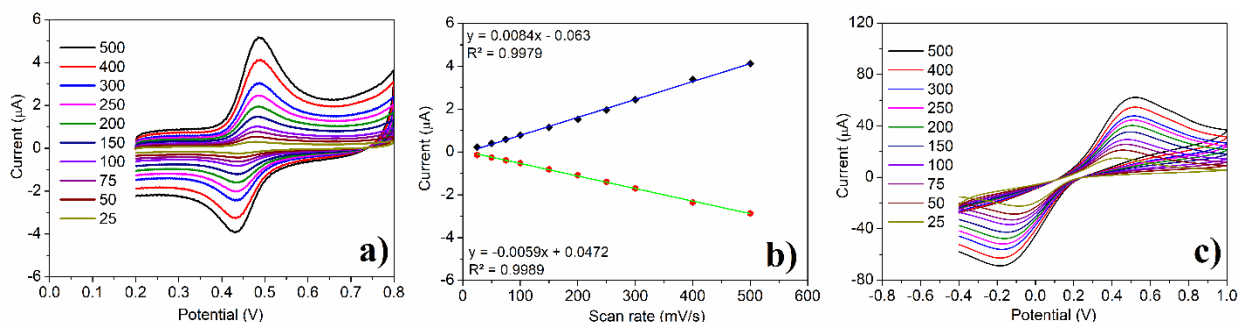


Figure 5. a) CV responses of 6 μM quercetin at various scan rates, b) Plot of I_{pa} and I_{pc} and c) CV of TEOS@Fe₂O₃/GCE in a solution containing K₃[Fe(CN)₆] and KCl at different scan rates in the ranging from 25 to 500 mV/s.

CV at different scan rates was performed to estimate the specific surface area of TEOS@Fe₂O₃ modified GCE in a solution containing K₃[Fe(CN)₆] and KCl by Randles-Sevcik equation (Figure 5c). The concentrations of KCl and K₃[Fe(CN)₆] were 0.1 M and 5.0 mM. where A , D_0 , and C_0 are the specific surface area (cm^2) of the TEOS@Fe₂O₃ modified GCE, the concentration of K₃[Fe(CN)₆] (5.0 mM) and diffusion coefficient ($7.6 \times 10^{-6} \text{ cm}^2/\text{s}$). The activated surface area of TEOS@Fe₂O₃-GCE was estimated as 0.103 cm^2 from the Randles-Sevcik equation by calculating the slope of I_p vs $\nu^{1/2}$ plot. This surface area was more remarkable than the unmodified GCE (0.071 cm^2).

Repeatability, Stability, Selectivity, and Comparison Of TEOS@Fe₂O₃/GCE Sensor

Anions and cations such as SO₄²⁻, NO₃⁻, K⁺, Na⁺, Mg²⁺, Ca²⁺, Fe³⁺, Ni²⁺ were examined to show the selectivity of the TEOS@Fe₂O₃ modified GCE sensor at 25 °C. Selectivity experiments were carried out by SWV method using 10 mM of anions and metal ions stock solutions in ultra-pure water. Besides, another interfering study was done in the presence of adenine purine base and ascorbic acid, and glucose solutions at concentration of 1 mM in water. Anions, metal ions and other interfering molecules had no significant effect (< 4%) on the electrochemical response on 6 μM quercetin (Figure 6 a and b).

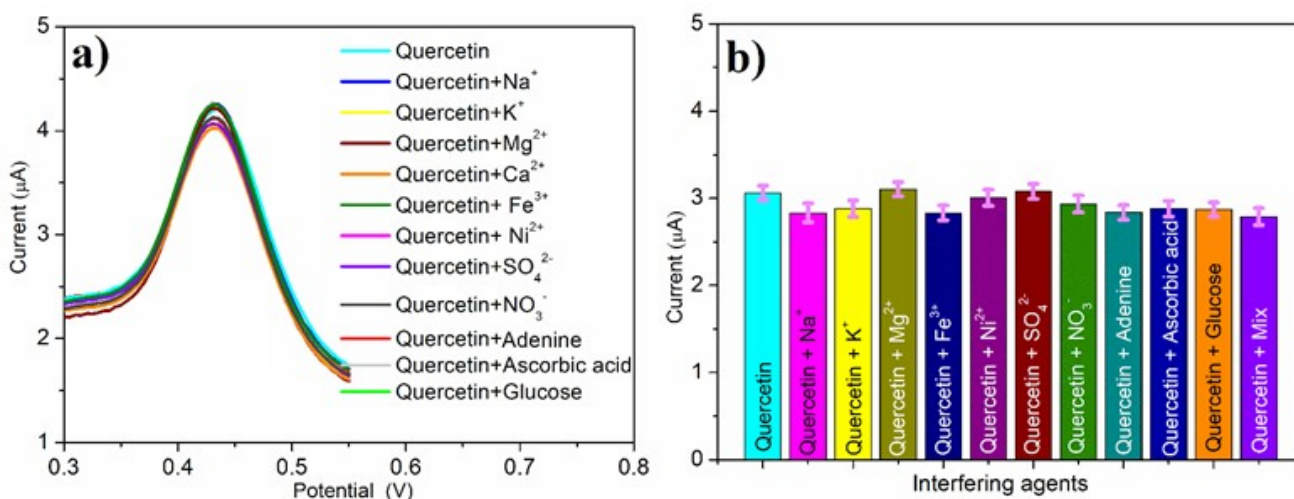


Figure 6. a) DPV curves in the presence of anions, cations, and bioanalytes and b) their column graph.

SWV technique was performed in the stability experiment of the sensor every weekday for the determination of quercetin. The electrochemical responses measured in a pH of 2 on TEOS@Fe₂O₃ modified GCE at 25 °C, which did not demonstrate any significant changes in comparison with the beginning response. RSD (Relative Standard Deviation) of the peak current values was found to

be 4.1%. Moreover, the repeatability test was done by 7 successive SWV of 6.0 µM quercetin on TEOS@Fe₂O₃/GCE, and the RSD was calculated to be 3.5%. It can be concluded that the results from these measurements TEOS@Fe₂O₃/GCE sensor showed high repeatability and stability for the determination of quercetin.

Table 1. Comparison of present electrochemical sensors with other reported methods for the determination of quercetin in various samples.

Methods	Working Electrode	LOD (nM)	Sample	References
SWV	TEOS@Fe ₂ O ₃ /GCE	92	Apple Tea	This work
SWV	Co nanoparticle/GCE	100	Tablet and urine	(37)
SWV	NiO-CNT/CPE	30	Onion, apple and capsule	(38)
DPV	MIP-GO/GCE	48	Apple juice	(39)
DPV	Carbon@Fe nanoparticle/GCE.	150	Human urine	(40)

MIP-GO: Molecularly imprinted polymer incorporated graphene oxide, CNT: Carbon nanotube, CPE: Carbon paste electrode.

TEOS@Fe₂O₃/GCE sensor system was compared with the other techniques data on the determination of quercetin given in Table 1. The obtained outcomes in this study demonstrated that TEOS coated Fe₂O₃ sensor system had excellent properties for the selective and sensitive determination of quercetin. The suggested TEOS@Fe₂O₃/GCE had some benefits in terms of LOD and linear range. In most quercetin determination studies, electrode modifications were done by carbon nanotube, graphene oxide, and metal nanoparticles. As known, carbon nanotubes have high toxicity, and graphene is expensive and challenging to synthesize. This sensor system has more sensitivity with a high surface area, but their stabilities are very low.

Moreover, some other metal nanoparticles containing studies were available in the literature among them. The TEOS@Fe₂O₃/GCE was suggested in this study. TEOS@Fe₂O₃ modified GCE demonstrated very high stability to evaluate quercetin in the apple tea sample. Moreover, the TEOS@Fe₂O₃ modified GCE was easy to prepare, cheaper, and fast electron transfer between quercetin and its surface compared to the electrodes.

Sample Analysis

The applicability of the TEOS@Fe₂O₃ modified GCE sensor in a commercially available apple tea sample was performed *via* standard addition method, as reported in (41). Tea sample was weighted as 0.5 g and thrown in a 10 mL ethanol. For better dissolution, the suspension was kept in an ultrasonic bath for an hour and centrifuged with 3000 rpm

speed. Then the supernatant of the sample suspension was separated from the suspension, and the solution was used to determine quercetin without any treatment by SWV technique from 0.0 to 1.0 V. 100 µL of the apple tea sample solution was added in a voltammetric cell to determine the amount of quercetin, and 1.0 µM of quercetin was added to the cell. The addition process of quercetin was repeated two times to 100 µL sample containing BR buffer solution. Average data and RSD (<5%) were estimated through successive measurements (**Table 2**). Moreover, the recovery of the measurements on the detection of quercetin was calculated as 104.16% and 106.04%. According to the real sample measurements, the suggested the TEOS@Fe₂O₃ modified GCE is fast, accurate, and efficient for the determination of quercetin.

CONCLUSION

In this study, TEOS-coated Fe₂O₃ to obtain spherical nanomaterials. A voltammetric determination of low concentrations of quercetin was performed using TEOS@Fe₂O₃ material modified GCE. The selectivity of TEOS@Fe₂O₃ modified GCE sensor to quercetin was examined in the presence of different anions, cations, and bio-analytes at the optimum operating conditions. The suggested protocol shows the successful application of TEOS@Fe₂O₃ modified GCE for the determination of quercetin in real samples with excellent selectivity and sensitivity due to its high synergistic effect of metal nanoparticles and TEOS. Also, reproducibility and stability of the sensor are excellent.

Table 2. Examples of quercetin detection by SWV on TEOS@Fe₂O₃ modified GCE in apple tea sample.

Addition (µM)	Measured (µM)	Recovery (%)	RSD (% , n=3)
0.00	1.18±0.04	-	-
1.00	2.22±0.04	104.16	4.19
2.00	3.30±0.05	106.04	4.07

REFERENCES

- Gao M, Li W, Dong J, Zhang Z, Yang B. Synthesis and characterization of superparamagnetic Fe₃O₄@ SiO₂ core-shell composite nanoparticles. *World Journal of Condensed Matter Physics*. 2011;1(2):49-54.
- Gupta AK, Gupta M. Synthesis and surface engineering of iron oxide nanoparticles for biomedical applications. *Biomaterials*. 2005;26(18):3995-4021.
- Sajjadi S, Khataee A, Bagheri N, Kobya M, Şenocak A, Demirbas E, et al. Degradation of diazinon pesticide using catalyzed persulfate with Fe₃O₄@MOF-2 nanocomposite under ultrasound irradiation. *Journal of Industrial and Engineering Chemistry*. 2019;77:280-90.
- Carraro G, Barreca D, Comini E, Gasparotto A, Maccato C, Sada C, et al. Controlled synthesis and properties of β-Fe₂O₃ nanosystems functionalized with Ag or Pt nanoparticles. *CrystEngComm*. 2012;14(20):6469-76.
- Kemer B, Demir E. A novel potentiometric pH electrode based on sulfated natural Fe₃O₄ and analytical application in food samples. *Journal of Food Measurement and Characterization*. 2018;12(4):2256-62.
- Surowiec Z, Gac W, Wiertel M. The synthesis and properties of high surface area Fe₂O₃ materials. *Acta Physica Polonica A*. 2011;119(1):18-20.
- Ziolo RF, Giannelis EP, Weinstein BA, O'Horo MP, Ganguly BN, Mehrotra V, et al. Matrix-Mediated Synthesis of Nanocrystalline γ-Fe₂O₃: A New Optically Transparent Magnetic Material. *Science*. 1992;257(5067):219-23.
- McBain SC, Yiu HH, Dobson J. Magnetic nanoparticles for gene and drug delivery. *International journal of nanomedicine*. 2008;3(2):169.
- Lu Y, Yin Y, Mayers BT, Xia Y. Modifying the Surface Properties of Superparamagnetic Iron Oxide Nanoparticles through A Sol–Gel Approach. *Nano Letters*. 2002;2(3):183-6.
- Cornejo D, Padrón-Hernández E. Study of magnetization process in ordered Fe nanowire arrays. *Journal of Magnetism and Magnetic Materials*. 2007;316(2):e48-e51.
- Demir E. A Simple and Sensitive Square Wave Stripping Pathway for the Analysis of Desmedipham Herbicide by Modified Carbon Paste Electrode Based on Hematite (α-Fe₂O₃ Nanoparticles). *Electroanalysis*. 2019;31(8):1545-53.
- Liao X, Luo J, Wu J, Fan T, Yao Y, Gao F, et al. A sensitive DNAzyme-based electrochemical sensor for Pb²⁺ detection with platinum nanoparticles decorated TiO₂/α-Fe₂O₃ nanocomposite as signal labels. *Journal of Electroanalytical Chemistry*. 2018;829:129-37.
- Nomnotho J, Sabela M, Kanchi S, Mdluli P, Xhakaza M, Arodola O, et al. MWCNTs- Fe₂O₃ nanoparticles nanohybrids based highly sensitive electrochemical sensor for the detection of kaempferol in broccoli samples. *Turkish Journal of Chemistry*. 2019;43:1229-43.
- DEMİR E. Sensitive and Selective Pathway of Total Antioxidant Capacity in Commercially Lemon, Watermelon and Mango-pineapple Cold Teas by Square Wave Adsorptive Stripping Voltammetry. *Gazi University Journal of Science*. 2019;32(4):1123-36.
- Lino FMA, de Sá LZ, Torres IMS, Rocha ML, Dinis TCP, Ghedini PC, et al. Voltammetric and spectrometric determination of antioxidant capacity of selected wines. *Electrochimica Acta*. 2014;128:25-31.
- Mosleh M, Ghoreishi SM, Masoum S, Khoobi A. Determination of quercetin in the presence of tannic acid in soft drinks based on carbon nanotubes modified electrode using chemometric approaches. *Sensors and Actuators B: Chemical*. 2018;272:605-11.
- Kuyumcu Savan E. Square Wave Voltammetric (SWV) Determination of Quercetin in Tea Samples at a Single-Walled Carbon Nanotube

- (SWCNT) Modified Glassy Carbon Electrode (GCE). *Analytical Letters*. 2020;53(6):858-72.
18. Morosanu AC, Benchea AC, Babusca D, Dimitriu DG, Dorohoi DO. Quantum-Mechanical and Solvatochromic Characterization of Quercetin. *Analytical Letters*. 2017;50(17):2725-39.
 19. Şenocak A, Basova T, Demirbas E, Durmuş M. Direct and Fast Electrochemical Determination of Catechin in Tea Extracts using SWCNT-Subphthalocyanine Hybrid Material. *Electroanalysis*. 2019;31(9):1697-707.
 20. Liu C, Zhang Y, Zhang P, Wang Y. Evaluating Modeling Units and Sub-word Features in Language Models for Turkish ASR2018. 414-8 p.
 21. Manokaran J, Muruganatham R, Muthukrishnaraj A, Balasubramanian N. Platinum-polydopamine @SiO₂ nanocomposite modified electrode for the electrochemical determination of quercetin. *Electrochimica Acta*. 2015;168:16-24.
 22. Ponnaiah SK, Periakaruppan P. A glassy carbon electrode modified with a copper tungstate and polyaniline nanocomposite for voltammetric determination of quercetin. *Microchimica Acta*. 2018;185(11):524.
 23. Ji Y, Li Y, Ren B, Liu X, Li Y, Soar J. Nitrogen-doped graphene-ionic liquid-glassy carbon microsphere paste electrode for ultra-sensitive determination of quercetin. *Microchemical Journal*. 2020;155:104689.
 24. Yao Z, Yang X, Liu X, Yang Y, Hu Y, Zhao Z. Electrochemical quercetin sensor based on a nanocomposite consisting of magnetized reduced graphene oxide, silver nanoparticles and a molecularly imprinted polymer on a screen-printed electrode. *Mikrochim Acta* [Internet]. 2017 2017/12//; 185(1):[70 p.]. Available from: <http://europemc.org/abstract/MED/29594565>, <https://doi.org/10.1007/s00604-017-2613-5>.
 25. Jing J, Shi Y, Zhang Q, Wang J, Ruan J. Prediction of Chinese green tea ranking by metabolite profiling using ultra-performance liquid chromatography–quadrupole time-of-flight mass spectrometry (UPLC–Q–TOF/MS). *Food Chemistry*. 2017;221:311-6.
 26. Abdullah AA, Yardım Y, Şentürk Z. The performance of cathodically pretreated boron-doped diamond electrode in cationic surfactant media for enhancing the adsorptive stripping voltammetric determination of catechol-containing flavonoid quercetin in apple juice. *Talanta*. 2018;187:156-64.
 27. Ravichandran R, Rajendran M, Devapiriam D. Antioxidant study of quercetin and their metal complex and determination of stability constant by spectrophotometry method. *Food Chemistry*. 2014;146:472-8.
 28. Pilařová V, Plachká K, Chrenková L, Najmanová I, Mladěnka P, Švec F, et al. Simultaneous determination of quercetin and its metabolites in rat plasma by using ultra-high performance liquid chromatography tandem mass spectrometry. *Talanta*. 2018;185:71-9.
 29. Şenocak A, Köksoy B, Demirbaş E, Basova T, Durmuş M. 3D SWCNTs-coumarin hybrid material for ultra-sensitive determination of quercetin antioxidant capacity. *Sensors and Actuators B: Chemical*. 2018;267:165-73.
 30. Hua Z, Deng Y, Li K, Yang S. Low-density nanoporous iron foams synthesized by sol-gel autocombustion. *Nanoscale Research Letters*. 2012;7(1):129.
 31. Tadic M, Panjan M, Damnjanovic V, Milosevic I. Magnetic properties of hematite (α -Fe₂O₃) nanoparticles prepared by hydrothermal synthesis method. *Applied Surface Science*. 2014;320:183-7.
 32. Stöber W, Fink A, Bohn E. Controlled growth of monodisperse silica spheres in the micron size range. *Journal of Colloid and Interface Science*. 1968;26(1):62-9.
 33. Şenocak A, Khataee A, Demirbas E, Doustkhah E. Ultrasensitive detection of rutin antioxidant through a magnetic micro-mesoporous graphitized carbon wrapped Co nanoarchitecture. *Sensors and Actuators B: Chemical*. 2020;312:127939.
 34. Ersin D, Ahmet S, Mouhoum FT-K, Erhan D, Hassan YA-E. Electrochemical Evaluation of the Total Antioxidant Capacity of Yam Food Samples on a Polyglycine-Glassy Carbon Modified Electrode. *Current Analytical Chemistry*. 2020;16(2):176-83.
 35. Şenocak A, Basova T, Demirbas E, Durmuş M. Direct and Fast Electrochemical Determination of Catechin in Tea Extracts using SWCNT-Subphthalocyanine Hybrid Material. *Electroanalysis*. 2019.
 36. Zhang Z, Gu S, Ding Y, Shen M, Jiang L. Mild and novel electrochemical preparation of β -cyclodextrin/graphene nanocomposite film for super-sensitive sensing of quercetin. *Biosensors and Bioelectronics*. 2014;57:239-44.
 37. Wang M, Zhang D, Tong Z, Xu X, Yang X. Voltammetric behavior and the determination of quercetin at a flowerlike Co₃O₄ nanoparticles

modified glassy carbon electrode. Journal of Applied Electrochemistry. 2011;41(2):189-96.

38. Karimi-maleh H, Gupta V, Golestani F, Ahmadzadeh S, Fazli G, Khosravi S. NiO/CNTs Nanocomposite Modified Ionic Liquid Carbon Paste Electrode as a Voltammetric Sensor for Determination of Quercetin. International journal of electrochemical science. 2014;10:3657-67.

39. Sun S, Zhang M, Li Y, He X. A molecularly imprinted polymer with incorporated graphene oxide for electrochemical determination of quercetin. Sensors (Basel). 2013;13(5):5493-506.

40. Wang S, Xu Q, Liu G. Differential Pulse Voltammetric Determination of Uric Acid on Carbon-Coated Iron Nanoparticle Modified Glassy Carbon Electrodes. Electroanalysis. 2008;20(10):1116-20.

41. Şenocak A, Köksoy B, Akyüz D, Koca A, Klyamer D, Basova T, et al. Highly selective and ultra-sensitive electrochemical sensor behavior of 3D SWCNT-BODIPY hybrid material for eserine detection. Biosensors and Bioelectronics. 2019;128:144-50.



Effect of Calcium Stearate on the Thermal Conductivity of Geopolymer Foam

Cansu KURTULUŞ^{1*} , M. Serhat BAŞPINAR² 

¹Afyon Kocatepe University, Engineering Faculty, Materials Science and Engineering Department, AFYONKARAHİSAR/TURKEY

²Afyon Kocatepe University, Technology Faculty, Metallurgy and Materials Engineering Department, AFYONKARAHİSAR/TURKEY

Abstract: Geopolymers are considered an alternative to conventional cement recently. The use of fly ash and blast furnace slag in geopolymer, which are waste products considered as an environmentally friendly product due to the solution to the storage of wastes also. Geopolymer concrete production is also reported to be 44-64% less than the cement that causes the most CO₂ emissions. CO₂ emissions are reduced due to the minimum processed natural minerals and industrial waste products used in the geopolymer system. For this reason, this study comes to the fore in terms of the evaluation of wastes. Production of porous geopolymers is potential in use in many industrial applications such as filtering, thermal insulation, light structural material, and catalysis. By controlling the pore type, pore size distribution, pore connectivity, and shape of porosities, potential usages are differentiated. In this study, closed porosity geopolymer foams were produced by the geopolymerization technique with the help of hydrogen peroxide and calcium stearate (CaS) as a surfactant. The thermal conductivity, density, and strength values was correlated with the changing pore size distribution depending on the amount of surfactant and foaming agent. In this study, porous geopolymers with density values 450-500 kg/m³, 0.069 W/mK thermal conductivity, and 2.1 MPa strength value was reached. The reduction in pore sizes due to CaS increase was analyzed. However, we did not observe a decrease in thermal conductivity values due to the reduction of the pore size. Exciting results for CaS content on thermal conductivity were reported.

Keywords: Calcium stearate, foam, geopolymer, porosity, thermal conductivity.

Submitted: December 17, 2019. **Accepted:** May 18, 2020.

Cite this: KURTULUŞ C, BAŞPINAR MS. Effect of Calcium Stearate on the Thermal Conductivity of Geopolymer Foam. JOTCSA. 2020;7(2):565-74.

DOI: <https://doi.org/10.18596/jotcsa.660727>.

***Corresponding author. E-mail:** cansudemir@aku.edu.tr.

INTRODUCTION

An incredible acceleration is seen in the construction sector in recent years, and the necessity of the technically superior parameters and values of the construction materials to be used pave the way for the use and application of many new construction materials. Significantly, the sustainability concept that arises due to the rapid consumption of fossil energy resources, air pollution caused by greenhouse gas, the effort to

minimize the amount of energy use, and the lack of proper use of the produced materials accelerates the research and development of these materials (1-3).

Today, in parallel to the increasing environmental awareness, national and international environmental policies are becoming more stringent. Kyoto Protocol has been signed by many countries, and studies have been started to reduce CO₂ emissions. The World Business Council for

Sustainable Development says it is responsible for the cement sector for about 5% of CO₂ emission. It is an indication that the cement sector has a significant impact on the increase in CO₂ emissions. (4). The concrete and cement sector has been criticized for not only high emissions of carbon dioxide but also consuming large amounts of natural resources and energy mainly from cement production. These justified criticisms are tried to be overcome by alternative solutions. With the addition of fly ash, industrial waste in cement-based systems (such as plaster, mortar, concrete) can be minimized, and carbon dioxide emission can be minimized, and the need for natural resources is reduced (5–12).

In our country, resources such as petroleum, coal, and natural gas are used for energy production. As presented in TÜİK 2015 and 2016 reports, coal use for energy production is expected to increase gradually by 2040 (13,14). It means that by-products such as fly ash and bottom ash formed as a result of the combustion of coal will also increase gradually. While Japan recycled 96% of fly ash in the context of cyclic economy and England, India, America, Australia recycles about 50% of the fly ash; this ratio remains 15% in Turkey (14). One of the other objectives of this study is the fact that the fly ash, which is generated as a waste of millions of tons per year, can be converted into added-value products.

Secondly, energy efficiency in buildings is always an important issue. Demand for energy, which is indispensable for human life, is increasing rapidly with population growth, industrialization, and urbanization. Meeting the increasing energy consumption in the world where there is limited energy supply has been a problem for many countries, and the dependence on foreign energy has increased (15). In Turkey, a large part of the energy consumption consists of housing under the name of city consumption. Heat insulation is one of the most critical measures that can be taken to ensure energy efficiency in houses.

Thermal insulation materials used in buildings are the most effective solution in reducing heat losses. In this way, it contributes to the almost zero energy target by reducing the heat energy requirement in buildings. It is necessary to produce a foam geopolymer with homogeneously distributed and closed porosity to provide thermal isolation (16,17).

Many articles on porous geopolymer production have been published. In the direct foaming method, which is the most commonly used method, foam materials are produced by adding gas-forming additives to a suspension or liquid medium. Foaming is usually done by adding H₂O₂,

Al powder, metallic Si, and sodium perborate as a foaming agent to the geopolymeric mixture and mixing them mechanically. After the decomposition of additives in an alkaline slurry, a bubble forms and a porous structure is formed (7,18–21). Besides, the amount of porosity, which depends on the amount of foaming agent used, also depends on whether the foams can remain stable in the mixture. Additives are needed to ensure that thermodynamically unstable gas bubbles are kept in the mixture and are homogeneously distributed. These additives are referred to as surfactants. Many studies have been conducted on butyric acid, valeric acid, butyl gallate, propyl gallate, hexylamine, oleic acid, and albumin as surfactants in foam geopolymer production (22–31). However, there are only limited numbers of publications on CaS, and its effect on the thermal conductivity properties. Cui et al. reached a minimum thermal conductivity value of 0.096W / mK from their work, depending on the amount of CaS. They observed that although samples containing a fixed amount of stearate reached a minimum value of 0.048W/mK by changing the water/binder amount, this negatively affected the mechanical properties (24,32).

This study was carried out on the development of porous geopolymer wall elements for insulation with the help of CaS as a surfactant. This study gains importance in CO₂ emission, cyclic economy, and energy fields thanks to the reduction of cement use, recycling of fly ash, and the development of thermally insulated wall elements. In this study, the effect of CaS on thermal conductivity is examined from a different perspective. CaS, which reduces the pore size, negatively affected the thermal insulation feature.

MATERIALS AND METHODS

The mixed composition of foam geopolymer includes fly ash, metakaolin, sodium hydroxide, sodium silicate, expanded perlite, water, and chopped polypropylene fiber (Table 1). Hydrogen peroxide was used as a foaming agent (%35), and CaS was used to obtain foam stabilization. Fly ash (FA) was taken from the Seyitömer Thermal Power Station, Turkey, and metakaolin was supplied from the Czech Republic. Chemical compositions of metakaolin and fly ash are presented in Table 2.

The principle of homogeneous mixing of solid components and liquid components in separate places was followed. First, the NaOH flakes were completely dissolved in water to obtain a 10M environment and then mixed with sodium silicate solution. Geopolymeric slurry was added by adding an alkaline solution to the mixture of metakaolin, fly ash, expanded perlite, and polypropylene fibers mixed separately. After the geopolymer slurry

became homogeneous, foaming agent and surfactant were added and mixed. Finally, a foam mixture was poured into 100x100x100 mm molds and cured at 60°C.

The compressive strength tests were conducted with a compressive testing machine on the samples whose dimensions were 100 × 100 × 100 mm. Compressive strength test was applied.

Table 1. Composition of foam geopolymer mixtures.

Code	Fly Ash(%)	Metakaolin (%)	CaS* (%)	Perlite (%)	Fiber (%)
1				0	
2	90	10	0.15	2	0.21
2				4	
4				8	
5				0	
6	90	10	0.45	2	0.21
7				4	
8				8	
9				0	
10	90	10	0.75	2	0.21
11				4	
12				8	

Table 2. Chemical content of Fly ash and Metakaolin.

	Fly Ash	Metakaolin
SiO ₂	50.30	54.10
Al ₂ O ₃	19.10	41.10
CaO	4.55	0.13
Fe ₂ O ₃	12.40	1.10
MgO	4.67	0.18
K ₂ O	2.16	0.80

After drying, the unmolded samples were stored in the laboratory conditions for 28 days. The thermal conductivity coefficient λ was calculated with a modified transient plane source. The bulk density of the product was calculated as the mass to volume ratio of the sample.

RESULTS AND DISCUSSION

Density and Porosity

According to scanning electron microscopy analysis, samples have closed porosity, pore morphology is pretty homogeneous, and pore dimensions are getting smaller following the surfactant amount (Figure 1). Measurements were taken from perlite-free samples. Samples contain 0.15%, 0.45% and 0.75% CaS, respectively. The pore sizes varying depending on the amount of

CaS are 928.8 μm , 659.5 μm , and 573.5 μm , respectively. Pore sizes were observed to change inversely proportional to the amount of CaS.

Density was effected directly proportional to the amount of surfactant in the foam geopolymer mixture. Utilizing H₂O₂, the gas bubbles formed in the geopolymer slurry were further kept in mixture with the effect of the increased amount of surfactant, and therefore the density decreased. Density values also gradually decreased inversely proportional to the amount of perlite added to the mixture. The lowest density value at different Ca stearate concentrations were obtained in samples containing 8% perlite. The highest density values were also measured in samples without perlite (Figure 2).

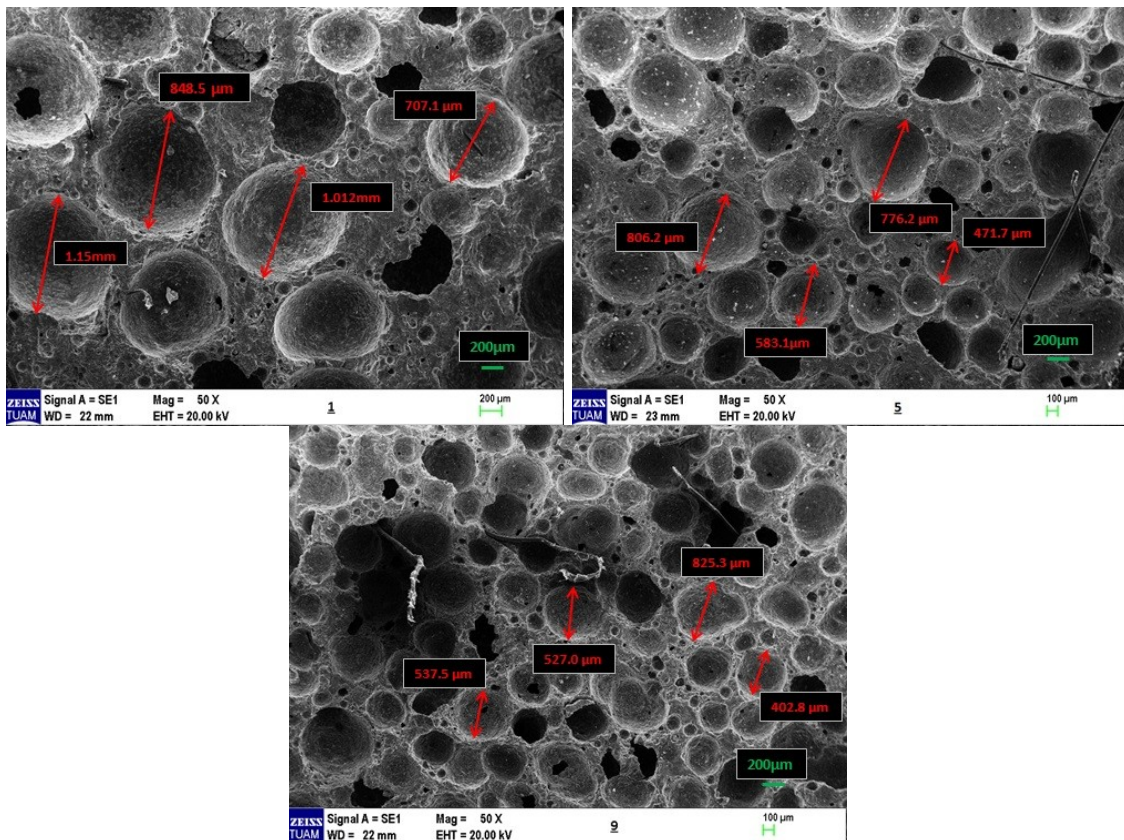


Figure 1. Scanning electron microscopy images of geopolymer foams at 50X magnification. Foams contains upper row, left) 0.15%, upper row, right) 0.45%, and lower row, center) 0.75% CaS.

Compressive Strength

The compressive strength values recorded from an average of three cubic specimens with dimensions of 100×100×100 mm³ cured during 28 days were tested. The results of the compressive strength of geopolymer foams are shown in Figure 3. The perlite-free foams had higher strength values compared to the samples containing 8% perlite. A gradual decrease in compression strength values was observed with the increase of perlite input into the composition. This decrease in compressive strength is due to the lower strength (0.1-0.4MPa) and porosity of perlite (33). It is also due to the highly crushable behavior of expanded perlite during compression (34). Besides, our work suggests that this is because of non-bonding between perlite and geopolymer foam.

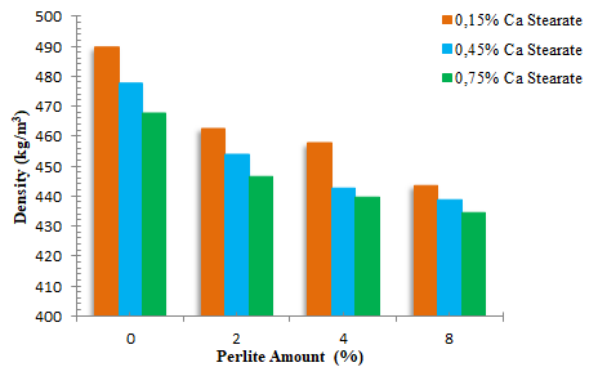


Figure 2. Density values of foam geopolymer samples according to perlite amount and CaS concentration.

In the samples without perlite, the strength values changed depending on the amount of CaS. The strength value of the sample without perlite containing 0.75% CaS was 2.14 MPa, while the strength of the sample containing 0.15% CaS was 1.82 MPa.

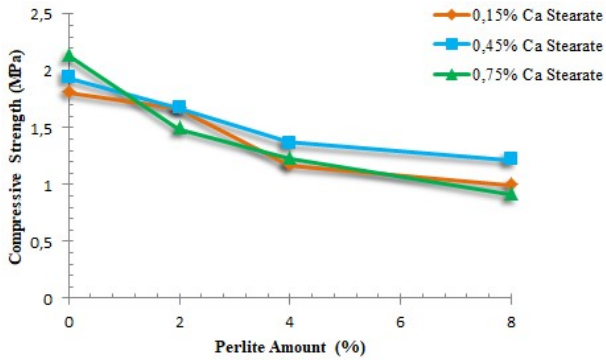


Figure 3. Compressive strength values of foam geopolymer samples according to perlite amount and CaS concentration.

Thermal Conductivity

Figure 4 presents the thermal conductivity performances of geopolymer mixtures. Thermal conductivity tests were carried out on all twelve geopolymer mixtures. It is evident that the perlite input into the mixture gradually reduces the thermal conductivity values for all samples. The minimum thermal conductivity value was obtained

at 8% perlite input for all samples.

Considering the amount of CaS, surprising results were obtained when the thermal conductivity values were examined. Considering the Knudsen effect (35,36), thermal conductivity is expected to decrease as the pore size decreases. According to theory, when the pore diameter of the material becomes less than the average free length of the path of gas molecules, the molecules only collide with pore surfaces without transferring energy. Baetans et al. (44) also summarized this statement and said that reducing cell sizes is a very effective way to reduce the thermal conductivity of insulating material. However, an increase was observed in contrast to the theory in thermal conductivity with cell reduction due to the increasing CaS amount. This situation most probably because water repellent property of CaS (45). As a result of this situation, CaS makes it challenging to remove the water in the sample during drying. **Table 3.** Foam geopolymer studies reported in the literature and the findings of this study.

Table 3. Foam geopolymer studies reported in the literature and the findings of this study.

Aluminosilicate Activator Precursor	Admixture	Aggregate	Foaming Agent	Pore Size	Strength (MPa)	Density (kg/m³)	Thermal Cond (W/mK)	Refs
Fly Ash	Water Sodium Silicate	-	-	H ₂ O ₂	-	0.4-1.43	270-375	0.071-0.092 (37)
Fly Ash Blast Furnace Slag	NaOH Sodium Silicate Distilled Water	-	-	Foaming Agent	-	3.0-50.0	600-1500	0.15-0.5 (38)
Fly Ash	NaOH Sodium Silicate Tap Water	-	-	H ₂ O ₂	-	1.9-3.4	400-650	0.083-0.127 (39)
Fly Ash Metakaolin	NaOH Sodium Silicate Distilled water	-	-	H ₂ O ₂	-	0.26-21	440-1100	0.082-0.227 (40)
Metakaolin Fly Ash	NaOH Sodium Silicate	-	-	H ₂ O ₂	-	1.23	560	0.107 (12)
Fly Ash Metakaolin	NaOH Sodium Silicate Distilled Water	-	Construction and demolition waste	H ₂ O ₂	0.198-31.88 μm	3.6-11.9	1000-1700	0.19-0.44 (41)
Fly Ash Blast Furnace Slag	NaOH Sodium Silicate Water	SDS	-	H ₂ O ₂	0-2mm	3.2-44.8	140-1020	0.183-0.646 (20)
Fly Ash Metakaolin	NaOH Sodium Silicate Water	Surfactant	-	Al	-	0.6-403	430-850	0.079-0.170 (42)
Fly Ash Metakaolin	NaOH Sodium Silicate Distilled Water	-	-	H ₂ O ₂	0.57-1.13mm	0.68-2.23	150-300	0.0622-0.0852 (43)
Fly Ash	-	Calcium Stearate	-	H ₂ O ₂	140 -4563 μm	1.45-1.65	310-360	0.095-0.139 (24)
FlyAsh-Metakaolin	NaOH Sodium Silicate Water	Calcium Stearate	Expanded Perlite	H ₂ O ₂	573-928 μm	0.925-2.14	435-490	0.069-0.1052 This work

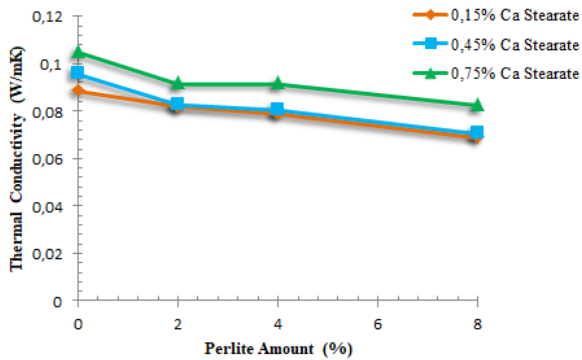


Figure 4. Thermal insulation performances of foam geopolymer samples according to CaS and perlite amount.

Table 3 gives the foam geopolymer studies reported in the literature. As mentioned earlier, there are not too many foam geopolymer studies using CaS as a surfactant. Cui et al. obtained the lowest conductivity when using CaS as a surfactant in fly ash based geopolymer foams is 0.096W/ mK (24). Minimum detectable thermal conductivity value among fly ash based foam studies for samples with a density of 150-300kg/ m³, 0.0622W / mK has been reached by Wu et al. (43). The best thermal conductivity value was recorded as 0.069W/mK in a sample containing 0.15% CaS and 8% perlite in this study.

CONCLUSION

The results show that hydrogen peroxide with CaS is useful in obtaining homogeneous pore morphology with low thermal conductivity. Density was effected directly proportional to the amount of surfactant in the foam geopolymer mixture. Also, the density decline continued with perlite added to the mixture. Although in the construction area, perlite is widely used as an aggregate because of its outstanding insulation characteristics and low weight, it decreases the compressive strength of the foam. The strength value of perlite-free samples increased in direct proportion with the amount of CaS.

An interesting result was encountered in thermal conductivity measurements. Contrary to what the thermal conductivity theorem states, there is no result that thermal conductivity decreases with decreasing pore size. On the contrary, the increased amount of CaS impairs the insulating properties of the sample. This situation was caused by the water repellent feature of CaS. The presence of perlite as an aggregate gave the material better-insulating properties in all samples where thermal conductivity decreased with increasing porous perlite input. The best thermal conductivity value was recorded as 0.069W/mK in a sample containing 0.15% CaS and 8% perlite in this study.

Foamed fly ash geopolymers have good potential in an application for lightweight building materials. These geopolymer mixtures where the amount of perlite is maximum 2% appear to meet the values specified in TSE 13655 ($> 1.5\text{MPa}$, $d < 450\text{-}550\text{kg/m}^3$ and $\lambda < 0.12\text{W / mK}$).

This study shows an environmentalist approach in terms of converting fly ash into value-added products and reducing the use of cement that causes CO₂ emission. It supports the protection of the limited energy resources by improving the thermal insulation feature of the walls that have the most energy loss in buildings.

ACKNOWLEDGEMENTS

A part of this study was presented orally in 4th International Powder and Porous Materials Symposium 09-11 September, 2019, Marmaris, Turkey. This work was financially supported by Afyon Kocatepe University under the contract of 19.Fen.Bil.01 BAP Project and also it is supported by a TÜBİTAK project 218M778.

REFERENCES

- Duxson P, Fernández-Jiménez A, Provis JL, Lukey GC, Palomo A, Van Deventer JSJ. Geopolymer technology: The current state of the art. *J Mater Sci.* 2007;42(9):2917-33.
- Dhananjay KP, V V. Fly Ash as Sustainable Material for Green Concrete - A State of Art. *Int J Res Eng Sci Technol.* 2015;1(2):17-24.
- Petrillo A, Cioffi R, Ferone C, Colangelo F, Borrelli C. Eco-sustainable Geopolymer Concrete Blocks Production Process. *Agric Agric Sci Procedia [Internet].* 2016;8:408-18. Available from: <http://linkinghub.elsevier.com/retrieve/pii/S2210784316300377>
- Duran Atiş C, Bilim C, Çelik Ö, Karahan O. Influence of activator on the strength and drying shrinkage of alkali-activated slag mortar. *Constr Build Mater.* 2009;23(1):548-55.
- Çevik S. The Effect of Oil Consumption and Oil Prices on CO₂ Emissions in the Industrial Sector. 2017;19(4):93-110.
- Dean, B., Dulac, J., Petrichenko, K., and Graham P. Towards a zero-emission, efficient, and resilient buildings and construction sector. In: *Global Status Report [Internet].* 2016. p. 1-48. Available from: [https://www.worldgbc.org/sites/default/files/UNEP188_GABC_en\(web\).pdf](https://www.worldgbc.org/sites/default/files/UNEP188_GABC_en(web).pdf)
- Abdollahnejad Z, Pacheco-Torgal F, Félix T, Tahri W, Barroso Aguiar J. Mix design, properties and cost analysis of fly ash-based geopolymer foam. *Constr Build Mater [Internet].* 2015;80(May 2010):18-30. Available from: <http://dx.doi.org/10.1016/j.conbuildmat.2015.01.063>

8. Jiménez Rivero A, De Guzmán Báez A, Navarro JG. New composite gypsum plaster - Ground waste rubber coming from pipe foam insulation. *Constr Build Mater*. 2014;55(2014):146-52.
9. Cha J, Seo J, Kim S. Building materials thermal conductivity measurement and correlation with heat flow meter, laser flash analysis and TCI. *J Therm Anal Calorim*. 2012;109(1):295-300.
10. Gunasekara C, Law DW, Setunge S. Effect of Composition of Fly Ash On Compressive Strength of Fly Ash Based Geopolymer Mortar. 23rd Australas Conf Mech Struct Mater. 2014;3(1):168-77.
11. Pacheco-Torgal F. Eco-efficient construction and building materials research under the EU Framework Programme Horizon 2020. *Constr Build Mater [Internet]*. 2014;51:151-62. Available from: <http://dx.doi.org/10.1016/j.conbuildmat.2013.10.058>
12. Novais RM, Buruberri LH, Ascensão G, Seabra MP, Labrincha JA. Porous biomass fly ash-based geopolymers with tailored thermal conductivity. *J Clean Prod*. 2016;119:99-107.
13. Özcan M, Özel G, Demirkol Ö, Babayiğit S. Kömür sektör raporu (İnçit) [Internet]. Ankara; 2017. Available from: http://www.tki.gov.tr/depo/file/2017_Kömür_Sektör_Raporu_21_02_19.pdf
14. Enerji Çalışma Grubu TMMOB. Enerji ve kömür raporu [Internet]. Ankara; 2015. Available from: http://www.maden.org.tr/resimler/ekler/22ed738b2c7ba36_ek.pdf
15. Türkyılmaz O, Bayrak Y, Aytaç O, Erkilet M. Türkiye Enerjide Nereye Gidiyor. TMMOB Makina Mühendisleri Odası Enerji Çalışma Grubu ve ODTÜ MD Enerji Kom [Internet]. 2017; Available from: http://www.inovasyon.org/pdf/O.Türkyılmaz.Türkiye'nin_Enerji_Görünümü_Tem.2016.pdf
16. Kang S, Choi JY, Choi S. Mechanism of heat transfer through porous media of inorganic intumescent coating in cone calorimeter testing. *Polymers (Basel)*. 2019;11(2).
17. Kamseu E, Nait-Ali B, Bignozzi MC, Leonelli C, Rossignol S, Smith DS. Bulk composition and microstructure dependence of effective thermal conductivity of porous inorganic polymer cements. *J Eur Ceram Soc*. 2012;32(8):1593-603.
18. Prud'homme E, Michaud P, Joussein E, Peyratout C, Smith A, Arrii-Clacens S, et al. Silica fume as porogent agent in geo-materials at low temperature. *J Eur Ceram Soc*. 2010;30(7):1641-8.
19. Vaou V, Panias D. Thermal insulating foamy geopolymers from perlite. *Miner Eng [Internet]*. 2010;23(14):1146-51. Available from: <http://dx.doi.org/10.1016/j.mineng.2010.07.015>
20. Xu F, Gu G, Zhang W, Wang H, Huang X, Zhu J. Pore structure analysis and properties evaluations of fly ash-based geopolymer foams by chemical foaming method. *Ceram Int [Internet]*. 2018;44(16):19989-97. Available from: <https://doi.org/10.1016/j.ceramint.2018.07.267>
21. Medri V, Papa E, Dedecek J, Jirglova H, Benito P, Vaccari A, et al. Effect of metallic Si addition on polymerization degree of in situ foamed alkali-aluminosilicates. *Ceram Int [Internet]*. 2013;39(7):7657-68. Available from: <http://dx.doi.org/10.1016/j.ceramint.2013.02.104>
22. Hajimohammadi A, Ngo T, Mendis P, Sanjayan J. Regulating the chemical foaming reaction to control the porosity of geopolymer foams. *Mater Des [Internet]*. 2017;120:255-65. Available from: <http://dx.doi.org/10.1016/j.matdes.2017.02.026>
23. Gonzenbach UT, Studart AR, Tervoort E, Gauckler LJ. Stabilization of foams with inorganic colloidal particles. *Langmuir*. 2006;22(26):10983-8.
24. Cui Y, Wang D, Zhao J, Li D, Ng S, Rui Y. Effect of calcium stearate based foam stabilizer on pore characteristics and thermal conductivity of geopolymer foam material. *J Build Eng [Internet]*. 2018;20(June):21-9. Available from: <https://doi.org/10.1016/j.jobe.2018.06.002>
25. Shao N ning, Zhang Y bo, Liu Z, Wang D min, Zhang Z tai. Fabrication of hollow microspheres filled fly ash based foam geopolymers with ultra-low thermal conductivity and relative high strength. *Constr Build Mater [Internet]*. 2018;185:567-73. Available from: <https://doi.org/10.1016/j.conbuildmat.2018.07.077>
26. Medpelli D, Seo JM, Seo DK. Geopolymer with hierarchically meso-/macroporous structures from reactive emulsion templating. *J Am Ceram Soc*. 2014;97(1):70-3.
27. Bai C, Colombo P. High-porosity geopolymer membrane supports by peroxide route with the addition of egg white as surfactant. *Ceram Int [Internet]*. 2017;43(2):2267-73. Available from: <http://dx.doi.org/10.1016/j.ceramint.2016.10.205>
28. Nushtaeva A V. Stabilization of emulsions and emulsion films by silica with hexylamine. *Mendelev Comm*. 2012;22(4):225-6.
29. Zhao W, Subhasree B, Park JG, Kim SY, Han IS, Kim IJ. Particle-stabilized wet foams to porous ceramics by direct foaming. *J Ceram Process Res*. 2014;15(6):503-7.
30. Cilla MS, Morelli MR, Colombo P. Open cell geopolymer foams by a novel saponification/peroxide/gelcasting combined route. *J Eur Ceram Soc [Internet]*. 2014;34(12):3133-7. Available from: <http://dx.doi.org/10.1016/j.jeurceramsoc.2014.04.001>
31. Krister Holmberg, Bo Jönsson, Bengt Kronberg, Björn Lindman. Wiley: Surfactants and Polymers in Aqueous Solution [Internet]. 2002. 0-471 p. Available from: <http://eu.wiley.com/WileyCDA/WileyTitle/productCd-0471498831.html>
32. Ash F. E ff ect of Calcium Stearate in the Mechanical and Physical Properties of Concrete with PCC and Fly Ash as Binders. 2020;
33. Torres ML, García-Ruiz PA. Lightweight pozzolanic materials used in mortars: Evaluation of their influence

- on density, mechanical strength and water absorption. *Cem Concr Compos* [Internet]. 2009;31(2):114–9. Available from: <http://dx.doi.org/10.1016/j.cemconcomp.2008.11.003>
34. Jamei M, Guiras H, Chtourou Y, Kallel A, Romero E, Georgopoulos I. Water retention properties of perlite as a material with crushable soft particles. *Eng Geol* [Internet]. 2011;122(3–4):261–71. Available from: <http://dx.doi.org/10.1016/j.enggeo.2011.06.005>
35. Qiao JH, Bolot R, Liao HL, Coddet C. Knudsen effect on the estimation of the effective thermal conductivity of thermal barrier coatings. *J Therm Spray Technol*. 2013;22(2–3):175–82.
36. Sundén B, Yuan J. Evaluation of models of the effective thermal conductivity of porous materials relevant to fuel cell electrodes. *Int J Comput Methods Exp Meas*. 2013;1(4):440–54.
37. Feng J, Zhang R, Gong L, Li Y, Cao W, Cheng X. Development of porous fly ash-based geopolymer with low thermal conductivity. *Mater Des*. 2015;65(November 2017):529–33.
38. Zhang Z, Provis JL, Reid A, Wang H. Mechanical, thermal insulation, thermal resistance and acoustic absorption properties of geopolymer foam concrete. *Cem Concr Compos* [Internet]. 2015 Sep 1 [cited 2018 Aug 28];62:97–105. Available from: <https://www.sciencedirect.com/science/article/pii/S0958946515000979>
39. Łach M, Korniejenko K, Mikuła J. Thermal Insulation and Thermally Resistant Materials Made of Geopolymer Foams. *Procedia Eng*. 2016;151:410–6.
40. Novais RM, Ascensão G, Buruberri LH, Senff L, Labrincha JA. Influence of blowing agent on the fresh- and hardened-state properties of lightweight geopolymers. *Mater Des* [Internet]. 2016;108:551–9. Available from: <http://dx.doi.org/10.1016/j.matdes.2016.07.039>
41. De Rossi A, Carvalheiras J, Novais RM, Ribeiro MJ, Labrincha JA, Hotza D, et al. Waste-based geopolymeric mortars with very high moisture buffering capacity. *Constr Build Mater* [Internet]. 2018;191:39–46. Available from: <https://doi.org/10.1016/j.conbuildmat.2018.09.201>
42. Novais RM, Ascensão G, Ferreira N, Seabra MP, Labrincha JA. Influence of water and aluminium powder content on the properties of waste-containing geopolymer foams. *Ceram Int* [Internet]. 2018;44(6):6242–9. Available from: <https://doi.org/10.1016/j.ceramint.2018.01.009>
43. Wu J, Zhang Z, Zhang Y, Li D. Preparation and characterization of ultra-lightweight foamed geopolymer (UFG) based on fly ash-metakaolin blends. *Constr Build Mater* [Internet]. 2018;168:771–9. Available from: <https://doi.org/10.1016/j.conbuildmat.2018.02.097>
44. Baetens R, Jelle BP, Thue JV, Tenpierik MJ, Grynning S, Uvsløkk S, et al. Vacuum insulation panels for building applications: A review and beyond. Vol. 42, *Energy and Buildings*. 2010. p. 147–72.
45. Izaguirre A, Lanas J, Álvarez JI. Effect of water-repellent admixtures on the behaviour of aerial lime-based mortars Effect of water-repellent admixtures on the behaviour of aerial lime-based mortars.



An improved isolation of trimyristin from *Myristica fragrans* as a renewable feedstock with the assistance of novel cationic gemini surfactant

Ayhan YILDIRIM , Serkan ÖZTÜRK , Haluk TÜRKDEMİR , Atakan KOLALI 
, Beyza Gökçem ATALAY , Hatice KOCATAŞ 

Bursa Uludağ University, Faculty of Arts and Sciences, Department of Chemistry, 16059, Bursa, Turkey.

Abstract: In the present work, a surfactant-assisted convenient extraction method was developed for the isolation of trimyristin from nutmeg. Commercially available monomeric surfactants and novel readily synthesized cationic dimeric surfactants were used as auxiliary chemicals. The improved isolation method herein revealed that the combination of dimeric surfactant with n-hexane allows selective extraction (without colored polar components of nutmeg) and maximum yield of triglyceride. Besides, the developed method is more practical than existing protocols and provides higher yields of trimyristin in a short period.

Keywords: Nutmeg, triglycerides, surfactant-assisted extraction, renewable materials.

Submitted: August 16, 2019. **Accepted:** May 18, 2020.

Cite this: YILDIRIM A, ÖZTÜRK S, TÜRKDEMİR H, KOLALI A, ATALAY BG, KOCATAŞ H. An improved isolation of trimyristin from *Myristica fragrans* as a renewable feedstock with the assistance of novel cationic gemini surfactant. JOTCSA. 2020;7(2):545-60.

DOI: <https://doi.org/10.18596/jotcsa.605805>.

***Corresponding author. E-mail:** yildirim@uludag.edu.tr.

INTRODUCTION

The necessary chemical raw materials required by the chemical, pharmaceutical, textile, and food industries have been provided for a long time from crude oil. However, the depletion of oil reserves, the cost of production and derivatization processes of different petrochemicals and excessive energy requirements have led both the academic and the industrial community to the search for new sources of raw materials. It is becoming increasingly popular to find more environmentally friendly, biodegradable, and renewable raw material resources. Among these feedstock sources, animal and vegetable-originated fats and oils are particularly remarkable (1, 2). Vegetable oils are biomass that has the potential to replace many chemicals in oil refineries, and the main component of this biomass is triglycerides, also

known as triacylglycerol (3). Triglycerides are receiving increased interest owing to their potential as a starting material for the production of biofuel and as a source for valuable renewable raw chemicals (4-6). As a result of pyrolysis or thermal and catalytic cracking processes performed with triglycerides, bio-based versatile chemicals can be prepared suitable for different industrial fields (7-9).

Lipids are often found in tissues with carbohydrates and proteins, which makes their isolation difficult. Triglycerides and many other natural compounds of the lipid class are generally isolated from plant sources like canola and *Jatropha curcas* by extraction techniques, and supercritical carbon dioxide is the widely used solvent along with other supercritical fluids (10-12). The triglyceride ratios and compositions of

lipid extracts obtained from several vegetable sources show variability. For instance, *Myristica fragrans* seeds (nutmeg) are rich in myristicin as one of the necessary components of its essential oil and trimyristin as a major triglyceride component (13-15). As known, trimyristin is a neutral lipid component, and non-polar solvents such as ether, n-hexane, and chloroform are suitable for its extraction. Trimyristin is a yellowish-white solid at room temperature, formed by esterification of glycerol with myristic acid as a saturated fatty acid. It is a raw material for the soap and oleochemical industries and widely used in the cosmetic industry (16). In the cosmetic industry, trimyristin can be classified as the following: emollient, refatting, skin conditioning, solvent, and viscosity controlling agent. It is used in makeup products, deodorants, creams and lotions, suntan and sunscreen products, hair conditioners, skincare, and skin cleansing products. Therefore, it is crucial to develop efficient extraction procedures to obtain this particular triglyceride with high yields. Unfortunately, it can be grown on an industrial scale only in regions with a tropical climate.

Beal reported a convenient ether-based isolation method with Soxhlet extractor, which requires a long time (24 to 72 hrs.), and the yield of the purified trimyristin was approximately 53% based on the mass of crude nutmeg extract (17). According to a procedure recommended by Ikan, extraction was carried out with chloroform as a solvent, and after the purification stage, trimyristin was obtained with a yield of 20% based on the mass of crushed nutmeg materials (18). Lagemwa used water-organic solvent mixtures for the isolation of trimyristin from nutmeg and obtained the desired triglyceride with a yield of only 8% at the end of 1 hour of extraction (19). On the other hand, some isolation methods designed as general chemistry experiments have also been developed but with a lower yield of trimyristin based on the mass of crude nutmeg extract (20, 21).

As is known, surfactants are both hydrophilic and lipophilic compounds which make them unique tools in isolation of various natural compounds via extraction processes (22-30). At the extraction stage, the combination of solvent with surfactant molecules facilitates the penetration of solvent molecules throughout seed cell walls. To the best of our knowledge, there has been no work investigating the surfactant-assisted isolation of trimyristin from nutmeg. In this work, we report the synthesis of a novel cationic gemini surfactant and its evaluation in an efficient extraction process of trimyristin from nutmeg.

EXPERIMENTAL SECTION

Reagents and chemicals

All reagents and solvents were purchased from either Merck or Sigma-Aldrich (St. Louis, MO) and used without further purification. Thin-layer chromatography (TLC) was performed using silica gel plates (60 F₂₅₄, Merck, Darmstadt, Germany).

Analytical techniques

Melting points were recorded by BÜCHI melting point B-540 apparatus (BÜCHI Labortechnik AG in Flawil, Switzerland). The Fourier Transformed Infrared (FTIR) spectra were measured using a PerkinElmer Spectrum 100 spectrometer. The Nuclear Magnetic Resonance (NMR) spectra were measured using Bruker Avance NEO 600 MHz NMR spectrometer (Santa Clara, CA, USA). Chemical shifts (δ) are reported in ppm, and J values in Hertz. A Hitachi 3100H dual-beam spectrophotometer (Tokyo, Japan) was used for the spectrophotometric analyses. Conductivity measurements were performed using a Thermo Scientific ORION 3 STAR digital conductometer (Madison, WI, USA). The elemental analyses were performed using a LECO CHNS-932 elemental analyzer (Saint Joseph, MI, USA).

Preparation of the surfactant

N¹,N¹,N⁶,N⁶-tetramethyl-N¹,N⁶-bis(4-((10-(5-(octylthio)-1,3,4-oxadiazol-2-yl)decyl)oxy)benzyl)hexane-1,6-diaminium chloride

N,N,N',N'-Tetramethyl-1,6-hexanediamine (0.15 g, 0.87 mmol) and two equivalents of 2-(10-(4-(chloromethyl)phenoxy)decyl)-5-(octylthio)-1,3,4-oxadiazole (31) (0.85, 1.72 mmol) are heated in MeCN at 80 °C for 24 h. After completion of the reaction, the mixture was cooled, and the excess of solvent was removed under reduced pressure. The residue is washed successfully with n-hexane. A white waxy product is obtained quantitatively in a sufficient purity.

Waxy solid (mp: 35–36 °C); FTIR (ATR): ν_{\max} 3351, 2919, 2852, 1667, 1612, 1586, 1514, 1484, 1474, 1433, 1367, 1306, 1252, 1183, 1146, 1043, 1018, 983, 958, 928, 865, 825, 795, 742, 718, 682, 617, 555, 522 cm⁻¹; ¹H NMR (600 MHz, CDCl₃) δ 7.50-7.47 (m, 4H, Ar), 6.87-6.85 (m, 4H, Ar), 4.74 (s, 4H, 2 x ArCH₂N⁺), 3.90 (t, J = 6.4 Hz, 4H, 2 x ArOCH₂-), 3.60 (t, J = 7.4 Hz, 4H, 2 x (CH₃)₃N⁺CH₂CH₂-), 3.18 (t, J = 7.4 Hz, 4H, 2 x HetSCH₂CH₂-), 3.15 (s, 12H, 2 x -N⁺(CH₃)₂), 2.77 (t, J = 7.4 Hz, 4H, 2 x HetCH₂CH₂-), 2.04-2.01 (m, 4H, 2 x HetSCH₂CH₂CH₂-), 1.77-1.70 (m, 12H, 6 x CH₂), 1.43-1.32 (m, 16H, 8 x CH₂), 1.28-1.23 (m, 32H, 16 x 1.36 CH₂), 0.84 (t, J = 7.1 Hz, 6H, 2 x -CH₂CH₃); ¹³C NMR (150 MHz, CDCl₃) δ 167.91,

164.24, 160.77, 134.57, 119.12, 114.90, 68.13, 67.27, 64.17, 49.24, 42.96, 32.47, 31.69, 29.42, 29.31, 29.29, 29.20, 29.11, 29.04, 29.03, 28.92, 28.91, 28.53, 26.36, 25.96, 25.35, 24.96, 22.56, 21.70, 14.03; Anal calc for $C_{64}H_{110}Cl_2N_6O_4S_2$ (1162.64): C 66.12, H 9.54, N 7.23, S 5.52. Found: C 66.15, H 9.49, N 7.27, S 5.50.

Conductivity measurements

Conductivity measurements were performed using a Thermo Scientific ORION 3 STAR digital conductometer apparatus (Madison, WI, USA). To measure the specific conductivity at each surfactant, we followed the step-by-step dilution-extraction method. The critical micellar concentration (cmc) value was estimated from the breakpoint on the curve of conductivity versus surfactant concentration.

Surface tension measurement at cmc

The capillary rise method is used to measure the surface tension of aqueous solution of the synthesized cationic surfactant at cmc (32, 33). The corresponding value was measured at 20 °C.

Emulsion stability

Emulsion stability was determined by mixing the aqueous solution of the surfactants with the mineral oil in a graduated cylinder with a plastic stopper. An aqueous solution of the surfactant at the cmc (10 mL) was poured into a 100 mL cylinder containing 10 mL mineral oil. The glass cylinder was closed with a stopper. The mixture was shaken by turning the glass cylinder vigorously up and down for 30 s at a constant speed, and then the time for the separation of 9 mL of clean surfactant solution was noted (34).

Ultraviolet (UV) spectrophotometric analysis

A Hitachi 3100H dual-beam spectrophotometer was used for spectrophotometric analysis. The spectra of the compounds were viewed at a wavelength range of 1100-190 nm. Since no peak was observed in the near IR and Visible (VIS) regions, comparative spectra were taken at a range of 500-190 nm. For the cationic surfactant, spectra of solutions with various concentrations (1.0×10^{-6} – 2.5×10^{-5}) M and separately 1.0×10^{-4} M on the curve were taken.

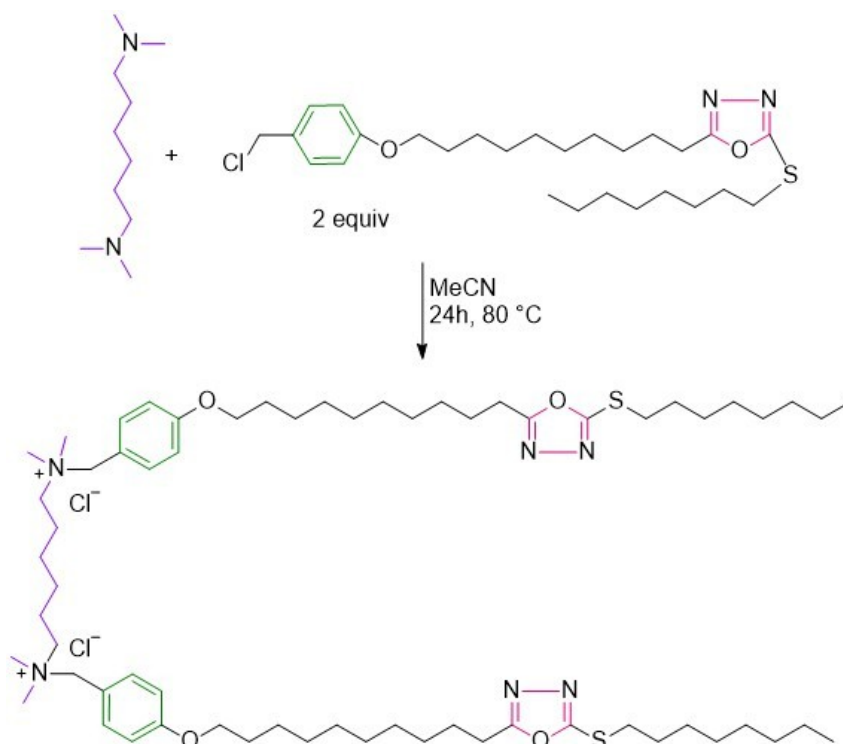
General extraction and purification procedure for trimyristin

The *Myristica fragrans* seeds were ground using a porcelain mortar and pestle at ambient temperature just before extraction to isolate triglycerides more efficiently. From this undried crushed sample, exactly 1 gram was weighed, placed in a 50 mL single-necked flask, and was extracted at 50 °C for 20 min with 20 mL of the solvent indicated in the present work. In the case of surfactant-assisted extractions, 5 mg of the related surfactant was also added into the flask. After that, the obtained mixture was filtered, and the filtrate was evaporated in a vacuum. The residue was weighed and recrystallized from acetone to afford pure trimyristin as a white solid with mp: 55–56 °C. However, the triglyceride is sufficiently pure and can be used for many purposes without further purification.

RESULTS AND DISCUSSION

Synthesis and physicochemical characterization of the surfactant

1,3,4-oxadiazole based long-chain benzyl chloride derivative (31) was treated with *N, N, N', N'*-tetramethyl-1,6-hexanediamine, as shown in Scheme 1, to prepare the cationic gemini type surfactant. The structure of the novel surfactant was confirmed by FTIR, 1H NMR, and ^{13}C NMR spectroscopic methods (Appendix A. Supplementary material, S2). The evaluation of 1H NMR spectrum showed that ($ArCH_2N^+$) benzyl protons appear as a singlet at 4.74; methylene protons of ($ArOCH_2-$) group also appear as a triplet peak at 3.90 ppm. The methylene protons next to the heterocyclic ring sulfur atom ($HetSCH_2CH_2-$) have a chemical shift of 3.18 ppm as a triplet peak. The methyl protons attached to the quaternary N atom [$N^+(CH_3)_2$] have a chemical shift of 3.15 ppm as a singlet peak, which are the essential characteristic peaks of this compound (Figure 1). The surfactant is not soluble in water at room temperature but is readily soluble by mild heating. Physicochemical parameters such as foam height and foam stability could not be determined because this compound did not form a permanent foam layer in water. However, various parameters like density (ρ), cmc, surface tension at cmc (γ_{cmc}), surface effectiveness (π_{cmc}), Gibbs free energy of micellization (ΔG_{mic}), and hydrophilic-lipophilic balance (HLB) value were measured and/or calculated for the surfactant. The results are summarized in Table 1.



Scheme 1: Synthesis of symmetrical heterocyclic gemini-type surfactant.

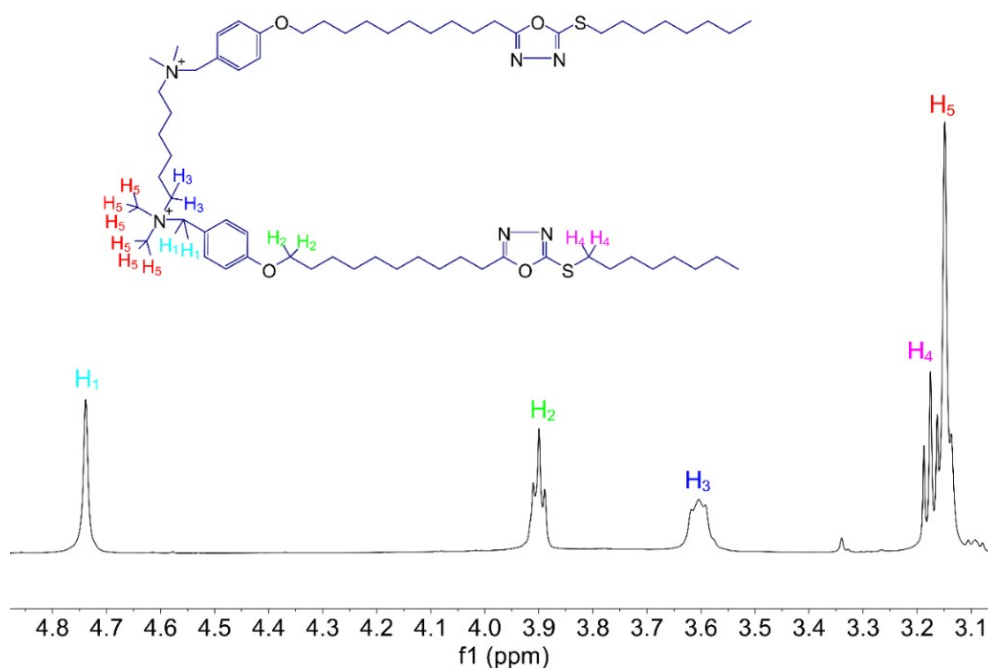


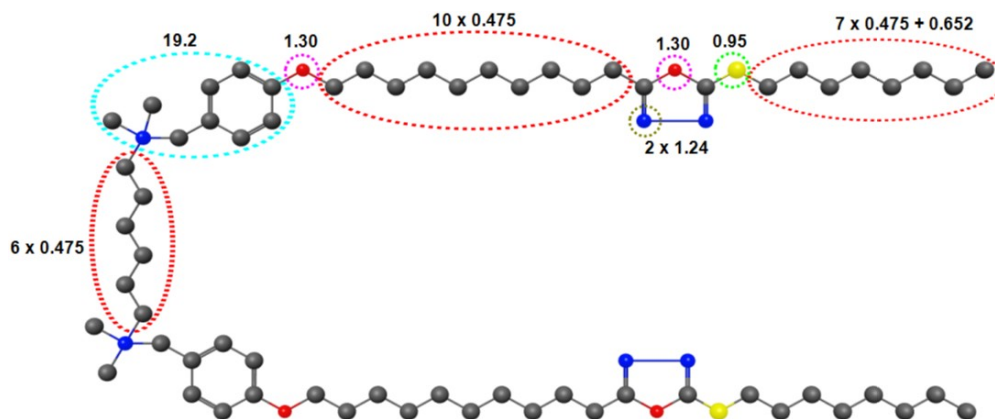
Figure 1: Some characteristic ¹H NMR peaks of the surfactant molecule.

Table 1: Experimental and calculated physicochemical properties of the surfactant catalyst.

ρ (g mL ⁻¹) ^{a,b}	cmc ($\times 10^{-5}$ mM) ^a	γ_{cmc} (dyn cm ⁻¹) ^a	Π_{cmc} (dyn cm ⁻¹)	ΔG_{mic} (kJ mol ⁻¹)	ES_1 (s) ^{a,b,d}	ES_2 (s) ^{a,c,d}
1.1227	26.36	33.01	39.79	- 36.9	164	38

HLB (Hydrophilic-lipophilic balance) value of the surfactant molecule

Hydrophilic and hydrophobic group contributions^e



$$HLB = \Sigma (\text{Hydrophilic group contributions}) - \Sigma (\text{Hydrophobic group contributions}) + 7$$

$$= (19.2 \times 2 + 4 \times 1.30 + 4 \times 1.24 + 2 \times 0.95) - (40 \times 0.475 + 2 \times 0.652)$$

$$= 30.2$$

^a Value measured at 20 °C.

^b Value measured at $1,0 \times 10^{-4}$ M of surfactant concentration.

^c Value measured at critical micelle concentration of the surfactant.

^d Emulsion stability in seconds.

^e Contributions were received from references (35, 36).

The cmc of the surfactant was determined by conductivity measurements. As seen in Figure 2, with the increase in conductivity, the concentrations also showed a linear increase. Besides, the concentration was determined as 26.36×10^{-5} mM at which the slope was changed. This concentration is the critical micelle concentration of the synthesized gemini surfactant and is relatively low in comparison with cmc values of previously synthesized cationic gemini surfactants (37). The surfactant's cmc plays an essential role in the Gibbs free energy of micellization. The value of Gibbs free energy of

micellization, which is calculated by the following equation, proves that as the cmc of the surfactant decreases, the tendency of the substance to form micelle increases. The negative value of Gibbs' free energy of micellization shows that micelle formation occurs spontaneously.

$$\Delta G_{mic} = RT \times \ln (cmc)$$

Where ΔG_{mic} is the Gibbs free energy of micellization, R is the ideal gas constant ($8.314 \text{ J mol}^{-1} \text{ K}^{-1}$), T is the absolute temperature (293 K).

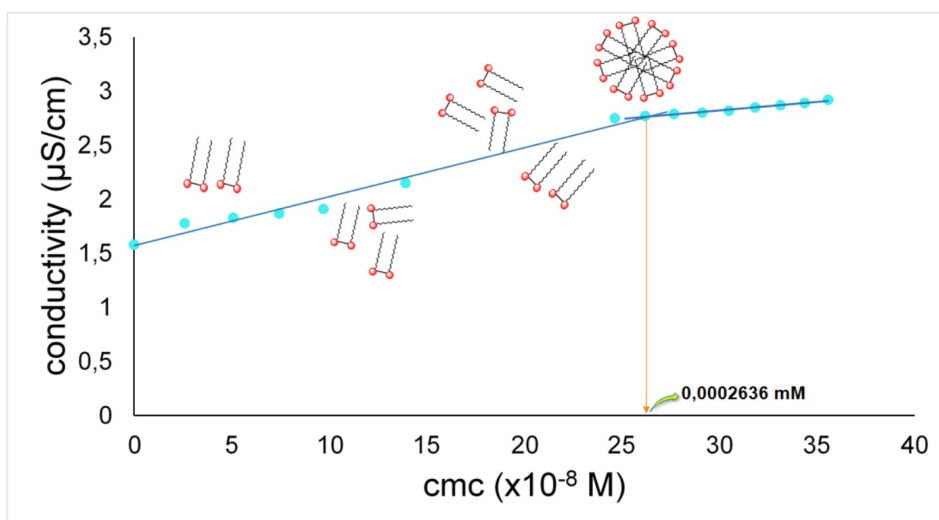


Figure 2. Conductivity as a function of surfactant concentration.

The surface tension was measured to evaluate the surface activity of the aqueous solution of the surfactant at cmc with a capillary rise method in accordance (32, 33). The effectiveness in surface tension reduction (π_{cmc}) is the amount of reduction in surface pressure attained at the cmc (38). It is defined by using the following equation:

$$\pi_{cmc} = \gamma_0 - \gamma_{cmc}$$

Where, γ_0 is the surface tension of pure solvent (water, 72.8 dyn cm⁻¹ at 20 °C) and γ_{cmc} is the surface tension of the solution at the cmc. This parameter (π_{cmc}) indicates the maximum reduction of surface tension caused by the dissolution of surfactant molecules and hence becomes a measure for the effectiveness of the surfactant to lower the surface tension of the solvent (39). The effectiveness value was calculated as 39.79 dyn cm⁻¹. This result indicates that the synthesized surfactant has the potential to reduce the surface tension in the aqueous system (40). The *HLB* value is also calculated for the synthesized surfactant according to the Davies method (41).

One of the essential properties of surfactant molecules is emulsion stability, and it reflects the capability of a surfactant to maintain an emulsion for a longer duration. It was determined as a time required to break down the emulsion formed between surfactant solution and mineral oil. The emulsification is realized by the effect of adsorption, and it forms a layer of adsorptive film in the interface of dispersed droplets. The emulsion stability of the synthesized surfactant was measured as the time required for separation of 9 mL of pure water from the emulsion formed between surfactant solution at cmc and mineral oil (10/10 mL). As depicted in Table 1, the emulsion stability was measured at two different

concentrations of the synthesized surfactant. ES_1 is the emulsion stability measured at 1.0×10^{-4} M of surfactant concentration, and ES_2 is the emulsion stability measured at cmc. Although the emulsion stability ES_1 was found higher than ES_2 , the results in Table 1 showed that the synthesized compound has a low emulsification tendency, and therefore, it can be used safely in various applications.

The UV spectra of the surfactant measured for different concentrations of aqueous solutions are given in Figure 3a. The UV spectrum of the slightly more concentrated surfactant solution (1.0×10^{-4} M) was also taken (Figure 3b). In these spectra, a maximum absorbance value was measured in the wavelength of 232 nm, and two narrow bands were also detected in the wavelength range of 272–280 nm.

As known, dimeric (gemini) surfactants are compounds consisting of more than one hydrophilic head group and a hydrophobic tail group linked by a rigid or a flexible spacer at or near the head groups. The spacer group may also possess hydrophobic or hydrophilic groups, short or long alkyl groups, rigid or flexible groups (42). These surfactants appear to be superior to the corresponding conventional monomeric surfactants. They have much lower cmc, are more efficient in lowering the surface tension of water, and have better wetting and lime-soap dispersing properties (43). Gemini surfactants have widespread use, some of which are using as a phase transfer catalyst and finding applications in adsorption (44), analytical separations (45), solubilization processes (46), nanotechnology (47) and oil recovery (48). They also find use in the dissolution of dyes and pigments in the spinning and weaving industry (49).

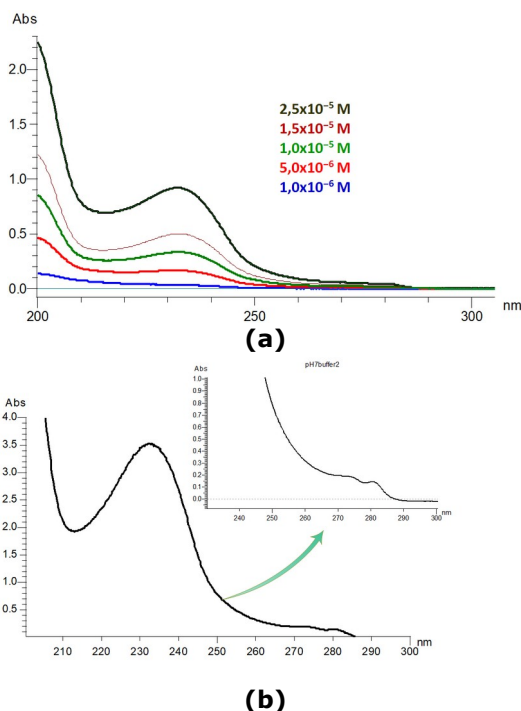
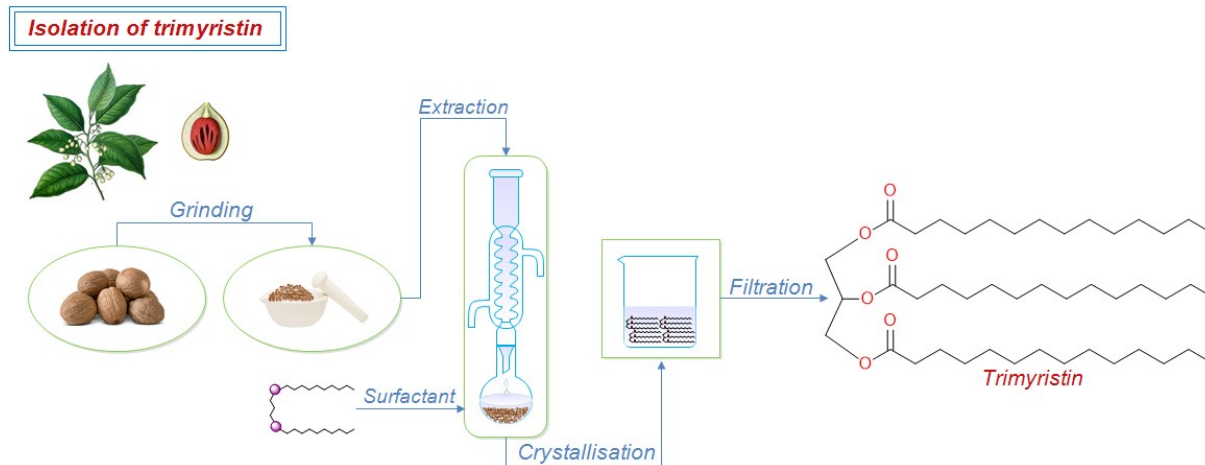


Figure 3. (a) UV spectra of aqueous solutions of the surfactant at different concentrations. Figure (b) UV spectrum of an aqueous solution of the surfactant at 1.0×10^{-4} M.

Extraction of trimyristin

In this study, a series of extraction studies were carried out for the isolation of trimyristin from nutmeg (Scheme 2). The extractions were performed by slightly polar solvents (CHCl_3 and THF) and n-hexane as a non-polar solvent, all of which have a relatively low boiling point. Cationic and anionic monomeric surfactants such as cetyltrimethylammonium bromide (CTAB), cetylpyridinium bromide (CPB), and sodium dodecyl sulfate (SDS) respectively were selected, and their effectiveness was compared with the gemini surfactant (GS), to determine surfactant assistance in the isolation process (Table 2). It should be noted that the percent recovery yield of trimyristin is the yield after crystallization from acetone and is based on the recovered crude extract. As can be seen from the table, n-hexane, including gemini surfactant, is the more efficient system comparing to the other extracting neat solvents and surfactant-based solvent systems. The crude extract obtained at the end of the extraction with n-hexane is quite clear and colorless, so the purification of trimyristin becomes a simple task. On the other hand, orange-colored extracts obtained by extraction processes with the other slightly polar solvents, indicating that some moderately polar components of nutmeg essential oil are also transferred to the solvent phase along with trimyristin.



Scheme 2. Schematic representation of the trimyristin isolation process.

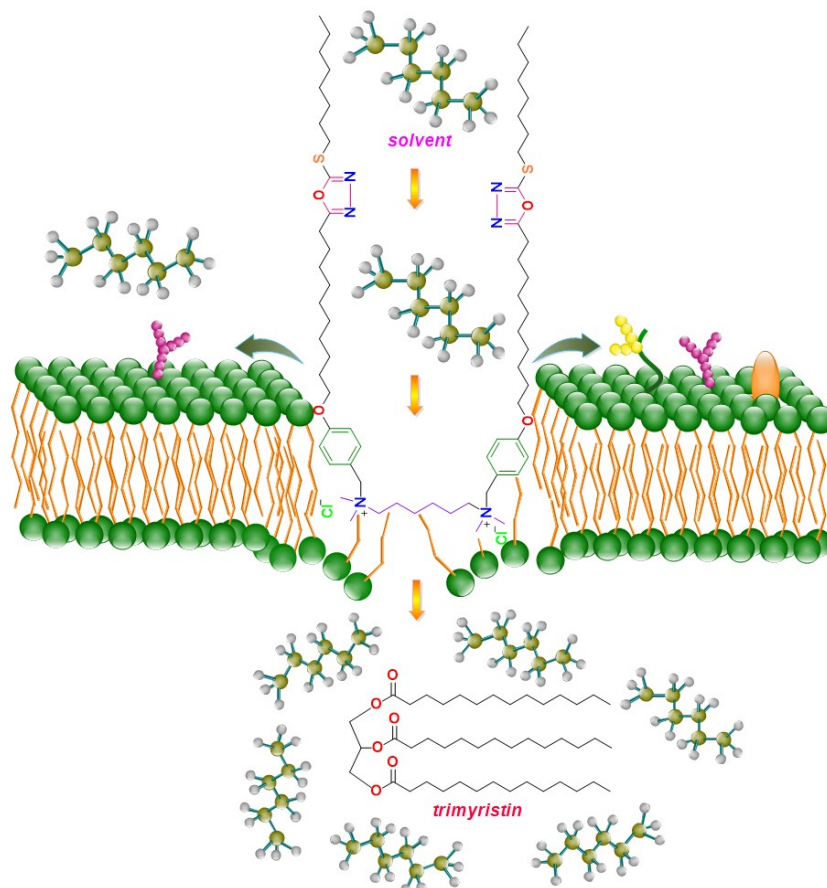
The possible role of the cationic surfactant during the extraction process can be expressed as in Figure 4. According to this figure, the surfactant molecules form a channel-like cavity for easier penetration of the non-polar solvent molecules from the semipermeable phospholipids based cell membrane. However, intriguing results were encountered in extractions with SDS as an anionic surfactant. As seen from Table 2, the amount of

recovered trimyristin slightly decreased with the use of CHCl_3 or n-hexane in combination with SDS compared with the same neat solvent (entries 10, 12, and entries 1, 3 respectively). The main possible reason for this result may be that the surface of the cell membrane composed of phospholipids and is negatively charged (50), which has a repellent effect against anions of SDS surfactant.

Table 2. Experimental conditions for the extraction of trimyristin.

Entry	Surfactant	Solvent	Surfactant (mg)	Time (min)	Temperature (°C)	Recovery yields based on crude extract (%) ^f
1	-	CHCl ₃	5	20	50	60
2	-	THF	5	20	50	62
3	-	n-hexane	5	20	50	63
4	CTAB	CHCl ₃	5	20	50	64
5	CTAB	THF	5	20	50	72
6	CTAB	n-hexane	5	20	50	69
7	CPB	CHCl ₃	5	20	50	71
8	CPB	THF	5	20	50	74
9	CPB	n-hexane	5	20	50	67
10	SDS	CHCl ₃	5	20	50	42
11	SDS	THF	5	20	50	69
12	SDS	n-hexane	5	20	50	57
13	GS	CHCl ₃	5	20	50	67
14	GS	THF	5	20	50	66
15	GS	n-hexane	5	20	50	76

^fAfter crystallization from acetone.

**Figure 4.** Plausible role of the surfactant molecule in the extraction process.

On the other hand, Table 2 shows that the ideal solvent and surfactant in the extraction process are n-hexane and GS, respectively. Accordingly, optimization studies were performed and the results obtained are shown in Figure 5. When these results are evaluated, it can be concluded that the optimum conditions for the extraction of trimyristin

with n-hexane should be as given in Figure 5, entry 5. As a result, the most apparent advantages of the method developed in this study compared with the existing ones are that it allows obtaining triglyceride with more practical, selective, and high yields.

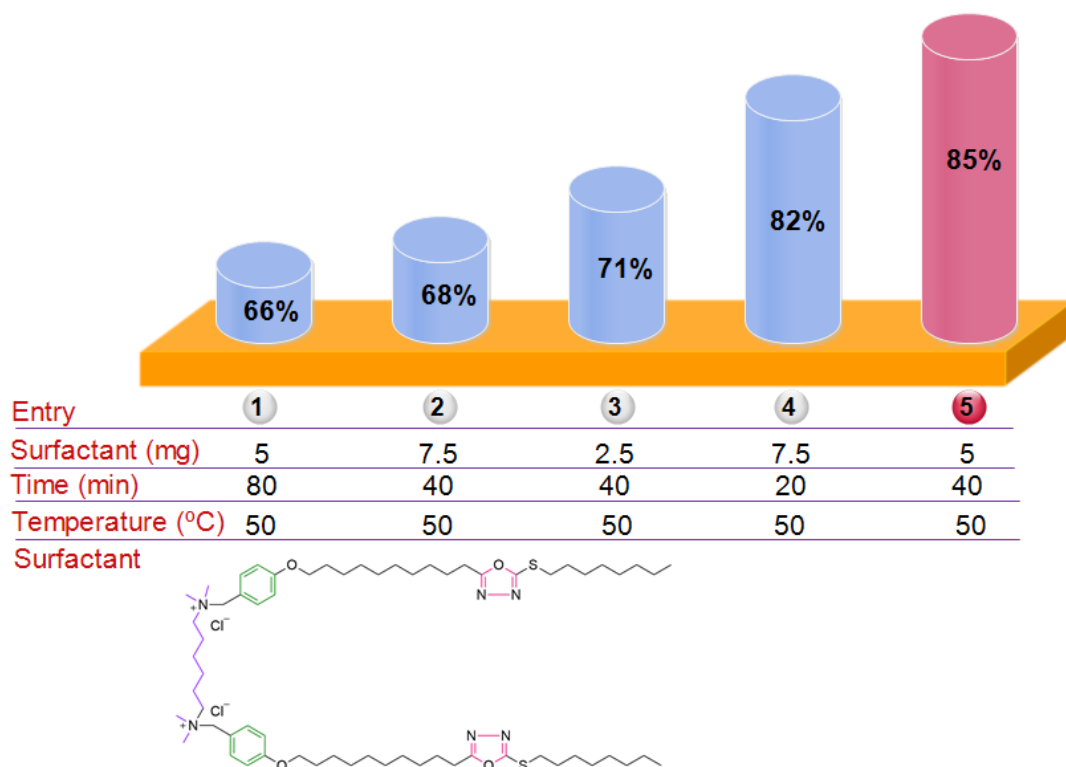


Figure 5. Optimization parameters for the recovery of trimyristin (percent yields are based on the crude extract after crystallization from acetone).

CONCLUSIONS

Herein, an extractive isolation method was developed for trimyristin from nutmeg as a valuable renewable raw material, and this method is more practical and effective than the existing isolation methods. Several different surfactants in combination with organic solvents, were used to make extraction more effective. It has been observed that monomeric and dimeric cationic surfactants, especially the newly synthesized gemini type surfactant, are more effective than the anionic surfactant (SDS) in the extraction process. The performed optimization studies revealed that to obtain the highest yield of the triglyceride, *n*-hexane and gemini surfactant are ideal as an organic solvent and as an auxiliary agent, respectively.

REFERENCES

- Metzger JO, Biermann U. Sustainable development and renewable feedstocks for chemical industry. In: Bozell JJ, Patel MK, editors. *Feedstocks for the Future, Renewables for the Production of Chemicals and Materials*. Washington, DC: American Chemical Society; 2006 Jan, Vol. 921, p. 13–26.
- Biermann U, Bornscheuer U, Meier MAR, Metzger JO, Schäfer HJ. Oils and fats as renewable raw materials in chemistry. *Angew. Chem. Int. Ed.* 2011 Mar; 50:3854–3871.
- Wiggers VR, Beims RF, Ender L, Simionatto EL, Meier HF. Renewable hydrocarbons from triglyceride's thermal cracking frontiers in bioenergy and biofuels. In: Lopes EJ, Zepka LQ, editors. *Frontiers in Bioenergy and Biofuels*. London: IntechOpen Limited; 2017 Jan, p. 407–424.
- Agyeman GA, Gyamerah M, Biney PO, Woldesenbet S. Extraction and characterization of triglycerides from coffeeweed and switchgrass seeds as potential feedstocks for biodiesel production. *J. Sci. Food Agric.* 2016 Mar; 96: 4390–4397.
- Kubickova I, Kubicka D. Utilization of triglycerides and related feedstocks for production of clean hydrocarbon fuels and petrochemicals: a review. *Waste Biomass Valori.* 2010 Aug; 1: 293–308.
- Lligadas G, Ronda JC, Galià M, Cádiz V. Oleic and undecylenic acids as renewable feedstocks in the synthesis of polyols and polyurethanes. *Polymers* 2010 Oct; 2: 440–453.
- Maher KD, Bressler DC. Pyrolysis of triglyceride materials for the production of renewable fuels and chemicals. *Bioresour. Technol.* 2007 Sep; 98: 2351–2368.
- Fréty R, Da Rocha MGC, Brandão ST, Pontes LAM, Padilha JF, Borges LEP, Gonzalez WA. Cracking and hydrocracking of triglycerides for renewable liquid fuels: alternative processes to transesterification. *J. Braz. Chem. Soc.* 2011 July; 22: 1206–1220.
- Crivello JV, Narayan R. Epoxidized triglycerides as renewable monomers in photoinitiated cationic polymerization. *Chem. Mater.* 1992 May; 4: 692–699.

10. Wells PA, Foster NR, Liong KK, Chaplin RP. Supercritical fluid extraction of triglycerides. *Sep. Sci. Technol.* 1990 Oct; 25: 139–154.
11. Temelli F. Extraction of triglycerides and phospholipids from canola with supercritical carbon dioxide and ethanol. *J. Food Sci.* 1992 March; 57: 440–443.
12. Chen WH, Chen CH, Chang CMJ, Chiu YH, Hsiang D. Supercritical carbon dioxide extraction of triglycerides from *Jatropha curcas* L. seeds. *J. Supercrit. Fluids* 2009 Dec; 51: 174–180.
13. Spricigo BC, Pinto LT, Bolzan A, Novais AF. Extraction of essential oil and lipids from nutmeg by liquid carbon dioxide. *J. Supercrit. Fluids* 1999 July; 15: 253–259.
14. Working paper, Food and Agriculture Organization of the United Nations, Rome, Nutmeg and derivatives, <http://www.fao.org/3/v4084e/v4084e.pdf/>, 1994 (accessed 10 June 2019).
15. Muchtaridi AS, Apriyantono A, Mustarichie R. Identification of compounds in the essential oil of nutmeg seeds (*Myristica fragrans* Hoult.) that inhibit locomotor activity in mice. *Int. J. Mol. Sci.* 2010 Nov; 1: 4771–4781.
16. Krishnamoorthy B, Rema J. Nutmeg and mace, in: Peter KV (Ed.), *Handbook of Herbs and Spices*, Woodhead Publishing, Cambridge, vol. 1, 2012, pp. 399–416.
17. Beal GD. Trimyrustin, *Org. Synth.* 1926; 6: 100.
18. Ikan R. *Natural Products a Laboratory Guide*, second ed., Academic Press, Inc., London, 1991, pp. 26–27.
19. Lugemwa FN. Extraction of betulin, trimyrustin, eugenol and carnosic acid using water-organic solvent mixtures. *Molecules* 2012 Aug; 17: 9274–9282.
20. Frank F, Roberts T, Snell J, Yates C, Collins J. Trimyrustin from nutmeg. *J. Chem. Educ.* 1971 Apr; 48: 255–256.
21. De Mattos MCS, Nicodem DE. Soap from nutmeg: an integrated introductory organic, chemistry laboratory experiment. *J. Chem. Educ.* 2002 Jan; 79: 94–95.
22. Leser ME, Luisi PL, Palmieri S. The use of reverse micelles for the simultaneous extraction of oil and proteins from vegetable meal. 1989 Nov; 34: 1140–1146.
23. Prevot AB, Gulmini M, Zelano V, Pramauro E. Microwave-assisted extraction of polycyclic aromatic hydrocarbons from marine sediments using Nonionic surfactant solutions. *Anal. Chem.* 2001 June; 73: 3790–3795.
24. Shi Z, Zhu X, Cheng Q, Zhang H. Micellar extraction and preconcentration of anthraquinone derivatives from rhubarb prior to their HPLC-DAD determination. *J. Liq. Chromatogr. Relat. Technol.* 2007 Feb; 30: 255–271.
25. Ugolini L, De Nicola G, Palmieri S. Use of reverse micelles for the simultaneous extraction of oil, proteins, and glucosinolates from cruciferous oilseeds. *J. Agric. Food Chem.* 2008 Feb; 56: 1595–1601.
26. Li F, Yu Y, Zhang H, Liu T, Lia Y, Duan G. Infrared-assisted non-ionic surfactant extraction as a green analytical preparatory technique for the rapid extraction and pre-concentration of picroside I and picroside II from *Picrorhiza scrophulariiflora* Pennell. *Anal. Methods* 2013 May; 5: 3747–3753.
27. Tuntiwattanapun N, Tongcumpou C, Haagensohn D, Wiesenborn D. Development and scale-up of aqueous surfactant-assisted extraction of canola oil for use as biodiesel feedstock. *J. Am. Oil Chem. Soc.* 2013 Apr; 90: 1089–1099.
28. Heng MY, Thio BJ, Ong ES. Surfactant-assisted pressurized liquid extraction at room temperature for radix glycyrrhizae by a new class of surfactants. *J. Chromatogr. Sci.* 2016 May-Jun; 54: 864–870.
29. Ramly NH, Zakaria R, Naim MN. Surfactant-assisted aqueous extraction of palm-pressed mesocarp fiber residual oil with Tween 80 solution. *Sep. Sci. Technol.* 2017 May; 52: 1796–1805.
30. Kadioglu SI, Phan TT, Sabatini DA. Surfactant-based oil extraction of corn germ. *J. Am. Oil Chem. Soc.* 2011 June; 88: 863–869.
31. Yıldırım A. Synthesis of novel alkyl-sulfanyl-1,3,4-oxadiazolyl-1,3,5,7-tetraazatricyclic ammonium chloride type cationic surfactants. *J. Het. Chem.* 2015 March; 52: 522–526.
32. Martino W, De la Mora JF, Yoshida Y, Saito G, Wilkes J. Surface tension measurements of highly conducting ionic liquids. *Green Chem.* 2006 Jan; 8: 390–397.
33. Sugden S. The determination of surface tension from the rise in capillary tubes. *J. Chem. Soc., Trans.* 1921; 119: 1483–1492.
34. Negm NA, Mohamed AS. Surface and thermodynamic properties of diquateryary bola-form amphiphiles containing an aromatic spacer. *J. Surf. Deterg.* 2004 Jan; 7: 23–30.
35. Akzo Nobel surface chemistry LLC, Technical information surface chemistry. HLB & emulsification description of hydrophile, lipophile balance and use of HLB in producing emulsions. <https://vdocuments.site/documents/akzonobel-tb-hlbemulsions.html/>, 2008 (accessed 10 June 2019).
36. Szymanowski J, Voelkel A. Hydrophile lipophile balance of hydroxyoximes in McGowan scale and their partition and extraction properties. *J. Chem. Tech. Biotechnol.* 1992 Oct; 54: 19–26.
37. Singh V, Tyagi R. Unique micellization and cmc aspects of gemini surfactant: an overview. *J. Disper. Sci. Technol.* 2014 Aug; 35: 1774–1792.
38. Öztürk S, Yıldırım A, Gece G, Türkdemir H. Flexible semicrown ether-linked symmetric cationic gemini surfactants: synthesis and evaluation as catalysts for

acceleration of diastereoselective [3 + 2] cycloaddition reaction in reversed phase micellar media. *J. Surf. Deterg.* 2019 Nov; 22: 197–208.

39. Dong B, Li N, Zheng L, Yu L, Inoue T. Surface adsorption and micelle formation of surface active ionic liquids in aqueous solution. *Langmuir* 2007 Mar; 23: 4178–4182.

40. El-Sayed R, Alotaibi HH, Elhady HA. Synthesis, surface parameters, and biodegradability of water-soluble surfactants for various applications. *J. Oleo Sci.* 2018 May; 67: 551–569.

41. Davies JT. A quantitative kinetic theory of emulsion type, I. physical chemistry of the emulsifying agent, in: Schulman JH. (Ed.), *Proceedings of the second international congress of surface activity: Gas-liquid and liquid-liquid interface.* Butterworths, London, 1957 pp. 426–438.

<http://citeseerx.ist.psu.edu/viewdoc/download?doi=10.1.1.473.424&rep=rep1&type=pdf/>, (accessed 10 June 2019).

42. Zana R, Xia J. Introduction, in: Zana R, Xia J. (Eds.), *Gemini Surfactants: Synthesis, Interfacial and Solution-Phase Behavior, and Application.* Marcel Dekker Inc., New York, 2004, pp. 1–8.

43. Tawfik SM. Synthesis, surface, biological activity and mixed micellar phase properties of some biodegradable gemini cationic surfactants containing oxycarbonyl groups in the lipophilic part. *J. Ind. Eng. Chem.* 2015 Aug; 28: 171–183.

44. Laschewsky A, Wattebled L, Arotçaréna M, Jiwan JLH, Rakotoaly RH. Synthesis and properties of cationic oligomeric surfactants. *Langmuir*, 2005 July; 21: 7170–7179.

45. Li W, Sun C, Hou B, Zhou X. Room temperature synthesis and catalytic properties of surfactant-modified Ag nanoparticles. *Int. J. Spectrosc.* 2012 July; 2012.

46. Han Y, Wang Y. Aggregation behavior of gemini surfactants and their interaction with macromolecules in aqueous solution. *Phys. Chem. Chem. Phys.* 2011 Jan; 13: 1939–1956.

47. Crescenzo AD, Germani R, Canto ED, Giordani S, Savelli G, Fontana A. Effect of surfactant structure on carbon nanotube sidewall adsorption. *Eur. J. Org. Chem.* 2011 Aug; 2011: 5641–5648.

48. Rosen M, Wang JH, Chen P, Zhu Y. Ultralow interfacial tension for enhanced oil recovery at very low surfactant concentrations. *Langmuir* 2005 Mar; 21: 3749–3756.

49. Idouhar M, Tazerouti A. Spectrophotometric determination of cationic surfactants using Patent Blue V: application to the wastewater industry in Algiers. *J. Surfactants Deterg.* 2008 Dec; 11: 263–267.

50. Pekker M, Shneider MN. Interaction between electrolyte ions and the surface of a cell lipid membrane. *J. Phys. Chem. Biophys.* 2015 Mar; 5: 1000177.

An improved isolation of trimyristin from *Myristica fragrans* as a renewable feedstock with the assistance of novel cationic gemini surfactant

Ayhan YILDIRIM, Serkan ÖZTÜRK, Haluk TÜRKDEMİR, Atakan KOLALI, Beyza Gökçem ATALAY, Hatice KOCATAŞ

Department of Chemistry, Faculty of Arts and Sciences, Bursa Uludağ University, Bursa 16059, Turkey

Supplementary material

Table of Contents:

FTIR spectrum for the gemini surfactant	Figure S1
¹ H NMR spectrum for the gemini surfactant	Figure S2
¹³ C NMR spectrum for the gemini surfactant	Figure S3

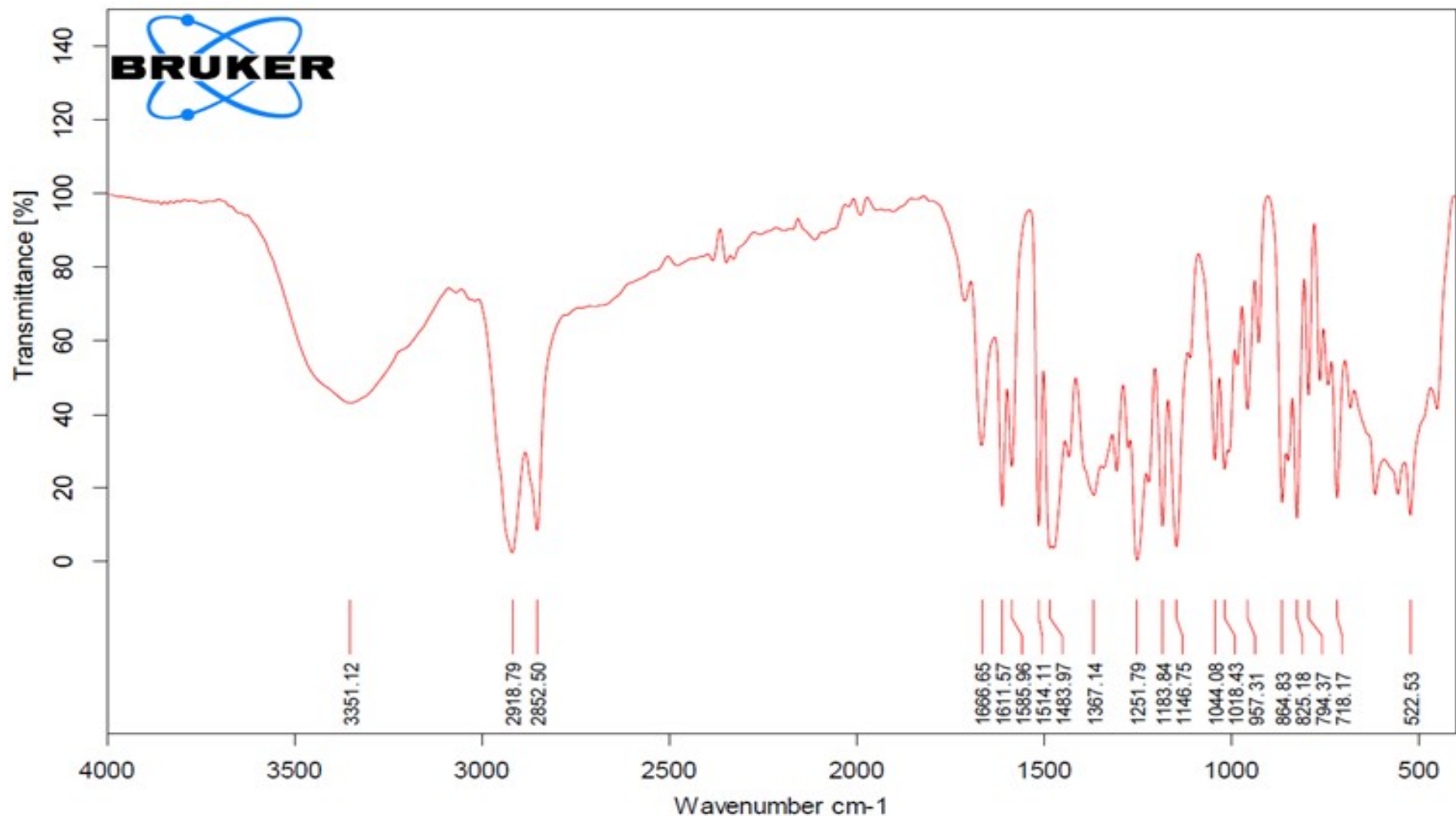


Figure S1. FTIR Spectrum.

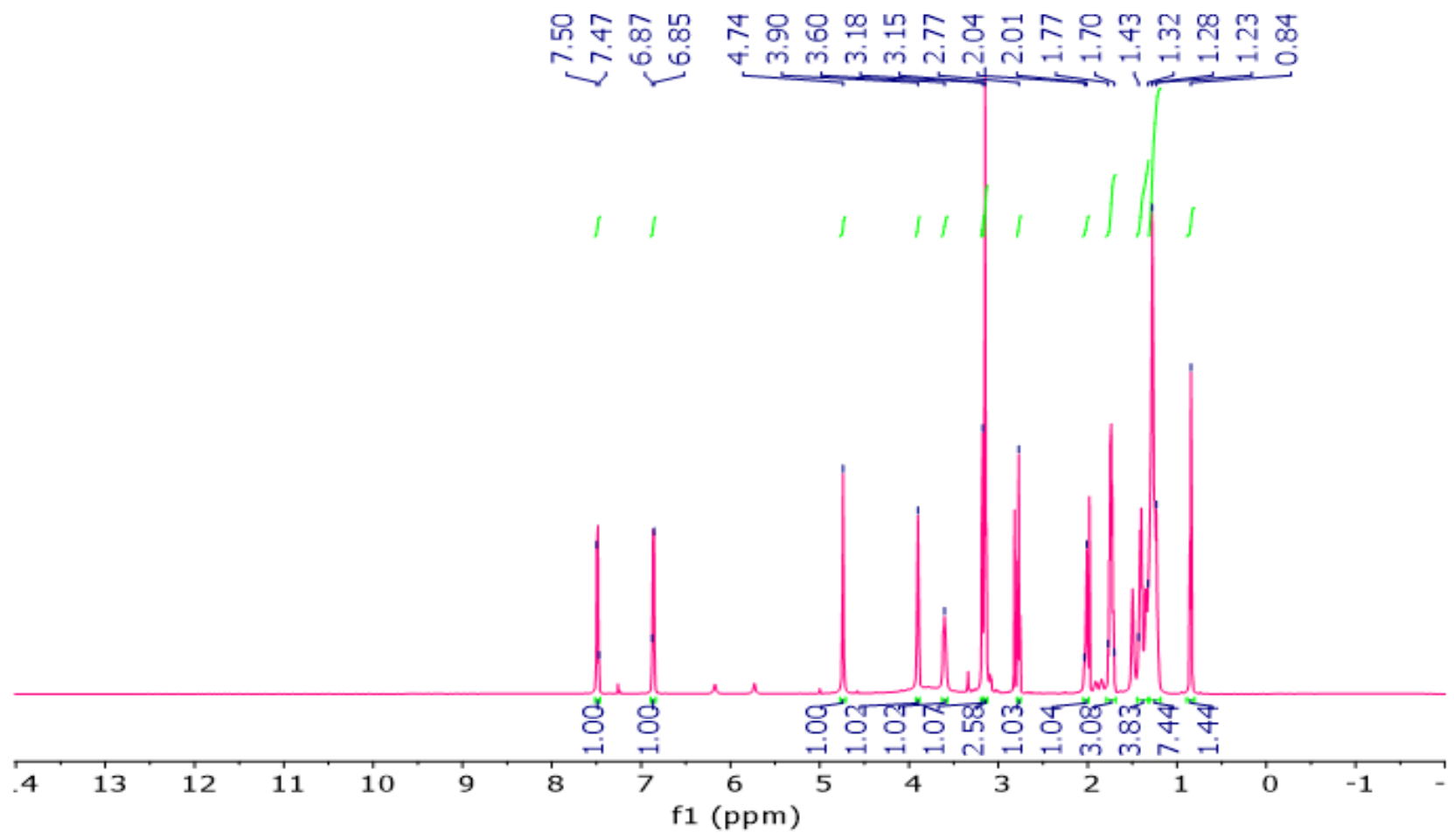


Figure S2. ¹H NMR Spectrum.

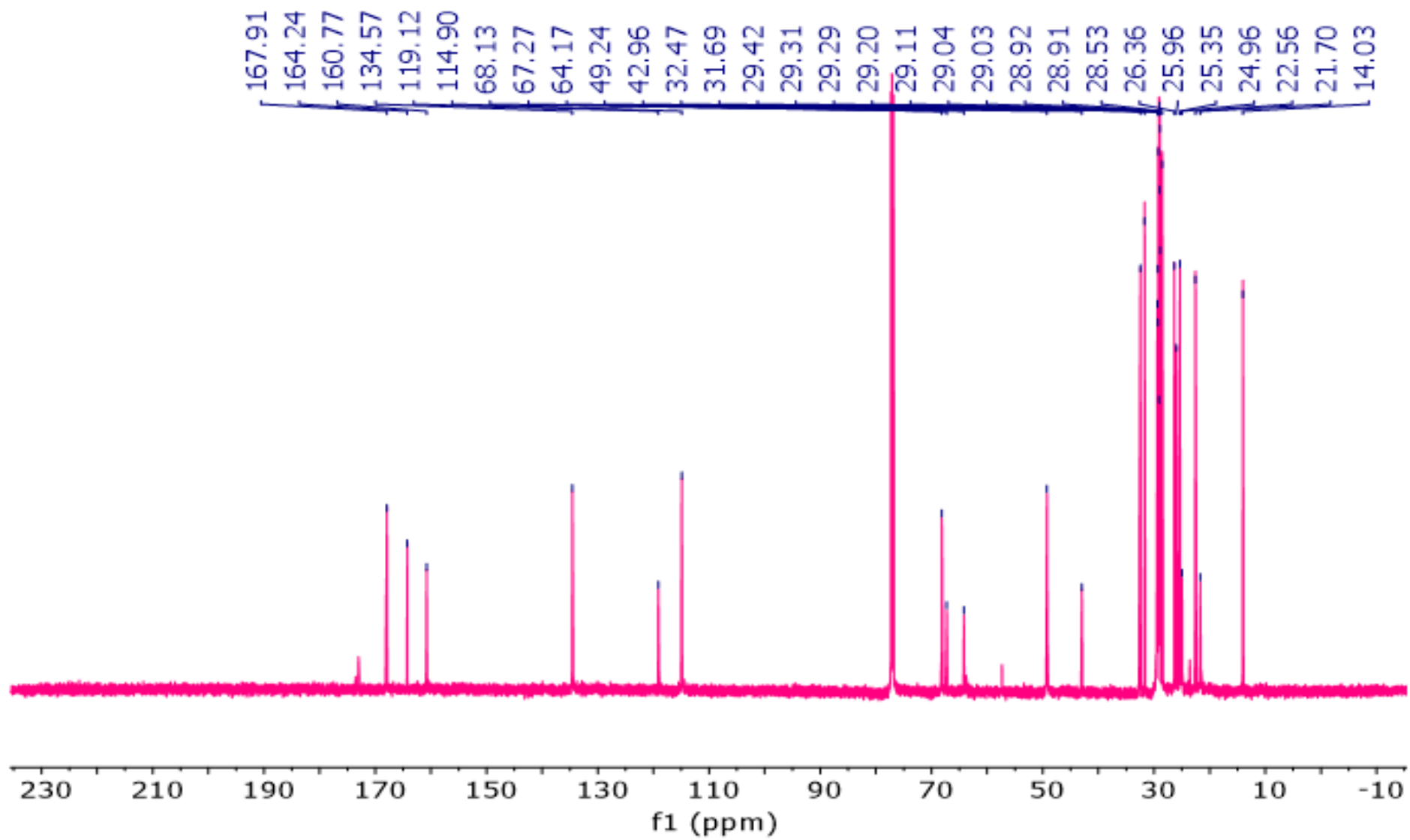


Figure S3. ^{13}C NMR Spectrum.



Copper Oxide Nanoparticles: Synthesis, Characterization, Antimicrobial Activities and Catalytic Reduction of Methylene Blue

Selda Doğan Çalhan^{1*}  , Mustafa Gündoğan²  

^{1*}Mersin University, Faculty of Pharmacy, Department of Pharmaceutical Biotechnology, 33169 Mersin, Turkey.

²Mersin University, Faculty of Pharmacy, Department of Pharmaceutical Technology, 33169 Mersin, Turkey.

Abstract: In recent years, metal nanoparticles have been applied in many areas due to their attractive properties. Copper oxide nanoparticles, in particular, have drawn much attention owing to their electrical, catalytic, optical, antibacterial, and antifungal properties. In this study, copper oxide nanoparticles were synthesized using *Onosma Sericeum Willd (Boraginaceae)* extract with a simple, economical, and eco-friendly method for the first time. The synthesized nanoparticles were characterized using ultraviolet-visible spectrophotometry, field emission scanning electron microscopy, and X-ray diffraction. The particle size distribution and zeta potential measurements of the copper oxide nanoparticles were measured with the dynamic light scattering technique. It was determined that the copper oxide nanoparticles with a particle size of less than 100 nm showed a catalytic effect in the reduction of methylene blue (MB). At room temperature, up to 90% MB dye degradation was achieved. Also, the antimicrobial properties of the copper oxide nanoparticles were investigated in this study. The results of the study showed that synthesized copper oxide nanoparticles could be used as a promising agent in nanotechnology applications.

Keywords: Copper oxide nanoparticles, *Onosma Sericum Willd*, Green synthesis, Catalysis, Antibacterial activity

Received: November 26, 2019. **Accepted:** May 19, 2020.

Cite this: Doğan Çalhan S, Gündoğan M. Copper Oxide Nanoparticles: Synthesis, Characterization, Antimicrobial Activities and Catalytic Reduction of Methylene Blue. JOTCSA. 2020;7(2):561–70.

DOI: <https://doi.org/10.18596/jotcsa.650993>.

***Corresponding author. E-mail:** seldadgn@gmail.com, seldadgn@mersin.edu.tr

INTRODUCTION

Metal nanoparticles are used in various fields due to properties including high surface area/volume ratio, differences in chemical reactivity and catalytic properties, and selective drug delivery to target organs and tissues with easy surface modification. They can be used in electrochemical processes and hydrogen production, electronic devices and communication systems, sensor design, and

biomedical and medical imaging technologies. They also have the potential to be used in many different fields, including material chemistry (1,2).

Copper oxide nanoparticles (CuONPs) attract attention with their catalysis (3), sensor (4), and superconducting applications (5) due to their superior physicochemical properties. These structures are also considered to be semiconductor materials with photocatalytic (6)

and photovoltaic (7) properties. Some studies have shown that CuONPs can be antibacterial agents (8) and used in the treatment of cancer (9).

CuONPs can be synthesized by different chemical methods such as chemical reduction (10), microwave radiation (11), and thermal decomposition (12). However, synthesis procedures performed with these methods involve the adsorption of toxic chemicals to the surface. It can cause serious side effects, especially in medical applications. The use of toxic chemicals, which pose a risk to the environment and human health, in chemical methods has led researchers to develop new alternative methods. Green chemistry (13), which is defined as the utilization of a dozen principles that prevent or reduce the emergence and use of substances that pose a danger to the environment and human health in the design, production, and use of chemical products, is an alternative approach that has been extensively researched in recent years. Association of green chemical principles with nanotechnology has been shown by Schmidt (2006) as the key to a sustainable society in the 21st century (14). The high toxicity and long biocompatibility of nanoparticle technologies, which have been known for a long time, have urged scientists to develop new synthetic procedures that are more secure, environmentally friendly, and producing as little waste as possible, using natural and renewable raw materials that can be easily integrated into biomedical applications. With this new green nanotechnology approach, it has become much easier to find solutions to the problems caused by the conventional synthesis procedure.

Green nanotechnology has been reported to use plants and extracts such as *Aloe vera*, *Azadirachta indica* (linden), *Camellia sinensis* (tea), *Jatropha curcas* (castor nuts), *Acalypha indica* (castor nettle), *Cymbopogon sp* (lemongrass) being preferred in metal nanoparticle synthesis as they are cheap and renewable natural resources. Also, microorganisms such as *Rhodococcus sp.*, *Sargassum wightii*, *Pseudomonas stutzeri*, *Candida glabrata*, M13 bacteriophage, *Fusarium oxysporum*, and *Thermomonospora sp.* are extensively used in the synthesis of metal nanoparticles as natural resources that serve the purpose of green synthesis (15, 16). Particularly in CuONP synthesis, the leaves and stems of the *Gundelia tournefortii* (kenger) plant (17), the leaves of the *Psidium guajava*

plant (18), lemon juice (19) and the *Gloriosa superba* L plant (20) are used.

Plants do not require any other agents in the production of metal nanoparticles because of the phenolic species they contain (21). Therefore, in recent years, studies on plants and plant extracts and nanoparticle synthesis have been conducted with increasing acceleration. *Onosma sericeum Willd* is a member of the *Boraginaceae* family and has been known for its wound healing properties for many years among people in Adiyaman, Turkey. The *Boraginaceae* family, found in tropical, subtropical, and temperate regions of the world, is represented by 154 genera and 2500 species (22).

Depending on the chemical composition and ionic features, several classes of dye molecules have been reported. Thiazine dyes such as MB are aromatic, organic, and toxic pollutants (23). Methylene blue, like the other organic dyes, are released by different industries such as cosmetic, textile, pharmaceutical, and plastic industries (24). There are findings in the literature that MB affects the central nervous system (25). Besides, this pollutant can be accumulated in soil and water and threaten human health. Therefore the investigation of catalytic degradation is essential. In recent years nanoparticles have been used in the degradation of the dye. Especially owing to their large surface area, CuONPs showed very high reactivity.

In this study, CuONP synthesis was carried out by using the root extract of the *Onosma Sericeum Willd* plant for the first time, the wound healing properties of which are well-known, and applying a completely green method without the need for any other organic solvents or stabilizing agents. The characterization of the CuONPs was elucidated using analytical methods. The antimicrobial activities of the obtained CuONPs against a range of Gram-positive and Gram-negative bacteria were evaluated. Its catalytic activity on the reduction of methylene blue, a harmful pollutant for the environment, in the presence of CuONPs was also studied.

MATERIALS AND METHODS

Materials

Copper(II) nitrate ($\text{Cu}(\text{NO}_3)_2$, 99%), methylene blue ($\text{C}_{16}\text{H}_{18}\text{ClN}_3\text{S}$, 95%), sodium borohydride (NaBH_4 , 99%) were obtained from Sigma. Gram-positive bacterial strains *Staphylococcus*

aureus (ATCC25925) and *Bacillus subtilis* (ATCC 6633), gram-negative bacterial strains *Escherichia coli* (ATCC25923), *Acinetobacter baumannii* (ATCCS 02026) and *Aeromonas hydrophila* (ATCC95080) were purchased from the Refik Saydam Hıfzısıhha Institute, Ankara, Turkey. All the chemicals used in the study were of analytical grade, and 18.2 mΩ of distilled water needed throughout the research was obtained through the Milli-Q A10 water purification system.

Instruments

All spectrophotometric measurements were conducted by using the Shimadzu UV-1800 spectrophotometer. The structural morphology of the CuONPs was obtained using a Zeiss / Supra 55 Field Emission Scanning Electron Microscope (FE-SEM). The XRD of the nanoparticles was studied by a high-resolution Rigaku SmartLab brand X-ray diffractometer (XRD). The size distribution of the CuONPs and zeta potential measurements were performed using a Zetasizer Nano-ZS (Malvern Instruments).

Preparation of Extract

The *Onosma Sericeum Willd* plant was collected from the Adiyaman-Besni region in Turkey between April and July 2018. The identification of the plant species was made by Assoc. Prof. Dr. Rıza Binzet of the Faculty of Arts and Sciences at Mersin University. The collected

plant samples were first cleaned from dust and impurities using tap water, followed by distilled water. The plant was left to dry in a clean and dry place. The root portions of the plant were extracted for the CuONP synthesis. For the extraction, 200 mL of distilled water was added to 20 g of roots that were cut into small pieces and subjected to maceration for 6 hours at a temperature that did not exceed 90 °C in a shaking water bath. The extract was filtered *in vacuo* and stored in a refrigerator. Great care was taken to keep the extract as fresh as possible.

Synthesis of the CuONPs

Copper(II) nitrate ($\text{Cu}(\text{NO}_3)_2$, Sigma) was used as the copper source. 5 mL of the extract (20 g / 200 mL) dropwise was added to the $\text{Cu}(\text{NO}_3)_2$ solution (25 mL), which was prepared in 100 mM and mixed in the magnetic stirrer. Next, 1000 μL of NaOH (0.1 M) was added to the mixture.

The gray-green color that developed within half an hour indicated the synthesis of CuONP. The resulting CuONPs were separated by centrifugation (10,000 rpm, 20 min), washed three times with deionized water, and dried in an oven at 80 °C for 12 hours. The oven-dried sample was heat-treated in an ash oven at 400 °C for 3 hours (Figure 1). The obtained samples were stored in a cool and dry environment until analysis.

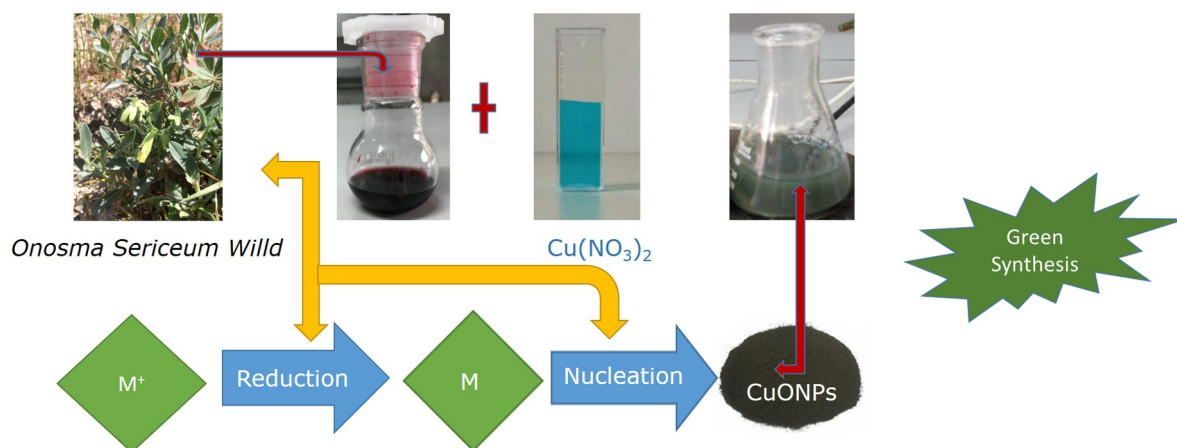


Figure 1. Schematic showing the synthesis procedure and mechanism of CuONPs

Characterization of the Synthesized CuONPs

The optical properties of the synthesized CuONPs were determined by an ultraviolet-visible (UV-Vis) absorption spectrophotometer. All measurements were performed in the range of 200-800 nm, in quartz tubes and with

Shimadzu brand UV-1800 spectrophotometer adjusted to 1 nm resolution. The structural morphology of the CuONPs was obtained using a Zeiss / Supra 55 Field Emission Scanning Electron Microscope (FE-SEM). A high vacuum sputter platinum coating device was used for sample preparation. The crystal structure of the

nanoparticles was illuminated by a high-resolution Rigaku SmartLab brand x-ray diffractometer (XRD) using Cu(K α) radiation (wavelength: 1.54 Å) operated at 40 kV and 40 mA at room temperature. The size distribution of the CuONPs and zeta potential measurements were performed using a Zetasizer Nano-ZS [Malvern Instruments]. Before size distribution and zeta potential measurements, CuONPs were suspended in deionized water at a concentration of 1 mg/10 mL and then sonicated using a sonicator at room temperature for 20 min at 40 W form a homogeneous suspension.

Catalytic Properties

A reduction of MB was observed in the presence of NaBH₄ and CuONPs catalysis. 10 mL of water, 1 mL of 10 mM 4MB, and 1 mL of 1mM NaBH₄ were mixed in a tube at 25 °C. Then, 1 mL of 0.01% CuONPs solution was added to this mixture. Samples were taken from the obtained mixture at intervals of one minute, and measurements were made between 200-800 nm by UV-Vis region absorption spectrophotometer, and reaction monitoring was performed. Also, MB degradation (%) was calculated using the following equation.

$$\text{Dye degradation (\%)} = \left(\frac{C_0 - C_t}{C_0} \right) \times 100 \quad (1)$$

C₀: Initial concentration of MB

C_t: Concentration of the dye solution after 45 minute

All dye concentrations were measured by UV-Vis absorption spectrophotometer. Results were

given as the average of the three measurements.

Antibacterial Activity

In vitro antibacterial activity studies were performed against *Staphylococcus aureus* (ATCC 25925), *Escherichia coli* (ATCC 25923), *Acinetobacter baumannii* (ATCC 02026), *Bacillus subtilis* (ATCC 6633) and *Aeromonas hydrophila* (ATCC 95080) bacteria using the resazurin microplate method (resazurin microtitre assay-REMA) (26). Ampicillin was used as the standard drug in these studies. The color change of resazurin from blue to pink or colorless was considered positive and, therefore, an indication of bacterial growth. The minimum inhibition concentration (MIC) value was determined as the lowest concentration that prevents the resazurin from blue to pink or colorless. All antibacterial activity assays were repeated three times.

RESULTS AND DISCUSSION

UV-Vis Analysis

UV-Vis spectra were taken to evaluate the optical properties of the CuONPs obtained by biosynthesis. It was observed that the solutions of CuONPs obtained in 1 mg / 10 mL water gave characteristic plasmon band at approximately 220 nm at room temperature. Surface plasmon absorbance due to the collective oscillation of the free conduction band electrons was very sensitive to determine CuONPs, which was in good agreement with previous works (27, 28). Figure 2 shows the UV-Vis spectra of the CuONPs and plant extract.

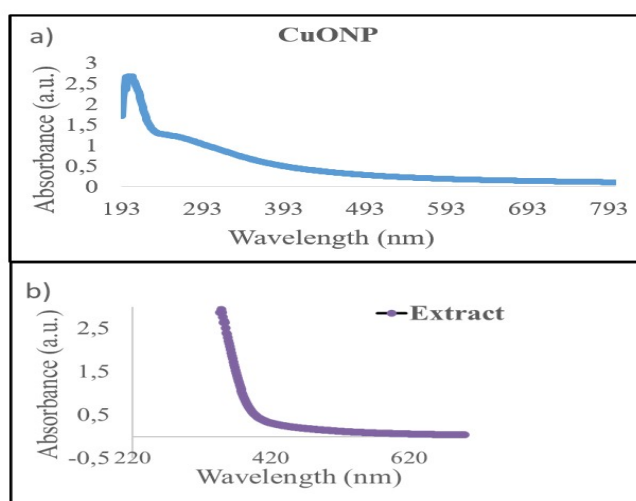


Figure 2. UV-Vis spectra a) CuONPs b) Extract of *Onosma Sericeum Willd.*

FESEM Image and Particle Size Distribution

FE-SEM analyses were performed to determine the surface morphology and particle size of the obtained CuONPs. The FE-SEM images showed that the CuONPs were spherical and approximately 70 nm in size. The dynamic light scattering (DLS) analysis results for size

distribution were also in support of the FE-SEM results (Figure 3). The particle size was ranging from 70 ± 6 nm in DLS measurements, which is an excellent agreement to FESEM particle size. DLS results were calculated by taking the average of the three measurements and standard deviation.

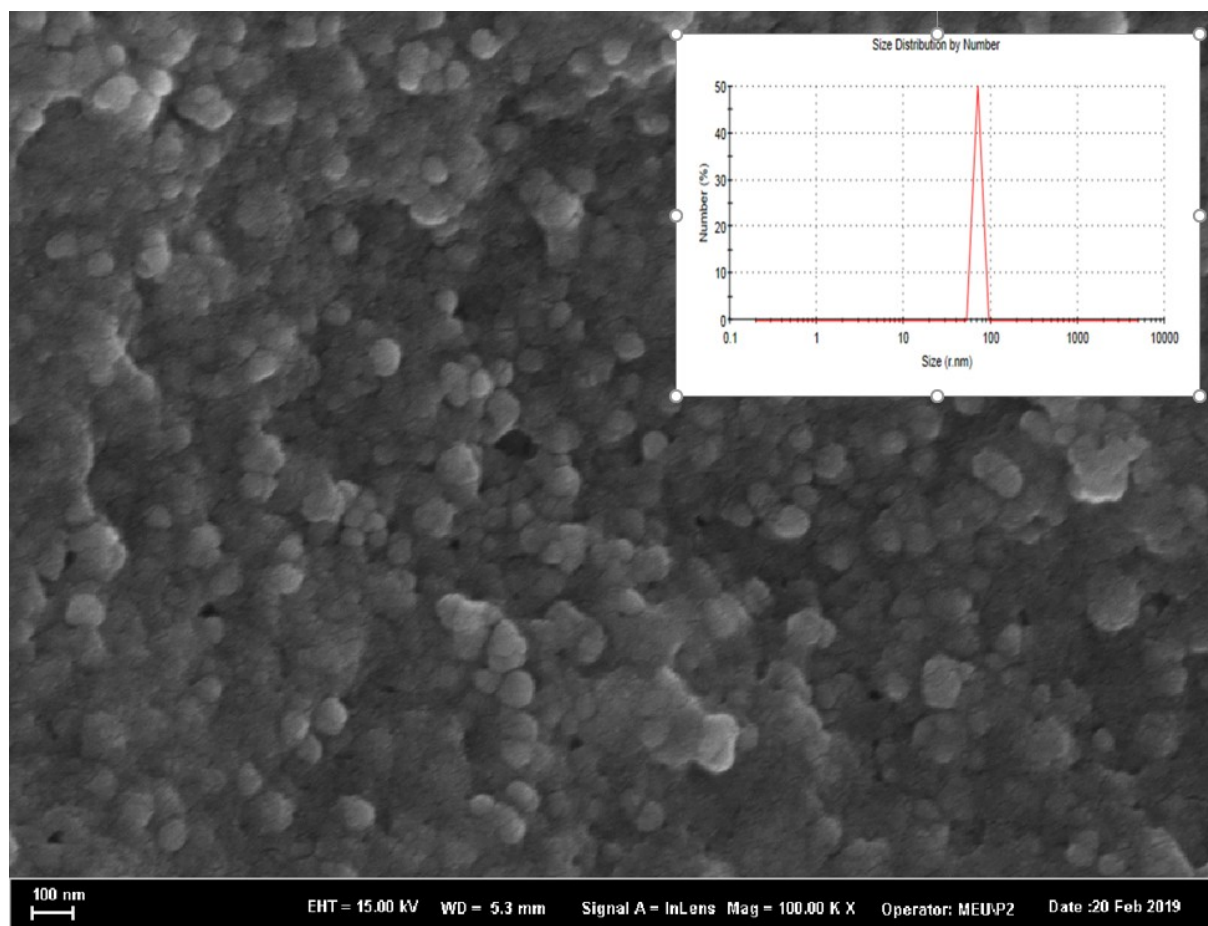


Figure 3. FESEM image and particle size distribution of CuONPs.

Zeta Potential Measurements

Zeta potential is an important parameter related to the stability of nanoparticles. The negative value of the zeta potential reveals that the CuONP negatively charged growths are coated and that electrostatic interaction between these nanoparticles may be responsible for the long-term stability of metal nanoparticles by preventing possible aggregation (28). In this study, the

biomolecules present in the *Onosma Sericeum Willd* plant as inducing and stabilizing agents are thought to be responsible for the electrostatic interaction between the species. The zeta potential (ζ -Pot, mV) for the CuONPs was measured as -13.7 ± 1.55 at 25°C (Figure 4). Zeta potential results were calculated by taking the average of the three measurements and standard deviation.

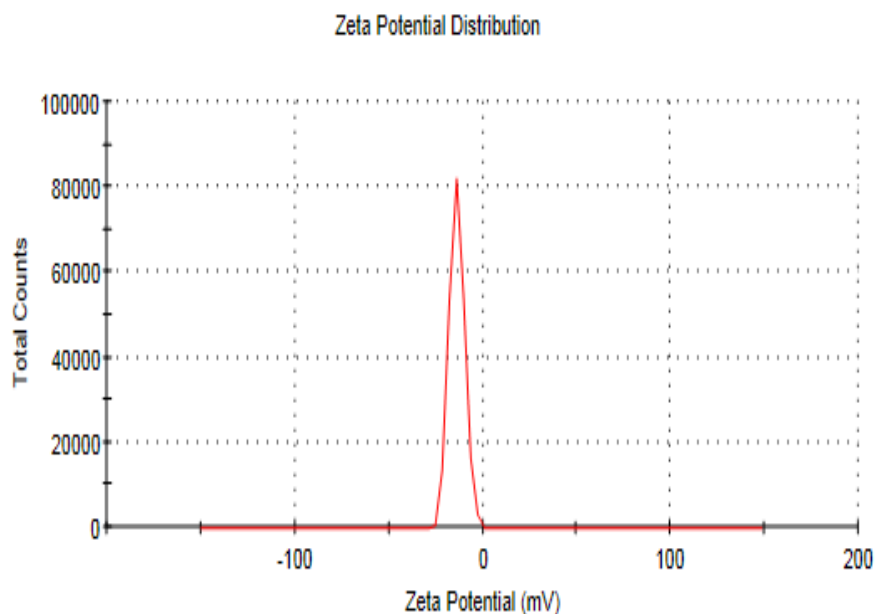


Figure 4. Zeta potential of CuONPs.

XRD Analysis

The powder X-ray diffraction technique was used to illuminate the CuONPs crystal structures obtained by biosynthesis. The diffraction patterns of XRD analyses, which were conducted to clarify the crystal structures, led to peaks observed at (111), (200), (202), (020), (202), (113), (311), (220) and (400).

These peaks confirmed the presence of CuONPs. The obtained XRD patterns were found to match those in the database of the Powder Diffraction Standards Joint Committee (JCPDS) file no: 89-7102. The information obtained was in agreement with the literature (29). The XRD spectrum obtained for the CuONPs is as shown in Figure 5.

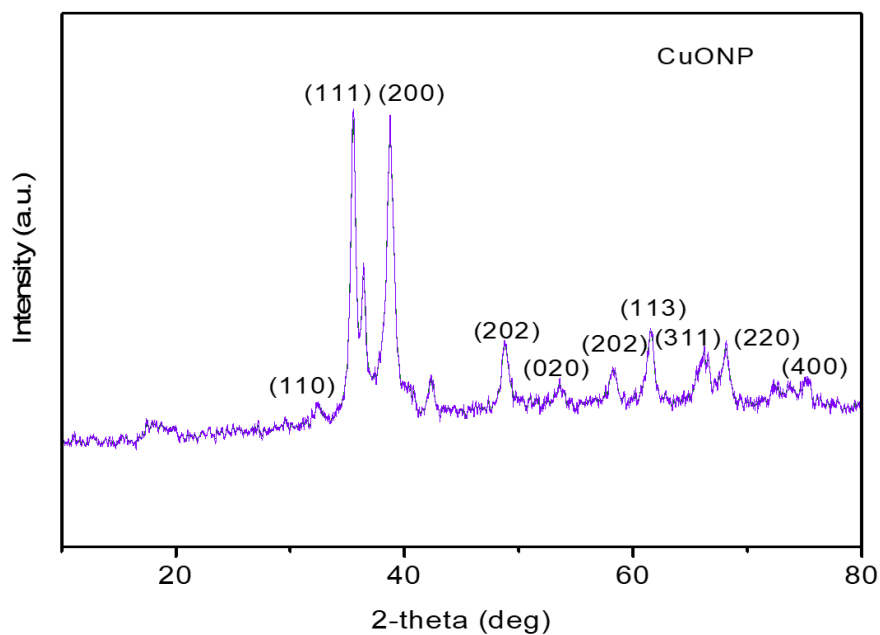


Figure 5. XRD spectra of CuONPs.

Catalytic Activities

As described in catalytic properties, it was found that four characteristic peaks of MB at 246, 292, 613, 664 nm changed only slightly before the addition of CuONPs. However, after adding 0.01% CuONPs solution to the same

mixture, the absorbances were reread at specific intervals. In the first 45 minutes, the characteristic blue color of MB was significantly reduced, and the absorbance intensity decreased (Figure 6).

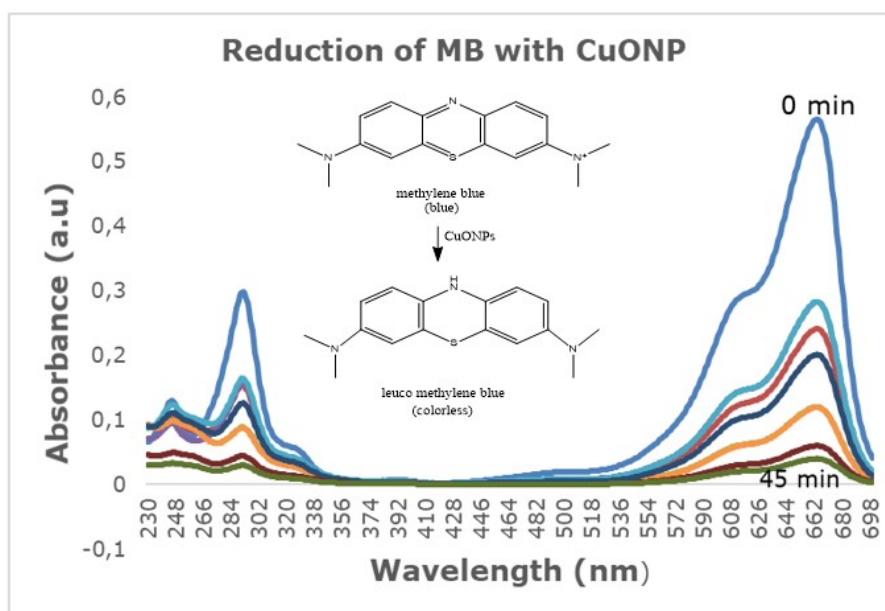


Figure 6. Reduction of MB with CuONP.

As a result of calculations, according to Equation 1, the rate of removal of >90% observed in 45 minutes. Schematic

representation of degradation mechanism MB to leuco-methylene blue is given in Figure 7.

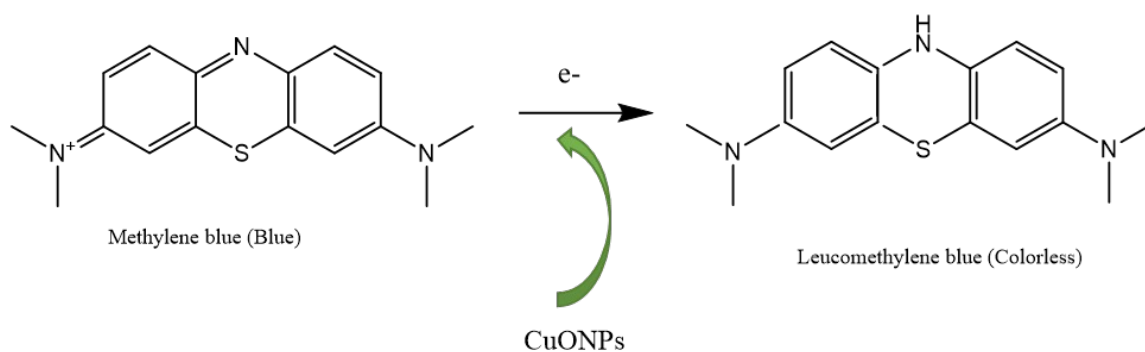


Figure 7. Schematic representation of degradation MB to leuco methylene blue.

MB is a heterocyclic aromatic industrial pollutant-dye, which can be reduced to leuco-methylene blue in the presence of NaBH_4 , but the reduction rate is prolonged. In this study forty-five minutes after the addition of the CuONPs to the dye, the absorbance is gradually decreased. The results show that CuONPs contribute to electron transfer, which plays an essential role in the reduction of methylene blue to leuco methylene blue. These results are in

agreement with the late studies on catalytic degradation of MB using biosynthesized CuONPs (29).

Antibacterial Activity

The results obtained by determining antibacterial activity using the resazurin microplate method are summarized in Table 1. The CuONPs showed antibacterial activity at a concentration of $250 \mu\text{g} / \text{mL}$ for *Bacillus*

subtilis (ATCC 6633), 500 µg / mL for *Staphylococcus aureus* (ATCC 25925), *Escherichia coli* (ATCC 25923) and *Aeromonas hydrophila* (ATCC 95080) and 500 µg / mL for *Acinetobacter baumannii* (ATCC 02026). The results determined that the CuONPs showed lower antibacterial activity against the standard drug Ampicillin. However, the increase of

CuONPs concentration also increases the antibacterial effect. It is due to the direct interaction between CuONPs and the external membrane surface of the bacteria (30). However, since high concentrations can cause toxic effects *in vivo*, these effects should be investigated in further studies.

Table 1. The MIC values (µg/mL) of CuONP against the bacteria.

Copper oxide Nanoparticle	<i>Staphylococcus aureus</i> (ATCC 25925)	<i>Escherichia coli</i> (ATCC25923)	<i>Acinetobacter baumannii</i> (ATCC 02026)	<i>Bacillus subtilis</i> (ATCC 6633)	<i>Aeromonas hydrophila</i> (ATCC 95080)
CuONP	500	500	>500	250	500
Ampicillin	31.25 µg/mL	15.62 µg/mL	125 µg/mL	0.9 µg/mL	31.25 µg/mL

CONCLUSION

In this study, CuONPs were successfully prepared using the extract of *Onosma Sericeum Willd* (*Boraginaceae*) in a simple, economical, and environmentally friendly way. The synthetic process was advantageous to other conventional methods because this process did not require any organic solvent or toxic reagents. The synthesized nanoparticles were characterized by UV-Vis spectrophotometer, FE-SEM, and XRD. The particle size distribution and zeta potential measurements of the CuONPs were determined by the DLS method. The obtained CuONPs were found to have a spherical structure and an average particle size of 70 nm. The synthesized CuONPs showed antimicrobial activity against *Staphylococcus aureus* (ATCC 25925), *Escherichia coli* (ATCC25923), *Acinetobacter baumannii* (ATCC 02026), *Bacillus subtilis* (ATCC 6633), *Aeromonas hydrophila* (ATCC 95080) at high concentration. The toxic effect of CuONPs, which increased antibacterial activity following the increase in the dose of CuONP, should be investigated in the future for *in vivo* studies. It also showed that the CuONPs performed excellently in the catalytic reduction of methylene blue. At room temperature, up to 90% MB dye degradation was achieved. In conclusion, it can be said that these nanostructures are candidate molecules for biomedical and biotechnological applications.

FUNDING

This study was funded by the Mersin University Scientific Research Project Unit with the Project No 2019-1-AP2-3412.

ACKNOWLEDGEMENTS

The authors would like to thank Assoc. Prof. Dr. Rıza Binzet of the Faculty of Arts and Sciences at Mersin University for identifying the *Onosma Sericeum Willd* species, the Mersin University Advanced Technology, Training, Research and Application Center (MEITAM) for providing access to their laboratory facilities and Dr. Mahmut Ulger of the Department of Microbiology, Faculty of Pharmacy at Mersin University for determining the antibacterial results. The non-extended version of this paper was presented as oral presentation at the "5th International Turkic World Conference on Chemical Sciences and Technologies (ITWCCST 2019)" which will take place in Sakarya, Turkey between 25-29 October 2019.

REFERENCES

1. Castro L, Blázquez ML, Muñoz JÁ, González FG and Ballester A. Mechanism and applications of metal nanoparticles prepared by Bio-Mediated process. RASE. 2014; 3:1-18.
2. Feldheim DL, and Foss CA. Metal nanoparticles synthesis, characterization and applications. Marcel Dekker Inc; 2002.
3. Avgouropoulos G, Papavasiliou J, Tabakova T, Idakiev V, Loannides T. A comparative study of ceria-supported gold and copper oxide catalysts for preferential CO oxidation reaction. Chem. Eng. J. 2006;124(1-3):41-5.
4. Tamaki J, Shimanoe K, Yamada Y, Yamamoto Y, Miura N, Yamazoe N. Dilute hydrogen sulfide sensing properties of CuO-SnO₂ thin film prepared by low-pressure evaporation method. Sens. Actuators. B. 1998;49(1-2):121-5.

5. Yu Y, Zhang J. Solution phase synthesis of rose like CuO. *Mater. Lett.* 2009;63(21):1840-3.
6. Sundaramurthy N, Parthiban C. Biosynthesis of copper oxide nanoparticles using pyrus pyrifolia leaf extract and evolve the catalytic activity. *IRJET.* 2015;2(6):332-8.
7. Michael JJ, Iniyan S. Performance analysis of a copper sheet laminated photovoltaic thermal collector using copper oxide – water nanofluid. *J. Sol. Energy.* 2015; 119:439-51.
8. Abboud Y, Saffaj T, Chagraoui A, El Bouari A, Brouzi K, Tanane O, Ihssane B. Biosynthesis, characterization and antimicrobial activity of copper oxide nanoparticles (CONPs) produced using brown alga extract (*Bifurcaria bifurcata*). *Appl. Nanosci.* 2014;4(5):571-6.
9. Gnanavel V, Palanichamy V, Roopan SM. Biosynthesis and characterization of copper oxide nanoparticles and its anticancer activity on human colon cancer cell lines (HCT-116). *J. Photoc. Photobio.B.* 2017;171:133-8.
10. Wu SH, Chen DH. Synthesis of high-concentration Cu nanoparticles in aqueous CTAB solutions. *J. Colloid. Interface. Sci.* 2004;273(1):165-9.
11. Wang H, Xu JZ, Zhu JJ, Chen HY. Preparation of CuO nanoparticles by microwave irradiation. *J. Cryst. Growth.* 2002; 244:88-94.
12. Xu CK, Liu YK, Xu GD, Wang GH. Preparation and characterization of CuO nanorods by thermal decomposition of Cu₂O₄ precursor. *Mater. Res. Bull.* 2002;38(21):2365-72.
13. Anastas P and Warner J. *Green chemistry: Theory and practice.* Oxford University Press, USA; 1998.
14. Schmidt K. Woodrow Wilson International Center for Scholars and The Pew Charitable Trusts. In American Chemical Society Meeting, Washington DC, 2006.
15. Mittal AK, Chisti Y and Banerjee UC. Synthesis of metallic nanoparticles using plant extracts. *Biotechnol. Adv.* 2013;31(2):346-56.
16. Shah M, Fawcett D, Sharma S, Tripath SK and Poinern GEJ. Green Synthesis of Metallic Nanoparticles via Biological Entities. *Materials.* 2015;8(11):7278-308.
17. Nasrollahzadeh M, Maham M, Sajadi SM. Green synthesis of CuO nanoparticles by aqueous extract of *Gundelia tournefortii* and evaluation of their catalytic activity for the synthesis of N-monosubstituted ureas and reduction of 4-nitrophenol. *J. Colloid Interface Sci.* 2015; 455:245-53.
18. Sreeju N, Rufus A, Philip D. Studies on catalytic degradation of organic pollutants and anti-bacterial property using biosynthesized CuO nanostructures. *J. Mol. Liq.* 2017; 242:690-700.
19. Mohan S, Singh Y, Verna DK, Hassan SH. Synthesis of CuO nanoparticles through green route using Citrus limon juice and its application as nanosorbent for Cr(VI) remediation: process optimization with RSM and ANN-GA based model. *Process Saf. Environ.* 2015; 96:156-66.
20. Naika HR, Lingarajua K, Manjunath K, Kumar D, Nagaraju G, Sureshd D, Nagabhushana H. Green synthesis of CuO nanoparticles using *Gloriosa superba* L. extract and their antibacterial activity. *J. Taibah. Univ. Sci.* 2015; 9:7-12.
21. Kumar V, Yadav SK. Plant-mediated synthesis of silver and gold nanoparticles and their applications. *J. Chem. Technol. Biotechnol.* 2009;84(2):151-7.
22. Akcin OE, Aktas T, Altıntas MY. Myosotis Alpestris F.W.Schmidt Boraaginaceae türünün anatomik özellikleri. *Ordu Univ. J. Sci. Tech.* 2013;3(1):61-8.
23. Nath I, Chakraborty J, Verpoort F. *Environment, energy, emerging, applications, and sustainability.* Elsevier, 2020.
24. Vidhu VK, Philip D. Catalytic degradation of organic dyes using biosynthesized silver nanoparticles. *Micron.* 2014; 56: 54-62.
25. Sultan M, Javeed A, Uroos M, Imran M, Jubeen F, Nouren S, Saleem N, Bibi I, Masood R, Ahmed W. Linear and crosslinked polyurethanes based catalysts for reduction of methylene blue. *J Hazard Mater.* 2018; 344: 210-9.
26. Gahlaut A, Chhillar AK. Evaluation of antibacterial potential of plant extracts using resazurin based microtiter dilution assay. *Int.J. Pharm.Pharm.Sci.* 2013;5(2):372-6.
27. Sivaraj R, Rahman PKSM, Rajiv P, Salam HA, Venckatesh R. Biogenic copper oxide nanoparticles synthesis using *Tabernaemontana divaricate* leaf extract and its antibacterial activity against urinary tract pathogen. *Spectrochim. Acta A.* 2014; 133:178-81.
28. Erci F, Koc RC and Isildak I. Green synthesis of silver nanoparticles using *Thymbra spicata* L. var. *Spicata* zahter aqueous leaf extract and evaluation of their morphology-dependent antibacterial and cytotoxic activity. *Artif. Cells. Nanomed. Biotechnol.* 2018;46(1):150-8.
29. Bordbar M, Sharifi-Zarchi Z, Khodadadi B. Green synthesis of copper oxide nanoparticles/clinoptilolite using *Rheum palmatum* L. root extract: high catalytic activity for reduction of 4-

Dođan alhan S. Gündođan M. JOTCSA. 2020; 7(2): 561-570.

RESEARCH ARTICLE

nitro phenol, rhodamine B, and methylene blue. J Sol-Gel Sci Technol. 2017; 81:724-33.

30. Das D, Nath BC, Phukon P, Dolui SK. Synthesis and evaluation of antioxidant and antibacterial behavior of CuO nanoparticles. Colloid Surface B. 2013; 101:430- 3.



Development of Gelatin-Alginate-TiO₂-SOD Biosensor for the Detection of Superoxide Radicals

Utku KARAKAYA  , Burak DERKUS*  , Emel EMREGUL  

Ankara University, Faculty of Science, Chemistry Department, 06100, Ankara, Turkey.

Abstract: In this work, a biosensor that uses gelatin and alginate hydrogels in addition to titanium dioxide (TiO₂) nanoparticles (NPs) as a sensor matrix was developed to detect superoxide radicals (O₂^{•-}), which play a role in carcinogenesis when present in excess levels. Parameters affecting the performance of the biosensor such as the amount of gelatin-alginate ratio, amount of TiO₂ NPs, the concentration of SOD enzymes, and glutaraldehyde (GA) cross-linker were investigated. Chronoamperometry was used as an electrochemical technique for the development of biosensor as well as characterization steps. The developed biosensor exhibited two linear ranges between 0.0009 mM – 0.125 mM and 0.25 mM – 2 mM, which was utilized as calibration curves. The detection limit of the biosensor was found 0.9 μM, which was at the appropriate level for the detection of O₂^{•-} in tumor samples. Finally, the constructed biosensor showed significant analytical performance, such as low detection limit, reusability, and reproducibility.

Keywords: Hydrogel, nanoparticle, biosensor, superoxide dismutase, cancer.

Submitted: November 13, 2019. **Accepted:** May 26, 2020.

Cite this: KARAKAYA U, DERKUS B, EMREGUL E. Development of Gelatin-Alginate-TiO₂-SOD Biosensor for the Detection of Superoxide Radicals. JOTCSA. 2020;7(2):571–80.

DOI: <https://doi.org/10.18596/jotcsa.646433>.

***Corresponding author.** E-mail: burakderkus@gmail.com, Tel: +90 (506) 906 9786.

INTRODUCTION

Reactive oxygen species (ROS) are a class of highly reactive reduced oxygen molecules and include various structures such as superoxide anions, hydroxyl radicals, and hydrogen peroxide (H₂O₂). Superoxide radicals, the primary species of ROPs, are present in low concentrations under normal physiological conditions, and they are converted to H₂O₂ and oxygen (O₂) as a result of dismutation with superoxide dismutase (SOD) enzymes (1).

Superoxide anions are often considered to be toxic since they are converted to other radicals in biological systems such as alkoxyl radicals (RO[•]), hydroxyl radicals (HO[•]), and peroxyxynitrite radicals (ONOO⁻). Increased superoxide anions result in mutagenesis and consequently, cell death (2-4). Besides, the concentration of superoxide may increase significantly in traumatic brain injuries (5,6). Superoxide radicals can also emerge as a consequence of gradual neurodegenerative

damages such as aging (7), cancer (8), and Parkinson's (9). Taken all together, developing sensitive platforms and tools towards detecting superoxide anions is essential.

So far, different sensing strategies have been followed for constructing biosensor systems aiming for the detection of superoxide anions. Fluorescence (10) and electrochemical (11) techniques are the most widely preferred ones. The biosensors developed by the modification of electrodes with hydrogels, without utilizing NPs, resulted in an insufficient detection limit (12, 13), while other designs containing nano-structures require multi-component recognition material (14, 15) or complex fabrication processes (16), which reduces the feasibility of the developed system. Moreover, a big part of the superoxide biosensors focusses on biosensor design but validating the system with biological samples such as blood or tissue (12, 14). Therefore, we need simple, low-cost, and sensitive biosensing tools for the determination of the level of superoxide anions in

biological samples, which might give information about the development of cancer.

Though enzymes catalyze biochemical reactions with unique celerity, they lack electrical conductivity due to their protein-nature, and therefore coupling enzymes with metal NPs might be an excellent strategy to enhance electron transfer to the electrode. By now, several types of NPs - such as Ag (17), Au (18), ZnO (19), and TiO₂ (20) NPs - have been used to develop biosensors. TiO₂ NPs have attracted a critical interest in their advantages, having a large surface area, high uniformity, and biocompatibility such that TiO₂ NPs have been used as a component of the sunscreen-technology as well as they are well accepted in the food industry. Researchers demonstrated a direct electron transfer between biomolecules and electrodes modified with TiO₂ NPs (21, 22). The improved catalytic activity of the developed biosensors has been attributed to their smaller sizes, enabling a larger surface area for biomolecule immobilization and a faster electron transfer from biomolecule to an electrode surface. All these superior properties make TiO₂ NPs a suitable material for electrode design.

In this work, we focused on creating SOD-based biosensor for fast, specific, easy, and sensitive detection of superoxide anions. To this end, we combined gelatin and alginate biopolymers as a carrier system and utilized from TiO₂ NPs to construct a nanocomposite material that brings various advantages such as high surface area, which enabled us to increase SOD immobilization efficiency, and semi-conductivity. SOD enzymes were bonded onto this nanocomposite material, which was coated onto platinum (Pt) electrode, via crosslinking with glutaraldehyde (GA) reagent. The developed gelatin-alginate-TiO₂-SOD biosensor was then tested for detecting superoxide radicals in cancer tissues.

EXPERIMENTAL SECTION

Preparation of gelatin-alginate-TiO₂-SOD biosensors

Gelatin-alginate-TiO₂-SOD electrodes were prepared following the previously published protocols (12, 23) -with small modifications-. After the gelatin was dissolved at 50 °C, different amounts of alginate and titanium dioxide (obtained from Sigma-Aldrich, with diameter <25 nm, in anatase form) were added and homogenized by vortexing. SOD enzymes dissolved in phosphate buffer were added to different units and re-vortexed for homogenization. Finally, the cross-linker glutaraldehyde was added to obtain stiff immobilization gel. The gels (25 µL) were modified on each surface of the Pt working electrode - square plate having 1 cm² surface area- with a total of 50 µL of gel, and were allowed to dry for 6 hours. Un-bonded enzymes were washed away with PBS for 3 times. Each step of electrode modification included coating the electrode with

gelatin-alginate, gelatin-alginate-SOD, gelatin-alginate-TiO₂, and gelatin-alginate-TiO₂-SOD were characterized with electrochemical impedance spectroscopy (EIS) technique. Pt square plate electrode with 1 cm² surface area was used as a counter electrode, and Ag/AgCl with saturated KCl was used as a reference electrode, which was introduced into the cell via a Luggin capillary. All electrochemical measurements were performed with Gamry Potentiostat-Galvanostat with Framework Version 5.50.

Optimization of gelatin-alginate-TiO₂-SOD biosensors

Firstly, different gelatin-alginate ratios (0.25, 0.5, 1, 2) were tried to optimize the immobilization conditions. TiO₂, SOD enzyme, and glutaraldehyde concentrations were kept constant in the immobilization gel. To optimize the cross-linking process, different electrodes were prepared by using different glutaraldehyde concentrations (0,001, 0,002, 0,004, 0,01, and 0,016 M). Also, to obtain an efficient electrochemical performance from the developed biosensors, amperometric responses were recorded for electrodes prepared with varying enzyme concentrations that change between 25 and 5000 U, which provided an optimal enzyme concentration. For TiO₂ NPs optimization, different amount of TiO₂ NPs (0.0001 - 0.0005 g) were tested by keeping the gelatin-alginate ratio (1 w/w), SOD concentration (100 U), and glutaraldehyde cross-linker concentration (0.004 M) constant. Finally, the level of xanthine, triggering the dismutation reaction, was optimized (0.0009-2 mM).

Reproducibility and reusability of biosensor

Amperometric measurements were recorded for 6 replica electrodes to examine the reproducibility of the gelatin-alginate-TiO₂-SOD biosensor, and consistency of the amperometric responses was examined. On the other hand, for reusability study of the developed biosensor, amperometric measurements were obtained every day, up to 10 days, against xanthine (2 mM) at +0.65 V. After each use, the electrodes were washed with phosphate buffer (0.05 mM, pH 7.4) and stored in the buffer at +4 °C until further use. Reproducibility and reusability of the biosensor were determined by interpreting the amperometric responses.

Obtaining the calibration graphs

A series of gelatin-alginate-TiO₂-SOD biosensors were prepared, and amperometric measurements were recorded for varying xanthine concentrations at +0.65 V. The obtained current densities were plotted against xanthine concentration to obtain calibration curves and equations. The sensing limit and linear ranges were determined from the obtained graphs. During the calibration study, the electrodes were stored in the phosphate buffer (pH 7.4) at +4 °C until use.

Clinical application of gelatin-alginate-TiO₂-SOD biosensor

Cancerous meningioma (grade I) tissue was obtained from Ankara University, Department of Neurosurgery. Biosensor response was tested on healthy and cancerous brain tissues to demonstrate the usability of the developed

biosensor in biological applications. After stabilizing the gelatin-alginate-TiO₂-SOD biosensors in the electrochemical cell containing phosphate buffer (0.05 M, pH 7.4), homogenized solutions containing healthy or cancerous tissue were added, and the changes in amperometric signal were determined.

RESULTS and DISCUSSION

Characterization of gelatin-alginate-TiO₂-SOD electrodes

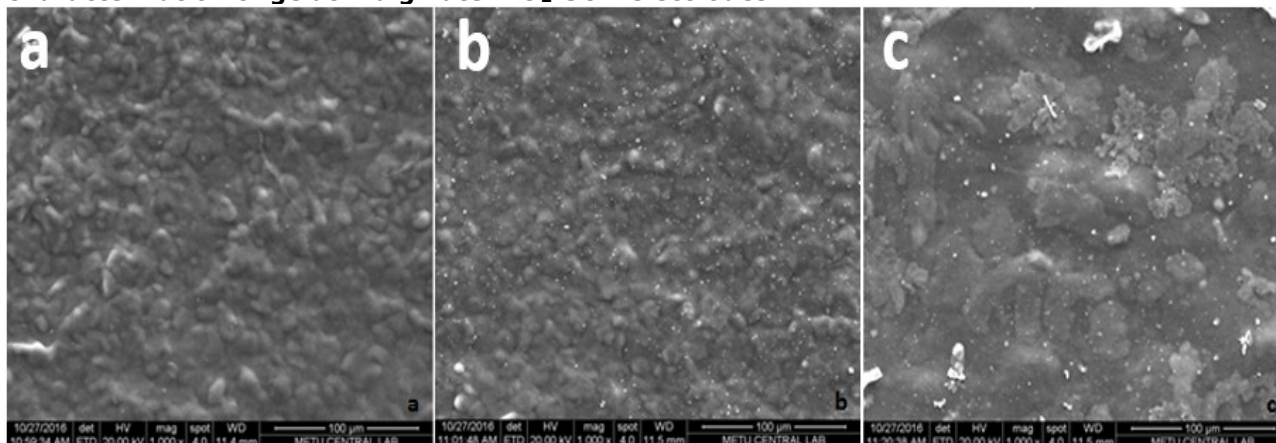


Figure 1. SEM images of gelatin-alginate (a), gelatin-alginate-TiO₂ (b), and gelatin-alginate-TiO₂-SOD (c) electrodes. Scale bars 100 μ m.

The design of surface topography is one of the critical parameters for building a successful biosensor. SEM images were obtained in comparison with gelatin-alginate and gelatin-alginate-TiO₂ modified electrodes to examine the surface properties of the developed gelatin-alginate-TiO₂ electrode. It was seen in the micrograph that the gelatin-alginate biopolymer mixture covered the electrode surface properly (Figure 1a) and evaluated as a proper matrix in this regard. When TiO₂ NPs were included in the biopolymer mixture, microstructures were turned in to lower-scale microstructures (Figure 1b) due to surface enhancing property of nanoparticles, and resulted in a suitable nanocomposite material for biosensor design. Some nanoparticle aggregates were visible on this micrograph. When SOD enzymes included via cross-linking to the system, besides some little salt crystals, SOD enzymes characterized by leaf-shaped appearance seemed efficiently immobilized onto the surface (Figure 1c). Hence, it can be concluded that the gelatin-alginate-TiO₂-SOD electrode was successfully prepared, and in terms of surface properties, it seems suitable for biosensing applications.

Electrode modifications were also characterized by an electrochemical technique, namely electroimpedance spectroscopy (EIS). The Nyquist plots of the bare electrode, gelatin-alginate electrode, gelatin-alginate-SOD electrode, gelatin-alginate-TiO₂ electrode, and gelatin-alginate-TiO₂-SOD electrode were obtained for a Randles circuit model (Figure 2). Each EIS spectrum consists of a

semicircle and a linear portion, which correspond to a charge transfer and diffusion process, respectively. The diameter of the semicircle is related to the charge-transfer resistance (R_{ct}) at the interface of the electrode surface and solution and can be used to evaluate the processes taking place on the electrode surface. Thus, in our strategy, change in R_{ct} values helps us to understand the success of modification steps. Unless conducting or nano-materials used, R_{ct} increases after electrode modifications due to the decreased electron transfer. While the charge transfer resistance of the bare electrode was nearly 25 Ω (Figure 2a), this value increased to 56 Ω when the Pt electrode was modified with gelatin-alginate composite, which shows the success of the modification (Figure 2b). SOD immobilization into gelatin-alginate composite hydrogel was further improved the R_{ct} from 56 Ω to 68 Ω (Figure 2c), indicating an efficient immobilization of SOD enzymes into the gelatin-alginate composite structure. Incorporation of TiO₂ NPs decreased R_{ct} of gelatin-alginate, 56 Ω , to 48 Ω (Figure 2d) as a result of both enhanced surface area owing to nano-size of the particles and their semi-conductive property. When SOD enzymes were immobilized into gelatin-alginate-TiO₂ nanocomposite structure, R_{ct} was increased from 48 Ω to 66 Ω (Figure 2e), which showed the success of the SOD immobilization. This increase in R_{ct} after SOD immobilization into gelatin-alginate-TiO₂ (about 18 Ω) was higher than that of SOD immobilization into gelatin-alginate (about 12 Ω), indicating a more efficient SOD immobilization in gelatin-alginate-TiO₂.

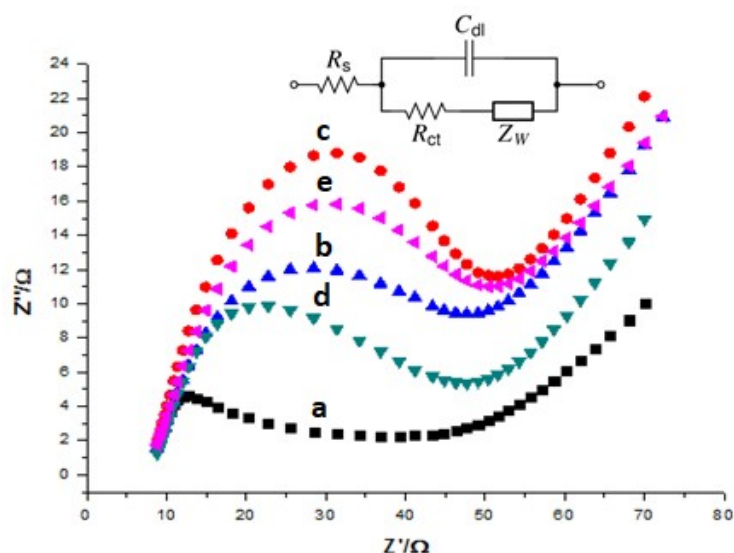


Figure 2. Nyquist Plot showing the change in charge transfer resistance after each modification step: (a) Bare electrode, (b) gelatin-alginate coated electrode, (c) gelatin-alginate-SOD coated electrode, (d) gelatin-alginate-TiO₂ modified electrode, and (e) gelatin-alginate-TiO₂-SOD electrode

Lastly, we obtained the Fourier-Transform Infrared (FTIR) spectra of gelatin-alginate-SOD and gelatin-alginate-TiO₂-SOD for further evaluate the effect of TiO₂ NPs on enzyme immobilization. Both spectra indicated the characteristic peaks of alginate and gelatin biopolymers (Figure 3). The peak near 1028 cm⁻¹ was of C-O stretching vibration of pyranose rings constituting the alginate, while the peaks at 1530 and 1637 cm⁻¹ related to amide I and II born of gelatin (24). Both spectra exhibited the peaks related to alginate and gelatin, which showed the success of composite preparation. Due to the chemically inert nature of TiO₂ NPs, no

specific peak related to TiO₂ NPs was observed. When the spectra of gelatin-alginate-SOD and gelatin-alginate-TiO₂-SOD compared, a slight increase in amide I and II bands in the spectrum of gelatin-alginate-TiO₂-SOD can be seen clearly. This slight increase in amide I and II bands in gelatin-alginate-TiO₂-SOD can be attributed to a higher enzyme immobilization via amide bond formation between gelatin (NH₂-) and enzyme -via glutaraldehyde crosslinker -. This finding consolidated our previous findings and led us to conclude that including the TiO₂ NPs into the system improved enzyme immobilization.

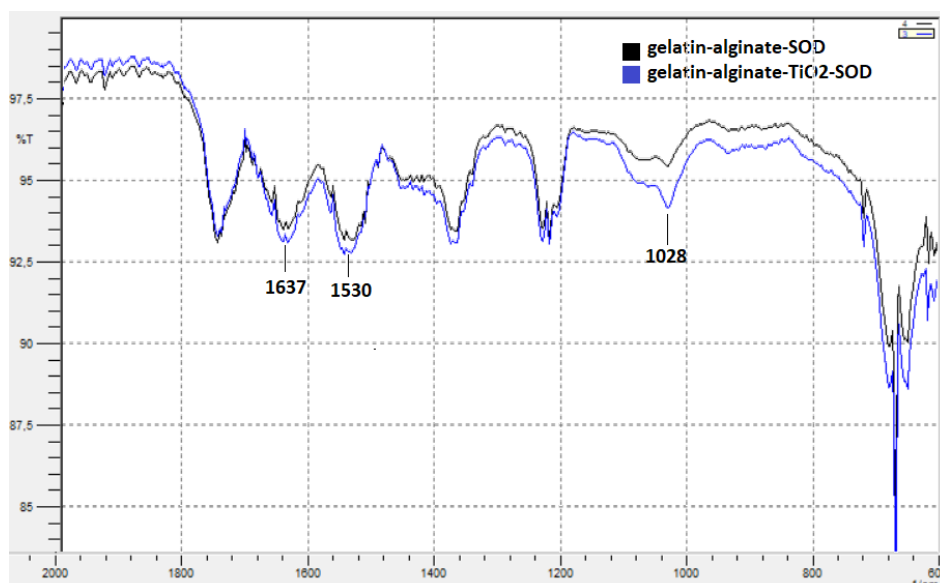


Figure 3. FTIR Spectra of gelatin-alginate-SOD (black) and gelatin-alginate-TiO₂-SOD (blue)

Optimization of gelatin-alginate-TiO₂-SOD biosensor

There are many parameters, namely biopolymer, crosslinker, nanostructure, and bio-recognizing element concentrations which affect biosensor performance, and need to be optimized before

further experiments. To this end, we tested different ratios of gelation: alginate biopolymers (0.25-2 w/w) as well as different concentrations of GA cross-linker (0.001-0.016 M), SOD enzyme (25-5000 U), and TiO₂ NPs (0.0001-0.0005 g).

For the optimization of gelatin: alginate ratio, we prepared different electrodes with varying concentrations of gelatin: alginate ratio (0.25-2 w/w) by keeping the GA (0.01 M), SOD (100 U), and TiO₂ (0.0003 g) constant. The optimal gelatin: alginate ratio was found to be 1 (w/w) at which the most efficient amperometric response was recorded (Figure 4a). At higher ratios, as a result of the change in the pore structure/size and thus the reduced electron transfer, a decrease in sensitivity was observed. On the other hand, at the lower ratios (0.25-0.5 w/w), similar reduced amperometric responses were observed unlikely due to mechanical instability. For an efficient enzyme immobilization, different GA cross-linker concentrations (0.001-0.016 M) were tested by keeping the gelatin: alginate ratio (1 w/w), SOD (100 U), and TiO₂ (0.0003 g) constant. 0.004 M GA was found to be the optimal concentration (Figure 4b). The increase in GA concentrations led to more efficient enzyme immobilization, thus a more intense amperometric current as a result of larger electrochemical reactions. However, when we further increased the GA concentration, a decrease in amperometric response was observed mainly due to enzyme inactivation and reduced electron diffusion through electrode surface due to smaller pore size (Figure 4b) (23). The concentration of bio-recognizing elements, SOD enzymes, in this

case, is another critical parameter for the electrochemical performance of enzymatic biosensors. Amongst different SOD concentrations (25-5000 U), the optimal value was determined as 100 U (Figure 4c) by keeping the gelatin: alginate ratio (1 w/w), GA (0.004 M), and TiO₂ (0.0003 g) constant. In lower SOD concentrations, lower current density was observed as a consequence of inadequate enzyme concentrations. In contrast, when we increased the SOD concentration over the optimal value, at this time, decreased current density was obtained due to enzyme-enzyme cross-linking in addition to over-saturation of pores with an excessive amount of enzymes that result in not-efficient diffusion of products and electrons through electrode surface (23). Finally, we optimized the amount of TiO₂ NPs, which were used to increase SOD immobilization and electron transfer rate by increasing the surface area. By keeping the gelatin: alginate ratio (1 w/w), GA cross-linker (0.004 M), and SOD (100 U) concentrations constant, we tested different amounts of TiO₂ NPs (0.0001 - 0.0005 g) and found the optimal value to be 0.0004 g (Figure 4d). Low amounts of nanoparticles were not able to increase the surface area as much as necessary, while too high amounts of nanoparticles completely covered the polymer surface, increased resistance, and inhibited electron transfer.

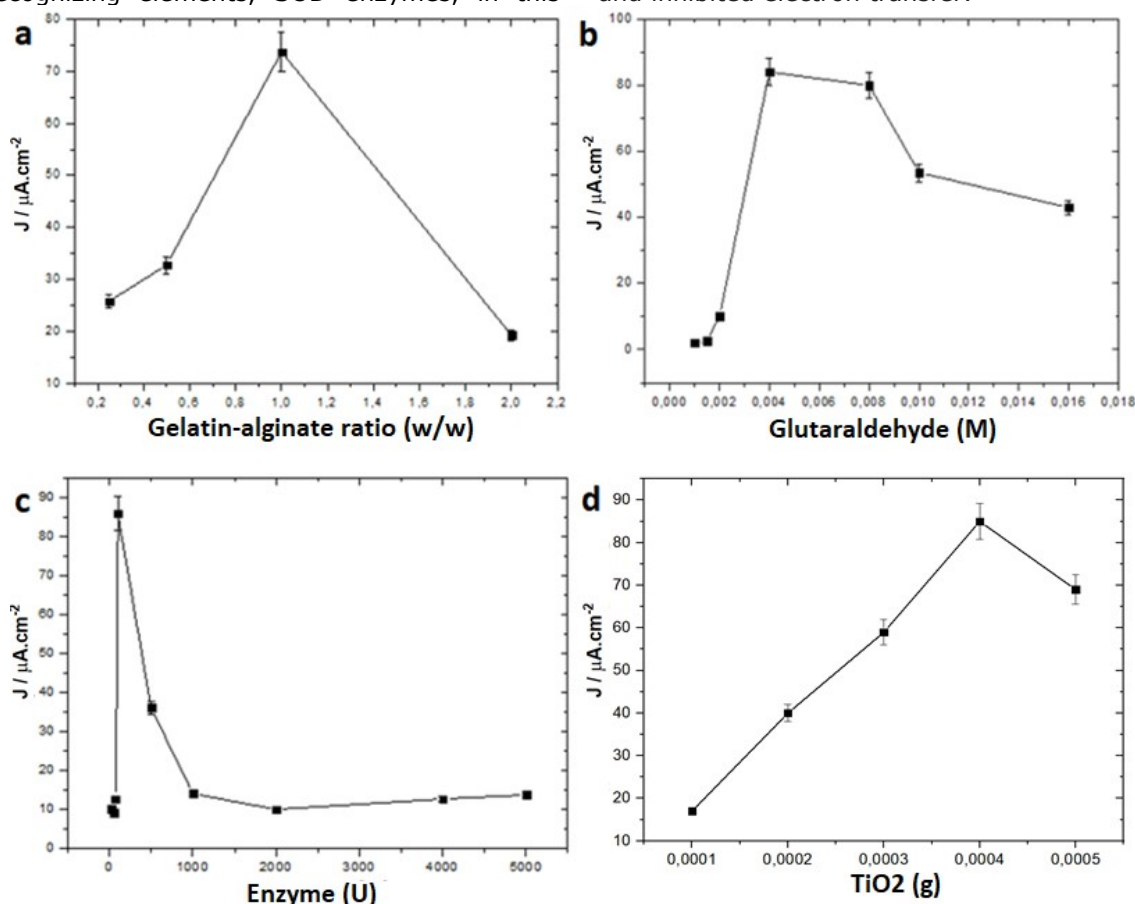


Figure 4. Effect of gelatin: alginate ratio (a), GA concentration (b), SOD concentration (c), and amount of TiO₂ (d) on the amperometric response of biosensor.

Reproducibility and reusability of the developed biosensor

Reproducibility and reusability are two parameters that are important in the practical use and commercialization of biosensors. To investigate the reproducibility and reusability potentials of the developed biosensor, we prepared 6 and 3 replicas, respectively, of a gelatin-alginate-TiO₂-SOD biosensor. For reproducibility study, after the 6 replica electrodes were stored at 4 °C for 1 day, amperometric measurements were performed by adding 2 mM xanthine into the electrochemical cell. Each measurement was performed triplicate. For the reusability study, amperometric measurements were recorded in the presence of 2 mM xanthine up to 10 days. After each use, electrodes were washed with phosphate buffer (pH 7.4) and stored in the refrigerator at 4 °C.

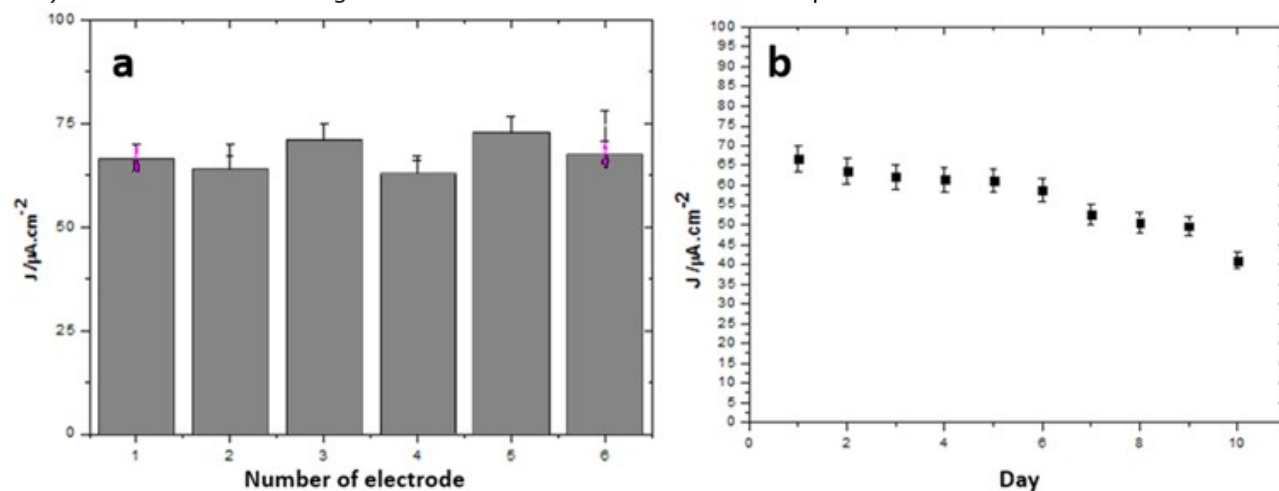


Figure 5. Reproducibility (a) and reusability (b) of gelatin-alginate-TiO₂-SOD electrodes.

Calibration study for gelatin-alginate-TiO₂-SOD electrode

Calibration study that defines the lower/higher measurement limits of a biosensor is another key step in biosensor design. To obtain calibration graph for gelatin-alginate-TiO₂-SOD electrode, we tested a broad range of xanthine concentration varying between 0.0009-2 mM. The amperometric current densities obtained within this range

The mean value and standard deviation for amperometric measurements with 6 replica electrodes in the context of reproducibility study were found to be 67.5 $\mu\text{A}\cdot\text{cm}^{-2}$ and 5.8%, respectively (Figure 5a). This finding showed that gelatin-alginate-TiO₂-SOD electrodes are reproducible with trust. On the other hand, the amperometric response of the gelatin-alginate-TiO₂-SOD electrodes decreased to % 61.6 of its initial performance (Figure 5b). This finding suggests that the developed biosensor has short-term reusability, up to 7 times, after which the response goes beyond 70%. One reason why the reusability of the gelatin-alginate-TiO₂-SOD electrode was not found better might be the distortive effect of NPs, which lead to detachment of nanocomposite film from the surface.

showed two linear graphs for 0.0250-2 mM (Figure 6a) and 0.0009-0.0125 mM (Figure 6b). Linear regression equations were expressed for gelatin-alginate-TiO₂-SOD electrode as $[J, \text{mM}] = (-2.5) + (32.8) \times [\text{Xanthine, mM}]$ for high xanthine concentrations (Figure 6a) and $[J, \text{mM}] = (0.13) + (22.8) \times [\text{Xanthine, mM}]$ for low xanthine concentrations (Figure 6b).

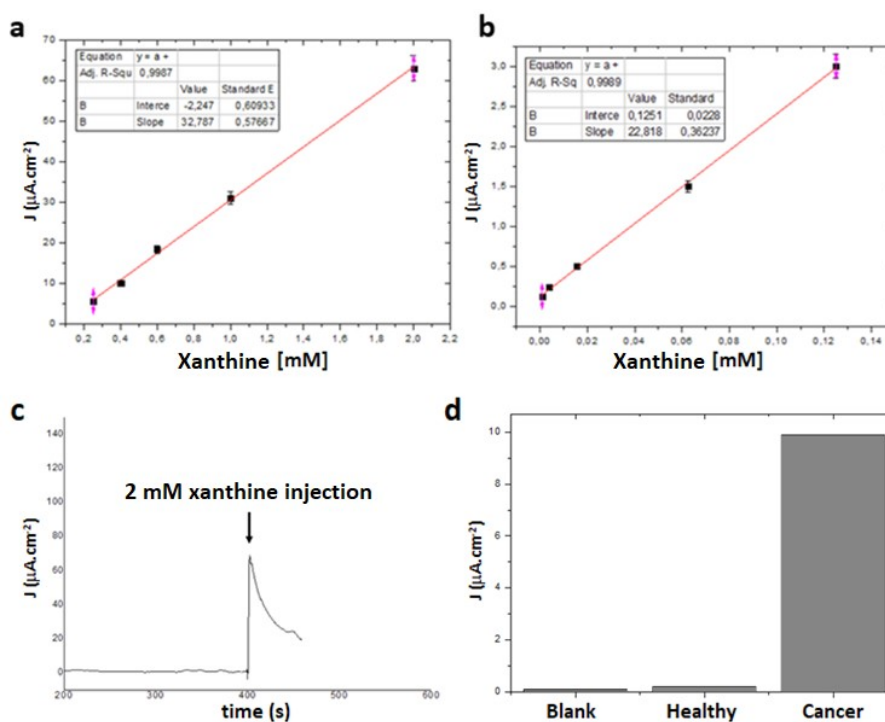


Figure 6. Calibration graphs of gelatin-alginate-TiO₂-SOD biosensor for high-range (a) and low-range (b) xanthine concentrations. (c) The amperometric response of gelatin-alginate-TiO₂-SOD biosensor after 2 mM xanthine injection. (d) Clinical application of gelatin-alginate-TiO₂-SOD biosensor.

The response of the electrode was proportional to the concentration of O₂^{•-} and the coefficient of determination (R²) was found 0.9987 and 0.9989 for high concentration range and low concentration range, respectively. The detection limit for the low linear range was determined as 0.9 µM. The amperometric response of gelatin-alginate-TiO₂-SOD biosensor after injection of 2mM xanthin was demonstrated in Figure 6c.

Clinical application of gelatin-alginate-TiO₂-SOD biosensor

The ultimate goal of biosensor studies is to apply the developed systems in human clinics to contribute to human health by providing easy-to-use, practical, and low-cost diagnostic tools. To examine the potential of the developed biosensor to be applied in clinics, we tested the electrodes in healthy and cancer tissues to detect superoxide radicals. The gelatin-alginate-TiO₂-SOD biosensor exhibited nearly 10-times higher amperometric response to cancer tissue homogenate compared to healthy tissue (Figure 6d). This result confirmed

our anticipation of the higher level of ROS in cancer cells and tissues compared to healthy ones (25, 26). Also, various groups utilized SOD-based biosensors for detecting superoxide radicals in cancer cells (27) and tissues (13, 28), and reported higher levels of superoxide radicals in the cancer samples. For instance, Campanella et al. (2000) has reported an approximately 15 times more intense amperometric response for cancerous renal tissue compared to healthy tissue (13). These reports support and consolidate our findings.

Various published works have lower or higher LOD and linear range compared to our design (Table 1). Our design exhibited a detection limit suitable to be used in superoxide detection; besides, it showed good performance when applied in real samples (cancer tissue). Consequently, the findings we obtained enabled us to conclude that the developed biosensor can be applied in cancer clinics after a comprehensive work, including repetitive biological trials.

Table 1. Comparison of gelatin-alginate-TiO₂-SOD sensors sensing with electrochemical (amperometry) with literature.

Electrode	LOD	Linear Range	Application	Reference
Gelatin-SOD	10.0 μ M	0.02-2 mM	Cancer tissue	12
GC-PEDOT-CNT-SOD	1.0 μ M	20-3000 μ M	Wine/Juice	15
PtPd-PDA-RGO-SOD	2.0 μ M	0.016-0.24 mM	-	29
GC-MPA-MnSOD	91.1 μ M	135.2-1160 μ M	-	30
Au-Fc-PEG-SOD	0.001 μ M	5-100 μ M	Cancer cells	16
Gelatin-Alginate-TiO ₂ -SOD	0.9 μ M	0.0009-2 mM	Cancer tissue	This work

GC: Glassy Carbon, PEDOT: Poly(3,4-ethylenedioxythiophene), CNT: Carbon Nanotube, PDA: Polydopamine, RGO: Reduced Graphene Oxide, MPA: 3-mercaptopropionic acid, PEG: Polyethylene glycol, Fc: Ferrocene.

CONCLUSION

Superoxide radicals take place in many biological processes such as cancer, and their detection might be crucial in particularly cancer cases. In this work, it was aimed to develop a sensitive biosensor which uses gelatin-alginate-TiO₂ nanocomposite as an electrode material, and SOD enzyme as a biorecognizing element. After optimization and calibration studies, the developed sensor found suitable for detecting O₂^{•-} in clinical samples. The developed biosensor might be a promising candidate to be applied in cancer clinics.









REFERENCES

- McCord JM and Fridovich I. Superoxide dismutase. An enzymic function for erythrocyte (hemocuprein). *Journal of Biological Chemistry*. 1969 Nov; 244: 6049-55.
- Halliwell B and Gutteridge JMC. Oxygen toxicity, oxygen radicals, transition metals and disease. *Biochemical Journal*. 1984 Apr; 219: 1-14.
- Kehrer JP. The Haber-Weiss reaction and mechanisms of toxicity. *Toxicology*. 2000 Aug; 149(1): 43-50.
- Auchere F and Rusnak F. What is the ultimate fate of superoxide anion in vivo? *Journal of Biological Inorganic Chemistry* 2002 Jun; 7: 664-7.
- Wrona MZ and Dryhurst G. Oxidation of serotonin by superoxide radical: implications to neurodegenerative brain disorders. *Chemical Research in Toxicology*. 1998 Jun; 11(6): 639-50.
- Vanella A, Di Giacomo C, Sorrenti V, Russo A, Castorina C, Campisi A, Renis M. and Perez-Polo JR. Free radical scavenger depletion in post-ischemic reperfusion brain damage. *Neurochemical Research*. 1993 Dec; 18(12): 1337-40.
- Cadenas E and Davies KJA. Mitochondrial free radical generation, oxidative stress, and aging. *Free Radical Biology and Medicine*. 2000 Aug; 29(3-4): 222-30.
- Floyd RA. Role of oxygen free radicals in carcinogenesis and brain ischemia. *The FASEB Journal*. 1990 Jun; 4(9): 2587-97.
- Kumar H, Lim H-W, More SV, Kim B-W, Koppula S, Kim IS, and Choi D-K. The role of free radicals in the aging brain and Parkinson's disease: Convergence and parallelism. *International Journal of Molecular Sciences*. 2012 Aug; 13(8): 10478-504.
- Zhou Y, Ding J, Liang T, Abdel-Halim ES, Jiang L, Zhu J-J. FITC doped rattle-type silica colloidal particle-based ratiometric fluorescent sensor for biosensing and imaging of superoxide anion. *ACS Applied Materials and Interfaces*. 2016 Feb; 8: 6423-30.
- Yildirim O, Derkus B. Triazine-based 2D covalent organic frameworks improve the electrochemical performance of enzymatic biosensors. *Journal of Materials Science*. 2020; 55:3034-44.
- Emregul E. Development of a new biosensor for superoxide radicals. *Analytical and Bioanalytical Chemistry*. 2005 Nov; 383: 947-54.
- Campanella L, Favero G, Persi L, Tomassetti M. New biosensor for superoxide radical used to evidence molecules of biomedical and pharmaceutical interest having radical scavenging properties. *Journal of Pharmaceutical and Biomedical Analysis*. 2000; 23: 69-76.
- Rahimi P, Ghourchian H, Refiee-Pour H-A. Superoxide radical biosensor based on a nano-composite containing cytochrome c. *Analyst*. 2011 June; 136: 3803-8.
- Braik M, Barsan MM, Dridi C, Ali MB, Brett CMA. Highly sensitive amperometric enzyme biosensor for detection of superoxide based on conducting polymer/CNT modified electrodes and superoxide dismutase. *Sensors and Actuators B*. 2016 June; 236:574-82.
- Crulhas BP, Recco LC, Delella FK, Pedrosa VA. A novel superoxide anion biosensor for monitoring reactive species of oxygen released by cancer cells. *Electroanalysis*. 2017; 29:1-7.
- Derkus B, Acar Bozkurt P. Multilayer graphene oxide-silver nanoparticle nanostructure as efficient peroxidase mimic. *Hacettepe Journal of Biology and Chemistry*. 2018; 46(2): 159-67.
- Yilmaz MS, Derkus B, Emregul E. Investigation of the use of collagen-gelatin-gold nanoparticle nanocomposite system as an aptasensor matrix. *Hacettepe Journal of Biology and Chemistry*. 2019; 46(4): 523-31.

19. Derkus B, Emregul E, Emregul KC. Copper–zinc alloy nanoparticle based enzyme-free superoxide radical sensing on a screen-printed electrode. *Talanta*. 2015;134:206-14.
20. Derkus B, Emregul E, Emregul KC, Yucesan C. Alginate and alginate-titanium dioxide nanocomposite as electrode materials for anti-myelin basic protein immunosensing. *Sensors and Actuators B*. 2014; 192: 294-302.
21. Bao S-J, Li CM, Zang J-F, Cui X-Q, Qiao Y, Guo J. New nanostructured TiO₂ for direct electrochemistry and glucose sensor applications. *Advanced Functional Materials*. 2008 Feb; 18(4): 591-9.
22. Luo Y, Liu H, Rui Q, Tian Y. Detection of Extracellular H₂O₂ Released from Human Liver Cancer Cells Based on TiO₂ Nanoneedles with Enhanced Electron Transfer of Cytochrome c. *Analytical Chemistry*. 2009 March; 81(8): 3035-41.
23. Emregul E, Kocabay O, Derkus B, Yumak T, Emregul KC, Sinag A, Polat K. A novel carboxymethylcellulose–gelatin–titanium dioxide–superoxide dismutase biosensor; electrochemical properties of carboxymethylcellulose–gelatin–titanium dioxide–superoxide dismutase. *Bioelectrochemistry*. 2013 Apr; 90:8-17.
24. Wang X, Han M, Bao J, Tu W and Dai Z. A superoxide anion biosensor based on direct electron transfer of superoxide dismutase on sodium alginate sol–gel film and its application to monitoring of living cells. *Analytica Chimica Acta*. 2012; 717: 61– 6.
25. Liou G-Y, Storz P. Reactive oxygen species in cancer. *Free Radical Research*. 2010 May; 44(5): 479-96.
26. Keshavarzian A, Zapeda D, List T, Mobarhan S. High levels of reactive oxygen metabolites in colon cancer tissue: Analysis by chemiluminescence prob. *Nutrition and Cancer*. 1992 Jan; 17(3): 243-9.
27. Mavrikou S, Tsekouras V, Karageorgou M-A, Moschopoulou G, Kintzios S. Detection of superoxide alterations induced by 5-Fluorouracil on HeLa cells with a cell-based biosensor. *Biosensors*. 2019 Oct; 9(4):126-38.
28. Han M, Guo P, Wang X, Tu W, Bao J, Dai Z. Mesoporous SiO₂–(L)-lysine hybrid nanodisks: direct electron transfer of superoxide dismutase, sensitive detection of superoxide anions and its application in living cell monitoring. *RSC Advances*. 2013 Aug; 3(43): 20456-63.
29. Tang J, Zhu X, Niu X, Liu T, Zhao H, Lan M. Amperometric superoxide anion radical biosensor based on SOD/PtPd-PDARGO modified electrode. *Talanta*. 2015 Jan; 137: 18-24.
30. Ye Q, Li W, Wang Z, Zhang L, Tan X, Tian Y. Direct electrochemistry of superoxide dismutases (Mn-, Fe-, and Ni-) from human pathogen *Clostridium difficile*: Toward application to superoxide biosensor. *Journal of Electroanalytical Chemistry*. 2014 July; 729: 21-6.



Antioxidant Enzyme Activities in Ascorbic Acid and Selenium Applied Hepatocellular Carcinoma Cells

Burcu Menekşe BALKAN^{1*}  , Öğünç MERAL²  , Görkem KISMALI²  ,
Tevhide SEL²  

¹Burdur Mehmet Akif Ersoy University, Faculty of Veterinary Medicine, Department of Biochemistry, Burdur – TURKEY

²Ankara University Faculty of Veterinary Medicine, Department of Biochemistry, Ankara - TURKEY

Abstract: Ascorbic acid and selenium have potential use in the prevention of cancer. The role of antioxidant enzymes against cancer is to prevent oxidative damage. In this study, the effects of L-selenomethionine (234 µM), SeO₂ (100 µM), ascorbic acid (0,313 mM, and 31,3 mM) on antioxidant enzyme activities in HepG2 cell line were studied. GPx, CAT, and SOD activities of the treated cells were measured spectrophotometrically. There was a significant increase in the activity of GPx in HepG2 cells treated with L-selenomethionine (234 µM), SeO₂ (100 µM), and ascorbic acid (0,313 Mm and 31,3 mM). However, the activity of CAT was found significantly decreased in L-selenomethionine (234 µM), SeO₂ (100 µM), ascorbic acid (31,3 mM) treated HepG2 cells. The SOD levels of HepG2 cells treated with ascorbic acid (0,313 mM and 31,3 mM) were found higher than the control cells. The results of the present study indicated that the antioxidant enzyme activities changed depending on L-selenomethionine, SeO₂ application, and CAT activities changed depending on ascorbic acid doses.

Key words: Antioxidant enzymes, Ascorbic acid, HepG2, Selenium

Submitted: April 21, 2020. **Accepted:** May 27, 2020.

Cite this: BALKAN BM, MERAL Ö, KISMALI G, SEL T. Antioxidant Enzyme Activities in Ascorbic Acid and Selenium Applied Hepatocellular Carcinoma Cells. JOTCSA. 2020;7(2):581-8.

DOI: <https://doi.org/10.18596/jotcsa.724117>.

***Corresponding author. E-mail:** burcualpaslan@yahoo.com.

INTRODUCTION

Free radical species are formed as a result of reactions of oxygen and may play a role in tumor formation (1). On the other hand, overproduction of reactive oxygen species (ROS) can also induce the apoptotic pathway in the tumor cells, and this approach has effectively been used as a critical point for anticancer treatment (2). Depending on tumor type and degree, cancer cells exhibit different redox statuses. Because of these differences, the cell may be affected differently by the oxidants (3). Since oxidative stress may involve the etiology of cancer, agents that can prevent oxidative stress such as exogenous antioxidants

have been extensively investigated to prove if they inhibit/reduce oxidative damage and prevent/slow cancer development (4). In addition to their protective effect on cancer, antioxidants like selenium (Se) and ascorbic acid (AA), exhibit pro-oxidant activity in cancer cells (5, 6). Se mediates ROS production in cancer cells, thus induces cytotoxicity (7, 8).

AA, a potent antioxidant, may act as a pro-oxidant when it reacts with metal ions in DNA. High doses of AA may prevent cancer, and it has been shown in limited studies that high dose ascorbate has promising results in the treatment of cancer (9). Because AA contributes to the production of superoxide and

may produce ascorbyl radicals, it is considered as an essential pro-oxidant of free radical reactions (6).

Selenium, which is an essential element for many biological functions, has been shown to have a protective effect against cancer (10, 11). Selenium has various biological activities (12, 13) and can be found as organically bound selenium forms (e.g., selenomethionine, selenocysteine) or inorganic forms (e.g., selenate, selenite) (14). Selenoproteins that contain organically bound selenium are found in living organisms, including humans, and some of their roles are well identified (15, 16, 17).

In the current study, it is aimed to investigate the effect of two different concentrations of AA and two different forms of selenium on antioxidant enzyme activities in the HepG2 cell line.

MATERIALS AND METHODS

Cell Culture

HepG2 cell line was used in this study (ATCC Cat No. HB- 8065). Cells were placed into 75-cm² tissue culture flasks and grown in RPMI 1640 Medium containing 10% Fetal Bovine Serum (FBS), 50 mg/l Gentamicin sulfate and 300 mg/l L-glutamine in a cell culture incubator at 37 °C in the presence of 5% CO₂.

For the determination of the effect of compounds in question on antioxidant enzyme activities, 0.313 mM and 31.3 mM AA (Merck, Cat No: 100468), 234 µM L-selenomethionine (Merck, Cat No: 561505), 100 µM SeO₂ (Sigma, Cat no: S-9379) concentrations, which were observed to significantly change the cell viability in previous studies (18, 19), were applied to HepG2 cells. Only RPMI 1640 Medium (containing 10% FBS, 50 mg/l Gentamicin sulfate and 300 mg/l L-glutamine) was applied to the control group.

Determination of Antioxidant Enzyme Activities

After treatments with AA, SeO₂ and L-selenomethionine for 24 h, cells were detached using a sterilized scrapper, lysed in ice-cold lysis buffer (0.1 M Tris/HCl, pH 7.4, containing 0.5% Triton X-100, 5 mM β-Mercaptoethanol, 0.1 mg/ml serine proteases inhibitor Phenylmethylsulfonyl fluoride) and centrifuged at 14.000 × g for 5 minutes at +4 °C. The supernatant was collected and kept at -80°C for CAT, SOD, and GPx analysis.

Superoxide dismutase (SOD) activities were determined using the SOD determination kit (Sigma-Aldrich, USA) according to the manufacturer's instructions. GPx activities were measured by spectrophotometric analysis at 340 nm according to the procedure described by Paglia and Valentine 1967 (20). CAT activity was also measured spectrophotometrically by the method stated by Aebi 1983 (21). This method is based on the measurement of the rate of decrease in the absorbance at 240 nm as the catalase enzyme breaks hydrogen peroxide down into water and oxygen. The rate decrease in absorbance is proportional to catalase enzyme activity. The specific activity of catalase is defined as k/g protein. k value was calculated from the equation $k=0.1175/t$ (t= Time in seconds, which is required for reduction of absorbance from 0.45 to 0.40).

Protein concentration in the cell lysate was determined by Bradford assay (22). All enzyme activity values were divided by protein concentration for specific activity determination. All experiments were repeated in triplicate for each group. Mean values were shown in Table 1.

Statistical Analysis

Statistical analysis between treated and control groups was performed with variance analysis (ANOVA), and differences between the groups were determined with the Duncan post hoc test. P values <0.05 were considered statistically significant.

RESULTS

GPx and SOD Enzyme Activities in HepG2 cells

GPx activities were significantly increased in HepG2 cells treated with 0.313 and 31.3 mM AA, 234 µM L-selenomethionine, and 100 µM SeO₂ compared to the control group (Figure 1). SOD activities were significantly increased in HepG2 cells at 0.313 and 31.3 mM of AA and 234 µM L-selenomethionine concentration compared to the control group (Figure 2). These results may indicate that increasing SOD activity 0.313 and 31.3 mM of AA and 234 µM L-selenomethionine have antioxidant effects in this concentration. Also, GPx levels are higher in L-selenomethionine-treated concentration than SeO₂. Hence, we may conclude that L-selenomethionine is less toxic or has more potent antioxidant properties than SeO₂, which is the inorganic form of selenium. The SOD activities of HepG2 cells treated with different doses of L-selenomethionine, SeO₂ and AA in comparison to the control group are presented in Figure 2.

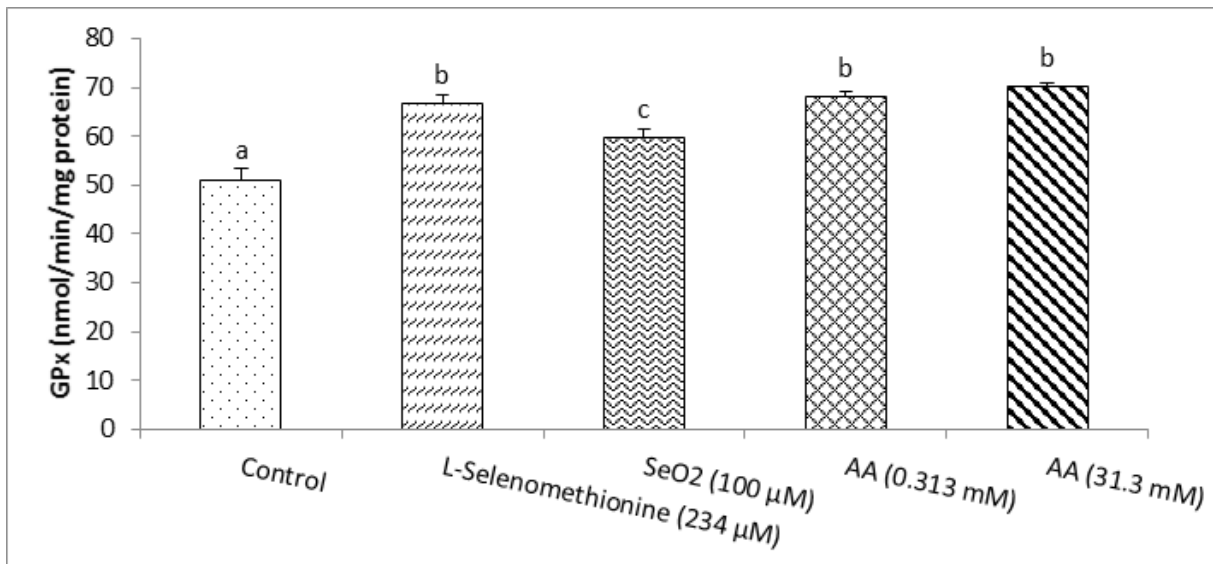


Figure 1. The GPx activities in HepG2 cells treated with 234 µM L-selenomethionine, 100 µM SeO₂, 0.313 mM, and 31.3 mM AA (Different letters indicate the differences between the groups).

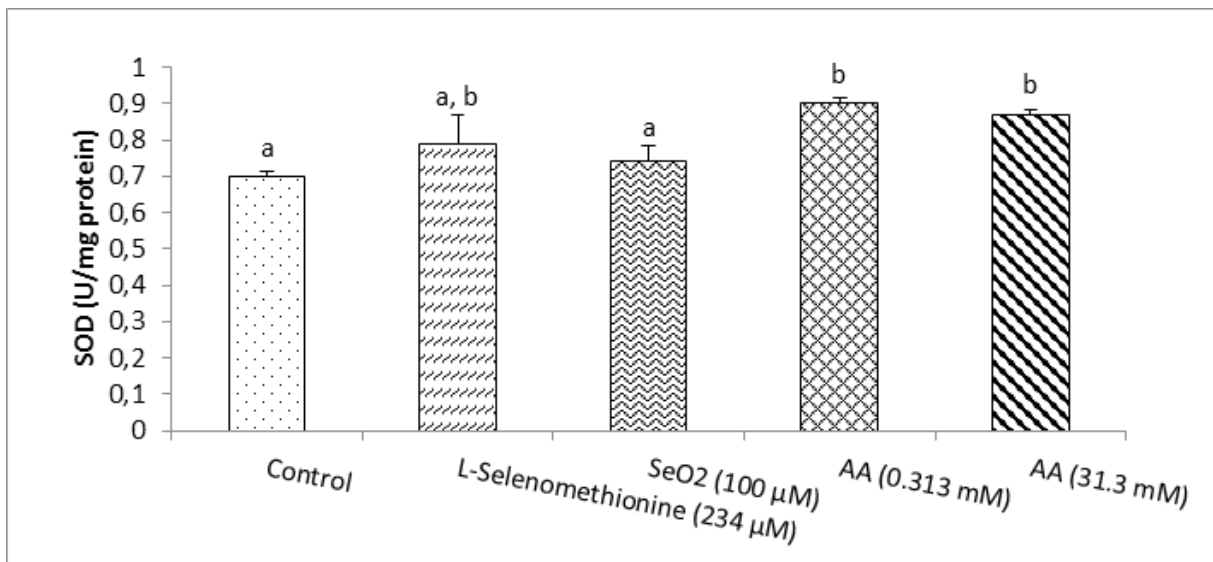


Figure 2. The SOD activities in HepG2 cells treated with 234 µM L-selenomethionine, 100 µM SeO₂, 0.313 mM, and 31.3 mM AA (Different letters indicate the differences between the groups).

CAT Enzyme Activities in treated HepG2 cells

CAT activities were significantly increased in HepG2 cells only at 0.313 mM AA concentration. CAT activities were significantly decreased in 31.3 mM AA, L-selenomethionine, and SeO₂ applied HepG2 cells compared to the control group (Figure 1). These results may indicate that depending on its dose, AA may have either antioxidant or pro-oxidant effects on HepG2 cells. Decreased activity of catalase

represents the conversion of hydrogen peroxide to more toxic hydroxyl radicals. The CAT activities of HepG2 cells which were treated with different doses of L-selenomethionine, SeO₂ and AA in comparison to the control group are presented in Figure 3.

0.313 mM and 31.3 mM AA (Different letters indicate the differences between the groups). The results of the study are summarized in Table 1.

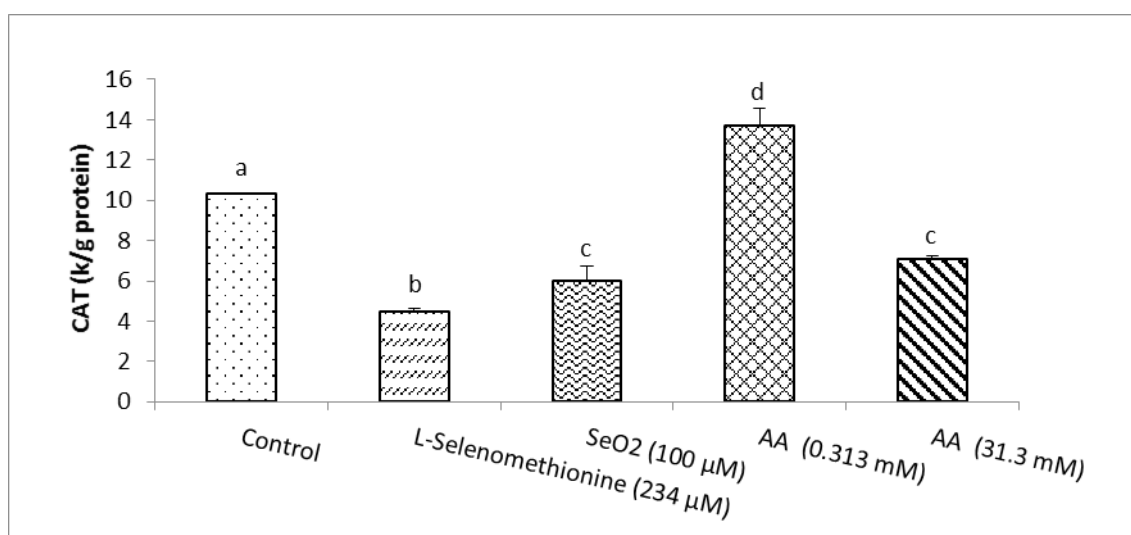


Figure 3. The CAT activities in HepG2 cells treated with 234 µM L-selenomethionine, 100 µM SeO₂, 0.313 mM and 31.3 mM AA (Different letters indicate the differences between the groups)

Table 1. The GPx, SOD and CAT enzyme activities of HepG2 cells treated with 234 µM L-selenomethionine, 100 µM SeO₂, 0.313 mM and 31.3 mM AA.

GROUPS	GPx (X±SD)	SOD (X±SD)	CAT (X±SD)
Control group	51.1±2.32 ^a	0.70±0.014 ^a	10.3±0.035 ^a
L-Selenomethionine (234 µM)	66.7±1.85 ^b	0.79±0.077 ^{a,b}	4.47±0.16 ^b
SeO₂ (100 µM)	59.7±1.79 ^c	0.74±0.042 ^a	5.99±0.714 ^b
AA (0.313 mM)	68.1±0.9 ^b	0.9±0.014 ^b	13.7±0.86 ^d
AA (31.3 mM)	70.1±0.9 ^b	0.87±0.011 ^b	7.09±0.15 ^c

Data are presented as (Mean±SD). SD: Standard deviation. Statistical analysis was performed using one-way ANOVA with post hoc Duncan test. P values<0,05 were considered statistically significant (GPx : nmol/min/mg protein; SOD: U/mg of protein; CAT: k/g of protein). Different letters in the same column are statistically significant.

DISCUSSION AND CONCLUSION

As oxidative stress causes DNA damage, it has a role in cancer pathogenesis (23). The antioxidant enzymes CAT and GPx can scavenge hydrogen peroxide, which is produced by SOD from superoxide radical. In some cases, hydrogen peroxide is converted to highly toxic hydroxyl radicals by Fenton reaction due to the low CAT level (24). For the normal cellular function, there should be an appropriate balance between Cu/Zn-superoxide dismutase (Cu/Zn-SOD), catalase, and selenium-glutathione peroxidase activities. CAT and SOD activity could demonstrate the positive or negative balance of the antioxidant defense system (25).

On the hepatic metastasis model, Heukamp et al. (26) found that vitamins A (retinol), C (ascorbic acid) and E (alpha-tocopherol)

increased GPx and SOD activities and decreased thiobarbituric acid-reactive substances (TBARS) levels. They concluded that these vitamins prevent oxidative stress in hepatocytes. In a study on young and aged rats, they found that the AA level decreased due to the increase in lipid peroxidation and MDA levels (27).

Although it is considered to be an antioxidant agent, at pharmacological doses (0.3-20 mM) AA, have been reported to be selectively toxic to cancer cells by producing ascorbate radicals, and inducing H₂O₂ formation (28). AA has also been reported in other studies to have cytotoxic effects on various types of cancer cells through a hydrogen peroxide generation (5, 29, 30, 31). Studies showed that specific protein transcription factors significantly decreased, and iron metabolism disrupted after AA treatment in colon cancer cells that are involved in cancer progression (32, 33). In

Ryszawy et al. (34) study, sodium ascorbate showed anti-tumor activity in glioblastoma multiforme cells. Gao et al. (35) demonstrated that AA could lead to liver cancer cells' death via intracellular reductive stress.

Increasing ROS production and oxidation, Se is known to induce apoptotic cell death in cancer cells (36, 37). Se, which is an essential element for many biological functions, has been shown to have cancer-protective effects in epidemiological and experimental animal studies. In addition to its protective effect against cancer, Se shows prooxidant activity and increased oxidative stress in cancer cells (38).

Wu et al. (39), demonstrated the therapeutic effect of selenite on peritoneal cancer in a mouse model. They indicated that selenite induced ROS production depending on its dose in the H22 cells and 4 mg Se/kg could be more effective than that of cisplatin in killing cancer cells. The mechanism of Se is related to endogenously formed selenium nanoparticles and its effect to hijack the Trx- and Grx-coupled GSH systems to produce ROS to kill cancer cells. Some organic Se components such as selenoamino acids, selenoproteins, and synthetic organic Se compounds have been reported to have cancer-protective effects (40, 41). Many preclinical, epidemiological studies and experimental animal models supported that Se compounds play a protective role against cancer. To date, studies have demonstrated the importance of the dose, which is administered, and the chemical structure of Se, which is used to determine the protective activity of Se components from cancer (42).

It is thought that there are many mechanisms in the anticancer activity of Se (43). But it was revealed that cell deaths that are related to Se applications were associated with ROS production (37, 38, 44, 45), and apoptotic cell death due to increased ROS production was observed through the caspase-independent apoptotic pathway (46). Estevez et al. (47) investigated the effects of chitosan-stabilized selenium nanoparticles, which were compared with other selenium-containing species on cell proliferation, apoptosis, and cell cycle pattern in HepG2 cells. They compared the effect of different type of Se compounds and concluded that cells which were exposed to Se(IV) showed strong induction of apoptosis and a significant population of cells when they are compared to control cells.

In our study, while the effects of AA on CAT activity were found to be dose-dependent, no changes were found in GPx and SOD activities. GPx activities increased, but CAT activities decreased in L-selenomethionine, and SeO₂

applied to HepG2 cells when they are compared to the control group. L-selenomethionine generated a significant increase in GPx activity than SeO₂. There were no statistical differences in SOD activity between L-selenomethionine and SeO₂ applied HepG2 cells. Compared to the control group: GPx activities increased in HepG2 cells treated with L-selenomethionine, SeO₂, and different doses of AA, but CAT activities decreased in all groups but increased in 0.313 mM AA applied cells compared to the control group.

The results of this study indicated that L-selenomethionine, SeO₂, and AA application increase GPx enzyme activities in HepG2 cells. L-selenomethionine and SeO₂ decrease CAT enzyme activities but do not change SOD enzyme activities. SOD enzyme activities are increased in both 0.313 mM and 31.3 mM AA concentrations. Depending on its doses, AA effects CAT enzyme activities. 0.313 mM AA increases, and 31.3 mM decreases CAT enzyme activities in HepG2 cells.

ACKNOWLEDGMENTS

This study was presented in the 1st International Conference on Natural Products for Cancer Prevention and Therapy, 31 August–2 September 2015, Istanbul, Turkey.

REFERENCES

1. Traber MG, Atkinson J. Vitamin E, antioxidant and nothing more. *Free Radic Biol Med*. 2007;43(1):4–15. Doi: 10.1016/j.freeradbiomed.2007.03.024.
2. Zou Z, Chang H, Li H, Wang S. Induction of reactive oxygen species: an emerging approach for cancer therapy. *Apoptosis*. 2017;22(11):1321–35. doi: 10.1007/s10495-017-1424-9.
3. Hatem E, Azzi S, El Banna N, He T, Heneman-Masurel A, Vernis L, et al. Auranofin/Vitamin C: A novel drug combination targeting triple-negative breast cancer. *J Natl Cancer Inst*. 2019;111(6):597–608. doi: 10.1093/ije/djy149.
4. Shaaban S, Ashmawy AM, Negm A, Wessjohann LA. Synthesis and biochemical studies of novel organic selenides with increased selectivity for hepatocellular carcinoma and breast adenocarcinoma. *Eur J Med Chem*. 2019;179:515–526. doi:10.1016/j.ejmech.2019.06.075.
5. Du J, Martin SM, Levine M, Wagner BA, Buettner GR, Wang SH, et al. Mechanisms of ascorbate-induced cytotoxicity in pancreatic cancer. *Clin Cancer Res*. 2010;16(2):509–20. doi: 10.1158/1078-0432.CCR-09-1713.
6. Paolini M, Pozzetti L, Pedulli GF, Marchesi E, Cantelli-Forti G. The nature of prooxidant activity of vitamin C. *Life Sci*. 1999;64(23):273–278. Doi: 10.1016/s0024-3205(99)00167-8.

7. Fernandes AP, Gandin V. Selenium compounds as therapeutic agents in cancer. *Biochim Biophys Acta - Gen Subj.* 2015;1850(8):1642–60. doi: 10.1016/j.bbagen.2014.10.008.
8. Misra S, Boylan M, Selvam A, Spallholz JE, Björnstedt M. Redox-active selenium compounds—from toxicity and cell death to cancer treatment. *Nutrients.* 2015;7(5):3536–56. doi: 10.3390/nu7053536.
9. Head KA. Ascorbic acid in the prevention and treatment of cancer. *Altern Med Rev.* 1998;3(3):174–86. PMID: 9630735.
10. Combs GF. Status of selenium in prostate cancer prevention. *Br J Cancer.* 2004;91(2):195–9. Doi: 10.1038/sj.bjc.6601974.
11. Knekt P, Marniemi J, Teppo L, Heliövaara M, Aromaa A. Is low selenium status a risk factor for lung cancer? *Am J Epidemiol.* 1998;148(10):975–82. Doi: 10.1093/oxfordjournals.aje.a009574.
12. Mandrioli J, Michalke B, Solovyev N, Grill P, Violi F, Lunetta C, et al. Elevated levels of selenium species in cerebrospinal fluid of amyotrophic lateral sclerosis patients with disease-associated gene mutations. *Neurodegener Dis.* 2017;17(4–5):171–80. doi: 10.1159/000460253.
13. Vinceti M, Chiari A, Eichmüller M, Rothman KJ, Filippini T, Malagoli C, et al. A selenium species in cerebrospinal fluid predicts conversion to Alzheimer's dementia in persons with mild cognitive impairment. *Alzheimer's Res Ther.* 2017;9(1):100. doi: 10.1186/s13195-017-0323-1.
14. Gammelgaard B, Jackson MI, Gabel-Jensen C. Surveying selenium speciation from soil to cell-forms and transformations. *Analytical and Bioanalytical Chemistry.* 2011;399:1743–63. doi: 10.1007/s00216-010-4212-8.
15. Brigelius-Flohé R, Flohé L. Selenium and redox signaling. *Arch Biochem Biophys.* 2017;617:48–59. doi: 10.1016/j.abb.2016.08.003.
16. Hatfield DL, Tsuji PA, Carlson BA, Gladyshev VN. Selenium and selenocysteine: Roles in cancer, health, and development. *Trends Biochem Sci.* 2014;39(3):112–20. doi: 10.1016/j.tibs.2013.12.007.
17. Labunskyy VM, Hatfield DL, Gladyshev VN. Selenoproteins: Molecular pathways and physiological roles. *Physiol Rev.* 2014;94:739–77. doi: 10.1152/physrev.00039.2013.
18. Balkan BM, Sel T. Vitamin C'nin HepG2 hücrelerinde apoptozis üzerine etkileri. *Ankara Üniv Vet Fak Derg.* 2014;61:237–41.
19. Balkan BM. HepG2 hücrelerinde selenyum ve vitamin C'nin apoptosis üzerine etkileri [Doktora Tezi]. [Ankara]: Ankara Üniversitesi; 2012.
20. Paglia DE, Valentine WN. Studies on the quantitative and qualitative characterization of erythrocyte glutathione peroxidase. *J Lab Clin Med.* 1967;70(1):158–69. PMID: 6066618
21. Aebi HE. Catalase in: H.U. Bermeyer (Hrsy). *Methods of enzymatic analysis.* Verlag Chemie; Weinheim, Bd. III; 1983. p. 273-286.
22. Bradford M. A rapid and sensitive method for the quantitation of microgram quantities of protein utilizing the principle of protein-dye binding. *Anal Biochem.* 1976;72(1–2):248–54. doi.org/10.1016/0003-2697(76)90527-3.
23. Athreya K, Xavier MF. Antioxidants in the treatment of cancer. *Nutrition and Cancer.* 2017;69:1099–104. doi: 10.1080/01635581.2017.1362445.
24. Guo Dong Mao, Thomas PD, Lopaschuk GD, Poznansky MJ. Superoxide dismutase (SOD)-catalase conjugates. Role of hydrogen peroxide and the fenton reaction in SOD toxicity. *J Biol Chem.* 1993;268(1):416–20. PMID: 8380162.
25. Michiels C, Raes M, Toussaint O, Remacle J. Importance of SE-glutathione peroxidase, catalase, and CU/ZN-SOD for cell survival against oxidative stress. *Free Radic Biol Med.* 1994;17(3):235–48. Doi: 10.1016/0891-5849(94)90079-5.
26. Heukamp I, Kilian M, Gregor JJ, Neumann A, Jacobi CA, Guski H, et al. Effects of the antioxidative vitamins A, C and E on liver metastasis and intrametastatic lipid peroxidation in bop-induced pancreatic cancer in Syrian hamsters. *Pancreatology.* 2005;5(4–5):403–9. Doi: 10.1159/000086541.
27. Van Der Loo B, Bachschmid M, Spitzer V, Brey L, Ullrich V, Lüscher TF. Decreased plasma and tissue levels of vitamin C in a rat model of aging: Implications for antioxidative defense. *Biochem Biophys Res Commun.* 2003;303(2):483–7. Doi: 10.1016/s0006-291x(03)00360-7.
28. Chen Q, Espey MG, Krishna MC, Mitchell JB, Corpe CP, Buettner GR, et al. Pharmacologic ascorbic acid concentrations selectively kill cancer cells: Action as a pro-drug to deliver hydrogen peroxide to tissue. *Proc Natl Acad Sci USA.* 2005;102(38):13604–9. Doi: 10.1073/pnas.0506390102.
29. Chen P, Stone J, Sullivan G, Drisko JA, Chen Q. Anti-cancer effect of pharmacologic ascorbate and its interaction with supplementary parenteral glutathione in preclinical cancer models. *Free Radic Biol Med.* 2011;51(3):681–7. doi: 10.1016/j.freeradbiomed.2011.05.031.
30. Du J, Cullen JJ, Buettner GR. Ascorbic acid: Chemistry, biology and the treatment of cancer. *Biochim Biophys Acta - Rev Cancer.* 2012;1826(2):443–57. doi: 10.1016/j.bbcan.2012.06.003.
31. Levine M, Padayatty SJ, Espey MG. Vitamin C: A concentration-function approach yields pharmacology and therapeutic discoveries. *Adv Nutr.* 2011;2(2):78–88. doi: 10.3945/an.110.000109.
32. Pathi SS, Lei P, Sreevalsan S, Chadalapaka G, Jutooru I, Safe S. Pharmacologic doses of ascorbic acid repress specificity protein (Sp) transcription factors and Sp-regulated genes in colon cancer cells. *Nutr Cancer.* 2011;63(7):1133–42. doi: 10.1080/01635581.2011.605984.

33. Schoenfeld JD, Sibenaller ZA, Mapuskar KA, Wagner BA, Cramer-Morales KL, Furqan M, et al. O₂·- and H₂O₂-mediated disruption of Fe metabolism causes the differential susceptibility of NSCLC and GBM cancer cells to pharmacological ascorbate. *Cancer Cell*. 2017;31(4):487-500. doi: 10.1016/j.ccell.2017.02.018.
34. Ryszawy D, Pudełek M, Catapano J, Ciarach M, Setkowicz Z, Konduracka E, et al. High doses of sodium ascorbate interfere with the expansion of glioblastoma multiforme cells in vitro and in vivo. *Life Sci*. 2019;232:116657. doi: 10.1016/j.lfs.2019.116657.
35. Gao P, Zhang H, Dinavahi R, Li F, Xiang Y, Raman V, et al. HIF-Dependent antitumorigenic effect of antioxidants in vivo. *Cancer Cell*. 2007;12(3):230-8. Doi: 10.1016/j.ccr.2007.08.004.
36. Susin SA, Daugas E, Ravagnan L, Samejima K, Zamzami N, Loeffler M, et al. Two distinct pathways leading to nuclear apoptosis. *J Exp Med*. 2000;192(4):571-9. Doi: 10.1084/jem.192.4.571.
37. Uğuz AC, Naziroglu M, Espino J, Bejarano I, González D, Rodríguez AB, et al. Selenium modulates oxidative stress-induced cell apoptosis in human myeloid HL-60 cells through regulation of calcium release and caspase-3 and -9 activities. *J Membr Biol*. 2009;232(1-3):15-23. doi: 10.1007/s00232-009-9212-2.
39. Wu X, Zhao G, He Y, Wang W, Yang CS, Zhang J. Pharmacological mechanisms of the anticancer action of sodium selenite against peritoneal cancer in mice. *Pharmacol Res*. 2019;147:104360. doi: 10.1016/j.phrs.2019.104360.
40. Chen T, Zheng W, Wong YS, Yang F. Mitochondria-mediated apoptosis in human breast carcinoma MCF-7 cells induced by a novel selenadiazole derivative. *Biomed Pharmacother*. 2008;62(2):77-84. doi: 10.1016/j.biopha.2007.12.002.
41. Rayman MP. The importance of selenium to human health. *Lancet*. 2000;356(9225):233-41. Doi: 10.1016/S0140-6736(00)02490-9.
42. El-Bayoumy K, Sinha R. Mechanisms of mammary cancer chemoprevention by organoselenium compounds. *Mutat Res*. 2004;551(1-2):181-97. Doi: 10.1016/j.mrfmmm.2004.02.023.
43. Whanger PD. Selenium and its relationship to cancer: an update. *Br J Nutr*. 2004;91(1):11-28. Doi: 10.1079/bjn20031015.
44. Gopee N V., Johnson VJ, Sharma RP. Sodium selenite-induced apoptosis in murine B-lymphoma cells is associated with inhibition of protein kinase C-δ, nuclear factor κB, and inhibitor of apoptosis protein. *Toxicol Sci*. 2004;78(2):204-14. Doi: 10.1093/toxsci/kfh072.
45. Shilo S, Tirosch O. Selenite activates caspase-independent necrotic cell death in Jurkat T cells and J774.2 macrophages by affecting mitochondrial oxidant generation. *Antioxidants Redox Signal*. 2003;5(3):273-9. Doi: 10.1089/152308603322110850.
46. Rudolf E, Rudolf K, Červinka M. Selenium activates p53 and p38 pathways and induces caspase-independent cell death in cervical cancer cells. *Cell Biol Toxicol*. 2008;24(2):123-41. Doi: 10.1007/s10565-007-9022-1.
47. Estevez H, Garcia-Lidon JC, Luque-Garcia JL, Camara C. Effects of chitosan-stabilized selenium nanoparticles on cell proliferation, apoptosis and cell cycle pattern in HepG2 cells: Comparison with other selenospecies. *Colloids Surfaces B Biointerfaces*. 2014;122:184-93. doi: 10.1016/j.colsurfb.2014.06.062.



Fabrication of Superhydrophobic Coatings on Glass based on Poly(dimethylsiloxane) and Fumed Silica

Esra KASAPGİL , Alper NERAT , Buse M. POYRAZ , İlke ANAÇ* 

Department of Materials Science and Engineering, Gebze Technical University, Gebze, Kocaeli, Turkey.

Abstract: This study reports the preparation of superhydrophobic covalently attached poly(dimethylsiloxane)(PDMS)/fumed silica composite coatings on glass via spin-coating and subsequent heating. The effect of PDMS molecular weight and fumed silica type (hydrophilic and three different hydrophobic) on the wettability and morphology were studied in detail, and the wettability and morphology of the coatings were characterized by contact angle measurements and scanning electron microscopy (SEM). Superhydrophobic coatings which have advancing contact angles of 172-174° and contact angle hysteresis (CAH) as low as 7-8° were obtained using 4% (w/v) PDMS modified hydrophobic fumed silica and all kinds of PDMS. The surfaces which were prepared by 4% (w/v) hydrophilic and dimethylsiloxymodified fumed silica had high advancing contact angles of 163-168°, but the CAH on these surfaces were higher than the ones prepared using PDMS modified fumed silica. It is due to the incompatibility of the hydrophilic and dimethylsiloxymodified fumed silica with the PDMS matrix also confirmed with the SEM results.

Keywords: poly(dimethylsiloxane), fumed silica, wetting, superhydrophobic coatings, contact angle, spin-coating

Submitted: February 21, 2020. **Accepted:** June 07, 2020.

Cite this: KASAPGİL E, NERAT A, POYRAZ BM, ANAÇ İ. Fabrication of Superhydrophobic Coatings on Glass based on Poly(dimethylsiloxane) and Fumed Silica. JOTCSA. 2020;7(2):589-96.

DOI: <https://doi.org/10.18596/jotcsa.692565>.

*Corresponding author. E-mail: ilkeanac@gtu.edu.tr.

INTRODUCTION

There is a great interest in the fabrication of artificial superhydrophobic surfaces over the last 20 years after Barthlott et al. reported the self-cleaning property of a lotus leaf in 1997, which is known as a "lotus effect" (1-5). Superhydrophobic surfaces, which have water contact angles (CA) larger than 150°, sliding angles lower than 5° or contact angle hysteresis (CAH) lower than 10°, can be used in various applications such as oil-water separation, self-cleaning, anti-icing, anti-fouling, and drop transport (5-7). There are two crucial factors when designing hydrophobic surfaces; (1) using a low energy material as a coating and (2) creating a rough surface, which will increase the hydrophobic surface character according to the Cassie Baxter wetting situation (8). Therefore, superhydrophobic

surfaces can be prepared either by modifying rough surfaces using low energy materials or by making a roughness using low energy materials (2-7,9).

To date, researchers used different techniques to create various superhydrophobic surfaces such as sol-gel, lithography, templating method, colloidal assembling and aggregation, layer-by-layer assembly, plasma method, chemical vapor deposition, phase separation, electrospinning and electrospraying, dip-coating and so on (4,10-11). These techniques are quite complicated and expensive due to multiple steps, specific equipment, and costly reagents. Besides, they can be applied to specific substrates. Overcoming such difficulties, different kinds of polymers, together with various nanoparticles, were used to fabricate superhydrophobic surfaces on different substrates

where the nanoparticles were used to create surface texturing on the surfaces (12-18). Silica-based nanofillers are the most used ones in the literature to create superhydrophobic and self-cleaning surfaces (14, 19-26). Manoudis et al. prepared superhydrophobic composite films containing hydrophilic silica nanoparticles and poly(methyl methacrylate) (PMMA) and commercial poly(alkyl siloxane) (Rhodorsil 224) on various substrates (glass, silicon, wood, concrete, aluminum, silk, marble) via spray coating (14). Superhydrophobic films were fabricated on glass via a drop-coating method using Sylgard 184 silicone (containing curing agent and poly(dimethylsiloxane) (PDMS) prepolymer) and silica particles (19). Chang et al. successfully prepared the superhydrophobic wood surfaces via a dip-coating method using PDMS Sylgard 184, curing agent, and hydrophobic silica particles (20). They also investigated the morphology, wetting behavior, and roughness of the coatings as a function of silica concentration (20). Superhydrophobic composite films containing hydrophobic fumed silica particles and different polymers (thermoplastic resin, PS, cross-linked epoxy resin, PDMS-urea copolymer, polyether-based polyurethane urea, PMMA, polycarbonate) were prepared on glass via spin-coating process or doctor blade coating method by Yilgor and coworkers (21-23). Cai et al. fabricated superhydrophobic fabrics via successive dip-coating of PDMS and silica suspensions and successive annealing steps (24). Also, bioinspired superhydrophobic cross-linked polyurethane-acrylate coatings containing hydrophobic fumed silica on glass were prepared via bar coating following UV curing by Fourmentin and coworkers (25). The superhydrophobic coating on cellulosic filter paper for oil-water separation was achieved via solution casting technique using PMMA copolymer and silica nanoparticles by Siriam et al. (26).

As noted above, several papers in the literature report the preparation of superhydrophobic coatings on various substrates such as glass, wood, aluminum, silicon wafer using PDMS, low surface energy material, and nanoparticles (14,19,20,24,27). Either these coatings are not covalently attached to the substrates (14), or they are prepared using curing agents (19,20,24, 27). In 2011, McCarthy and coworkers showed, for the first time, that linear polysiloxanes containing only Si-O-Si in their main chain react with inorganic surfaces containing hydroxyl groups upon heating to desired temperature (especially 100 °C for 24 h) (28). Furthermore, they reported that they obtained low hysteresis surfaces and concluded that they could control the thickness of the PDMS layers on silica by changing the molecular weight of the PDMS.

In the present study, we have prepared superhydrophobic PDMS/silica coatings which are covalently attached to glass via a simple spin-

coating process and subsequent heating. The wettability and surface morphology of PDMS/silica composites on glass were characterized by contact angle measurements (equilibrium, advancing and receding contact angle) and scanning electron microscopy (SEM), respectively. The effect of PDMS molecular weight, silica concentration, and silica type on coatings' morphology and contact angles were also systematically studied, and the results were compared with the findings reported in the literature.

EXPERIMENTAL DETAILS

Materials

Polydimethylsiloxane (PDMS) with three different weight average molecular weight (M_w) of 2000 (2k), 63000 (63k) and 117000 (117k) were obtained from Alfa Aesar (Massachusetts, USA). Amorphous hydrophobic fumed silicon (IV) oxide (~50 nm; PDMS modified, referred to as FS) was obtained from Alfa Aesar. Amorphous hydrophobic pyrogenic silica with different particle sizes and different surface modification (~40 nm; dimethylsiloxyl modified; referred as H15 and ~30 nm; PDMS modified; referred as H18) and amorphous hydrophilic pyrogenic silica (~25 nm; referred as N20) were obtained from Wacker (Burghausen, Germany). Toluene was obtained from Sigma-Aldrich. Ethanol, sulfuric acid (H_2SO_4 , 95-97%), hydrogen peroxide (H_2O_2 , 30%), and ultra-pure water were obtained from Merck (Darmstadt, Germany). All reagents were used as received without further purification. Glass microscope slides were obtained from ISOLAB GmbH (Wertheim, Germany) and cut into 25 mm x 35 mm x 1 mm pieces. Deionized water ($18.2 M\Omega cm^{-1}$) was obtained through a system including pretreatment, reverse osmosis, and ion exchange steps (Elga Option Q15).

Preparation of PDMS-silica Coatings

Glass microscope slides were cleaned by ethanol and then activated by piranha solution before the coating procedure. Glass slides were immersed into freshly prepared piranha solution, which is a 7:3 (v:v) mixture of concentrated H_2SO_4 and 30% H_2O_2 . They were kept at 80 °C for 2 h and then left at room temperature overnight. Then the glass slides were washed with deionized water and dried at 125 °C for 30 min in an oven. Activated glass slides were used immediately for PDMS-silica composite film preparation.

The coating solution was prepared as follows; the desired amount of silica particles (to obtain x% w/v for the toluene volume, where x is 0, 0.4, 1.2, 2, 3, and 4) were added to 1 % w/ v PDMS toluene solution. The polymer solution was mixed with a magnetic stirrer for 1 h and then sonicated for 30 min at room temperature. 10 μL of the homogeneous polymer solution was dropped onto

the freshly activated glass slide and spin-coated at 2000 rpm for 60 s. Then the coatings were kept at 100 °C for 24 h in an oven (Figure 1).

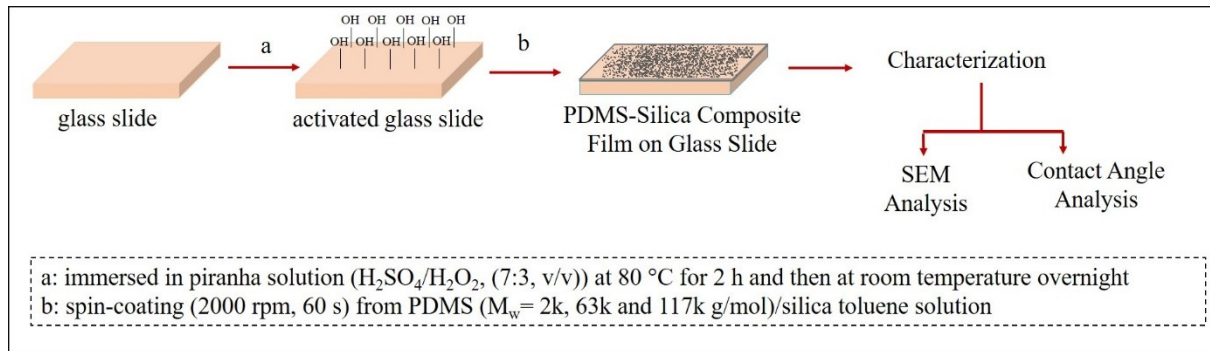


Figure 1: Schematic illustration of the PDMS-silica composite film preparation and characterization procedure.

Characterization of The Coatings

The surface morphology of the coatings was characterized by scanning electron microscopy (SEM, Philips XL 30 SFEG). PDMS-silica composite films were coated with a gold layer before SEM analysis to prevent charging effects. Contact angles were measured by a contact angle meter (KSV-CAM 200) with a PC controlled motorized syringe using ultra-pure water under air at room temperature. Static contact angles (Θ_e) were measured by forming 5 μL drops of water on samples, and the values recorded 2 s after the release of the needle. Advancing contact angles (Θ_a) were measured by increasing the volume of the water droplet on the surface from 3 to 8 μL , and receding contact angles (Θ_r) were measured by decreasing the volume of a water droplet from 10 to 3 μL by using the automatic dispenser through the needle. The needle was kept within the water droplet during the Θ_a and Θ_r measurements. The reported values were calculated by taking the averages of 5 different measurements made on the same sample.

Chemical stabilities of PDMS/silica composite coatings were tested by washing the samples with toluene for 5 minutes and dried at 100 °C for 24 h in the oven. SEM images were again taken, and contact angle (Θ_e , Θ_a , and Θ_r) values were again measured after washing with toluene, and the results were compared with the unwashed samples' results.

RESULTS AND DISCUSSION

In this study, covalently attached superhydrophobic PDMS/silica coatings were prepared on piranha-cleaned glass slides. The superhydrophobic coatings were prepared via a spin-coating of silica/PDMS dispersions and subsequent heating at 100 °C for 24 h. The covalent attachment was achieved via heating, as reported in the literature by McCarthy et al. (28). PDMS with three different molecular weights, hydrophilic, and three different hydrophobic fumed silica were used to prepare the

coatings. The effect of hydrophobic fumed silica concentration on surface morphology and wettability were also studied.

Table 1 shows the effect of fumed silica concentration on the equilibrium (Θ_e), advancing (Θ_a) and receding (Θ_r) contact angle and contact angle hysteresis (CAH) values of composite films. The composites films were prepared by two different molecular weights (63k and 117k g/mol) of PDMS and five different concentration of hydrophobic fumed silica (0.4, 1.2, 2.3 and 4% w/v) where hydrophobicity is achieved by modification with PDMS (~50 nm; referred as, FS). As seen in Table 1, the Θ_e , Θ_a and Θ_r values of bare PDMS coating increase from $108\pm 1^\circ$, $111\pm 1^\circ$ and $96\pm 2^\circ$ to $119\pm 1^\circ$, $120\pm 1^\circ$ and $103\pm 2^\circ$ respectively as the molecular weight of PDMS increases from 63 k to 117 k. This trend is similar to the results reported in the literature [28]. The Θ_e , Θ_a , and Θ_r values of the coatings increased with an introduction of hydrophobic fumed silica (FS) as depicted in Table 1 regardless of PDMS molecular weight. As the concentration of hydrophobic fumed silica (FS) increased from 0.4 to 4 % w/v, and increase in Θ_e , Θ_a and Θ_r values were seen up to $169\pm 2^\circ$, $173\pm 1^\circ$, $166\pm 1^\circ$, and $170\pm 2^\circ$, $172\pm 2^\circ$ and $164\pm 1^\circ$ for the coatings prepared by 63k and 117k PDMS respectively (Table 1). The highest contact angle values and lowest CAH (7° for 63k PDMS and 8° for 117k PDMS) were obtained at 4 % w/v silica concentration for PDMS coatings prepared by different molecular weights. The highest Θ_e value (164°) of cross-linked silicone-based coatings prepared by spray coating using $\text{CaCO}_3/\text{SiO}_2$ particles on glass by Yang et al. (27) was lower than our results. Manoudis et al. reported that they obtained siloxane-based coatings via spraying on glass using 2% w/v hydrophilic silica particles with a Θ_a of 164° and CAH of 3° . The CAH hysteresis value (3°) is better than our values (7° for 63k PDMS and 8° for 117k PDMS), but the information on the chemical composition and the molecular weight of

the poly(alkyl siloxane) which was used to prepare the coating was not given in the paper (14).

Table 1. Equilibrium (Θ_e), advancing (Θ_a) and receding (Θ_r) contact angle and contact angle hysteresis (CAH) values of PDMS/SiO₂ composite films prepared by hydrophobic fumed silica (FS) and PDMS with different molecular weights. The PDMS (1% w/v) was prepared by dissolving PDMS (63k or 117k) in toluene.

PDMS (M _w (g/mol))	Silica/toluene (% w/v)	Θ_e (°)	Θ_a (°)	Θ_r (°)	CAH (°)
63k	0	108±1	111±1	96±2	15
63k	0.4	119±2	124±1	108±2	16
63k	1.2	161±1	168±2	150±1	18
63k	2	167±1	171±1	155±2	16
63k	3	169±1	172±2	164±1	8
63k	4	169±2	173±1	166±1	7
117k	0	119±1	120±1	103±1	17
117k	0.4	129±2	146±1	107±1	39
117k	1.2	166±2	167±1	142±1	25
117k	2	167±1	168±1	134±1	34
117k	3	169±2	172±1	159±2	13
117k	4	170±2	172±2	164±1	8

The Θ_e , Θ_a , Θ_r , and CAH values of bare PDMS and composite coatings before and after washing with toluene were shown in Table 2. The coatings were prepared using PDMS with different molecular weights (2k, 63k, and 117k) and 4 % w/v hydrophobic fumed silica (FS). As seen in Table 2, the Θ_e , Θ_a , Θ_r values of the bare 2k PDMS and 63k PDMS coatings were slightly decreased (1-2°) or increased (1-2°) after washing with toluene, but the decrease in Θ_e , Θ_a , Θ_r values of the coating prepared using 117 k PDMS were higher compared to the other coatings. The increase in all the contact angle values was seen as the molecular weight of the PDMS rises, as shown in Table 2, and the trend did not change after washing with toluene. Similar to the bare PDMS coatings, there was a slight change (1-2°) in the Θ_e , Θ_a , Θ_r values of the composite coatings prepared using 4 % w/v silica (FS) after washing with toluene. The results in Table 2 clearly show that bare PDMS and composite coatings were covalently attached to the piranha cleaned glass slides, and the superhydrophobic character of the composite coatings did not alter after washing with toluene.

Figure 2 shows the SEM images of the coatings prepared by PDMS with different molecular weights PDMS/silica (FS) composite before and after washing with toluene. All the SEM pictures in Figure

2 a-c clearly show that the homogenous PDMS/silica (FS) composite coatings were obtained with a similar morphology regardless of the PDMS molecular weight. No change in the homogeneity of the composite coatings was observed after washing with toluene. (Figure 2 d-f).

After investigating the effect of silica concentration on coatings' wettability, 4 % w/v silica concentration and 63k PDMS were chosen to study the effect of silica size and type on coating morphology and wettability (Table 3 and Figure 3). The Θ_e , Θ_a , Θ_r , and CAH values of PDMS/silica composite films prepared using different types and size fumed silica were shown in Table 3. The Θ_e contact angles of the PDMS coating increased up to 159-172° with an addition of different types and sizes of fumed silica (Table 3). Although high Θ_a values were obtained for the coatings prepared by hydrophilic fumed silica (N2O) (168±2°) and dimethylsiloxy modified hydrophobic fumed silica (H15) (N2O) (163±2°), the surfaces were not superhydrophobic due to the high CAH hysteresis (24° and 16° respectively). Superhydrophobic composite coatings were obtained when two different sizes of PDMS modified fumed silica particles (FS; ~50 nm and H18; ~30nm) were used to prepare the coatings. The Θ_a , Θ_r , and CAH values of the coating prepared using FS and N18 were

measured as $173\pm 1^\circ$, $166\pm 1^\circ$, 7° , and $174\pm 1^\circ$, $166\pm 1^\circ$, 8° respectively. These differences can be due to the incompatibility of the hydrophilic (N20) and dimethylsiloxo modified hydrophobic (H15) fumed silica and compatibility of the PDMS modified hydrophobic (FS and H18) fumed silica with the PDMS matrix.

Table 2. Equilibrium (Θ_e), advancing (Θ_a) and receding (Θ_r) contact angle and contact angle hysteresis (CAH) values of PDMS/SiO₂ composite before and after washing with toluene. The composite films composed of hydrophobic fumed silica (FS) and PDMS with different molecular weights. The PDMS (1% w/v) was prepared by dissolving PDMS (2k, 63k, or 117k) in toluene.

PDMS (M _w (g/mol))	Silica/toluene (% w/v)	Washing	Θ_e (°)	Θ_a (°)	Θ_r (°)	CAH (°)
2k	-	No	94±1	95±2	81±1	14
2k	-	Toluene	92±2	99±2	82±1	17
2k	4	No	170±1	173±2	166±1	7
2k	4	Toluene	168±1	172±1	162±1	10
63k	-	No	108±1	111±1	96±2	15
63k	-	Toluene	109±1	110±1	96±1	14
63k	4	No	169±2	173±1	166±1	7
63k	4	Toluene	168±1	172±1	165±2	7
117k	-	No	119±1	120±1	103±1	17
117k	-	Toluene	110±2	117±1	98±1	19
117k	4	No	170±2	172±2	164±1	8
117k	4	Toluene	171±2	173±2	165±1	8

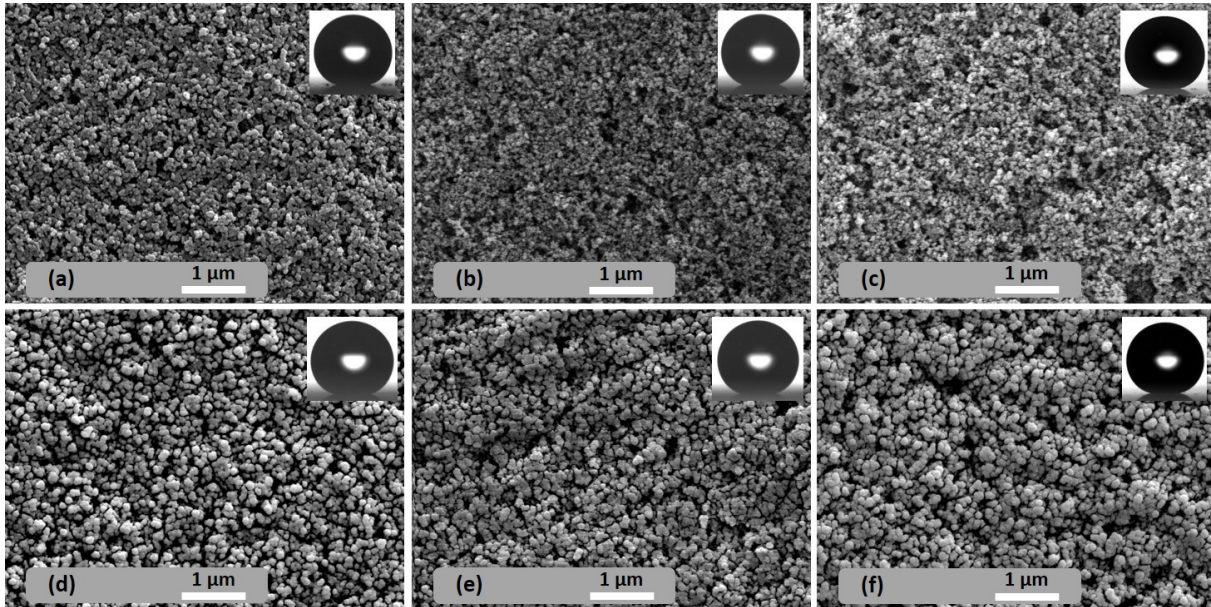


Figure 2. SEM pictures and water droplets of PDMS-silica composite films prepared with fumed silica (FS) and PDMS with different molecular weights : (a) 2k PDMS; (b) 63k PDMS; (c) 117k PDMS; (d) 2k PDMS, washed with toluene; (e) 63k PDMS, washed with toluene; and (f) 117k PDMS, washed with toluene (Silica concentration is 4 % w/v).

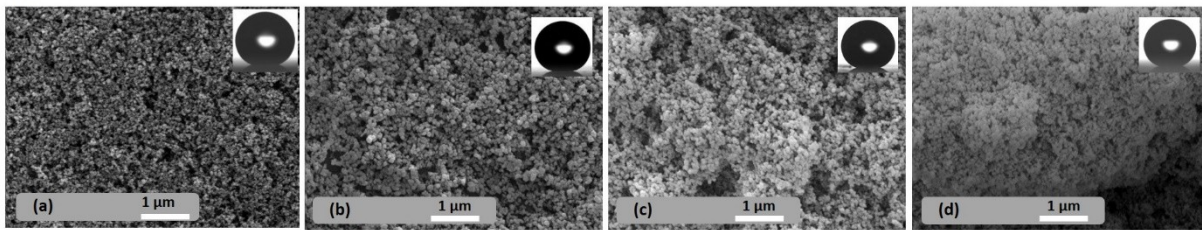
Table 3. Equilibrium (θ_e), advancing (θ_a) and receding (θ_r) contact angle and contact angle hysteresis (CAH) values of PDMS/SiO₂ composite films with hydrophilic and three different hydrophobic fumed silica and PDMS (63k). The PDMS (1% w/v) was prepared by dissolving PDMS (63k) in toluene.

Silica type	Silica/toluene (% w/v)	θ_e (°)	θ_a (°)	θ_r (°)	CAH (°)
-	-	108±1	111±1	96±2	15
FS	4	169±2	173±1	166±1	7
N2O	4	163±2	168±2	144±2	24
H15	4	159±1	163±1	147±1	16
H18	4	172±2	174±1	166±1	8

SEM pictures of the PDMS/fumed silica coatings which were prepared using 4% w/v PDMS modified hydrophobic fumed silica (FS and H18) and dimethylsiloxo modified fumed silica (H15) and hydrophilic fumed silica (N2O) are depicted in Figure 3 a, b, c, and d respectively. Figure 3 a and b shows that the coatings prepared using FS and N10 are homogenous and very small aggregates of the fumed silica were seen on the surfaces confirming

the compatibility of the PDMS modified fumed silica with the PDMS matrix. Distinct big aggregates of fumed silica, which is embedded in the PDMS matrix and non-homogeneous coating formation were observed as seen in Figure 2 c and d when dimethylsiloxo modified fumed silica (H15) and hydrophilic fumed silica (N2O) were used conforming the non-compatibility of the particles with the PDMS matrix.

I.



II.

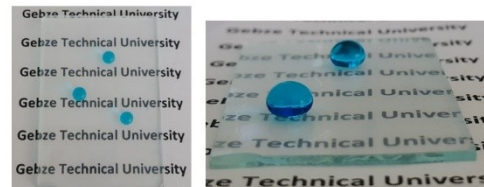


Figure 3. I. SEM pictures and water droplets of PDMS-silica composite films prepared with 63k PDMS and three different hydrophobic and hydrophilic fumed silica particles: (a) FS (b) H18, (c) H15 and (c) N20 (Silica concentration is 4% w/v). II. Photographs of superhydrophobic PDMS-silica composite film (63k PDMS, 4% w/v FS) coated glass slide (water droplets were dyed with methylene blue).

CONCLUSIONS

Summarizing, in this paper, we have demonstrated the preparation of covalently attached superhydrophobic PDMS/silica composite coatings on activated glass slides via an easy and straightforward spin-coating process. SEM and contact angle measurements were used to characterize the morphology and the wettability of the surfaces. The superhydrophobic coatings were obtained when PDMS modified fumed silica (FS and H18) were used, and the concentration of the fumed silica was 4 % w/v whereas the superhydrophobic surfaces were not obtained when hydrophilic (N2O). Dimethylsiloxy-modified (H15) fumed silica were used due to the high CAH. To obtain a superhydrophobic surface using PDMS and fumed silica via a spin coating process, the type and the concentration of the fumed silica need to be optimized.

ACKNOWLEDGMENTS

This research is supported by Gebze Technical University Research Fund. (Project Number: GTU 2016-A17) and originates from Alper Nerat's MS Thesis (#523031). We thank Mr. Ahmet Nazim in the Materials Science and Engineering Department of Gebze Technical University for taking the SEM images.

REFERENCES

- Barthlott W, Neinhuis C. Purity of the sacred lotus, or escape from contamination in biological surfaces. *Planta* 1997; 202 (1): 1-8.
- Chen W, Fadeev AY, Hsieh MC, Oner D, Youghblood J et al. Ultrahydrophobic and ultralyophobic surfaces: some comments and examples. *Langmuir* 1999; 15 (10): 3395-9.
- Erbil HY, Demirel AL, Avci Y, Mert O. Transformation of a simple plastic into a superhydrophobic surface. *Science* 2003; 299 (5611): 1377-80.
- Yan YY, Gao N, Barthlott W. Mimicking natural superhydrophobic surfaces and grasping the wetting process: a review on recent progress in preparing superhydrophobic surfaces, *Advances in Colloid and Interface Science* 2011; 169 (2): 80-105.
- Roach P, Shirtcliffe NJ, Newton MI. Progress in superhydrophobic surface development. *Soft Matter* 2008; 4 (2); 224-40.
- Feng L, Li SH, Li YS, Li HJ, Zhang LJ et al. Superhydrophobic surfaces: from natural to artificial. *Advance Materials* 2002; 14 (24): 1857-60.
- Liu K, Tian Y, Jiang L. Bio-inspired superoleophobic and smart materials: design, fabrication, and application. *Progress in Materials Science* 2013; 58 (4): 503-64.
- Cassie ABD, Baxter S. Wettability of porous surfaces. *Transactions of the Faraday Society* 1944; 40: 546-51.
- Erbil HY. The debate on the dependence of apparent contact angles on drop contact area or three-phase contact line: A review. *Surface Science Reports* 2014; 69 (4): 325-65.
- Atici EG, Kasapgil E, Anac I, Erbil HY. Methyltrichlorosilane polysiloxane filament growth on glass using low cost solvents and comparison with gas phase reactions. *Thin Solid Films* 2016; 616: 101-10.
- Kasapgil E, Atici EG, Cicek R, Anac I, Erbil HY. Superhydrophobic polysiloxane filament growth on non-activated polymer coatings. *RSC Advances* 2016; 6: 74921-8.
- Tuteja A, Choi W, Ma M, Mabry JM, Mazzella SA, Rutledge GC, McKinley GH, Cohen RH. Designing superoleophobic surfaces. *Science* 2007; 318 (5856): 1618-22.

13. Jung YC, Bhushan B. Mechanically durable carbon nanotube-composite hierarchical structures with superhydrophobicity, self-cleaning, and low-drag. *ACS Nano* 2009; 3: 4155-63.
14. Manoudis PN, Karapanagiotis I, Tsakalof A, Zuburtikubis I, Panayiotou C. Superhydrophobic composite films produced on various substrates. *Langmuir* 2008; 24 (19): 11225-32.
15. Hsieh CT, Chen JM, Kuo RR, Lin TS, Wu CF. Influence of surface roughness on water- and oil-repellent surfaces coated with nanoparticles. *Applied Surface Science*. 2005; 240(1):318-26.
16. Chibowski E, Holysz L, Terpolowski K, Jurak M. Investigation of superhydrophobic effect of PMMA layers with different fillers deposited on glass support. *Colloids and Surfaces A: Physicochem. Eng. Aspects*. 2006; 291 (1-3): 181-90.
17. Yang J, Pi P, Wen X, Zheng D, Xu et al. A novel method to fabricate superhydrophobic surfaces based on well-defined mulberry-like particles and self-assembly of polydimethylsiloxane. *Applied Surface Science* 2009; 255 (6): 3507-12.
18. Yuze YM, Demirel AL, Menzel F. Tuning the surface hydrophobicity of polymer/ nanoparticle composite films in the Wenzel regime by composition. *Langmuir*, 2005; 21(11): 5073-8.
19. Ke Q, Fu W, Jin H, Zhang L, Tang T et al. Fabrication of mechanically robust superhydrophobic surfaces based on silica micro-nanoparticles and polydimethylsiloxane. *Surface & Coatings Technology* 2011; 205 (21-22): 4910-4.
20. Chang H, Tu K, Wang X, Liu J. Fabrication of mechanically durable superhydrophobic wood surfaces using polydimethylsiloxane and silica nanoparticles. *RSC Advances* 2015; 5 (39): 30647-53.
21. Soz CK, Yilgor E, Yilgor I. Influence of the average surface roughness on the formation of superhydrophobic polymer surfaces through spin-coating with hydrophobic fumed silica. *Polymer* 2015; 62: 118-28.
22. Soz CK, Yilgor E, Yilgor I. Simple processes for the preparation of superhydrophobic polymer surfaces. *Polymer* 2016; 99: 580-93. doi: 10.1016/j.polymer.2016.07.051
23. Yilgor I, Bilgin S, Isik M, Yilgor E. Facile preparation of superhydrophobic polymer surfaces. *Polymer* 2012; 53 (6): 1180-8.
24. Cai R, Glinel K, De Smet D, Vanneste M, Mannu N et al. Environmentally friendly super-water-repellent fabrics prepared from water-based suspensions. *ACS Applied Materials and Interfaces* 2018; 10 (18): 15346-51.
25. Fourmentin A, Galy J, Charlot A, Gerard J-F. Bioinspired silica-containing polyurethane-acrylate films: Towards superhydrophobicity with tunable water adhesion. *Polymer* 2018; 155: 1-12.
26. Sriram A, Kumar A. Separation of oil-water via porous PMMA/SiO₂ nanoparticles superhydrophobic surface. *Colloids and Surfaces A: Physicochemical and Engineering Aspects* 2019; 563: 271-9.
27. Yang J, Pi P, Wen X, Zheng D, Xu et al. A novel method to fabricate superhydrophobic surfaces based on well-defined mulberry-like particles and self-assembly of polydimethylsiloxane. *Applied Surface Science* 2009; 255 (6): 3507-12.
28. Krumpfer JW, McCarthy TJ. Rediscovering silicones: "Unreactive" silicones react with inorganic surfaces. *Langmuir* 2011; 27 (18): 11514-9



In situ Crosslinking System of Gelatin with Acrylated β -cyclodextrin Towards the Fabrication of Hydrogels for Sustained Drug Release

Mehmet ARSLAN^{1*}  

¹University of Yalova, Faculty of Engineering, Department of Polymer Materials Engineering, 77200, Yalova, Turkey.

Abstract: Cyclodextrins (CDs) are of interest in the fabrication of various polymeric platforms, especially the crosslinked networks that possess unique advantages in biomedical applications. When one benefits from the abilities of CDs to form inclusion complexes with hydrophobic drug molecules, hydrogel-based supported drug platforms employ CDs as nano-buckets in the network structure. In the current study, we report on the fabrication of gelatin-based hydrogels chemically crosslinked with acrylated β -cyclodextrin (β -CD) as sustained drug release platforms. A practical and straightforward synthesis of crosslinked networks was achieved by Michael's addition reaction of gelatin amino functionalities onto acryloyl groups of modified β -CD. Tunable synthesis of hydrogels incorporating a different amount of β -CD molecules was maintained by simple adjustment of the reaction stoichiometry between amine and acrylate groups. The resulting hydrogels were characterized by their surface morphology, equilibrium swelling ratios, and rheological properties. Thus obtained hydrogels were evaluated in terms of their drug loading capacities and sustained release efficiencies. The results demonstrated that the amount of drug loading and prolonged release is dependent on the amount of β -CD in the gel network. Thanks to their in situ gel-forming abilities, these hydrogels can be used as injectable formulations for various biomedical applications.

Keywords: Drug releasing hydrogels, β -cyclodextrin, aza-Michael addition, injectable hydrogels.

Submitted: April 10, 2020. **Accepted:** June 07, 2020.

Cite this:

DOI: <https://doi.org/10.18596/jotcsa.717856>.

***Corresponding author.** E-mail: mehmet.arslan@yalova.edu.tr, Tel: +90-226-811-5959.

INTRODUCTION

Hydrogels purvey some unique and advantageous properties that make them ideal candidates in several biomedical applications. (1–3) Significant research has been devoted to engineered hydrogels in practical clinical utilization, such as in controlled/sustained drug release platforms or tissue construction scaffolds. In tissue engineering, hydrogels are employed as environments for adhesion, encapsulation, growth, or directed spread of cells. (4–6) In therapeutic applications, hydrogels are exploited as slow drug releasing platforms in which the rate of release can be controlled via response toward external stimuli such as temperature or pH of the local environment. (7–9) While the eximious features of hydrogels are advantageous, the challenges associated with the

practical introduction of the hydrogels into the body might limit their routine clinical implementation. Surgical implantation of the pre-formed hydrogels to defect sites is often associated with patient compliance and discomfort. In this context, non-invasive techniques such as employment of injectable hydrogel formulations to administrate regenerative factors or therapeutics to the body have been addressed. (10–12) In situ cross-linkable hydrogels that can form the network structure in vivo through physical or chemical interaction of gel, precursors could allow straightforward inclusion of drugs, (13) growth factors (14) or genes (15) to the target body tissues.

Gelatin is a biopolymer of animal-origin, derived from collagen by partial hydrolysis and denaturation. Due to essential characteristics such

as excellent biocompatibility, nontoxicity, high resemblance to extracellular matrix in a gel state, and low immunogenicity make gelatin widely used in the biomedical fields. (16–18) Gelatin contains peptide sequences that can bind to cell surface integrins, which is notable for cellular recognition. (19) Improved cell attachment and proliferation make gelatin-based scaffolds ideal for tissue regeneration, cell encapsulation, and 3D cell culture applications. (20–22) The utility of gelatin-based controlled-release systems covers a wide variety of drug and gene delivery applications. (23) Although gelatin can form temperature-induced physical gelation, a much-sought strategy is the fabrication of chemically crosslinked hydrogels to increase the stability of the gels. Toward this, several injectable gel-forming systems such as dextran-gelatin hydrogels via oxidized dextran and gelatin, (24) gelatin polymers with pendant norbornene (GelN) or tetrazine (GelT) groups, (25) and UV-curable acrylated gelatin hydrogels (26) have been reported.

Cyclodextrins (CDs) are torus-shaped molecules that are derived mainly degradation of starch. The structures of CDs possess an interesting molecular property with a hydrophobic inner cavity and hydrophilic outer structure. CDs can form inclusion complexes through the hydrophobic inner cavities with molecules that are physically compatible with the cavity size. The dynamic inclusion complexation abilities of CDs with low polarity organic compounds make them ideal materials in the fabrication of biomaterials augmenting the properties in various

applications. (27,28) To date, CDs have been employed in the fabrication of diverse hydrogel-based polymeric drug delivery systems, especially to modify the release kinetics. (29–32) While the overall hydrophilic nature of CDs increases the swelling state of the network structure, the hydrophobic inner core enables enhanced loading and prolonged/sustained release of hydrophobic therapeutic compounds.

In this contribution, we report on the synthesis of gelatin-based hydrogels incorporating β -cyclodextrin residues towards sustained drug release applications. Briefly, hydrogels were prepared via reacting gelatin amino groups with acrylate modified β -CD in aqueous buffer solutions (Figure 1). The method demonstrated a facile and efficient crosslinking process via aza-Michael addition of complementary functional precursors, which can be employed as an injectable gel-forming system. A series of hydrogels displaying tunable physical properties were obtained by changing the stoichiometric balance between gelatin amino groups and acrylate modified β -CD crosslinker. Drug loading and sustained release studies of fabricated hydrogels were investigated by using poorly water-soluble anti-inflammatory drug diclofenac sodium. The results indicated that the amount of drug loading and release profiles could be controlled by changing the β -CD crosslinker ratio. It is believed that the benign gelation methodology outlined here can be utilized in the design and synthesis of bulk and injectable hydrogels for tissue engineering, drug delivery, and various other biomaterial applications.

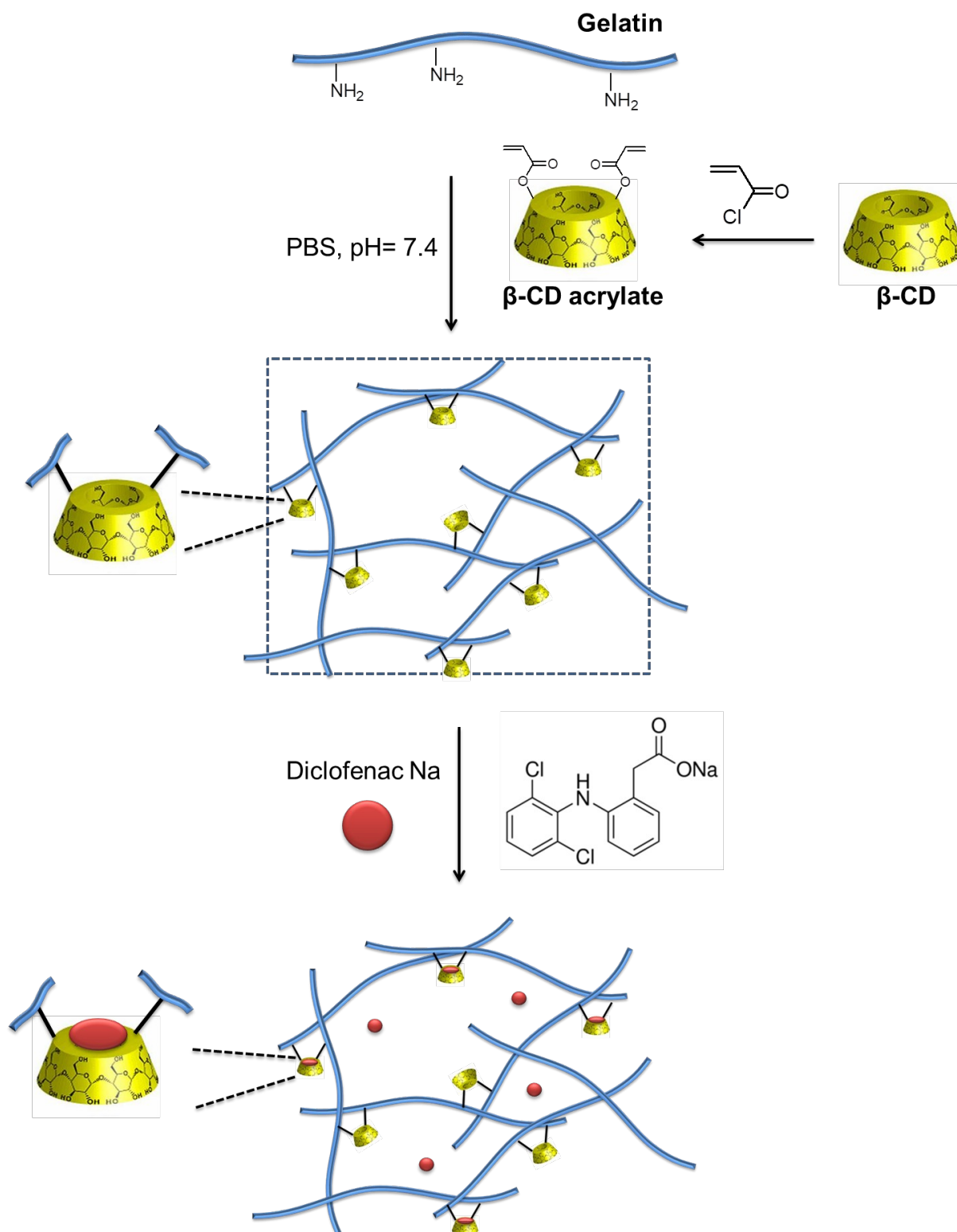


Figure 1. Schematic representation of the gelatin-based hydrogel synthesis with a β -CD-based crosslinker and the diclofenac Na loading into the hydrogel augmented by the inclusion complex formation.

EXPERIMENTAL SECTION

Materials and characterization

β -cyclodextrin, acryloyl chloride, diclofenac sodium salt, 1,8-diazabicyclo(5.4.0)undec-7-ene (DBU), gelatin from porcine skin (type A, 300 g bloom,

average M_n : 50.000-100.000 g/mol) were obtained from Aldrich Chemical Co. All solvents and inorganic materials were obtained from Merck Co. and used as received unless otherwise noted. Synthesis of acryloyl-modified β -cyclodextrin (β -CD-acrylate, the average degree of acetylation ~ 5.9

per molecule. Detailed synthesis procedure is given in Supporting Information) was carried out based on the reported procedure. (33) Characterization of β -CD acrylate was performed using ^1H NMR spectroscopy (Varian 400 MHz). Fourier-transform infrared spectroscopy analyses were conducted on a Nicolet 380 spectrometer. Scanning electron microscopy analysis was carried out using an ESEM-FEG/EDAX Philips XL-30 (Philips, Eindhoven, The Netherlands) instrument with 10 kV accelerating voltage. The rheological measurements were performed using an Anton Paar MCR 302 rheometer between 0.05-100 rad/s at 37 °C. UV-vis studies were carried out using a Varian Cary 50 Scan UV/Vis spectrophotometer.

Methods

Synthesis of gelatin-based β -CD incorporated hydrogels

In a vial, gelatin (100 mg) was placed and dissolved in 1 mL PBS buffer (phosphate-buffered saline, pH of 7.4) at 37 °C. In a separate vial, a pre-determined amount of β -CD-acrylate and DBU (0.1 molar equivalents to acrylate groups) were placed and dissolved in 200 μL of PBS solution. The two-ingredient solutions were thoroughly mixed and sonicated briefly. The mixture solution was heated at 37 °C for 6 h for a crosslinking reaction. After that, the resultant hydrogel was washed with distilled water several times to remove unreacted species. Dried hydrogels were obtained after the freeze-drying of water-swollen samples.

Equilibrium swelling ratios (ESRs)

Equilibrium swelling of hydrogels in distilled water was determined at 25 °C. 20 mg hydrogel was conditioned in distilled water, and the mass increase of sample as a function of time was recorded until a constant weight was attained. The percent swelling was determined using empirical equation 1:

$$\text{ESR (\%)} = (W_{\text{wet}} - W_{\text{dry}}) / W_{\text{dry}} \times 100 \quad (\text{Eq. 1})$$

The swelling tests were performed in triplicate for each sample, and average data with standard deviation was used for obtaining swelling curves.

Rheological characterization

The rheological properties of hydrogels were studied by dynamic oscillatory experiments at a constant 1

% strain. Loss (G'') and storage (G') moduli of disk-shaped water-equilibrated hydrogels were measured at 37 °C between 0.05 and 100 rad/s angular frequency. 8 mm diameter parallel plate was used for measurements and the plate distance was set to 2.0 mm.

Drug loading and release studies

Diclofenac-Na was loaded into the hydrogels by employing solution absorption. Briefly, 50 mg water-swollen gel sample was soaked in 0.5 wt.% drug solution in PBS (pH: 7.4). The hydrogel was incubated at 37 °C for 24 h, protected from light. Total drug loading was determined from the concentration difference between initial and final soaking solutions using a UV-Vis spectrophotometer (276 nm absorption maxima of diclofenac-Na in PBS solution).

Drug release profiles of hydrogels were investigated by immersing gel samples in 3 mL of PBS solution at 37 °C. Aliquots of the release medium (1 mL) were taken out and replaced with the new solution at pre-determined intervals. The total drug content in the collected medium was determined spectrophotometrically at 276 nm. The experiments were performed triplicate, and the release profiles were expressed in terms of cumulative release.

RESULTS AND DISCUSSION

Synthesis and characterization of gelatin-based β -CD containing hydrogels

Hydrogels composed of a gelatin matrix and distinct β -CD units were fabricated via amine-acrylate Michael addition of gelatin amino functionalities onto acryloyl groups of modified β -CD (Figure 2). Though it may vary depending on the source, the amino acid composition of gelatin mostly consists of glycine, proline, and hydroxyproline. Amine-containing lysine residues also constitute the structure of both bovine and porcine skin gelatin. (34) In chemical derivatization and modification of gelatin, amino groups of lysine have been exploited in reactions with isocyanates, (35) aldehydes, (36) vinyl sulfones(37), and genipin. (38) Towards the synthesis of gelatin-based hydrogels, reactive amino groups of amino acid chain strands were utilized in crosslinking reaction with activated carbonyls (39) as well as a modification with photo-curable acrylate functionalities. (26)

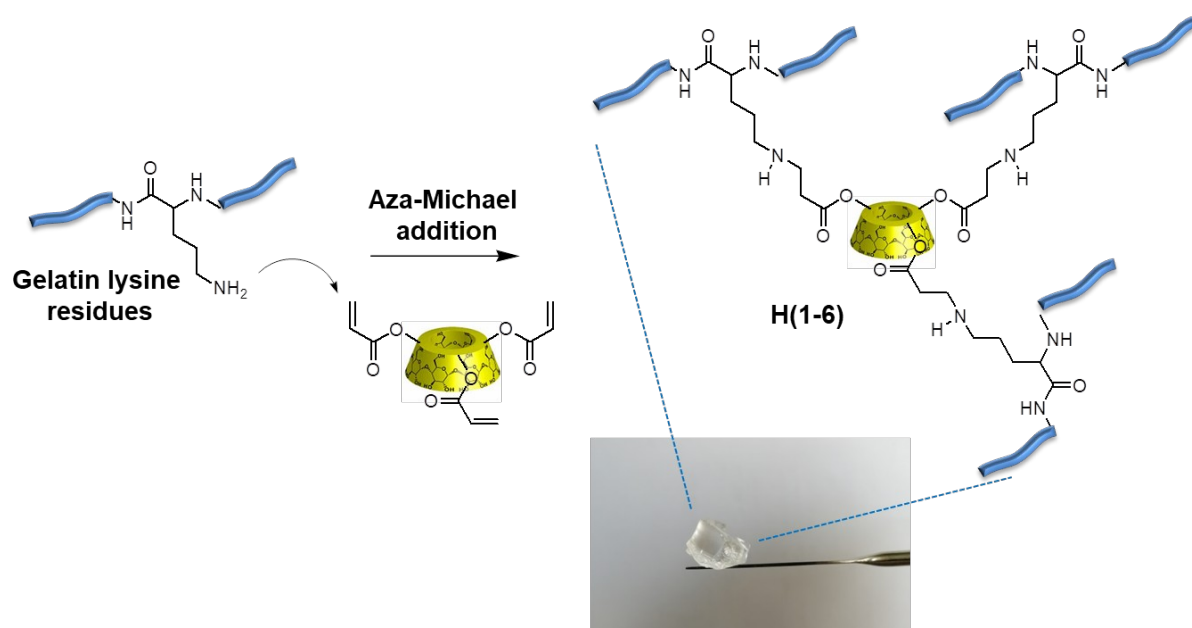


Figure 2. Crosslinking mechanism via multi-addition of gelatin amino groups onto acrylate functionalities of β -CD-acrylate. Representative picture of transparent hydrogel H-4.

A series of hydrogels composed of different β -CD-acrylate crosslinker ratio were synthesized in aqueous PBS buffer environment at 37 °C reaction temperature. Due to the multiple additions of amine groups onto acryloyl functionalities, relatively fast network formation was established within minutes. To ensure maximum available crosslinking, gelation reactions were continued for 6 h. Although the efficiency of the crosslinking process was prominent in uncatalyzed conditions (Table 1, Entry 1 and 2), gel formation was further promoted by using organo-catalysts DBU (Table 1, Entry 3-6). In aqueous conditions, β -CD is an efficient catalyst for aza-Michael addition of various amines onto electron-deficient carbonyls. (40) On the other hand, DBU possesses superior promotion of nitrogen

nucleophile reactivity towards α,β -unsaturated carbonyl compounds. (41)

A strong hydrogenation reaction was confirmed by FT-IR characterization of reaction ingredients and resulting hydrogels (Figure 3). The spectrum of β -CD-acrylate shows characteristic vibrations at 1720 cm^{-1} and 1664 cm^{-1} due to the stretchings of C=O and C=C, respectively. In the FT-IR spectrum of gelatin, typical amide peaks are resolved at 1639 cm^{-1} and 1535 cm^{-1} . The spectrum of hydrogel H-4 is characterized by the presence of the typical vibration peaks of both gelatin and β -CD-acrylate, demonstrating the structural integration of the hydrogelation components into the matrix network.

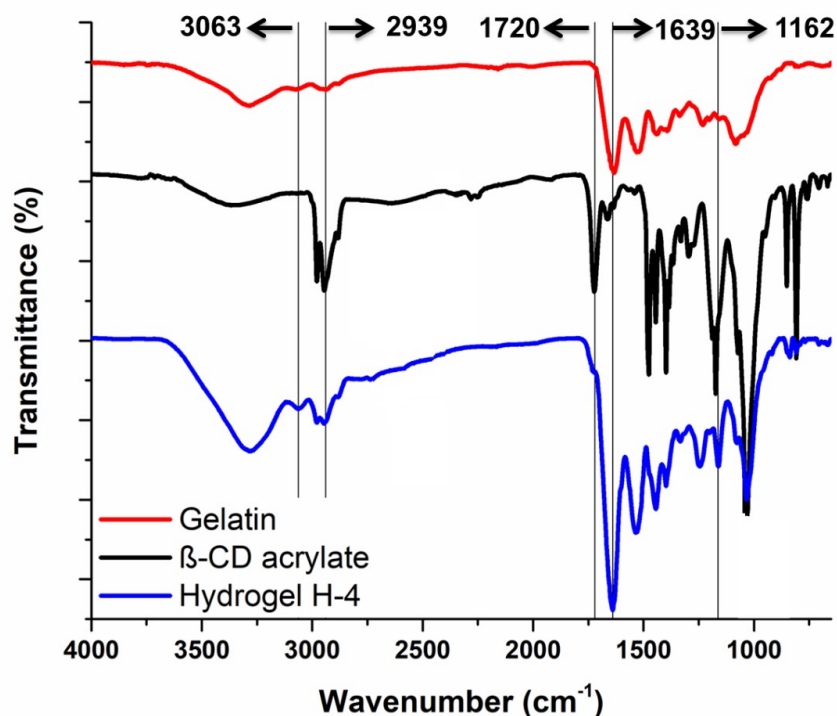


Figure 3. FT-IR structural analysis of gelatin, β -CD-acrylate, and hydrogel H-4.

The properties of fabricated hydrogels are summarized in Table 1. As expected, increased β -CD-acrylate feed in gel formulation resulted in higher gel conversions. The catalytic introduction of DBU in the gelation process has led to enhanced crosslinking efficiencies in different β -CD-acrylate

feeds. Obtained hydrogels are clear transparent samples in the water-swollen state (Figure 2). The morphological characterization of hydrogels using SEM analysis on freeze-dried samples revealed interconnected porous structures with varying pore sizes (Figure 4).

Table 1. Properties of hydrogels with varying gelatin / β -CD-Ac ratio.

Entry	Hydrogel ^a	Feed	Gel Conv. (%)	ESR ($\times 100\%$)	Drug Load (mg/g dry gel)
		Gelatin (mg) : β -CD-acrylate (mg)			
1	H-1	100.0 : 5.0	67	-	-
2	H-2	100.0 : 10.0	71	-	-
3	H-3	100.0 : 5.0	73	9.4 (± 2.7)	11.9 (± 4.4)
4	H-4	100.0 : 10.0	77	6.7 (± 2.1)	18.7 (± 5.8)
5	H-5	100.0 : 15.0	82	5.8 (± 1.8)	27.1 (± 5.3)
6	H-6	100.0 : 20.0	87	3.9 (± 1.3)	31.7 (± 7.4)

^a H-1 and H-2: No organo-catalyst; H (3-6): DBU catalystr.

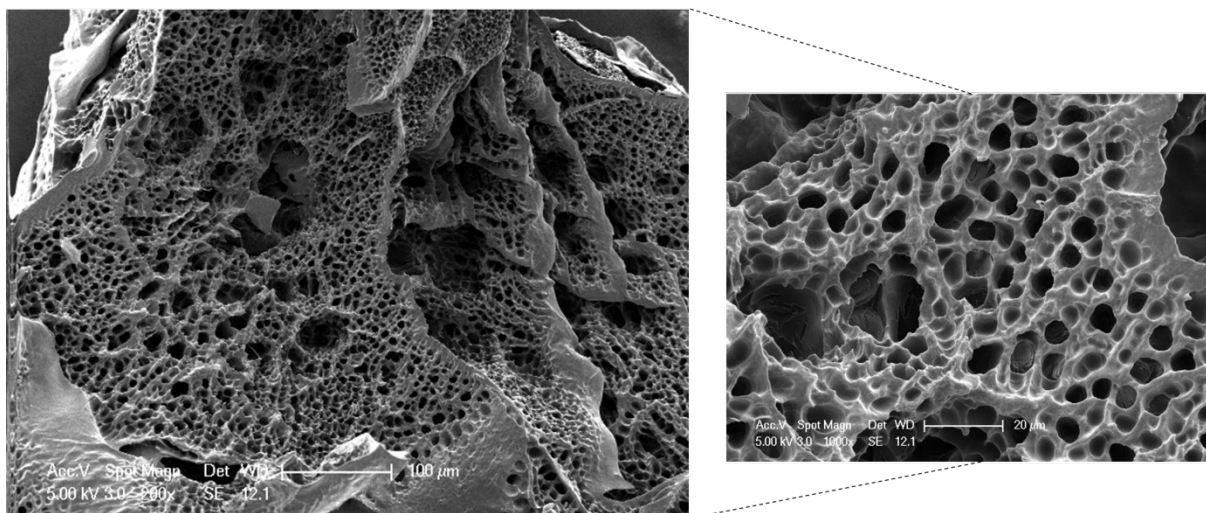


Figure 4. Representative SEM images of freeze-dried hydrogel H-4 with two different magnification (Scale bars: 100 μm for larger image and 20 μm for smaller image).

Equilibrium water uptake ratio of a hydrogel is an essential physical property in addressing gel mechanical properties, surface and network properties, and diffusion of solutes. (1) Though various parameters (i.e., pH, temperature) can contribute to ascertain the water uptake, maximum swelling is mostly related to the nature of polymer matrix and crosslinking degree. The swelling properties of the fabricated hydrogels were investigated in aqueous PBS conditions (pH: 7.4, 25 $^{\circ}\text{C}$). All the hydrogels displayed pronounced swelling degrees ($\sim 940\text{-}390\%$ to the mass of gel sample)

because of the hydrophilic groups present on the gelatin backbone and cyclodextrin crosslinker (Figure 5). Equilibrium water uptakes were reached in relatively short periods in applied experimental conditions. It was observed that hydrogels exhibit maximum water uptake dependency on the feed ratio of the gelatin matrix and $\beta\text{-CD}$ -acrylate crosslinker. Relatively higher maximum swelling degrees were observed in case of a lower crosslinker ratio in the feed. This can be attributed to higher free gel volumes and voids of network possessed by lower crosslinking degree.

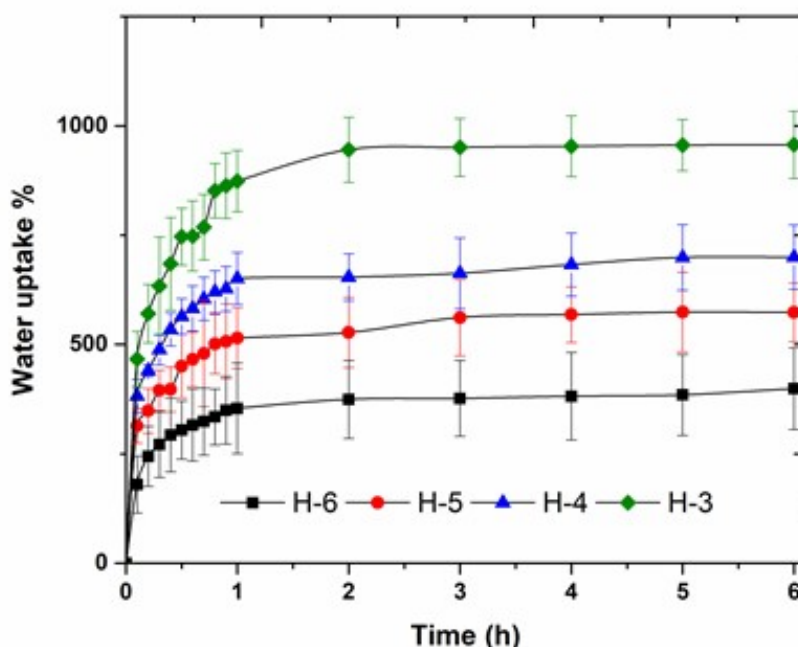


Figure 5. Equilibrium swelling profiles of gelatin-based $\beta\text{-CD}$ containing hydrogels in PBS buffer.

Hydrogel viscoelastic properties were examined via dynamic frequency scan analysis of prepared hydrogels at 37 $^{\circ}\text{C}$. The tests of hydrogels having different crosslinker ratios were performed at a

constant 1.0 % strain between 0.05-100 rad/s. As it can be seen in Figure 6, all samples exhibited permanent elastic character in the test frequency interval where storage moduli (G') were higher than

loss moduli (G''). According to the results, G' and G'' values of the samples show relatively low oscillation frequency dependency maintaining highly homogenous crosslinking of gel networks. (42) An increase in the ratio of β CD-based crosslinker has

resulted in higher moduli, which could be due to the increased network structure. The damping factors ($\tan \delta$, G''/G') of hydrogels were less than 1 in all cases representing the higher elastic character of networks over viscous behavior. (43)

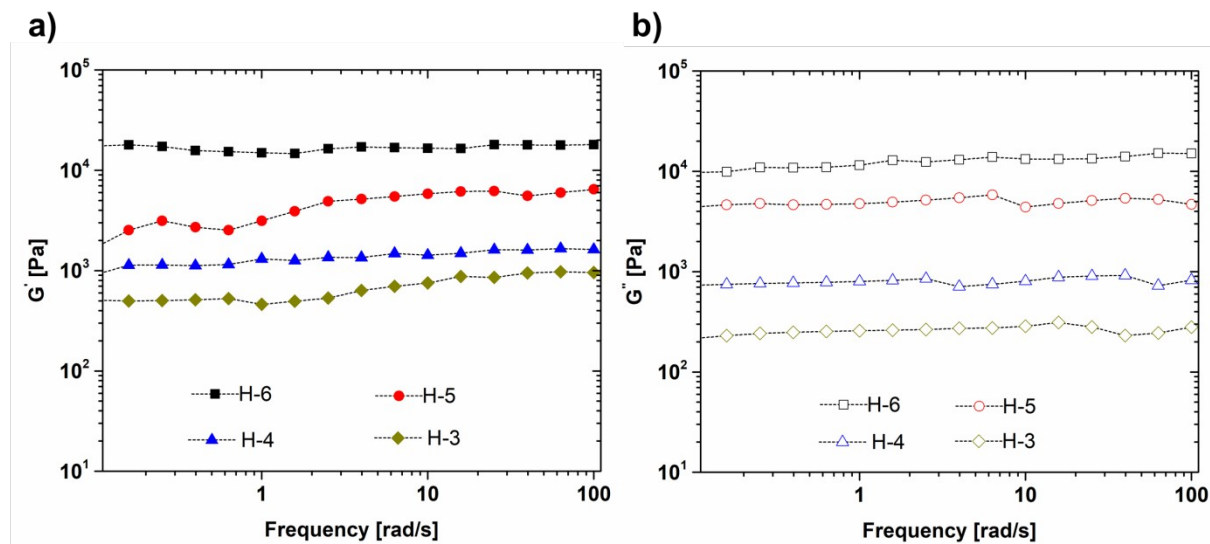


Figure 6. Dynamic frequency scan analysis of hydrogels: a) Storage and b) loss moduli.

Drug loading and release studies

Loading and sustained/controlled release of drugs, biomolecules, and other therapeutically relevant materials using hydrogels procure great potentials in realizing effective administration systems. The typical strategy for loading and release of drugs is based on the diffusion phenomena governed by weak interactions of the hydrogel matrix with subject molecules. In hydrogel networks that accommodate cyclodextrins as molecular buckets, inclusion complexation between hydrophobic molecules and cyclodextrins ensures another means of drug loading. Diclofenac-Na, widely used as a non-steroidal anti-inflammatory drug for various complaints and diseases, was employed as a model hydrophobic molecule to study the drug loading and release studies of fabricated hydrogels. It has been established that diclofenac-Na can form a molecular inclusion complex with β -cyclodextrin. (44) Hydrogels prepared as disk-shaped samples were loaded with the drug by solution absorption at 37 °C. 0.5 wt.% soaking solution was used for 24 h incubation, which is the required time to reach equilibrium as determined by UV-spectrophotometry. The drug loading efficiencies of hydrogels determined from the difference between initial and final soaking concentrations were given in Table 1. According to the results, the loaded drug amount increased from 11.9 (mg/g) to 31.7 (mg/g) for different hydrogels. A direct relation between crosslinker amount and drug levels was accounted for, where increased β -CD-acrylate crosslinker in the hydrogel resulted in considerably higher drug loading. The enhanced drug loading could be due to the higher available binding sites of cyclodextrin

cavities to complex with diclofenac-Na molecules. The inclusion complexation might have increased the solubility of slightly hydrophobic drug molecules within the hydrophilic gel network.

In vitro drug release profiles of the hydrogels containing different β -CD-acrylate crosslinker ratios were investigated in PBS buffer (pH: 7.4) at 37 °C. Initially, drug-loaded hydrogels taken from soaking solutions were gently washed with PBS buffer and then placed in the release medium. Aliquots of the release medium were taken out and replaced with the fresh solution at pre-determined intervals to resemble the physiological conditions. Time-dependent release profiles determined via UV-spectrophotometry were given in Figure 7. Overall, hydrogel H-3 having the lowest β -CD-acrylate, released its content faster than other hydrogels. An initial accelerated release was observed for all four hydrogels, which could be attributed to the burst removal of drug molecules present in the aqueous phase and adsorbed on the network matrix. (45) As expected, H-6 with the highest crosslinker content showed the lowest initial burst release and followed by H-4 and H-5. Incorporation of higher β -CD-acrylate caused a higher crosslinking degree of the network as well as enhanced drug/cyclodextrin complexation interactions, yielding slow diffusion of diclofenac-Na from the hydrogels. After the initial burst releases, all gelatin-based hydrogels exhibited sustained release profiles over a couple of days. In a specific time, relatively slower and lower total drug release from higher cyclodextrin content hydrogel could be ascribed to enhanced molecular inclusion interactions.

In an overall structure-property relationship of fabricated hydrogels, it was observed that the amount of β -CD content in the hydrogels maintained enhanced drug/matrix interactions. Hydrogel physical properties can also be manipulated by adjusting the crosslinking degrees, which of them are simply controlled by the stoichiometric ratios of

gelatin and β -CD-acrylate in gel formulations. The efficient covalent crosslinking reaction allows in situ gel formation that might improve the versatility of material to injectable drug release systems. One can suggest that the demonstrated approach could be utilized in the design and synthesis of hydrogel-based controlled/sustained drug delivery systems.

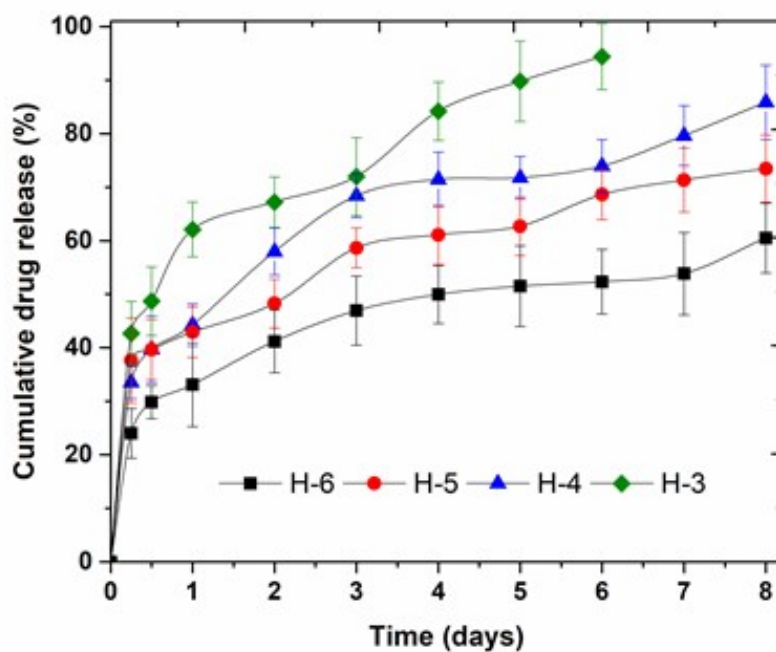


Figure 7. Cumulative release profiles of diclofenac-Na from gelatin-based β -CD containing hydrogels at 37 °C in PBS buffer (pH 7.4). Data with mean \pm SD (n=3).

CONCLUSION

A series of gelatin-based hydrogels incorporating β -CD units were fabricated under benign reaction conditions. Chemical crosslinking was established by utilizing unmodified pristine porcine gelatin via azo-Michael addition reaction. Practical and straightforward synthesis methodology allowed tunable control of the β -CD-based crosslinker amount in gel networks. It was shown that hydrogel physical properties could be tuned by adjusting the stoichiometry between amine and acrylate groups of precursor materials. The potential sustained drug release application of hydrogels was investigated by employing diclofenac-Na as a model hydrophobic molecule capable of inclusion complex formation with β -CD. The results suggested that the amount of β -CD content in the hydrogels maintained enhanced drug/matrix interactions leading to higher drug loading into the gel network. Lower initial burst releases and more sustained drug release for days was also attained in case of higher β -CD incorporation. It is believed that the efficient covalent crosslinking reaction demonstrated here could be utilized in the fabrication of biologically relevant gelatin and cyclodextrin based biomaterials.

REFERENCES

1. Peppas NA, Hilt JZ, Khademhosseini A, Langer R. Hydrogels in biology and medicine: From molecular principles to bionanotechnology. *Advanced Materials*. 2006. doi:10.1002/adma.200501612
2. Caló E, Khutoryanskiy V V. Biomedical applications of hydrogels: A review of patents and commercial products. *European Polymer Journal*. 2015. doi:10.1016/j.eurpolymj.2014.11.024
3. Hoffman AS. Hydrogels for biomedical applications. *Advanced Drug Delivery Reviews*. 2012. doi:10.1016/j.addr.2012.09.010
4. Lee KY, Mooney DJ. Hydrogels for tissue engineering. *Chemical Reviews*. 2001. doi:10.1021/cr000108x
5. Wang H, Heilshorn SC. Adaptable Hydrogel Networks with Reversible Linkages for Tissue Engineering. *Advanced Materials*. 2015. doi:10.1002/adma.201501558
6. Geckil H, Xu F, Zhang X, Moon S, Demirci U. Engineering hydrogels as extracellular matrix mimics. *Nanomedicine*. 2010. doi:10.2217/nmm.10.12
7. Li J, Mooney DJ. Designing hydrogels for controlled drug delivery. *Nature Reviews Materials*. 2016. doi:10.1038/natrevmats.2016.71

8. Qiu Y, Park K. Environment-sensitive hydrogels for drug delivery. *Advanced Drug Delivery Reviews*. 2012. doi:10.1016/j.addr.2012.09.024
9. Hoare TR, Kohane DS. Hydrogels in drug delivery: Progress and challenges. *Polymer*. 2008. doi:10.1016/j.polymer.2008.01.027
10. Yang JA, Yeom J, Hwang BW, Hoffman AS, Hahn SK. In situ-forming injectable hydrogels for regenerative medicine. *Progress in Polymer Science*. 2014. doi:10.1016/j.progpolymsci.2014.07.006
11. Yu L, Ding J. Injectable hydrogels as unique biomedical materials. *Chemical Society Reviews*. 2008. doi:10.1039/b713009k
12. Li Y, Rodrigues J, Tomás H. Injectable and biodegradable hydrogels: Gelation, biodegradation and biomedical applications. *Chemical Society Reviews*. 2012. doi:10.1039/c1cs15203c
13. Tiller JC. Increasing the local concentration of drugs by hydrogel formation. *Angewandte Chemie - International Edition*. 2003. doi:10.1002/anie.200301647
14. Cai S, Liu Y, Xiao ZS, Prestwich GD. Injectable glycosaminoglycan hydrogels for controlled release of human basic fibroblast growth factor. *Biomaterials*. 2005. doi:10.1016/j.biomaterials.2005.03.012
15. Paul A, Hasan A, Kindi H Al, Gaharwar AK, Rao VTS, Nikkhah M, et al. Injectable graphene oxide/hydrogel-based angiogenic gene delivery system for vasculogenesis and cardiac repair. *ACS Nano*. 2014. doi:10.1021/nn5020787
16. Yue K, Santiago GT, Tamayol A, Annabi N, Khademhosseini A, Hospital W, et al. Synthesis, properties, and biomedical applications of gelatin methacryloyl (GelMA) hydrogels. *Biomaterials*. 2016. doi:10.1016/j.biomaterials.2015.08.045.Synthesis
17. Olsen D, Yang C, Bodo M, Chang R, Leigh S, Baez J, et al. Recombinant collagen and gelatin for drug delivery. *Advanced Drug Delivery Reviews*. 2003. doi:10.1016/j.addr.2003.08.008
18. Yue K, Trujillo-de Santiago G, Alvarez MM, Tamayol A, Annabi N, Khademhosseini A. Synthesis, properties, and biomedical applications of gelatin methacryloyl (GelMA) hydrogels. *Biomaterials*. 2015. doi:10.1016/j.biomaterials.2015.08.045
19. Davidenko N, Schuster CF, Bax D V., Farndale RW, Hamaia S, Best SM, et al. Evaluation of cell binding to collagen and gelatin: a study of the effect of 2D and 3D architecture and surface chemistry. *J Mater Sci Mater Med*. 2016. doi:10.1007/s10856-016-5763-9
20. Gasperini L, Mano JF, Reis RL. Natural polymers for the microencapsulation of cells. *Journal of the Royal Society Interface*. 2014. doi:10.1098/rsif.2014.0817
21. Chen YC, Lin RZ, Qi H, Yang Y, Bae H, Melero-Martin JM, et al. Functional human vascular network generated in photocrosslinkable gelatin methacrylate hydrogels. *Advanced Functional Materials*. 2012. doi:10.1002/adfm.201101662
22. Pepelanova I, Kruppa K, Scheper T, Lavrentieva A. Gelatin-methacryloyl (GelMA) hydrogels with defined degree of functionalization as a versatile toolkit for 3D cell culture and extrusion bioprinting. *Bioengineering*. 2018. doi:10.3390/bioengineering5030055
23. Young S, Wong M, Tabata Y, Mikos AG. Gelatin as a delivery vehicle for the controlled release of bioactive molecules. *Journal of Controlled Release*. 2005. doi:10.1016/j.jconrel.2005.09.023
24. Draye JP, Delaey B, Van De Voorde A, Van Den Bulcke A, De Reu B, Schacht E. In vitro and in vivo biocompatibility of dextran dialdehyde cross-linked gelatin hydrogel films. *Biomaterials*. 1998. doi:10.1016/S0142-9612(98)00049-0
25. Koshy ST, Desai RM, Joly P, Li J, Bagrodia RK, Lewin SA, et al. Click-Crosslinked Injectable Gelatin Hydrogels. *Advanced Healthcare Materials*. 2016. doi:10.1002/adhm.201500757
26. Chen B, Hu X. An injectable composite gelatin hydrogel with pH response properties. *Journal of Nanomaterials*. 2017. doi:10.1155/2017/5139609
27. Arslan M, Sanyal R, Sanyal A. Cyclodextrin embedded covalently crosslinked networks: Synthesis and applications of hydrogels with nano-containers. *Polymer Chemistry*. 2020. doi:10.1039/c9py01679a
28. Arslan M, Sanyal R, Sanyal A. Cyclodextrin-containing hydrogel networks. In: Mishra M, editor. *Encyclopedia of Biomedical Polymers and Polymeric Biomaterials*. Taylor and Francis: New York; 2015. p. 2243-58. Available from: <https://www.taylorfrancis.com/books/e/9781466501799/chapters/10.1081%2FE-EBPP-120050543>
29. Arslan M, Aydin D, Degirmenci A, Sanyal A, Sanyal R. Embedding well-defined responsive hydrogels with nanocontainers: Tunable materials from telechelic polymers and cyclodextrins. *ACS Omega*. 2017. doi:10.1021/acsomega.7b00787
30. Arslan M, Gevrek TN, Sanyal A, Sanyal R. Cyclodextrin mediated polymer coupling via thiol-maleimide conjugation: Facile access to functionalizable hydrogels. *RSC Advances*. 2014. doi:10.1039/c4ra12408a
31. Arslan M, Gevrek TN, Sanyal R, Sanyal A. Fabrication of poly(ethylene glycol)-based cyclodextrin containing hydrogels via thiol-ene click reaction. *European Polymer Journal*. 2015. doi:10.1016/j.eurpolymj.2014.08.018
32. Arslan M, Yirmibesoglu T, Celebi M. In situ Crosslinkable Thiol-ene Hydrogels Based on PEGylated Chitosan and β -Cyclodextrin. *J. Turk. Chem. Soc., Sect. A: Chem.*, 2018, 5, 1327-1336.
33. Slavkova M Iv, Momekova DB, Kostova BD, Momekov G Tz, Petrov PD, *Bulgarian Chemical Communications*, 2017, Volume 49, Number 4, 792 - 799.
34. Hafidz RNRM, Yaakob CM, Amin I, Noorfaizan A. Chemical and functional properties of bovine and porcine skin gelatin. *Int Food Res J*. 2011.
35. Bertoldo M, Bronco S, Gragnoli T, Ciardelli F. Modification of gelatin by reaction with 1,6-diisocyanatohexane. *Macromol Biosci*. 2007. doi:10.1002/

mabi.200600215

36. De Carvalho RA, Grosso CRF. Characterization of gelatin based films modified with transglutaminase, glyoxal and formaldehyde. *Food Hydrocoll.* 2004. doi:10.1016/j.foodhyd.2003.10.005
37. Honda I, Arai K, Mitomo H. Characterization of cross-links introduced in gelatin. *J Appl Polym Sci.* 1997. doi:10.1002/(SICI)1097-4628(19970606)64:10<1879::AID-APP2>3.0.CO;2-F
38. Bigi A, Cojazzi G, Panzavolta S, Roveri N, Rubini K. Stabilization of gelatin films by crosslinking with genipin. *Biomaterials.* 2002. doi:10.1016/S0142-9612(02)00235-1
39. Liu C, Zhang Z, Liu X, Ni X, Li J. Gelatin-based hydrogels with β -cyclodextrin as a dual functional component for enhanced drug loading and controlled release. *RSC Advances.* 2013. doi:10.1039/c3ra42532k
40. Surendra K, Krishnaveni NS, Sridhar R, Rao KR. β -Cyclodextrin promoted aza-Michael addition of amines to conjugated alkenes in water. *Tetrahedron Letters.* 2006. doi:10.1016/j.tetlet.2006.01.124
41. Yeom CE, Kim MJ, Kim BM. 1,8-Diazabicyclo[5.4.0]undec-7-ene (DBU)-promoted efficient and versatile aza-Michael addition. *Tetrahedron.* 2007. doi:10.1016/j.tet.2006.11.037
42. Siemoneit U, Schmitt C, Alvarez-Lorenzo C, Luzardo A, Otero-Espinar F, Concheiro A, et al. Acrylic/cyclodextrin hydrogels with enhanced drug loading and sustained release capability. *Int J Pharm.* 2006. doi:10.1016/j.ijpharm.2005.12.046
43. Jin R, Moreira Teixeira LS, Dijkstra PJ, Karperien M, van Blitterswijk CA, Zhong ZY, et al. Injectable chitosan-based hydrogels for cartilage tissue engineering. *Biomaterials.* 2009. doi:10.1016/j.biomaterials.2009.01.020
44. Das S, Subuddhi U. Studies on the complexation of diclofenac sodium with β -cyclodextrin: Influence of method of preparation. *J Mol Struct.* 2015. doi:10.1016/j.molstruc.2015.07.001
45. Huang X, Brazel CS. On the importance and mechanisms of burst release in matrix-controlled drug delivery systems. *Journal of Controlled Release.* 2001. doi:10.1016/S0168-3659(01)00248-6

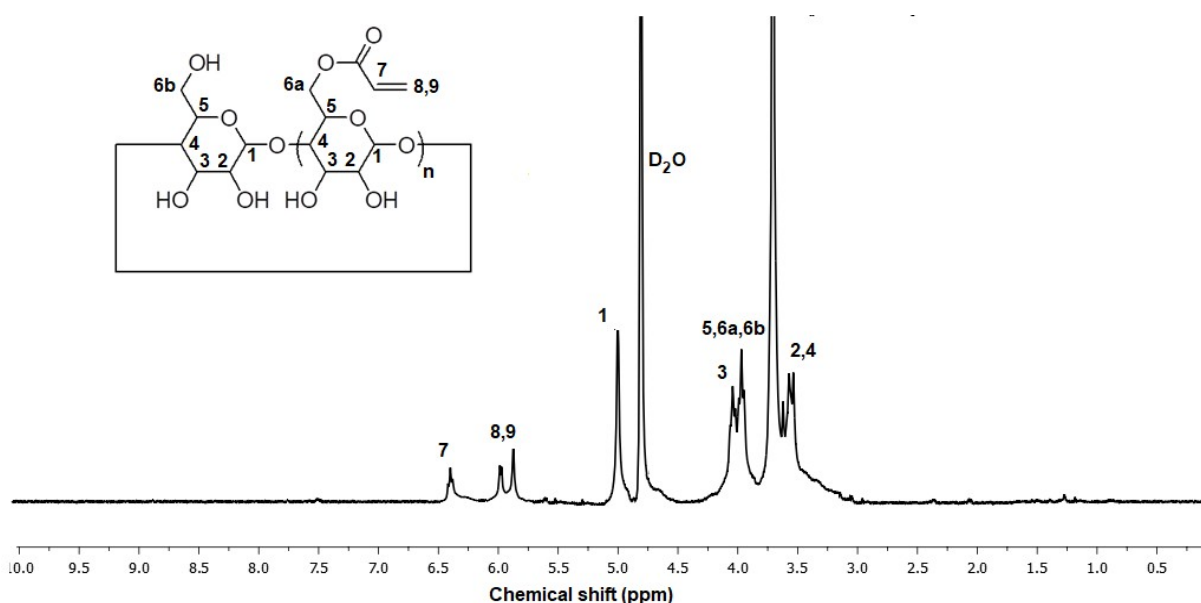
SUPPORTING INFORMATION

In situ Crosslinking System of Gelatin with Acrylated β -cyclodextrin Towards the Fabrication of Hydrogels for Sustained Drug Release

Mehmet Arslan

University of Yalova, Faculty of Engineering, Department of Polymer Materials Engineering, 77200, Yalova, Turkey.

Synthesis of Acryloyl-modified β -cyclodextrin (β -CD-acrylate): Synthesis of the β -CD-acrylate was conducted by following a previously reported procedure. (1) β -CD (1.0 g, 0.88 mmol) previously dried by lyophilization, and triethylamine (0.5 mL, 6.16 mmol) were dissolved in 10 mL dry dimethylformamide. The mixture was cooled to 0 °C in an ice bath and acryloyl chloride (0.85 mL, 6.16 mmol) was added dropwise. The reaction was continued for 16 h at room temperature. After the reaction was complete, a white precipitate was removed by filtration. The purified product was obtained by precipitation of the mixture into cold acetone and filtration (Yield: 41%). The structure of the compound is consistent with the reported literature data (Figure S1). Degree of acetylation based on peak integrals of H1 protons at 5.03 ppm and vinyl protons at 5.82 - 6.40 ppm revealed average degree of acetylation \sim 5.9 per molecule.



References:

1. Slavkova M Iv, Momekova DB, Kostova BD, Momekov G Tz, Petrov PD, *Bulgarian Chemical Communications*, 2017, Volume 49, Number 4, 792 - 799.



A comprehensive study on electrospinning of poly (vinyl alcohol): effects of the TCD, applied voltage, flow rate, and solution concentration

Gokhan Acik*  

Piri Reis University, Faculty of Science and Letters, Department of Chemistry, Tuzla, TR-34940 Istanbul, Turkey

Abstract: In the present work, the electrospun fibers of poly (vinyl alcohol) (PVA) are fabricated from its solution in water under ambient conditions, and the effect of altered working parameters used such as tip-to-collector distance (TCD), applied voltage, flow rate and solution concentration on the average diameter and frequency distribution of them is deeply discussed. The mean electrospun PVA fiber diameters and its distributions are estimated by a combination of the Scanning electron microscope (SEM) and the ImageJ analyzer program, which is extensively utilized in respective sciences. The achieved results from the experiments indicate that higher both TCD and applied voltage used decrease the average electrospun PVA fiber diameter. Conversely, when the flow rate or solution concentration is increased, diameters of achieved fibers are soared. It is anticipated that this comprehensive study will be beneficial to academia and industry working on potential PVA fiber applications.

Keywords: electrospinning; poly (vinyl alcohol); scanning electron microscope; working parameters.

Submitted: May 22, 2020. **Accepted:** June 11, 2020.

Cite this: Acik G. A comprehensive study on electrospinning of poly (vinyl alcohol): effects of the TCD, applied voltage, flow rate, and solution concentration. JOTCSA. 2020;7(2):609–16.

DOI: <https://doi.org/10.18596/jotcsa.741452>.

***Corresponding author.** E-mail: (gacik@pirireis.edu.tr), Tel: (+90 216 581 00 50/1665), Fax: (+90 216 581 0051).

INTRODUCTION

To date, with the increasing global interest, considerable research efforts have been generated aiming at the production of fibers of both natural or synthetic polymers and inorganic materials for a remarkable range of application areas such as chemistry, medicine, material science, nanotechnology, textile, and so on (1-8). In this respect, the most well-known fiber production methods mentioned in the literature are mechanical drawing, self-assembly, hydrothermal processing, electrospinning, melt blowing, phase separation, template synthesis, extraction, vapor-phase polymerization, and solvent casting (7, 9). Among them, especially, electrospinning process, which can be applied as the spinning of the wet or dry solution, melt at elevated temperatures, gel, and emulsion has emerged as an efficient, affordable, and most extensively utilized method. A typical relatively simple electrospinning instrument setup

consists of a metallic nozzle, syringe pump, voltage supply, and collector (screen or roller) apparatus for making fibers with diameters ranging from few nanometers to a few hundred nanometers. Generally, the setup is designed for feeding ranging from $\mu\text{L}\cdot\text{h}^{-1}$ to $\text{mL}\cdot\text{min}^{-1}$ and making 0–40 kV voltage value over distances of 0–40 cm between the nozzle and collector. During the experiments, after the voltage is imposed, the polymer droplet that emerged on the nozzle is transformed into a conical shape (known as Taylor cone) via potential difference formed. The continuously elongated polymeric jet that is ejected from the pendant droplet by overcoming the surface tension of the spinning solution reaches the collector while the solvent is evaporated. Many types of electrospinning parameters such as TCD distance, applied voltage, flow rate and needle diameter (process parameters), the solvent used, concentration, viscosity and conductivity of the solution, molecular weight, solubility, glass-transition temperature,

chain entanglement density of polymer (molecular parameters), relative humidity, pressure and temperature of surrounding (ambient parameters) can strongly influence the various properties and structure of the final product (10). Producing the long lengths fibers, providing the higher surface area to volume ratio and superior mechanical properties, and allowing the functionalization and tunable surface morphologies are some of the advantages that it provides. Moreover, the electrospinning process offers many advantages due to its ease controllability, economic competitiveness, and versatility in broad range potential fields such as biosensor technology, enzyme immobilization, optoelectronics, filtration, tissue engineering, drug delivery, wound dressings, self-cleaning, environmental remediation, and etc (11).

PVA is biodegradable and biocompatible, semicrystalline and water-soluble industrial polymer, and is available as entirely (91-99%), moderately (92-96%) or partially (87-89%) hydrolyzed forms produced by sequential polymerization of vinyl acetate monomer and hydrolysis of achieved poly (vinyl acetate) (PVAc). Depending on its hydrolysis degree, the mechanical, chemical, and physical properties of PVA, such as rigidity, tensile strength, flexibility, solubility, crystallinity, and biodegradability are in a wide range (9, 12). As an FDA-approved material, PVA based products have been in use for advanced widespread industrial, commercial, food, and medical applications, including textile, paper, antimicrobial packaging, tissue engineering, wound dressing, contact lenses, and drug delivery on account of its excellent features (13-15). Hence, PVA has piqued the interest of industry and academia for many years due to the information mentioned above. Furthermore, PVA aqueous solution can be easily prepared and electrospun; thus, the present comprehensive study will be promising for the scientists working on different PVA fiber applications.

This study aims to demonstrate the influence of a variety of electrospinning parameters on the average diameter and frequency distribution of electrospun PVA fibers to create a detailed database for scientists and industry workers. The morphological analysis of PVA fibers was studied through scanning electron microscopy and accurate image processing.

EXPERIMENTAL SECTION

Materials

During the experiments, the utilized commercially available fully hydrolyzed Poly (vinyl alcohol) (PVA, $M_w = 60,000 \text{ g.mol}^{-1}$) was purchased from Merck (Darmstadt, Germany). To prepare the PVA electrospinning solutions, water (H_2O , ultrapure grade) procured from Merck (Steinheim, Germany)

was used. Rectangular microscope cover glasses used as fiber accumulated substrate (3×1 inch) were supplied from ISOLAB (Istanbul, Turkey). No necessary purification and distillation procedures were implemented for all chemicals and solvents used.

Preparation of electrospinning solutions

Commercially available, fully hydrolyzed PVA was dissolved in distilled H_2O by vigorously stirring on a magnetic stirrer at $60 \text{ }^\circ\text{C}$ for 3 h to obtain 11, 13, and 15% (w/w) solutions to be used in the electrospinning process for determining the effect of solution concentration.

Electrospinning procedure of PVA

To fabricate the electrospun fibers of PVA achieved previously from its solutions at different concentrations, a transparent chamber of electrospinning setup equipped with a syringe pump (NE-500, New Era Pump Systems Inc., Turkey), a high voltage power source (ElectroSis, PW1010, Turkey). A 5 mL plastic syringe with metal needle and rectangular microscope cover glasses, which are cleaned two times with chromic acid solution-distilled water cycle, having 3×1 inch dimensions stuck aluminum plate collector was utilized. To conduct the detailed investigation on the effect of different parameters on electrospinning, 15, 20 and 25 kV are applied on PVA solutions at 11, 13 and 15% concentrations when they are fed by 0.6, 1.0 and 1.4 mL.h^{-1} rates fixed to 7, 10 and 13 cm TCDs, separately. During the experiments, relative humidity and temperature were 41% and $24.1 \text{ }^\circ\text{C}$ and almost constant. After conducting the electrospinning experiments, electrospun fiber coated glasses were kept in a desiccator to remove the residual H_2O for 72 h at room temperature to be used for SEM analysis. Electrospinning time was 5 min for all experiments.

Characterizations

Surface morphologies and characteristics of each PVA fibers obtained by using different electrospinning parameters were examined with the help of scanning electron microscopy (SEM, at 10.0 kV, JEOL JSM-6335F, Tokyo, Japan, after coating with Pt (Platin) by sputter coater device (Polaron SC7620, East Sussex, United Kingdom). The average diameters and histograms of fibers were determined to utilize Image J processing software application (National Institutes of Health; USA).

RESULTS AND DISCUSSION

The electrospinning variables influencing the full range of features of the fibers have motivated the investigators in many types of research for use in diverse applications (16, 17). In our study, electrospinning parameters mentioned elsewhere in the literature were changed; a variety of optimum spinning conditions were utilized to achieve the

smooth and uniform PVA fibers without the free beads. Some SEM images selected were presented in Figures (a)-(e) to provide seeing the micrometer scale, unimodal, cylindrical, and beadless structure and smooth surface of the achieved PVA fibers to readers. As can be easily seen from the $\times 2,500$ and $10,000$ zoomed SEM images, while the flow rate and solution concentration fixed, if the applied voltage or TCD is increased to higher values, it is visibly evident that average diameter of the obtained fibers decreases to lower, as expected. Moreover, the obtained PVA fiber structures were almost the same in these conditions.

The primary purpose of this study was to provide researchers with a comprehensive overview of how several electrospinning parameters would affect the average fiber diameters of PVA fibers and their distribution. In this respect, the detailed Table 1 and some selected histograms (Figures 2(a)-(e)) were presented.

The effect of polymer solution concentration on the diameter of electrospun fibers has been studied in the literature by several groups. Indeed, the uniaxial stretching of a charged jet, which can strongly be affected by the solution concentration mentioned in the Introduction part, is the essential phenomenon in the electrospinning technique. Based on the literature results, it is well-known that the increasing solution concentration caused to an increase in solution viscosity and formation of uniform fibers after the critical chain entanglement value, and increasing average diameter of fibers as well (18, 19). Firstly the effect of solution concentration on the average diameter of electrospun PVA fibers was investigated, and PVA solution concentration was varied from 11 to 15% (w/w). After the solution concentration was increased from 11 to 13 or 15%, the mean diameter of PVA fibers gradually was increased. The obtained results were in good agreement with the literature, as tabulated in Table 1 (20).

As stated in previous information, feeding or flow rate is another parameter that affected the resulted

average diameter of fibers in the electrospinning process. Higher flow rate produces fibers with relatively larger diameter or vice versa due to the formation of a higher accumulated amount of suspended droplet on the spinneret that can lead to insufficient time to elongation of polymer chains (21). In our study, the flow rate was varied in the range of 0.6 and 1.4 mL.h^{-1} . One can see in Table 1, after the used flow rate was increased, the mean diameter of electrospun PVA fibers was increased, supporting the above-stated results achieved from concentration changes.

The reverse influences solution concentration and flow rate effects were obtained by altering both TCD and applied voltage parameters. The prevention of bead formation and adjusting the fiber diameter can be taken control by selecting the optimal TCD providing adequate time to complete solvent evaporation from the fibers before reaching the collector (19). As can be seen in Figures 1(a)-(e) and 2(a)-(e), and Table 1 as well, while the electrospinning TCD changed from 7 to 13 cm , the mean PVA fiber diameter decreased probably due to the reason mentioned above. On the other hand, the applied voltage that is known as driving force to jet initiation during electrospinning was the other examined parameter for solution electrospinning of PVA. In this respect, in our present study, PVA solution having different either concentrations and feed rates or varied TCD was electrospun with 15 , 20 , or 25 kV applied voltage. The average diameter of all the electrospun fibers achieved as uniform without bead formation decreased gradually with the increasing applied voltage from 15 to 25 kV , supporting the trend of mean diameter change when the TCD increased from 7 to 13 cm . These applied voltage changing results combined with the TCD alteration results were attributable to producing ultrafine or nanofibers resulting from higher electrostatic force to stretch the jet during electrospinning. Also, the observed results were in good agreement with the literature, as expected (22).

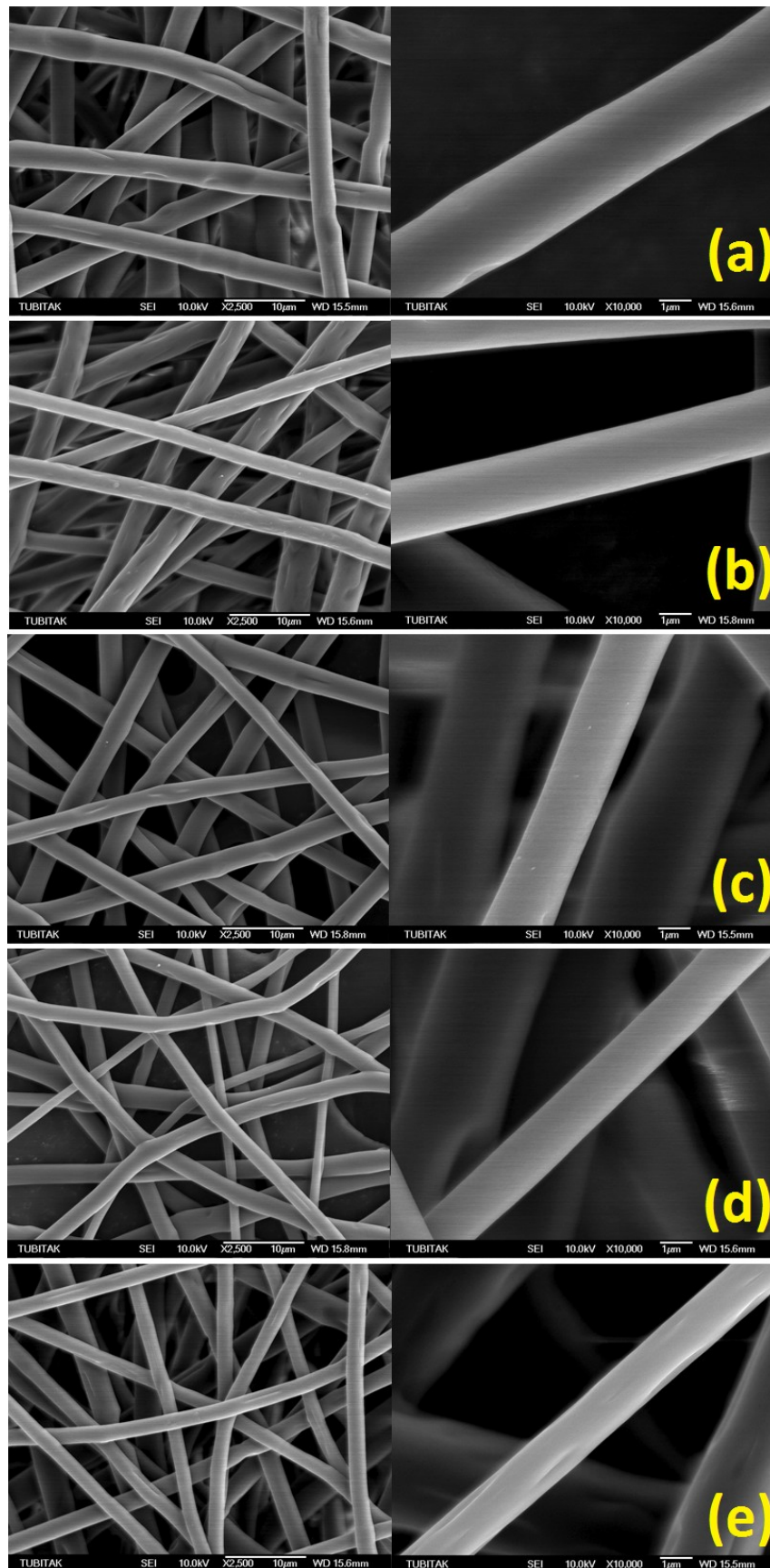


Figure 1. The SEM images (left, $\times 2,500$) and their magnified micrographs (right, $\times 10,000$) of electrospun PVA fibers obtained from $1 \text{ mL} \cdot \text{h}^{-1}$ flow rate, 13% (w/w) solution concentration, (a) 15 kV (7 cm TCD) (b) 20 kV (7 cm TCD) (c) 25 kV (7 cm TCD) (d) 25 kV (10 cm TCD) (e) 25 kV (13 cm TCD) applied voltages.

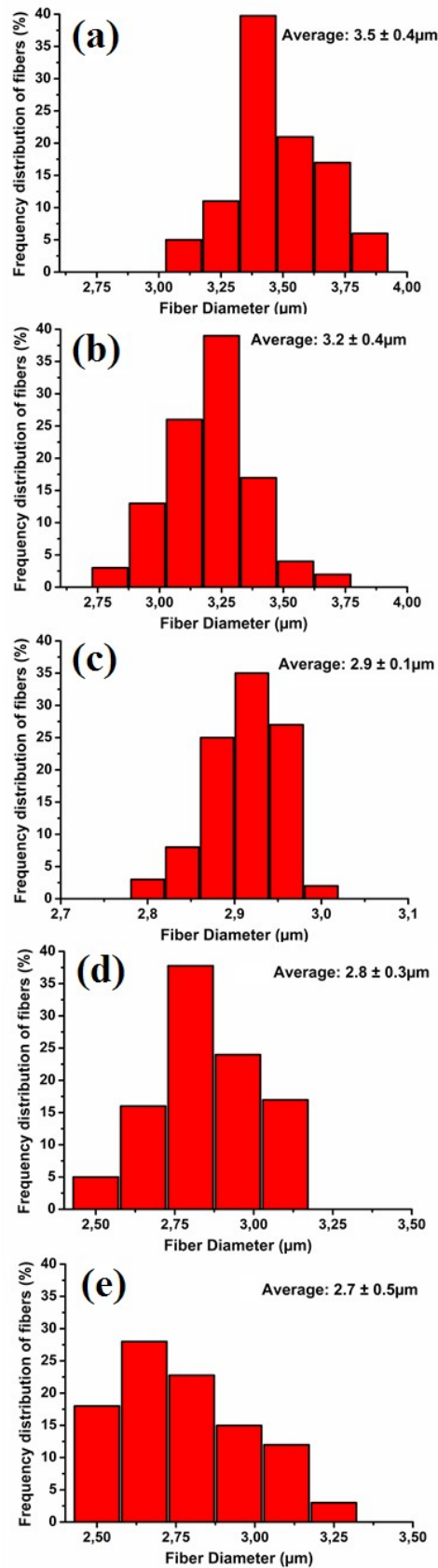


Figure 2. Frequency distribution and average diameter histograms of electrospun PVA fibers obtained from $1 \text{ mL} \cdot \text{h}^{-1}$ flow rate, 13% (w/w) solution concentration, (a) 15 kV (7 cm TCD) (b) 20 kV (7 cm TCD) (c) 25 kV (7 cm TCD) (d) 25 kV (10 cm TCD) (e) 25 kV (13 cm TCD) applied voltages.

Table 1. The data of experiments carried out at each variable of tip-to-collector distance, solution concentration, applied voltage, and solution flow rate.

Experiment No	Tip-to-Collector Distance, x= 7, 10 and 13 (cm)			Average Fiber Diameter \pm std dev. (μm)		
	Solution Conc. (%w/w)	Applied Voltage (kV)	Solution Flow Rate ($\text{mL}\cdot\text{h}^{-1}$)	x=7cm	x=10cm	x=13cm
1	11	15	0.6	3.1 \pm 0.3	3.0 \pm 0.1	2.9 \pm 0.7
2	11	15	1.0	3.1 \pm 0.5	3.0 \pm 0.5	3.0 \pm 0.1
3	11	15	1.4	3.1 \pm 0.9	3.1 \pm 0.4	3.0 \pm 0.9
4	11	20	0.6	2.9 \pm 0.4	2.7 \pm 0.1	2.6 \pm 0.8
5	11	20	1.0	2.9 \pm 0.9	2.9 \pm 0.2	2.8 \pm 0.8
6	11	20	1.4	3.0 \pm 1.0	3.0 \pm 0.6	2.9 \pm 0.9
7	11	25	0.6	2.7 \pm 0.5	2.6 \pm 0.9	2.4 \pm 0.2
8	11	25	1.0	2.8 \pm 0.1	2.7 \pm 0.7	2.6 \pm 0.7
9	11	25	1.4	2.8 \pm 0.5	2.9 \pm 0.5	2.9 \pm 0.1
10	13	15	0.6	3.4 \pm 0.3	3.2 \pm 0.3	3.1 \pm 0.1
11	13	15	1.0	3.5 \pm 0.4	3.4 \pm 0.6	3.2 \pm 0.4
12	13	15	1.4	3.6 \pm 0.3	3.4 \pm 0.2	3.3 \pm 0.3
13	13	20	0.6	3.0 \pm 0.4	2.9 \pm 0.3	2.8 \pm 0.3
14	13	20	1.0	3.2 \pm 0.4	3.1 \pm 0.5	2.9 \pm 0.4
15	13	20	1.4	3.3 \pm 0.4	3.2 \pm 0.3	3.1 \pm 0.6
16	13	25	0.6	2.8 \pm 0.2	2.7 \pm 0.3	2.5 \pm 0.3
17	13	25	1.0	2.9 \pm 0.1	2.8 \pm 0.3	2.7 \pm 0.5
18	13	25	1.4	3.0 \pm 0.5	2.9 \pm 0.1	2.8 \pm 0.7
19	15	15	0.6	3.6 \pm 0.5	3.5 \pm 0.4	3.3 \pm 0.5
20	15	15	1.0	3.7 \pm 0.4	3.6 \pm 0.3	3.5 \pm 0.3
21	15	15	1.4	3.8 \pm 0.3	3.6 \pm 0.7	3.6 \pm 0.1
22	15	20	0.6	3.4 \pm 0.5	3.2 \pm 0.5	3.1 \pm 0.3
23	15	20	1.0	3.4 \pm 0.8	3.3 \pm 0.7	3.2 \pm 0.1
24	15	20	1.4	3.6 \pm 0.4	3.6 \pm 0.8	3.5 \pm 0.9
25	15	25	0.6	3.1 \pm 0.3	2.9 \pm 0.3	2.8 \pm 0.1
26	15	25	1.0	3.2 \pm 0.5	3.1 \pm 0.7	3.1 \pm 0.2
27	15	25	1.4	3.2 \pm 0.8	3.2 \pm 0.2	3.1 \pm 0.9

CONCLUSION

In this study, the influence of electrospinning parameters such as polymer solution concentration, solution flow rate, tip-to-collector distance, and applied voltage was investigated deeply for the electrospun PVA fiber morphology, frequency distribution, and average diameter by conducting 27 separate experiments. Fiber properties such as fiber mean diameter, morphology, frequency distribution, etc. can be fully controlled with an appropriate combination of process, solution, and environmental parameters in the electrospinning process for the desired functions. The effect of these different variables on the resulted PVA fibers was tried to be explained logically by correlating with the previously published electrospinning literature papers. Depending on the attained results from the present comprehensive study, PVA fibers thus offer many attributions to scientists working on PVA fiber applications.

FUNDING

This research did not receive any specific grant from funding agencies in the public, commercial, or not-for-profit sectors.

CONFLICT OF INTEREST

The authors declare that they have no known competing financial interests or personal relationships that could have appeared to influence the work reported in this paper.

REFERENCES

1. Sankar S, Sharma CS, Rath SN, Ramakrishna S. Electrospun fibers for recruitment and differentiation of stem cells in regenerative medicine. *Biotechnology journal*. 2017;12(12):1700263.

2. Lee C-G, Javed H, Zhang D, Kim J-H, Westerhoff P, Li Q, et al. Porous electrospun fibers embedding TiO₂ for adsorption and photocatalytic degradation of water pollutants. *Environmental science & technology*. 2018;52(7):4285-93.
3. Dzenis Y. Spinning continuous fibers for nanotechnology. *Science*. 2004;304(5679):1917-9.
4. Toshniwal L, Fan Q, Ugbohue SC. Dyeable polypropylene fibers via nanotechnology. *Journal of applied polymer science*. 2007;106(1):706-11.
5. Sanjay M, Arpitha G, Naik LL, Gopalakrishna K, Yogesha B. Applications of natural fibers and its composites: An overview. *Natural Resources*. 2016;7(3):108-14.
6. Neves A, Bointon TH, Melo L, Russo S, De Schrijver I, Craciun MF, et al. Transparent conductive graphene textile fibers. *Scientific reports*. 2015;5:9866.
7. Acik G, Kamaci M, Cansoy CE. Superhydrophobic EVA copolymer fibers: the impact of chemical composition on wettability and photophysical properties. *Colloid and Polymer Science*. 2018;296(11):1759-66.
8. AÇIK G, Kamaci M, ÖZATA B, ÖZEN CANSOY CE. Effect of polyvinyl alcohol/chitosan blend ratios on morphological, optical, and thermal properties of electrospun nanofibers. *Turkish Journal of Chemistry*. 2019;43(1).
9. Teixeira MA, Amorim MTP, Felgueiras HP. Poly (Vinyl Alcohol)-Based Nanofibrous Electrospun Scaffolds for Tissue Engineering Applications. *Polymers*. 2020;12(1):7.
10. Cui W, Li X, Zhou S, Weng J. Investigation on process parameters of electrospinning system through orthogonal experimental design. *Journal of applied polymer science*. 2007;103(5):3105-12.
11. Acik G, Altinkok C. Polypropylene microfibers via solution electrospinning under ambient conditions. *Journal of Applied Polymer Science*. 2019;136(45):48199.
12. Chahal S, Kumar A, Hussian FSJ. Development of biomimetic electrospun polymeric biomaterials for bone tissue engineering. A review. *Journal of Biomaterials Science, Polymer Edition*. 2019;30(14):1308-55.
13. Arslan M, Acik G, Tasdelen MA. The emerging applications of click chemistry reactions in the modification of industrial polymers. *Polymer Chemistry*. 2019;10(28):3806-21.
14. Yu Z, Li B, Chu J, Zhang P. Silica in situ enhanced PVA/chitosan biodegradable films for food packages. *Carbohydrate polymers*. 2018;184:214-20.
15. Liu B, Xu H, Zhao H, Liu W, Zhao L, Li Y. Preparation and characterization of intelligent starch/PVA films for simultaneous colorimetric indication and antimicrobial activity for food packaging applications. *Carbohydrate polymers*. 2017;157:842-9.
16. Lin J, Ding B, Yang J, Yu J, Sun G. Subtle regulation of the micro- and nanostructures of electrospun polystyrene fibers and their application in oil absorption. *Nanoscale*. 2012;4(1):176-82.
17. Huang L, Bui NN, Manickam SS, McCutcheon JR. Controlling electrospun nanofiber morphology and mechanical properties using humidity. *Journal of polymer science part B: Polymer physics*. 2011;49(24):1734-44.
18. Oliveira JE, Mattoso LH, Orts WJ, Medeiros ES. Structural and morphological characterization of micro and nanofibers produced by electrospinning and solution blow spinning: a comparative study. *Advances in Materials Science and Engineering*. 2013;2013.
19. Shao H, Fang J, Wang H, Lin T. Effect of electrospinning parameters and polymer concentrations on mechanical-to-electrical energy conversion of randomly-oriented electrospun poly (vinylidene fluoride) nanofiber mats. *RSC advances*. 2015;5(19):14345-50.

20. Motamedi AS, Mirzadeh H, Hajiesmaeilbaigi F, Bagheri-Khoulenjani S, Shokrgozar M. Effect of electrospinning parameters on morphological properties of PVDF nanofibrous scaffolds. *Progress in biomaterials*. 2017;6(3):113-23.
21. Zong X, Kim K, Fang D, Ran S, Hsiao BS, Chu B. Structure and process relationship of electrospun bioabsorbable nanofiber membranes. *Polymer*. 2002;43(16):4403-12.
22. Liu Y, Dong L, Fan J, Wang R, Yu JY. Effect of applied voltage on diameter and morphology of ultrafine fibers in bubble electrospinning. *Journal of Applied Polymer Science*. 2011;120(1):592-8.



Antioxidant and Anticholinesterase Properties of *Sideritis perfoliata* subsp. *athoa* (Papan. & Kokkini) Baden and *Sideritis trojana* Bornm. Teas from Mount Ida-Turkey and Their Phenolic Characterization by LC-MS/MS

Sema CARIKCI*  

*Izmir Democracy University, Vocational School, 35140, Izmir, Turkey

Abstract: The phenolic profile, antioxidant, and anticholinesterase activities of teas prepared from two *Sideritis* (L.) species: *Sideritis perfoliata* subsp. *athoa* (Papan. & Kokkini) Baden and *Sideritis trojana* Bornm., collected from Mount Ida (Kaz Dağı) Turkey, were determined. The teas were prepared by infusion and decoction methods. The quantitative amounts of the phenolic contents were determined by liquid chromatography-tandem mass spectrometry (LC-MS/MS). The significant phytochemicals were found to be fumaric acid for infusion and decoction samples of *S. trojana* and infusion of *S. perfoliata* subsp. *athoa*, chlorogenic acid for decoction of *S. perfoliata* subsp. *athoa*. The tea samples prepared by the decoction method were found to be rich in phenolics. Apart from the fact that the decoction sample of *S. trojana* exhibited the best antioxidant effect in 2,2-diphenyl-1-picrylhydrazyl (DPPH), β -carotene bleaching and cupric (Cu^{2+}) ion reducing power assay (CUPRAC) methods among the tested samples at all concentrations, and showed significant inhibition effect at 200 $\mu\text{g}/\text{mL}$ against acetylcholinesterase and butyrylcholinesterase enzymes (59.74%, 64.99%, respectively).

Keywords: *Sideritis*, *Sideritis perfoliata* subsp. *athoa* (Papan. & Kokkini) Baden, *Sideritis trojana* Bornm., Antioxidant activity, Anticholinesterase activity, Phenolics.

Submitted: April 11, 2020. **Accepted:** June 15, 2020.

Cite this: CARIKCI S. Antioxidant and Anticholinesterase Properties of *Sideritis perfoliata* subsp. *athoa* (Papan. & Kokkini) Baden and *Sideritis trojana* Bornm. Teas from Mount Ida-Turkey and Their Phenolic Characterization by LC-MS/MS. JOTCSA. 2020;7(2):617–32.

DOI: <https://doi.org/10.18596/jotcsa.718274>.

*Corresponding author. E-mail: sema.carikci@idu.edu.tr. Tel:+90 232 2621001. Fax:+90 232 2621004.

INTRODUCTION

For centuries, herbal teas have been used as herbal remedies to treat infections, ailments, and diseases. For the usage as a health-promoting beverage, the evaluation of the functional and bioactive composition of the tea, such as polyphenols, carotenoids, vitamin C, vitamin E, as well as essential major, minor, and trace elements are essential. Some studies have been reported their antioxidative, antimicrobial, anticarcinogenic, antihypertensive, antimutagenic, and antiangiogenic activities. These activities have shown that they are related to different bioactive components included in herbal teas (1–4).

The antioxidant activity is based on the availability of electrons to neutralize any free radicals. Phenolic compounds are known to be antioxidant compounds. The antioxidant activity of plants is attributed mainly to their phenolic compounds (1,3–4). Alzheimer's disease (AD) is the most common form of dementia. In addition to synthetic drugs, the treatment of this disease has gained significant importance with natural treatments. Therefore, finding natural sources to inhibit acetylcholinesterase (AChE) and butyrylcholinesterase (BChE), which AD begins as a deficiency in the production of the neurotransmitter acetylcholine inhibitors, has been the subject of many studies recently.

The genus *Sideritis* (L.), a member of the Lamiaceae plant family, is distributed mainly in the Mediterranean area over 150 annual and perennial species (5,6). In Turkey, as well as in the world, *Sideritis* species is very widely consumed as herbal tea and has been used in folk medicine for their activities such as anti-inflammatory, antirheumatic, antispasmodic, and antimicrobial (7-11). In Turkey, the genus *Sideritis* is divided into three sections (Hesiodia, Burgsdorfia, and Empedoclia), and Turkey is the gene center of the Empedoclia section (5). They represented 46 species (52 taxa) with a very high endemism ratio (almost 80%) (9). Most of the studies carried on *Sideritis* species are focused on their bioactive constituents; essential oils, diterpenoids, glycosides- and activities of their extracts, and isolated pure compounds (1,3,6-13). Although they have been used as a tea for a long time, the studies of aqueous extracts of the genus *Sideritis* have recently become more popular. Traditionally, *Sideritis* teas are prepared via the infusion method using flowering branches of the plant. The studies showed that the main chemicals of the infusions are composed of water-soluble polyphenolic compounds, many of which have related to their potent antioxidant properties, also minerals and vitamins. The phytochemical composition and several activities of some *Sideritis* tea; *Sideritis scardica*, *S. raeseri*, *S. syriaca*, and *S. clandestina* subsp. *clandestina* have been reported previously (1,3,15-17).

Mount Ida, which is one of the wealthiest mountains concerning rareness and endemic species, is located

between Balıkesir and Canakkale boundaries in Turkey. *Sideritis perfoliata* subsp. *athoa* (Papan. & Kokkini) Baden., and *S. trojana* Bornm. are grown at Mount Ida. *S. trojana* is an endemic species, widely known as "Sarıköz çayı" and *S. perfoliata* subsp. *athoa* is known as "Kedi kuyruğu çayı". The teas prepared from both species are widely consumed with a view to its distinctive flavor and possible pharmacological effects such as common cold, including fever, flu, and bronchitis, and to relieve gastric disorders (18). Both species have been investigated for their essential oil, diterpenoids, and glycoside composition, and several activities in some studies (Table 1). There is no study on the detailed phenolic composition and anticholinesterase activity of teas prepared from *S. trojana* and *S. perfoliata* subsp. *athoa*.

The objective of the present study is to determine phenolic composition as well as antioxidant and anticholinesterase activity of the *S. trojana* and *S. perfoliata* subsp. *athoa* herbal teas. Two methods were used to prepare tea samples: infusion and decoction. The determined phenolic contents, divided of mainly three groups: flavonoids and derivatives, phenolic acids, and dicarboxylic acid, were screened by LC-MS/MS. Antioxidant properties were determined based on 2,2-diphenyl-1-picrylhydrazyl (DPPH), β -carotene linoleic acid, and cupric (Cu²⁺) ion reducing power assay (CUPRAC). The anticholinesterase activity was also evaluated. This study is the first one on the phenolic composition and activity of the *S. trojana* and *S. perfoliata* subsp. *athoa* herbal teas.

Table 1. Previous studies on *S. trojana* and *S. perfoliata* subsp. *athoa*.

	<i>S. trojana</i>	<i>S. perfoliata</i> subsp. <i>athoa</i>
Major comp. of Essential oil (EO)	β -pinene α -pinene (19) Valeranone α -bisabolol β -caryophyllene (20)	Myrcene β -pinene Ar-curcumene (25)
Diterpenoids	7- <i>epi</i> -Candicandiol Siderol Sideridiol Isocandol B Candol A acetate <i>Ent</i> -7 α -acetoxo-kaur-15-ene <i>Ent</i> -7 α -acetoxo-15 β ,16 β -epoxy-kaurane (7-Acetyl-sideroxol) <i>Ent</i> -2 α -hydroxy-8(14),15-pimaradiene (21)	Linearol Foliol Sidol <i>Ent</i> -3 β ,7 α -dihydroxy-kaur-16-ene <i>Ent</i> -7 α ,18-dihydroxy-beyer-15-ene 7- <i>epi</i> -Candicandiol <i>Ent</i> -3 β -hydroxy-kaur-16-ene Athonolone <i>Ent</i> -3 α ,18-dihydroxy-kaur-16-ene (26, 27)
Phenolics, Flavonoids and derivatives	Melittoside 10- <i>O</i> -(<i>E</i>)-feruloylmelittoside 10- <i>O</i> -(<i>E</i>)- <i>p</i> -coumaroylmelittoside Stachyoside E Stachyoside G Verbascoside	

	Isoacteoside Lamalboside Leonoside A Isolavandulifolioside Isoscutellarein 7-O-[6'''-O-acetyl- β -alloypyranosyl-(1 \rightarrow 2)]- β -glucopyranoside 4'-O-Methylisoscuteallarein 7-O-[6'''-O-acetyl- β -alloypyranosyl-(1 \rightarrow 2)]- β -glucopyranoside 3'-Hydroxy-4'-O-methylisoscuteallarein 7-O-[6'''-O-acetyl- β -alloypyranosyl-(1 \rightarrow 2)]- β -glucopyranoside Di-O-methylcrenatin (22)	
Activity	Antistress (23) Antimicrobial activity of EO (20) Antioxidant and antidiabetic activity (24)	<i>Candida albicans</i> Inhibitory (28) Insecticidal (29)

MATERIALS AND METHODS

General

LC-MS/MS experiments were performed by a Zivak® HPLC and Zivak® Tandem Gold Triple quadrupole (Istanbul, Turkey) mass spectrometry, equipped with a Synergy Max C18 column (250 x 2 mm i.d., 5- μ m particle size). The compounds used as standards in LC-MS/MS analyses and the experimental details are given in the supplementary data. For the antioxidant and anticholinesterase activities, absorbances (UV and visible range of 230 nm to 750 nm) were measured using a multiplate reader (Beckman Coulter DTX 880 Multimode Detector).

Plant Material

Sideritis perfoliata subsp. *athoa* (Papan. & Kokkini) Baden. were collected from natural habitats in B1, Balıkesir-Edremit, Mount Ida (Kazdağı, Kapıdağ), around the fire tower, rocky areas, 1350 m altitude, July 2013, Turkey (herbarium number TD 3805).

Sideritis trojana Bornm., originated in Balıkesir-Edremit, Mount Ida, near Sarıkız hill, limestone rocks, 1750 m altitude, July 2013, Turkey (herbarium number TD 3818). The species were identified by Prof. Dr. Tuncay Dirmenci (Balıkesir University), voucher specimens have been deposited at Balıkesir University Necatibey Education Faculty Herbarium. The plant samples were allowed to dry in the shade.

Preparation of decoction and infusion samples

Herbal teas were prepared as following the traditional preparation method: infusion and decoction.

Infusion: Two grams of the dried aerial parts of the plant were added in a beaker which contained 100 mL of distilled boiled water and allowed to stay for 15 minutes. Then it was filtered through Whatman No.1 filters (Sigma-Aldrich). The filtrate (25 mL) was diluted with 25 mL of distilled water.

Decoction: Two grams of the dried aerial parts of the plant were added to 100 mL of distilled water in a beaker and brought to boiling. After the boiling was stopped, the mixture was left for 15 min and filtered. The filtrate (25 mL) was diluted with 25 mL of distilled water.

Infusion samples were named as **SPAI** (infusion sample of *S. perfoliata* subsp. *athoa* (Papan. & Kokkini) Baden.) and **STI** (infusion sample of *S. trojana* Bornm.), decoction was **SPAD** (decoction sample of *S. perfoliata* subsp. *athoa* (Papan. & Kokkini) Baden.) and **STD** (decoction sample of *S. trojana* Bornm.).

Antioxidant Activities

The antioxidant activity was evaluated using in vitro the free radical scavenging activity using 2,2-diphenyl-1-picrylhydrazyl (DPPH \cdot) (DPPH assay) (30), β -carotene-linoleic acid model system (31) and CUPRAC (32). BHT (butylated hydroxytoluene) and BHA (butylated hydroxyanisole) were used as standards in DPPH and β -carotene-linoleic acid assay. In CUPRAC assay ethanol was used as a negative control; whereas curcumin was used as a positive control. A detailed experimental procedure for the activity studies were given in the supplementary data.

Anticholinesterase activity

For the measurement of anticholinesterase activity, inhibition of AChE and BChE were measured by the slightly modified spectrophotometric method developed by Ellman, Courtney, Andres, and Featherston (33). A detailed procedure was given in supplementary material.

LC-MS/MS experiments

In the LC-MS/MS experiments the mobile phase was composed of water (A, 0.1 % formic acid) in methanol (B, 0.1 % formic acid), the gradient program of which was 0-1.00 minute 55 % A and 45

% B, 1.01-20.00 minutes 100 % B and finally 20.01-23.00 55 % A and 45 % B. The flow rate of the mobile phase was 0.25 mL/min, and the column temperature was set to 30 °C. The injection volume was 10 µL.

The mobile phase was composed to be a gradient of acidified methanol and water system because of its fragmented ion stability. The optimum ESI (Electrospray Ionization) parameters were identical to those described in the recent study (13-14). Detailed information, validation of experiments and uncertainty evaluation is given in supplementary data.

Preparation of test solution for LC-MS/MS

A one mL of each sample was added 4 mL of the ethanol-water mixture (50:50 v/v). A portion of 1 mL of this stock solution was transferred into a 5 mL

of another volumetric flask, and 50 mL of curcumin solution was added as internal standard and diluted to the volume with methanol and mixed. The solution was filtered through a 0.45 µm Millipore Millex-HV filter and the final solution (1 mL) was transferred into a capped auto sampler vial and 10 mL of sample was injected to LC for each run. The samples in the auto sampler were kept at 15 °C during the experiment.

Statistical Analysis

In both antioxidant and anticholinesterase activity tests, the experimental data were calculated as the mean ± standard deviation and analyzed. Variance ANOVA was studied, including one-way analysis. Significant differences between means were recorded by Duncan's multiple range tests. $p < 0.05$ was regarded as significant, and $p < 0.01$ was very significant.

RESULTS AND DISCUSSION

Table 2. Phenolic composition of *Sideritis trojana* and *S. perfoliata* subsp. *athoa*

Flavonoids and derivatives				
	SPAI	SPAD	STI	STD
Rutin (1)	1.64±0.11	-	1.70±0.11	-
Quercitrin (2)	-	15.17±0.97	-	-
Apigenin (3)	-	-	12.17±0.98	16.61±1.34
Penduletin (4)	16.73±1.7	58.53±5.93	2.92±0.3	59.30±6.01
Quercetagenin-3,6-dimethylether (5)	110.87±20.76	-	-	27.32±5.12
Luteolin-7-O-glucoside (6)	7.34±0.37	22.26±2.27	-	1.84±0.19
Luteolin-5-O-glucoside (7)	-	4.60±0.3	-	-
Pelargonin (8)	7.30±0.37		46.21±2.35	47.86±4.87
Total (mg/kg)	143.88	100.56	63.00	152.93
Phenolic acids				
p-Coumaric acid (9)	2.65±0.41	-	-	-
Caffeic acid (10)	34.65±6.86	28.36±5.61	22.89±4.53	15.53±3.07
t-Ferulic acid (11)	201.26±14.06	-	107.32±7.5	-
Chlorogenic acid (12)	205.28±28.43	210.89±29.2	18.20±2.52	184.86±25.6
Rosmarinic acid (13)	3.94±0.3	3.73±0.29	4.19±0.32	4.57±0.35
Gallic acid (14)	4.65±0.32	4.55±0.32	4.63±0.32	4.54±0.31
Syringic acid (15)	-	2.92±0.2	-	28.80±1.94
Total (mg/kg)	452.43	250.945	157.23	218.30
Dicarboxylic acid				
Fumaric acid (16)	281.06±19.49	206.49±14.32	310.62±21.54	462.14±32.05
Total (mg/kg)	281.06	206.49	310.62	462.14
Total (mg/kg)	877.37	557.50	530.85	853.37

Major compounds of the extracts showed as **bold**.

Phenolic Profile

The characterization of the phenolic components of decoction and infusion samples of *S. perfoliata* subsp. *athoa* and *S. trojana* was achieved by LC/MS

analysis. The results were given in Table 2. In the tea samples, around 10 to 12 phenolic compounds were determined. *S. perfoliata* subsp. *athoa* was found to be rich in phenolic acids, whereas *S.*

trojana was rich in dicarboxylic acid. SPAI was found to be the richest in terms quantity (877.37 mg/kg) and numbers of determined components (12 phenolic compounds).

Fumaric acid was the main component for the infusion sample of *Sideritis perfoliata* subsp. *athoa*, infusion sample of *S. trojana* (STI) and decoction sample of *S. trojana* (STD) (281.06, 310.62, 462.14 mg/kg, respectively). For decoction sample of *S. perfoliata* subsp. *athoa* (SPAD), chlorogenic acid was determined as the main component (210.89 mg/kg). The three main components for tea samples were determined as follows: fumaric acid, chlorogenic acid, t-ferulic acid for SPAI; chlorogenic acid, fumaric acid, penduletin for SPAD; fumaric acid, t-ferulic acid, pelargonin for STI and fumaric acid, chlorogenic acid, penduletin for STD. It was previously shown that *Sideritis* extracts, especially methanolic, were rich in phenylpropanoids like verbascoside and martinoside; flavones like apigenin and penduletin; and flavone glucosides like isoscutellarein and hypolaetin (12,13,34–36). In the aqueous extract, in addition to these compounds, mainly chlorogenic acid, ferulic acid, cinnamic acid, and caffeic acid, were determined (3,15,37,35). The results are consistent with previous studies.

Antioxidant and Anticholinesterase Activities

Since a higher correlation between phenolics and antioxidant activity has been demonstrated by several studies in aromatic and medicinal plants (39–42), there is a growing interest in phenolic compounds and flavonoids, which are the most widely occurring chemicals in plants having strong antioxidant properties. Due to the toxic effect of synthetic derivatives humans prefer taking these compounds supplied by nutritional sources such as fruits, vegetables, and herbal tea, which have high phenolic content and good antioxidant capacity.

Antioxidant activities of teas were determined according to three methods: DPPH, β -carotene, and CUPRAC. The results are given in Table 3. For DPPH and β -carotene, the activity tests were carried on four different concentrations: at 10 $\mu\text{g/mL}$, 25 $\mu\text{g/mL}$, 50 $\mu\text{g/mL}$, 100 $\mu\text{g/mL}$. In the DPPH method, for all concentrations, SPAI, SPAD, and STD showed very high radical scavenging activity (up to 60%), while STI had relatively lower activity. STI has showed the best inhibition activity at a concentration of 100 $\mu\text{g/mL}$ with 42.34%, while BHA was 62.39% and BHT was 80.82%.

Considering that these three tea samples are rich in fumaric acid and chlorogenic acid, it can be said that these compounds are responsible for the significant antioxidant activity of the teas. Most studies on phenolic contents of herbal teas showed that the antioxidant activity of the teas could be attributed to the presence of phenolic compounds. Notably, the antioxidant capacities of the teas having chlorogenic

acid were found to be reasonably high (3,43,44). Although it is not a phenolic compound, fumaric acid is a compound commonly detected in plant extracts, and plants carrying this compound at a high amount have been found to exhibit high antimicrobial and antioxidant activity (14,45). Furthermore, in the β -carotene-linoleic acid method, the SPAI has had the best activity value, like the standard BHA. In the CUPRAC, $\text{TEAC}_{\text{CUPRAC}}$ values of the teas were calculated by using curcumin as a reference. $\text{TEAC}_{\text{CUPRAC}}$ of curcumin was found as 0.9 mmol TR g^{-1} (in Trolox mM equivalents of 1 mM antioxidant solution which studied). The tea samples prepared by the decoction method were showed higher activity (for SPAD 2.21 mmol TR g^{-1} and for STD 2.23 mmol TR g^{-1}), while the lowest activity was showed by STI (0.43 mmol TR g^{-1}), which was the lowest tea sample in terms of total phenolic content (Table 3).

The anticholinesterase activities of the tea samples were determined at a concentration of 200 $\mu\text{g/mL}$, and inhibition % values were calculated against AChE and BChE activities. The results are given in Table 4. AChE and BChE were inhibited by galantamine, which was used as a standard, at a rate of 86% and 77%, respectively. Among the tea samples, the best inhibition values against the AChE enzyme were shown by STD of 59.74% and SPAI of 58.30%. For the BChE enzyme, the results were similar. STD and SPAI had the best inhibition values; 64.99% and 53.60%, respectively. STI has the lowest inhibition against both enzymes. Although the antioxidant activities of the tea samples resulted from their high phenolic acid contents, Orhan et al., (2007) (46) reported that there was no correlation between AChE and BChE enzyme inhibition with phenolic contents. They had reported that some of these compounds are not inhibitor for AChE and BChE. Rather than phenolic acids, flavonoid derivatives such as quercetin, genistein, luteolin-7-O-rutinoside were found to be more effective inhibitors. If the flavonoid content of the tea samples were compared, it was found that STD and SPAI samples with higher flavonoid content (in total 152.93 and 143.88 mg/kg, respectively) were showed higher enzyme inhibition. STI, with the lowest amount of flavonoid content, has the lowest inhibition. These results are consistent with the literature.

		Table 3. Activity results of SPA and ST.			
		10 µg/mL	25 µg/mL	50 µg/mL	100 µg/mL
DPPH (Inhibition %)	SPAD	68.92±0.70	68.98±0.68	62.78±0.65	65.83±0.30
	STD	69.38±0.93	68.47±0.40	65.92±0.90	62.98±1.20
	SPAI	66.25±0.72	67.31±2.70	64.73±2.54	62.33±1.24
	STI	4.88±0.84	4.99±1.18	8.85±2.63	42.34±3.26
	BHA	22.75±2.15	30.97±4.14	48.17±3.94	62.39±2.99
	BHT	73.09±2.62	77.68±0.74	78.79±0.76	80.82±1.56
β-carotene- linoleic acid (Inhibition %)	SPAD	53.44±1.55	61.27±1.12	59.25±0.67	47.82±0.23
	STD	70.47±1.55	69.88±2.13	66.34±2.15	54.83±2.55
	SPAI	39.96±2.6	85.87±0.46	70.49±3.77	76.95±0.54
	STI	5.77±1.45	68.38±6.47	54.72±1.73	62.24±2.58
	BHA	81.90±1.95	85.54±1.73	85.98±2.42	79.54±4.13
	BHT	82.56±5.03	72.38±11.8	77.12±2.93	71.02±1.01
CUPRAC		mmol TR/g			
	SPAD	2.21			
	STD	2.53			
	SPAI	1.43			
	STI	0.43			
	Curcumin	0.90			

Table 4 Anticholinesterase Activity of *S. trojana* and *S. perfoliata* subsp. *athoa*

Tea Samples	Anticholinesterase Activity	
	AChE	BChE
SPAI	58.30 ± 0.48	53.60 ± 0.33
SPAD	46.82 ± 0.74	32.40 ± 0.22
STI	30.06 ± 0.67	22.78 ± 0.04
STD	59.74 ± 0.80	64.99 ± 0.36
Galantamine	86.73 ± 1.25	77.13 ± 1.48

% inhibition values at 200 µg/mL concentration of tea samples.

Galantamine was used as a standard.

CONCLUSION

In conclusion, *Sideritis perfoliata* subsp. *athoa* and *S. trojana* were found as a crucial antioxidant source in different *in vitro* tests like DPPH, β -carotene linoleic acid, and CUPRAC assays. Also, they have the best inhibition results on two enzymes, which have essential roles in Alzheimer's Disease. The quantities of some phenolics of the infusion and decoction of *S. perfoliata* subsp. *athoa* and *S. trojana* were successfully characterized by LC-MS/MS, and chlorogenic acid, t-ferulic acid, penduletin, and fumaric acid were determined as the most abundant chemicals for tea samples. The antioxidant and anticholinesterase activities of the *S. perfoliata* subsp. *athoa* and *S. trojana* were probably their phenolic and flavonoid composition. Furthermore, the activity could be attributed to the possible synergistic interaction between phenolic and non-phenolic components in its chemical composition. According to the results, it can be said that *S. trojana* and *S. perfoliata* subsp. *athoa* can be used as a supportive food for an antioxidant source for daily take.

Supplementary data

Method validation parameters of LC-MS/MS measurements, standards chromatogram of secondary metabolites, structures of the determined phenolics and procedures of biological activity assays can be found in the Supplementary Information section of this document.

Conflict of interest

The author declares no competing financial interest.

Funding

This research did not receive any specific grant from funding agencies in the public, commercial, or not-for-profit sectors.

REFERENCES

1. Irakli M, Tsifodimou K, Sarrou E, Chatzopoulou P. Optimization Infusions Conditions for Improving Phenolic Content and Antioxidant Activity in *Sideritis scardica* Tea Using Response Surface Methodology. *J Appl Res Med Aromat Plants*. 2018;8:67-74.
2. Silveira TFF da, Meinhart AD, Ballus CA, Godoy HT. The Effect of the Duration of Infusion, Temperature, and Water Volume on the Rutin Content in the Preparation of Mate Tea Beverages: An Optimization Study. *Food Res Int*. 2014;60:241-5.
3. Goulas V, Exarchou V, Kanetis L, Gerothanassis IP. Evaluation of the Phytochemical Content, Antioxidant Activity and Antimicrobial Properties of Mountain Tea (*Sideritis syriaca*) Decoction. *J Funct Foods*. 2013;6:248-58.
4. Ozer Z. Investigation of Phenolic Compounds and Antioxidant Activity of *Mentha spicata* L. subsp. *spicata* and *M. longifolia* (L.) subsp. *typhoides* (Briq.) Harley Decoction and Infusion. *JOTCSA*. 2018;5(2):445-56.
5. Güvenç A, Duman H. Morphological and Anatomical Studies of Annual Taxa of *Sideritis* L. (Lamiaceae), With Notes on Chorology in Turkey. *Turk J Bot*. 2010;34:83-104.
6. Obon de Castro C, Rivera-Nunez D. A Taxonomic revision of the section *Sideritis* genus *Sideritis* (Labiatae). In: Cramer J (Eds.), Berlin-Stuttgart, pp 86. 1994.
7. Fraga BM. Phytochemistry and Chemotaxonomy of *Sideritis* Species from the Mediterranean Region. *Phytochemistry*. 2012;76:7-24.
8. González-Burgos E, Carretero ME, Gómez-Serranillos MP. *Sideritis* spp.: Uses, Chemical Composition and Pharmacological Activities— A review. *J Ethnopharmacol*. 2011;135:209-25.
9. Kilic T, Topcu G, Goren AC, Aydogmus Z, Karagoz A, Yildiz YK, Aslan I. Ent-kaurene Diterpenoids from *Sideritis lycia* with Antiviral and Cytotoxic Activities. *Rec Nat Prod*. 2020; 14(4):256-68.
10. Çarıkçı S, Özer Z, Dereli S, Açar D, Gören AC, Kılıç T. Essential Oil Composition of Five *Sideritis* Species Endemic to Turkey. *SDU J Nat Appl Sci*. 2018;22(Special Issue):301-5.
11. Çarıkçı S, Kılıç T, Azizoğlu A, Topçu G. Chemical Constituents of Two Endemic *Sideritis* Species from Turkey with Antioxidant Activity. *Rec Nat Prod*. 2012;2:101-9.
12. Halfon B, Çiftçi E, Topçu G. Flavonoid Constituents of *Sideritis caesarea*. *Turk J Chem*. 2013;37:464-72.
13. Sagir ZO, Carikci S, Kilic T, Goren AC. Metabolic Profile and Biological Activity of *Sideritis brevibracteata* P. H. Davis Endemic to Turkey. *Int J Food Prop*. 2017;20(12):2994-3005.
14. Özer Z, Gören AC, Kılıç T, Öncü M, Çarıkçı S, Dirmenci, T. The Phenolic Contents, Antioxidant and Anticholinesterase Activity of Section *Amaracus* (Gled.) Vogel and *Anatolicon* Ietsw. of *Origanum* L. Species. *Arab J Chem*. 2020; 13:5027-39.
15. Vasilopoulou CG, Kontogianni VG, Linardaki ZI. Phytochemical Composition of "Mountain Tea" from *Sideritis clandestina* subsp. *clandestina* and Evaluation of Its Behavioral and Oxidant / Antioxidant Effects on Adult Mice. *Eur J Nutr*. 2013;107-16.

16. Danesi F, Saha S, Kroon PA, Glibeti M. Bioactive-rich *Sideritis scardica* tea (Mountain Tea) is as Potent as *Camellia sinensis* Tea at Inducing Cellular Antioxidant Defences and Preventing Oxidative Stress. *J Sci Food Agric*. 2013;3558-64.
17. Petreska J, Stefova M, Ferreres F, Moreno DA, Tomás-barberán FA, Stefkov G, et al. Potential Bioactive Phenolics of Macedonian *Sideritis* species Used for Medicinal "Mountain Tea". *Food Chem*. 2011;125:13-20.
18. Selvi S, Dağdelen A, Kara S. Medicinal and Aromatic Plants Consumed as Herbal Tea and Collected from Ida Mountains (Balıkesir -Edremit). *J Tekirdag Agricul Facul*. 2013;10(2):26-33.
19. Kirimer N, Baser KHC, Demirci B, Duman H. Essential Oils of *Sideritis* Species of Turkey Belonging to the Section *Empedoclia*. *Chem Nat Compd*. 2004; 40:18-21.
20. Kirmizibekmez H, Karaca N, Demirci B, Demirci F. Characterization of *Sideritis trojana* Bornm. Essential Oil and Its Antimicrobial Activity. *Marmara Pharm J*. 2017; 21(4): 860-5.
21. Topçu G, Gören A, Kılıç T, Yıldız YK, Tümen G. Diterpenes from *Sideritis trojana*. *Nat Prod Lett*. 2002; 16:33-7.
22. Kirmizibekmez H, Ariburnu E, Masullo M, Festa M, Capasso A, Yesilada E, Piacente S. Iridoid, Phenylethanoid and Flavonoid Glycosides from *Sideritis trojana*. *Fitoterapia*. 2012; 83:130-6.
23. Öztürk Y, Aydın S, Öztürk N, Başer KHC. Effects of Extracts from Certain *Sideritis* Species on Swimming Performance in Mice. *Phytotherapy Res* 1996; 10:70-3.
24. Celep E, Seven M, Akyüz S, İnan Y, Yesilada E. Influence of Extraction Method on Enzyme Inhibition, Phenolic Profile and Antioxidant Capacity of *Sideritis trojana* Bornm. *S Afr J Bot*. 2019; 121:360-5.
25. Özek T, Baser KHC. The Essential Oil of *Sideritis aethoa* Papanikolaou et Kokkini. *J Essent Oil Res*. 1993; 5:669-70.
26. Kilic T, Goren AC, Tumen G, Topcu G. Phytochemical Analysis of Some *Sideritis* Species of Turkey. *Chem Nat Comp*. 2003;39:373-374.
27. Topçu G, Gören AC, Yıldız YK, Tümen G. Ent-kaurene Diterpenes from *Sideritis aethoa*. *Nat Prod Lett*. 1999; 14(2):123-9.
28. Dulger B, Gonuz A, Aysel V. Inhibition of Clotrimazole-resistant *Candida albicans* by Some Endemic *Sideritis* Species from Turkey. *Fitoterapia*. 2006; 77:404-5.
29. Aslan I, Kılıç T, Gören AC, Topçu G. Toxicity of Acetone Extract of *Sideritis trojana* and (*Say*), *Sitophilus granarius* (L.) and *Ephestia kuehniella* (Zel.). *Ind Crop Prod*. 2006; 23:171-6.
30. Blois MS. Antioxidant Determinations by the Use of A Stable Free Radical. *Nature*.1958;181:1199-1200.
31. Marco GJ. A Rapid Method for Evaluation of Antioxidants. *J American Oil Chem Soc*. 1968; 45:594-8.
32. Apak R, Güçlü K, Özyürek M, Celik S E. Mechanism of Antioxidant Capacity Assays and the CUPRAC (cupric ion reducing antioxidant capacity) assay. *Microchimica Acta*. 2008;160(4):413-9.
33. Ellman GL, Courtney KD, Andres V, Featherston RM. A New and Rapid Colorimetric Determination of Acetylcholinesterase Activity. *Biochem Pharmacol* 1961; 7: 88-95.
34. Charami MT, Lazari D, Karioti A, Skaltsa H, Hadjipavlou-Litina D, Souleles C. Antioxidant and Antiinflammatory Activities of *Sideritis perfoliata* subsp. *perfoliata* (Lamiaceae). *Phytother Res*. 2008;22:450-4.
35. Gabrieli CN, Kefalas PG, Kokkalou EL. Antioxidant Activity of Flavonoids from *Sideritis raeseri*. *J Ethnopharmacol* 2005; 96:423-8.
36. Kirmizibekmez H, Ariburnu E, Masullo M, Festa M, Capasso A, Yesilada E, et al. Iridoid, Phenylethanoid and Flavonoid Glycosides from *Sideritis trojana*. *Fitoterapia*. 2012;83(1):130-6.
37. Deveci E, Tel-çayan G, Duru ME. Phenolic Profile, Antioxidant, Anticholinesterase, and Anti-tyrosinase Activities of the Various Extracts of *Ferula elaeoachyris* and *Sideritis stricta*. *Int J Food Prop* 2018; 21:771-83.
38. Zengin G, Sarikurkcu C, Aktumsek A. *Sideritis galatica* Bornm.: A Source of Multifunctional Agents for the Management of Oxidative Damage, Alzheimer's and Diabetes Mellitus. *J Funct Foods*. 2014; 11:538-47.
39. Baki S, Tufan AN, Altun M, Özgökçe F, Güçlü K, Özyürek M. Microwave-assisted Extraction of Polyphenolics from Some Selected Medicinal Herbs Grown in Turkey. *Rec Nat Prod*. 2018; 12(1), 29.
40. Yılmaz H, Çarıkçı S, Kılıç T, Dirmenci T, Arabacı T, Gören AC. Screening of Chemical Composition, Antioxidant and Anticholinesterase Activity of Section *Brevifilamentum* of *Origanum* (L.) Species. *Rec Nat Prod*. 2017; 5:439-55.

41. Gülçin İ. Antioxidant Activity of Food Constituents: An Overview. *Arch Toxicol* 2012; 86(3):345-91.
42. Vergine M, Nicolì F, Negro C, Luvisi A, Nutricati E, Accogli RA, Sabella E, Miceli A. Phytochemical Profiles and Antioxidant Activity of *Salvia* species from Southern Italy. *Rec Nat Prod*. 2019; 13(3):205-15.
43. Erkan N, Cetin H, Ayranci E. Antioxidant Activities of *Sideritis congesta* Davis et Huber-Morath and *Sideritis arguta* Boiss et Heldr.: Identification of Free Flavonoids and Cinnamic Acid Derivatives. *Food Res Int*. 2011;44(1):297-303.
44. Silva BA, Malva O, Dias ACP. St. John' s Wort (*Hypericum perforatum*) Extracts and Isolated Phenolic Compounds are Effective Antioxidants in Several in Vitro Models of Oxidative Stress. *Food Chem*. 2008;110:611-19.
45. Jaberian H, Piri K, Nazari J. Phytochemical Composition and in Vitro Antimicrobial and Antioxidant Activities of Some Medicinal Plants. *Food Chem*. 2013; 136(1):237-44.
46. Orhan I, Kartal M, Tosun F, Şener B. Screening of Various Phenolic Acids and Flavonoid Derivatives for Their Anticholinesterase Potential. *Z Naturforsch C* 2007; 62(11-12):829-32.

SUPPLEMENTARY DATA

Antioxidant and Anticholinesterase Properties of *Sideritis perfoliata* subsp. *athoa* (Papan. & Kokkini) Baden and *Sideritis trojana* Bornm. Teas from Mount Ida-Turkey and Their Phenolic Characterization by LC-MS/MS

Sema CARIKCI*

*Izmir Democracy University, Vocational School, 35140, Izmir, Turkey

***Corresponding authors**

Tel :+90 232 2621001

Fax :+90 232 2621004

E-mail: sema.carikci@idu.edu.tr

ORCID: 0000-0003-3657-9926

Table S1. Method Validation Parameters of LC-MS/MS Measurements

Compounds	Linear regression equation	R ²	LOD (mg/L)	LOQ (mg/L)	RSD (%)
Kaempferol	y=0.2040x+0.0573	0.9925	0.002	0.008	5.47
Kaempferon-3-O-Rutinoside	y=0.1080x+0.0135	0.9977	0.014	0.045	8.15
Salvigenin	y=0.0355x+0.8620	0.9912	0.036	0.119	5.21
Penduletin	y=0.1630x+0.0262	0.9965	0.089	0.297	9.47
Isorhamnetin	y=0.0739x+0.5100	0.9608	0.088	0.294	3.67
Quercetin	y=0.1150x+0.0078	0.9938	0.001	0.002	0.11
Quercetagenin-3,6-dimethylether	y=0.0181x+0.0202	0.9924	0.022	0.074	0.1
Isoquercetin	y=0.0115x+0.0215	0.9959	0.199	0.665	9.42
Quercitrin	y=0.0290x+0.0058	0.9918	0.001	0.002	4.28
Luteolin	y=0.2120x+0.0699	0.9937	0.062	0.207	0.16
Luteolin-7-glucoside	y=0.1350x+0.0246	0.9957	0.022	0.072	8.56
Luteolin-5-glucoside	y=0.2300x+0.0413	0.9926	0.01	0.034	1.12
Apigenin	y=0.1780x+0.0850	0.9961	0.15	0.501	4.01
Rutin	y=0.0232x+0.0008	0.9969	0.01	0.034	7.9
p-Coumaric acid	y=0.2670x+0.1810	0.9774	0.006	0.021	6.39
Caffeic Acid	y=0.3300x+0.0036	0.9924	0.028	0.093	8.04
t-ferulic acid	y=0.0655x+0.0266	0.9925	0.047	0.158	5.21
Chlorogenic Acid	y=0.2620x+0.0674	0.998	0.445	1.483	5.45
Rosmarinic acid	y=0.1960x+0.0043	0.9982	0.022	0.072	3.73
Fumaric Acid	y=0.0569x+0.0177	0.9912	0.003	0.01	5.44
Pyrogallol	y=0.0438x+0.0073	0.9803	0.001	0.002	5.47
Ellagic acid	y=0.0244x+0.0048	0.9951	0.02	0.068	0.11
Vanillin	y=0.0982x+0.0158	0.9982	0.019	0.064	6.57
Syringic acid	y=0.0305x+0.0079	0.9973	0.022	0.073	8.39
Salicylic acid	y=0.0255x+0.1780	0.9701	0.211	0.704	0.21
p-OH benzoic acid	y=0.1230x+0.0280	0.9939	0.002	0.007	4.78
IS* Curcumin*			369.3	176.9	20

* Used as internal standard

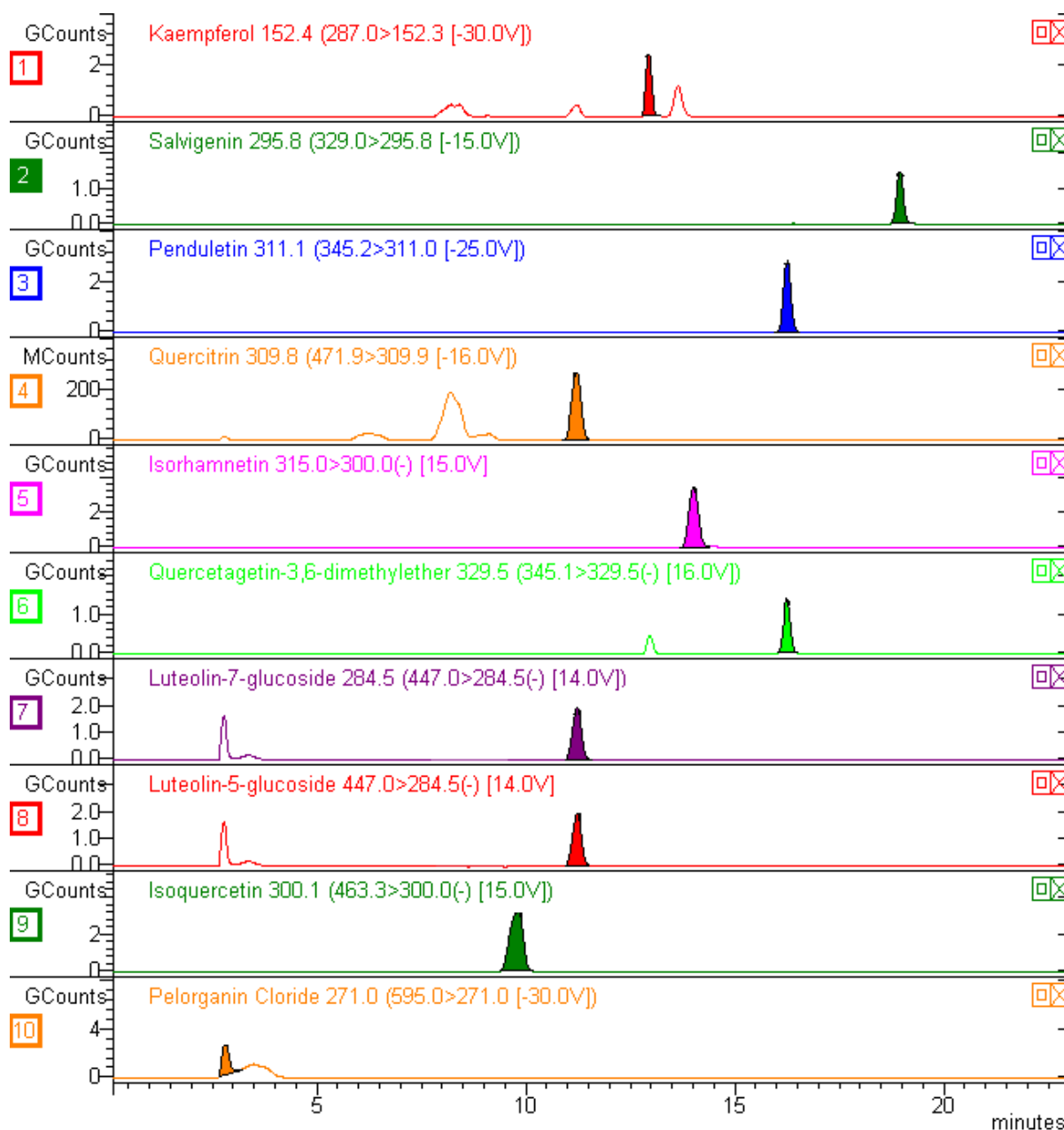


Figure S1 : Standards Chromatogram of Secondary Metabolites (Flavonoids) by LC-MS/MS (5 mg/L)

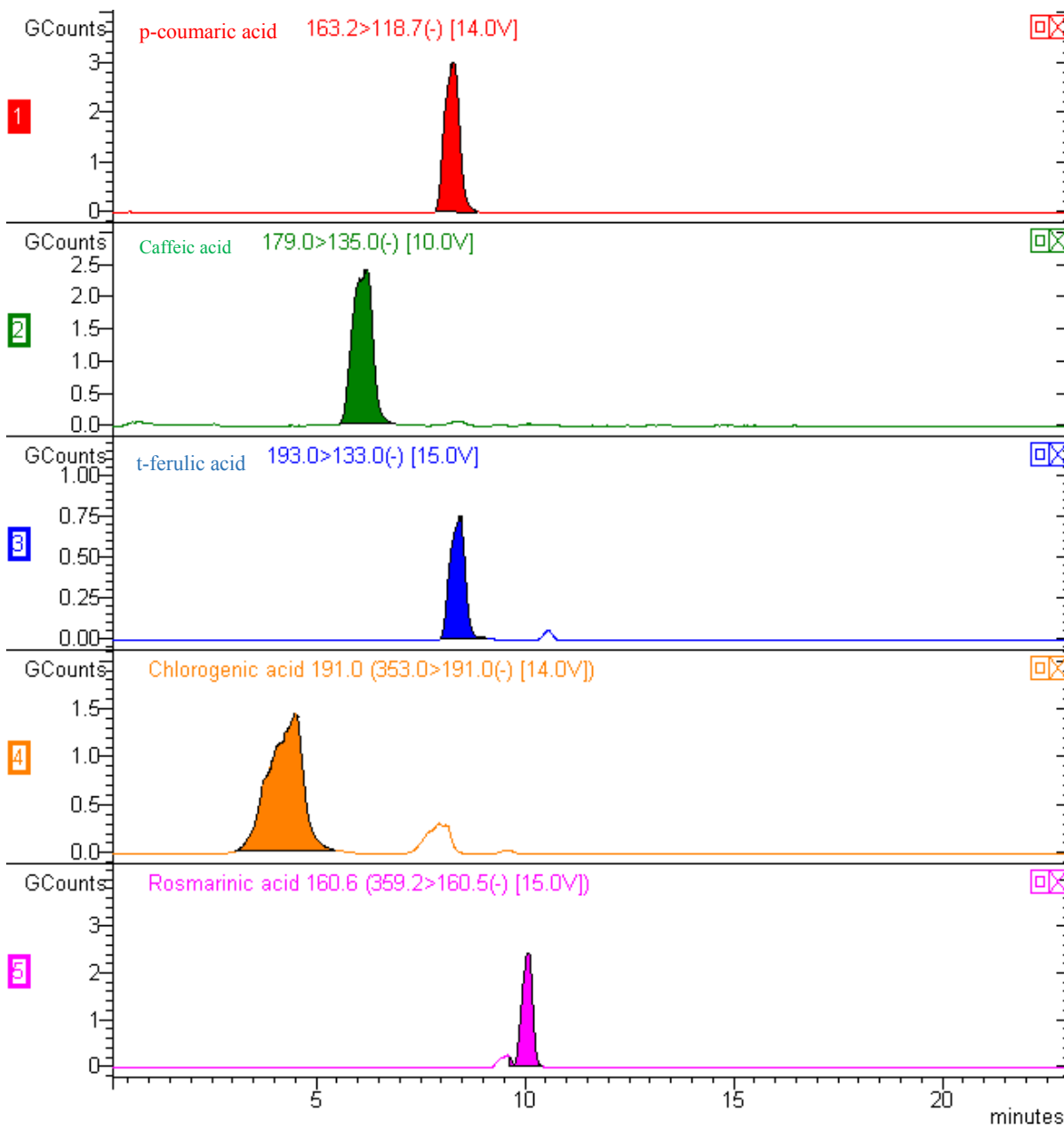


Figure S2: Standards Chromatogram of Secondary Metabolites (Phenolics and Others) by LC-MS/MS (5 mg/L)

Figure S2 (Continued)

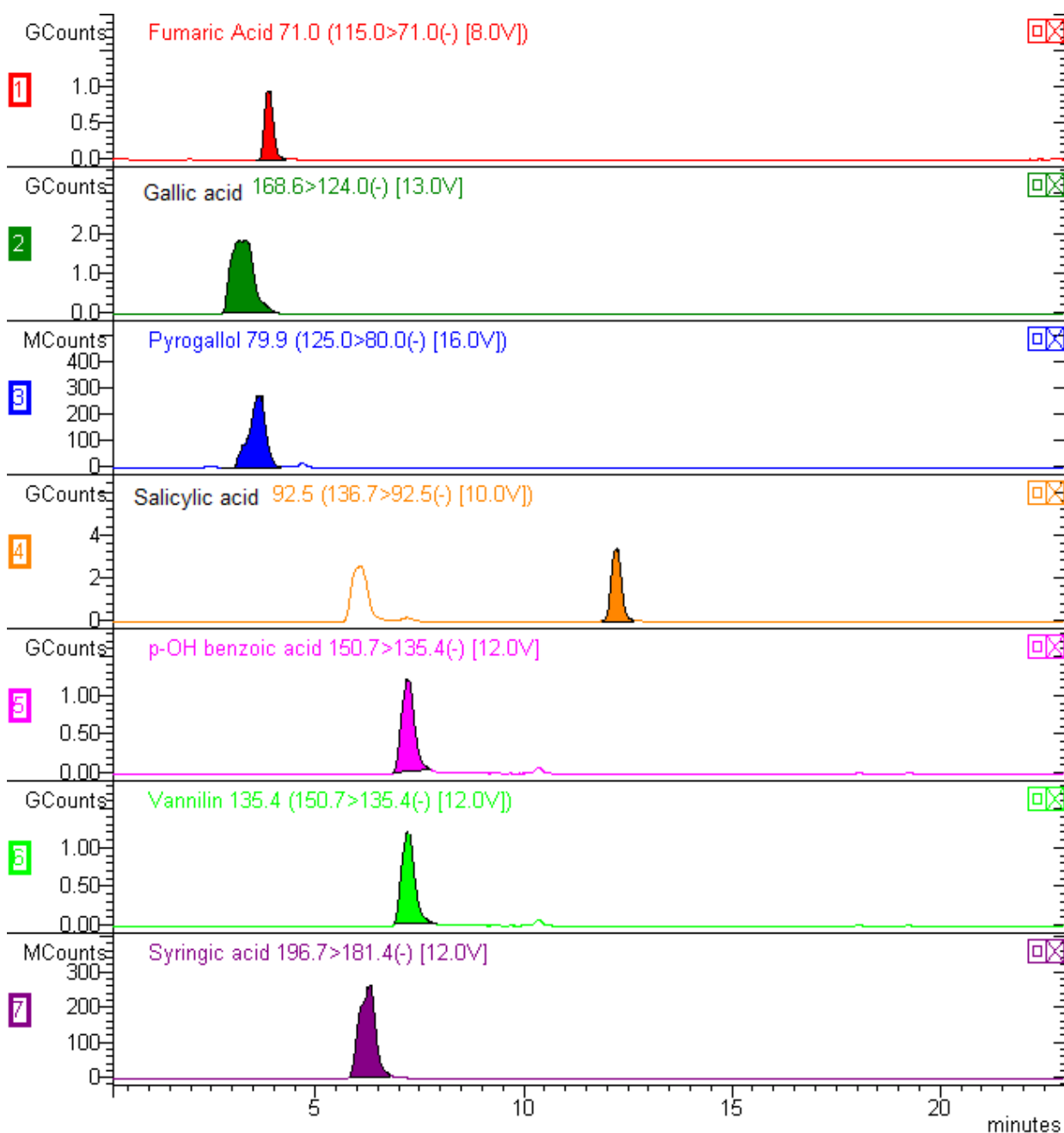


Table S2. Structures of the determined phenolics

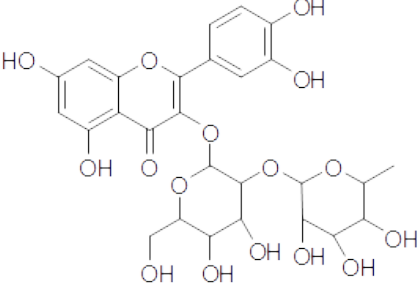
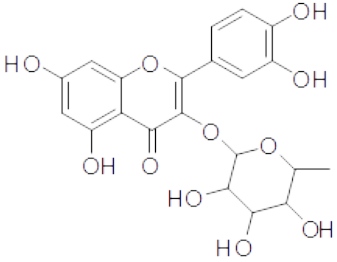
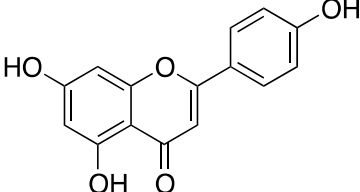
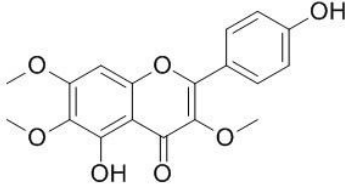
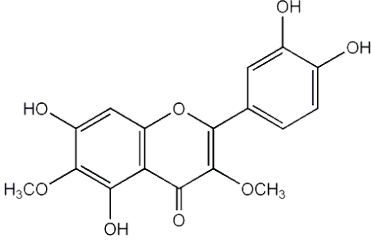
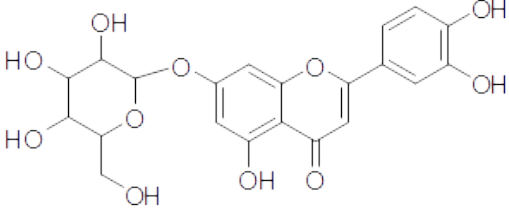
1	Rutin	
2	Quercitrin	
3	Apigenin	
4	Penduletin	
5	Quercetagetin-3,6-dimethylether	
6	Luteolin-7-O-Glucoside	

Table S2 (continued)

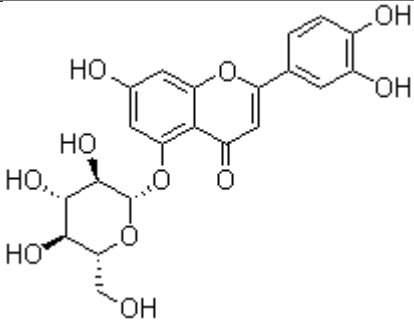
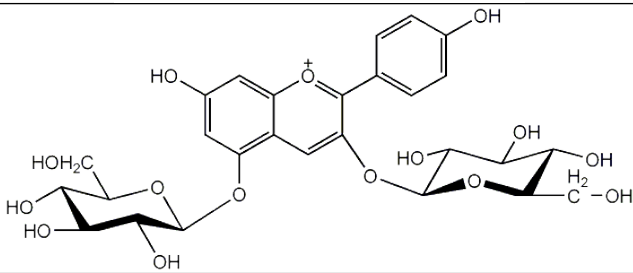
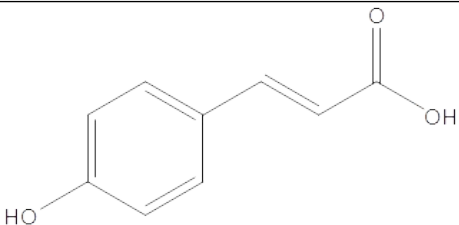
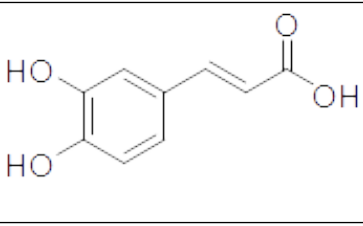
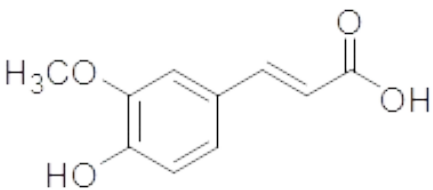
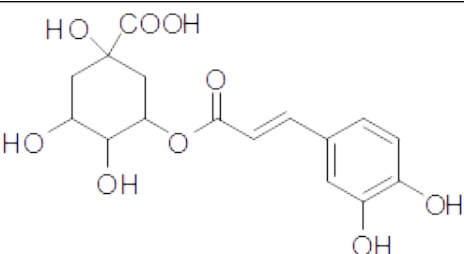
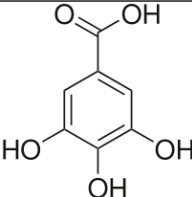
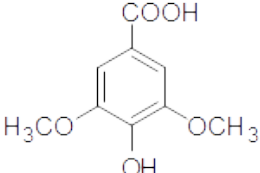
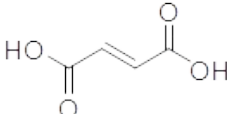
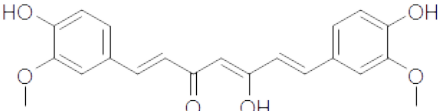
7	Luteolin-5-O-Glucoside	
8	Pelargonin	
9	p-coumaric acid	
10	Caffeic acid	
11	t-ferulic acid	
12	Chlorogenic acid	

Table S2 (continued)		
14	Gallic acid	
15	Syringic acid	
16	Fumaric acid	
IS	Curcumin-IS	

MATERIAL AND METHODS

Chemicals

The following compounds were used as standards in LC-MS/MS analyses: fumaric acid (99%, Sigma-Aldrich), pyrogallol (98%, Sigma-Aldrich), rutin (94%, Sigma-Aldrich), chlorogenic acid (95%, Sigma-Aldrich), gallic acid (99%, Merck), syringic acid (95%, Sigma-Aldrich), t-ferulic acid (99%, Sigma-Aldrich), caffeic acid (98%, Sigma-Aldrich), pelargonin chloride (98%, Sigma-Aldrich), quercitrin (97%, Sigma-Aldrich), salicylic acid (99%, Sigma-Aldrich), p-coumaric acid (98%, Sigma-Aldrich), luteolin-7-O-glu (99%, AppliChem), rosmarinic acid (96%, Sigma-Aldrich), pyrogallol (98%, Sigma-Aldrich), apigenin (95%, Sigma-Aldrich), kaempferol (96%, Sigma-Aldrich), and isorhamnetin (98%, ExtraSynthese, Genay-France).

LC-MS/MS experiments

Due to its fragmented ion stability, the best mobile phase solution was determined to be a gradient of acidified methanol and water system. The optimum ESI parameters were determined as 2.40 mTorr CID gas pressure, 5000.00 V ESI needle voltage, 600.00 V ESI shield voltage, 300.00 °C drying gas temperature, 50.00 °C API housing temperature, 55 psi Nebulizer gas pressure, and 40.00 psi drying gas pressure.

Procedures of Biological Activity Assays

Determination of the Anticholinesterase Activity

Inhibitory activities of acetyl- and butyryl-cholinesterase were measured by slightly modified spectrophotometric method, developed by Ellman, Courtney, Andres and Featherston (1). Acetylthiocholine iodide and butyrylthiocholine iodide were used as substrates of the reaction and DTNB method was used for the measurement of the anticholinesterase activity. Hundred and fifty microlitres of 100 mM sodium phosphate buffer (pH 8.0), test tea samples at different concentrations. Solution of AChE or BChE were mixed and incubated for 15 min at 25 °C, and 0.5 mM DTNB was added. The reaction was then initiated by the addition of acetylthiocholine iodide (0.71 mM) or butyrylthiocholinechloride (0.2 mM). The hydrolysis of these substrates were monitored spectrophotometrically by the formation of yellow 5-thio-2-nitrobenzoate anion as a result of the reaction of DTNB with thiocholine, released by the enzymatic hydrolysis of acetylthiocholine iodide or butyrylthiocholine chloride, at a wavelength of 412 nm. Methanol was used as a solvent to dissolve the controls. Percentage of inhibition of AChE or BChE was determined by a comparison of the rates of reaction of samples relative to blank sample (ethanol in phosphate buffer pH 8.0) using the formula:

$$\text{Inhibition \%} = [(E-S)/E] \times 100$$

where E is the activity of enzyme without test sample. and S is the activity of enzyme with test sample. Galanthamine was used as a reference compound.

Determination of the Antioxidant Activity with the β -Carotene Bleaching Method (2)

β -Carotene (0.5 mg) in 1 mL of chloroform was added to 25 μ L of linoleic acid, and 200 mg of Tween 40 emulsifier mixture. After evaporation of chloroform under vacuum, 100 mL of distilled water saturated with oxygen, was added through vigorous shaking. A mixture of four thousand microliters was transferred into different test tubes containing different concentrations of the sample. As soon as the emulsion was added to each tube, the zero-time absorbance was measured at 470 nm using a spectrophotometer. The emulsion system was incubated for 2 h at 50 °C. A blank, devoid of β -carotene, was prepared for background subtraction. BHT (butylated hydroxytoluene) and BHA (butylated hydroxyanisole) were used as standards. The bleaching rate (R) of β -carotene was calculated using the following equation: $R = \ln(a/b) / t$, where: \ln =natural log, a =absorbance at time (0 min), and b =absorbance at time t (120 min). The antioxidant activity (AA) was calculated in terms of percent inhibition relative to the control, using the equation below:

$$AA = [(R_{\text{control}} - R_{\text{sample}}) / R_{\text{control}}] \times 100$$

Determination of Antioxidant Activity with the DPPH Free Radical Scavenging Method (3)

The free radical scavenging activity of the methanol extract was determined spectrophotometrically by the DPPH (1,1-diphenyl-2-picrylhydrazyl) assay. In its radical form, DPPH absorbs at 517 nm, but upon reduction by an antioxidant or a radical species, its absorption decreases. Briefly, 0.1 mM solution of DPPH in methanol was prepared and 160 μ L of this solution was added to 40 μ L of sample solutions in methanol at different concentrations. After 30 min, the absorbance was measured at 517 nm. The lower absorbance of the reaction mixture indicates the higher free radical scavenging activity. The capability of scavenging the DPPH radical was calculated using the following equation:

$$\text{DPPH scavenging effect (\%)} = [(A_{\text{control}} - A_{\text{sample}}) / A_{\text{control}}] \times 100$$

The CUPRAC Experiment (4)

The CUPRAC method was performed as described, with some minor modification, since experiments were performed in 96-well plates.

Briefly, 1 mM dimethylformamide (DMF), 10 mM CuCl_2 , 7.5 mM neocuproine, 1 M $\text{NH}_4\text{CH}_3\text{COO}$ (pH 7.0) solution, and distilled water were mixed in a volume ratio of 1:1:1:0.6. Then, 180 μ L of the mixture was dispersed into the wells. 25 μ L diluted compounds (dilution ratio 1:20) in EtOH. After waiting for 30 minutes, the absorbance at 450 nm was measured against a reagent blank by Beckman Coulter DTX 880 Multimode Detection System. Ethanol was used as a negative control; whereas curcumin was used as a positive control.

$\text{TEAC}_{\text{CUPRAC}}$ of curcumin was found as 0.9 mmol TR g^{-1} , by using calculation formula.

$\text{TEAC}_{\text{CUPRAC}}$ values of compounds were calculated by using references. TEAC of plant extracts (mmol TR g^{-1}) = $(\text{Absorbance} / \epsilon_{\text{TR}}) (205/25) (20/1) (2/0.02)$. Here, absorbance comes from the instrument; $\epsilon_{\text{TR}} = 16700$ (1); 205 is total reaction volume; 25 is compound volume added to the reaction; 20/1 is the dilution factor; 2 is the solvent volume (mL) in which plant extracts; 0.02 is weight of plant extract as grams.

REFERENCES

1. Ellman GL, Courtney KD, Andres V, Featherstone RM. A new and rapid colorimetric determination of acetylcholinesterase activity. *Biochem Pharma*. 1961; 7:88-95.
2. Marco GJ. A rapid method for evaluation of antioxidants. *J American Oil Chem Soc*. 1968; 45:594-8.
3. Blois MS. Antioxidant determinations by the use of a stable free radical. *Nature*. 1958;181:1199-1200.
4. Apak R, Güçlü K, Özyürek M, Celik S E. Mechanism of antioxidant capacity assays and the CUPRAC (cupric ion reducing antioxidant capacity) assay. *Microchimica Acta*. 2008;160(4):413-9.

